Investigating the Key Controls on Mine Water Temperature in the United Kingdom

Mylène Receveur

Doctor of Philosophy

THE UNIVERSITY OF EDINBURGH

2024

To my nephew and niece, Manoé and Lola

Abstract

Following the 2015 Paris Climate Agreement, the UK Government announced that gas boilers will be banned in all new homes from 2025. Among the developing low-carbon energy sources available to decarbonise residential and commercial heating across the UK, the thermal energy within abandoned, flooded coal mines has significant potential. Mine workings access a large volume of rock and are easily accessible from the surface. With 25% of the UK population living over legacy workings, they also represent an opportunity to reduce fuel poverty in deprived rural areas within former coalfields. Understanding what determines the temperature of mine-water is essential to characterise the heat available and accessible by mine-water heating systems in the long-term, and therefore promote the development of the resource in the UK.

This research aims to characterise the key controls on the mine-water temperature (MWT) in UK coalfields and the mechanisms of heat recharge. These aims are first constrained through the compilation of monitoring data available from The Coal Authority in a geodatabase, which includes temperature profiles, temperature and water level times series, flow rate and discharge rate measurements. Each acquisition was associated with the status of the mine-water block (MWB) at the time of acquisition, the site characteristics (e.g. location, type of site), mine history (e.g. abandonment date) and historic temperature measurements available from the literature. The data analysis highlighted a clear linear relationship between the average MWT in pumping and monitoring shafts and the average depth of the observations.

Discrepancies in MWT observed between different sites within the same coalfield were then investigated numerically by looking at the effect of a range of thermal and hydraulic properties, pumping scenarios, hydraulic recharge scenarios and geometrical parameters on the temperature distribution and heat extraction rate in mines, considering models of simple geometries. Solutions for groundwater flow and heat transfer equations were calculated using the open-source finite-element numerical modelling software OpenGeoSys. The results indicated the key effects of the pumping depth relative to the seam depth and the nature of hydraulic recharge. The latter was shown to significantly alter the temperature distribution in the pumping and monitoring shafts, both during pumping and water rebound. Subsequently, the nature and temperature of recharging mine water were shown to determine the extent of the thermal disturbances following a period of dewatering and water rebound, with the discrepancies between the observed and predicted geothermal gradient decreasing with time since the mine abandonment. Although the permeability of longwall panels was suggested to not significantly impact the thermal steady-state conditions, transient analyses revealed the key control of the permeability contrasts between the mined-out area and the surrounding fractured media on the rate at which heat is mined from the rock and conveyed to the shaft. Additionally, the total recoverable heat from a mine-water reservoir was highly influenced by the total thickness of the mined area.

Mine-water reservoirs are highly complex geometrical and hydraulic systems and are subject to numerous uncertainties, due to the long history of mining, poor mapping and documentation, and the inability to characterise the current state of the mine workings. Hence, no standard modelling approach to quantify the potential thermal resource available has yet been developed. To that aim, a numerical model for the Dawdon High Main seam in the area surrounding the pumping Theresa shaft in the NE England Coalfield, UK, was finally developed to investigate the effect of geometrical simplifications on the heat potential assessment for more complex mine workings including open roadways, pillar-and-stall and longwall panels. Results showed that appropriate estimates of the long-term heat potential of mines can be undertaken for large-scale studies using equivalent porous media approaches, which simplify the model development process and decrease the computational time.

In conclusion, this research has successfully characterised the key controls on MWT and the key features controlling the heat distribution and heat extraction rate in mines. This provides insights into the essential parameters to consider when assessing the heat potential of flooded coal mines, with the ultimate aim of contributing to the development of a generic conceptual tool for the assessment of the sustainable rate of heat recovery, both in the UK and beyond. This includes the potential to develop a method based on calculations of the relative distribution of permeability and porosity for individual mining depth intervals.

Lay Summary

Mine-water resources are a potential low-carbon resource available in the UK that can be used for hot water, space heating and cooling applications. The UK has an extensive coal mining history and today, all underground coal mines are closed. Following the cessation of mining and dewatering activities, water has generally been left to rise back to its natural level, filling the large voids left by the mining activities. This provides the opportunity to pump water at a large flow rate and harness the 12-20°C heat using a heat pump, to provide a local source of heating and cooling to the inhabitants living above former collieries. The accessibility of the mines from the surface makes it an advantageous solution, that also has the potential to reduce fuel poverty in rural areas.

To date, there is no clear understanding of the key controls on the temperature of mine water and the resources available in the subsurface in the long term. A key issue is establishing how fast the mine-water reservoir can be replenished in heat if one or several users are pumping water and extracting heat. Past studies have shown that the mine water temperature observed in shafts and boreholes is not directly related to the geothermal gradient (i.e. the temperature does not increase with depth). Further research is therefore needed to understand what determines the mine-water temperature (e.g. the geology, the hydraulic recharge, etc) within the mines and across UK coalfields, in order to characterise the sustainability of heat extraction.

Following a thorough analysis of existing data acquired by the Coal Authority and other literature data sources, numerical models with simplified geometry were developed to investigate the effect of a range of controlled parameters on the temperature distribution and rate of heat extraction from the different materials that form the mine. This includes the effect of the geothermal gradient, rock heat conductivity, seam permeability, flow rate, etc. Results suggest the key role of the permeability contrasts between the mine workings and the surrounding fractured zone, in relation to the seam depth, the geothermal gradient, and the pumping depth (for pumped coalfields). A third model representing a small area around the pumping shaft at Dawdon, NE England Coalfield, already pumped for mine-water treatment purposes, is developed to look into the effects of different mine features (e.g shafts, roadways, collapsed material in galleries) on the circulation of cold water and the rate of heat extraction, accounting for the nature and the source of water recharge. A series of models with different levels of simplifications are compared, showing that in the long term, the detailed structure of mine workings can be simplified for large-scale studies into a uniform material with averaged hydraulic and thermal properties. These results are used to develop a best-practice method to assess the long-term heat potential of flooded coal mines.

Acknowledgements

I first want to thank my supervisors for their trust, guidance and endless support over the past four years. Thanks to my principal supervisor, Dr Christopher McDermott, for taking me through the hidden side of numerical modelling with OpenGeoSys, adapting the code to my ambitions and dealing with my heavy models. Thanks for reminding me to stay focused when new ideas pop into my mind, and for accepting to provide 'negative' feedback on my work! Thanks to Gus, Dr, Andrew Fraser-Harris, for always checking on me, for making complex modelling concepts accessible, and for all your insightful comments that pushed me to develop critical thinking. Thanks to Dr Stuart Gilfillan, for helping me set priorities and share my research with the real world, teaching me all about the science of writing papers and understanding journal editors.

A huge thank you to Dr Fiona Todd for your priceless technical and moral support since my first PhD day. Thanks for introducing me to the geothermal community as I first set foot in the UK, tracking my progress through weekly catch-ups and reviewing most of my thesis. Among the Coal Authority team, a special thanks to Dr Charlotte Adams for being so supportive in times of doubt and for allowing me to co-chair an EGC1 conference session, it has been a real honour. Thanks to Dan Mallin-Martin for allowing me to expand my technical skill set by joining on-site activities that helped me put my research into context (and being part of a drilling site photo shoot!). Thanks to Ian Watson for your guidance in the early stage of my PhD, and to Jez Crooks, who left this world but whose conviction and ambition to promote mine-water heat resources have been an inspiration. Thanks to Alison Monaghan and Andres Quiros Gonzalez for facilitating my transition from PhD to a full-time position at the BGS.

Thanks to my family for always believing in me even when I don't, and for understanding that despite the pain of a PhD, I found my home in Scotland. Many thanks to Becca for playing such a significant role in my integration into this new country. I am so grateful for the friendship we cultivated throughout our PhD journeys (and countless hours of teaching). Thanks for being there whenever I needed support and constantly reminding me to trust myself. Thanks to Gina for all the fun adventures during the COVID lockdown, for your precious company that made this hard time bearable, and for offering me a productive writing retreat in California. Thanks to Phil for being an understanding and supportive housemate as I was trying to complete this PhD whilst starting a new job. Thanks to Sara for your endless support and words of encouragement over the past weeks, and for all the workout sessions that kept me going throughout the PhD years and helped me regain my strength after periods of illness. Finally, a heartfelt thank you to Stephanie, Sophie and Carole from the PGR team for your continuous efforts to improve our PhD experience and assistance throughout the PhD challenges.

Funding for this research was provided by NERC through an E4 DTP studentship (NE/ S007407/1) and by the Coal Authority through a CASE partnership.

Declaration

I declare that this thesis was composed solely by myself, that the work contained herein is my own except where explicitly stated otherwise in the text by reference or acknowledgement, and that it has not been submitted for any other degree or professional qualification. Where work that has formed part of jointly-authored publications has been included, my contributions and those of the other authors to this work have been explicitly indicated below.

The work presented in Chapter 5 has been submitted for publication in the GeoEnergy journal from the Geological Society London as '*Quantifying vertical borehole heat exchanger sustainability from a geothermal resource perspective in the UK*'. This study was conceived by myself and my supervisors Christopher McDermott, Stuart Gilfillan, Andrew-Fraser Harris and Ian Watson. I carried out the numerical modelling, data analysis, interpretation and visualisation and led the writing of the paper. Christopher McDermott defined the scope of the study, contributed to the development of the methodology and updated the OpenGeoSys source code for calculations of energy change. Andrew Fraser-Harris provided technical support for the numerical analysis. Ian Waston provided the GIS data. Stuart Gilfillan contributed to the drafting of the manuscript. All co-authors validated the interpretation of the results, and reviewed and approved the final version of the manuscript.

An initial version of Chapter 6 included in Appendix 6 was previously published in the proceedings for the World Geothermal Congress 2020 as *'Key Controls on Mine-water Temperature in Flooded Mine Shafts: Insights from Temperature Profiles and Numerical Modelling'*. This study was conceived by myself and my supervisors Christopher McDermott, Stuart Gilfillan, Andrew-Fraser Harris and Ian Watson and reviewed by all the co-authors. I defined the scope of the study, carried out the numerical modelling, data analysis, interpretation and visualisation and led the writing of the paper.

Chapter 8, in preparation for submission to the proceedings for the Energy Geoscience Conference 1, has been conceived by myself and the co-authors Christopher McDermott, Stuart Gilfillan, Andrew-Fraser Harris and Fiona Todd.

Mylène Receveur

Contents

Appendices

Figures and Tables

Figures

Tables

Chapter 1

Introduction

1.1 Introduction

1.1.1 Context

Heat demand for residential and commercial heating represents more than 30% of the energy consumption in the United Kingdom and about 50% in Scotland. With about 78% of UK dwellings using natural gas to fuel central heating, it is responsible for 23% of the nations' greenhouse gas emissions in 2022. Following the 2015 Paris Climate Agreement, both the UK Government and Scotland agreed to reach their net-zero emission goal by 2050 and 2045 (Climate Change Act 2008 and Climate Change (Scotland) Act 2009, Stark (2019)), respectively. To reach this target, efforts are being focused on the need to decarbonise residential heating. Scotland aims to replace gas boilers with low-carbon heating systems in all new homes by 2025 and to supply up to 35% and 70% of low-carbon energy for domestic and non-domestic heating by 2032, respectively (*Clean Growth - Transforming Heating*, 2018). Mine water within abandoned, flooded legacy coal mines has been increasingly seen as a potential low-carbon and renewable source of heating and cooling that could contribute to this ambitious target (Adams & Younger, 2001; Banks, Skarphagen, Wiltshire, & Jessop, 2004; Farr et al., 2016; Watzlaf & Ackman, 2006). In the UK, 9 out of 10 of the largest urban centres are underlain by coal workings. This proximity makes it a valuable resource, that could also participate in the reduction of energy poverty in deprived rural areas in former coalfields, where a quarter of the population remains.

Legacy flooded coal mine workings contain a large volume of interconnected voids inherited from the mining activities, that form highly permeable flow pathways from which mine water can be stored and abstracted at relatively high rates (Bailey, Moorhouse, & Watson, 2013; Malolepszy, Demollin-Schneiders, & Bowers, 2005). Those large interconnected voids provide significant potential for heat exchange between the host rock and the mine water over the whole depth range spanned by the worked coal seams, up to 100s of meters below the surface (Banks et al., 2004). Mine-water temperatures (MWT) are generally warmer than the natural groundwater temperature in Carboniferous aquifers at the same depth. In UK mines, it is in the order of 12℃ - 21℃, against 10℃ - 12℃ for aquifers shallower than 100 mbgl

(B. O Dochartaigh, 2009). Using open-loop mine-water-based heat pump systems, heat can be harnessed from the mine water and used as a source of heating or cooling that could be distributed to local users and industries connected to a district heating network (Fig.1.1). Although the collapse of roof materials and ground subsidence may have partially filled the galleries, many shafts, roadways or drifts remained open following the abandonment of the mines (Banks, Younger, Arnesen, Iversen, & Banks, 1997; P. Younger & Robins, 2002). If not backfilled and capped, shafts can provide easy access to the resource whilst avoiding costs associated with the drilling of new boreholes. Hence, mine-water-based heat pump systems offer cost-effective solutions relative to conventional GSHP systems (S. A. Ghoreishi-Madiseh, Ghomshei, Hassani, & Abbasy, 2012).

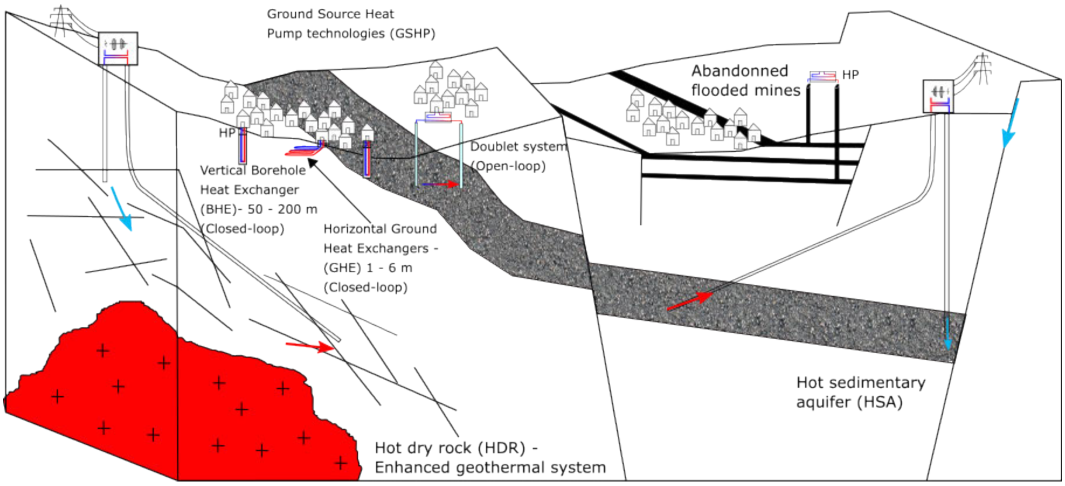

Figure 1.1: Type of geothermal systems available in the UK. Among them, mine-water-heat resources, which are available in former coalfield areas and are easily accessible from the surface, can be used for heating and cooling applications.

The Coal Authority (TCA), who is responsible for managing the legacy mine workings across the United Kingdom, currently operates 80 active and passive mine-water treatment schemes across the UK (TCA annual report 2022-2023). Those treatment schemes aim at reducing the concentration of pollutant minerals before allowing the mine water to discharge at the surface or in the sea, thereby preventing unwanted contamination of the environment. About 3000 L/s of mine water are pumped from more than 50 abandoned coal mines, which was suggested to represent about 100 MW of potential low enthalpy heat energy (Banks, Fraga Pumar, & Watson, 2009). In Scotland, Todd, McDermott, Harris, Bond, and Gilfillan (2019) showed that mine-water heating systems could contribute to about 7% of Scotland's heat requirement for hot water or domestic space heating or cooling. Although cost-effective mine-water heating systems can be created from those already being pumped for treatment purposes (Loredo, Roqueñí, & Ordóñez, 2016), local authorities and private industries have shown an increasing interest in developing local systems accessing the underlying mine workings.

To promote the development of mine-water heat extraction schemes in the UK, it is essential to understand the geothermal resources available in mines and why mine waters have reached a certain temperature. The long-term geothermal potential of mine-water heating systems depends on the rate at which water can be extracted from flooded mine workings without significantly depleting the heat stored in the system (Watzlaf & Ackman, 2006). Concerns have arisen from the potential interference risks between users accessing a group of inter-connected collieries, highlighting the necessity to better understand the source of heat, the spatial extent of the heat accessed by a typical heat extraction scheme and the rate at which the system is replenished in heat. Currently, there is no heat ownership model in the UK. In some countries such as in Spain, this tends to hinder the development of shallow geothermal resources (Garcia-Gil et al., 2020). Licensing heat is essential to control production, avoid over-exploitation and interference between users, and provide a better regulatory framework for financial risks and therefore promote investments.

This research therefore aims at improving the hydrogeological and heat flow models of flooded mines to support the development of a regulatory framework that ensures the sustainable use of mine-water heat resources. It can be summarised in three points:

- **Assessing the key controls on MWT**. Although the regional geothermal gradient is suggested to exert the most influence over the MWT, other potential drivers and their relative contribution need to be better understood.
- **Characterising the sustainability of heat extraction from mines**. This requires a better understanding of the source and rate of heat recharge and the thermal footprint of heat extraction on the heat in place.
- **Identifying the key mine features controlling the long-term heat recovery rate at the scale of a mine.** This includes the effect of the type of workings, the extent of the fault/fracture network and the mine geometry.

A key outcome is the development of an integrated predictive conceptual tool/best practice numerical approach that enables the scientific estimation of the extent and nature of the heat available from mine workings in the long term.

1.1.2 UK Mining history

Most of the collieries in the United Kingdom are located in Central and North-East England, Scotland and Wales (Fig. 1.2). After being first mined in the UK by the Romans in Northumberland, coal mining was abandoned for a thousand years (Hall, 1981). Some traces of coal mining have been found during the 12 - 13th century, but it only emerged during the 16th Century and significantly increased in extent during the 17th Century. In the early times of mining, coal was mostly extracted from shallow mines using the pillar-and-stall method. In the early 18th, the invention of the Newcomen steam engine enabled the pumping of water more efficiently, allowing access to deeper parts of mines. This engine was first installed in the UK at Dudley Castle in Staffordshire in 1712. From the 1950s, longwall mining was the main extraction method in deep mines, and many areas initially mined by the room-and-pillar method were latterly reworked using this method (B. J. Andrews, Cumberpatch, Shipton, & Lord, 2020). In 1979, 70% of the coal sales in Britain were used for electricity generation (Manners, 1991), produced from deep mines in 223 National Coal Board (NCB) collieries. However, the commitment of the government to increase shares of oil and nuclear for electricity generation progressively led to a drop in the demand for coal. Hundreds of collieries closed between 1958 and 1959, and 23 additional mines closed following the 1984 miners' strike. Only 50 mines were still open in 1992. The last underground coal mine, the Kellingley Colliery, closed in 2015. Following the closure of mines, dewatering activity generally ceased, allowing groundwater to rebound back to its natural level and fill the voids inherited from the mining activities (P. Younger & Adams, 1999), turning mines into 'anthropogenic aquifers' (Adams & Younger, 2001; Banks et al., 1997).

Figure 1.2: Distribution of coalfields and mine-water blocks in Wales, Scotland and England (GIS data provided by TCA under an academic license).

1.1.3 Review of existing mine-water heating projects and technologies

GSHP technology

Open-loop or closed-loop ground source heat pump (GSHP) systems are well-known technologies that can be used to extract heat from geothermal resources. In open-loop systems, the pumped mine water circulates through a heat pump-heat exchanger unit before being discharged to a mine-water treatment system (e.g. Caphouse Colliery, UK, N. Burnside, Banks, and Boyce (2016)), to surface water ponds (e.g. Mieres, Spain), or re-injected back to the mine in another seam (e.g. the Shettleston & Lumphinnans, Scotland, Banks et al. (2009)). The heat exchanger is used to transfer heat from the mine water to a refrigerant (e.g. glycol), whose temperature is then increased to useful levels for its utilisation in heat distribution systems (Malolepszy, 2003). In a standing column arrangement such as in Markham, UK, the water pumped from a flooded abandoned mine shaft is reinjected back into the mine at a different depth through the same shaft after its passage through the heat exchanger unit (Athresh, Al-Habaibeh, & Parker, 2016). Whilst deep mines can provide access to higher temperatures, shallower mine levels are generally used for the re-injection of cooled water. Open-loop systems generally have a high efficiency of thermal exchanges compared to other systems as the fluid carrying heat directly enters into contact with the surrounding rock (Luo, 2014). In a closed-loop system, a calorific fluid circulates through a heat exchanger submerged in the flooded mine void. This technology has been implemented in the Folldal Mine, Norway (Banks et al., 2004) and in the mine-water treatment lagoon in the Caphouse Colliery, UK (Banks, 2016).

International projects

Whilst the potential of flooded mine workings to provide sustainable heat energy has been extensively investigated, a limited number of mine-water-based heat pump systems are currently operating worldwide. About 96% of those systems are implemented in underground coal mines. This includes the Oranje Nassau Colliery in Heerlen, The Netherlands (Ferket, Laenen, & Van Tongeren, 2011; Verhoeven et al., 2014); the Barredo-Figaredo coal mines in Asturias, Mieres, Spain (Andrés, Ordóñez, & Álvarez, 2017; Jardón, Ordóñez, Alvarez, Cienfuegos, & Loredo, 2013), the Nowa Ruda mine in Poland (Malolepszy et al., 2005), the Springhill coal mine in Nova Scotia, Canada (Jessop, 1995), and mines at Park Hill, Missouri and Houghton, Michigan in the US.

The first abandoned coal mine water-power station opened at Heerlen in the Netherlands in 2008 (Ferket et al., 2011). There, the 32℃ water is extracted from underground coal workings via five 700 m deep wells, providing heating/cooling to a district heat system composed of 350 dwellings, commercial floor space and community buildings (Verhoeven et al., 2014). This system has been considered to decrease CO_2 emissions by 55% compared to conventional water heating systems (Thomas, 2017). Seasonal production and heat storage were proved to increase the overall efficiency and sustainability of the system by balancing the extraction and recharge in heat (Banks, 2008). In Mieres, Northern Spain, the 4 MWt geothermal installation has been functioning since 2010 (Díaz Noriega, Fernández, & Alvarez, 2020). Four underwater pumps abstract the 22℃ - 26℃ mine water from the flooded Barredo-Santa Bárbara coal mines at a rate of 215 m^3/h. Heat is extracted via three 500 kW$_{th}$ heat exchangers and used to provide air conditioning to the Vital Álvarez Buylla Hospital, a research centre and a student dormitory located near the mine (Andrés et al., 2017; Loredo et al., 2017).

Additional abandoned collieries have been investigated for their mine-water heat resource potential. This includes the Plzenska coal basin in the Czech Republic (Baier, Polak, Sindelar, & Uhlik, 2011), the Vouters coal mine in France (Hamm & Bazargan Sabet, 2010), the Gaspe mine in Canada (Raymond & Therrien, 2008), the Pittsburg or the Krimich II coal mine in the USA (Uhlík & Baier, 2012). In addition to coal mines, the geothermal potential of potassium and uranium mines have also been assessed in Germany (Renz, Rühaak, Schätzl, & Diersch, 2009), Norway (Cu, Zn and S Folidal mine and Kongsberg silver mine), in Hungary (Recsk mine), in the Pribram region in Czech Republic (Baier et al., 2011), in Poland (Nowa Ruda coal mine) and in Canada (Con gold mine; Ropak Can Am Coal mine, Nova Scotia).

UK projects

In the UK, ground source heat pump technology was first implemented at a temporary pilot site in Mossend, Scotland, in 1992. Two permanent small-scale (i.e. 65 kW) open-loop mine-water-based ground source heating schemes were commissioned in 1999-2000 in Shettleston, near Glasgow, and Lumphinnans, near Cowdenbeath in Fife (Banks et al., 2009). The 12℃ and 14.5℃ mine water was pumped from 100 mbgl and 172 mbgl at a rate of 5-10 L/s and heated to 55℃ via a heat exchanger, providing heat to 16 and 18 dwellings in Shettleston and Lumphinnans, respectively. In both systems, water was reinjected at a temperature of 3℃ in the Carboniferous strata via 50 and 60 m deep boreholes located 20 and 100 m away from the pumping wells (Banks et al., 2004). Clogging of the heat pump systems by the highly ferrous mine water caused the system failure that led to the cessation of the operation.

Among other terminated projects, a small-scale 35 kW scheme located in the Crynant Dulais Valley in South Wales was installed in 2014, pumping 11.5℃ waters from flooded workings located at 65 m depth in the Coal Measures (Farr et al., 2016; Farr & Tucker, 2015; Manju, 2014). The Caphouse Colliery, pumped since 1996 for water management purposes, has also recently been investigated for its heat resource potential. A 10 kW heat pump was installed in April 2015, and two options were considered to access heat from the 12°to 15℃ mine water:

a closed-loop heat exchanger submerged in the aeration pond of the treatment site, or an open-loop heat exchanger system through which a fraction of the mine water pumped at the Hope Shaft would be directed (N. Burnside et al., 2016). However, both projects have been terminated.

The two largest mine-water heating systems currently operating in the UK have been developed at Lanchester Wines' warehouse facilities in Gateshead, North-East England (Banks, Steven, Black, & Naismith, 2022). Those have a combined installed capacity of about 3.6 MW. In addition, a large-scale mine-water-based district heating system has been commissioned by the Gateshead City Council to reduce and replace the utilisation of gas in the energy centre, which will provide 6 MW of heat from the underlying mine workings (Gateshead Council, 2021). Smaller scale systems currently operating in England include the 20 kW scheme in Markham, Bolsover (N. M. Burnside, Banks, Boyce, & Athresh, 2016), and a 12 kW scheme in Dawdon, County Durham (Bailey et al., 2013). In Dawdon, a demonstration system was initially implemented by TCA in 2013 and has since then continuously been abstracting a 20℃ mine water at a rate of 100-150 L/s. The Seaham Garden Village now plans to use the mine water pumped from the Dawdon colliery to provide 6 MW of heating to a newly built district heating network.

Recent assessments of the heat potential of the Caerau and Coegnant Collieries in the upper Llynfi Valley, South Wales Coalfield, which closed in the late 1970s, have recently been carried out as part of the Trailblazing project (Brabham et al., 2020; Thomas, 2017). Based on the flow of about 32000 L/s being drained from the Caerau colliery at an average temperature of 13.4℃, the heat resource available was estimated to 72 MW. A feasibility study near the Taff Merthyr mine-water treatment works (Farr et al., 2016) finally suggested that 220 kW could be produced from the mine. Additional projects in North-East England (Sunderland, Hebburn and Holborn) and in Fife (Dollar) are moreover currently under consideration and/or development.

In addition to commercial projects, the UK Geoenergy Observatory in Glasgow was developed by the British Geological Survey to enable researchers to study the geothermal characteristics of flooded coal mines and the potential for using mine water as a renewable heat energy resource (A. A. Monaghan et al., 2021). The research facility is located on the western side of the central Coalfield of the Midland Valley of Scotland. It comprises 12 boreholes accessing the three main seams worked in the area (i.e. Glasgow Upper, Glasgow Ell and Glasgow Main) on the site of the former Farm Colliery closed in 1921, with the deepest borehole reaching 199 mbgl. Data acquired since the drilling of the first well in 2018 (i.e. temperature, water movement, geochemistry, environmental monitoring) have aimed at getting a better understanding of the water circulation and heat transfers in abandoned mine workings, and quantify the heat that can be extracted from mine waters (A. Monaghan et al., 2017).

1.2 Research plan

The three main research questions for this research, a description of the research gaps and of the thesis structure are summarised in this section.

1.2.1 Research questions

- What are the main heat sources controlling the MWT in flooded coal mines? (chapters 3, 5 and 6)
- What are the main heat extraction/recovery mechanisms during pumping and water rebound? What is the impact of past mining activities on the thermal state and temperature distribution in mines? (chapter 6 and 7)
- What are the key features controlling steady-state heat potential and long-term dynamic heat recovery in mines? (chapter 8)

1.2.2 Research gap

Key control on MWT

A recent study on the temperature distribution in flooded coal mines in Scotland highlighted the lack of correlation between the MWT and the depth of the measurements (Gillespie et al., 2013). In addition to the natural geothermal heat flux, other factors were suggested to control the temperature in mines. This includes energy inputs from solar and anthropogenic sources, heat production from exothermic pyrite oxidation reactions or the decay of radioactive elements (Farr et al., 2016). In addition, the architecture of the near surface geology and rock property distribution was also suggested to disturb the heat flow and the temperature distribution in mines. This includes trapped heat or ‘thermal blanketing’ effect as well as refracted heat phenomenon, that are commonly observed under low conductivity strata such as coal seams (Farr et al., 2020). Convective heat transport associated with the circulation of mine water within the network of interconnected open voids (e.g. galleries, roadways, shafts) has also been considered to overprint the natural conductive heat profile and cause discrepancies between the predicted and observed MWT in mine shafts (Beamish & Busby, 2016). Anomalous temperatures, e.g. where the water temperature is greater than the rock temperature, would either be caused by pumping or the existence of free or ’natural’ heat convection generated by salinity and density-related temperature gradients in large open voids (Hamm & Bazargan Sabet, 2010; C. Nuttall, Adams, & Younger, 2002; Renz et al., 2009).

Farr et al. (2020) observed that mine waters in UK mine shafts are generally warmer than predicted by the geothermal gradient above 200 mbgl, and colder below. However, the authors highlighted the necessity for further analysis to understand whether this warming effect is typical of any coalfield and pumping scenarios and whether it is localised or spread within the hydraulically connected parts of a mine. Fluctuations in the post-pumping temperature profiles measured in Horden, North-East England, were for example interpreted to result from fluctuations in the pumping rate. Other factors such as the depth range spanned by the mined seams (Banks et al., 2004), the temperature and depth of the most productive workings (Farr et al., 2020), the existence of colder rainwater or shallow groundwater inflow were also suggested to impact the observed temperature profile in pumped shafts. Such analysis was however considered challenging due to the lack of data within mine galleries and the complexity of mine networks.

The first aim of this research is therefore to characterise the key controls on the near-surface MWT and its distribution at the scale of the mine or a network of mines. Using a combination of data analysis, analytical and numerical modelling, the relative contribution of different heat sources, rock properties and the effect of the local hydrogeology on the thermal state of mines are investigated.

Static heat potential, dynamic heat recharge and thermal footprint

Characterising the initial heat capacity of a mine-water reservoir, the thermal footprint of heat extraction around a production well, and the mechanisms and rate of thermal recovery are essential to determine the sustainability of heat extraction from mines. Although the undisturbed geothermal gradient is commonly used to assess the initial heat content of flooded coal mines (Raymond, Comeau, Malo, & Blessent, 2017), a few authors highlighted the existence of long-term disturbances of the thermal state of mines resulting from extensive periods of mining and dewatering (Malolepszy, 2003). However, the extent and impact of a potential residual anomaly on the initial heat potential assessment of a mine-water reservoir (i.e. before geothermal utilisation starts) is unclear. In addition, the dynamic of heat recovery and heat recharge is not well studied and highly depends on the complex structure and geometry of mines (Chu, Dong, Gao, Wang, & Sun, 2021). This adds to uncertainties to the nature of hydraulic recharge, including the source and pathways of the recharging mine water (e.g. deep warm water, rainwater infiltration, infiltration from shafts or losing rivers, reinjected water), and the water residence time.

Hence, the research presented in this thesis aims to scope out the size of the temperature resources available to use in legacy mine workings. This includes an assessment of the initial heat potential of mine-water reservoirs, and the use of numerical modelling to assess the extent of potential disturbances caused by past dewatering activities. Numerical modelling is used to characterise the dynamics and mechanisms of heat recharge (i.e. heat recovery rate) to support the development of a methodology to guide the licensing of heat.

Conceptualisation of dynamic heat recovery

Various approaches have been developed in the literature to estimate the heat potential of mine water reservoirs, using both empirical and analytical solutions (Rodríguez & Díaz, 2009) and numerical modelling approaches (Loredo et al., 2016). Analytical models have been used to solve for the exact mathematical solutions of heat transfer through the consideration of homogeneous systems and simple geometries (Banks et al., 2009; Loredo et al., 2017). Those have been described as a useful tool to get an insight into the sustainability of heat abstraction from geothermal systems at the early stage of feasibility studies.

Numerical codes allow solving for coupled groundwater flow and heat and mass transfer equations for more realistic representations of mining scenarios, through approximations (Andrés et al., 2017; Bao & Liu, 2019a; Diersch, Rühaak, Schätzl, Bauer, & Heidemann, 2010; Ferket et al., 2011; S. A. Ghoreishi-Madiseh et al., 2012; P. Guo, He, Zheng, & Zhang, 2017; Hamm & Bazargan Sabet, 2010; Malolepszy, 2003; Raymond & Therrien, 2008; Renz et al., 2009). Although numerical models allow for more complex geometries, they also require more data and additional computational time and are subject to numerical instabilities that can limit their reliability (Malolepszy, 2003; Renz et al., 2009). Part of the modelling difficulties are linked to the complexity of the geometry of mine workings, the lack of pre-mining data, uncertainties in the nature and distribution of the mining voids (i.e. collapsed roof material, backfilled voids with different degrees of compaction, fractured rock, open voids and roadways) and the current state of the galleries. In addition, the application of governing equations can be challenging. Flow and heat coupling between the different mining domains is not well understood (Heinze & Pastore, 2023) and local equilibrium assumptions generally considered in geothermal reservoir modelling might not be valid under the high flow rates conditions expected in open mining voids. The large permeability contrasts and high velocities in mining voids are also prone to generate numerical instabilities. Simplifications of the geometry and controlling mechanisms are therefore generally required, but no standardised approach has yet been developed to simulate heat extraction from mine-water reservoirs (Renz et al., 2009).

By comparing different modelling approaches, this research aims to identify the key geometrical features and rock properties controlling the rate of heat extraction from mines. This is used to provide guidance on the best-practice modelling approach and develop a conceptual tool that can predict the sustainable rate of heat extraction from mines to guide the licensing of heat for potential users.

1.2.3 Thesis organisation

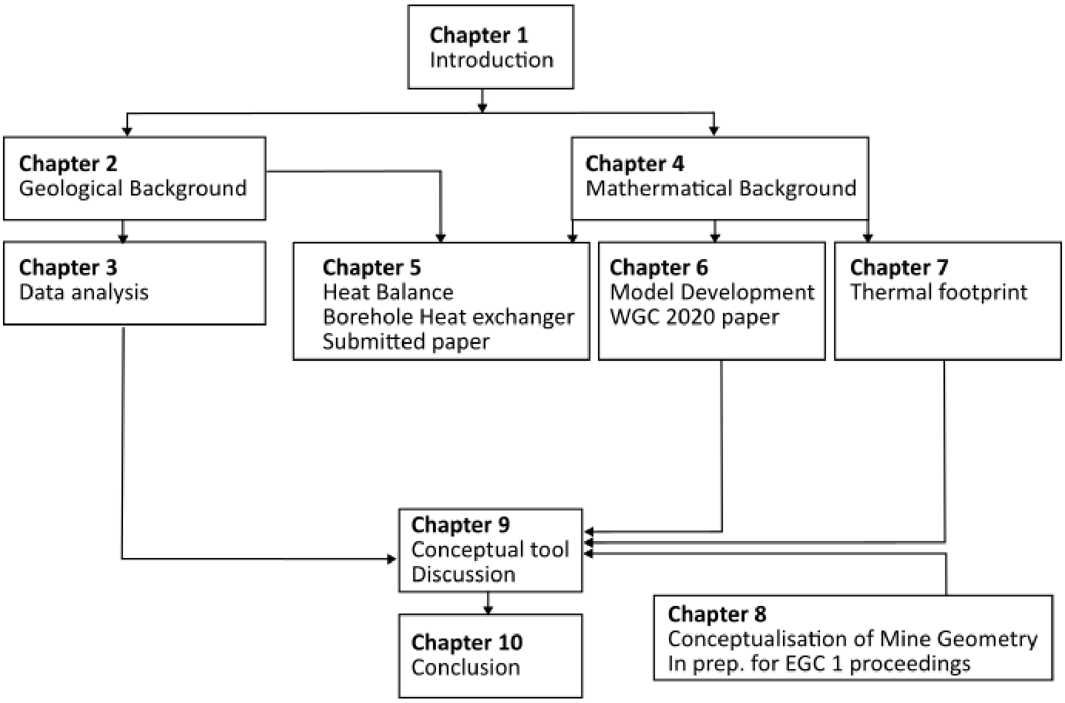

Figure 1.3: Relationship between chapters

The first part of the research involved the collation and analysis of available data from TCA and other literature sources. The second part consisted of the development of numerical models for the study of groundwater flow and heat transfers in mine-water reservoirs. The relationship between the different chapters is summarised in Fig. 1.3.

Chapter 2 describes the geology of the UK coalfields and the conceptualisation of mine workings. This includes an overview of the structure, hydrogeology, heat sources (e.g. geothermal, solar, radiogenic heat) and transport processes controlling the thermal state of flooded coal mines.

Chapter 3 describes the development of a geodatabase designed to facilitate data analysis. The database compiles legacy geological data (e.g. BGS GeoIndex database), historic temperatures available in various archives (e.g. Geothermal Catalogue for the UK, Burley et al. (1984)) and monitoring data from in situ sensors acquired by TCA. A total of 199 temperature logs and 220 temperature time series collected between 2000 and 2023 at 140 different sites were processed and integrated into the database. A thorough analysis of the relationship between the MWT monitored in mine shafts by TCA and the local geological, geothermal and hydrogeological conditions is performed, accounting for the spatial distribution of the dataset.

Using visual inspection, TCA temperature profiles are moreover described to understand the relationship between the temperature distribution and hydraulic state of mines (e.g. pumped, rebounding, discharging). In addition, a statistical analysis of the rock type distribution is performed to characterise the potential effect of the geology on the observed MWT.

Chapter 4 provides the mathematical description of the governing equations for groundwater flow and heat transfer, and of the modelling approaches used in the literature to investigate the heat potential of flooded coal mines. In particular, a description of the finite-element method is provided together with an introduction to the OpenGeoSys (OGS) numerical modelling code used in this study. Based on the analytical solutions, benchmarking results associated with heat transport, coupling and non-linear flow with OGS are presented.

Chapter 5 implements numerical modelling to study the sub-surface heat balance in UK coalfields, based on the typical geological succession introduced in Chapter 2. The thermal footprint induced by heat extraction from a borehole heat exchanger (BHE) is calculated based on the typical heat consumption for a single-family house in the UK. The 1D model assumes heat conduction only and suggests that sustainable heat extraction cannot be achieved within densely populated areas when relying on geothermal heat recharge only. This chapter has been submitted for publication in the Geoenergy journal (Geological Society London).

Chapters 6 and 7 consist of the development of groundwater flow and heat transfer models of flooded coal mines, based on the conceptualisation of mine workings described in Chapter 2. OGS is used to simulate coupled groundwater flow and heat transfer processes in 2D models of simple geometry and better understand the geological, hydrogeological and thermal controls on the temperature distribution, heat extraction and heat recovery rate in mines. In the model development Chapter 6, a sensitivity analysis is conducted to assess the relative effect of thermal and hydraulic properties on the observed temperature in shafts and the heat extraction rate from mine workings. In Chapter 7, the effect of long-term dewatering on the initial heat potential of a mine with dipping seams is determined. The model is used to understand the effect of convective flow in highly connected subsurface voids, the influence of local and regional groundwater recharge, and the mechanisms/dynamics of heat recovery.

Chapter 8 focuses on understanding the effect of geometrical simplifications on the thermal plume propagation and heat extraction rate from mine workings. 3D porous and multi-element models of the Dawdon Seam E mine workings, North-East England Coalfield, UK, are developed and compared to determine the key geometrical features controlling the heat mining rate from flooded coal mines, accounting for the nature of hydraulic recharge. This research, which highlights the possibility of modelling mine workings at a large scale using an equivalent porous material approach, has been prepared for submission in the Energy Geosciences Conference 1 proceedings.

Chapters 9 and 10 are the general discussion and conclusion of the thesis, respectively.

Chapter 2

Geological background and conceptualisation of mine-water reservoirs

2.1 Introduction

Developing a numerical model to assess the geothermal potential of geothermal systems requires the development of comprehensive conceptual models and an understanding of the underground geological, hydrogeological and thermal processes involved. Geological systems are inherently complex and simplifications of the reservoir geometry and rock property distribution are often necessary (Kruse & Younger, 2009). This applies all the more to mine-water reservoirs, where interconnected mining voids create highly heterogeneous and anisotropic systems with complex groundwater flow patterns that tend to disturb the natural subsurface temperature distribution and heat flow (Bailey, Gandy, Watson, Wyatt, & Jarvis, 2016). As discussed further in Chapter 4, this complexity makes it difficult to build computationally efficient models, and simplifications of the controlling mechanisms of groundwater flow and heat transfer involved are generally required.

The first section of this chapter describes the geology and hydrogeology of the Carboniferous succession in the UK, with a focus on the Midlothian and North-East England coalfields. In the second section, the concept of mine-water reservoirs is introduced, including a description of the structure and hydrogeology of mines. The third section describes the thermal state of mines, the volumetric heat assessment methods, and the concept of heat recovery from galleries, based on a review of past research works.

2.2 Geological background

2.2.1 Carboniferous succession

The Devonian-Carboniferous sedimentary succession in UK basins consists of sequences of non-metamorphosed sandstones, siltstones and mudstones with beds of limestone, coal, fireclay, ironstone and oil shale. These were deposited in 10 m thick cycles in shallow non-marine basin environments, and locally intersected by andesitic/basaltic lava flows and pyroclastic rocks up to several kilometres in thickness (Cameron & Stephenson, 1985). In the Midland Valley of Scotland (MVS), this sedimentary succession is subdivided into four groups: the Inverclyde, Strathclyde, Clackmannan and the Scottish Coal Measures (Browne et al., 1999). The oldest sedimentological lithologies below the lavas of the Early Carboniferous are part of the Devonian (Framenian) Stratheden Group (Knox Pulpit Formation, present in Fife) and Devono-Carboniferous Inverclyde Group (Kinnesswood, Ballagan and Clyde Sandstone Formation), initially known as the Old Red Sandstone Formation (Forsyth, Hall, & McMllan, 1996). Following the recent review of the stratigraphy, the Ballagan Formation, which is also found in northern England, now defines the base of the Carboniferous (Tournaisian). The overlying Strathclyde Group (Visean), mainly consists of the Clyde Plateau Volcanic Formation, Gullane Formation, West Lothian Oil Shale and Lawmuir Formation (Fig. A.1).

The Clackmannan Group lies unconformably on top of the deposits of the Strathclyde Group. It consists of:

- The Upper Limestone Formation, previously referred to as Upper Limestone Group (ULGS), is characterised by cyclical sequences of limestone, mudstone, sandstone, siltstone, seatrock and coal. Depositional environments are interpreted to range from shallow seas to deltaic and alluvial plains;
- The Limestone Coal Formation (LSC), comprises cycles of coal, mudstone, siltstone, sandstone, seatearth and coal with some thicker mudstone intervals, ironstone and limestone;
- The Lower Limestone Formation, previously referred to as Lower Limestone Group (LLGS), is dominated by repeated upward-coarsening cycles of limestone, bedded mudstone, siltstone and sandstone with minor seatrock and thin coal and ironstone deposited in a quiet marine and non-marine backwater.

Whilst the Lower and Upper Limestone formations represent relatively marine successions, the Limestone Coal Formation characterises a return to non-marine conditions in which large quantities of coal have accumulated. The Clackmannan Group terminates with the Passage Formation (equivalent to the fluvial-deltaic ’Millstone Grit’ lithofacies in the Pennine Basin). The Passage Formation consists of coarse-grained sandstone with mudstone, seatclay and fireclay deposited during the Namurian-early Westphalian (Browne et al., 1999), and marks the transition into the Coal Measures Group.

The Coal Measures Group consists of fluvial-deltaic facies deposited during the Westphalian in cyclical sequences of mudstone, siltstone, seatearth, sandstone and coal, in a coastal deltaic plain with frequent occurrence of coal swamp conditions. The Scottish Coal Measures Group (CMS) is distinguished from the Pennine Coal Measures (PCM) found in North-East England to account for the different definitions of the base of the groups (Dean, Browne, Waters, & Powell, 2011). The succession is subdivided into Lower (LCMS), Middle (MCMS) and Upper Coal Measures formations (UCMS) in Scotland, in a similar way to the PCM, referred to as Pennine Lower (PLCM), Middle (PMCM) and Upper (PUCM) Coal Measures Formations, respectively. The succession has been suggested to exceed 1790 m in the MVS (Dean et al., 2011).

Most of the coal produced in the UK originates from the Middle Coal Measures and the Limestone Coal Formation (Clackmannan Group). The thickness of coal seams typically ranges between 1 m and 3 m, depending on the thickness of the sedimentary cycle, with some exceptional seams reaching 15 m in thickness (J. H. Rippon, 2002). In the following sections, we further describe the geology of the Midlothian Coalfield and Durham area, which have been selected as case studies for this research.

Midlothian Coalfield

The MVS is a 80 km wide, 150 km long WSW-ENE trending Carboniferous sedimentary basin that developed on the eroded and deformed remnant of the Caledonian Mountains (Cameron & Stephenson, 1985; Read, Browne, & Stephenson, 2002; Underhill, Monaghan, & Browne, 2008). It is separated from the Northern Highlands and Grampian Highlands by the Highland Boundary Fault, and from the Southern Uplands by the Southern Upland Fault (Fig. 2.1). Both of these SW-NE striking faults formed major lineaments during the Caledonian Orogeny (Cameron & Stephenson, 1985). The MVS contains a complex arrangement of several Upper Palaeozoic sedimentary basins, and Lower Palaeozoic metamorphic rocks (i.e. crystalline basement) that only outcrop along the main faults together with Devonian rocks (Bluck, 2002; Cameron & Stephenson, 1985; Underhill et al., 2008). The metamorphic basement, which underlies most of Scotland, is intersected by intrusions of granitic and basic ingenious rocks, generally in the form of laccoliths. Highly metamorphosed granitic and basaltic intrusions observed at outcrop in the Northwest Highlands are likely to be similar to rocks found in the deepest part of Scotland (Gillespie et al., 2013). The MVS only has a few small granite intrusions at outcrop although it contains numerous minor intrusions, mainly of basaltic and andesitic composition. According to geophysical data, the basement-cover boundary is situated at about 8 km depth in the central part of the MVS (Cameron & Stephenson, 1985; Gillespie et al., 2013).

The Midlothian Coalfield is situated in the Midlothian Syncline, on the South-east of the MVS, where the Southern Upland Fault joins the NNE-SSW striking Leven Syncline (Fig. 2.2). It is bounded on the north by the reverse NE-trending Pentland Fault, the main basin bounding structures that has a throw of up to 1.8 km, and on the south by the Dunbar-Gifford (DGF) and the Lammermuir faults (LF). It is suggested that the Midlothian-Leven Syncline was formed by syn-sedimentary growth within a dextral strike-slip regime during the Early Carboniferous (i.e. during deposition of the Limestone Coal Formation), which was followed by fold tightening and reverse faulting during the Late Carboniferous (i.e. during deposition of the Coal Measures Group) (Underhill et al., 2008). The truncation of some of the faults by sediments and volcanic rocks suggests that some of them became inactive after the Early Carboniferous. Some Late Carboniferous structures are however truncated by E-W striking Latest Carboniferous-Early Permian normal faults, quartz-dolerite dyke swarms and extensional fractures, which indicates that their formation was completed by the end of the Carboniferous (A. Monaghan & Parrish, 2006; J. Rippon, Read, & Park, 1996; D. Stephenson, Loughlin, Millward, Waters, & Williamson, 2003).

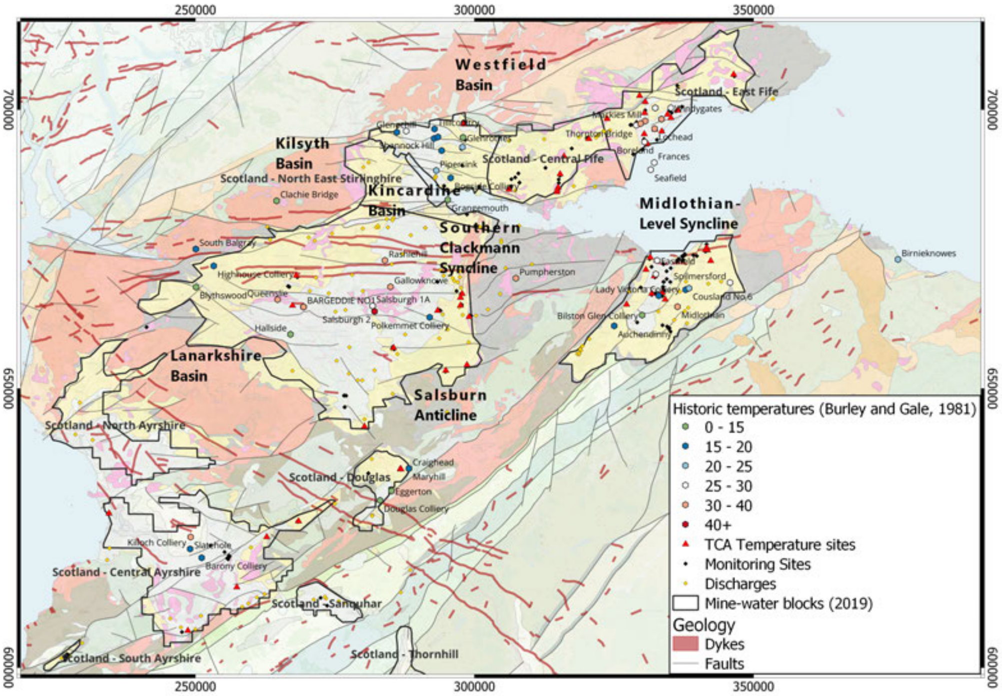

Figure 2.1: Geological map of the Midland Valley of Scotland. The 625k Bedrock geology, dykes and fault lines are provided by the British Geological Survey under the Open Government Licence v3.0. Borehole temperatures (℃) are from Burley et al. (1984). The mine-water block outlines, monitoring sites, discharges and temperature sites are provided by the Coal Authority under an academic license.

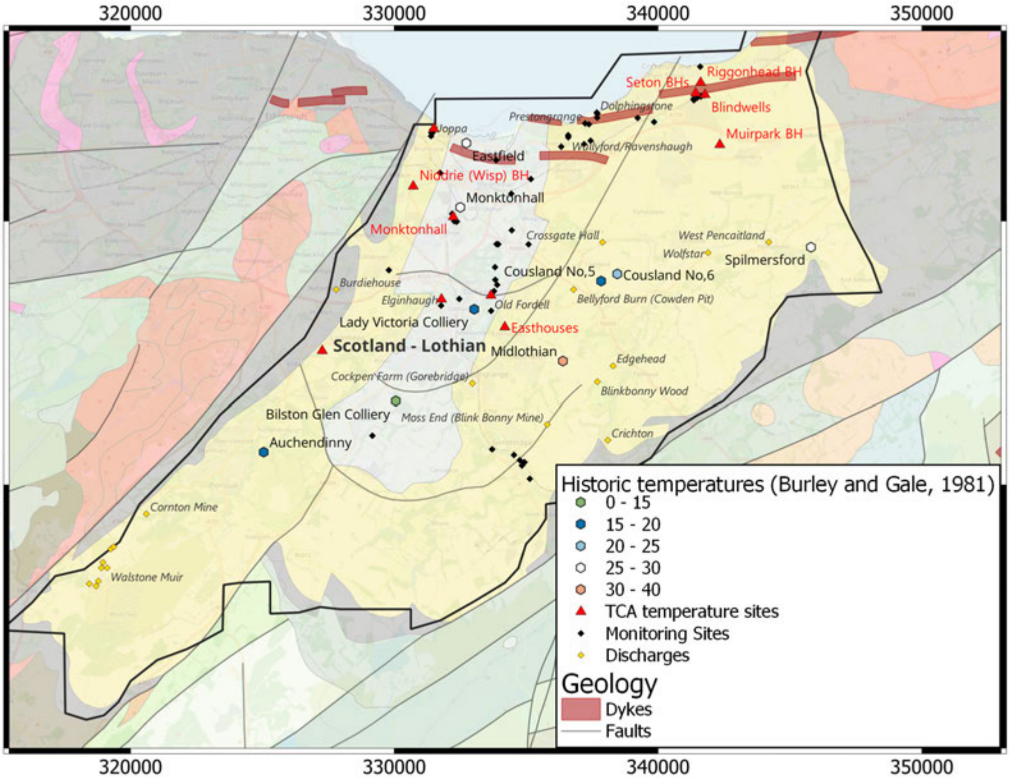

Figure 2.2: Geological map of the Lothian Coalfield. The 625k Bedrock geology, dykes and fault lines are provided by the British Geological Survey under the Open Government Licence v3.0. Historical temperatures (℃) are from Burley et al. (1984). The outline of the coalfields, monitoring sites, temperature sites and discharges are provided by the Coal Authority under an academic license. A list of TCA temperature monitoring sites is provided in Fig.A.8.

Magmatic activity in the MVS extended from the Carboniferous to the Permian for a period of about 90 Ma (Upton, Stephenson, Smedley, Wallis, & Fitton, 2004). It is suggested that volcanism led to an increase in the heat flow during the Carboniferous, especially in the active eastern region. Early magmatic activity occurred in the Pentland Hills during the Lower Devonian, in the form of lava flows and ash layers of basaltic, andesitic, trachytic and rhyolitic composition. During the Visean (Lower Carboniferous), basaltic to rhyolitic lavas and intrusions were formed from short-lived volcanoes that erupted in a floodplain environment, releasing a vast amount of tuff materials (e.g. Garleton Hills, Arthur's Seat, Clyde Plateau Volcanic Fm). Later Visean and Namurian activity (e.g. Kinghorn and Bathgate Hills volcanic Fms) was dominated by basaltic lavas and tuffs (Smedley, 1986; D. Stephenson et al., 2003; Upton et al., 2004). In the Late Carboniferous, short-lived episodes of tholeiitic magmatism extended across the MVS (A. Monaghan & Parrish, 2006; Timmerman, 2004). Those mostly occurred in the form of dolerite sills (e.g. Salisbury Crags) and ENE-to ESE-trending tholeiitic dykes intruded along extensional faults, cross-cutting the shortened and inverted Carboniferous basins (Cameron & Stephenson, 1985; J. Rippon et al., 1996). From the Latest Carboniferous to Permian, alkaline magmatism (i.e. Mauchlin Volcanic Formation) occurred in response to the broader post-orogenic extension associated with the opening of the Atlantic (Neumann et al., 2004; Upton et al., 2004), accompanied by the intrusion of NNE- to NW-trending dykes (Upton et al., 2004). The more widespread thermal effect around tholeiitic sills/dykes compared to alkaline ones has been suggested by Murchison and Raymond (1989), as a result of their emplacement in dry and compacted sediments. Those likely exerted a major influence on hydrocarbon maturity within the lower Limestone Coal, Lower Limestone and upper West Lothian Oil Shale formations, in the Central Coalfield and Midlothian-Leven basins (A. Monaghan, 2014).

From the Paleogene, Scotland has been subjected to an increasing amount of regional uplift caused by the underplating of a magmatic plume associated with the opening of the North Atlantic (Hillis, Thomson, & Underhill, 1994). This event (60 Ma) coincided with the end of the sedimentation in the MVS and led to the significant erosion of the Late and post-Carboniferous sedimentary rocks, especially at basin margins and between the Midlothian–Leven Syncline and Clackmannan Syncline, where the D'Arcy-Cousland Anticline developed (Vincent et al., 2010). The Coal Measures represent the youngest observable set of sedimentary rocks in the Midlothian Coalfield, mostly preserved in the centre of the synclines and basins, where the full sedimentary sequence has been preserved (i.e. Permian sediments are still visible).

Durham area, North-East England

The Dawdon-Horden collieries are located in the East Durham Coalfield in North-East England (Fig. 2.3). The geology in Durham County consists of a Lower Palaeozoic basement overlain by Carboniferous and Permo-Triassic sequences. The Carboniferous Pennine Coal Measures (PCM) have extensively been mined for coal. They are divided into Lower (LCM), Middle (MCM) and Upper (UCM) formations, and consist of alternating layers of mudstone, sandstone and coal seams, with the occurrence of ironstone bands. At least eleven marine bands consisting of shelly mudstone are present, suggesting cyclical change between marine and alluvial environments. Of these, the 'Quarterburn' marine band defines the base of the LCM whilst the 'Harvey' and 'Down Hill' marine bands represent the contacts between the LCM-MCM and MCM-UCM formations, respectively (Stone et al., 2010).

The PCM dip eastwards toward the North Sea (1 - 5°) where they are found at increasing depth offshore. When not at outcrop, they are unconformably overlain by Permo-Triassic rocks via an erosion surface, with the Yellow Sands Formation forming the base of the Permian (Streetly et al., 2009). In the Dawdon-Horden area, the PCM are almost entirely concealed by the Permian Magnesian Limestone aquifer. The Permian strata outcrop east of the PCM and gently dip to the southeast. Underlying the PCM, the Yoredale Group (including the Millstone Grit or Stainmore Formation) and the Carboniferous Limestone Formation (Great Scar Limestone Group) can be found toward the west (Benton, Cook, & Turner, 2003).

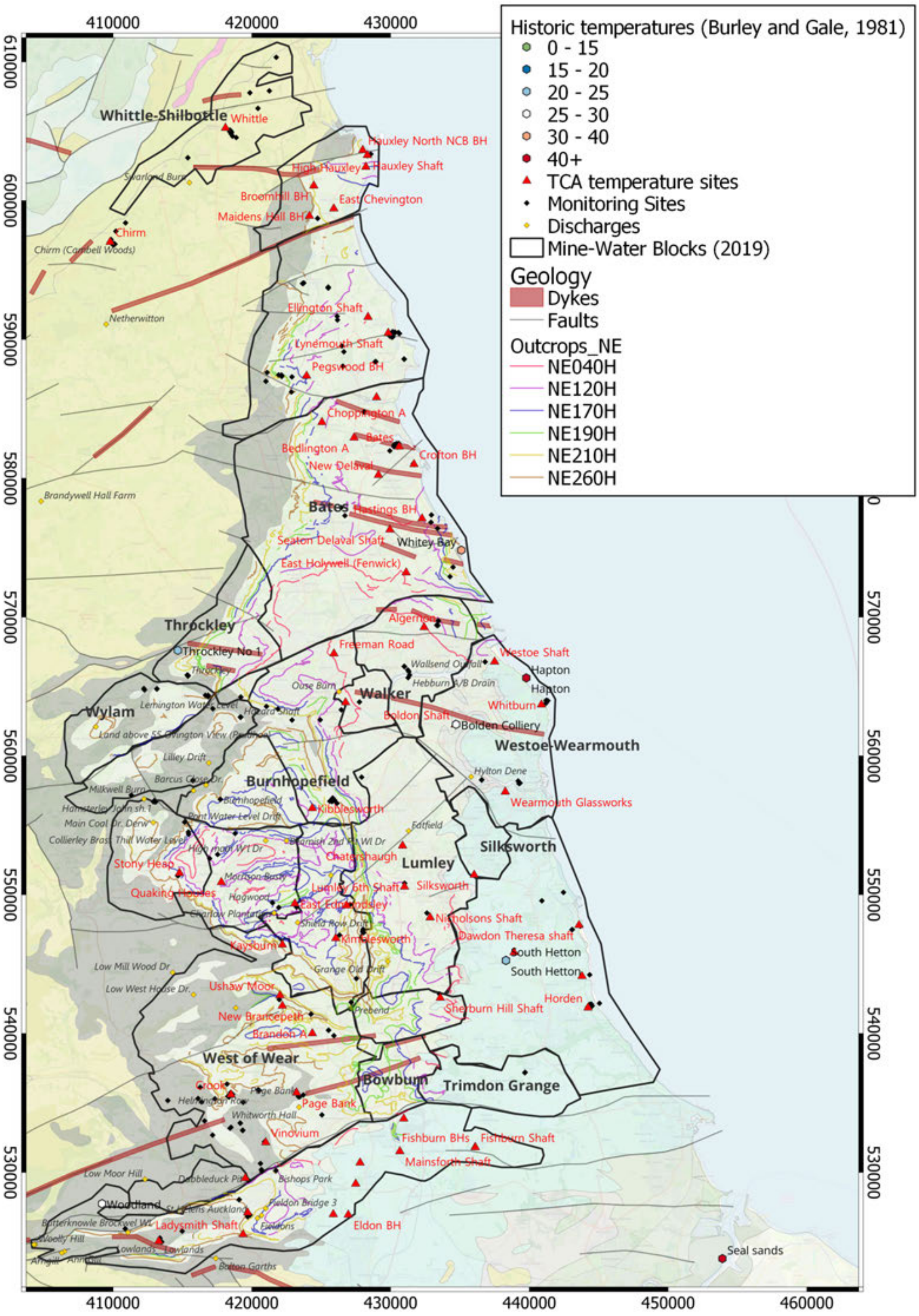

Figure 2.3: Geological map of the North-East Coalfield. The 625k Bedrock geology, dykes and fault lines are provided by the British Geological Survey under the Open Government Licence v3.0. Available historical temperatures (℃) are from Burley et al. (1984). The outline of the mine-water blocks, outcrops, monitoring sites, temperature sites and discharges are provided by the Coal Authority under an academic license.

The CM succession is cut by WSW-ENE striking tholeiitic quartz-dolerite dykes (including the Hett Dyke and the Ludworth Dyke, which splits the Dawdon-Horden block into two parts) to the south of Durham, associated with the late Carboniferous volcanic activity (Stone et al., 2010). Additional volcanic activity during the early Permian has moreover led to the intrusion of the 30 m-thick quartz-dolerite Whin Sill and associated igneous dykes into the sedimentary sequence. The sill underlies the larger part of the county and extends beneath the North Sea (D. Stephenson et al., 2003).

2.2.2 Rock properties

Table 2.1 provides the thickness of each Carboniferous formation encountered in the Carrington-1 well, located in the Midlothian area in Scotland (A. Monaghan, 2014) and the harmonic mean thermal properties for each of them. The harmonic mean heat conductivity values are from J. P. Busby (2019) and were calculated based on sample laboratory measurements and formation thicknesses from boreholes in Scotland and England. The harmonic mean density, heat capacity and radiogenic heat production (RHP) for each formation were calculated as part of this research work. Those were determined based on the relative thickness of each lithology (e.g. sandstone, clay, limestone) within each Carboniferous formation encountered by the Carrington-1 well (Table A.3), and their respective density, specific heat capacity (S. M. Watson & Westaway, 2020), and RHP values (Hasterok et al., 2018; Osimobi et al., 2018; Vilà et al., 2010), summarised in Table 3.1. The total harmonic means for the full stratigraphic column were then calculated based on the relative thickness of each formation in the Carrington-1 well and their respective density, heat capacity and RHP values.

The density and heat capacity are parameters controlling the amount of heat stored and released from rocks under a temperature change. Except for coal, these are fairly similar among rock types and the approximation of the volumetric heat capacity calculated using the approach described in Chapter 4 (Eq. 4.29) yields an error which has little impact on the heat storage (Raymond, Sirois, Nasr, & Malo, 2017). Using harmonic means allows a relatively accurate estimate of the thermal capacity of a reservoir. In contrast, the heat conductivity, which ranges between 0.4 W/℃.m for coal and 4.54 W/℃.m for sandstone in the Carboniferous formation (Table. 3.1), is a key control on the rate of heat transport in areas where conductive processes are dominant (Dethlefsen, Beyer, Feeser, & Köber, 2016). This will impact the rate of recoverable heat over time, which is investigated further in chapter 6.

Formation	Thickness (m)	λ (W/℃.m)	ρ (kg/m^3)	c (J/kg.K)	RHP (µW/m^3)
MSCM	69	2.02	2605	877	1.713
LSCM	132	1.91	2553	858	1.812
PGP	108	2.91	2534	891	1.018
ULGS	87	2.25	2513	871	1.641
LSC	92	2.24	2581	846	1.299
LLGS	53	1.88	2593	835	1.824
WLO	260	4.36	2500	950	1.824
GUL	162	4.36	2500	950	1.812
ART	37	2.2	2500	950	0.540
Mean		2.22	2557	865	1.75184

Table 2.1: Harmonic mean heat conductivity λ, density ρ, heat capacity c and radiogenic heat production (RHP) for the Carboniferous formations in UK coalfields. The heat conductivity values are from J. P. Busby (2019). The harmonic mean density, heat capacity and RHP values for each formation were derived using the percentage of rock types in each formation (Table A.3) and their corresponding density, heat capacity and RHP values (Table 3.1). The thickness of each formation was determined from the Carrington-1 well (A. Monaghan, 2014)). MSCM: Middle Coal Measures; LSCM: Lower Coal Measures; PGP: Passage Formation; ULGS: Upper Limestone Formation, LSC: Limestone Coal Formation; LLGS: Lower Limestone Formation; WLO: West Lothian Oil-Shale; GUL: Gullane Formation and ART: Arthur's Seat Formation.

2.2.3 Hydrogeology

Dochartaigh et al. (2015) classified the aquifers in the UK according to the bedrock type and by distinguishing the formations impacted by mining. Unmined coal-bearing strata in the Carboniferous Coal Measures have been described as complex multi-layered minor aquifers. They are characterised by alternating low permeability (i.e. mudstone) and high permeability (i.e. sandstone or limestone) layers, laterally compartmentalised by the intrusion of igneous rocks (dykes, sills, plugs), and faults that can either act as permeable pathways or hydraulic barriers. This natural layering tends to create complex flow paths, dominated by horizontal intergranular flow and fracture flow. Those aquifers can be found in both confined or unconfined conditions, and are generally described as minor or moderately productive (Ball, 1999; MacDonald, Robins, Ball, & O Dochartaigh, 2005; Robins, 1990), providing borehole yields in the range 5-15 L/s. In these formations, groundwater residence time has been estimated to be over 60 years (B. E. O Dochartaigh, Smedley, MacDonald, Darling, & Homoncik, 2011). The Passage Formation forms an extensive productive aquifer where groundwater moves dominantly by intergranular flow (Ball, 1999). The typical permeability values for the aquifers in the Carboniferous formations are reported in Table 2.2.

Formation	Thickness tested (m)	Typical K (m/s)	Max K (m/s)
Sherwood Sandstone Formation	22	1×10^{-5}	2×10^{-5}
Permian	22	8×10^{-8}	9×10^{-8}
Middle CM above Deep Main	232	$<1\times 10^{-10}$	5×10^{-8}
Main Coal Seams	377	$<1\times 10^{-10}$	2×10^{-9}
Lower CM below Blackshale	243	6×10^{-10}	1×10^{-9}
Namurian	50	4×10^{-10}	

Table 2.2: Average and maximum hydraulic conductivity K (m/s) for different Carboniferous formations (K. R. Whitworth, 2002).

Although the presence of coal seams generally adds low-permeability layers between the sandstone units (Table A.7), the increase in void space where coal seams have been mined out tends to increase the transmissivity, productivity and storage capacity of the aquifers in the CM and parts of the Clackmannan Group (Dochartaigh et al., 2015).

Steeply dipping normal and strike-slip faults are very common in the Limestone Formation and Limestone Coal Formation, offsetting the stratigraphic succession from a few centimetres to several meters (B. O Dochartaigh E, MacDonald, Fitzsimons, & Ward, 2015). Extensive mineralisation along the fault planes within coal has been suggested to provide evidence of flow within the structures, which would over time reduce the connectivity and permeability of the fracture network and hinder future fluid flow (B. Andrews, Shipton, Lord, & McKay, 2020). In UK coal mines, this has led miners to mine coal along the fault strikes, potentially creating barriers to the flow across the faults. Although the effect of the fault structure is not investigated thoroughly in this study, future work should consider the evolution of faults and the surrounding damage zone, as well as potential reactivation during subsidence (Donnelly, 2020) to better characterise the fluid and convective heat flow in mines.

2.3 Structure and hydrogeology of mines

2.3.1 Mining approaches

Coal has been mined using two main approaches, pillar-and-stall (Fig. 2.4) and longwall mining (Fig. 2.5). The pillar-and-stall method was used in the early stage of mining and therefore forms the oldest and shallower mine workings (B. J. Andrews et al., 2020). This approach consists of extracting coal from *stalls* or *rooms*, leaving in place regularly spaced rectangular pillars to support the roof (Garrard & Taylor, 1988; Wardell & Wood, 1966). Abandoned coal mine plans indicate that the pillar sizes can range from around 5 × 5 m to > 30 × 15 m, whilst the stall width is dependent upon the volume of material mined and on the strength of the overburden (Todd et al., 2019). In the Carboniferous Coal Measures, stalls were generally 6 to 9 m wide and pillars 9 to 30 m wide (P. Younger & Adams, 1999). The total proportion of coal extracted using this approach is highly variable, estimated to range between 15–90% (Gee et al., 2017) or 30–60% (Edmonds, 2018).

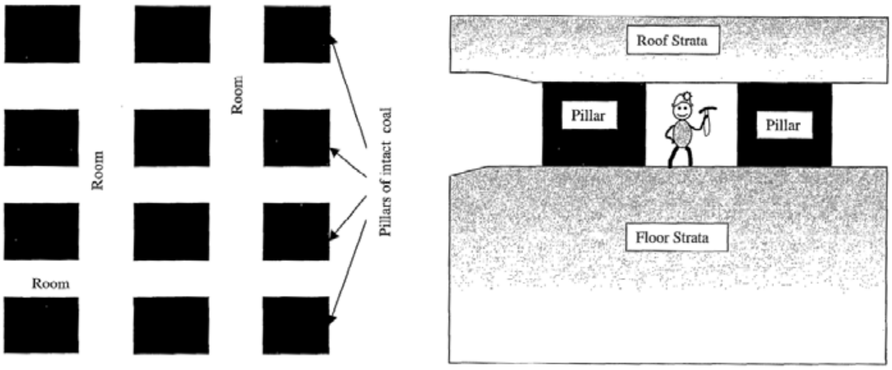

Figure 2.4: Layout of the stoop and room mine workings, on a plan view (left) and profile view (right) (P. Younger & Adams, 1999).

Longwall mining is a method developed since 1795 and mostly used from 1950 (P. Younger & Adams, 1999). Many areas initially mined by the room-and-pillar method were later reworked using the longwall extraction method. This method involves driving tunnels to the farthest extent of the mine and removing coal laterally from the working face of the seam. Colliery areas were divided into sections of about 4-8 ha around which thick stone walls were built and pillars progressively removed, leading to an extraction rate of up to 80%. The coal panel between the roadways is typically 100 to 250 m wide (P. Younger & Robins, 2002), with coal face area and tailgate/headgate entries being about 4.5 m and 90 m wide, respectively (Esterhuizen & Karacan, 2005). This method allowed the overburden roof to collapse behind the advancing longwall face, forming an accumulation of blocks of rocks containing high void ratios called ‘goaf’ (Fig. 2.5).

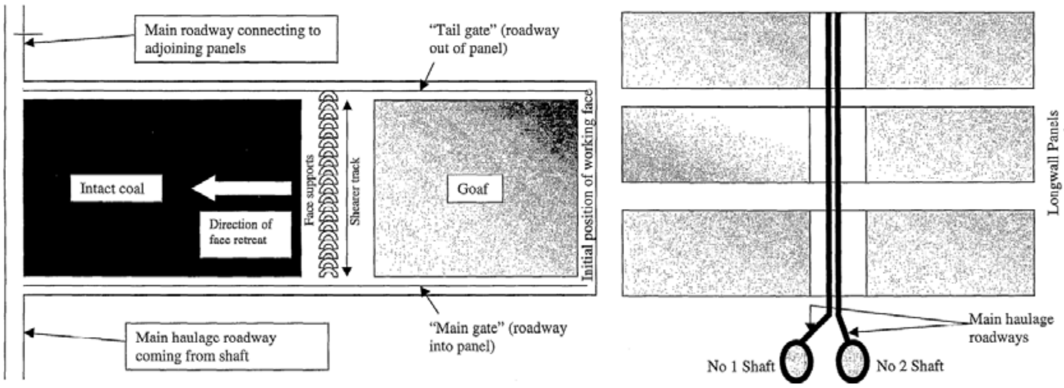

Figure 2.5: Layout of typical individual longwall mine workings (left) and of a series of panels in relation to the main haulage and shaft access (right) (P. Younger & Adams, 1999).

2.3.2 Hydrogeological model

Mine-water reservoirs are formed of large interconnected voids inherited from the mining activities in which groundwater has generally been allowed to rebound back to its natural levels following the cessation of mining and of the dewatering activities (P. Younger & Adams, 1999). In the literature, they have been referred to as 'anthropogenic aquifers' (Adams & Younger, 2001; Banks et al., 1997), conceptually divided into three main domains:

- The mine **open voids** (i.e. shafts, drifts, roadways), which are considered as tunnels of simple geometries that act as preferential pathways into or from mine-water reservoirs (Malolepszy et al., 2005). Whilst shafts may be backfilled and capped, most of the roadways or drifts remain open after the closure of mines (P. Younger & Robins, 2002). Those interconnected and highly transmissive voids are generally attributed large permeability and porosity values (e.g. $k = 10^{-7}$ m^2 and Φ = 99%, Adhikary and Guo (2015)), and turbulent flow can be generated at high flow velocities. They also provide significant potential for heat exchange between the host rock and the mine water over the whole depth range spanned by the worked coal seams (Banks et al., 2004).
- The **mined area,** which consists of the volume surrounding the open mine voids affected by mining-induced secondary porosity and fracturing (Andrés et al., 2017; Esterhuizen & Karacan, 2007; P. Guo et al., 2018; Ordóñez, Jardón, Álvarez, Andrés, & Pendás, 2012; Wolkersdorfer, 2008). The porous media (i.e. goaf/backfilling material, driving and caverns), where linear Darcy flow dominates, accounts for a considerable proportion of the void volume in mines and hence contains the major portion of the mine-water (Renz et al., 2009). Whilst galleries may partially be filled by collapsed roof materials following the abandonment of the mine, ground subsidence was shown to promote the development of fractures in the strata overlying the mined panels, increasing the permeability of the overburden. On the contrary, the progressive compaction of the goaf material by the subsiding rock mass was shown to reduce the transmissivity and storage capacity of the backfilled voids over time, until a state of equilibrium is reached (Esterhuizen & Karacan, 2007; P. Younger & Robins, 2002).
- The **undisturbed rock mass,** characterised by the pre-mining properties of the unmined coal beds and overlying rocks (Esterhuizen & Karacan, 2007).

Understanding the void volume and permeability distribution above longwall panels resulting from subsidence has been of particular interest in the literature and was suggested to influence both the piezometric response (Booth, 2002) and the geothermal potential of abandoned mine workings (P. Guo et al., 2018). In general, longwall areas can be divided into four main deformation zones (Fig. 2.6).

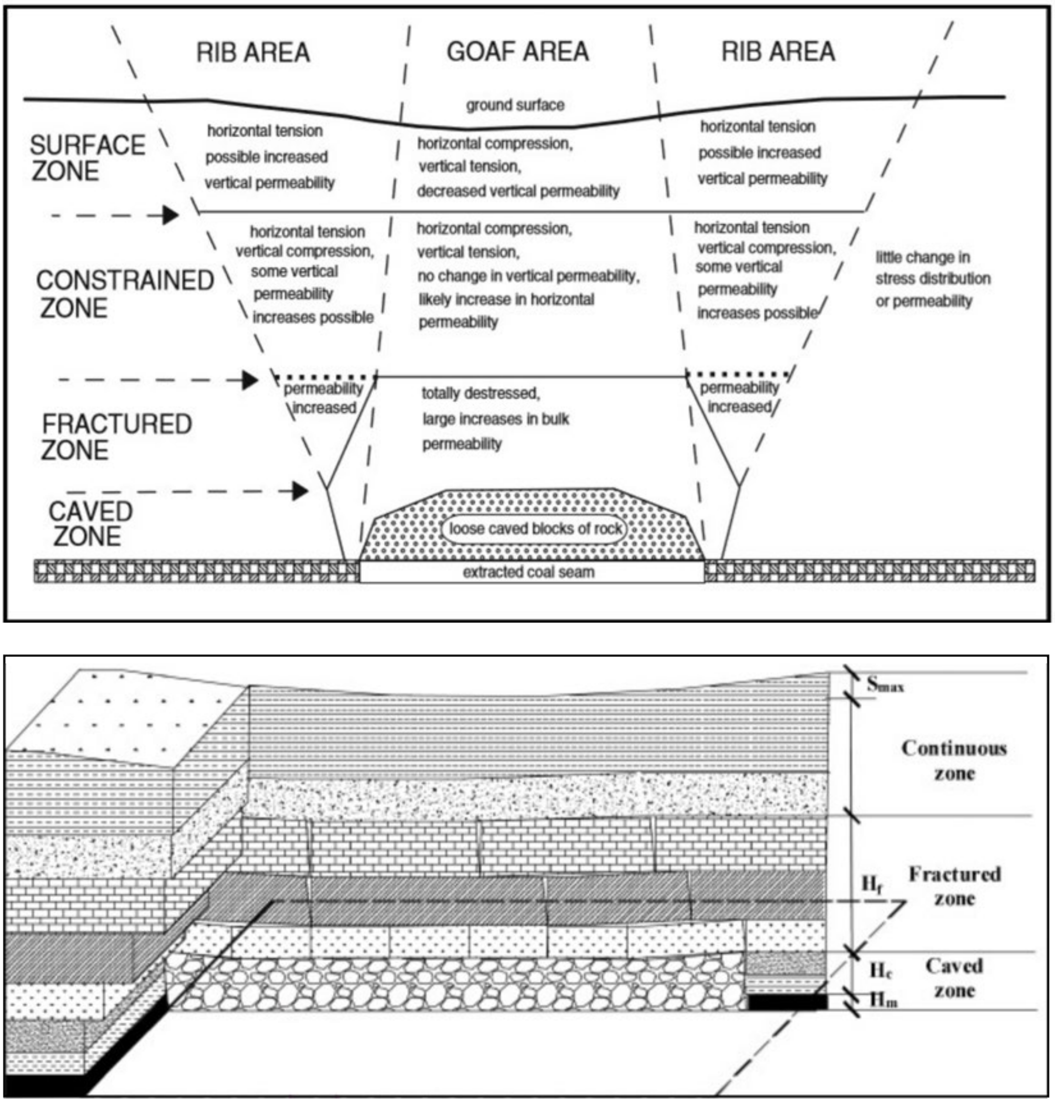

Figure 2.6: Distribution of the deformation zones and associated permeability changes induced by the collapse of goaf material and overburden subsidence above a longwall panel. The models presented on the left and right are from Forster and Enever (1992) and P. Guo et al. (2018), respectively.

- **A caved zone**, characterised by broken blocks of rock detached from the roof, representing 4-6 times the extraction thickness (Adhikary & Guo, 2015; Mucho et al., 2000). Using a hydraulic conductivity of 1×10^6 m/s in the lower part of the goaf (Hoek & Bray, 1981; D. J. Stephenson, 1979), Esterhuizen and Karacan (2007) showed using numerical modelling that the highly permeable 'fully caved zone' extends about 1.5 times the mining height, and that this permeability rapidly decreases upward in the 'partially caved zone', until reaching 100 mD at about 6 - 9 m height.
- **A fractured zone**, characterised by bending of the rocks, fracturing, joint opening and bed separation, whose thickness has been extensively discussed in the literature. For Adhikary and Guo (2015), the fractured zone extends about 15 to 40 times the extraction thickness. In the UK, an observation-based 'ten times the height of the mine working' rule was used during mining activities to describe the vertical migration of fractures in the bedrock overlying mine workings (A. A. Monaghan et al., 2021). Whilst B. J. Andrews et al. (2020) documented the main deformation zone to extend to a range of 5–15 m above collapsed, 2 m-thick pillar-and-stall workings (with faulting extending up to 50 m above the collapsed workings), P. Younger and Adams (1999) suggested that the fractured zone height is in the range of 40 to 100 m for typical longwall panel widths of 100-250 m. The height and the permeability of the fractured zone were however shown to highly depend on the geology and the roof strength (P. Guo et al., 2018).
- **A constrained zone** of variable thickness, without significant fracturing or alteration to the original geomechanical properties (Adhikary & Guo, 2015)
- **A surface zone** less than 20 m thick, dominated by tensile fracturing.

Table 2.3 summarises the different zones thickness determined by Adhikary and Guo (2015), Mucho et al. (2000), Gillespie et al. (2013), Booth (2002) and Esterhuizen and Karacan (2007).

Zone	M1	M2	M3	M4
Near-surface	20 m		-	Open fracturing
Constrained	Variable		W/9	Little fracturing
Fractured	15-40 × H		W/3	30-40 × H (Vertical fractures)
Caved	5 × H	4-6 × H	-	2-8 × H (Collapsed material)
Fully caved	1.5 × H*		-	-
Seam	H	H	W	-

Table 2.3: Hydrogeological models comparison for a longwall panel, with W the panel width and H the height of the mined seam (m). M1: Adhikary and Guo (2015), M2: Mucho et al. (2000), M3: Gillespie et al. (2013), M4: Booth (2002), *Esterhuizen and Karacan (2007).

A key element to developing a hydrogeological model is the identification of the recharge and discharge zones and the potential hydraulic connections between different parts of a mine system. To characterise the nature of hydraulic recharge in mines, K. R. Whitworth (2002) described a system composed of four depth-controlled mining units, dividing water inflows into 3 categories:

- **Shaft water,** that characterises the interconnection between a mine and a major aquifer. Those can be determined from pumping data;
- **Coal measures inflow**, that represents small inflow (< 330 m^3/day) from minor aquifers, or larger flow from major sandstone aquifers situated above or below the mine workings or from faults. Coal Measures inflow rate generally starts declining once the water recovery reaches the level of inflow (i.e. when the hydraulic gradient between the mine workings and the source aquifer decreases);
- **Shallow working waters** (i.e. shaft, Coal Measures aquifers and surface waters), which affects the water level in old shallow workings in the later stages of recovery but can gravitate to deeper workings via mine connections. Seasonal fluctuations in water inflow are linked to variations in rainfall, with the interconnection between mine workings and surface features (i.e. drains, shafts, streams) offering a potential for rapid recharge in response to precipitation events (Farr et al., 2016).

In mines, the location/elevation of outcrops, the permeability, depth and thickness of the worked seams and of the surrounding strata as well as the presence of faults are key geological features likely to influence the nature of recharge and flow pathways. Mining infrastructures can also play a major role, acting either as a barrier (e.g. closed dam) or a pathway (e.g. roadway) to flow, connecting the underground workings to surface discharge (e.g. shafts, drifts) or within the mine systems. Hydraulic recharge is also possible where connections exist between neighbouring collieries within the same coalfield. As water is rebounding, new connections might also be created via mining infrastructures (e.g. tunnels), connecting over large areas and depth range hydrogeological units that were previously isolated, and adding to the complexity of groundwater flow (Bailey et al., 2016). Those hydrogeological units are referred to as 'mine-water blocks' (MWB) by the Coal Authority (TCA) and can themselves be divided into sub-blocks (e.g. Bates, North-East England), where gaps in the recorded connections between adjacent collieries exist. A thorough evaluation of mine plans and underground surveys is therefore essential to identify the location, interconnectivity and state of those elements and develop a reliable conceptual model.

2.3.3 Residual void volume

Several methods have been deployed in the literature to derive estimates of the residual water-bearing void volume in mines (Vélez Márquez et al., 2018), which is required to conduct volumetric heat potential assessments of mines. The most common approach consists of multiplying the estimated workings area A in each seam by the average seam/extraction thickness h, and scaling the estimated void volume by a factor f accounting for backfilling, subsidence and induced fracturing (Eq. 2.1).

$$V_{void} = \sum_{1}^{n}(Ah) \times f \tag{2.1}$$

with n the number of workings in the mine volume. The void space in the mine workings was alternatively calculated by Banks, Frolik, Gzyl, and Rogoż (2010) accounting for the dip of the seams α and the available porosity in mine void c (Eq. 2.2).

$$V = \frac{Ah}{cos\alpha}c \tag{2.2}$$

A complete review of the volumetric assessment method employed by Banks et al. (2010) is given in Appendix A.1.2.

The compression factor f or residual void volume c has been extensively discussed in the literature. Malolepszy (2003) suggested that 5% to 40% of the initial mined volume is likely to remain open depending on the mining method employed. In room-and-pillar areas, only small and local convergence of the roof/floor is expected as pillars were generally left in place, whilst the accumulation of small amounts of debris resulting from roof falls is assumed to be compensated by the creation of voids in the overlying rock. For P. L. Younger, Banwart, and Hedin (2002), 50% of the mining voids are therefore likely to remain open if no collapse occurs, although the extent of fracturing above the mined seam is often unknown. In longwall mining, Gillespie et al. (2013) suggested that about 20% of the mining voids remain after subsidence of the overburden rock, whilst P. Younger and Adams (1999) estimated a goaf porosity of 30% after subsidence and fracturing. Jessop (1995) alternatively found that 25% of the initial void volume remains whether the panel has been mined using the longwall or pillar-and-stall methods. In areas of total extraction, K. R. Whitworth (2002) showed that residual voids represent 10% of the extracted height. For a 200 m wide longwall panel, subsidence was shown to account for 90% and 35% of the extracted thickness at 100 m and 500 m depth, respectively.

Alternatively, some authors such as Malolepszy et al. (2005) calculated the residual void volume from the coal production data (i.e. tonnage of coal extracted). A mean excavated rock density was used together with a factor of 25% to account for subsidence and backfilling (Jessop, 1995), with additional corrections applied to account for the exploitation depth and the type of the mine workings. In Bazargan and Demollin (2008) and He, Sousa, Elsworth, and Jr (2011), the volume of water-filled voids $V_{residual}$ was determined by subtracting the volume of coal extracted $V_{extracted}$ by the backfilled volume $V_{backfilled}$ and the volume of subsided rock $V_{subsidence}$ (Eq. 2.3).

$$V_{residual} = V_{extracted} - cV_{backfilled} - V_{subsidence} \tag{2.3}$$

with c the residual volume fraction or bulking rate (with c = 0.7 for caving and 0.85 for a working backfilled with compacted sand).

Other studies used a combination of dewatering and water rebound data to quantify the residual volume of interconnected underground mining voids (Banks et al., 2010; K. R. Whitworth, 2002). Water extraction rates used for the dewatering of mine workings during mining activities are generally assumed to balance the inflow of water in mines and can therefore be used to assess the hydraulic recharge rate to the model. When available, they can be used jointly with water rebound time series to estimate the water recovery rate and get insight into the residual volume of connected voids following the abandonment of the mine (P. Younger, 2001). K. R. Whitworth (2002) used long-term pumping and inflow rates from the East Fife Coalfield to simulate mine-water recovery and predict the timing and size of potential water discharge, distinguishing between areas of total and partial extractions in longwall mining areas and considering the roadway size. Andrés et al. (2017) calculated the void volume in the Asturias mine (NW Spain) accounting for the method of operation and the presence of shafts and galleries. The amount of water that infiltrated the reservoir during the groundwater rebound, estimated from effective rainfall, was used to calibrate the residual voids, giving an average mined area porosity of 20%. Typical borehole yields used to maintain low water levels during mining in Scottish mines are provided for reference in Table A.9.

2.4 Thermal state and heat potential of mines

In mines, groundwater transports the energy released by the earth's natural heat flux and mineral oxidation through laterally extensive voids inherited from coal extraction (Raymond & Therrien, 2010). In addition to natural heat sources, anthropogenic heat sources such as instantaneous fires, air ventilation, or forced heat convection due to pumping have been suggested to impact the thermal state in mines (Fig. 2.7). In this section, the potential sources contributing to the renewal of the heat stored in the subsurface are described, excluding the effect of dynamic heat recharge via the groundwater flow. An example of the contribution of different heat sources in the Midlothian Coalfield is also provided in Appendix A.1.4.

2.4.1 Heat sources

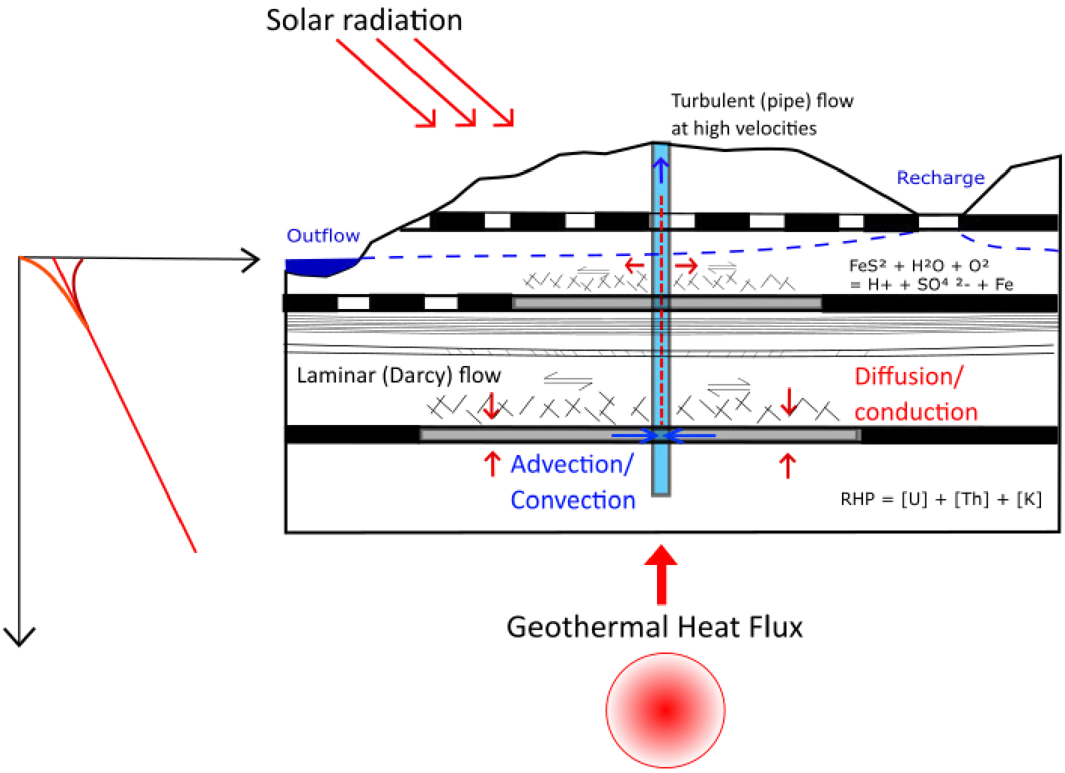

Figure 2.7: Conceptual model of a mine-water reservoir representing the different heat sources (i.e. geothermal heat flux, solar radiation, RHP, pyrite oxidation), the groundwater flow (i.e. Darcy flow, turbulent flow) and heat transfer processes (i.e. conductive and convective) in flooded coal mines. The mine comprises longwall panels, pillar-and-stall workings, fractured zones and the undisturbed rock mass.

Geothermal gradient

In undisturbed parts of the subsurface, the rock temperature generally increases according to the local geothermal gradient, which is determined by the geothermal heat flux q and the thermal conductivity of rocks λ (W/m.K) (J. Busby, Kingdon, & Williams, 2011). Using bottom-hole temperatures (BHT) from 61 boreholes < 1.3 km depth, corrected for topographic effects (Jaeger, 1965) and reported in the BGS Catalogue of Geothermal Data for the UK (UKGC) (Burley et al., 1984), Gillespie et al. (2013) calculated the average geothermal gradient for coalfields in Scotland. Values ranging from 3.7℃/km to 45℃/km were obtained for each borehole, with a mean of 22.5℃/km and a combined average of 30.5℃/km (Fig. 2.8). Using 133 BHT from 72 offshore wells in the North West Margin area, Gatliff et al. (1996) moreover observed an increase in the geothermal gradient from about 35.8℃/km at 1 - 3.5 km to 46.7℃/km at 3.5 - 5 km, relatively consistently across Scotland, and independent of the location (i.e. onshore or offshore) and the type of rock (i.e. sedimentary, crystalline basement). When plotted together, onshore and offshore temperature measurements indicated an average geothermal gradient of 31.9℃/km (Gillespie et al., 2013). An average heat flow of 56 mW/m^2 was determined from a compilation of 35 heat flow measurements reported in the UKGC (Burley et al., 1984; K. Rollin, 1982; K. E. Rollin, 1987), collected in onshore boreholes $\leq$ 400 m depth, with values ranging from 29 mW/m^2 to 82 mW/m^2. Apparent 'hot spots' corresponding to granite intrusions were identified in the central part of the MVS and the East Grampians region, with heat flows of 60 mW/m^2 and 70 mW/m^2, respectively (Gillespie et al., 2013). Updates of heat flow maps for the UK published by J. Busby (2010) including measurements from 390 deep (>1 km) boreholes confirmed an average of 55 mW/m^2, with the highest perturbations being associated with granite intrusions.

Although the temperature in mines is expected to follow the local geothermal gradient, mine-water temperatures (MWT) measured down to 1500 m depth in nine shafts from the MVS and reported in the UKGC were shown not to correlate well with the measurement depths (Gillespie et al., 2013) (Fig. 2.8). Using a more comprehensive dataset including historic coal strata temperatures measured in-situ in dry operational mines, equilibrium temperatures from onshore hydrocarbon exploration wells and monitoring temperatures from pumped and un-pumped mine shafts and boreholes (sourced from TCA, Natural Resources Wales, UKGEOS-Glasgow, Environment Agency and Bridgend County Council datasets), Farr et al. (2020) provided a more detailed mapping of the temperature distribution in UK coalfields. Their results showed equilibrium temperature gradients varying from 17-21℃/km for the Warwickshire and Fife coalfields, to 34℃/km for the North-East Coalfield, with a median geothermal gradient of 24.1℃/km calculated for all British coalfields. The authors additionally suggested that although mine water in un-pumped flooded shafts tends to reach thermal equilibrium with the surrounding strata, mine waters in pumped coalfields generally display greater temperatures near the surface.

It is important to note that estimates of the subsurface conductive heat flux are often associated with many uncertainties, such as potential disturbances of the measured temperature by convective heat (i.e. presence of groundwater flow), by paleo-climate (i.e. responsible for lower apparent gradient at the surface), or by cooling of rock by drilling fluid. A few studies in the UK have been conducted over time to re-evaluate the equilibrium geothermal gradient and the subsurface conductive heat flux accounting for those effects (J. Busby et al., 2011; S. M. Watson & Westaway, 2020). However, corrections are generally local and site-specific, which tends to reduce the reliability of the 'undisturbed geothermal gradient' dataset to represent the true equilibrium state at the national scale.

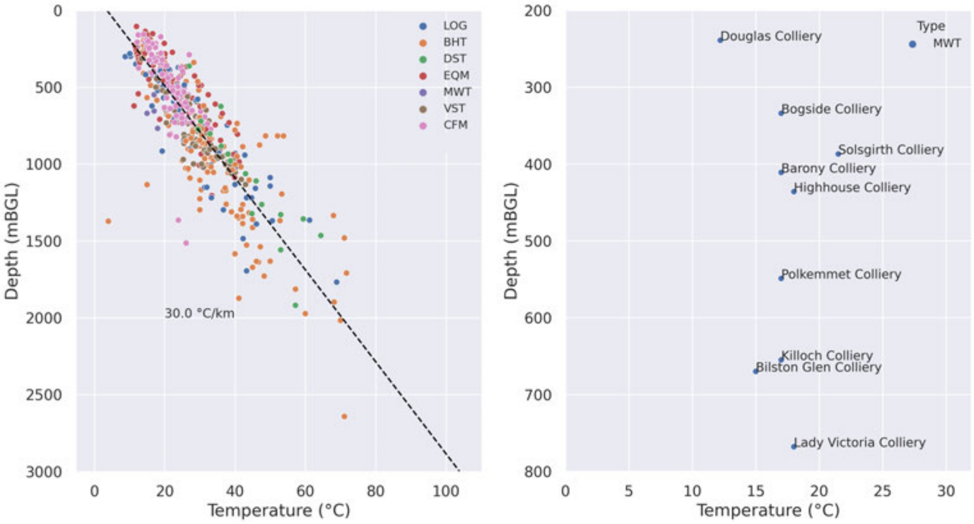

Figure 2.8: Historical temperature data available from the Geothermal Catalogue for the UK (left) and mine-water temperatures only (right) (Burley et al., 1984). LOG: temperature measured during geophysical logging; BHT: Bottom-hole temperature; DST: drill-stem test measurement; EQM: Equilibrium temperature; MWT: Mine Water Temperature; VST: Virgin strata temperature; CFM: coalfield measurement. A list of the historical temperature sites is provided by Gillespie et al. (2013).

Radiogenic heat production (RHP)

The Earth's natural heat flow is generally attributed to the combination of a primordial heat inherited from the formation of Earth, and up to 45% to the natural decay of radioactive isotopes (Pollack & Chapman, 1977). Due to geochemical differentiation, partial melting and magma crystallisation processes, the upper crust is generally enriched in heat-producing elements (HPEs) compared to lower levels, with the Uranium, Thorium and Potassium being radiogenic elements found in minerals in most crustal lithologies (Beamish & Busby, 2016). Measurements of RHP in continental rocks have shown that acidic rocks have the highest heat production rate (i.e granites), followed by basic and ultrabasic rocks (Browne et al., 1999; Cermak, 1982; L. Rybach, 1976). Lachenbruch (1970) revealed the existence of a linear relationship between the surface heat flow and the RHP, with the heat produced by HPEs decreasing exponentially with depth (Beamish & Busby, 2016). In the UK, the linear relationship between heat flow and RHP was confirmed for crustal materials ranging from granite to low-grade metasediments (Richardson & Oxburgh, 1979), according to Eq. 2.4.

$$q_0 = 27 + 16.6 \times A_0 \tag{2.4}$$

with q_0 the heat flux (mW/m^2), and $A_0 = 10^{-5}\rho \times (9.52[U] + 2.56[Th] + 3.48[K])$ the radiogenic heat production from rocks (µW/m^3) determined from the sum of the contribution from the four main HPEs, with [U], [Th] and [K] the concentrations of Uranium ^{238}U and ^{235}U (ppm), Thorium ^{232}Th (ppm) and Potassium ^{40}K (wt%), and ρ the average rock density (kg/m^3) (O'Neill, 2016; K. Rybach, Hokrick, & Eugester, 1988; Vilà et al., 2010). Although the distribution of radiogenic elements provides an important control on the temperature distribution within the Earth's lithosphere (Sandiford & McLaren, 2006), it was shown that this simple RHP distribution model does not apply when heterogeneous lithologies are considered (Furlong & Chapman, 1987).

Scotland is located on a geologically stable part of Earth's crust, where only granite intrusions contain sufficient concentration of U, T and K elements to generate radiogenic heat at significant levels and thus represent an additional source of in-situ heat (Gillespie et al., 2013). The largest and greatest concentration of intrusions is located in the block of crystalline rocks bounded by the Highland Boundary Fault and the Great Glen Fault. Some granite intrusions can be found south of Inverness and near Aberdeen, but only have small heat-producing (HP) values (0.6–2.2 μW/m^3), and in the Grampian Highlands and the Northern Highlands (HP of 2.2 to 7.3 μW/m^3). Two large intrusions (Fleet and Criffel), with HP values of 3 μW/m^3 and 2.2 μW/m^3 were emplaced in Southern Scotland at the end of the Caledonian Orogeny (410–390 Ma). Only one intrusion of significant size, the Distinkhorn intrusion, can be found in the MVS and consists of diorite and granodiorite with relatively low HP capacity (2.0 μW/m^3). In the west of the MVS, an anomalous region of higher heat flow has been attributed to several potential factors, including 1) a crustal thinning, 2) a higher crustal radiogenic heat production, 3) the upward flow of groundwater, 4) residual heat production from Tertiary igneous activity, or 5) a combination of these factors (J. Busby et al., 2011; Robins, 1990). A combined determination of the geothermal heat flux and RHP can therefore be used to constrain the thermal field within the crust where the heat flow is not disturbed by heat convection (Mareschal & Jaupart, 2013).

Solar heat recharge

The surface heat flux can be described as the rate of heat transfer between the atmosphere and the ground surface. The heat exchanges at the ground surface highly depend on the relative temperature difference between the air and the ground surface, but also on complex interactions between subsurface processes, including evapotranspiration and convective processes, and on the amount of absorbed and back-scattered longwave and shortwave radiations (Banks, 2008). According to Trenberth, Fasullo, and Kiehl (2009), the land surface absorbs about 2 W/m^2 from solar radiation, much of which will return to the atmosphere as latent/sensible heat. In a balanced system, only a limited proportion of this absorbed energy will be conducted downward into the ground, depending on e.g. the soil saturation, humidity, wind speed, ground reflectivity and emissivity, which are often unknown or uncertain (Liang, Wang, He, & Yu, 2019).

The decrease in near-surface temperature induced by heat extraction and/or cold water inflow is generally assumed to increase the heat flow from the surface (Rivera, Blum, & Bayer, 2015b). However, the extent of the surface heat recharge will highly depend on the distance of the heat sink from the surface, the amplitude of the thermal drawdown and the conductivity of the ground. Seasonal variations in surface heat flux have been described to impact the yearly ground temperature within the top 10-20 meters below the surface (L. Rybach & Eugster, 2010). However, the contribution to the heat recharge of the downward solar heat flux below that depth of influence relative to the upward geothermal flux is highly uncertain (Banks et al., 2004), with solar recharge likely to prevail at shallow depth. In Chapter 5, the ground surface heat balance is determined numerically, accounting for the yearly average air/soil temperature and solar radiations in Scotland. The relative contribution of downward surface heat flux induced by heat extraction from a vertical borehole heat exchanger located in a typical Carboniferous sedimentary succession is moreover calculated.

Exothermic reactions

Mine waters generally contain a high concentration of iron that results from the oxidation of sulphide minerals contained within the coal deposits (i.e. pyrite, marcassite, sphalerite, galena) by dissolved oxygen (Raymond & Therrien, 2010).

In mines, the oxidation of crystalline pyrite to ferrous iron generally occurs when water is lowered by pumping and mineral surfaces exposed to water enter in contact with oxygen (Banks et al., 1997; Farr et al., 2016). It can be described by Eq. 2.5 (Stumm & Morgan, 2012):

$$FeS_2(s)+\frac{7}{2}O_2+H_2O \rightarrow Fe^{2+}+2SO_4^{2-}+2H^+ \tag{2.5}$$

Oxidation reactions are exothermic and therefore likely to contribute to the overall temperature in mines. According to the CRC Handbook of Chemistry and Physics, the reaction described by Eq. 2.5 has a standard molar enthalpy ΔHr_0 = -1443 kJ/mol. In Banks (2008), Eq. 2.6 was used to calculate the temperature change ΔT_{FeS_2} induced by such a reaction.

$$\Delta T_{FeS_2} = \frac{\Delta H}{c_p} \tag{2.6}$$

With ΔH (kJ/mol) the enthalpy of the overall reaction (< 0 means exothermic) and c_p the molar heat capacity of water. Their analysis showed that 1400-1500 kJ/mol of heat energy could be released in mine waters through pyrite oxidation (Banks, 2008). Based on the adit discharge rate at Ynysarwed in the South Wales Coalfield, Farr et al. (2016) alternatively estimated that pyrite oxidation can generate a temperature increase of 0.5°K/L of water with an iron content of 76.85 mg/L (0.001377 mol/L).

The abundance of sulphide minerals in the coal seams, together with the degree of rock exposure and the hydrogeological processes affecting groundwater circulation is expected to determine the significance of sulphide oxidation processes as a heat source in mines. Although the presence of ongoing chemical reactions might explain mine-water temperature anomalies, the energy input from exothermic sulphide oxidation reactions is expected to be negligible in flooded mine workings and mainly occur above or within the zone of fluctuation of the water table (Banks et al., 2004). The temperature change induced by such reaction during mining activities has however been suggested to be mainly taken by the water, with no significant accumulation of heat in the surrounding rock (Krige & Schonland, 1939). New reactions might be triggered during the operation of a mine-water system, as the rock enters into contact with oxygen. However, this effect is outwith the scope of this project, and further work involving chemical modelling should be undertaken to understand the contribution of exothermic reaction to the heat renewal in flooded mines.

Instantaneous fires

Instantaneous fires in mines typically occur due to spontaneous combustion of coal (i.e. “spontaneous heating”) resulting from self-heating and the auto-oxidation of coal (Eq. 2.7). As it reacts with oxygen in the air at ambient temperature, coal liberates heat which can accumulate in the mine. This process can ultimately lead to spontaneous fires if the interaction rate increases (R. V. K. Singh, 2013). A classic example of a burning Colliery is that of Centralia in Pennsylvania, which has been burning since 1962 (Thomas, 2017). Kim and Chaiken (1993) calculated that the oxidation of coal could produce 93.7 kcal/mole (4.2 kJ/mol) of carbon. However, it is uncertain if those events can significantly alter the rock temperature and if any residual heat remains following flooding.

$$C + O_2 = CO_2 + Heat \tag{2.7}$$

2.4.2 Heat flow disturbances

Reduced heat flows in groundwaters above mine workings have been documented by (S. M. Watson, Westaway, & Burnside, 2019). Those were calculated using bottom-hole temperature from boreholes in the Glasgow area. Compared to the regional average temperature gradient calculated in unmined succession, those reduced heat flows were attributed by (S. M. Watson et al., 2019) to:

- the reduction of the upward conductive heat flow above the mine voids as heat is dispersed laterally through the workings, which can result from pumping
- the downward flow of groundwater through the connected workings, which would decrease the upward flow of heat

This suggests that temperature data in mines are not representative of the actual heat flow, with the present thermal state of mines reflecting the changes that occurred since mining and retaining no ‘memory’ of the pre-mining thermal state (S. M. Watson et al., 2019; Westaway & Younger, 2016).

In addition, the geological dip and folding of the Carboniferous strata are likely to influence the groundwater flow and the thermal recharge and discharge into mine-water reservoirs. In the Midlothian Coalfield for example, the mined strata in the Limestone Coal Formation on the western limb of the syncline dip at a rate of up to 60°, whereas the overlying Coal Measures strata dip at 3-10°. Such variation is expected to create complex patterns in the advection of heat and disturb the temperature profiles compared to a typical profile for horizontal sedimentary successions (Farr et al., 2020). Additional disturbances might moreover result from heat refraction processes, due to the presence of dipping low conductivity layers such as unmined coal seams or shale in the succession. On the other hand, mining-induced fractures and faults are likely to increase heat transfer processes between the mine water and the rock mass surrounding the mine workings. This has the potential to increase the size of the mine-water reservoir (A. A. Monaghan et al., 2021), or be detrimental to the reservoir quality if it is accompanied by the collapse of material filling the mine workings (B. J. Andrews et al., 2020). The effect of dipping strata and the fractured zone permeability on the temperature in mines is discussed further in chapters 7 and 8, respectively.

2.4.3 Volumetric heat assessment

Volumetric assessments aim to assess the heat-in-place or initial (static) heat capacity of a geothermal reservoir (see Appendix A.1.4). The thermal capacity of flooded coal mines is generally determined based on the total volume of water-filled space V (m^3) and the geothermal gradient. Assuming that the mine-water temperature is in equilibrium with the reservoir temperature, the energy available in the subsurface or heat in place E_{HIP} (J or Wh) is commonly expressed as:

$$E_{HIP} = V[\phi \rho_w c_w + (1-\phi)\rho_r c_r](T_d - T_0) \tag{2.8}$$

with T_d and T_0 the reservoir temperature at the depth of interest and the reference temperature (°C), respectively, ϕ the reservoir porosity, and ρ_w and ρ_r the density (kg/m^3) and c_w and c_r the heat capacity (J/°C.kg) of the water and rock, respectively (Vélez Márquez et al., 2018). Depending on the approach, the reference temperature T_0 can represent the average temperature of the hottest/coldest month (Bao & Liu, 2019a), the yearly average surface temperature (Chu et al., 2021), the minimum/maximum temperature cooled/heated by a heat exchanger (Ngoyo Mandemvo, Comeau, Raymond, Grasby, & Terlaky, 2023), the reinjection temperature or the recharge water temperature.

For Ngoyo Mandemvo et al. (2023), the total heat content of a mine H_{tot} (W) can be divided into the energy held in the host rock (H_{rock}), the mine water (H_{MW}) and the recharging groundwater (H_{GW}), so that:

$$H_{tot} = H_{rock} + H_{MW} + H_{GW} \tag{2.9}$$

The potential heat energy P_{MW} (W) that can be harnessed from mine waters can alternatively be defined based on the rate at which the mine water is abstracted (Banks, 2008):

$$P_{MW} = Q \times \Delta T \times c_v \tag{2.10}$$

Where Q (m^3/s) is the abstraction or discharge rate, c_v is the volumetric heat capacity of water (J/°C.m^3) and ΔT is the temperature change across the heat exchanger. Current regulations in the UK impose a difference of <8 °C between the inlet and outlet heat exchanger temperatures (Environmental Agency, 2012).

In a mine-water geothermal system, a heat pump is used to raise the temperature extracted from the mine water via a heat exchanger to useful levels. The thermal energy delivered by the heat pump to the end user P_{heat} equals the sum of the thermal potential of mine waters P_{MW} and the energy required by the air compressor P_e (Chu et al., 2021), which depends on the system coefficient of performance (COP), so that:

$$P_{heat} = \frac{P_{MW} \times COP}{COP - 1} \tag{2.11}$$

with COP = $\frac{P_{heat}}{P_e}$ (Banks, 2008).

Given the high heat capacity of water and large volume of open voids in flooded coal mines, those have been increasingly considered for their high energy production and storage potential (Adams & Younger, 2001). However, estimates of the 'static heat potential' of a geothermal system tend to overestimate the extent of the resource available over the long term (Chu et al., 2021). The recoverable heat H_{RH} (W) that can be extracted from a reservoir will depend on some other factors, such as the nature of the infrastructure (i.e. open/closed loop), the well design, the geometry and permeability of the reservoir, the purpose of utilisation (i.e. heat/electricity) and the duration of the operations (Agemar, Weber, & Moeck, 2018; Frey et al., 2023). In the geothermal assessment of conventional reservoirs, a recovery factor R varying from 0.2 to 20% is generally used to account for those factors (Calcagno, Baujard, Guillou-Frottier, Dagallier, & Genter, 2014), so that:

$$H_{RH} = R\frac{E_{HIP}}{t} \tag{2.12}$$

The sustainability of heat extraction from geothermal reservoirs is, on the other hand, impacted by the recharge from adjacent aquifers, the fluid chemistry and the heat demand in the vicinity of the mine (Banks, 2016; Ordóñez et al., 2012). Injection of cold water enhances the risk of thermal short-circuiting, which might cause an early thermal breakthrough and reduce the sustainability of heat extraction and the efficiency of a heat pump system. In those scenarios, cyclical production and the reinjection of heat are essential to ensure balance in the system over the long term. However, one of the key limitations of volumetric assessment is that it does not account for those complex factors. Based on the study from Bao and Liu (2019a), Chu et al. (2021) developed a method accounting for both the static heat content of a mine E_s, and the heat resupply during the operation of the system, that is the dynamic convective heat recharge E_d^{flow} and conductive heat transfers through the rock E_d^{rock}, so that:

$$E_{tot} = E_s + E_d^{rock} + E_d^{flow} \tag{2.13}$$

$$E_d^{rock} = \sum_i^n (q\pi D_i Z_i)t \tag{2.14}$$

with n the number of open infrastructures (e.g. shaft, roadway/gallery, stopes), q the heat flux (W/m^2), D and Z the diameter and length of the open void (m), where the porosity ϕ = 1, and t the time (s).

$$E_d^{flow} = \theta\mu\rho_r c_r V_r (T_r - T_0) \tag{2.15}$$

With T_0 the reference temperature, θ the recharge factor and μ the energy conversion efficiency factor. Estimates of the recharge factor are however complex and will depend on the recharging water characteristics such as its temperature and thermal properties, on the flow velocity/residence time that itself depends on the permeability of the seams/rock, the pumping rate and volumetric recharge rate.

Although numerical modelling can overcome some of the challenges linked to the parameters uncertainties, there remains to date a lack of conceptual understanding of the dynamic heat replenishment of mine-water reservoirs and the structural differences between shafts, galleries and goaf (Chu et al., 2021). This makes it challenging to analytically quantify the potential of mine-water resources, and define governing equations of flow and heat transport (see Chapter 4).

2.5 Summary

This chapter provided a description of the background geology in the UK as well as a conceptualisation of the structure of coal mines, that will be used for the development of the numerical models (chapters 6, 7 and 8). It also sets the context for the analysis of available monitoring data (Chapter 3) and of the subsurface heat balance and thermal footprint induced by heat extraction from a vertical borehole heat exchanger in the UK (Chapter 5).

Chapter 3

Data analysis and identification of the heat sources in coal mines

3.1 Chapter Overview

This chapter consists of the analysis of thermal, hydraulic and geological data available from UK coalfields, through the development of a geodatabase (not available publicly). The analysis aims to identify the key factors controlling the mine-water temperature (MWT) and the heat redistribution in flooded mines by identifying potential correlations between the local geology, the historical temperature, the MWT and the hydraulic parameters monitored by The Coal Authority (TCA) at the scale of a monitoring site, mine-water block (MWB) or coalfield. To do so, geological logs from the BGS GeoIndex Onshore Database are collected and digitised to perform statistical analysis on the rock type distribution across the UK. In parallel, historical temperature measurements acquired in the corresponding and/or neighbouring boreholes were collected from the literature (Burley et al., 1984) together with monitoring data (time series and temperature profiles) acquired by TCA in boreholes and shafts in mining areas. Data were formatted and classified according to their measurement location, the nature of the measurement and the mine status/type of site at the time of acquisition, and included in a Python geodatabase to facilitate the data processing and analysis.

Key questions:

- Is the MWT solely controlled by the undisturbed geothermal gradient?
- Does the local geology influence the MWT distribution in UK coalfields?
- Is the temperature distribution in mine shafts dependent on the nature/hydraulic state of the coalfield/MWB?

Hypotheses

- The geothermal gradient dominates the temperature profiles in mines over radiogenic heat production and exothermic reactions.
- The MWT in un-pumped shafts mainly depends on the extent of hydraulic mixing in the shaft, i.e. the seams depths, temperature of recharge water and seam permeability.
- The pumped MWT mainly depends on the origin of recharge water and pumping depth.

3.2 Introduction

Mine water is being increasingly viewed as a low-carbon heating resource that could contribute to the decarbonisation of residential and industrial heating in the UK. Recent studies (Farr et al., 2020; Gillespie et al., 2013) showed that the MWT measured in shafts and boreholes in UK coalfields is generally higher than the groundwater temperature at shallow depths, in both unpumped areas and pumped coalfields (Fig. 3.1). This near-surface warming makes mine waters a valuable heat resource that can be harnessed via ground source heat pumps (GSHP). However, there is to date a lack of understanding of the key controls on MWT and therefore, it is uncertain if the shallow warming and deep cooling effect is prevailing in all pumping situations and spread within interconnected parts of a mine and at the scale of a coalfield (Farr et al., 2020). This makes it challenging to determine the sustainability of this resource for large-scale and long-term utilisation.

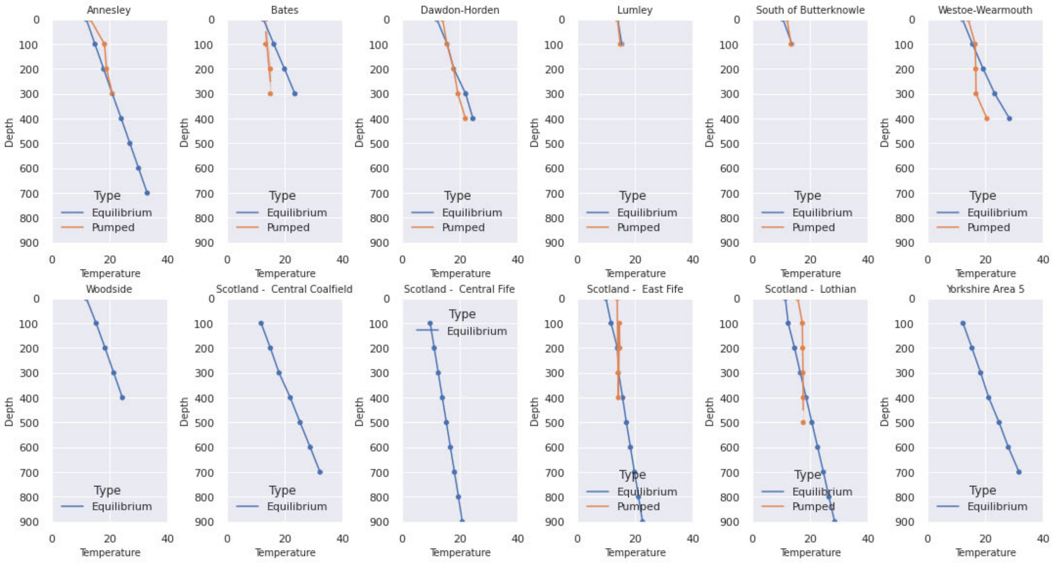

Figure 3.1: Equilibrium and pumped temperature profiles calculated by Farr et al. (2020) averaged at the scale of the mine-water blocks per 100 m depth intervals. Temperatures are in ℃ and depths are in meters below ground level (mbgl) A comparison of the profiles suggests that pumped temperature gradients are generally lower than the predicted undisturbed geothermal gradient. In most cases, the temperature measured in pumped shafts and boreholes is higher than the equilibrium temperature at shallow depths (i.e. above 100-200 mbgl), whilst temperatures in pumped coalfields are lower than in the equilibrium coalfields at 300-500 m depth (Farr et al., 2020). This latter observation was interpreted to either reflect the lack of deep data or respond to the effect of warmer waters being drawn from deeper and more productive seams intercepting the pumping shafts.

Collieries in the UK have accessed coal from the Coal Measures and the Limestone Coal Formation down to depths of about 1400 m below ground level (bgl), with the deepest shafts reaching depths of about 1000 mbgl. This large depth range implies that the MWT can significantly vary between the uppermost and lowermost levels depending on the local geothermal gradient. Robins (1990) reported a range of temperature between 8℃ and 15℃ for water circulating above 200 m, whilst average temperatures of 11.5℃-13.3℃ and 14℃-15℃ were reported for the Crynant, South Wales Coalfield (Farr et al., 2016) and the Caphouse Colliery, Yorkshire (N. Burnside et al., 2016), respectively. Samples collected as part of the Scotland Baseline Project in Autumn 2008 indicated pumped MWT of 11.7℃ and 14.5℃, in accordance with the typical groundwater temperature in Carboniferous aquifers in the Midland Valley of Scotland (MVS), against 19.2℃ for the sample collected in the pumped Polkemmet shaft, and 9.8℃ for the gravity discharge (B. E. O Dochartaigh et al., 2011). Gillespie et al. (2013) reported temperatures from 12℃ to 21℃ for nine boreholes in the MVS, with a mean and median value of 17℃. The authors however highlighted the lack of correlation between the MWT and the depth of measurements, suggesting that the geothermal gradient might not be the only controlling parameter on the MWT (Fig. 2.8).

A few mechanisms have been suggested to be responsible for temperature anomalies in flooded mines (Fig. 3.2). This includes the existence of free density-related flow within vertical open shafts (Hamm & Bazargan Sabet, 2010; C. Nuttall et al., 2002) or forced convective flow generated by pumping (N. Burnside et al., 2016). A comparison between temperature data from pumped shafts/boreholes and equilibrium temperatures in MWB indeed showed that pumping significantly alters the temperatures predicted by geothermal gradients (Farr et al., 2020). Difficulties in predicting the temperature of pumped mine waters arise from the fact that waters of different temperatures might enter the shaft at different depths. Faults can also have a substantial impact on the subsurface temperatures, acting either as a flow barrier or a highly conductive flow pathway allowing cold water recharge from the surface, deep warm water recharge or recharge of saline water from the coast (Dochartaigh et al., 2015). The accumulation of heat below low conductivity coal seams (i.e. 'trapped heat') or heat refraction on inclined strata are also common phenomena in mines likely to create temperature anomalies (Gillespie et al., 2013). Quantifying the amplitude of those effects requires a deep understanding of the local geology (i.e rock heat conductivity, strata geometry), the heat transfer processes and their relative contribution to the heat recharge. In addition to the natural geothermal heat flux and radiogenic heat production, exothermic reactions such as pyrite oxidation (Banks, 2008; Farr et al., 2016) and instantaneous fires (Thomas, 2017) that occur in active mines have been suggested to represent an additional source of heat that could contribute to the development of those anomalies. However, the residual heat left from those processes after the flooding of the mine is uncertain.

In this study, a geodatabase containing geological, historical and monitoring data was developed to optimise the processing and cross-correlation analysis of the different data types. This chapter describes the database structure, including the data sources, the different attributes for each database table (also referred to as *entity*) and the data analysis approaches. Digitised geological logs are used to perform a statistical analysis of the rock types distribution

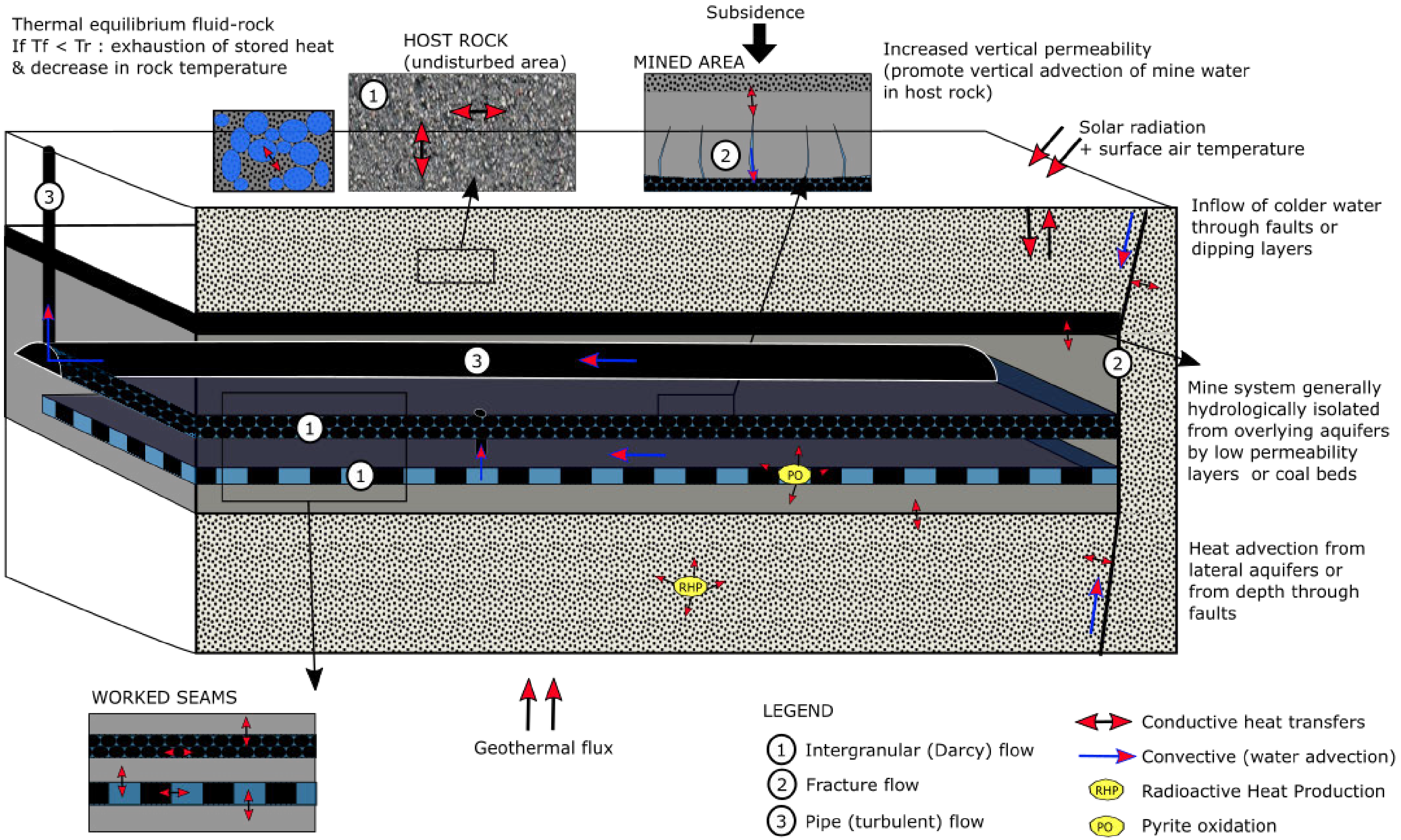

Figure 3.2: Diagram representing the different thermal, hydraulic and mechanic processes likely to impact the temperature distribution in different mining and geological units (i.e. pillar-and-stall, longwall panel, fractures zone, faults, porous host rock). The different sources of heat (e.g. geothermal heat flux, solar radiation, RHP, pyrite oxidation) are represented together with the main heat transfer processes. Heat conduction is represented as dominant in the porous and fractured host rock, in the mined area and the goaf material (e.g. collapsed material in longwall panel). Heat convection is described in the open voids (e.g. stalls), the roadways and faults.

in UK coalfield, and to identify potential correlations between the rock properties (e.g. heat conductivity, heat capacity), their heat production potential (e.g. radiogenic heat production) and the MWT monitored by TCA. Historical temperatures available for the UK (J. Busby, 2010; J. Busby & Terrington, 2017; Farr et al., 2020; Gillespie et al., 2013) are used to assess the relative contribution of the local geothermal gradient on the apparent MWT. In addition, hydraulic parameters such as the pumping/discharge rate or water level are used to identify potential discrepancies between the predicted and observed MWT in shafts, accounting for the site location, the nature and status of the site at the time of acquisition and the type of measurement.

3.3 Methods

3.3.1 Data sourcing

Historical temperature data

Farr et al. (2020) provided a map and synthesis of the temperature of Britain's coalfields at the scale of the MWB by comparing equilibrium temperatures to recent pumped MWT measured by TCA (Fig. 3.1). The undisturbed geothermal gradient in each coalfield was calculated from different datasets:

- historical temperature measurements from onshore hydrocarbon exploration wells reported in the BGS Catalogue of Geothermal Data for the UK or UKGC (Burley et al., 1984; K. E. Rollin, 1987),
- historical in-situ coal strata temperatures measured in dry operational coal mines between 1848 and 1924 (Farr et al., 2020),
- post-closure mine temperature data measured in un-pumped monitoring boreholes/shafts in both recovered and recovering coalfields (i.e. TCA, Natural Resources Wales, UKGEOS-Glasgow, Environment Agency and Bridgend County Council).

In their study, Farr et al. (2020) highlighted a good correlation between historical in-situ coal strata temperatures measured in dry operational mines (1848 - 1924) and more recent downhole temperatures measured from flooded abandoned mines in UK coalfields (BGS UKGC). This was interpreted to indicate the existence of a thermal equilibrium between the mine water in un-pumped flooded shafts and the surrounding strata, suggesting the thermal equilibration is a relatively rapid process (tens of years). For the same depth interval, a larger range of equilibrium temperature was however observed for the BGS UKGC data relative to the in-situ equilibrium temperatures in each MWB. The larger variability in the UKGC data was suggested to be caused by the effect of measurements taken inside and outside the mining areas, or an indication that UKGC data had not reached thermal equilibrium at the time of measurements. In addition, historical in-situ temperatures used to calculate the undisturbed geothermal gradient were measured in active mines, where the rock temperature in galleries could have been disturbed by air ventilation or by the circulation of recharge water in highly permeable voids.

In this study, both the temperatures compiled in the UKGC and the equilibrium gradients calculated by Farr et al. (2020) using a more comprehensive dataset were used to reflect the undisturbed thermal state of the mines. For each temperature value integrated into the database, the type and source of the data, the measurement depth and the heat flux associated with the temperature measurements (when available in the literature) were reported. In addition, the characteristics of the measurement site (e.g. borehole name, location, depth) and borehole were informed based on the data provided by TCA and on information available in the BGS geoIndex database. This is described further in section 3.3.2.

Monitoring data

A total of 462 MWT and water level data measured in 140 sites within UK coalfields (including the East and West Midlands, North-East and North-West England, Yorkshire, South Wales and Scotland coalfields) were compiled from the TCA dataset, made available through an academic license. The dataset comprises 199 temperature logs from 83 boreholes and shafts, 220 continuous water level and temperature time series data collected between 2000 and 2023 in pumping and monitoring shafts, boreholes, cascade outflow and discharge zones as well as 42 on-site manual measurements acquired since 1995 and a pumping test. Each data file was reformatted to a standard format (e.g. column names, depth below ground level/above reference datum) to systematise the analysis. For each data/acquisition, the site location (i.e. borehole/shaft name and coordinates), the nature of the site, the nature of measurement (i.e. data logger, temperature profiles, manual reading), and the acquisition period were collected. When available, the water level and/or flow rate and the probe/pump depth were integrated to investigate potential correlations between thermal and hydraulic parameters and identify any anomalies caused by forced convection (i.e. pumping).

Water level loggers installed in monitoring shafts and boreholes collect hydrostatic pressure values at successive equally spaced out points in time, usually every 10 or 15 minutes. Whilst some loggers directly re-transmit data, those sequences of acquisition are usually extracted manually during repeated site visits, resulting in a series of files covering different periods. Time series are generally processed (i.e. converted to water level based on the air pressure and water pressure), corrected for potential shifts in the logger depth between two acquisitions (using manual readings) and compiled by TCA after each site visit. However, there is no clear consistency between the data sets, especially for older time series. Here, the time series were reformatted by cleaning the data, merging the time series acquired at the same location, and converting the dates to the same format and the water level to the same unit. Depths given relative to Ordnance Datum (mAOD) were converted to meters below ground level (mbgl) using the ground surface elevation (mAOD), or calculated from the probe depth and water level above the probe (mAP). Any temperature and flow rate time series associated with the water level acquisition were appended as additional columns to the text file. Generally, only recent time series (i.e. post-2000) have consistent temperature measurements at a few selected monitoring sites. Although a single time series file is generally created for each site, it is important to note that those can include gaps in acquisition periods, faulty loggers measurements, and covers periods where the state of the mine has changed (i.e. from rebounding to pumped or discharging).

In addition to time series, temperature-conductivity (ECT) logs have been acquired at selected sites over single or repeated surveys. Those are generated for depth intervals ranging from 0.01 to 1 m, from the surface to the bottom of the borehole/shaft. Similarly to the time series, temperature profiles were here reformatted (i.e. converted to a mbgl), and corrected for any measurement error. This includes removing the upper $\sim$2 meters in profiles where a temperature shift at the water level depth is interpreted to be influenced by the air temperature. In addition, each acquisition is given a *Filename* to be referred to in the database.

Geological data

Geological logs. A total of 70 geological logs were collected and manually digitised from the BGS GeoIndex Onshore database, distributed across the onshore parts of the UK coalfields (Tables A.12 and A.13). Those logs were selected through an iterative filtering process. First, shapefiles for the locations of 1) existing geological borehole scans (generated from the Onshore BGS GeoIndex viewer), 2) historical temperature measurements (manually digitised from Burley et al. (1984)) and 3) the monitoring sites (provided by TCA) were imported into a GIS project (Fig. 3.3). A total of 113 non-confidential boreholes > 30 m depth and located at a distance < 500 m from boreholes/shafts with available temperature data were initially selected. The reference of each borehole contained in the BGS shapefile (i.e BGS index) was then used to identify and retrieve the corresponding borehole scan in the viewer. Borehole scans collected at the start of the research project in 2020 were made available as .png (i.e. one image per page), making the downloading process time-consuming. From 2023, scans were made available in PDF after an update of the GeoIndex database, facilitating the digitising process. After visual inspection of the geological logs, the selection was narrowed down to 70 boreholes by filtering out those manually written and difficult to decipher. The list of boreholes is provided in full in Appendix A.2.

All the information related to the geological logs, i.e. the X and Y coordinates of the borehole or shaft, its height, depth, the coalfield and the BGS index, was also collected and reported in the *GLOG* entity, described in section 3.3.2.

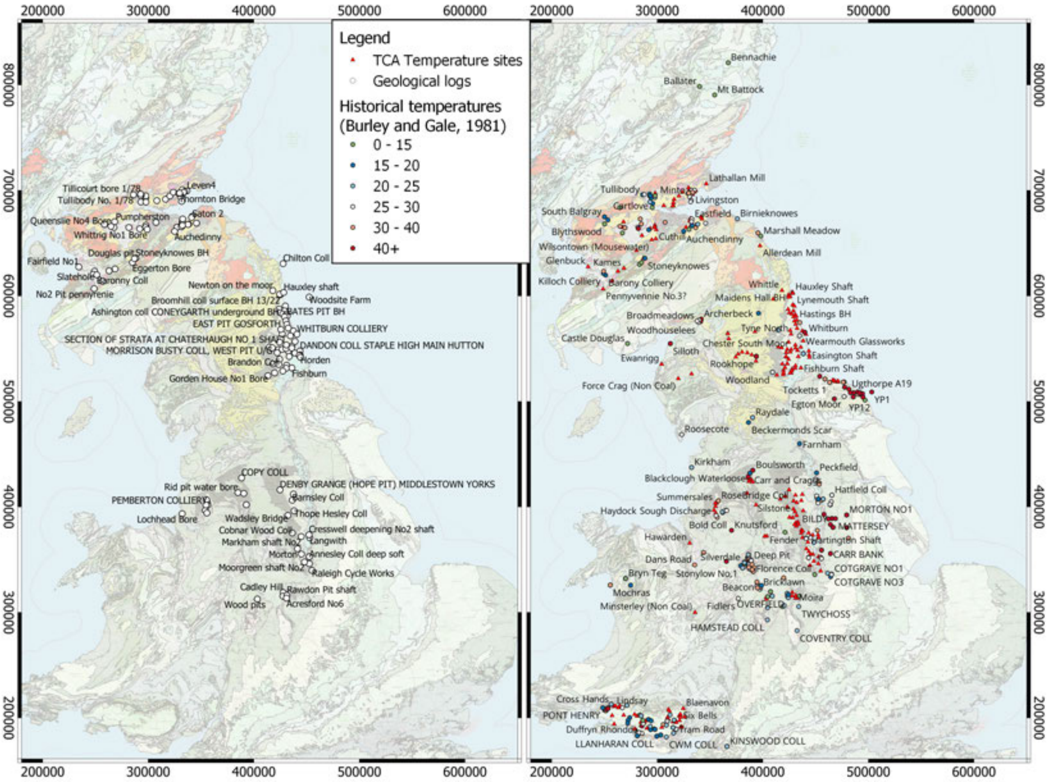

Figure 3.3: Geological maps of the UK showing the location of selected geological boreholes from the BGS GeoIndex Database (left), and the TCA temperature monitoring sites and historical temperatures (℃) from Burley et al. (1984).

Seams inset. The depth of the coal seams intersected by mine shafts where temperature profiles have been acquired was collected from TCA reports or geological logs downloaded from the BGS GeoIndex database. In total, 58 seams inset files have been created for a total of 95 shafts with available data.

Rock properties. To understand the link between the local geology and the thermal state of flooded mines, the heat conductivity, heat capacity, density and radiogenic heat production values for each rock type reported from the geological logs were compiled.

3.3.2 Database development

This section describes the structure of the geodatabase (Fig. 3.4) and the relationship between the different entities presented in Appendix A.2.3. Each entity consists of a series of *entries* (i.e. line, row) that corresponds to a specific acquisition. An entry is itself characterised by a series of *attributes*, that is a column in an entity that provides specific information regarding the acquisition. Attributes, if informed in different entities, can be used to link different entities from a geodatabase with each other.

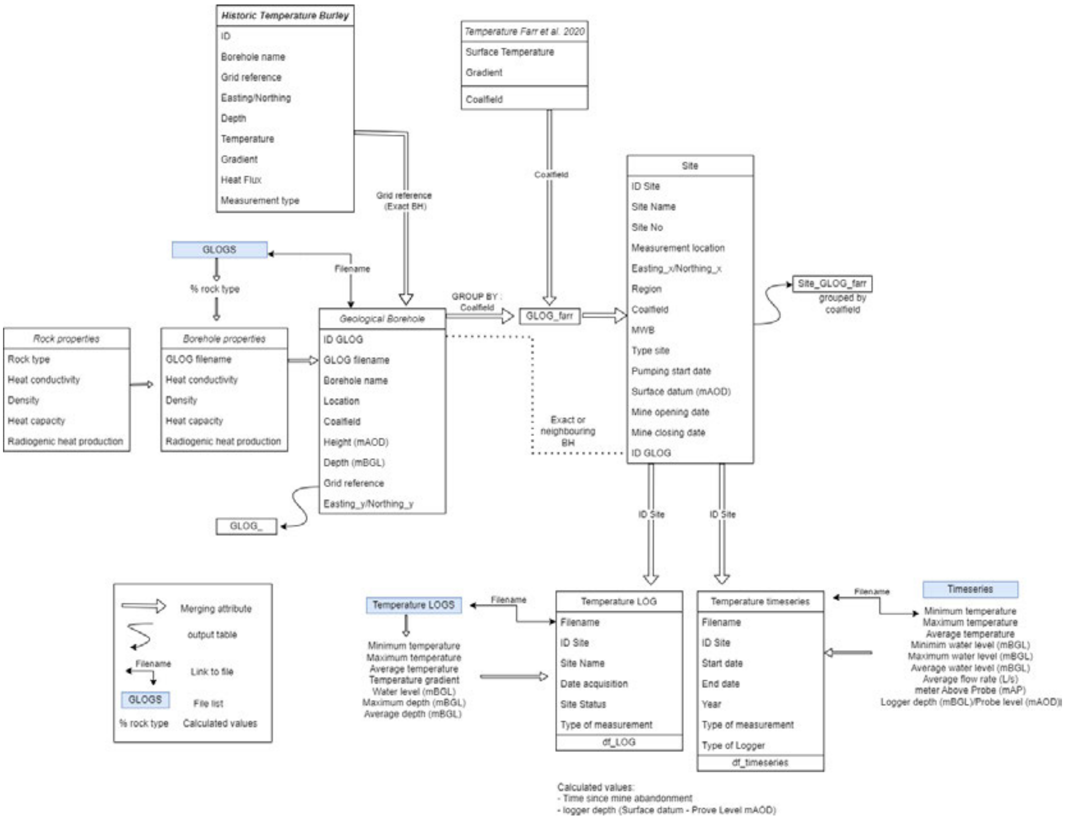

Figure 3.4: Diagram representing the database structure and the relationship between the entities and the different attributes in each of them.

The **Rock properties** entity (Fig. A.9) gathers the list of heat conductivity, heat capacity and density values reported in Table 3.1 as well as the calculated volumetric heat capacity ρc and heat diffusivity $\alpha = \frac{\lambda}{\rho c}$ for each lithology.

The **Geological Borehole** entity (GLOG) gathers the geological and geothermal information available for each geological borehole (Fig. A.10). It consists of 20 attributes, including the borehole *ID* and name, its location (i.e. site name, X and Y coordinates, BGS grid reference, MWB and coalfield) and geometrical characteristics (i.e. height and depth). Although temperature measurements have not been acquired in all geological boreholes, equilibrium temperature data available from the referred borehole or a neighbouring borehole located within a 500 m radius is manually appended to the corresponding entry via the **historical Temperature (Burley)** entity. Those include historical gradients from Burley et al. (1984) and equilibrium temperature gradients determined by Farr et al. (2020) for the corresponding MWB (Fig. 3.1). Appended information includes the historical temperature and measurement depth, the data type (e.g. LOG, BHT, EQM, see Burley et al. (1984) for details of the measurement types), the calculated geothermal gradient and/or heat flux, the borehole name and the data source. Each entry is linked to the corresponding digitised and formatted borehole scan via the *REFERENCE GEOL LOG* attribute, which refers to the digitised GLOG scan filename.

Lithology	λ (W/℃.K)	ρ (kg/m^3)	c (J/kg.K)	RHP ($\mu W/m^3$)
Sandstone	4.54[1] [3.58[11] - 4.9[5]]	2460[8] - 2640[9]	775[10] - 930[10]	0.9
Siltstone	2.22[2] [1.84[7] - 3.02[3]]	2680[9]	910[9]	1.44
Seatrock	1.83[12] - 2.42[3]	2680[7]	860[7] - 1000[10]	2.725
Mudstone	1.41[4] - 1.73[8]	2600[10]	770[10]	2.725
Limestone	2.09[8] - 2.85[5]	2760[7]	880[9]	0.93
Ironstone	2.35[12] - 2.85[5]	2760[7]	880[7]	0.7
Coal	0.4[6]	1350[9]	1300[9]	0.5
Dolerite	1.81[7]	2870[7] - 2900[9]	858[7] - 900[9]	0.324

Table 3.1: Properties of rock from the Carboniferous succession, estimated based on laboratory measurements made on water-saturated samples extracted from boreholes. λ is the rock thermal conductivity, ρ the rock density, c the specific heat capacity and RHP the radiogenic heat production. [1]Wheildon et al. (1984), [2]Downing and Gray (1986), [3]Oxburgh (1982), [4]Bullard and Niblett (1951), [5]England et al. (1980), [6]Herrin and Deming (1996), [7]S. Watson et al. (2020), [8]Westaway and Younger (2016), [9]Waples (2004), [10]Robertson (1988), [11]J. P. Busby (2019), [12]Benfield and Lenox-Conyngham (1939).The specific heat capacity c and density ρ values from S. M. Watson and Westaway (2020) have been determined from rocks sampled in UK coalfields. The RHP values are from Hasterok et al. (2018); Osimobi et al. (2018); Vilà et al. (2010).

The **Site** entity (Fig. A.11) lists all the temperature monitoring sites managed by TCA. The site *ID* is used to link each acquisition from the **Temperature time series** and **Temperature LOG** entities to the corresponding site, whilst *ID GLOG* links the sites to their geological characteristics provided in the **GLOG** entity. Other attributes include the site name and number (as referred to by TCA), the nature/name of the measurement location, the type of infrastructure (i.e. cascade, discharge, shaft, borehole), the type of site (e.g. monitoring, pumped, discharge), the site coordinates, the coalfield and MWB (Farr et al., 2020), the surface datum, pumping start date (if relevant) and the opening and abandonment dates of the collieries. The opening and abandonment dates of the mines are used as proxies for the duration of dewatering activities and the flooding rate since the closure of the mine.

The **Temperature Farr et al. (2020)** entity consists of the average surface temperature and undisturbed temperature gradient calculated by Farr et al. (2020) for each coalfield/MWB, with the coalfield name being used as the entity index (Fig. A.12). It is linked to the **GLOG** entity via the *Coalfield* attribute.

The **Temperature Log** entity gathers the information related to the temperature logs acquired by TCA, including the site name and acquisition time (Fig. A.13). It is linked to the corresponding temperature log file via the *Filename* attribute and to the **Site** entity via *ID Site*, which gives for each acquisition the information related to the nature of the site. Additional attributes such as the status of the site/MWB at the time of acquisition (i.e. pumped, rebounding, rebounded) are reported to allow a thorough analysis of the differences in measured temperature according to the hydrogeological conditions of the site.

Similarly, the **Temperature time series** entity gathers information related to the temperature time series acquired by TCA (Fig. A.14). It is linked to the corresponding time series file via the *Filename* attribute and to the **Site** entity via the *Site ID* attribute. For each entry/time series file, the acquisition start and end date, the logger type, measurement type (i.e. data logger, manual reading), the probe depth (mbgl) and/or logger level (mAOD), are provided, if known.

3.3.3 Data analysis approach

The data analysis presented in this chapter is divided into three axes:

- An analysis of the relationship between monitoring hydraulic and thermal data acquired in mine shafts averaged at the scale of the site, MWB or coalfield.
- A visual inspection of the temperature distribution in shafts, accounting for the type of site (i.e. pumping, monitoring shaft) and the hydraulic state of the mine at the time of acquisition (i.e. recovering, discharging, pumped), at a local and regional scale
- An analysis of the effect of the local geology on the monitored and historical temperatures.

The minimum, maximum and average temperature and measurement depth, the temperature gradient (for LOGS) and the rate of temperature and water level change throughout the acquisition period (for time series) are calculated to facilitate the analysis of the relationships between the datasets (i.e. time series and temperature profiles).

Following an initial manual calculation of the average values (which allowed a visual inspection of the time series and temperature profiles), a Python script was developed to automatically calculate those values from the formatted and corrected files. Although this second approach reduced the opportunity to spot any outliers or discrepancies in the data, it permitted speeding up the analysis as new data were added or new parameters were calculated. Overall, any error from the unprocessed time series or temperature profiles was assumed not to change significantly the results of the correlation analysis. Those calculated parameters were dynamically appended in the corresponding entity during the data analysis (i.e. not written in hard in the imported text file).

Although the correlation analysis requires the use of statistical values, the use of averaged temperatures tends to remove valuable information regarding the temperature distribution in mine shafts. A thorough analysis of the temperature profiles acquired in boreholes and shafts is therefore conducted to get a better understanding of the effect of the mine structure and hydraulic regime on the apparent MWT distribution. Profiles were both analysed as a single entity, accounting for the depth of the seams insets, or at a larger scale together with other profiles acquired in the MWB or coalfield to assess potential interactions between sites. The relationship between the monitored temperature profiles and the undisturbed geothermal gradient calculated by Farr et al. (2020) was moreover considered.

A statistical analysis of rock type distribution is finally used to analyse the effect of the geology on the undisturbed temperatures and the MWT monitored by TCA. After digitising the geological logs, the harmonic mean heat conductivity λ, volumetric heat capacity ρc and radiogenic heat production (RHP) were calculated for each log (Fig. A.15). Those were determined from the relative proportion of rock types in the available borehole log (Fig. 3.5) and from rock property values reported in the **Rock properties** entity (Table A.9). Some of the rock names used by the operators in the original logs were modified according to Table A.14 to correspond to the rock names given in Table 3.1. This was done to ensure the consistency between the borehole logs and calculate the harmonic means.

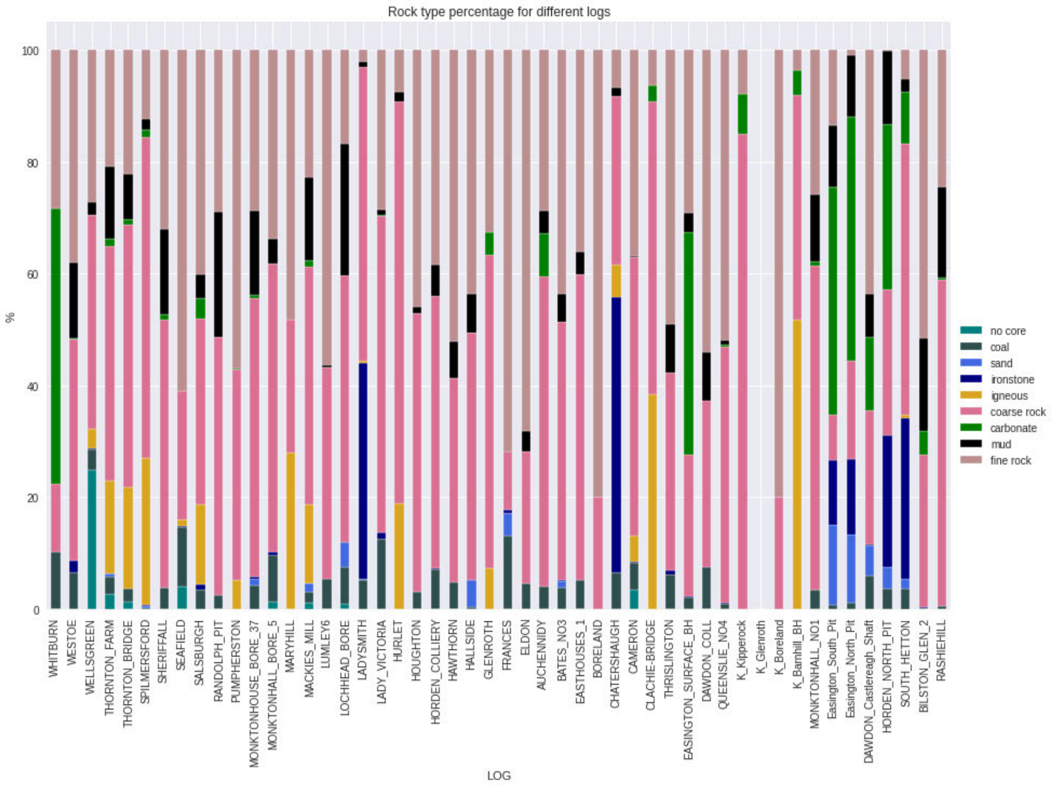

Figure 3.5: Relative proportion of rock types in the considered boreholes and shafts in the UK (based on GeoIndex database). The rock types are grouped by categories to improve the readability of the data and facilitate the comparison between the different borehole logs. 'Igneous' rocks include basalt, lava, dolerite, tuff, dyke and agglomerate; 'coarse rock' include coarse-grained sedimentary rocks (e.g. sandstone, conglomerate); 'fine rock' include fine-grained sedimentary rocks (e.g. siltstone, clayrock, seatrock, shale, mudstone); 'carbonate' include limestone and dolomite and 'mud' include clay, fireclay, etc (see details Table A.14).

3.4 Results

This section first provides the results of the analysis of the temperature profiles, classified per coalfield and MWB (Fig. 3.6). The nature of each monitoring shaft is summarised in Fig. A.8. Cross-correlation analyses between the monitoring, historical and geological data are then described.

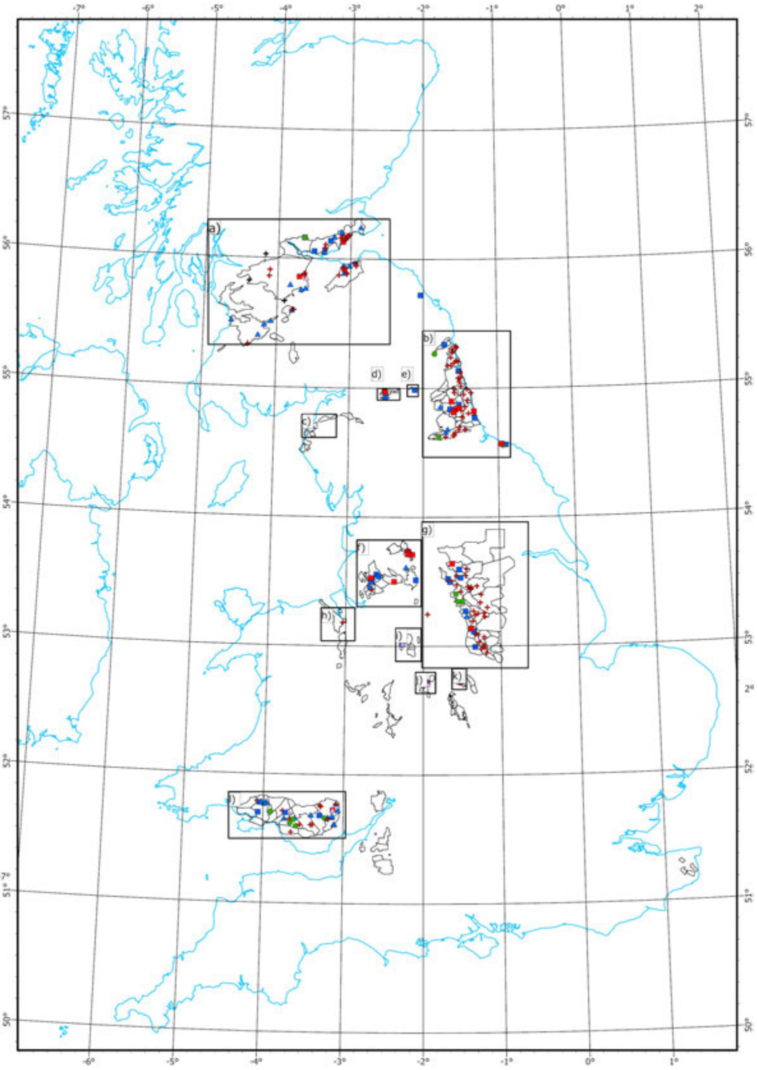

Figure 3.6: Location map for the monitoring and geological data available within UK coalfields. The black squares are the overviews of the coalfield maps displayed in section 3.4.1. The GIS data have been made available by TCA under an academic license.

3.4.1 Temperature profiles description

Nottinghamshire - Derbyshire

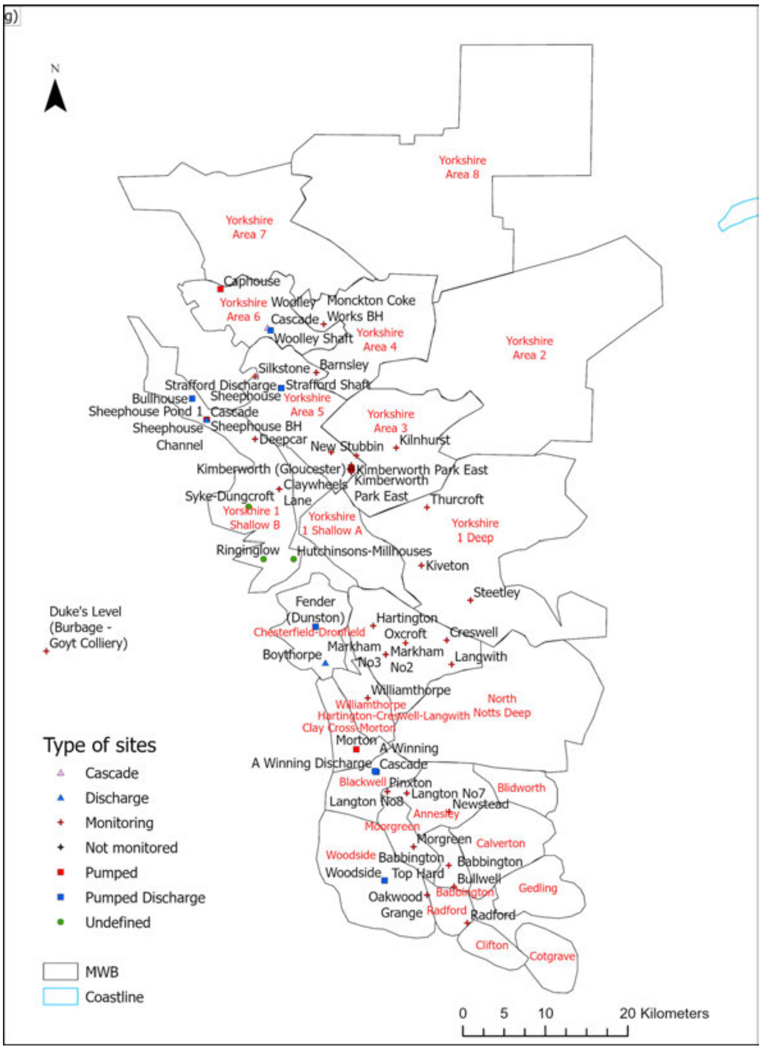

Figure 3.7: Location map for the monitoring sites in the Yorkshire and Nottinghamshire coalfields, showing the outline of the different MWB. The red and black labels refer to the MWB and site names, respectively (TCA data available via an academic license).

In the early 1980s, seven pumping stations were used to prevent mine waters in the Nottinghamshire - Derbyshire coalfield from flowing from shallow outcrop workings to the deeper operational mines located further east (K. Whitworth, 2012). Those included the Oxcroft, Langwith, Williamthorpe, Morton, A Winning, Langton and Woodside pumping stations (Fig. 3.7). Pumping at Woodside remained active following the closure of the last collieries, Annesley Bentinck in 2000, when pumping at A Winning ceased, and at Calverton in 2002, to prevent overflow to deep mine workings via Moorgreen and potential surface mine water discharges (K. Whitworth, 2012). Water has been pumped at Woodside at a rate of 100-150 L/s, thereby slowing down the water rebound in the southern section of the Nottinghamshire-Derbyshire Coalfield (Turner, 2012). In 2018, pumping at A Winning resumed with the construction of a mine-water treatment scheme aiming at controlling the water level in the Derbyshire Coalfield and preventing the pollution of an important source of drinking water (Coal Authority, 2018).

Profiles acquired in the Pinxton, Babbington and Newstead boreholes (Fig. 3.8), which are assumed to be isolated from the mined seams, display a linear increase in temperature with depth. Those profiles are inferred to have been used to determine the undisturbed geothermal gradient calculated by Farr et al. (2020).

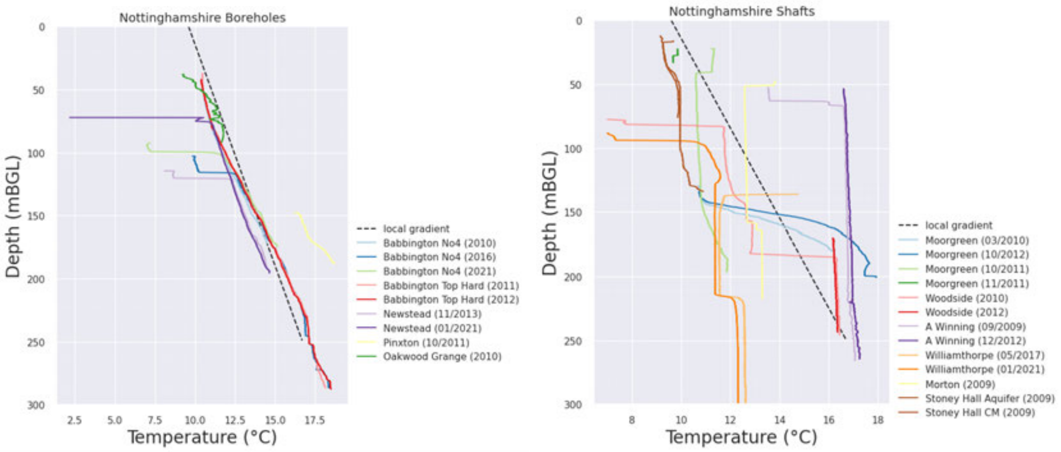

Figure 3.8: Temperature profiles acquired in boreholes (right) and shafts (left) in Nottinghamshire over the 2009 - 2021 period. The dotted line represents the local undisturbed geothermal gradient calculated by Farr et al. (2020). Borehole temperature profiles tend to follow a linear trend along the undisturbed geothermal gradient. Shaft profiles are characterised by uniform temperature distribution with shifts assumed to coincide with the pump depth, seam depths and water level. In profiles where the near-surface water temperature is influenced by the winter air surface temperature (Newstead, Babbington, A Winning), the upper ~2 meters were deleted before including the profiles in the database and avoid bias in the calculations.

Profiles acquired in the monitoring A Winning shaft (Blackwell MWB), at the time of acquisition, display a constant temperature from the inferred water level to the shaft bottom, that is higher than the temperature predicted by the geothermal gradient (Fig. 3.8). The pumped 2010 Woodside (Woodside MWB) temperature profiles depict a large shift at about 180 mbgl that is inferred to coincide with the location of the pump, reducing the temperature by about 3.8℃ in the top part of the shaft (Fig. 3.9). There, the temperature at the water level surface equals the temperature predicted by the undisturbed geothermal gradient at that depth, whilst the MWT equals the temperature predicted by the undisturbed geothermal gradient (Farr et al., 2020) at the bottom of both the Woodside and A winning shafts.

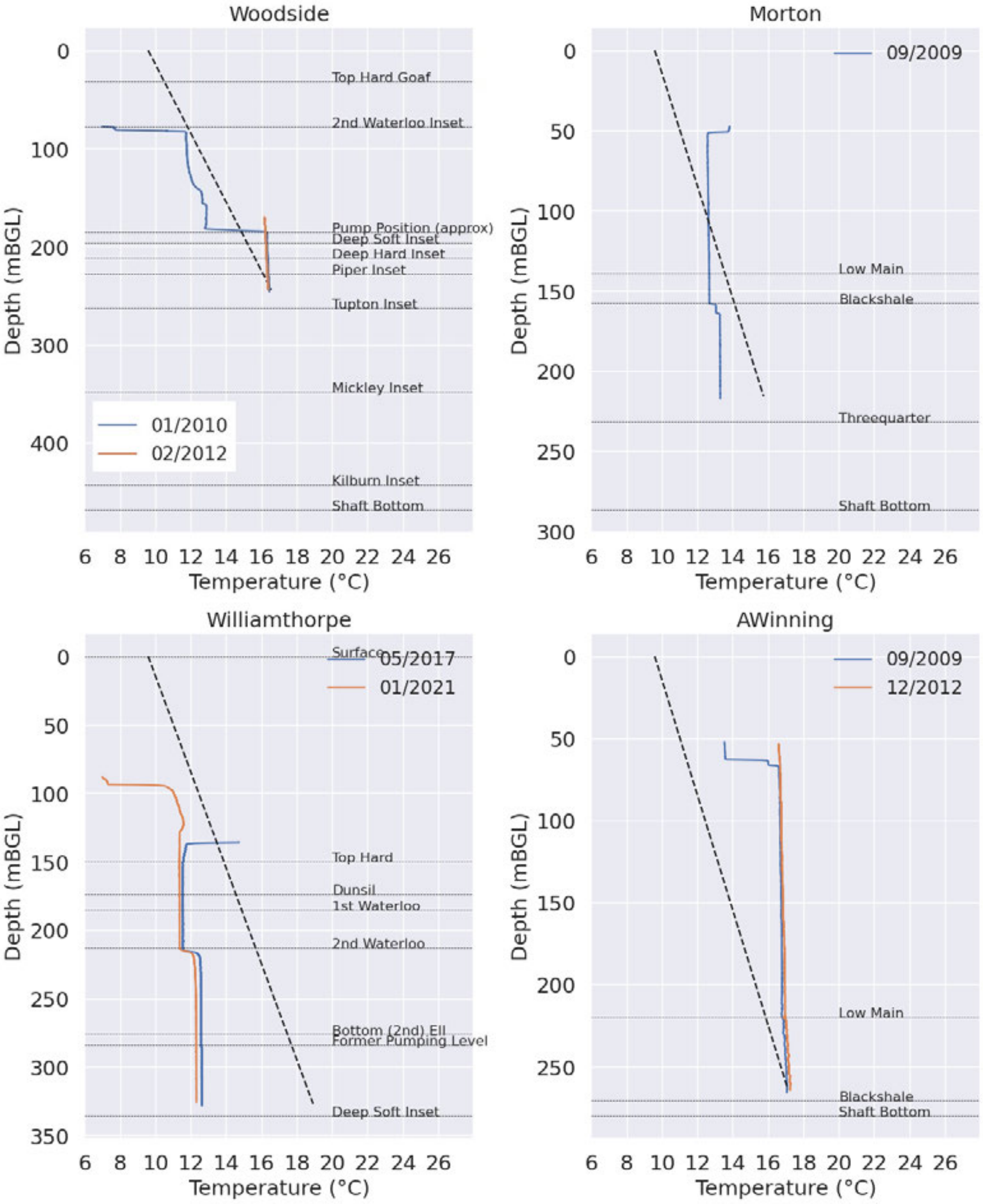

Figure 3.9: Temperature profiles at Woodside, Morton, Williamthorpe and A Winning, with the location of the seams insets. The temperature shifts at the water level depth were deleted before including the profiles in the database and avoid bias in the calculations.

The Moorgreen monitoring shaft is located about 5 km to the northeast of Woodside, in a neighbouring MWB. In both 2010 and 2012 profiles, a large shift towards lower temperatures is observed above 150 mbgl (Fig. 3.8). The temperature at that depth correlates well with the temperature measured in the shallower Stoney Hall profiles. The monitoring Morton shaft, which ceased pumping in 2000, and the Williamthorpe shaft, also display a relatively uniform temperature distribution that is lower than the one predicted geothermal gradient, over the bottom part or whole profile depth. Most profiles in the area depict temperature shifts at about 130-140 mbgl and 200-220 mbgl, which coincide with the depths of the Morton Backshale seam, the Williamthorpe 2nd Waterloo seam and the A Winning Low Main seam insets at $\sim$100 m, $\sim$210 and $\sim$220 m depth, respectively.

Repeated acquisitions in the Langton shaft (Annesley MWB, Nottinghamshire), which ceased pumping in 1982, depict multiple temperature shifts that coincide with the depths of the Top Hard, Waterloo and Deep Hard Seams insets (Fig. 3.10). The profiles indicate a general cooling in 2021 relative to 2013, which was interpreted as a response of the Langton shaft to pumping at A Winning, located 5 km to the north in the neighbouring Blackwell MWB (Lee Wyatt, personal communication). A return to the pre-pumping temperature is observed in the upper part of the shaft above the Waterloo seam inset in 2022, although the temperature between the Top Hard (the most widely worked seam in the coalfield; Edwards 1967) and the shaft bottom remains lower than the one predicted by the undisturbed geothermal gradient. Since the end of 2022, evidence of cooling has been measured at shallow depths.

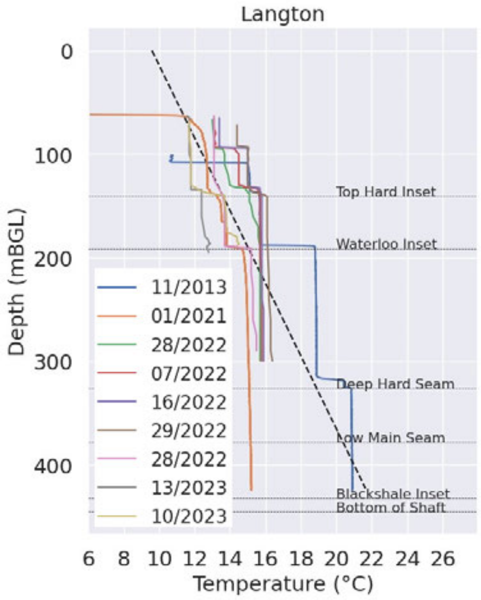

Figure 3.10: Langton temperature profiles (Nottinghamshire) acquired between 2013 and 2023. The undisturbed geothermal gradient is from Farr et al. (2020). In profiles where a temperature shift is observed at the water level depth, the upper $\sim$2 meters were deleted before including the profiles in the database and avoid bias in the calculations.

Pumping ceased in Oxcroft in the late 1990s and at Hartington in 2006, allowing water to rebound in the old workings in the Hartington MWB, located in northern Nottinghamshire (K. Whitworth, 2012). Although mine-water pumping has continued at Langwith, Creswell and Williamthorpe after 2006 (K. Whitworth, 2012), the overflow of water from Markham has been suggested to cause the rebound of mine-water at Creswell and Langwith. Pumping has since then stopped at all locations and both shafts are currently used for water level monitoring purposes. Whilst both the 400 m deep Creswell and 300 m deep Langwith shafts display a constant temperature of ∼ 23-24℃ from the shaft bottom, a shift in temperature corresponding to the High Main seam is observed at about 180 m depth in the 2022 Langwith profile (Fig. 3.11). A similar temperature shift is observed at 300 m depth in the Markham shaft. Although recharge is thought to be occurring from Oxcroft to Hartington and Creswell (Lee Wyatt, personal communication), both the Oxcroft and Hartington shafts, whose depth range is smaller than the other shafts (i.e. ∼ 220 m), display a much lower temperature than at Creswell, Langwith and Markham (∼ 12 and 14℃, respectively), suggesting that the main hydraulic recharge in those shafts occurs from shallower and cooler waters.

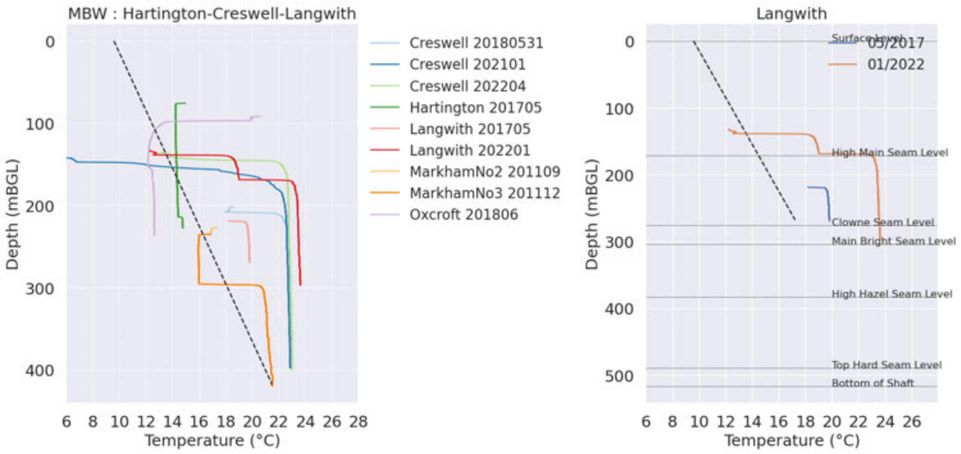

Figure 3.11: a) Temperature profiles in the Hartington-Creswell-Langwith MWB shafts. b) Langwith temperature profiles at different acquisition times, showing the location of the seams insets. The undisturbed geothermal gradient is from Farr et al. (2020). In profiles where a temperature shift is observed at the water level depth, the upper ∼2 meters were deleted before including the profiles in the database and avoid bias in the calculations.

South Derbyshire and Lancashire

Mine-water levels in the South Derbyshire Coalfield (Fig. 3.12) have recovered to a level where mine water is discharging at the surface (K. Whitworth, 2012). As previously observed for boreholes, the Netherseal monitoring boreholes depict a linear increase in temperature from the water level to the shaft bottom (Fig. 3.13). A slight increase in gradient is observed at about 70 mgbl, suggesting a change in lithology (e.g. change in surrounding rock thermal conductivity).

Profiles from the Collin Greens shafts (colliery closed in 1931) are the only profiles available in the Lancashire area, where water had been shown to have recovered at a rate of 8 m in 10 years (K. Whitworth, 2012). The profiles depict a quasi-constant temperature distribution from the shaft top, where the temperature equals the temperature predicted by the geothermal gradient, to the shaft bottom. A slight shift in temperature is observed at 70 mbgl, suggesting the intersection of the shaft with a mined coal seam.

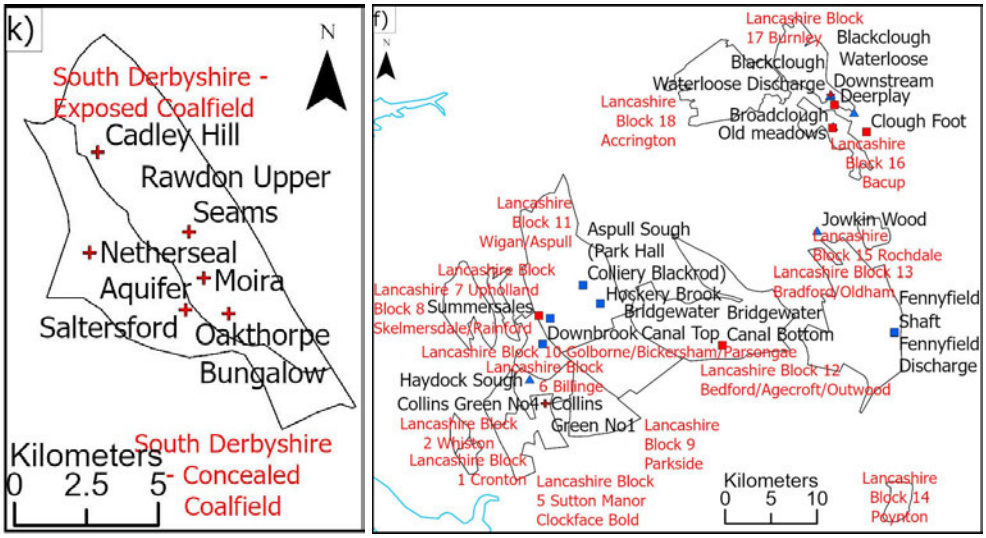

Figure 3.12: Location map for the monitoring sites in the Derbyshire and Lancashire coalfields, showing the outline of the different MWB. The red and black labels are the MWB and site names, respectively (TCA data available via an academic license).

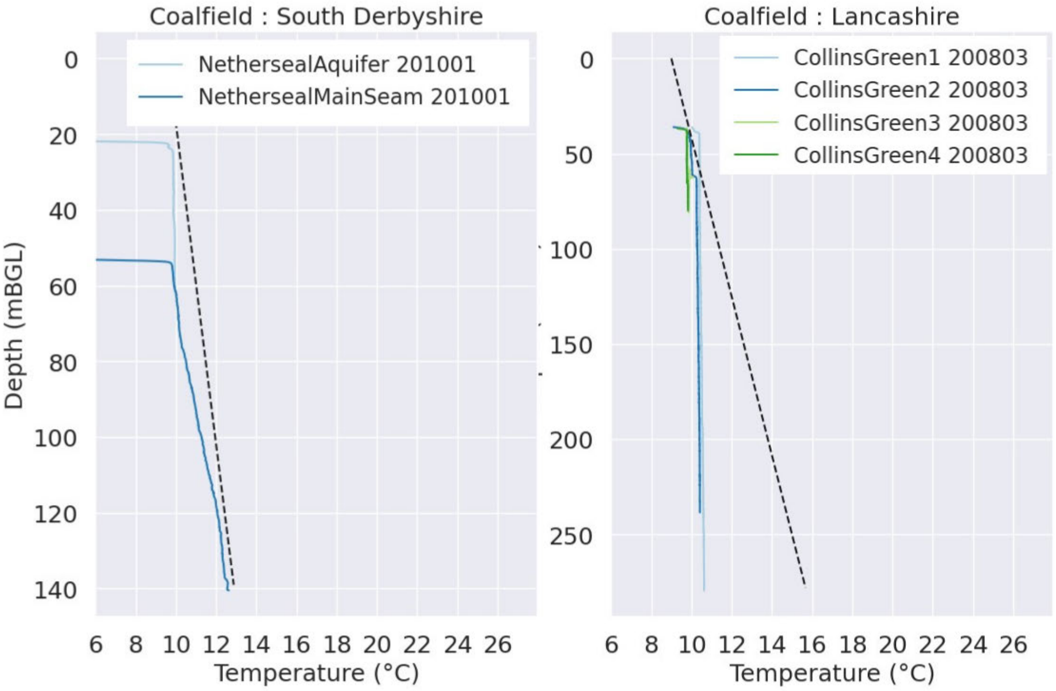

Figure 3.13: Derbyshire boreholes and Lancashire shafts temperature profiles. The undisturbed geothermal gradient is from Farr et al. (2020). In profiles where a temperature shift is observed at the water level depth, the upper ∼2 meters were deleted before including the profiles in the database and avoid bias in the calculations.

Yorkshire

The Yorkshire Coalfield is located North of Nottinghamshire (Fig. 3.7). Following the cessation of the mining activities and water rebound, pumping has resumed at several locations including the Caphouse Hope shaft, the Strafford shaft, and the Bullhouse, Sheephouse and Woolley pumping stations, where the water was initially allowed to discharge about 170 L/s (Burrell & Whitworth, 2000). Collieries in this area are generally interconnected to the areas to the east via roadway connections or narrow barriers (K. Whitworth, 2012).

At Strafford, where water has been described as having recovered to near the surface since 1999-2000, the Coal Measures are exposed and the western boundary of the area is defined by the outcrops of the worked seams (K. Whitworth, 2012). There, the temperature profiles measured in the flooded mine shaft in 2008 and 1016 display a uniform temperature of 14 ℃ from the top to shaft bottom, which equals the monitored temperature in the Thorpe Hesley shaft, located 10 km to the south-east of Strafford in the same MWB, and in the Barnsley shaft. Both the monitored Thorpe Hesley and Barnsley shafts, which were described as having stable water levels since 2008 (K. Whitworth, 2012), however, depict a slight shift in temperature at 150 mbgl, which corresponds to the depth of the Silkstone seam inset (Fig. 3.14). There, the measured MWT equals the temperature predicted by the undisturbed geothermal gradient at that depth.

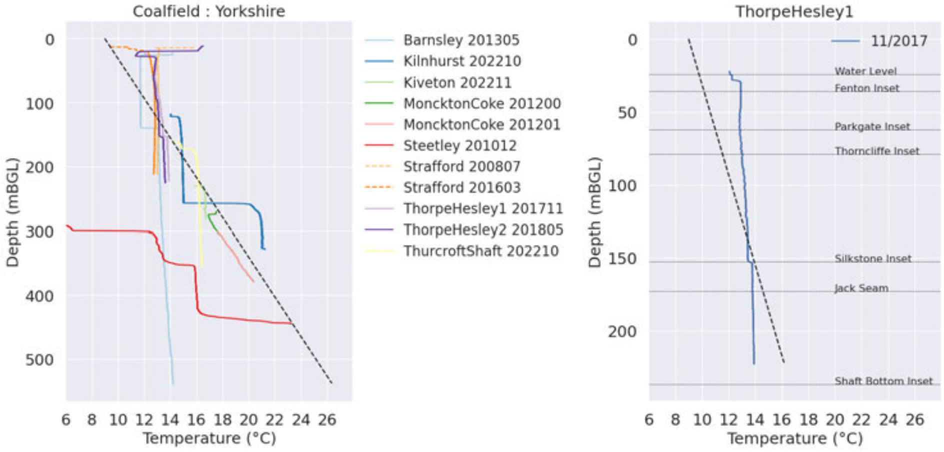

Figure 3.14: Yorkshire shafts and borehole temperature profiles (left) and Thorpe Hesley 1 temperature profile with the location of the seam insets (right). The undisturbed geothermal gradient is from Farr et al. (2020). In profiles where a temperature shift is observed at the water level depth, the upper ∼2 meters were deleted before including the profiles in the database and avoid bias in the calculations.

Other monitoring shafts in this area (i.e. Kilnhurst, Steeley, Thurcroft) depict constant temperature intervals between large temperature shifts. Whilst the temperature in the deep Steetly shaft appears cooler than the temperature in the shallower Kilnhurst and Thurcoft shafts, relative to the undisturbed geothermal gradient, all profiles tend to average 14-16℃, which coincides with the temperature measured at shallower depth at Strafford and Thorpe Hesley. As previously observed for boreholes, the temperature at the Mockton Coke Bore displays a linear increase in temperature with depth.

Scotland

Water has been rebounding in the Scottish coalfields (Fig. 3.15) since the closure of the mines. In the Lothian coalfield (Midlothian area), water has rebounded at an average rate of 20 m/yr since 2006 in the shallow Limestone Measures workings of the Burghlee and Roslin collieries on the western side, and of the Lady Victoria, Lingerwood and Easthouses collieries on the eastern side of the syncline (Bamforth, 2014). Those were suggested to drain into the deeper Bilston Glen mine workings, in which water was shown to rebound at a similar rate (Fig. 3.16).

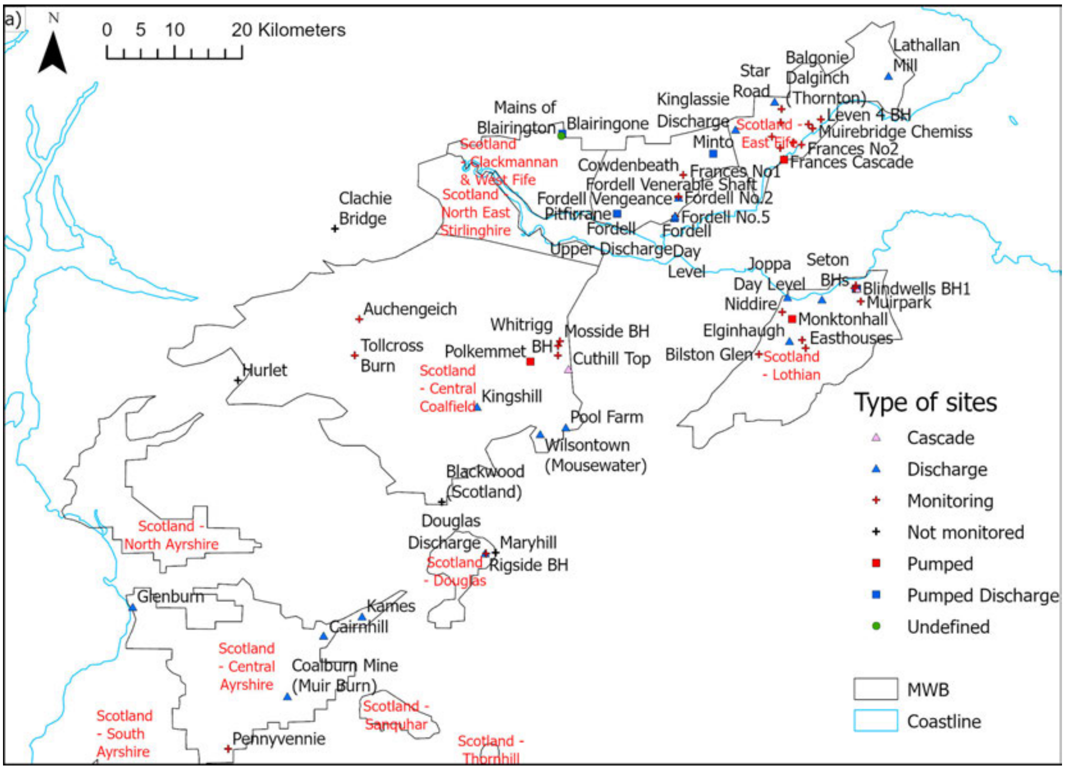

Figure 3.15: Location map for the monitoring sites in the Scotland coalfields, showing the outline of the different MWB. The red and black labels are the MWB and site names, respectively (TCA data available via an academic license).

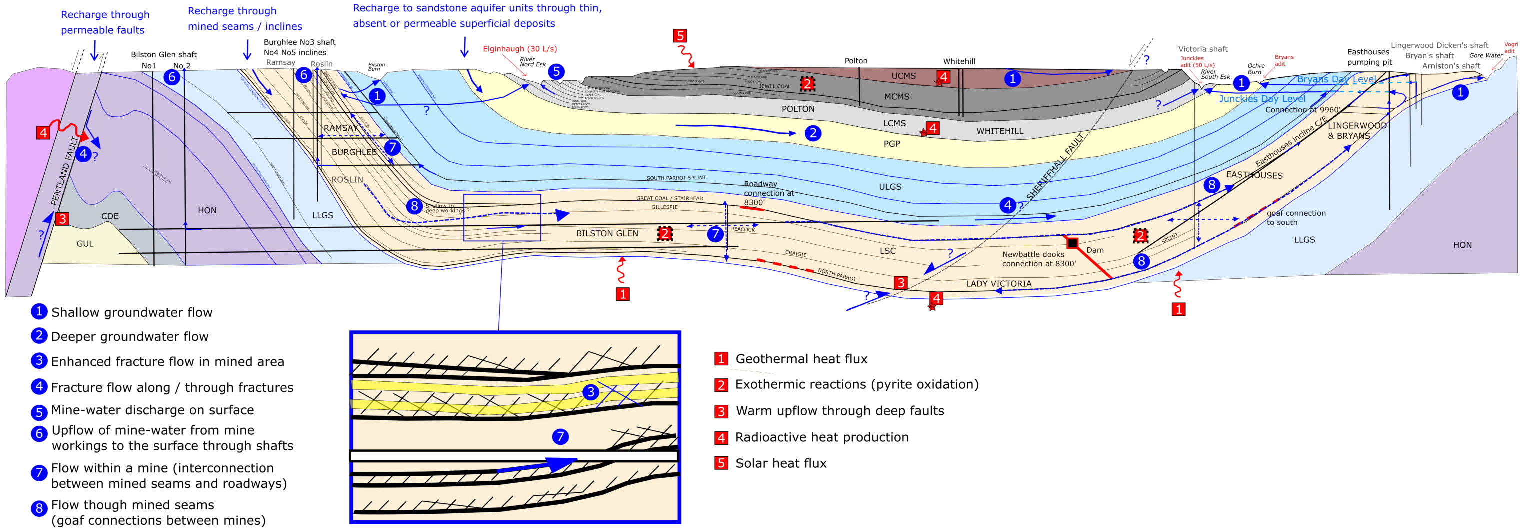

Figure 3.16: Geological and structural NW-SE section across the Midlothian coalfield showing the location and interconnection between collieries, the heat transfer processes and assumed groundwater recharge pathways.

Whilst the Easthouses borehole displays a relatively linear increase in temperature with depth until 200 m depth, the Bilston Glen shaft, located on the other side of the Midlothian syncline, depicts a constant temperature distribution from the water level to the shaft bottom (Fig. 3.17). In opposition to many shafts that directly intersect a gallery or roadway within worked coal seam, the Bilston Glen shafts No.1 and No.2 are connected to a set of steeply dipping seams via two quasi-horizontal roadways intersecting the shaft at 612 and 704 mbgl. This suggests that the temperature in the shaft might result from the mixing water of different temperatures across a large depth range in the mined area before entering the shaft at those two levels.

In the Central Scotland coalfield (Fig. 3.17), the undisturbed geothermal gradient calculated by Farr et al. (2020) matches the historical temperature profile measured in the Hurlet borehole, whilst the Maryhill borehole displays a slightly higher temperature gradient. The pumped Polkemmet shaft profile alternatively depicts a uniform temperature distribution slightly higher than the Bilston Glen profiles. Pumping at Polkemmet started in 1998 with the implementation of a mine-water pumping and treatment scheme, following the closure of the colliery in 1986 and the recovery of water to the near-surface (K. Whitworth, 2012). There, the mine-water system is principally in the Limestone Coal Group and is considered to be isolated from shallow mine workings in the Middle and Lower Coal Measures.

Although deep mining in Fife finished in 1988 with the closure of the Seafield/Fife collieries, pumping at Frances and Michael only stopped in 1995, following which six additional mine water level monitoring boreholes (Cameron, Lochhead, Randolph, Muiredge, Muirespot and Dalginch) were drilled (K. Whitworth, 2012). In 2000, a mine-water treatment scheme was constructed at the Frances Colliery and pumping resumed in 2004 to maintain the water level below 14 mBOD, and reduce the risk of contamination and surface discharges. The pumping rate at Frances increased to 90 L/s in 2006 and to 120 L/s in late 2008 to take account of the total re-saturation of the workings in the East Fife Coalfield. Temperature profiles acquired in Frances indicate an average of 15°C down to 250 m, with a slight temperature shift at about 100 mbgl (Fig. 3.17). This is greater than the temperature predicted by the undisturbed gradient defined by the Clachie-Bridge borehole, located in the same MWB. Shifts in temperature are also observed at the Chemiss and Bowhouse seams insets in the monitoring Michael shaft, where the temperature averages 12°C (i.e. the temperature at the Chemiss seam inset).

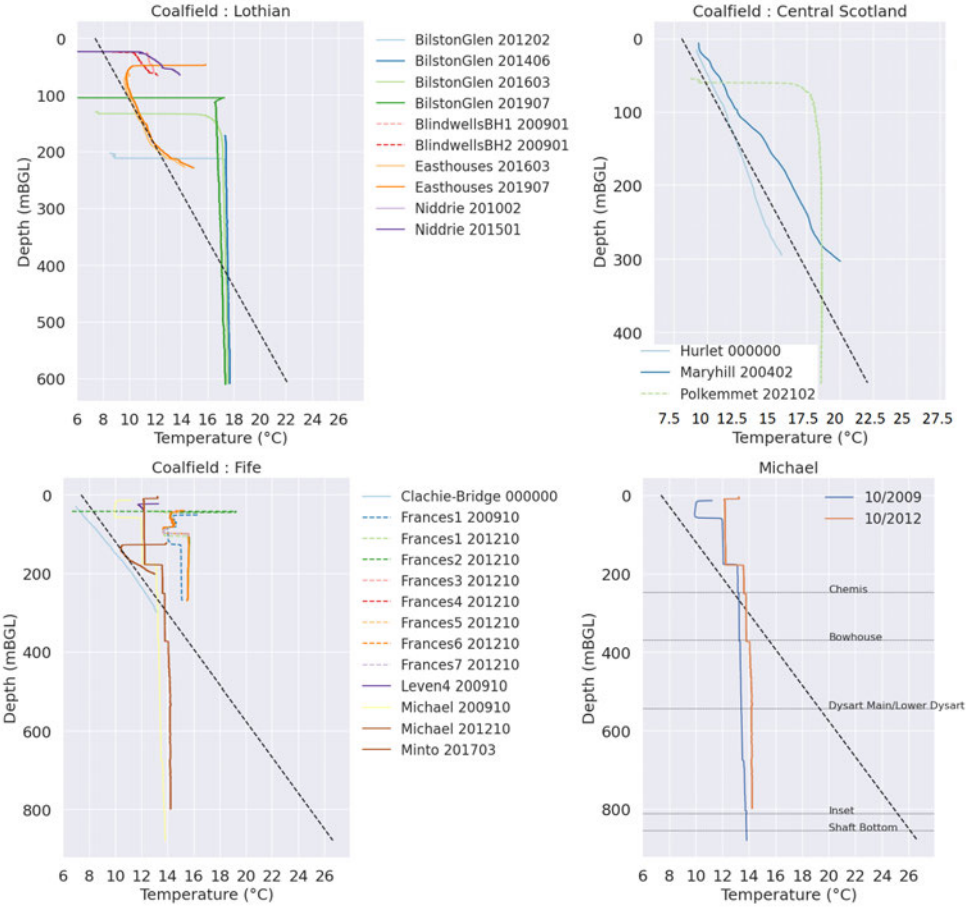

Figure 3.17: Temperature profiles in a) the Lothian shafts, b) Central coalfield boreholes, c) Fife shafts and d) Michael shaft with the location of the seams insets. The undisturbed geothermal gradient is from Farr et al. (2020). In profiles where a temperature shift is observed at the water level depth, the upper ∼2 meters were deleted before including the profiles in the database and avoid bias in the calculations.

South Wales

The South Wales coalfield (Fig. 3.18) is an E-W trending syncline crossed by normal NNW-SSE trending faults with throws up to over 500 m. Most of mine discharges in South Wales are gravity-driven (Robins, Davies, & Dumpleton, 2008), except at Six Bells (Vivian Colliery) where mine water is abstracted at 217 m depth to be pumped to a treatment scheme (Farr et al., 2016). There, high inflow rates have been interpreted as resulting from the high local rainfall (K. Whitworth, 2012). Only three temperature profiles from three boreholes are available in South Wales (Fig. 3.19). Whilst a quasi-uniform temperature distribution is measured between 20 mbgl and 160 mbgl in Cefn in 2010, a linear temperature gradient of 40℃/km is observed between 160 mbgl and 275 mbgl in Ogmore in 2012. In Rhonda, a temperature gradient of 30℃/km is measured between about 55 mbgl and 185 mbgl, and increases to a linear rate of 58℃/km between 185 mbgl and the borehole bottom at 300 mbgl, suggesting a change

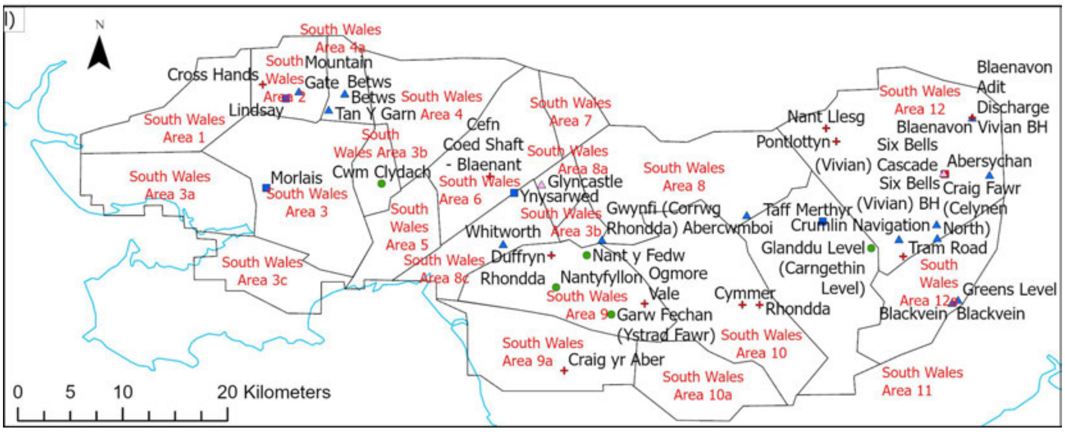

Figure 3.18: Location map for the monitoring sites in the South Wales coalfield, showing the outline of the different MWB. The red and black labels are the MWB and site names, respectively (TCA data available via an academic license).

in the surrounding host rock properties. Close to the surface (0 - 50 mbgl), the gradient gets reversed, with a maximum temperature of 13.11 ℃ observed at about 3 mbgl and a minimum of 11.75 ℃ measured at 25 mbgl, which is interpreted as the warming effect caused by higher air/surface temperatures.

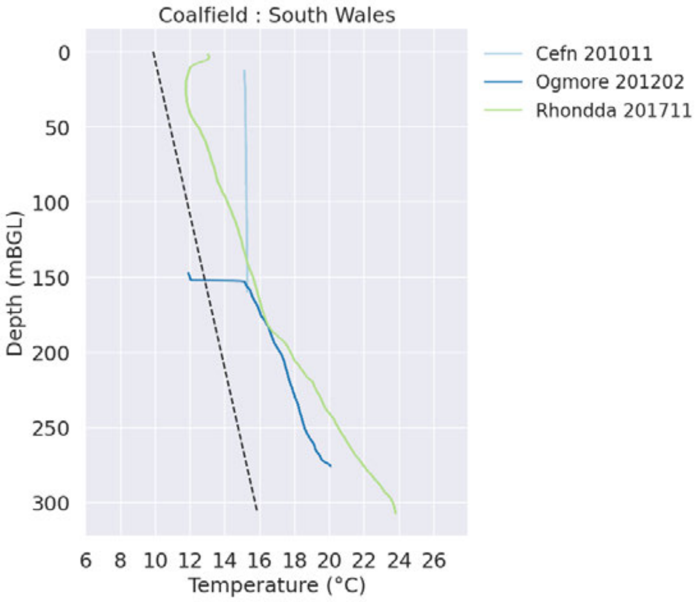

Figure 3.19: Temperature profiles for monitoring sites in South Wales. The undisturbed geothermal gradient is from Farr et al. (2020).

North-East England

The North-East England Coalfield is the largest in the UK (Fig. 3.20).

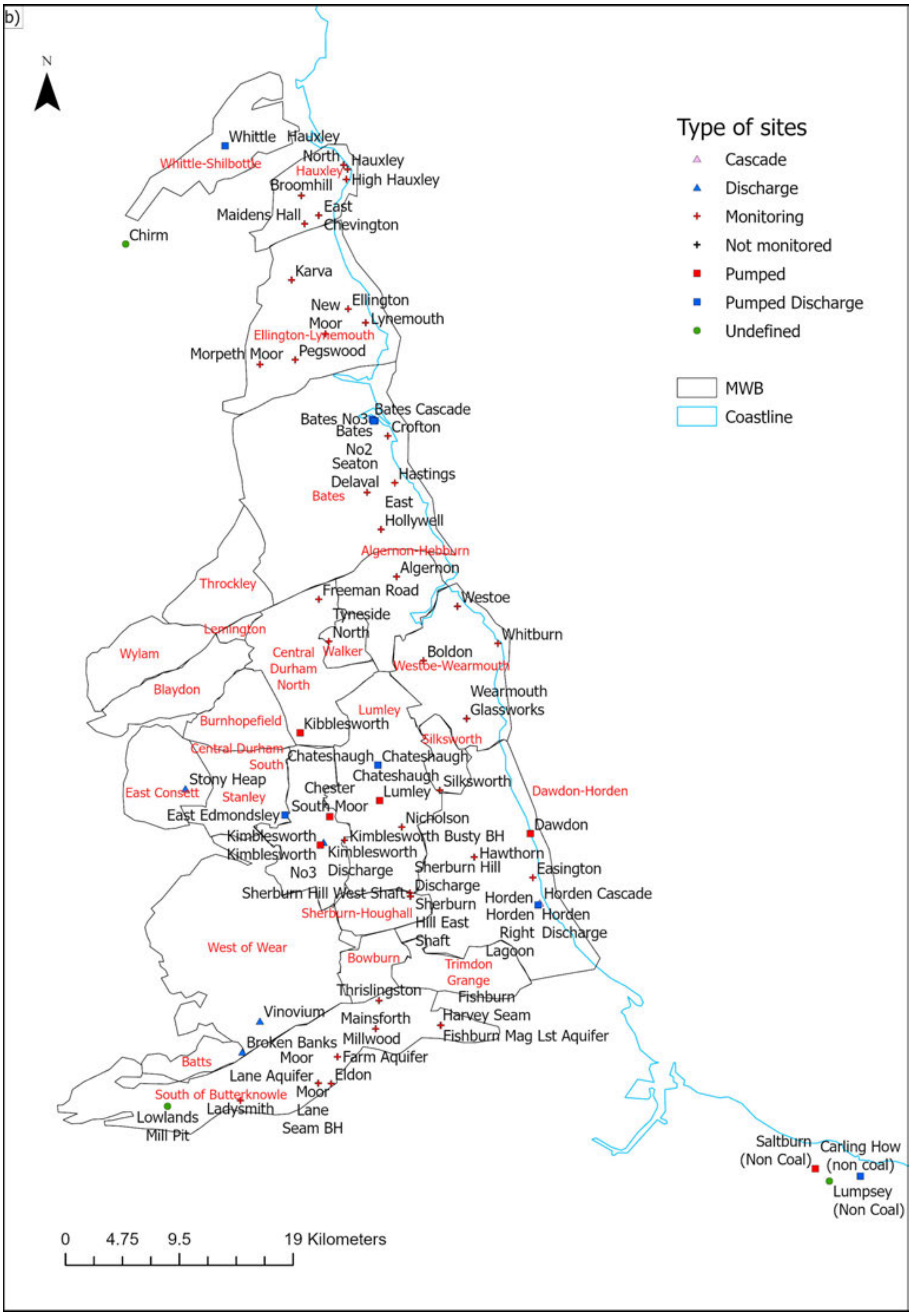

Figure 3.20: Location map for the monitoring sites in the North-East England coalfield, showing the outline of the different MWB and sub-blocks. The red and black labels are the MWB and site names, respectively (TCA data available via an academic license).

In the north part of the coalfield, the mine-water level is controlled by pumping at Bates No.3. The pumping head is kept to a minimum to minimise electricity consumption, which has allowed the coalfield to reach a natural equilibrium water level (P. L. Younger, 2016). The profiles displayed in Fig. 3.21 depict a uniform temperature distribution with depth, with a shift in temperature observed at the Bates No.3 Harvey seam and the Bates No.2 Yard G seam insets, where the MWT matches the temperature predicted by the local geothermal gradient.

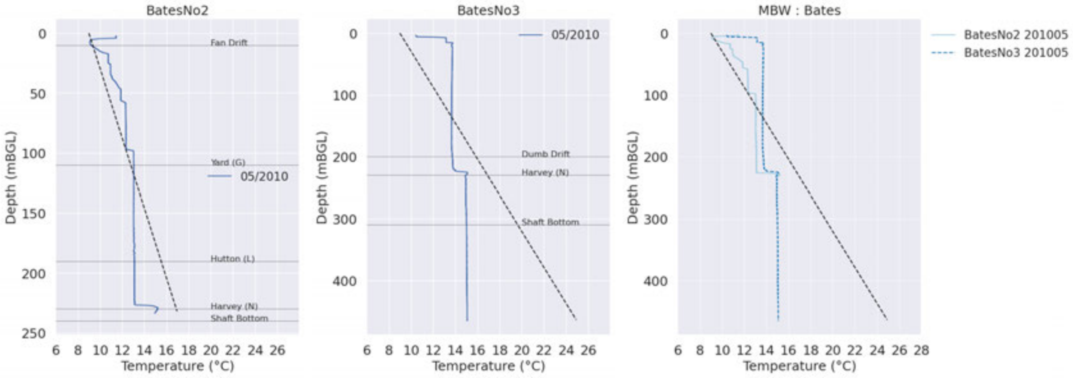

Figure 3.21: Temperature profiles in the monitoring Bates No.2 and pumped Bates No.3 shafts. The undisturbed geothermal gradient is from Farr et al. (2020). The temperature shifts at the water level depth were deleted before including the profiles in the database and avoid bias in the calculations.

North of Bates is the Ellington-Lynemouth MWB, where water is still rebounding. Connections between Bates and Lynemouth-Ellington have been described as sealed, therefore not allowing any significant flow between the two areas (K. Whitworth, 2012). Both the Ellington and Lynemouth collieries closed in 2005 after having merged into a single colliery in 1983 (K. Whitworth, 2012). In the Lynemouth and Ellington shafts, the MWT at the DE and G2 seams equal the temperature predicted by the undisturbed geothermal gradient at those depths, suggesting that most of the inflow to the shafts occurs via those respective insets (Fig. 3.22).

South of Bates is the Westoe-Wearmouth MWB, where MW has been rising at a rate of about 16 m/yr. Workings from the Westoe, Whitburn and Wearmouth collieries extend under the North Sea and are separated from adjacent collieries to the north, south and west by pillars of unworked coal. Water has been recovering since the abandonment of Westoe and Wearmouth Collieries in 1993 and all the mine workings in the area (i.e. Harton (closed in 1969), Boldon (closed in 1982), Whitburn (closed in 1968) and Hylton (closed in 1979)) were fully re-saturated by 2012 (K. Whitworth, 2012). Both the Boldon No.1 shaft and the Westoe crown shaft monitor mine-water levels in the Boldon, Westoe and Whitburn mining units (K. Whitworth, 2012). The temperature profiles in the Boldon shaft (Fig. 3.23) depict a slight linear increase in temperature between the water level and the 450 m deep Hutton seam. Whilst the MWT is higher than the temperature predicted by the undisturbed geothermal

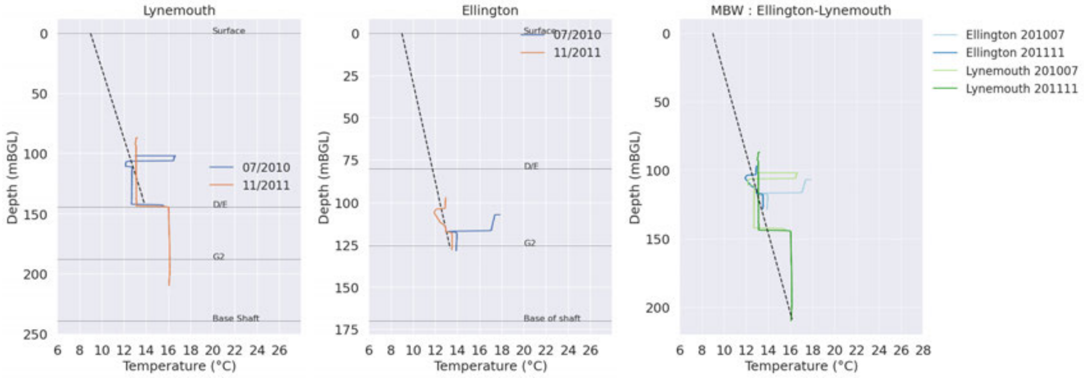

Figure 3.22: Temperature profiles for the Ellington and Lynemouth shafts. The undisturbed geothermal gradient is from Farr et al. (2020).

gradient above 200 mbgl, the temperature shifts by -7℃ at the Hutton seam, suggesting a major inflow zone. Although more complex, the Westoe Crown Shaft temperature profile tends to follow the geothermal gradient above the 923’ level (200 mbgl), below which the profile depicts a cooling along the trend of the Boldon shaft profiles. At 200 mbgl, a large cooling in the Westoe shaft is interpreted to result from the inflow of cold surface water recharge via the 923’ seam. The temperature observed at the Westoe 923’ and 1350’ levels moreover coincide with the temperatures observed at similar depths in Boldon, suggesting connections between those shafts. The Whitburn borehole, installed in 2010, was also shown to monitor the same water level as in Westoe, suggesting connections between the two areas (K. Whitworth, 2012). In the Whitburn and Wearmouth boreholes, the temperature however increases linearly with depth, suggesting that the conductive flux is dominant.

Mine-water levels in the historically called ’East of Wear’ area (i.e. including the interconnected Dawdon-Horden, Lumley and Sherburn Hill blocks, see Appendix A.2.5) are controlled by a combination of pumping at Horden and Dawdon, and by gravity discharge at Chatershaugh in the Lumley block (K. Whitworth, 2012). The Horden mine-water treatment site was commissioned in 2004, abstracting mine water from the Horden Colliery at an initial rate of 45 L/s, which increased to an average of 100 L/s in 2006 (Farr et al., 2020). In 2008, an active mine-water treatment plant became operational in Dawdon, abstracting 100 L/s from the Dawdon mine whilst the pumping rate at Horden was reduced to 50 L/s, allowing 50 L/s to be discharged at Chatershaugh (Bailey et al., 2013; K. Whitworth, 2012). Since the closure of the mines and the cessation of pumping in 1993 at Easington, mine-water levels have been continuously monitored by TCA at the Dawdon, Horden, Easington and Hawthorn shafts within the Dawdon-Horden MWB. Repeated temperature profiles have also been acquired in all four shafts since 2000, highlighting the good connectivity between the Dawdon, Easington and Horden sites despite the existence of the E-W trending Ludworth Whin Dyke splitting the Horden-Dawdon MWB into two sub-blocks (see Chapter 2).

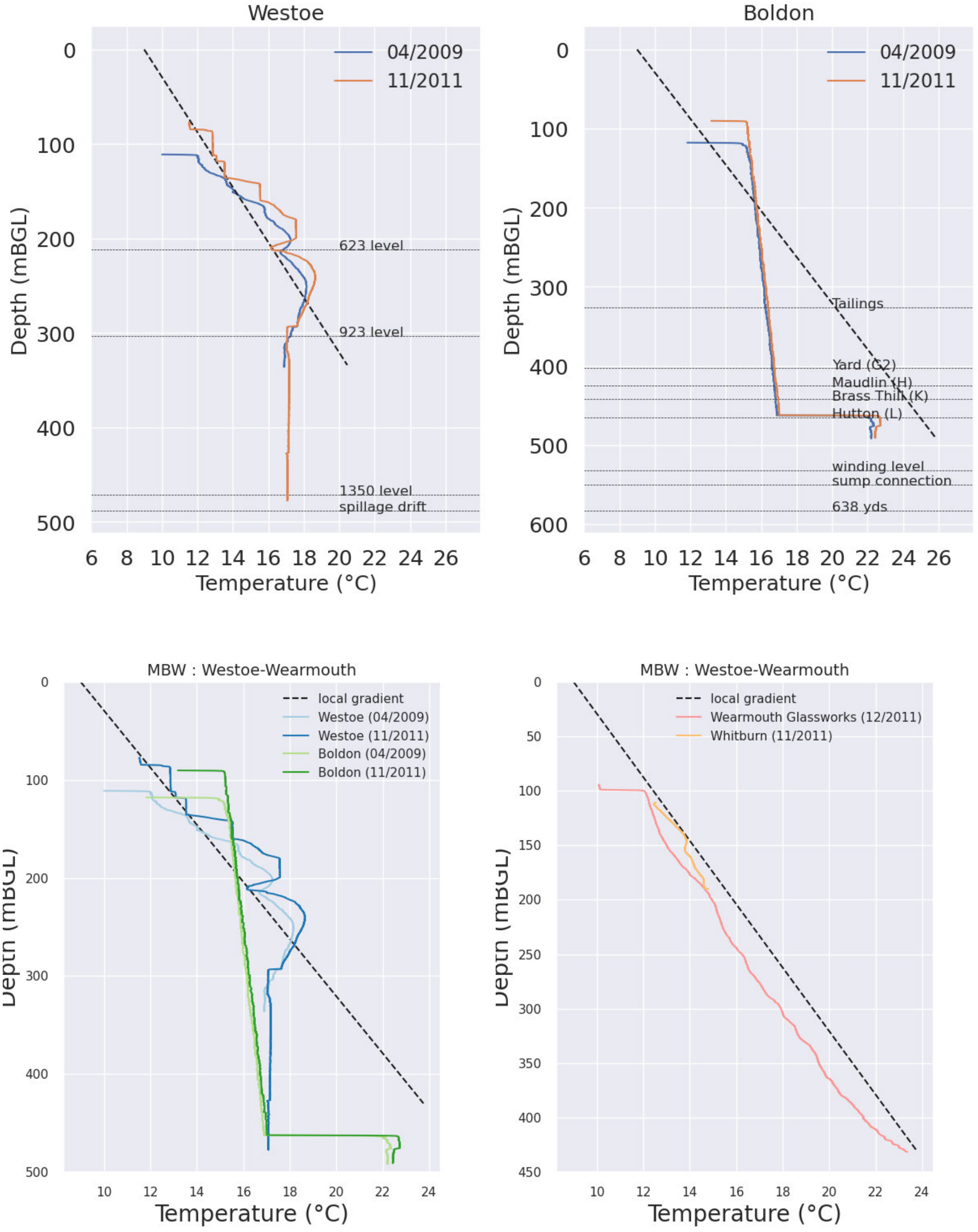

Figure 3.23: Westoe-Wearmouth shafts and boreholes temperature profiles. The undisturbed geothermal gradient is from Farr et al. (2020). Boreholes generally follow the trend of the undisturbed geothermal gradient whilst the shaft profiles display more complex temperature distribution associated with convection cells.

Temperature profiles acquired before the onset of pumping in Horden and Dawdon in 2004 and 2008, respectively, show that the temperature at the seams insets is generally slightly below the temperature predicted by the geothermal gradient in the MWB (Fig. 3.24). Mismatches between the different shafts might be interpreted as resulting from the differences in elevation and the relative depth of the seams, which are dipping toward the East. As pumping was initiated in Horden in December 2003 (with the pump at about 100 mbgl), general warming is observed at shallow depth in the Horden shaft and more significantly in the Dawdon shaft, suggesting connections between the two locations (Farr et al., 2020). More information about each shaft is provided in Appendix A.2.5 together with a detailed description of the temperature profiles (Fig. A.22).

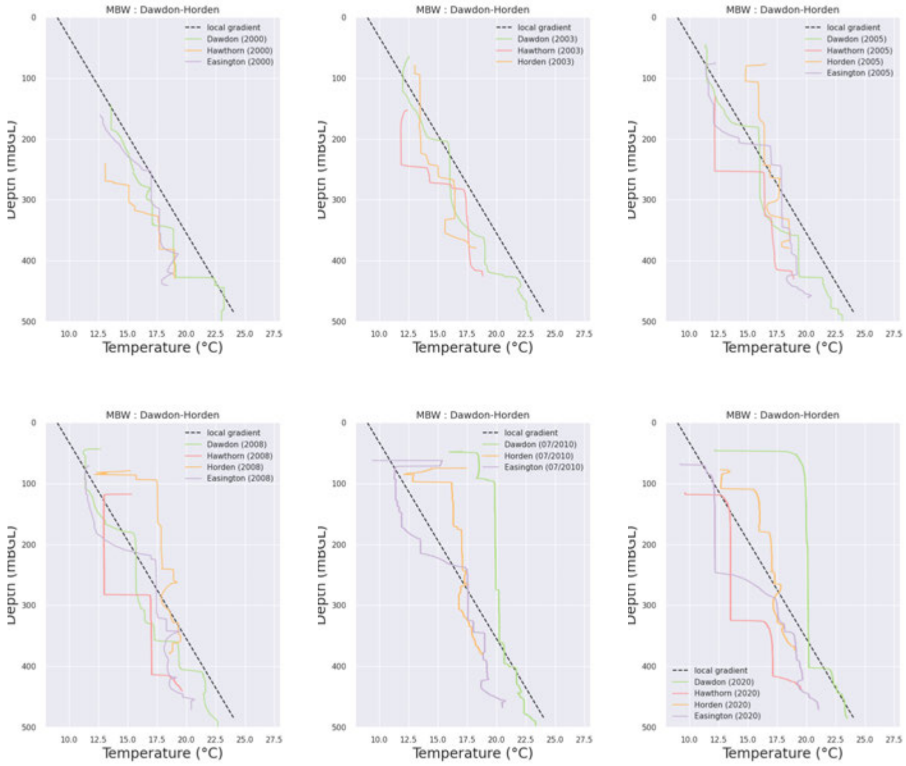

Figure 3.24: Temperature profiles for the Horden, Hawthorn, Easington and Dawdon shafts grouped per acquisition date. The undisturbed geothermal gradient is from Farr et al. (2020). Before pumping (2004), the temperature profiles depict a similar trend of increase in temperature with depth for all shafts. From the onset of pumping at Horden in 2004 and in Dawdon in 2008, warming is observed in the corresponding shaft.

To better highlight potential seam connections between the shafts (e.g. in response to pumping), the relative changes in temperature between two acquisition times were calculated for each shaft. The profiles displayed in Fig. 3.25 suggest multiple connections between the Dawdon and Easington shafts, that depict a similar warming pattern above the Easington Low Main and Dawdon Maudlin coal seams between 2000 and 2005, also visible above the

Hawthorn Low Main. This pattern is suggested to reflect the warming resulting from pumping at Horden. Similarly, Easington and Horden display a similar cooling pattern between 2005 and 2008, which reflects the cooling induced by pumping at Dawdon, observed in the top part of the Dawdon shaft. Strong warming observed above the Dawdon Low Main seam also correlates well with warming above the Horden Low Main, suggesting a strong connection between those shafts. The temperature increase along the Dawdon Theresa Shaft profile observed after a period of pumping was already interpreted by Farr et al. (2020) as the upflow of deeper, warmer waters being drawn into the shaft and replaced or mixed with cooler water. Although the Hawthorn shaft depicts similar variations in temperature as the other shafts above the Low Main seam, the general warming of the bottom half of the Dawdon shaft between 2005 and 2008 can be retrieved in the Hawthorn shaft.

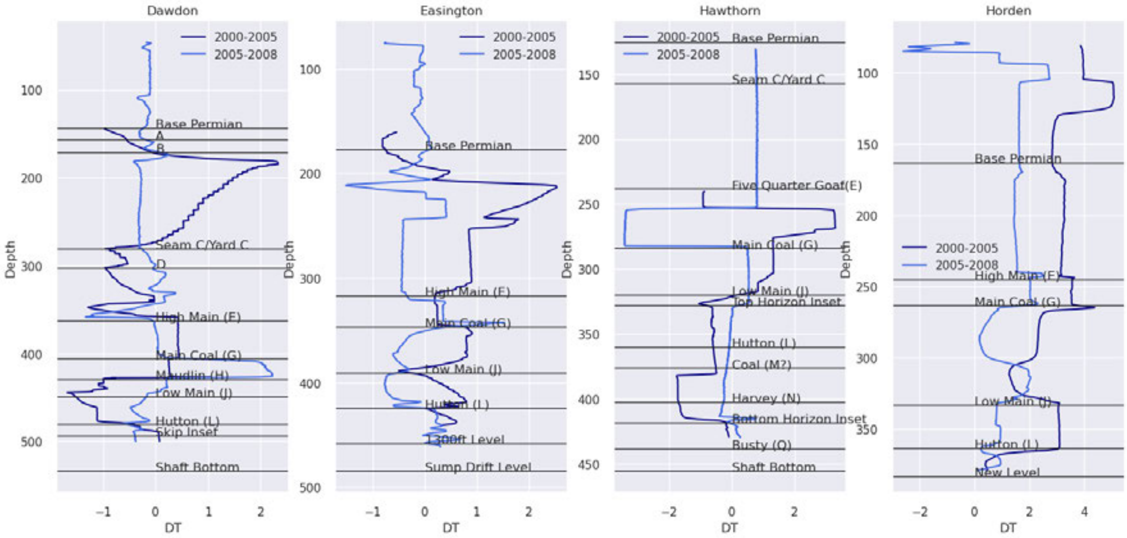

Figure 3.25: Temperature change ΔT between two acquisition dates in the Dawdon, Horden, Easington and Hawthorn shafts.

Following the cessation of deep mining in the East of Wear area, pumping at Lumley 6th resumed in 2005 to control the mine-water recovery in the Lumley MWB in addition to the construction of the gravity discharge at Chatershaugh (K. Whitworth, 2012). Pumping at Lumley 6th stopped again in 2008, resulting in a rise in mine-water levels at Lumley and Nicholsons, and a discharge to the River Wear via Chatershaugh in 2009. In Lumley, Nicholson and Chatershaugh, the temperature down to 150 mbgl tends to be greater than the geothermal gradient (Fig. 3.26). Main inflow zones can be inferred from the shifts in temperature at the Lumley and Chatershaugh Five Quarter seams whilst the shifts observed at Nicholsons correlate poorly with the depth of the deeper Main and Maudlin seams.

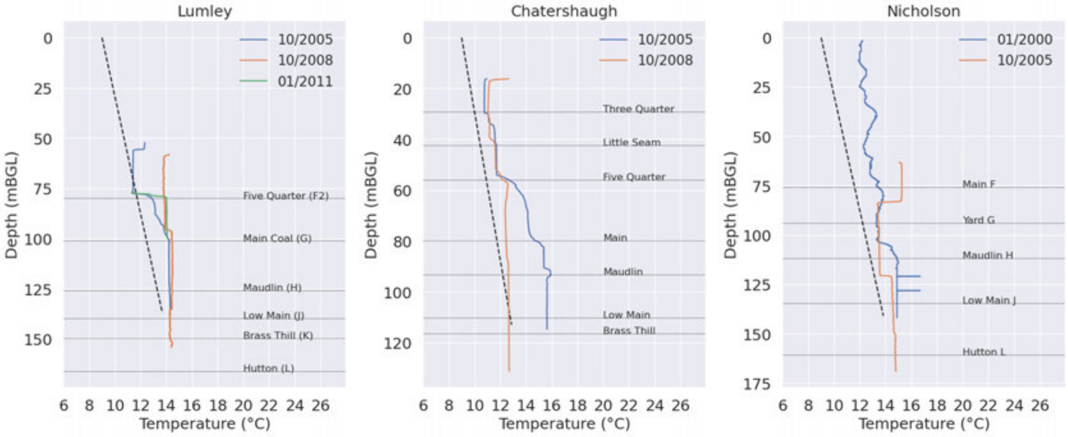

Figure 3.26: Lumley, Chatershaugh and Nicholson temperature profiles (Lumley MWB) with the depth of the seams inset in each shaft. The undisturbed geothermal gradient is from Farr et al. (2020).

The South of Butterknowle block is located in the southern part of the North-East Coalfield, where the mine water has fully recovered. The water level is monitored in the eastern part of the block at Thrislington, Mainsforth and Eldon, where the Coal Measures are concealed by the overlying Permian aquifer, and in the exposed section of the coalfield at Ladysmith and Woodhouses. Most of the shafts in this area depict cooler temperatures below 100 mbgl and warmer temperatures than the ones predicted by the geothermal gradient in the top part of the shaft, with relatively constant temperatures across the profile depth. Most boreholes depict a quasi-linear increase in temperature with depth (Fig. 3.27). The amplitude of the temperature shifts in the Thrislington and Mainsforth shafts are limited, mostly focused around the Thislington Low Main seam, the Mainsforth Yard and the Mainsforth Bottom Hutton seam in the earlier acquisition times. From 2013, a general warming observed above the Mainsforth Bottom Hutton seam and Thrislington Low Main seam tends to equalise the temperature along the profile depths and erases the temperature shifts at shallower depths.

Other temperature profiles available for the North-East Coalfield (Fig. 3.28) suggest that:

- As for all boreholes described in the previous MWB, the Hauxley North borehole displays a linear increase in temperature with depth. However, the gradient is much lower than the undisturbed gradient calculated by Farr et al. (2020) for the North-East Coalfield.
- The Blenkinsopp shaft, located in an isolated block, displays a significant change in the depth of the temperature shift between 2008 and 2010, from about 50 mbgl to 90 mbgl. Following the cessation of mining in the area, mine water was allowed to recover to near the surface before pumping and treatment at the Smallburn Shaft by TCA started in January 2005. The Blenkinsopp pumping borehole was then installed in 2006, abstracting mine water from shallow workings at a rate of about 15 L/s (K. Whitworth, 2012).

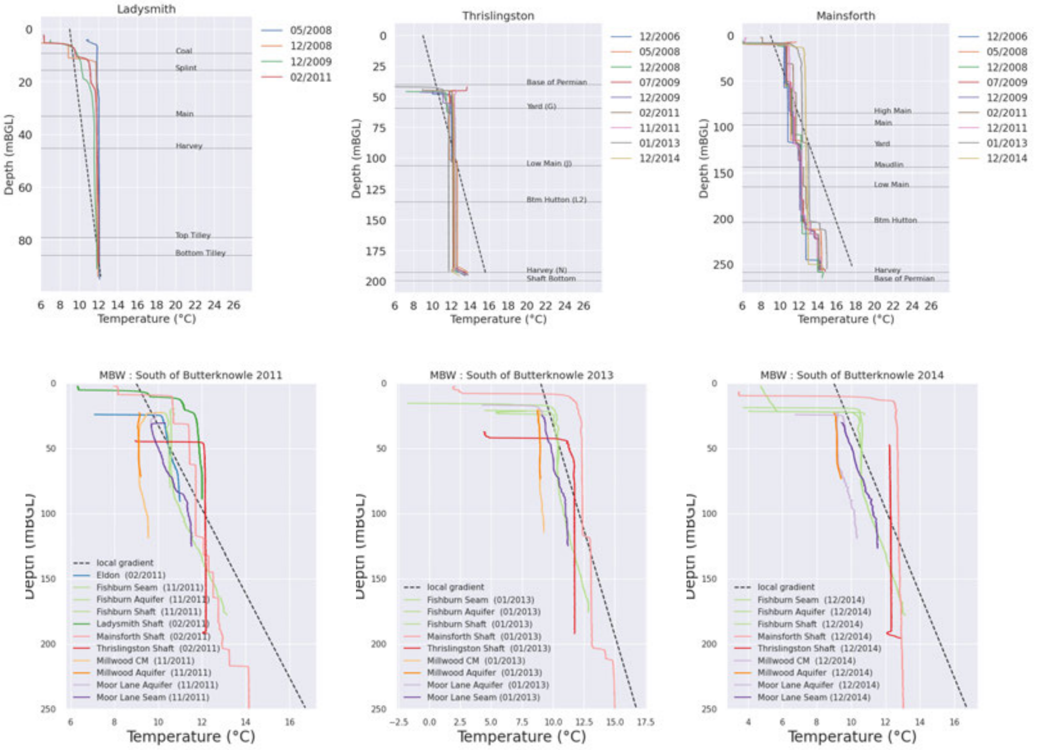

Figure 3.27: South of Butterknowle shafts profiles. The undisturbed geothermal gradient is from Farr et al. (2020). The temperature shifts at the water level depth were deleted before including the profiles in the database and avoid bias in the calculations.

- In Central Durham South, the pumped Kimblesworth and Chester South Moor shafts display a similar temperature distribution pattern, with a 2-3 ℃ temperature shift at about 120 mbgl and 110 mbgl, respectively. Those shafts are located 2.5 km away from each other, west of the Lumley Block. Kibblesworth, the pumping station used to control the mine-water level in Central Durham North, displays a uniform temperature distribution of about 14 ℃, which corresponds to the temperature predicted by the geothermal gradient at about 175 mbgl. All three sites, Kibblesworth, Kimblesworth and Chester South Moor, were initially pumping stations used to protect the operational collieries between Ryhope and Horden to the east (K. Whitworth, 2012). Together with the discharge at Chatershaugh, those are still used to control the water level in the interconnected collieries in Central Durham, pumping at an average rate of about 350 L/s, 220 L/s and 130 L/s since 1999, respectively (K. Whitworth, 2012).

- The temperature in the monitoring Vivonium shaft coincides well with the temperature at Chester South Moor, suggesting potential connections between the blocks. Vivonium is located in the West of Wear Block, situated in the southern part of the North-East Coalfield, just north of the South of Butterknowle block (e.g. Mainsforth-Thrislington block) and south of Central Durham North. Historically, the closure of the Vivonium pumping station was associated with the construction of a controlled gravity discharge at Page Bank (K. Whitworth, 2012).
- In the monitoring Sherburn hill shaft, a temperature shift at about 130 mbgl matches well the temperature predicted by the undisturbed geothermal gradient at that depth, whilst the temperature is constant below that depth and therefore cooler. Sherburn Hill is located in a MWB neighbouring Dawdon-Horden to the west and south of the Lumley MWB, which are both pumped. However, no connection has been identified between those MWB, making Sherburn Hill a rather isolated block.

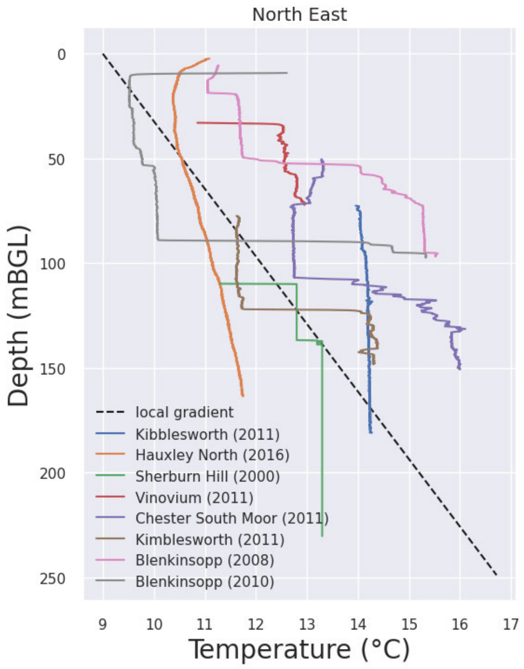

Figure 3.28: Other North-East Coalfield shaft profiles, including the pumped Kibblesworth, Kimblesworth, Blenkinsopp and Chester South Moor shafts, the Sherburn Hill and Vinovium monitoring shafts, and the Hauxley North monitoring borehole. Those are located in different MWB. The undisturbed geothermal gradient representing the average gradient across the NE coalfield is from Farr et al. (2020). In profiles where a temperature shift is observed at the water level depth, the upper ∼2 meters were deleted before including the profiles in the database and avoid bias in the calculations.

3.4.2 Spatial and temporal correlations between monitoring data

Temperatures profiles

The geodatabase is used to analyse the relationship between the calculated average temperature and mean depth calculated for each temperature log. When plotting all the types of sites together (Table 3.2), a good linear correlation is found between the average temperature and the average logging depth, with a gradient of 24℃/km (Fig. 3.29), in accordance with the median geothermal gradient of British coalfields calculated by Farr et al. (2020). The average profile temperature is also linearly correlated to the water level, although a gradient of only 12.5℃/km is calculated when all the sites are plotted together. A large range of temperature can indeed be observed for a given water level, with some coalfields displaying cooler surface water at greater depths, such as in the rebounding Nottinghamshire shafts or monitoring Yorkshire shafts. This suggests that as the rebound is not completed, the system has not returned to thermal equilibrium yet. This is discussed further in the next section.

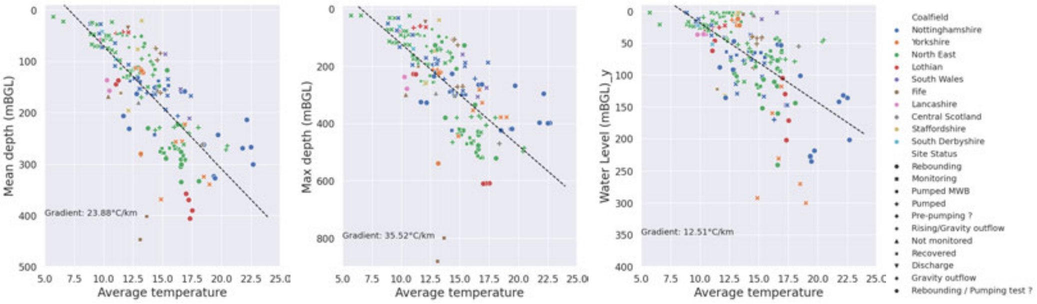

Figure 3.29: Relationship between the average shaft temperature (℃) and the water level, the mean depth and the shaft/boreholes depth for each temperature log. Data points are classified per type of site at the time of acquisition (Table 3.2) and coloured per coalfield. When considered together, a linear relationship best describes the relationship between the average temperature and the considered variable. The strongest relationship is observed for the maximum measured depth, with a gradient of 35.5℃/km.

When looking at the monitoring shafts only, the average profile temperature and depth depict a best-fitting gradient of 28℃/km. Similarly, a good correlation exists between the average log temperature and the maximum shaft depth, with a calculated gradient of 36℃/km. Rebounding sites in the Lothian Coalfield and in Nottinghamshire however depict lower average temperatures at greater depth and higher temperatures at shallower depth, respectively, whilst colder average temperatures are observed in the deep monitoring shafts in the pumped Fife Coalfield (Fig. 3.30).

Type	Definition	System	Limitations
Pre-pumping	Data acquired before pumping implemented in the shaft/borehole	Unknown	
Rebounding	Data acquired in MWB where the water level actively rising	Dynamic	
Recovered	Monitored shaft/borehole where the water rebound is completed	Static	
Pumped	Pumping implemented in the shaft/borehole where the data is acquired	Dynamic	
Pumped MWB	Data collected in an unpumped shaft/borehole located in a pumped MWB	Dynamic	Monitored site could be out of the zone of influence of the pumped site
Discharge	Data acquired at a surface discharge	Outflow	Surface data
Rising/gravity outflow	Site located in a rebounding MWB and/or discharging at the time of acquisition	Dynamic	Status applying to the MWB and not the site where data is acquired
Monitoring	Not described as rebounding or pumped	Unknown	Can include recovered MWB
Pumping test	Data acquired during a pumping test	Dynamic	Not the natural state

Table 3.2: Summary of the classification for the different types of sites. Each category is based on TCA terms and defines the type of site at the time of acquisition of a given dataset.

Time series

Loggers have been installed in monitoring boreholes and shafts to continuously monitor changes in water level, near-surface water temperature and/or flow rate over time. The average of those time series is used to analyse the potential relationship between the near-surface temperature at a given site, the measured flow and water level and the probe depth. The objective is to get a first insight into the potential effect of the hydraulic and measurement settings on the observed MWT, which will be investigated numerically in chapters 6 and 7.

Results first suggest two trends of increase in temperature with increasing logger depth (Fig. 3.31). Whilst temperatures ranging from 10℃ to 17℃ can be measured for a probe situated just below the water table in most discharged and pumped sites (i.e. for mAP < 1 m, with mAP expressing the water level in meter above probe), the average temperature in monitoring sites tends to increase quasi-linearly with an increase in the probe depth. Similarly, the near-surface water temperature appears to be slightly dependent on the depth of the water level

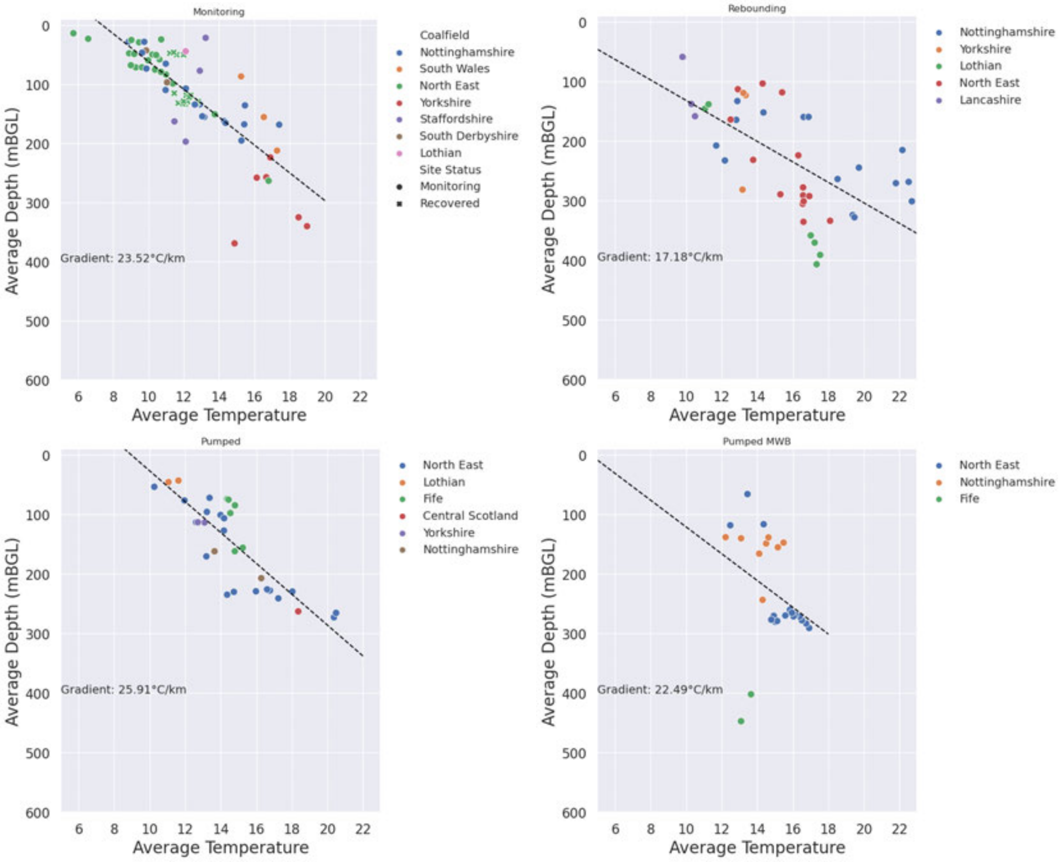

Figure 3.30: Relationship between the average MWT calculated from the monitoring, pumped and discharging coalfields (°C) and the average profile depth.

and the flow rate (see Fig. A.19), increasing at a linear rate of only 4°C/km when plotting all the sites together. When looking at monitoring sites only, the average probe temperature is found to increase with increasing water level depth at a rate of 26°C/km (not displayed on the figure). This suggests that the near-surface temperature depends on the geothermal gradients in monitoring sites, where equilibrium between the mine water and surrounding rock might exist.

3.4.3 Cross-correlation analysis

This section analyses the relationships between the average MWT calculated from TCA dataset, the undisturbed rock temperatures available in the literature and the local geology. In addition to looking at the relationship for each acquisition/site, values averaged at the scale of the MWB and/or coalfield (e.g. MWT, undisturbed geothermal gradient, heat conductivity, heat capacity) are used to mitigate the potential effect of outliers, errors in the estimates that might occur when looking at each site individually, and lack of data.

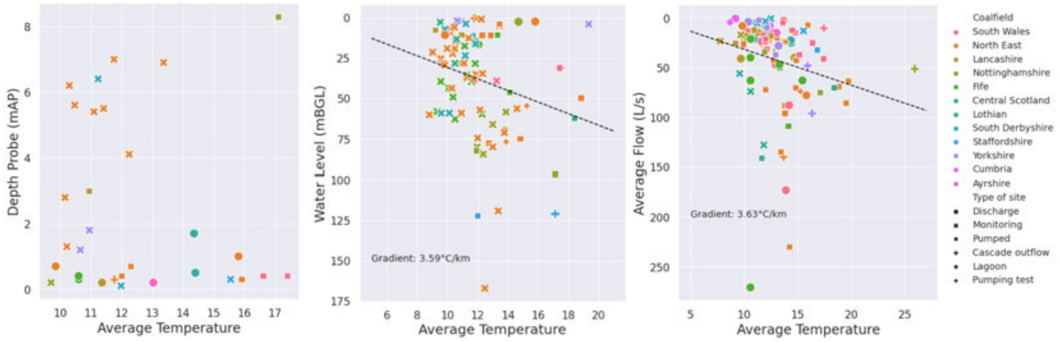

Figure 3.31: Relationship between the average temperature of the selected time series (℃) and the probe depth relative to the water table (meters above probe or mAP), the water level, and the flow rate.

Effect of pumping, water rebound and discharges on MWT

Overall, the monitoring temperatures acquired by TCA (i.e. LOG and time series) confirm a good linear relationship between the average temperatures and the depth of the measurements. Plotted together, results for each acquisition suggest an increase in the average temperature per increasing mean depth of 24℃/km, in accordance with Farr et al. (2020). Taken separately, pumped and monitoring sites depict a higher gradient of 26℃/km (Fig. 3.32). This suggests that deeper waters are generally warmer, following the effect of the geothermal gradient. No clear correlation is however observed between the average temperature in discharge areas and the acquisition depth (only of 3℃/km), where the temperature of minewater reaching the surface is expected to be impacted by the air temperature.

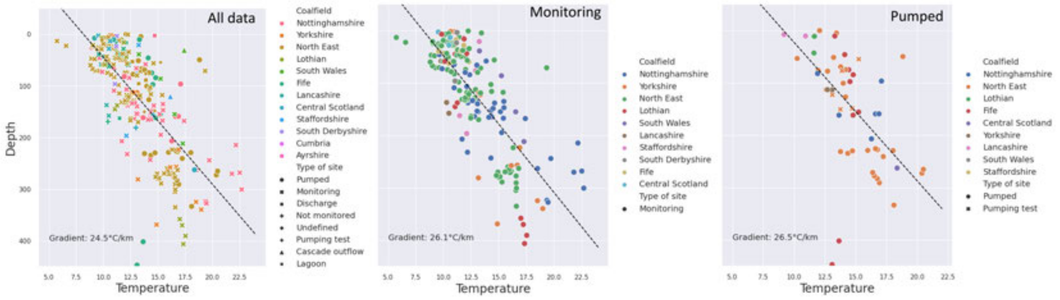

Figure 3.32: Relationship between the average coalfield MWT (℃) and the measurement depth (mbgl) for all data, the monitoring sites only and the pumped coalfields only.

The same observation is made when comparing the average temperatures to the water level, with the MWT in monitoring, pumping and discharging/rebounding shafts generally increasing as the depth to the water level increases, at a rate of about 11℃/km (Fig. 3.33).

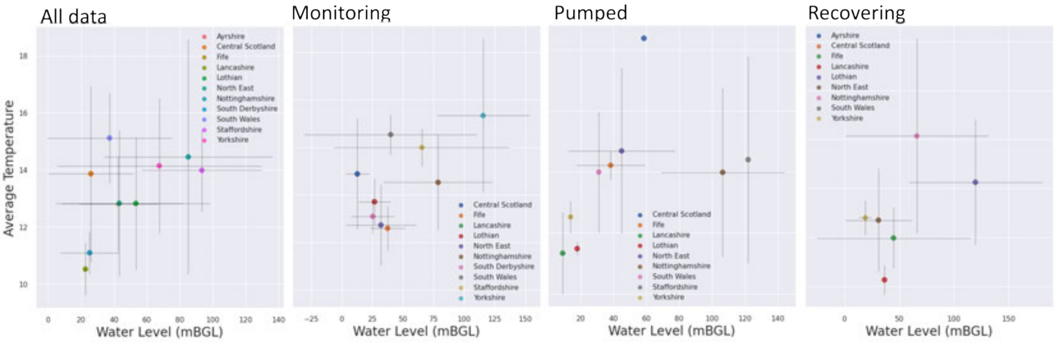

Figure 3.33: Relationship between the MWT collected by TCA (℃) and the monitored water level for all data, for the monitoring sites only, the pumped coalfields only and the rebounding/discharging sites only, averaged at the coalfield scale. The pumped data include the 'pumped' and 'Pumping tests'. The rebounding data include the 'Rebounding', 'Rising/Gravity outflow', 'Recovered', 'Discharge' and 'Gravity outflow' data. The vertical and horizontal lines represent the range of temperatures and water levels within each coalfield (i.e. minimum and maximum values), respectively.

Equilibrium and monitored temperature

To verify the hypothesis of the control of the geothermal gradient on the MWT, the average MWT dataset is compared to the historical temperatures and equilibrium geothermal gradients from Burley et al. (1984) and Farr et al. (2020). Given the limited number of historical measurements available in the BGS UK Geothermal Catalogue relative to the number of mine-water monitoring sites managed by TCA, both datasets are here averaged at the scale of the coalfield to reduce the scattering effect of single acquisitions. Results suggest that the average MWT in coalfields generally increases with increasing geothermal gradient (Fig. 3.34), although this trend is less notable when using the temperature gradients from Farr et al. (2020).

The large variability in both the historical gradients and MWT within a given coalfield suggested by the extensive error bars in Fig. 3.34 indicates a potential influence of other controlling factors on the thermal state of the mines. To better characterise the potential discrepancies between the monitored MWT and predicted undisturbed geothermal gradient, the full monitoring temperature dataset (i.e. TCA LOG and time series) averaged at the coalfield scale is plotted against the corresponding average for the historical/equilibrium temperature gradients (Burley et al., 1984; Farr et al., 2020), accounting for the state of the MWB at the time of acquisition (i.e. rebounding, pumped, discharging). Results presented in Fig. 3.35 suggest a positive linear relationship between the different datasets that is the strongest for the pumping sites (i.e. 0.22℃/(℃/km)) compared to the monitoring (i.e. 0.02℃/(℃/km)) or discharging/rebounding coalfields (i.e. 0.16℃/(℃/km)).

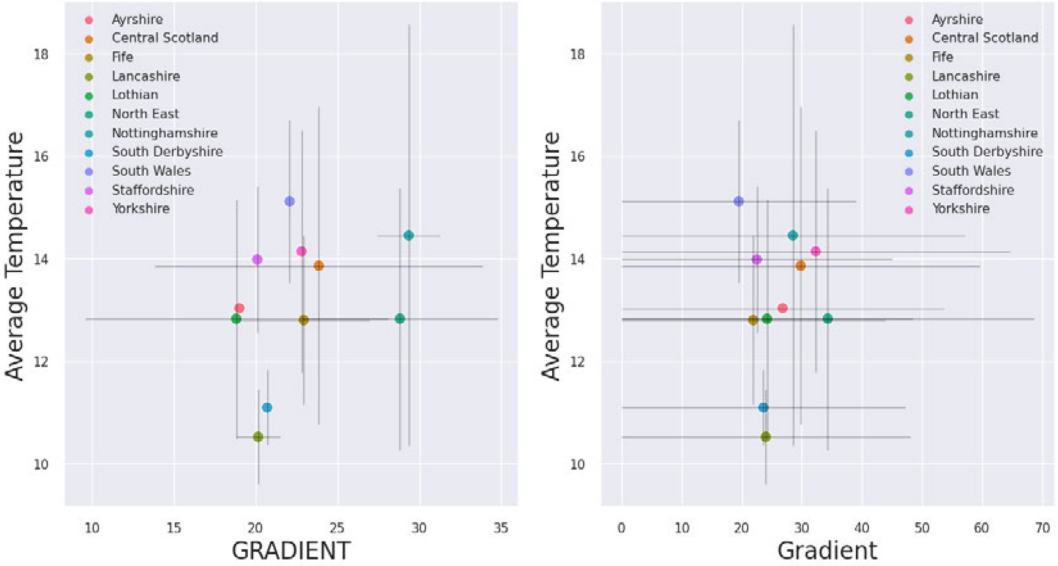

Figure 3.34: Relationship between the average coalfield logging/profile temperature (℃) collected by TCA and the historical temperature gradients (℃/km) from Burley et al. (1984) (left) and Farr et al. (2020) (right) averaged at the coalfield scale. The vertical and horizontal lines represent the range of temperatures and temperature gradients within each coalfield (i.e. minimum and maximum values), respectively.

Return to equilibrium

The data is examined to ascertain the potential effect of a slow thermal recovery following the cessation of mining activities. The linear regression performed on the full data set (i.e. temperature profiles and time series) suggests that the average MWT decreases as the time since abandonment increases, with mines being closed more recently generally displaying higher average MWT (Fig. 3.36). This relationship is somewhat unclear and the distribution of the data points highly depends on the coalfield and site status, with both pumped and monitored temperatures covering a large range of temperatures. In Nottinghamshire, the rebounding mine water gets cooler as the time since abandonment increases whilst the reversed effect is observed in the North-East Coalfield. This suggests that the cooling or warming effect of rebounding mine water might depend on the nature of the hydraulic recharge or the local geology.

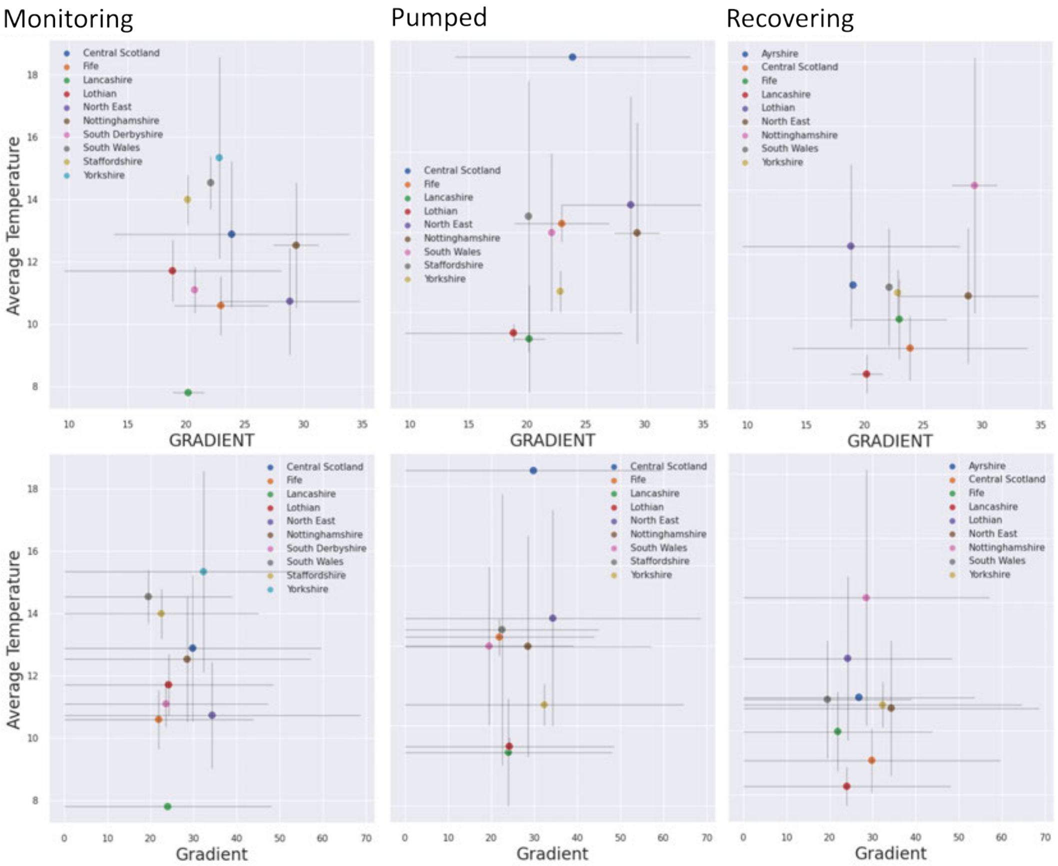

Figure 3.35: Relationship between the average logging and profile MWT (℃) and the historical gradient (℃/km) from Burley et al. (1984) (top row) and Farr et al. (2020) (bottom row) for the monitoring, pumped and recovering/discharging coalfields. The pumped data include the 'pumped' and 'Pumping tests'. The rebounding data include the 'Rebounding', 'Rising/Gravity outflow', 'Recovered', 'Discharge' and 'Gravity outflow' data. The vertical and horizontal lines represent the range of temperatures and temperature gradients within each coalfield (i.e. minimum and maximum values), respectively.

Statistical rock type distribution and temperature correlation

The potential effect of the geology on the thermal state of the mine is finally investigated at both regional and national scales. Here, the relationships between the historical geothermal gradients from Burley et al. (1984) and the subsurface thermal characteristics determined from the relative distribution of rock types in the corresponding or neighbouring borehole/shaft are first analysed (Fig. A.17). To reduce the scattering effect induced by the use of discrete values and overcome the effect of a limited number of historical temperature measurements from Burley et al. (1984), the analysis is then repeated using the more comprehensive dataset

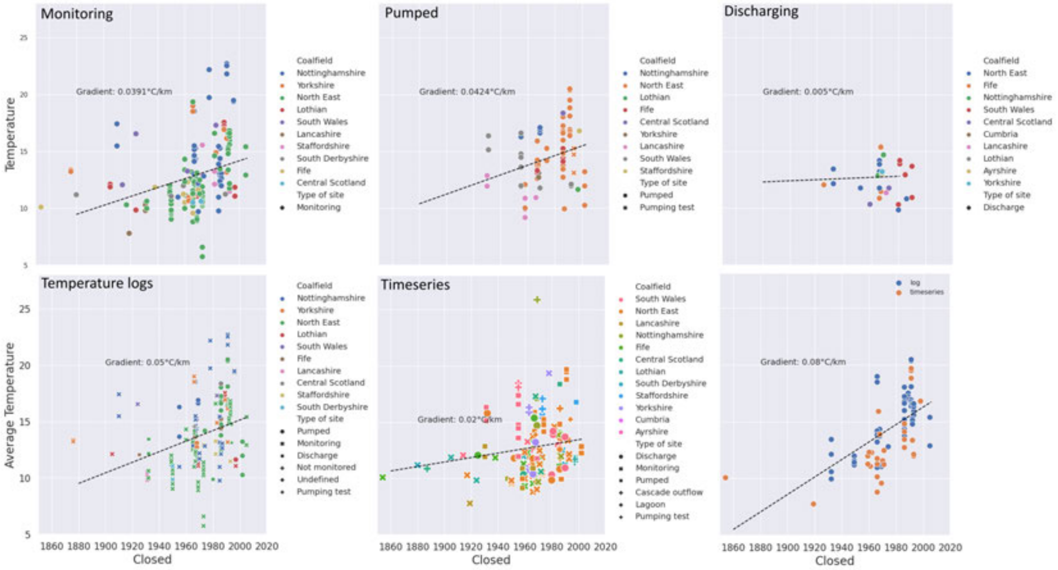

Figure 3.36: Relationship between the MWT collected by TCA (℃) and the time since abandonment (i.e. closing date) for the monitoring sites, the pumped coalfields and the discharging sites, classified by coalfield. The top row analyses those relationships for all data. The bottom row looks at results for the temperature profiles and time series individually and for data where geological logs are available only.

compiled by Farr et al. (2020), which provides the equilibrium temperature gradients at the coalfield scale. To do so, the harmonic mean rock thermal property values for each borehole are averaged at the coalfield scale (Fig. A.16). A similar analysis is presented in Appendix A.2.4 for values being averaged at the MWB scale (Fig. A.18).

Results suggest that the equilibrium temperature gradient increases with increasing subsurface heat conductivity. When averaged at the coalfield scale (Fig. 3.37), this relationship is more pronounced when using the geothermal gradients from Farr et al. (2020), which were calculated accounting for the local average surface temperatures within coalfields. This approach is suggested to improve the estimates of the geothermal gradient relative to the approach from Burley et al. (1984), where a uniform surface temperature of 9 ℃ was assumed at the scale of the UK (see discussion in section 3.5.2). This hypothesis is supported by the relatively clear linear relationship observed between the harmonic mean thermal conductivity of single boreholes within the same coalfield and the geothermal gradient from Burley et al. (1984), despite larger discrepancies observed for the Queenslie and Maryhill boreholes (Fig. A.17). Based on Eq. 6.1, this analysis suggests that the geothermal heat flux increases in coalfields where the geothermal gradient is the highest.

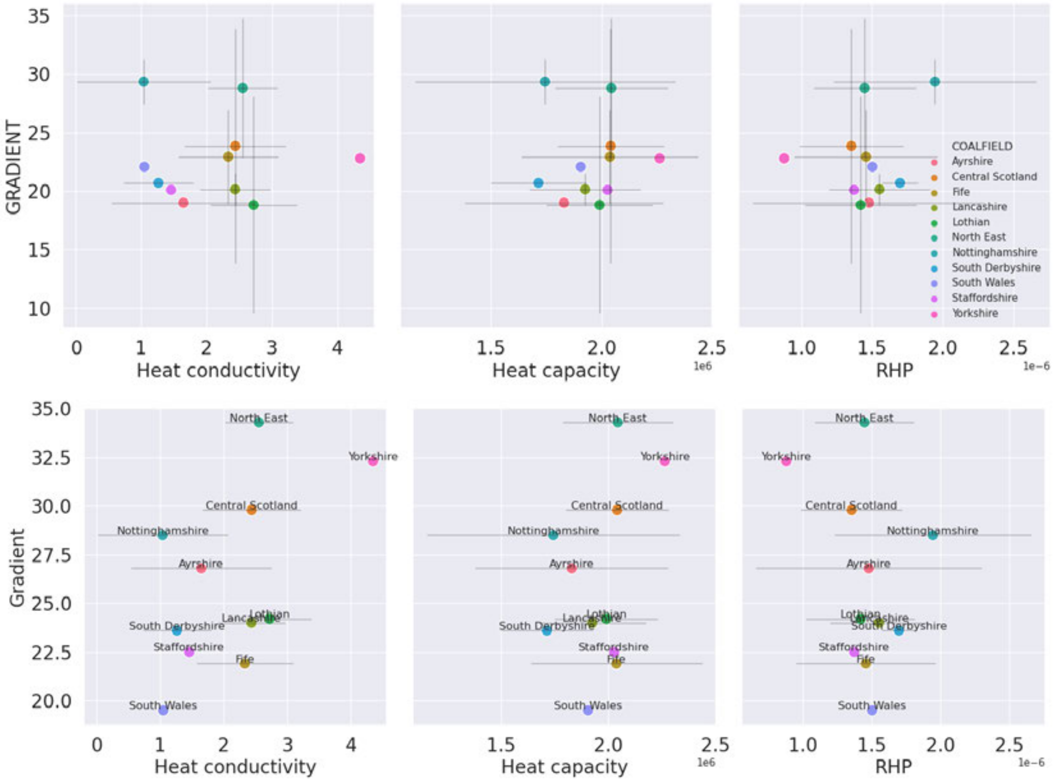

Figure 3.37: Relationship between the harmonic mean heat conductivity (W/℃.m), heat capacity (J/℃.kg), and RHP (μW/m^3) and the geothermal gradient (℃/km) from Burley et al. (1984) (top row) and Farr et al. (2020) (bottom row), averaged at the coalfield scale (Fig. A.12). The vertical and horizontal lines represent the range of temperature gradients and property values calculated for each coalfield (i.e. minimum and maximum values), respectively. A positive linear relationship can be inferred between the conductivity and the geothermal gradient, especially using the dataset from Farr et al. (2020). However, the heat capacity and RHP is relatively independent from the gradient.

On the other hand, no clear trend is observed between the geothermal gradient and the volumetric heat capacity calculated from each borehole (Fig. A.17) or at the coalfield (Fig. 3.37) and MWB (Fig. A.18) scales. Although an increased RHP is expected to increase the amount of heat produced in the system, its effect on the equilibrium temperature gradient is also negligible.

In parallel, the effect of the local geology on the MWT monitored by TCA is analysed, accounting for the nature of the site at the time of acquisition (Fig. 3.38). Here, the trend between the heat conductivity and the MWT is somewhat reversed compared to the one observed for the historical temperatures, with the average apparent MWT in mine shafts decreasing with increasing subsurface heat conductivity. This is particularly true for the monitoring sites. The MWT also slightly increases with increasing rock heat capacity when looking at the full data set, whilst the RHP does not clearly impact the MWT.

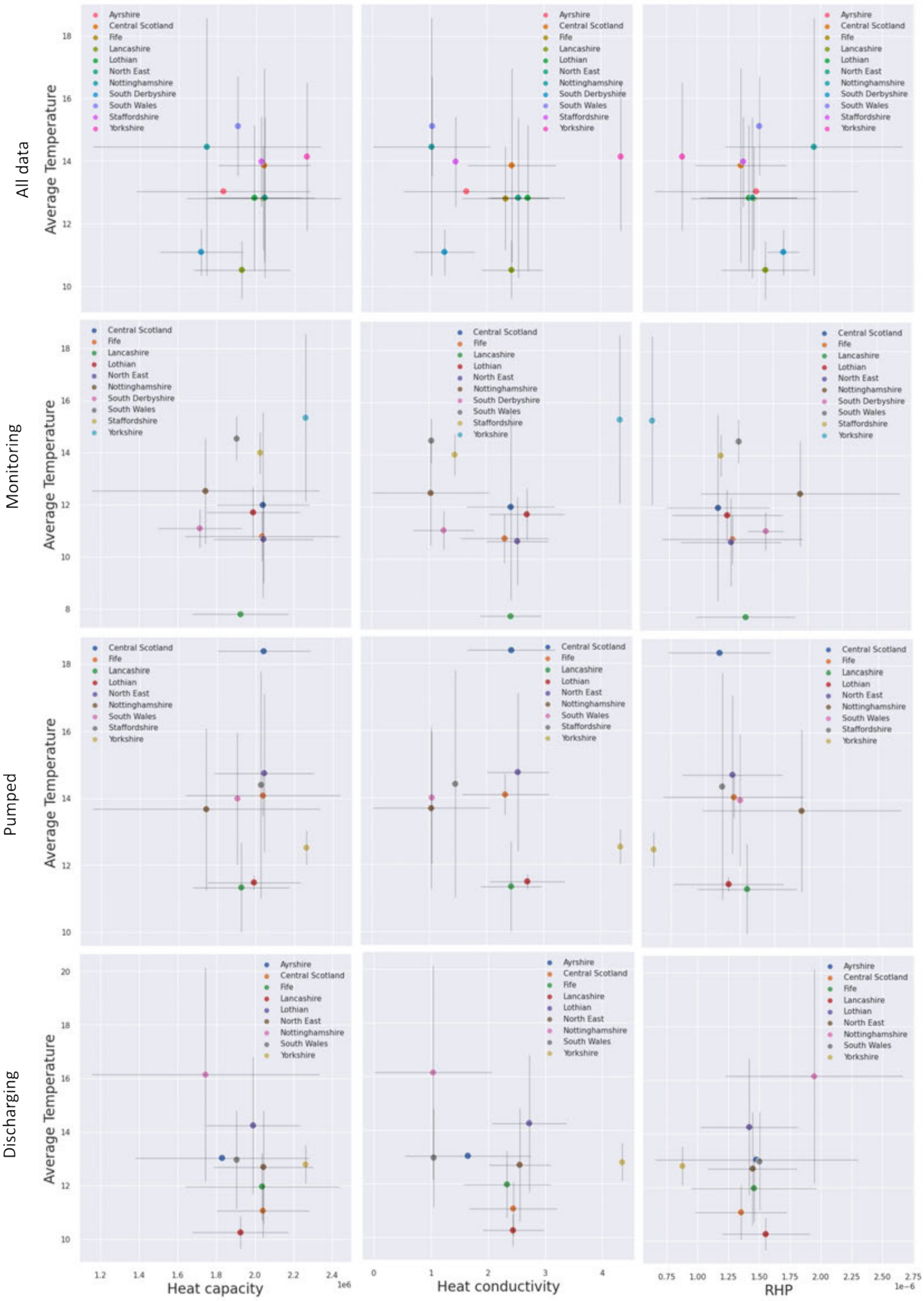

Figure 3.38: Relationship between the average MWT calculated from the monitoring, pumped and discharging coalfields data and the averaged rock property values (heat capacity (J/℃.kg), heat conductivity (W/℃.m), and RHP (μW/m^3)) within the coalfield. The vertical and horizontal lines represent the range of temperatures and property values calculated for each coalfield (i.e. minimum and maximum values), respectively.

3.5 Discussion

3.5.1 Data limitations, measurement errors and uncertainties

The data analysis presented in this chapter is subject to many uncertainties and unknowns linked to the nature of the data and potential processing errors. This includes:

- the lack of undisturbed pre-mining temperature data and geological data across the coalfields for each corresponding well. This makes it difficult to have a representative and detailed statistical distribution of the geology within a coalfield.
- uncertainties in the estimated undisturbed geothermal gradients from the literature. This includes uncertainties in the approaches used by Burley et al. (1984), in the datasets used by Farr et al. (2020) or in the extent of the corrections for paleo-climate applied.
- the lack of monitoring data and consistent parameters (e.g. water level, flow rate, logger depth) measured at each monitoring site. Not all sites monitored for water level are monitored for temperature, and only a few sites have repeated temperature profile acquisitions, which makes it impossible to perform a systematic analysis of spatial (i.e. through interconnected parts of a mine) and temporal changes (i.e. as the hydraulic state of the colliery changes) in temperature for those sites.
- the lack of information on the pump set-up (e.g. depth) for each acquisition and uncertainty in the type of measured parameters (i.e. mBGL, mAOD, mAP) that might lead to false interpretations. The depth of the measurement and/or relative to the water level is often unknown, which limits the significance of the data.
- potential errors in the digitising of geological logs and the categorising of ’rock types’ (Table A.14)
- uncertainty in the values of rock properties (extracted from the literature) that might vary between locations
- the use of averaged and unprocessed time series of temperatures and water level without accounting for the change in the state/the hydrodynamic of the mine.
- the unknown state of the mine at the time of acquisition for some temperature profiles
- the absence of seams inset depths for many temperature profiles.

3.5.2 Geothermal heat flux and paleo-gradient

The data correlation and statistical analysis suggested the key control of the geothermal gradient on the observed average MWT in shafts, with the average shaft temperature increasing with the deepening of shafts and the seams accessed. Determining the relative contribution of the purely conductive geothermal heat flux on the thermal state of mines however requires a proper estimate of the undisturbed geothermal gradient. This is challenging, as most temperatures have been measured in operational mines and could be disturbed by mining or by the convective heat flow resulting from mine-water circulation in rebounding or flooded mines.

Several methods have been used in the past to calculate the geothermal gradient. Theoretically, the geothermal gradient is determined by calculating the temperature difference (Δ T) between the measured temperature at depth and the yearly mean average surface air temperature (T_S) divided by the depth at which the subsurface temperature was measured (Everett, 1986). In the Geothermal Catalogue for the UK, Burley et al. (1984) calculated the geothermal gradient from available temperature measurements in UK boreholes. The surface temperature was calculated based on the average sea level temperature for the UK, adding 1 ℃ to account for the difference in air-land surface temperature and deducing 0.6 ℃ for every 100 m elevation above sea level. More recent studies however suggested that the subsurface temperature tends to equal the yearly average mean surface temperature down to a depth of 10 mbgl (Banks, 2012). Although this threshold depends on the rock type and amplitude of the yearly air temperature variations, it suggests that the mean air temperature can directly be used to assess the near-surface temperature.

Historical data available for boreholes compiled in the geodatabase (Fig. A.10) overall suggested a good linear relationship between the temperatures and measurement depths (Fig. 3.39). When plotting data for all the coalfields, this gradient averages 34.5 ℃/km, which is higher than the median geothermal gradient of 24.1 ℃/km calculated by Farr et al. (2020) using a more comprehensive dataset. This dataset included the BGS UKGC data, in-situ coal strata temperatures measured in operational mines and unpumped MWT measured more recently by TCA. A key limitation of the gradients calculated in Burley et al. (1984) lies in the use of the same air surface temperature of 9 ℃ averaged at the scale of the UK, which does not account for localised variations and might therefore overestimate or underestimate the gradient in some coalfields. By using deep offshore borehole temperatures and averaging values at the scale of the MWB, and utilising regional yearly mean surface air temperature values, Farr et al. (2020) optimised the estimates of the local geothermal gradient in some of the coalfields. However, discrepancies might be generated at the UK scale from the lack of data in some areas, and by ignoring the effect of the nature of the recharge that might disturb the purely conductive geothermal gradient.

Despite temperatures measured below 1.5 km depth being assumed to be only little affected by surface perturbations, several studies moreover mentioned the importance of considering the effects of past climatic variations on the shallow geothermal gradient at high latitudes (i.e. Gosnold, Majorowicz, Klenner, and Hauck (2011); Majorowicz et al. (2012); Raymond (2018)). Paleo-climate signals have been described as a series of mean surface temperature changes before the present day, that propagate downward by conduction and tend to superimpose onto the quasi-steady state thermal field associated with the Earth's internal heat, from which heat fluxes are calculated (Beltrami, Matharoo, & Smerdon, 2015). While the extent of the perturbations mainly depends on the magnitude and time scale of the past temperature variations, the amplitude of the temperature change due to surface disturbances tends to

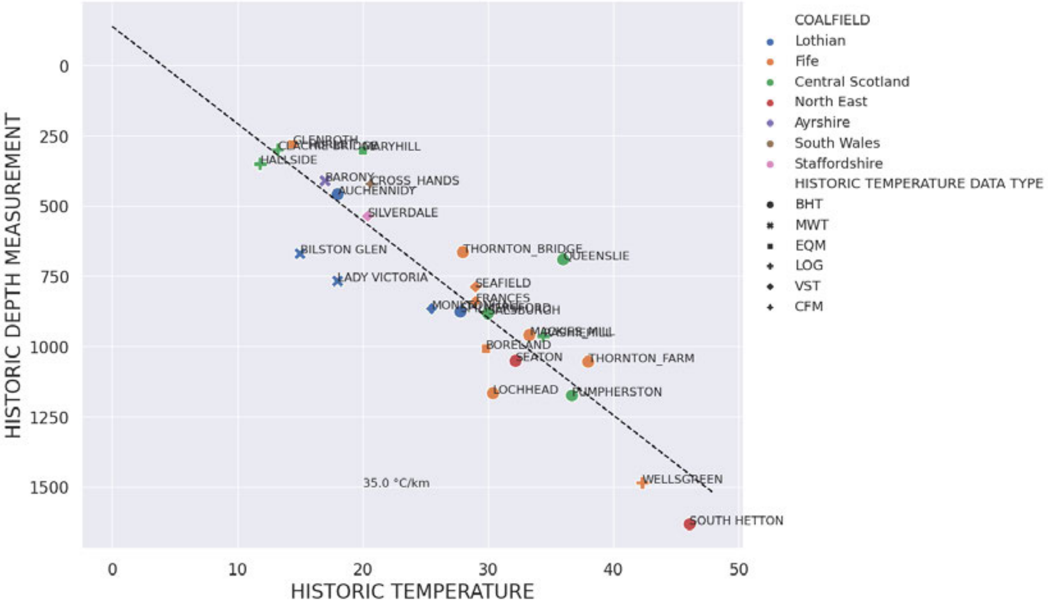

Figure 3.39: Relationship between the historical temperatures (℃) and measurement depths (mbgl) for each borehole with available geological data collected in the database (UKGC data, Burley et al. (1984)), averaged at the coalfield scale.

decrease exponentially with increasing depth depending on the thermal conductivity of the ground, and with a time lag since the onset of the surface perturbations (Beamish & Busby, 2016; J. Busby, 2015; Westaway & Younger, 2013). In the UK, Wheildon and Rollin (1986) suggested that boreholes $<$ 100 m depth are sensitive to surface temperature variations over the past 500 years, while Beltrami et al. (2015) showed that past climatic signals $>$ 1000 years B.P are still contributing to the thermal state of the subsurface down to 500 m depth, resulting in a lower temperature gradient near the surface. Using individual temperature measurements from shallow depth ($<$ 400 m) would therefore tend to underestimate the true "steady-state" background geothermal gradient and thus the extent of the geothermal resource at depth (J. Busby, 2015). When extrapolated to the surface, the best-fit shallow geothermal gradient estimated from boreholes $<$ 400 m depth indeed indicates a surface temperature of 4.0 ℃, which is lower than the current yearly average surface temperature in Scotland of about 9℃ (Gillespie et al., 2013). Recent studies aiming at re-evaluating the subsurface heat flow in the UK accounting for paleo-climate have concluded that heat fluxes measured in shallow boreholes in Scotland need to be increased by 18 mW/m^2 to account for the effects of the last prolonged glaciation (Westaway & Younger, 2013). The correction would be reduced to 8.8 - 13.5 mW/m^2 for 1 km deep boreholes and 0.2 - 9.1 mW/m^2 for 1.5 km deep boreholes. S. Watson et al. (2020) showed that applying paleo-climatic corrections to the Maryhill borehole (Glasgow area) increases the heat flow by 20 mW/m^2, leading to higher extrapolated temperatures at depth and therefore higher resource estimates. Estimating the local geothermal gradients based on observed temperature without correcting for past climatic effects as in Farr et al. (2020) might therefore underestimate the heat renewal rate in mines.

3.5.3 Effect of heat advection and recharge

The analysis of the temperature profiles in mine shafts suggests that most of the hydraulic flow occurs at the seams insets, i.e. where the worked seams intersect the shaft. In rebounding and monitoring shafts in un-pumped coalfields, the temperature in the shaft generally appears higher than predicted by the geothermal gradient, with the temperature at the deepest seam inset controlling the temperature in the bottom part of the shaft. This is however not verified for all shafts, suggesting that depending on the nature of the recharge, rebounding water sourced from a lower level or the surface might progressively lead to a cooling of the shaft temperature, or progressively return to a warmer pre-pumping equilibrium temperature once flooding is completed. An example of this has been suggested from the temperature profiles and cross-correlations analyses in Nottinghamshire, where seams are outcropping at the surface. There, cold recharge from shallow workings was interpreted to cause the progressive cooling of the deeper mine workings. On the contrary, deep mines confined under the Permian aquifer in the North-East Coalfield were suggested to benefit from deep recharge, favouring a long-term replenishment in heat.

Pumping shafts generally display a large shift in temperature at the pump location. As pumping progresses, only the most productive seams contribute to the hydraulic recharge, leading to a homogenisation of the temperature along the shafts and a reduction of the temperature shifts at the less productive seam insets. In those shafts, where pumping is generally performed at shallow depth, the temperature typically appears higher than predicted by the geothermal gradient at shallow depth, and lower in the bottom part of the shaft. Monitoring shafts in pumped coalfields generally display patterns similar to the pumping shafts, provided good hydraulic connections exist between the shafts. Additional mixing and thermal discrepancies might be caused in coalfields with dipping seams (i.e. Dawdon-Hawthorn).

In discharging shafts, the surface temperature was suggested to largely influence the temperature in the top part of the shaft. As profiles return to thermal equilibrium after the system has reached a hydraulic equilibrium, the temperature at the seam insets would return to the temperature predicted by the geothermal gradient at those depths.

Conductive heat exchanges between the advective mine-water and tunnel walls are known to be a slow process relative to heat convection, as suggested by the limited effect of the local rock heat conductivity values on the MWT (Fig. 3.38). The infiltration of surface water over decades of dewatering promoted by a high-pressure gradient between the mine and the surface might have cooled down the rock temperature, disturbing over the long-term the thermal equilibrium state of the mine. It is therefore of interest to understand the potential long-term disturbances of the rock temperature induced by the nature (i.e. temperature) of the recharging water and the flow rate during and following water rebound. This is even more important considering that most of the Carboniferous layers are tilted, potentially inducing the mixing of waters with different temperatures throughout a large depth range. This effect, suggested by the relationship between the MWT and the time since the closure of the mine (Fig. 3.31) is investigated further in Chapter 7 using numerical modelling.

A summary of the different controlling factors on the MWT, based on a qualitative analysis of the results, is provided in Table 3.3.

Parameter	Monitoring	Pumped	Pumped MWB	Rebounding	Discharging
Gradient	x	x		x	x
Average depth	x	x	x	x	x
Max depth	x	x	x	x	x
Water level	x	x	x	x	
Depth probe	x				x
Flow rate		x			x
Abandonment	x			x	
Heat conductivity	x				
RHP					x

Table 3.3: Summary of the controlling factors on the MWT based on the data analysis (qualitative analysis). The North-East (NE) and Lothian coalfields depict the stronger dependence of the MWT on the heat conductivity, whilst the NE, Yorkshire and Derbyshire coalfields depict the highest dependence of the MWT on the probe depth. Despite the good relationship between the MWT and the water level for all data types, the MWT in the South Wales and Central Scotland coalfields tends to be warmer for shallower levels, especially in pumped boreholes (whilst it tends to be colder in the Derbyshire and Lancashire coalfields and for the monitoring Yorkshire boreholes). The time since abandonment or rebound rate tends to impact the MWT differently depending on the coalfield, with the MWT being generally warmer in the NE Coalfield and colder in Nottinghamshire, which suggests the dominance of deep and shallow surface water recharge, respectively. The pumped MWT in Fife is generally colder for greater average/maximum shaft depth, whilst the monitored MET in Nottinghamshire is generally warmer. In the Lothian coalfield, the average MWT in the monitored shafts also tend to be colder.

3.6 Summary

The data and statistical analysis presented in this study suggest that although discrete temperature measurements in shafts can appear unrelated to the geothermal gradient at specific observation depths, the average MWT in shafts is strongly related to the average temperature predicted by the undisturbed geothermal gradient within a given depth interval. The geothermal gradient therefore plays a key role in controlling the MWT entering the shaft at the seam insets. However, convective heat flow mechanisms will tend to dictate the temperature distribution where shafts intersect mined coal seams and the extent of mixing, suggesting the importance of the distribution of mining voids.

Due to the lack of information associated with the nature of measurement, and uncertainties in the geology and the hydraulic boundaries of each mine-water system, it is however difficult to isolate the relative effect of different processes. In addition, the limited amount of data in mine galleries makes it challenging to isolate the effects of pumping and determine if the equilibrium state with the surrounding rocks is localised in the shaft or spread within the hydraulically connected parts of a mine or network of mines (Farr et al., 2020). Numerical modelling will therefore be used to investigate further the effect of a range of controlled parameters such as the rock properties, hydraulic recharge and pumping scenarios or the mine infrastructures. This will allow getting a clearer picture of the relative contribution of different controlling parameters/processes on the MWT and temperature distribution within flooded mines (chapters 6 and 7).

Chapter 4

Mathematical review of groundwater and heat transport modelling and introduction to numerical methods

4.1 Introduction

Determining the sustainability of heat extraction from mine-water reservoirs requires understanding the key mechanisms of heat transfer between the rock and the circulating fluid as well as the time required for thermally spent water to recover its initial temperature as it flows towards the extraction well (Banks, Athresh, Al-Habaibeh, & Burnside, 2019). This cannot be done without a proper characterisation of the hydrological components of flooded mine workings and their interactions in response to production (N. Burnside et al., 2016).

Different modelling approaches have been used in the literature to answer those questions and determine the long-term heat potential of geothermal systems. Depending on the nature and complexity of the problem, analytical and numerical modelling approaches can be used to solve the governing equations that describe the mechanisms of heat transport and fluid flow in the subsurface. Before developing a numerical model, hydraulic and thermal processes need to be defined mathematically through the establishment of a conceptual model. The conceptualisation process requires simplification of the real processes, and past research involving the modelling of abandoned flooded coal mines has faced important difficulties linked to the complex geometry and hydrogeology of the mine workings. The main challenge arises from the necessity to solve simultaneously for groundwater flow and heat transfer within a porous matrix (i.e. undisturbed rock mass, galleries, "goaf", caverns and drivings), open pipes (i.e. shafts, roadways, tunnels) and fractures (Ferket et al., 2011; Renz et al., 2009).

Based on the conceptual understanding of the structure and hydrogeology of mines provided in Chapter 2, this chapter presents a summary of the main thermal and hydraulic processes occurring in mines and of the main modelling approaches. The first two sections introduce the physics of groundwater flow and heat transport and provide a derivation of the governing equations for both subsurface processes (see parameters symbols and units in Table 4.1).

The derivation is here expressed following Christopher McDermott's lecture 'Hydrogeology 2: Simulation of Groundwater Flow and Transport' prepared for the University of Edinburgh. Analytical solutions and numerical modelling approaches applied to mine-water reservoirs are then reviewed using examples from the literature. The last section introduces OpenGeoSys (Kolditz et al., 2012), the open-source finite element modelling (FEM) code used in this study to simulate coupled groundwater flow and heat transfer in mines (i.e. chapters 5, 6, 7 and 8). Benchmarking results are presented to validate heat transport, coupling and non-linear flow processes implemented in the code as part of this research.

4.2 List of symbols and units

Property	Symbol	Unit
Rock temperature	T_r	℃
Water temperature	T_w	℃
Heat conductivity	λ	W/(℃.m)
Specific heat capacity	c	J/(℃.kg)
Heat transfer coefficient	h_c	W/℃/m^2
Density	ρ	kg/m^3
Hydraulic conductivity	K	m/s
Permeability	k	m^2
Storage	S	
Flow rate	Q	m^3/s
Velocity	v	m/s
Water dynamic viscosity	μ	Pa.s

Table 4.1: List of general symbols and units used in the thesis.

4.3 Groundwater flow

4.3.1 Physics of Groundwater flow

Groundwater flow strongly affects the transport of heat in the subsurface (Cherubini, Cacace, Scheck-Wenderoth, & Noack, 2014). Hydraulic processes are controlled by a series of reservoir properties, including:

- the hydraulic conductivity, that describes the ease with which water flows through a porous or fractured material. In opposition to the permeability, which is an intrinsic property of a porous material, the hydraulic conductivity also depends on the property of the fluid.

- the storage. In a confined aquifer, that remains saturated with water, the storativity or specific storage S_s is defined as the volume of water released from, or added to storage per unit volume of an aquifer per unit decrease in the hydraulic head owing to compressibility. In an unconfined aquifer, storage is expressed as the specific yield S_y, which corresponds to the volume of water that drains by gravity (dewatering of the aquifer material) per unit change in head and per unit area.
- the transmissivity, which corresponds to the product of the hydraulic conductivity and the reservoir thickness.
- the porosity, that characterises the proportion of primary or secondary/induced voids.

Underground flooded coal mines are particularly complex 'triple-porosity' systems composed of the primary rock porosity (i.e. unaffected rock mass), mining-induced fractures (i.e. secondary porosity), and the open mining voids (i.e. galleries, shafts, roads...), where intergranular porous flow, fracture flow and conduit/channel flow interact (Kruse & Younger, 2009; Wolkersdorfer, 2008). The large permeability contrasts are responsible for the complexity of the flow regime (Andrés et al., 2017), which extends from purely linear to a turbulent flow (R. Singh, Ngah, & Atkins, 1985).

In general, laminar flow is considered to be dominant in both the host rock and the mine workings (e.g. in the backfilling or collapsed 'goaf' materials) and in the fractured media surrounding the mine workings, where fluid velocities are relatively low (Renz et al., 2009). Laminar flow describes a linear dependency of flow velocity on the hydraulic head or pressure gradient. When considering viscous single-phase flow in a saturated porous medium, the Darcy equation (Eq. 4.4) can be used to determine the advective fluid velocity (or instantaneous discharge rate), which will in turn be used to solve for the heat transfer equation (section 4.4). Darcy flow has been described to be valid for Reynolds numbers (Eq. 4.1) Re < 2.3 (Fand, Kim, Lam, & Phan, 1987), with

$$Re = \frac{\rho v L}{\mu} = \frac{D v}{\mu} \tag{4.1}$$

where ρ is the fluid density (kg/m^3), μ is the dynamic viscosity (Pa.s) and L is the length of the fluid flow (characteristic length). The right term is used to calculate the Reynolds number in a pipe with inside diameter D (m) and average cross-sectional flow velocity v (m/s).

At higher flow rates, the flux and hydraulic gradients are non-linearly related and the Forchheimer flow regime emerges (L. Wang et al., 2022). Although the threshold at which this transition occurs is uncertain, with variations depending on the media and fluid characteristics, non-linear flow has been suggested to be initiated for Reynolds number > 1-10 (5 < Re < 80). Non-linear turbulent flow tends to develop for Re > 120-2000 (Fand et al., 1987) as a result of very high velocities. Turbulent flow in the open mining voids (roadways, shafts and galleries) is usually developed with lower Reynolds numbers ($\sim$ 100), due to the high roughness and the large diameter of the mine voids (Wolkersdorfer, 2008). Pipe flow models defined by the Poiseuille law are sometimes used to represent the flow through those highly transmissive voids in a similar way to a karstic system (Adams & Parkin, 2002). In many of the open voids with low pumping rates, or under natural conditions, velocities are however quite low and the flow is laminar. Forced convective flow and free density-driven convective flow in large open voids in response to salinity and temperature gradients are also common in mines and are described further in the next section (Hamm & Bazargan Sabet, 2010; Wieber, Stemke, Wonik, Enzmann, & Kersten, 2019).

In addition to characterising the nature of the flow, developing a reliable conceptual model of a hydrogeological system requires identifying the source of recharge, discharge and flow pathways through the subsurface. The monitoring of mine-water recovery in several coalfields in the UK suggests that mine workings behave in a way similar to a confined aquifer (Burrell & Whitworth, 2000). Recharge and discharge zones are generally highly dependent on the head distribution and on the topography. In mines, inflow can occur via the infiltration of water at the surface via shafts or shallow workings, leakage from overlying confined aquifers, or regional flow from connected hydrogeological systems or neighbouring mine workings (see Chapter 2). Surface discharge generally occurs where the head rises above the lowest topographic point in the basin or in mine-water blocks (i.e. a hydrogeological unit of interconnected mines), to rivers or via existing infrastructures (e.g. shafts, drifts). However, mines are dynamic systems and new hydraulic connections between adjacent systems are likely to be created as water is rebounding following closure and abandonment of the mine. This suggests that over time, the recharge and discharge or 'decant' points (e.g. connected mine, mine infrastructure, surface level) as well as the groundwater flow regime might change depending on the void space and head gradient (Adams & Younger, 2001), adding to the complexity of groundwater flow modelling (Ferket et al., 2011; P. Younger & Robins, 2002).

4.3.2 Groundwater flow equations

Linear Darcy flow

In fluid mechanics, the energy in a fluid system can be expressed in terms of the Bernoulli Equation. Bernoulli's principle states that, in a steady, isotropic, non-viscous flow, the sum of internal (pressure) energy, kinetic energy and potential energy remains constant. An increase in the fluid velocity therefore occurs simultaneously to a decrease in static pressure or in the fluid's potential energy (Batchelor, 1967). This principle is only applicable when turbulence, frictional forces and non-adiabatic processes are negligible. Bernouilli's law can be expressed in terms of total pressure (Eq. 4.2) or head (Eq. 4.3), as follows:

$$c = p + \frac{1}{2}\rho v^2 + \rho g z \tag{4.2}$$

$$H = z + \frac{v^2}{2g} + \frac{p}{\rho g} \tag{4.3}$$

With H the hydraulic head (m), v the fluid velocity (m/s), g the acceleration due to gravity (m/s^2), z the elevation of the point above a reference plane (m), p the pressure (Pa) and ρ the fluid density (kg/m^3).

Saturated confined aquifer flow In this section, the governing equations for 3D groundwater flow in a confined aquifer with source-term are derived based on Darcy's law (Eq. 4.4).

$$q = \frac{\Delta P}{L} \times \frac{k}{\mu} = K \times \frac{\Delta H}{\Delta x} \tag{4.4}$$

With q the discharge per unit area or Darcy flux (m/s), k the absolute permeability (m^2), ΔP the total pressure drop (Pa), μ the dynamic viscosity (Pa.s) and L the length of the sample (m). The right term expresses the Darcy flow q in terms of the hydraulic conductivity K of the porous media (m/s) and of the hydraulic head H (m).

The flux of fluid mass into the volume equals the flux of fluid mass out of the volume plus the change in mass stored within the volume (Fig. 4.1).

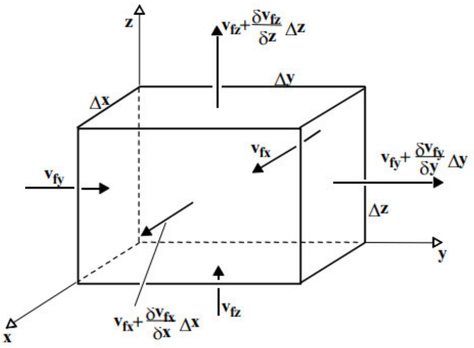

Figure 4.1: Control volume for 3D groundwater flow (source: 'Hydrogeology 2: Simulation of Groundwater Flow and Transport' lecture notes, Christopher McDermott, University of Edinburgh)

The conservation of volume for a given time step can first be expressed by:

$$\frac{\Delta V_w}{\Delta t} = Q_{in} - Q_{out} \tag{4.5}$$

Considering that:

$$Q_{in} = v_{fx}\Delta y\Delta z + v_{fy}\Delta x\Delta z + v_{fz}\Delta x\Delta y \tag{4.6}$$

$$Q_{out} = (v_{fx} + \frac{\delta v_{fx}}{\delta x}\Delta x)\Delta y\Delta z + (v_{fy} + \frac{\delta v_{fy}}{\delta y}\Delta y)\Delta x\Delta z + (v_{fz} + \frac{\delta v_{fz}}{\delta z}\Delta z)\Delta x\Delta y \tag{4.7}$$

one obtain,

$$Q_{in} - Q_{out} = -\frac{\delta v_{fx}}{\delta x}\Delta x\Delta y\Delta z - \frac{\delta v_{fy}}{\delta y}\Delta x\Delta y\Delta z - \frac{\delta v_{fz}}{\delta z}\Delta x\Delta y\Delta z \tag{4.8}$$

with v_f the fluid velocity. According to the balance equation, this difference equals the net change in water volume within the control volume, which is proportional to the change in hydraulic head, so that:

$$\frac{\Delta V_w}{\Delta x\Delta y\Delta z} \approx a\Delta H \tag{4.9}$$

where a is the correlation coefficient.

In a confined aquifer, the change in water volume mainly results from the compression of the aquifer structure, with the pore space increasing or decreasing with increasing/decreasing hydraulic head, which is proportional to water pressure P according to the relationship $P = \rho g H$. Because these pressure or head changes are assumed to be small, it is correct to assume a linear relationship between ΔV_w and ΔH, with the proportionality coefficient a corresponding to the specific storage coefficient S_s [1/L]. One can therefore rewrite Eq. 4.9, so that:

$$\Delta V_w = S_s \Delta H \Delta x\Delta y\Delta z \tag{4.10}$$

Where $S_s = \rho g(\alpha + n\beta)$, with n the porosity and α and β the compressibility of the aquifer framework and of the pore water $[M^{-1}LT^2]$, respectively. Replacing Eqs. 4.8 and 4.10 into Eq. 4.5, one can write:

$$S_s\frac{\Delta H}{\Delta t} = -\frac{\delta v_{fx}}{\delta x} - \frac{\delta v_{fy}}{\delta y} - \frac{\delta v_{fz}}{\delta z} \tag{4.11}$$

Thus, at any particular time,

$$S_s\frac{\delta H}{\delta t} = -\frac{\delta v_{fx}}{\delta x} - \frac{\delta v_{fy}}{\delta y} - \frac{\delta v_{fz}}{\delta z} \tag{4.12}$$

According to the Darcy law (Eq. 4.4), the flux components for an isotropic aquifer are given by $v_{fx} = -\frac{K\delta H}{\delta x}$, $v_{fy} = -\frac{K\delta H}{\delta y}$ and $v_{fz} = -\frac{K\delta H}{\delta z}$. Inserting those into Eq. 4.11, one can write:

$$S_s\frac{\delta H}{\delta t} = \frac{\delta}{\delta x}\frac{K\delta H}{\delta x} + \frac{\delta}{\delta y}\frac{K\delta H}{\delta y} + \frac{\delta}{\delta z}\frac{K\delta H}{\delta z} \tag{4.13}$$

Considering a source or sink term, one can then write:

$$S_s \frac{\delta H}{\delta t} = \frac{\delta}{\delta x} K \frac{\delta H}{\delta x} + \frac{\delta}{\delta y} K \frac{\delta H}{\delta y} + \frac{\delta}{\delta z} K \frac{\delta H}{\delta z} - q \tag{4.14}$$

where $q = q(x,y,z,t)$ represents the volume of water removed or added to the aquifer per unit time and unit volume (i.e. injection/extraction rate or groundwater recharge).

Anisotropy may be quantified by involving different K values for each component of the 3D space, namely K_x, K_y and K_z.

$$S_s \frac{\delta H}{\delta t} = \frac{\delta}{\delta x} K_x \frac{\delta H}{\delta x} + \frac{\delta}{\delta y} K_y \frac{\delta H}{\delta y} + \frac{\delta}{\delta z} K_z \frac{\delta H}{\delta z} - q \tag{4.15}$$

At steady-state conditions, $S_s = 0$ and $\frac{\delta H}{\delta t} = 0$. Assuming that the aquifer is homogeneous, Eq. 4.14 can be simplified to a form referred to as the Poisson equation:

$$\frac{\delta^2 H}{\delta x^2} + \frac{\delta^2 H}{\delta y^2} + \frac{\delta^2 H}{\delta z^2} = \frac{q}{K} \tag{4.16}$$

This can finally be simplified to Eq. 4.17 for cases without source-terms.

$$\frac{\delta^2 H}{\delta x^2} + \frac{\delta^2 H}{\delta y^2} + \frac{\delta^2 H}{\delta z^2} = 0 \tag{4.17}$$

Unconfined aquifer In an unconfined aquifer (i.e. free water surface), the change in water volume is mostly due to a change in the hydraulic head instead of owing to the compressibility of the aquifer. The groundwater flow equation can be derived in a similar manner to the equations for a confined aquifer by considering the saturated thickness h (water table) and replacing the specific storage S_s by the storage coefficient S (with S being about three orders of magnitude higher than S_s) and the flux q by Q, the water volume added to or removed from the aquifer per unit time and per unit surface area (Table 4.2). Therefore:

$$S \frac{\delta h}{\delta t} = \frac{\delta}{\delta x} T_x \frac{\delta h}{\delta x} + \frac{\delta}{\delta y} T_y \frac{\delta h}{\delta y} + \frac{\delta}{\delta z} T_z \frac{\delta h}{\delta z} - Q \tag{4.18}$$

with $T_x = K_x h$, $T_y = K_y h$ and $T_z = K_z h$ the transmissivities in the x, y and z directions [L^2/T].

	Confined	Unconfined
Storage	Specific storage S_s (m^{-1}) $S_s = \rho g(\alpha + n\beta)$	Specific Yield (S_y)
Storativity	$S = bS_s$	$S = S_y + bS_s$
Mechanism	Compressibility	Dewatering
Transmissivity (m^2/s)	T = K × b	T = K × h
Flow (m^3/s)	q [1/T]	Q [L/T]

Table 4.2: Difference in hydraulic properties between confined and unconfined aquifers, with b and h representing the aquifer thickness and saturated thickness (m), respectively.

Pipe flow

As mentioned earlier, the flow in a pipe can be described using the Poiseuille law, which expresses the pressure drop through a long cylindrical pipe of constant cross-section for a linear incompressible Newtonian fluid flow.

$$\Delta P = \frac{8\pi\mu LQ}{A^2} \tag{4.19}$$

with ΔP the pressure between the two ends of the pipe (Pa), L the pipe length (m), μ the fluid dynamic viscosity (Pa.s), Q the volumetric flow rate (m^3/s) and A the cross-sectional area of the pipe (m^2). This law was later extended to turbulent flow by inferring an effective turbulent viscosity (Hagen–Poiseuille law).

Non-linear Forchheimer and Turbulent flow

For high fluid velocities v, the Darcy and Poiseuille laws are inadequate to represent fluid flow in porous media and a pipe as inertial effects become important relative to viscous effects (Eq. 4.2). The Forchheimer law can be used to represent those inertial effects, by adding to the Darcy law a term proportional to the fluid density and a second one quadratic to the flow rate (Lenci, Zeighami, & Di Federico, 2022), so that:

$$\nabla P = (AQ + BQ^2) = \frac{\mu}{k_f}q + \rho\beta q^2 = (\frac{\mu}{k_f} + \rho\beta q)q \tag{4.20}$$

with k_f the Forchheimer permeability (m^2), β the Forchheimer coefficient (m^{-1}) and q the specific discharge (m/s). The values of β have been reported to vary over several orders of magnitude (Lenci et al., 2022), from 300 for granular materials (Bordier & Zimmer, 2000) up to 6 × 10^6 m^{-1} for fine sands (Ovalle-Villamil & Sasanakul, 2019).

Non-linear turbulent flow has been described to occur at larger flow rates. In turbulent regimes, friction losses along pipe walls are proportional to the square of the mean flow velocity. This effect is expressed in the empirical Darcy–Weisbach equation as a dimensionless friction factor, that can be used to determine the resistance to flow and the pressure loss due to friction for an incompressible fluid (G. O. Brown, 2012).

Fracture flow

Fracture flow describes the movement of fluid through a single fracture or fracture network in geological formations (Kresic, 2010). Depending on the complexity of the system, different equations have been developed in the literature to calculate the hydraulic conductivity and the flow rate through fractured media. Those are based on the Darcy and Forchheimer laws, modified to account for the geometry of the fractures (i.e. aperture, thickness, spacing, orientations). For a single fracture flow, the hydraulic conductivity of a fracture with aperture B has been defined by Witherspoon (2000) as:

$$K = B^2 \frac{\rho g}{12\mu} \tag{4.21}$$

And the flow through a cross-sectional area A (with $A = Ba$) is:

$$Q = Av = -a(\frac{\rho g}{12\mu})\frac{dH}{dx}B^3 \tag{4.22}$$

where B and a are the fracture aperture and the fracture height perpendicular to the flow direction, respectively, $\frac{dH}{dx}$ is the change in the hydraulic head along the flow direction, ρ and μ are the fluid density and viscosity, respectively, and g is the acceleration of gravity (Kresic, 2010). A common approximation for fracture flow is the cubic law, which considers that the aquifer volume acts as an equivalent porous medium (Witherspoon, 2000). It is expressed as:

$$\frac{Q}{dH} = \frac{CB^3}{f} \tag{4.23}$$

where C is a constant that depends on the geometry of the flow field and f is the fracture roughness.

When considering a fracture network, the flow will depend on the spatial geometry of the individual fractures and their interconnectivity Kresic (2010). The hydraulic conductivity of a set of parallel fractures (K_f) can be expressed as:

$$K_f = \frac{NB^2}{12}\frac{\rho g}{\mu} \tag{4.24}$$

with N the number of fractures per unit distance, B the average fracture aperture, and NB the fracture set porosity (Snow, 1968). Assuming that the fractured system acts as an equivalent porous medium, the hydraulic conductivity of a representative isotropic three-dimensional aquifer volume is (Snow, 1968):

$$K_{3f} = \frac{NB^2}{6}\frac{\rho g}{\mu} \tag{4.25}$$

Although fracture flow can be implemented in mine-water reservoirs modelling, the models developed in this research consider the fractured zone as a porous media with higher permeability relative to the surrounding undisturbed host rock (Chapters 6 to 8, where flow is described using the Darcy law.

4.4 Heat transport

4.4.1 Physics of heat transport

Heat transfer processes in the subsurface can either be triggered by the introduction or extraction of energy, or in response to other processes such as groundwater flow (Loredo et al., 2016). In mines, heat is transported both via heat conduction and 'free' natural (i.e. induced by density-viscosity contrasts) or forced (i.e. induced by pumping) heat convection through a network of roadways, drift, shafts (Dethlefsen et al., 2016).

Conduction characterises the transfer of heat through molecular interaction in response to a temperature gradient, i.e. from higher to lower temperatures. Conduction is generally the dominant heat transfer process in porous materials in low-velocity regimes, such as in the backfilled materials and undisturbed rock mass in unpumped mines, where water levels are fully recovered (Bailey et al., 2016; Ryan & Euler, 2017).

The conductive heat flux can be expressed as:

$$q = \lambda \frac{\Delta T}{\Delta z} \tag{4.26}$$

with λ the heat conductivity (W/°C.m), and $\frac{\Delta T}{\Delta z}$ the temperature gradient (°C/m).

Convection is the transfer of heat due to the movement of a fluid in the subsurface (advection). Free or natural convection is a buoyancy-driven flow that can be triggered in response to the mixing of mine waters with different temperatures, due to the presence of a natural vertical geothermal gradient, or due to salinity contrasts. Thermohaline stratification is commonly observed in large open voids and has been described as playing a major role in the transfer of heat in unpumped mines (Bao, Cao, Qin, Jiang, & Liu, 2020; Bao & Liu, 2019a; Hamm & Bazargan Sabet, 2010). The onset of free convective heat transport is often described from the Rayleigh number Ra (Appendix A.3). On the other hand, forced convection occurs when fluid flow is induced through external forces, a result of the injection or abstraction of fluid.

The basic relationship for heat transfer by convection is:

$$\dot{Q} = h_c A (T_s - T_f) \tag{4.27}$$

where $\dot{Q}$ is the heat transferred per unit time (W), A the surface area of heat transfer (m^2), h_c is the heat transfer coefficient (W/(m^2 ℃)), T_s is the solid surface temperature and T_f is the fluid temperature (℃).

The convective heat transfer coefficient h_c is dependent upon the physical properties of the fluid and the physical situation.

$$h_c = \frac{q}{\Delta T} \tag{4.28}$$

with q the heat flux (W/m^2) and ΔT the temperature contrast.

Thermal processes are controlled by a series of reservoir properties, including:

- the heat conductivity of the media λ_m (W.℃$^{-1}$.m^{-1}), which defines the ease with which heat flows via conduction, i.e. the rate at which heat is exchanged within and between the rock mass and the pore water. In mines, the rock and mine water conductivity is expected to control the long-term heat extraction rate from the system (S. A. Ghoreishi-Madiseh et al., 2012).
- the specific heat capacity c (J.℃$^{-1}$.kg^{-1}), which describes the quantity of heat (J) absorbed or released per unit mass of the material (kg) when its temperature increases or decreases by 1 ℃.
- the density ρ (kg.m^{-3}), which corresponds to the ratio of the mass of a sample and its volume. Taken together, the density and specific heat capacity are defined as the volumetric heat capacity ρc , which is an essential parameter to determine the heat potential of geothermal systems (Eq. 2.8).

The relative importance of conductive versus convective heat flow from the surrounding rock in a mine heat system is still debated in the literature. Whilst Malolepszy (2003) suggests that conduction is over 20 times greater than terrestrial heat flow, Raymond and Therrien (2008) considers that the geothermal heat flux has more control on the mine-water temperature compared to advection or conduction. The advection of heat with groundwater is generally predominant in open voids (e.g. shafts, drifts, roadways, galleries), where the fluid velocity can be the highest in the presence of a hydraulic gradient (Bridger & Allen, 2014).

S. Ghoreishi-Madiseh, Hassani, Mohammadian, and Radziszewski (2013) showed that the hydraulic conductivity is an approximate criterion to judge whether conduction or natural convection is the dominant heat transfer mode. Hamm and Bazargan Sabet (2010) and Bao and Liu (2019b) moreover showed that natural convection produced by buoyancy forces is the main heat transfer mechanism in shafts and highly depends on the permeability contrasts in the system. A recent analytical approach developed by Chu et al. (2021) suggested that the rechargeable factor, which depends on the volume ratio between the surrounding rock and the mine water, is a key parameter to assess the contribution of convection heat recharge from the rocks relative to the conductive flow. In Chapter 3, the linear correlation between the average log temperature and average depth of temperature profiles suggested a clear control of the geothermal gradient on the mine water temperature. However, no clear correlation was observed between the temperature and the rock heat conductivity, suggesting that conductive heat transfers might be overprinted by other processes associated with the nature of groundwater flow.

Although the transport of heat is slower than groundwater flow/pressure diffusion, as some heat is absorbed into the matrix, heat convection within the interconnected mine voids represents a substantial risk of short-circuiting in mines, i.e an early thermal breakthrough induced by direct connections between an injection and production point.

4.4.2 Heat transport equations

In this section, the governing equations for diffusion-dispersion heat transport are presented, based on the principle of energy conservation and heat flow equations to a control volume.

First, the total energy stored in a control volume (Fig. 4.2) can first be expressed as $\rho_m c_m T$, where $c_m \rho_m$ is the volumetric heat capacity of the porous media (Eq. 4.29), and T is the temperature of the porous media (℃).

$$\rho_m c_m = \phi \rho_w c_w + (1-\phi)\rho_r c_r \tag{4.29}$$

with ϕ the effective porosity of the media, c_w and ρ_w the specific heat capacity and the density of the pore water, and c_r and ρ_r the specific heat capacity and density of the solid rock, respectively.

The total energy in the control volume is therefore:

$$c_m \rho_m T \Delta x \Delta y \Delta z \tag{4.30}$$

The energy flux F_x [M/L2T] through the faces of the control volume can be expressed as:

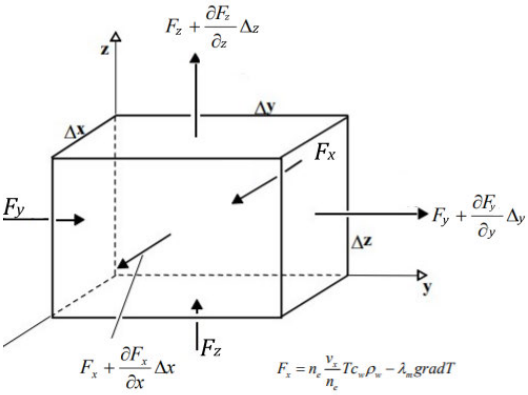

Figure 4.2: Control volume for 3D heat transport (source: adapted from 'Hydrogeology 2: Simulation of Groundwater Flow and Transport' lecture notes, Christopher McDermott, University of Edinburgh)

$$F_x = \phi \frac{v_x}{\phi} T c_w \rho_w - \lambda_m \nabla T \tag{4.31}$$

In this equation, the first and second terms represent the advective and diffusive energy fluxes, respectively. There,

- Advection describes the transport of heat via the linear Darcy flow (fluid motion), represented by the specific discharge q (m/s). Due to the nature of the porous media, the average velocity field $v = v_{x,y,z}$ is higher than the Darcy flux/specific discharge, as the water can only flow through the connected pore space and individual molecules will spread at different speeds (dispersion) so that $v = \frac{q}{\phi}$ (m/s).
- Diffusion characterises the transport driven by the motion of molecules along a temperature gradient. The law of heat conduction (Fourier's law) states that the conductive heat flux through a porous material is proportional to the negative temperature gradient in the temperature (transport towards decreasing temperature values). The rate of conductive heat transfer depends on the thermal conductivity of the media λ_m, which can be calculated based on the thermal conductivity of the porous matrix λ_r and of the pore water λ_w (Eq. 4.32):

$$\lambda_m = \phi \lambda_w + (1 - \phi) \lambda_r \tag{4.32}$$

Where ϕ is the rock porosity.

Assuming that the energy flux changes linearly along the distance Δx, the energy fluxes through the faces normal to the x-axis can be written as F_x and $F_x + \frac{\delta F_x}{\delta x} \Delta x$. This assumption is justified for sufficiently small control volumes. The net energy flux parallel to the x-axis is therefore:

$$F_x - (F_x + \frac{\delta F_x}{\delta x}\Delta x) = -\frac{\delta F_x}{\delta x}\Delta x \tag{4.33}$$

Following the same reasoning for the net flux through the control volume parallel to the y-axis and z-axis, the net energy transported through the faces of the control volume within a time interval Δt is:

$$-(\frac{\delta F_x}{\delta x} + \frac{\delta F_y}{\delta y} + \frac{\delta F_z}{\delta z})\Delta x \Delta y \Delta z \tag{4.34}$$

If there are no heat sources or sinks, the temporal change of energy in the control volume within the time interval Δt is the same as the energy passing through the control volume, so the energy balance is:

$$c_m \rho_m \Delta T \Delta x \Delta y \Delta z = -(\frac{\delta F_x}{\delta x} + \frac{\delta F_y}{\delta y} + \frac{\delta F_z}{\delta z})\Delta x \Delta y \Delta z \Delta t \tag{4.35}$$

which can be written as:

$$c_m \rho_m \frac{\Delta T}{\Delta t} = -(\frac{\delta F_x}{\delta x} + \frac{\delta F_y}{\delta y} + \frac{\delta F_z}{\delta z}) \tag{4.36}$$

Heat sources or sinks may occur due to the addition or the removal of energy. This can be expressed as a source-term q (J/s), that represents the energy unit added or removed per second:

$$c_m \rho_m \frac{\Delta T}{\Delta t} + (\frac{\delta F_x}{\delta x} + \frac{\delta F_y}{\delta y} + \frac{\delta F_z}{\delta z}) = q \tag{4.37}$$

The amount of energy added to or removed from the control volume during the time step Δt therefore equals $q\Delta t \Delta x \Delta y \Delta z$. If Δt tends to 0 (i.e. a point in time), one obtains:

$$c_m \rho_m \frac{\delta T}{\delta t} + \nabla \cdot F = q \tag{4.38}$$

Where divergence $\nabla \cdot F$ is a vector operator defined in 3D Cartesian coordinate system, which operates on the energy flux to produce a temperature field.

Considering $F_x = \phi \frac{v}{\phi} c_w \rho_w T - \lambda_m \nabla T$, one can now write

$$c_m \rho_m \frac{\delta T}{\delta t} + \nabla \cdot (c_w \rho_w v T - \lambda_m \nabla T) = q \tag{4.39}$$

Neglecting the source-term, the general transient heat diffusion equation can be written as:

$$c_m \rho_m \frac{dT}{dt} = -c_w \rho_w v \nabla T + \lambda_m \nabla^2 T \tag{4.40}$$

There, the first term on the right side represents the advective term, where the mass flow is characterised by the product of the water density ρ_w and velocity v, and the second term is the conductive heat transfer.

Dividing Eq. 6.5 by $c_m \rho_m$, one can express this equation in terms of temperature instead of energy.

$$\frac{\delta T}{\delta t} = \nabla \cdot D \nabla T - \frac{c_w \rho_w}{c_m \rho_m} v \nabla \cdot T - \frac{q}{c_m \rho_m} \tag{4.41}$$

Where the heat diffusion-dispersion tensor $D = D_m + v_i \beta_i$ (J/Kms) contains a component for pure heat conduction/diffusion and a component for dispersion due to advection (Marsily & G, 1986). v_i is the advective flow velocity in the direction i (m/s) and $\beta_i = \alpha_i \frac{c_w \rho_w}{c_r \rho_r}$ is the heat dispersion coefficient (J/Km). D_m is the thermal diffusivity of the medium. With the advective term being negligible relative to the diffusive term, one can assume that the heat diffusion-dispersion coefficient $D = D_m = \alpha$, with.

$$\alpha = \frac{\lambda_m}{c_m \rho_m} \tag{4.42}$$

For 1D transport (where $\nabla = \frac{\delta}{\delta x}$ and $\nabla \cdot = \frac{\delta}{\delta x}$) in a homogeneous system without source-term and homogeneous flow (v = constant and D = constant), the equation is reduced to:

$$\frac{\delta T}{\delta t} + \frac{c_w \rho_w}{c_m \rho_m} v \frac{\delta T}{\delta x} - \alpha \frac{\delta^2 T}{\delta x^2} = 0 \tag{4.43}$$

4.5 Modelling approaches

Different modelling approaches have been developed in the literature to investigate groundwater flow and heat transfers in mines. Whilst many studies initially focused on modelling mine-water rebound following the abandonment of the mine, analytical and numerical models have been increasingly employed to characterise the heat recovery potential of flooded mines. Choosing the best modelling approach depends on the nature and complexity of the problem and the scale of the analysis (Adams & Younger, 2001).

4.5.1 Analytical solutions

Analytical models solve for the exact mathematical solutions of flow and heat transport by considering homogeneous systems and require geometrical simplifications. They are often employed at an early stage of a feasibility study to get a first insight into heat transfers and the sustainability of heat extraction from geothermal systems (Banks et al., 2009; Loredo et al., 2017). Although necessary to validate numerical models, those generally express single processes at the time and do not give an overall understanding of the heat fluxes and recharge potential.

The heat transfer problem in open roadways and shafts has been viewed in a similar way to heat exchangers, allowing to solve the 1D heat transfer equations. Based on this assumption, different approaches have been developed in the literature to solve for heat conduction from open channels using either analytical models (Lauwerier, 1955; Pruess & Bodvarsson, 1984) or semi-empirical method (Rodríguez & Díaz, 2009).

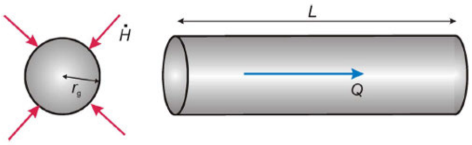

Figure 4.3: Scheme of a mine gallery as an approximately circular tunnel with radial heat flow. r_g = tunnel radius, H = heat flow to/from the tunnel, Q = volumetric water flow rate in the tunnel, L = tunnel length (Loredo et al., 2017).

The solution developed by Rodríguez and Díaz (2009) describes radially divergent conductive heat transfers from cylindrical mine shafts and tunnels. In this approach, the open pipe representing the gallery, shaft or tunnel of radius r_g is divided into a series of sections of length l_i. The rock mass temperature T_r is higher than the fluid temperature T_f and heat transfers are simulated as pure conduction between the rock mass and the circulating mine-water through an iterative process that generates the temperature output of each slice (Eq. 4.44). The fluid enters the increment at a temperature T_{ei} and volumetric flow rate Q, and exits the section on the other side at a temperature T_{si}. The water exit temperature from the i$_{th}$ increment is:

$$T_{si} = \frac{2\pi r_g l_i U_i T_r + (\rho_w c_w Q - \pi r_g l_i U_i) T_{ei}}{\rho_w c_w Q + \pi r_g l_i U_i} \tag{4.44}$$

Where c_w and ρ_w refer to the fluid heat capacity and density. The function U_i is defined as:

$$U_i = \frac{1}{\frac{1}{h_c} + \frac{r_g}{\lambda_r} ln(\frac{r_{0i}}{r_g})} \tag{4.45}$$

With λ_r the heat conductivity of the surrounding rock, h_c the heat transfer coefficient given by combining the Nusselt (Nu), Reynolds (Re) and Prandtl (Pr) numbers of the fluid in the tunnel (see Appendix A.3) and r_{0i} the effective thermal radius of the front of heat perturbation from the i$_{th}$ segment of tunnel.

The heat power gain can here be expressed as (Eq. 4.46):

$$H_i = 2\pi r_g l_i U_i (T_w - \frac{T_{ei} - T_{si}}{2}) \tag{4.46}$$

Alternatively, the Lauwerier-Pruess-Bodvarsson approach considers a parallel linear conductive heat flow from the water-bearing horizon. This approach, which gives more conservative values for the heat exchange capacity of the mine tunnel relative to the Rodríguez-Díaz solution, was shown to be more applicable to tabular mined void geometries (Loredo et al., 2017). Eq. 4.47 describes the formula to predict the temperature of water T_s at a distance x from the injection point in a fracture/channel of area A (Pruess & Bodvarsson, 1984).

$$T_s - T_r = (T_e - T_r) erfc(\frac{xP}{2qc_w}\sqrt{\frac{\lambda_2 \rho_2 c_2}{t - \frac{xA\rho_w}{q}}}) U(\Theta - \varepsilon) \tag{4.47}$$

where Θ is a dimensionless time related to real-time t since injection commenced, ε is a dimensionless distance in the flow direction, T_e is the injected water temperature and T_r is the host rock initial temperature, q is the injection flow rate, P is the effective perimeter perpendicular to the flow direction and erfc characterises the error function (Kschischang, 2017). c_w is the heat capacity of the pore water, and λ_2, ρ_2 and c_2 refer to the heat conductivity, density and capacity of sand outside the injection layer, respectively.

A general heat transport solution for a heat pulse and continuous injection of heat is here derived based on the mass transport solutions given by Lapidus and Amundson (1952) and Ogata and Banks (1961). This solution assumes an initial uniform temperature in the domain, and a constant temperature boundary to simulate heat injection at time t. This solution will be used in the section 4.6 to validate the numerical results for heat transport using the OpenGeoSys software.

$$T(x, 0 < t < t_0) = T_i + (T_0 - T_i) \times A(x,t) \tag{4.48}$$

$$T(x, t > t_0) = T_i + (T_0 - T_i) \times A(x,t) - T_0 \times A(x, t - t_0) \tag{4.49}$$

with $T_i = T(x, t = 0)$ the initial temperature distribution, T_0 the temperature of the pulse, x the distance from the source to the observation point (m) and where A is defined as follows (Eskilson, 1987):

$$A(x,t) = \frac{1}{2} erfc(\frac{Rx - vt}{\sqrt{4D'tR}}) + \frac{1}{2} \exp\frac{vx}{D'} erfc(\frac{Rx - vt}{\sqrt{4D'tR}}) \tag{4.50}$$

$$A(x,t-t_0) = \frac{1}{2} erfc(\frac{Rx - v(t-t_0)}{\sqrt{4D'(t-T_0)R}}) + \frac{1}{2} \exp\frac{vx}{D'} erfc(\frac{Rx - v(t-t_0)R}{\sqrt{4D'(t-t_0)R}}) \tag{4.51}$$

where $t_0 = 0.5$ the length of pulse (sec), $D' = DR$, $R = \frac{c_m \rho_m}{c_w \rho_w}$ the retardation factor, $D = D_m + v\alpha$ the dispersion coefficient (Eq. 4.42), v the Darcy velocity, $\alpha = 0.5x$ the dispersivity (with x the mesh resolution).

4.5.2 Numerical methods

Numerical approaches are used to solve more complex problems (e.g. coupled groundwater flow and heat and mass transfer equations) and more realistic representations of mining scenarios (e.g. heat exchanges between the circulating mine water and the surrounding rock), through approximations of the heat and mass flow equations (S. A. Ghoreishi-Madiseh et al., 2012; Loredo et al., 2016; Renz et al., 2009). Numerical modelling approaches include the Finite Difference Method (FDM, e.g. P. Guo et al. (2018)), the Finite Volume Method (FVM, e.g. S. Ghoreishi-Madiseh, Hassani, and Abbasy (2015)), and the Finite Element Method (FEM, C. Chen et al. (2019); Hamm and Bazargan Sabet (2010)). Finite difference simulators (FDM) such as SHEMAT (Ferket et al., 2011), finite element modelling software (FEM) such as TOUGH2 (P. Guo et al., 2017; Malolepszy, 2003), FEFLOW (Andrés et al., 2017; Diersch et al., 2010; Renz et al., 2009), HydroGeosphere (Raymond & Therrien, 2008), OpenGeoSys (C. Chen et al., 2019), or finite volume algorithm (FVM), such as MARTHE, FLUENT (Hamm & Bazargan Sabet, 2010), THEMUT (S. A. Ghoreishi-Madiseh et al., 2012) or OpenFOAM (Bao & Liu, 2019a) have been used in the literature for mine-water reservoir modelling applications.

The FDM discretises space and time in a rectangular grid, which does not represent accurately irregular boundaries and complex geometries. The FVM approach uses volume integral formulation to discretise the heat and groundwater flow equations. This approach is generally used to solve for pumping shaft analyses or for turbulent and source-term dominated flows in pipe-type schemes (Loredo et al., 2016). Of particular interest are the FEM, which solves for the approximation of partial differential equations within a discretised spatial domain. In FEM approaches, the domain is indeed divided into an unstructured mesh of triangle-based elements that give larger flexibility in representing complex geometries and subsurface structures, and therefore allow for more accurate representations of flow, heat/mass transport and deformation processes in geological systems.

In FEM, solutions for the partial differential equations of groundwater flow are solved at each node, providing a head value that can then be used to calculate the elemental flow velocities. The flow velocities are then used to derive the solution of the heat transport equation. FEM approaches are based on the principle of energy minimization, which assumes that the most stable system is the one with the smallest potential energy.

1. Meshing. In the FEM, the domain is subdivided into elements of arbitrary shape and size. The geometric object is represented by a mesh of I-D, 2-D and/or 3-D basic elements such as bars, triangles, quadrilaterals, tetrahedrons, hexahedra and pyramids, connected through a system of points called nodes. Within each finite element, a certain number of grid points is defined, which are located along the sides/faces of the element. At these points, the unknown functions have to be determined. The total number of unknowns (function values, function derivatives) is denoted as the degree of freedom of the discrete system. The mesh is modelled to include the material and structural properties that describe how the structure will respond to particular loading and boundary conditions.

2. Discretisation. Sets of matrix equations representing the integral (weak) formulations of the governing partial differential equations are solved for each discretised element in a mesh using discrete or iterative methods. In general, integral formulations of the continuum mechanic field are derived using the variational principles or the method of weighted residuals (MWR). The Galerkin method is a MWR commonly used to discretise general conservation equations (i.e. to convert volume to surface integrals) and transform the original partial differential equations to ordinary differential equations represented by a mass matrix, evaluated for each element.

3. Interpolation. The weak formulation allows discontinuities in the solution to appear. Interpolation functions are used to approximate the unknown values of field variables, minimizing the estimates of the error in the step changes between adjacent elements and the actual function. The interpolation functions are attached to each node and, therefore, correspond to the degree of freedom of the discrete system. Standard FEM is based on local interpolation, i.e. interpolation functions are chosen to be locally defined polynomials within each element and being zero outside the considered element. The construction of interpolation/shape function depends on the element type and different factors, such as function completeness, domain geometry, solution accuracy, and computation effort. Those have been described in (Kolditz, 2002). The residual is a measure of the accuracy of approximation or the error introduced by the discretisation method.

4.5.3 Model parameters

Initial and boundary conditions

The hydraulic and thermal boundary conditions (BC) are a key component of the conceptualisation of a groundwater system. Those are also required for numerical simulations to solve the second-order partial differential equation for fluid flow and heat transport through the domain, with head and temperature as the dependent variables (Reilly & Harbaugh, 2004). In mine modelling, knowing the lateral and vertical interconnectivity of different parts of the mines is essential to determine the model boundary conditions (Watzlaf & Ackman, 2006), together with the recharge area (Pruess & Bodvarsson, 1984; Rodríguez & Díaz, 2009).

Boundary conditions can be defined by:

- **Type 1 or Dirichlet BC**, which corresponds to the primary variables, such as the hydraulic head for a groundwater flow model (i.e. water level in a lake or river), or the temperature (e.g. mean annual surface temperature) for a heat transfer model.
- **Type 2 or Neumann BC**, which corresponds to the derivative of the primary variable. In a groundwater model, the flow rate can be used to represent recharge via precipitation or simulate pumping/injection from a well (i.e. sink/source-term). In a heat transfer model, Neumann BC is generally used to define the geothermal flux at the bottom boundary.
- **Cauchy BC (Type 3)**, which is a source-term dependent on the field variables and a transfer coefficient (i.e. conductance $\lambda_c = \frac{K_D}{d}$ in s^{-1}, with K_D the hydraulic conductivity of the medium (m/s) and d the distance (m)). In a groundwater flow model, this boundary can be used to simulate surface stream drainage (Baier et al., 2011).

Time, spatial discretisation and stability criteria

For the simulation to converge towards a stable solution in the resolution of the partial differential equations, it is essential to define appropriate mesh resolution (i.e. spatial discretisation of the domain) and time step length (i.e. time discretisation). At each time iteration of the simulation loop, solutions for the primary variables are calculated at each node, and hence choosing an appropriate mesh and time resolution is critical to finding the best compromise between the accuracy of the result and the simulation time. In mine modelling, smaller elements are generally required around pumping shafts or roadways, where the flow rate is the greatest, or at boundaries where the contrasts in hydraulic or thermal properties are likely to vary the most. Similarly, the number and length of time steps must allow both the temporal complexity of head and temperature distribution to be calculated and ensure that the stresses imposed on each cell (i.e. the volume of water taken out or injected) are not greater than the cell volume.

Three main criteria can be used to evaluate the stability of the results:

- the Courant number, which relates to the propagation of an advective front relative to the mesh element/cell size

$$C_o = \frac{v\Delta t}{\Delta x} \tag{4.52}$$

- the Neumann stability criteria, which relates the amount of diffusion/dispersion to the mesh size

$$\frac{\alpha\Delta t}{\Delta x^2} < 0.5 \tag{4.53}$$

  with $D = \alpha|v| + D_m$, $D_m = \frac{\lambda}{\rho c}$ and $\alpha = \frac{1}{2}\Delta x$. This stability criterion relates to both the temporal and spatial discretisation and is only valid for linear problems (Kolditz, 2002).

- the Peclet number, which is a combination of the Courant and Neumann criteria and corresponds to the ratio of diffusive to advective transport

$$Pe = \frac{v\Delta x}{D} = \frac{v\Delta x}{\alpha} \tag{4.54}$$

In the model developed in the subsequent chapters of this thesis, an isotropic heat dispersion coefficient of 0.5 m is considered to prevent instabilities in the shafts. There, the element size is the smallest (i.e. triangular elements are 1 m) as the permeability and therefore the fluid velocity is the highest.

Material properties

Assigning thermal and hydraulic properties to each cell is finally key to defining the different materials and heterogeneities in the system. An appropriate definition of the distribution of those properties (Table 4.1) is inherently part of the groundwater flow and heat transfer equations, and will therefore highly impact the determination of the primary variable distribution, i.e. head or temperature (Reilly & Harbaugh, 2004).

4.5.4 Examples of application

This section summarises examples of modelling approaches for the analysis of the heat recovery potential of flooded coal mines, discussed in more detail in Chapter 8.

A common method to simulate groundwater flow and heat transfers in mine is the porous media approach and has been used in many studies (P. Guo et al., 2018; Hamm & Bazargan Sabet, 2010; Raymond & Therrien, 2008; Renz et al., 2009). P. Guo et al. (2018) considered the mining area as a dual-porosity medium composed of a homogeneous caved zone (i.e. isotropic goaf material) and an overlying fractured zone (i.e. anisotropic medium with regular vertical fractures) surrounded by a large continuous media (i.e. surrounding host rock), where linear Darcy flow dominates. Andrés et al. (2017) similarly modelled the Asturias mine in Spain considering the unaltered rock mass, mined volume and open voids, as porous materials with different porosity and hydraulic conductivity values. To get a more accurate estimation of the heat capacity of mines using 2D porous models, Renz et al. (2009) developed a method including a "heat capacity equivalent" to account for the large storage capacity of the goaf, driving and caverns. Hamm and Bazargan Sabet (2010) later compared 2D and 3D porous media models to coupled 2D Darcy flow model integrating either laminar or turbulent one-dimensional flow to represent the structure of a coal mine in France. In their porous media approach, the shafts and galleries were considered as a special porous media where the porosity is such that the section open to flow is equal to the gallery/shaft cross-section. By comparing a high-velocity regime in the network of highly conductive shafts/galleries (i.e. equivalent porous media) to a regime with low-velocity in the less permeable porous rock mass (i.e assuming permeability contrasts of 10^5 between the galleries and shafts), Hamm and Bazargan Sabet (2010) showed that assuming an equivalent porous media for mine workings is adequate when considering large-scale modelling. Results from Renz et al. (2009) however showed that the overall heat storage from large mining voids was better accounted for in 1D/2D models, whilst 2D models were not able to properly account for free density-dependent convective movements compared to 3D porous models. Developing numerical methods accounting for free water flow and turbulent regime in open pipes, where velocities and pressure losses are high, was therefore suggested to be essential for more accurate results (Hamm & Bazargan Sabet, 2010).

To account for turbulent flow, Renz et al. (2009) used a combination of approaches including the Darcy equation to solve for laminar flow in the 2D porous rock mass, the Hagen–Poiseuille equations for slow-moving laminar pipe flow and the empirical Manning–Strickler equation to represent turbulent flow in 1D pipes (Diersch, 2005). Open vertical shafts and horizontal roadways were here considered as 1D elements, whilst driving and caverns were modelled as a 2D triangular finite element mesh representing a porous medium of high hydraulic conductivity, allowing to simplify the application of Manning's equation. Similarly, Raymond and Therrien (2008) combined laminar flow within 3D porous media and turbulent 1D pipe flow in mining voids using non-linear 3D Navier strokes calculations (Wolkersdorfer, 2008). The pipe network (i.e. shafts and roadways) was modelled as 1D elements embedded within a 3D mesh representing the porous mine aquifer. Although interactions between the intact strata of the mine aquifer and the conduits in mined-out areas have been successfully modelled, this approach has been considered unfeasible for a whole complex mine system due to the high computational requirements. Ferket et al. (2011) alternatively used coupled analytical models of heat transfer in mine void and discrete 'pipe network' hydraulic models based on a semi-empirical approach (Rodríguez & Díaz, 2009) to determine the heat capacity of the Asturias mine in Spain. This model was able to simulate both heat transfers between water and pipe walls and advective flow within a system of complex geometry, using a hybrid node-loop approach. The authors suggested that future work should include additional approaches to model turbulent flow in mine workings, including testing the Darcy–Weisbach approach.

4.5.5 Limitations

The numerical modelling of mine-water reservoirs has diverse challenges, including:

- the physics of heat transfer and groundwater flow. Computational challenges arise from the necessity to solve simultaneously for heat transfers and groundwater flow within open pipes, the porous matrix and fractures (Ferket et al., 2011; Renz et al., 2009). Whilst the porous media approach is often used to simulate flow in mines, velocities in open voids (e.g. shaft, roadways) can reach values of up to 400-2500 m/day (Wolkersdorfer, 2008), indicating potential turbulent flow in mine conduits that makes the use of the Darcy law for laminar flow modelling inadequate. However, the interactions between the different domains is not fully understood (Shen, Cheng, Wang, Teng, & Liu, 2002) and the mathematical implementation equations describing the coupling between those processes (e.g. Darcy linear flow, turbulent pipe flow, fracture flow) are often not available in classical groundwater simulation software (A. A. Monaghan et al., 2021). On the other hand, the implementation of the diverse equation describing those processes within a complex full-scale porous model for long-term simulations is computationally unfeasible and simplifications are generally required (Wood, He, & Apte, 2020).
- the computational cost. The implementation of the 3D mine geometry requires the consideration of elements of small dimensions (e.g. shafts, roadways) within large 3D volumes. In those elements, high-velocity and/or turbulent groundwater flow and advective heat transport generally dominate and mesh refinements around those structures are generally required, which can lead to large simulation time. The use of discrete 1D or 2D discrete elements embedded in the 3D domain has been seen as a solution to this problem, but the mathematical formulation there requires the inclusion of a factor allowing adjustment for the spatial dimension of the structure (e.g. cross-sectional area, hydraulic conductivity, thickness).
- the model parameterisation. In mining hydrogeology, building reliable groundwater flow models is often limited by uncertainties in the assumed parameters, material properties, boundary conditions, and the lateral/vertical mine interconnectivity (Szczepiński, 2019). Overall, the lack of pre-mining data and monitoring data in different parts of an interconnected network of mines makes it difficult to calibrate and validate models. In addition to the digitising process being an arduous task, mine plans are often uncertain, and so is the state of the galleries following the abandonment of the mine.
- the commonly used assumption of local rock-fluid thermal equilibrium (LTE) might not be valid at high velocities (Heinze & Pastore, 2023).

4.6 OpenGeoSys benchmarking

OpenGeoSys (OGS) is an open-source finite-element numerical modelling software used for the simulation of fully coupled effects of thermo-hydro-mechanical-chemical (THMC) processes in fractured porous media (Kolditz et al., 2012). The code allows solving for complex spatial, temporal and non-linear interactions between different processes, based on the balance equations for mass, momentum and energy conservation laws. This code has been used to simulate geothermal processes in the earth's subsurface, such as borehole heat exchanger (Schulte et al., 2016) or geothermal reservoir analysis (Watanabe et al., 2011).

In OpenGeosys, diffusive-advective heat transport in porous media can be simulated using jointly the GROUNDWATER_FLOW and HEAT_TRANSPORT processes. GROUNDWATER_FLOW calculates the head distribution H (m) at each node based on the hydraulic conductivity values K (m/s) attributed to each material. Alternatively, coupling between heat transport and hydraulic flow can be implemented using the LIQUID_FLOW process, which considers pressure distribution P (Pa) and permeability values k (Da). GROUNDWATER_FLOW and LIQUID_FLOW are used to calculate the change in water level/pressure in a saturated, confined porous aquifer according to the Darcy flow equations. The characteristics of both hydraulic processes are compared in Table 4.3 and the parameters for the linear solvers used to ensure convergence in the reference groundwater flow and liquid flow models in Chapter 6, 7 and 8 are given in Tables A.15. Those are further described in the OpenGeoSys manual (Kolditz et al., 2008).

PROCESS	LIQUID FLOW	GROUNDWATER FLOW
Primary variable	PRESSURE1	HEAD
Symbol	P	H
Unit	Pa	m
Hydraulic property	Permeability (m^2)	Hydraulic conductivity (m/s)

Table 4.3: Comparison between the parameters for the LIQUID_FLOW and GROUNDWATER_FLOW processes in OpenGeoSys.

The following equation allows converting the pressure distribution outputs (P) from the LIQUID_FLOW simulations into heads (H):

$$H = \frac{P}{\rho g} + z = \frac{P}{1000 \times 9.80665} + z \tag{4.55}$$

With z the elevation head (m), H the head (m), P the pressure (Pa), ρ (kg/m^3) the fluid density and g the gravitational constant of acceleration (m^2).

The hydraulic conductivity K can be converted to permeability values using Eq. 4.56, which is equivalent to multiplying all hydraulic conductivity values K by 10^{-7}.

$$K = \frac{k}{\nu}\rho g \tag{4.56}$$

With k the intrinsic permeability of the material (m^2) and μ the fluid viscosity (Pa.s).

4.6.1 Linear Darcy flow in saturated aquifers

To validate the groundwater flow and heat transfer processes, numerical solutions for heat transport obtained with OGS are compared against analytical solutions for a heat pulse and continuous heat injection in a 1D model composed of 1000 line elements (see section 4.5.1). The model properties for the fully-saturated porous matrix are provided in Table 4.4. Assuming a dispersivity $\alpha = 0.001$, results suggest a good fit between the analytical and numerical results (Fig. 4.4).

Parameter	value
Thermal Conductivity Fluid λ_w	0.63
Thermal Conductivity Rock λ_r	2.78
Heat Capacity Fluid c_w	4068
Heat Capacity Rock c_r	1280
Density Fluid ρ_w	1000
Density Rock ρ_r	2250
Porosity ϕ	0.25
Thermal Conductivity Media λ_m	2.24
Heat Capacity Media $\rho_m c_m$	3417000
Darcy Velocity v (m/s)	2.53×10^{-4}
Advective Velocity $q = \frac{v}{\phi}$	1.01×10^{-3}
Dispersion coefficient α	0.001
Thermal Diffusion Coefficient $D_{media} = \frac{\lambda_m}{\rho_m \beta_m}$	6.56×10^{-7}
Dispersion $D = D_{media} + v\alpha$	9.09×10^{-7}
Retardation factor $R = \frac{\rho_m \beta_m}{\rho_w \beta_w}$	0.84
Effective thermal dispersion factor $D' = DR$	7.64×10^{-7}
Initial temperature T_i (℃)	0
Duration of continuous injection/pulse t_0 (s)	999.9 / 0.5
Temperature of pulse T_0 (℃)	100
Time observation t (s)	1000
Distance observation x (m)	0.1

Table 4.4: Model properties, parameters, initial conditions and boundary conditions for the OGS benchmarking model for groundwater flow and heat transfers.

The temperature time series at a distance x = 0.1 m from the injection point is subsequently calculated for a range of dispersivity values. Fig. 4.5 suggests large sensitivity of the results to the dispersion coefficient. The best fit is calculated for α = 0.001, whilst α = 0.0016 leads to a temperature of up to half the one predicted by the analytical solution.

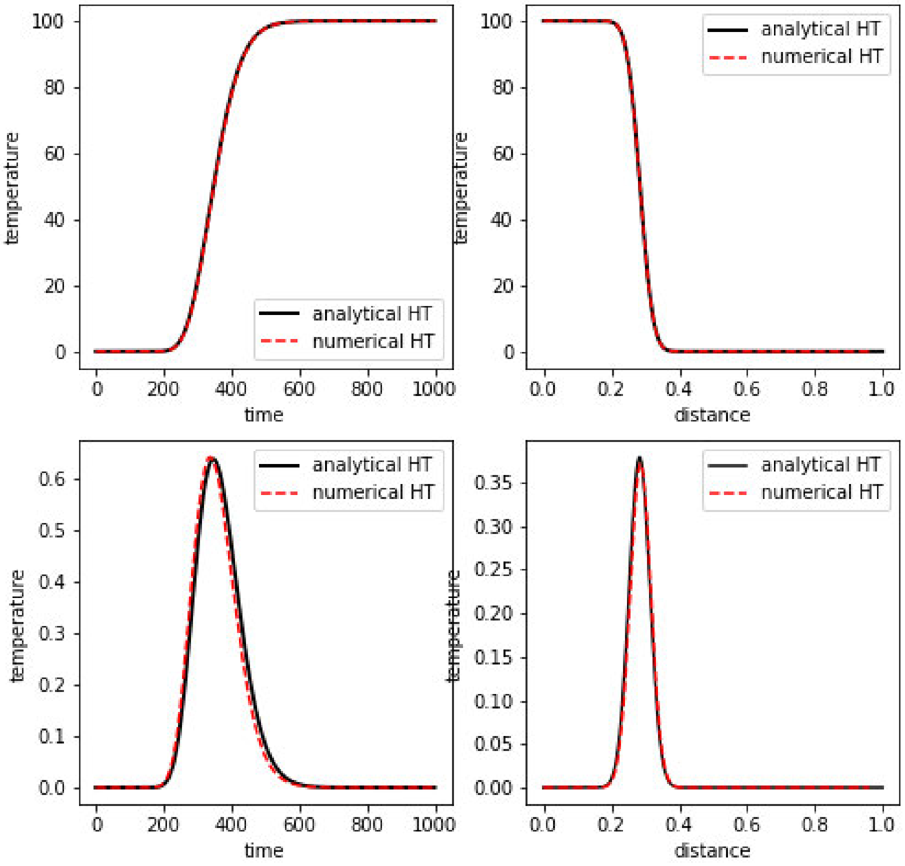

Figure 4.4: Comparison of the analytical and numerical solutions for heat transport as a function of time in seconds (left) and distance in meters (right) for continuous (top row) and heat pulse (bottom) injection for a solid and saturated matrix. The temperature is in ℃.

4.6.2 HT coupling in saturated aquifers

The effects of viscosity and density coupling are then evaluated using a 3D model and two equivalent 2D models in the XY and XZ planes. Coupling is solved at each time step via an inner loop of two to five iterations (Fig. 4.6). Those inner loop iterations are used to correct the non-linearities at a given time step and solve the current time step until it reaches a desired residual level.

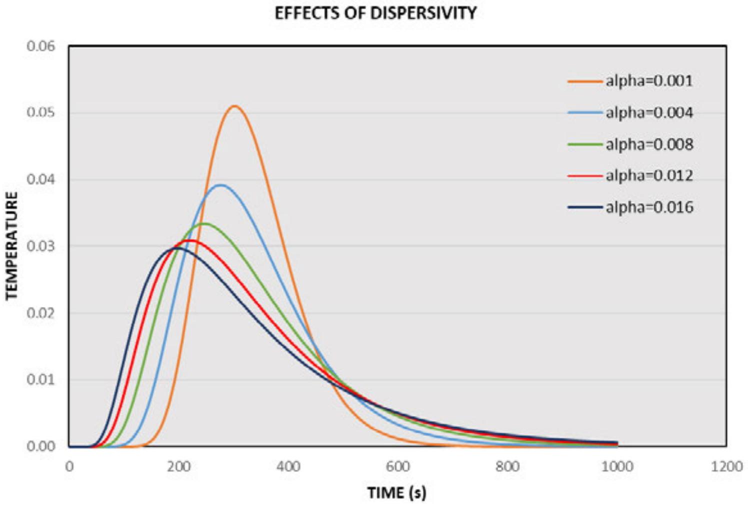

Figure 4.5: Effect of numerical dispersivity on heat pulse (time solution). The smaller the dispersivity, the later, greater and shorter the temperature pulse.

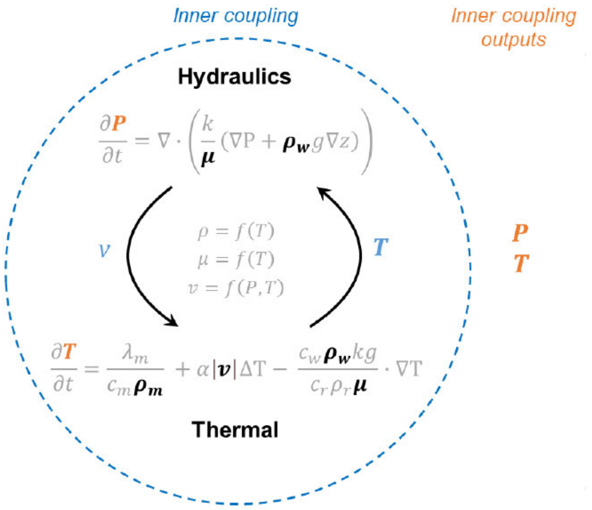

Figure 4.6: Coupling mechanisms between the thermal and hydraulic processes. Inner loops are used to solve for the fluid pressure (P) and temperature (T) as a result of changes in the temperature-dependent parameters (the fluid density ρ and viscosity μ) and of the fluid velocity that is itself a function of the temperature and pressure (modified from Todd (2023)).

Here, a maximal tolerance per degree of freedom or DOF of 1×10^5 is set (the maximum absolute difference of DOF variable in the domain between two iterations). At each iteration, the fluid density/viscosity is updated based on the calculated fluid temperature. Once the time step is solved, the simulation time progresses to the next outer loop iteration to solve for the next time step.

Fig 4.7 shows the relationship between the fluid dynamic viscosity/density and the temperature, implemented as density and viscosity curves in OGS.

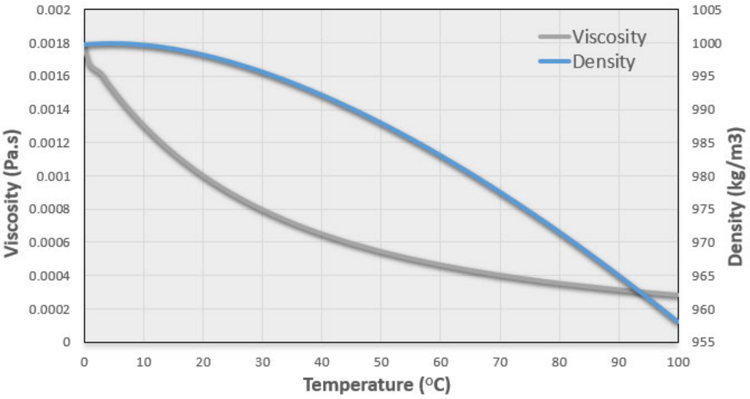

Figure 4.7: Density and viscosity curves for Hydro-Thermal Coupling implemented in OpenGeoSys by Christopher McDermott. Those depict the change in the fluid properties due to a temperature change.

Density coupling: the Elder Curve. The 3D model consists of a cuboid composed of 8192 hexahedron elements, whilst the 2D (XY and XZ) models consist of a rectangle with 8192 quadrilateral elements. In the Elder scenario, the top half right surface of the 3D model (or the top half right line for the 2D models) maintains a constant pressure of 0 Pa, which corresponds to the initial pressure condition. During the simulation, the bottom surface (line) has a constant pressure of 1.47×10^6 Pa and the top half left surface (line) maintains a constant temperature of 0℃. The system is initially assumed to have a uniform temperature of 20℃.

The velocity XZ vectors represented in Fig. 4.8 confirm the density effects induced by temperature contrasts in the model. Comparison with results from the 2D models suggests that the XZ set-up does not permit calculating properly the velocity vectors. However, similar results to the 3D model are obtained within the XY set-up, which requires the utilisation of the keyword $LIQUID_FLOW_YDEPTH in association with the liquid flow process in the input files.

Heat convection: Density-viscosity coupling In the heat convection scenario, where the effect of viscosity is also considered, the bottom surface (line) maintains a pressure of 1.47×10^6 Pa, according to the initial pressure gradient $P_z = P_0 - 9810z$, with $P_0 = 0$ Pa at $z = 75$ m. The lines (or points in the 2D models) at the top right and top left corners are attributed a temperature of 5℃ whilst a horizontal surface (line) centred toward the bottom of the cuboid generates heat via a constant temperature boundary of 50℃.

Fig. 4.9 shows the temperature distribution induced by density-viscosity coupling. Similar results are obtained for the 3D model and the corresponding 2D models. Density coupling promotes the natural convection of heat upward and cooling below the heating surface. This generates an anomaly of -3℃ to 5.5℃ relative to a scenario without coupling. However, the effects of viscosity are rather limited, contributing to an additional anomaly of only -0.4℃ to 0.6℃ relative to a scenario with density coupling only (Fig. 4.10).

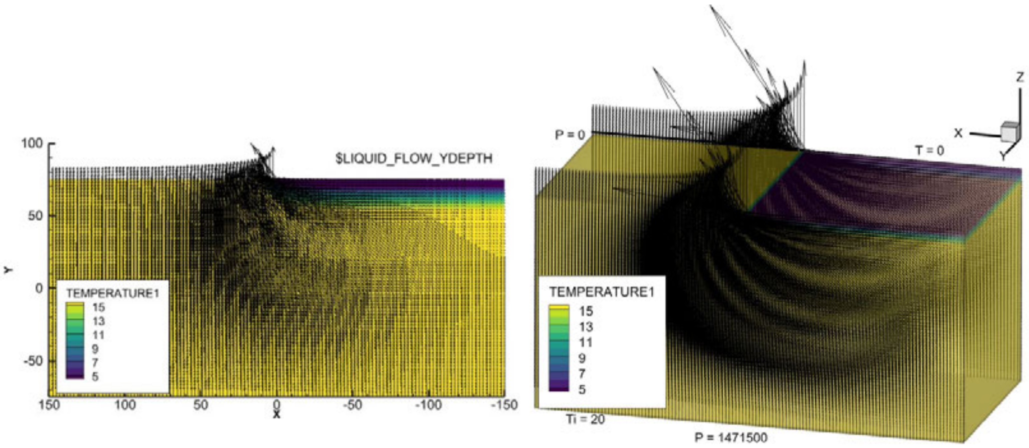

Figure 4.8: Temperature distribution (℃) and density-related flow vectors for the Elder model, calculated from a 2D (left) and 3D (right) mesh.

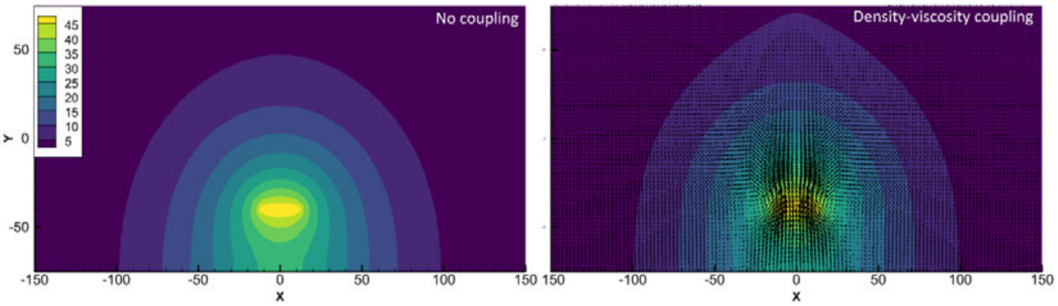

Figure 4.9: 2D temperature distribution for an uncoupled (left) and fully density-viscosity coupling scenario (℃). The fully coupled model depicts free heat convection cells highlighted by flow vectors. Those originate from the heat source and are directed towards the surface.

A source term is then added to investigate the combined effects of free and forced convection on the pressure and temperature distribution. A pump is added on the east part of the model extracting -2 $\times$ 10^{-7} $m^3/(s.m^2)$. Results confirm the combined effect of upward natural convection and eastward forced convection toward the pump (Fig. 4.11).

4.6.3 Non-linear flow and turbulent heat transport

Solutions for the Forchheimer equations can be calculated in OpenGeosys to simulate non-linear flow in porous materials or open channels. Further details about the active functions in the code (namely case 4 and case 5) can be found in the OGS manuals Kolditz et al. (2008) and are summarised in Appendix A.3.

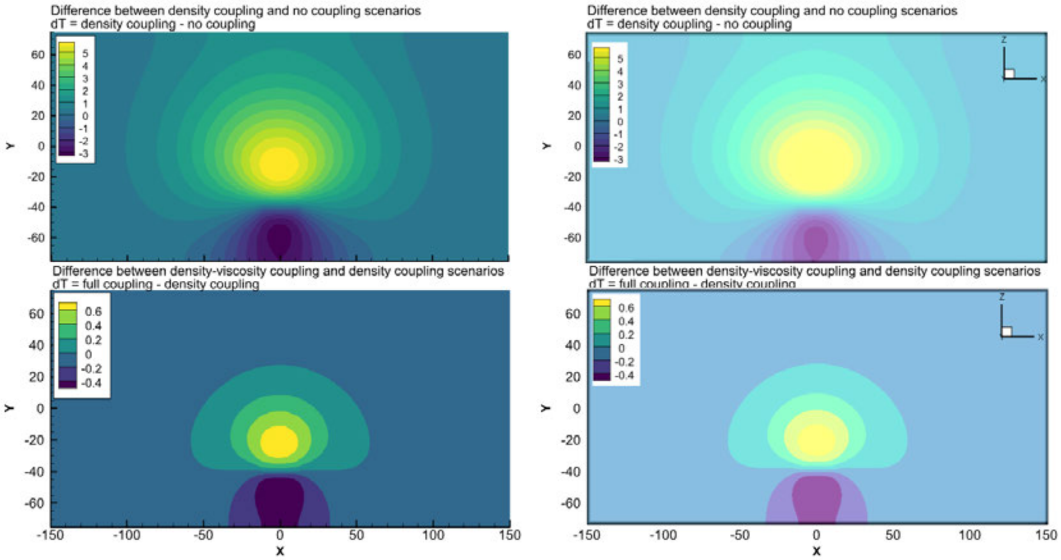

Figure 4.10: Difference induced by density and density-viscosity coupling in the heat convection model for the 2D (left) and equivalent 3D (right) models. Density coupling generates temperature anomalies of up to 5℃ relative to a scenario without coupling. Adding the effect of temperature-related viscosity changes only adds up to 0.6℃ to that thermal anomaly. Results confirm the equivalence between the 2D and 3D models.

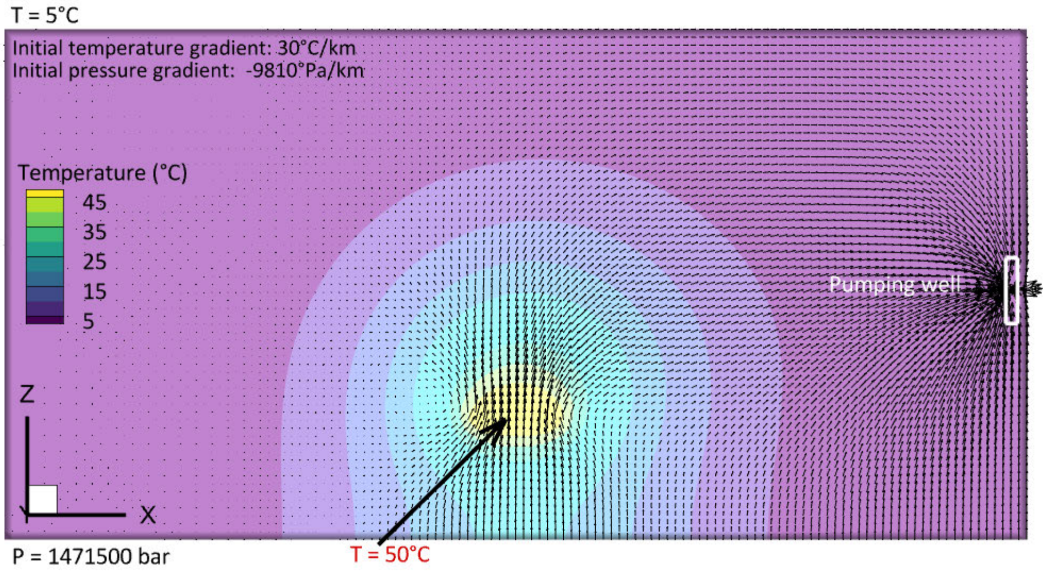

Figure 4.11: Temperature distribution in the 3D heat convection model resulting from the combination of free and forced convection. Results confirm the effect of pumping on the displacement of the thermal plume toward the right boundary, where pumping is implemented.

The numerical analysis consists of a simple 1D model composed of 960 line elements. A constant pressure $P = 0$ Pa is set on the right boundary whilst a source-term q on the left boundary defines a progressive increase in the flow rate (velocity) at each of the eleven time-steps, from 1 × 10^{-7} m^3/s to 2.05 × 10^{-4} m^3/s. The OGS code solves for the non-linear flow over a number of iterations that allow the system to reach a satisfactory pressure solution before calculating the velocity at a given time step (Fig. 4.12). The model assumes a material porosity of 100%, a fluid viscosity of 0.001 Pa.s, and a reference permeability of 1×10^{-9} m/s.

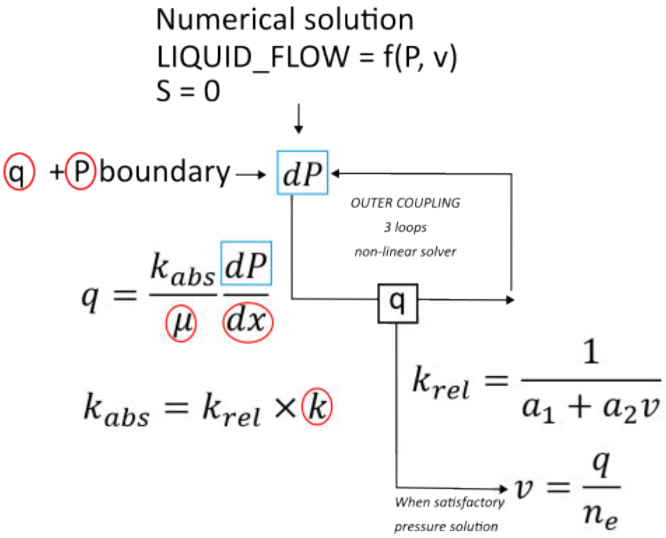

Figure 4.12: Implementation of the non-linear Forchheimer pressure solution in OGS. Outer coupling is used to derive a stable pressure solution at each time step in response to a change in the flow velocity v, through a series of iterations. The stable solution is then used to calculate the new velocity field at the considered time step. The velocity is a secondary variable for a pressure solution (i.e. depends on a pressure gradient dP/dx) and controls the relative permeability k_{rel} that itself modifies the flow q and therefore the pressure dP. k, k_{abs}, μ, n_e are the reference permeability, absolute permeability, fluid viscosity, and effective porosity, respectively. a_1 and a_2 are the Forchheimer coefficients (case 4).

For each set of Forchheimer coefficient and velocity range summarised in Table 4.5, the relationship between the velocity and the pressure gradient is calculated under the Forchheimer conditions based on the numerical implementation of case 4 in OGS. Results of the numerical analysis confirm the non-linearity of the relationship, with the velocity becoming increasingly less sensitive to an increase in the pressure gradient for all scenarios (Fig. 4.13).

Parameter	Min value	Max value	Increment
a_1	1×10^0	1×10^4	1×10^1
a_2	1×10^4	1×10^9	1×10^1
v (m/s)	1×10^{-9}	1×10^0	1×10^1

Table 4.5: Range of values for the Forchheimer coefficients a_1 and a_2 and velocities v used for the analysis of the Forcheimer code in OpenGeoSys, for case 4 (upper section) and case 5 (lower section).

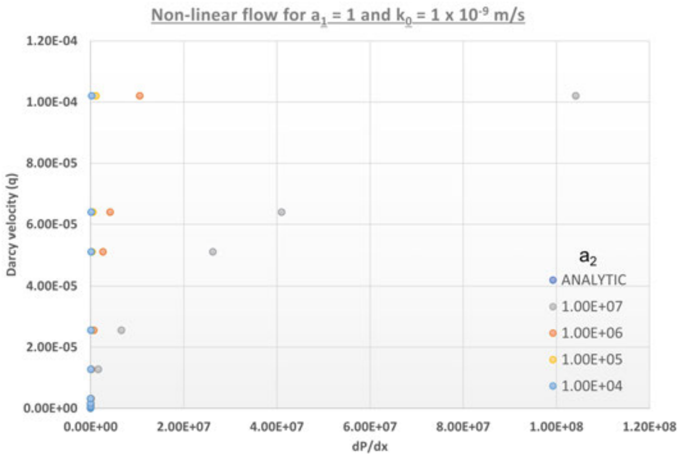

Figure 4.13: Numerical results for the Forchheimer solution (case 4) showing the relationship between the Darcy velocity (m/s) and pressure gradient (Pa/m), for different Forchheimer coefficients a_2.

4.7 Summary

This chapter provided a description of the physics and governing equations for groundwater flow and heat transfer in the subsurface. A review of the different analytical and numerical approaches used in the literature to solve for those equations, accounting for the conceptualisation of flooded coal mine workings was provided. In addition, the key features of the OpenGeoSys modelling code used for the study of groundwater flow and heat transfer in mines in this study were introduced. This sets the background for the numerical analysis implemented in chapters 5, 6, 7 and 8.

Chapter 5

Quantifying vertical borehole heat exchanger sustainability from a geothermal resource perspective in the UK.

5.1 Chapter Overview

This chapter consists of the manuscript submitted to the Geoenergy journal from the Geological Society London. It characterises the available heat for utilisation via a vertical Borehole Heat Exchanger for a single-family house in the Midland Valley of Scotland (MVS) in the UK, which is an area representative of Carboniferous sedimentary basins with low geothermal heat flow, moderate insolation levels, and relatively high heating demand. This chapter aims at characterising the subsurface heat balance in sedimentary basins in the UK, introducing the effect of heat extraction in areas where convective heat transfers are absent (i.e. worst case scenario), and highlighting the risk of over-exploitation. Using both analytical and numerical models based on conductive heat transfers only (i.e. no groundwater flow), we indeed demonstrate that the low rate of renewable heat does not allow the subsurface to naturally recharge under continuous heat extraction from a 100 m deep BHE, leading to the continuous expansion of the area mined in heat, potentially leading to interactions with other future installations. To prevent the depletion of shallow geothermal resources, we recommend the establishment of new heat utilisation regulations incorporating directives on a minimum reinjection percentage, rather than a minimum BHE spacing. Drawing insights from data related to the MVS, we show that local artificial sources of heat such as industrial 'waste' heat or heat from solar collectors can effectively increase the renewal rate of stored heat in the subsurface. In most areas, reinjecting the equivalent of 30-40% of the average annual heating requirements can effectively restrict the thermal footprint of heat extraction and alleviate interferences after 30 years of operation, whilst addressing the energy needs.

5.2 Abstract

Low-temperature geothermal energy is viewed as a renewable resource that could contribute to the decarbonisation of residential heating in the UK. As a first step toward licensing the utilisation of heat, this study constrains the geothermal potential of the shallow subsurface to provide the heating requirements of a typical single-family house via a vertical Borehole Heat Exchanger (BHE). Using a combination of analytical and numerical models, we calculate the heat balance for a typical house with an average garden size in urban areas based on the geological properties of the Carboniferous sedimentary basins in the UK. Our results show that large-scale deployment of Borehole Heat Exchangers can lead to thermal interference causing heat mining. This is because the geothermal flux, insulation rate and radiogenic heat production cannot replenish the heat at < 100 m used on a yearly average by a single household, within the recommended BHE separation distance of 6 m. Under most designs, the lack of natural recharge causes the continuous expansion of the thermal footprint over time at an average rate of 18 m^2/yr over 30 years. Using the distribution of the heat demand in the Midlothian and Edinburgh areas of Scotland as an example, we show that reinjecting artificially $\sim$35% of the heat load extracted yearly, using solar-assisted systems or local industrial waste heat, can guarantee the sustainability of the resource in areas of high demand and limit the areal impact of heat mining. Our work shows that such heat recharge needs to be incorporated into the design of a regulatory framework for Borehole Heat Exchangers to ensure that they provide a resilient long-term sustainable geothermal resource within urban areas.

5.3 Introduction

Heat demand for domestic and industrial space heating accounts for around half of the energy consumption in the United Kingdom. Currently, around 85% of this energy is supplied by natural gas, contributing to about 34% of the nation's Greenhouses Gas Emissions (BEIS, 2019). Following the Paris Agreement, the UK committed via the 2019 Climate Change Act to reach net zero carbon emission by 2050, while Scotland has set this ambition to 2045. To achieve this goal, there is an urgent need to decarbonise residential heat via the replacement of gas boilers with new domestic low-carbon energy sources by mid-2030. Geothermal ground-source heat exchanger, or pump (GSHP), technologies have been increasingly used in Europe since the 1980s for cooling and heating applications (L. Rybach, Megel, & Eugster, 2000). Their deployment has been slower in the UK, where they currently only supply about 0.2% of the total heat demand (Hannon, 2015; Lund & Boyd, 2016). Closed-loop GSHPs are commonly used to access geothermal resources in environments where no groundwater is available via a working fluid circulating in a ground heat exchanger (GHE). Heat pumps are used to raise this low-grade heat to useful temperatures. In contrast to shallow horizontal GSHP systems that are installed down to 6 m depth and are able to harness 'solar' heat, vertical borehole heat exchangers (BHE) can access resources situated down to 200 m depth. There, the ground temperature is mostly controlled by the geothermal gradient and remains stable through the year (Lund & Boyd, 2016). Although the drilling requirements of vertical BHEs imply higher installation costs, vertical BHEs are advantageous in areas of high land price due to the lower land-surface requirements (Trillat-Berdal, Souyri, & Achard, 2007). The higher temperatures accessed by vertical BHEs also allow greater temperature contrasts (ΔT) between the working fluid in the BHE and the surrounding ground, ensuring higher system performances compared to shallow horizontal GHE (C. Chen et al., 2019).

The performance and sustainability of BHEs have been extensively discussed in the literature Lazzari, Priarone, and Zanchini (2010); Lyu et al. (2017); L. Rybach and Eugster (2010); Signorelli, Kohl, and Rybach (2005); Stylianou, Florides, Tassou, Tsiolakis, and Christodoulides (2017); Zanchini, Lazzari, and Priarone (2012); Zhang et al. (2016). Whether isolated or in an array, BHEs are often considered sustainable if the production temperature reaches a quasi-constant value over time, ensuring a stable system coefficient of performances (COP) Rees (2016). This is possible if the ground temperature in the vicinity of the borehole reaches a quasi-steady-state (C. Chen et al., 2019). However, this is not indicative of the rate of heat recharge away from the borehole. L. Rybach and Eugster (2010) used numerical models calibrated on ground temperatures to determine the effect of heat extraction from a single 105 m deep family-house BHE in Switzerland, accounting for the geothermal heat flux and the air temperature (L. Rybach, 2002). Their results showed that the temperature in near-field around a single BHE in heating mode can reach quasi-steady-state after a few years of production, and quasi-total thermal recovery is possible several years after the cessation of the operations. A similar conclusion was obtained by Signorelli et al. (2005) for a BHE array in Switzerland. The authors demonstrated that the lower production temperature and risk of interference linked to an increased temperature decline around BHEs in an array can be compensated by deeper boreholes. Lazzari et al. (2010) assessed the long-term performances of BHEs for different geometries, configurations and working conditions in an environment with negligible groundwater flow. Using a periodic specific heat extraction rate (i.e. the heat load per unit BHE length q) of 20-30 W/m (Luo, Zhang, & Rohn, 2020), the authors showed that steady-state production temperature can be reached when a single BHE is operating even when no reinjection is performed during the summer. However, they also cite that at least partial compensation is required for BHE arrays to reach a constant production temperature.

Where GSHP systems operate in heating mode only, thermal imbalance in the subsurface can have adverse effects on the system efficiency (Capozza, Zarrella, & De Carli, 2015; Dacquay, Lohrenz, & Fujii, 2021; De Carli, Fiorenzato, & Zarrella, 2015; Diersch, 2005; Rivera, Blum, & Bayer, 2015a; Rivera et al., 2015b; Sáez Blázquez et al., 2017). Ground freezing can occur if more heat is extracted than is recharged (Yang, Kong, & Chen, 2015). Hence, determining the ground energy balance, including the rate of heat recharge from the surface and geothermal heat fluxes, is essential to determine the sustainability of long-term BHE operation (Rivera, Blum, & Bayer, 2016). As the number of GSHP systems is expected to increase in the near future, management of the thermal anomalies around a BHE or BHE array also requires consideration of the density of multiple users and their specific heat demand. Walch, Mohajeri, Gudmundsson, and Scartezzini (2021) discussed the risks of interference and over-exploitation of the ground heat capacity due to a dense deployment of BHEs in urban centres in western Switzerland. The results suggest that the technical potential of BHEs of 15.5 kWh/m^2 is insufficient to satisfy the heating demand in a densely populated area. Morchio and Fossa (2019) developed a numerical approach to detail the long-term behaviour of deep (500-800 m long) coaxial BHEs and investigate their thermal performance, independently of the interference issues. In the UK, the Microgeneration Certification Scheme (MCS, Department of Energy and Climate Change (2011)) recommends a minimum separation distance of 6 m between BHEs. However, L. Rybach and Eugster (2010) noted that after 30 years of cyclical production in heating mode only, a cooling of more than 1.5℃ is observed at such distance, with the area cooled by more than 0.1℃ extending up to 50 m away from the BHE in Switzerland. Alternatively, Signorelli et al. (2005) suggested a minimum borehole spacing of 7-8 m, based on the analysis of an array of six 100 m-deep BHEs in Switzerland.

To date, there is no heat ownership model in the UK (Abesser, Schofield, Busby, Bonsor, & Ward, 2018) and no consistent regulations regarding the use of shallow geothermal resources throughout Europe (Tsagarakis, 2020; Vienken, Schelenz, Rink, & Dietrich, 2015). In Germany and Switzerland, the VDI 4640 recommends a maximum thermal load per unit length of borehole of 50 W/m of BHE, which is also the average specific heat extraction rate generally obtained in sedimentary areas (Blum, Campillo, & Kölbel, 2011; Lazzari et al., 2010; Luo et al., 2020; VDI, 2012; H. Wang, Qi, Du, & Gu, 2009). In Spain, the absence of a clear definition of shallow geothermal resources has prevented the implementation of legislation at national levels, making the licensing process of geothermal systems a barrier to the development of the market (Garcia-Gil et al., 2020). Hence, it is crucial to identify the thermal resources available within a given area to guide decision-making and the development of a regulatory framework for the licensing of heat resources and ensure that a large deployment of BHEs can provide a resilient long-term sustainable geothermal resource in urban areas.

In this study, we quantify the heat mining effect of a stand-alone vertical BHE on the shallow geothermal resources (< 100 m) in the Midlothian area located in the Midland Valley of Scotland (MVS), United Kingdom (Browne et al., 1999). The MVS (see Fig. A.26 in Supplementary Material (SM) 1, Appendix A.4.1) is characteristic of mid-latitude regions with a temperate climate in terms of solar insolation, and of low geothermal heat flux typical of Carboniferous deposits/coal mining regions. As a large proportion of the population resides in rural areas that were extensively mined for coal and are today more likely to suffer from energy poverty, shallow vertical BHEs represent a means to comply with the heat demand, whilst achieving the decarbonisation of residential heating. This study aims to assess how far from a BHE heat is accessed to provide the heating requirements of a private user, knowing that the overall spatial disturbance linked to BHEs interferences as multiple users are accessing the same resource will respond to superimposition effects (Spitler & Bernier, 2016). We first perform a thorough analysis of the subsurface heat balance to calculate the heat in place in the MVS, based on the geological and climatic conditions in this area. We analytically quantify the volume of rock that would be required to provide that heat load using the yearly heating consumption of a single-family house in the UK. Based on the impact area for a 100 m BHE, we quantify the rate of natural heat recharge, i.e. how fast the subsurface can be naturally replenished in stored heat via conductive heat transfers when a stand-alone BHE is operating in heating mode, accounting for the relative contribution from the geothermal heat flux, the radiative recharge from the atmosphere (i.e. solar and thermal radiations) and the natural decay of radioactive heat-producing elements (i.e. radiogenic heat production, RHP) (Pollack & Chapman, 1977). Although the sizing of BHE is generally based on the maximum heat load of a property, using the average annual heat consumption is of key importance in the designing of conduction-based systems such as BHE. This approach enables the quantification of the amount of heat mined from the subsurface and demonstrates the requirements for engineered heat recharge. Based on the results from the analytical analysis, we then use transient numerical simulations to investigate the rate of heat mining for a range of scenarios with and without axial and radial heat recharge, assuming a geothermal flux of 0.057 W/m^2. For each scenario, we quantify the transient axial and radial sub-surface heat fluxes over 30 years of production to highlight the source of stored heat accessed by a 100 m and 40 m long BHE and the potential impact on neighbouring BHEs (Rivera et al., 2016).

In contrast to BHE in arrays, interferences between multiple stand-alone BHEs raise the question of heat ownership and not only performance. Hence, we do not aim to compete with the previous studies on the performances of BHEs. Multiple modelling studies are available in the literature, presenting a thorough analysis of the behaviour of BHEs for different scenarios and case studies. This study aims to provide the reader with an alternative perspective on the potential over-exploitation of shallow, low-temperature geothermal resources in temperate and areas with low heat flow and suggests a new heat ownership model, which is of critical importance where multiple BHE are to be constructed. Using geological properties that are characteristic of the Carboniferous successions found in the world, we quantify the maximum heat load that can be extracted from a given area (i.e. the maximum density of BHEs that would permit sustainable utilisation of a low-temperature geothermal resource by multiple users) and the amount of reinjection required to make of BHE a sustainable means of utilising this resource in populated areas. Hence, we ignore the effect of groundwater flow as a prerequisite to the design of heat utilisation regulations.

Although thermal advection does not impact the subsurface conductive heat balance (Hein, Zhu, et al., 2016), it has been suggested to have beneficial effects on the long-term performance of BHEs (Angelotti, Alberti, La Licata, & Antelmi, 2014; Chiasson, Rees, & Spitler, 2000; Dehkordi & Schincariol, 2013; Smith & Elmore, 2018; H. Wang et al., 2009; H. Wang, Yang, Xie, & Qi, 2013; Zanchini et al., 2012). Rivera et al. (2015a) showed that groundwater flow can promote thermal recovery at a given BHE as it increases the area from which heat can be sourced, and promotes the advection of the cold plume away from it, reducing the temperature anomalies in the BHE vicinity (Dehkordi, Schincariol, & Olofsson, 2015; Hu, 2017). Above a certain flow velocity (i.e. 10^{-6} m/s), Angelotti et al. (2014) however suggested that the migration of the cold anomaly downstream reduces the efficiency of heat recovery from reinjection after a heat extraction period. Potential concerns might moreover arise from the migration of this cold plume and the potential impact on BHE users located downstream, especially if those are closely spaced. When no groundwater flow occurs and thermal loads are unbalanced, insufficient BHEs spacing or borehole size can moreover decrease the system performance over time (Lazzari et al., 2010). Our work provides a first insight into the minimal thermal footprint of heat extraction that will need to be taken into account for regulations and guide the licensing of heat in such environments, questioning the minimum recommended separation distance between BHEs of 6 m. It moreover adds crucial geological models to existing engineering models of heat pumps. Through the treatment of the ground as a finite resource, we regard the sustainability issues of BHE from a geological rather than an engineering perspective; we clarify the concept of “steady-state” temperature and show that geological conditions in typical Carboniferous basins in mid-latitude areas cannot naturally provide sustainable heat to vertical BHEs unless they are very widely spaced, or cyclical production with artificial sub-surface heat recharge is implemented.

5.4 Material and methods

The thermal state of the Earth’s crust and the effective ground temperature is controlled by a long-term energy balance between the radiative and geothermal heat fluxes(Beltrami et al., 2015) and by the radiogenic heat production (RHP). Using analytical approaches, we calculate the subsurface heat balance to obtain an estimate of the geothermal resource available and the renewal rate of the heat utilised by a stand-alone BHE, assuming a homogeneous system with a simplified design and no groundwater flow. We then use numerical approaches to simulate the transient subsurface diffusive heat fluxes induced by heat extraction and make realistic assessments of the thermal footprint induced by heat mining. This is used to calculate the amount of engineered recharge that would be required to constrain the thermal plume and regulate the utilisation of shallow geothermal resources.

5.4.1 Subsurface heat balance

Heat in place

The heat in place (Q) corresponds to the total energy contained in a given volume of rock (V) and is controlled by the temperature distribution in the system and the thermal properties of the rocks. Using Eq. 5.1, we can determine the heat that can be extracted from it for a rock temperature change ΔT (i.e. temperature difference at the heat exchanger).

$$Q = \Delta T V \rho c = \Delta T V [(1 - \Phi)\rho_r c_r + \Phi \rho_w c_w] \tag{5.1}$$

Here, we calculate the volume of rock that would be required to meet the yearly average heat demand of a single-family house in the UK via mining of the heat stored in the ground. We consider a rock porosity ϕ = 0.1 and densities and specific heat capacities ρ_r = 2500 kg/m3, c_r = 898 J/kg℃, ρ_w = 1000 kg/m^3 and c_w = 4186 J/(℃.kg), with r and w referring to the rock and pore water, respectively (Table 5.1). The average ρ_r and c_r for the Carboniferous succession in the MVS is calculated using the average ρ_r and c_r for each formation weighted by the formation thickness, as described in the Carrington-1 borehole (A. Monaghan, 2014), situated in the Midlothian area. For each formation, ρ_r and c_r were calculated using the values for each rock type given by Watson (S. M. Watson & Westaway, 2020) (SM1, Appendix A.4.1) and the percentage lithology in each formation determined from geological logs from the BGS GeoDatabase. Although the volumetric heat capacity of the succession will depend on the relative proportion of each rock type and their conductivity (here ρc = 2.44 $\times$ 10^6 J/(℃.m^3)), we show that for an increase in (ρc of 24% (i.e. between dolerite and coal), V decreases by 31%. Among the energy delivered by a heat pump (H), part of it is supplied in the form of electrical heat (E), which reduces the amount of energy that needs to be extracted from the ground (G) to an extent that depends on the system COP (Eq. 5.2) (Banks, 2008).

$$G = H(1 - \frac{1}{COP}) \tag{5.2}$$

With COP = H/E. Using the borehole length h_{BHE} as a reference for the thickness of the cooled sub-surface layer, we can then calculate the areal impact of the extraction of the heat load G using Eq. 5.3, which will be used for the heat balance analysis and estimates of the rate of heat renewal in the MVS.

$$A = \frac{V}{h_{BHE}} \tag{5.3}$$

Formation	Thickness (m)	λ (W/℃.m)	ρ (kg/m^3)	c (J/kg.K)	RHP (μ W/m^3)
MSCM	69	2.02	2605	877	1.713
LSCM	132	1.91	2553	858	1.812
PGP	108	2.91	2534	891	1.018
ULSC	87	2.25	2513	871	1.641
LCS	92	2.24	2581	846	1.299
LLCS	53	1.88	2593	835	1.824
WLO	260	4.36	2500	950	1.824
GUL	162	4.36	2500	950	1.812
ART	37	2.2	2500	950	0.540
Mean		2.2	2557	865	1.75184

Table 5.1: Harmonic mean heat conductivity, density, heat capacity and radiogenic heat production for each Carboniferous Formation. The harmonic mean heat conductivity values are from J. P. Busby (2019) and were calculated based on sample laboratory measurements and formation thicknesses from boreholes in Scotland and England. The harmonic mean density, heat capacity and RHP for each formation were here calculated using rock density and heat capacity values from S. M. Watson and Westaway (2020) and the rock RHP values from Hasterok et al. (2018); Osimobi et al. (2018); Vilà et al. (2010) and the thickness of each rock type determined from the Carrington-1 (A. Monaghan, 2014) borehole, as detailed in Fig. A.27

.

Heat recharge

Geothermal flux. Geothermal energy is often considered as an infinite resource. However, sustainable production is only achieved if the rate of heat recharge to the ground balances the rate of heat extraction over time, but also over a controlled footprint area. The geothermal heat flux (Eq. 5.4) depends on the geothermal gradient of the subsurface ($\frac{\delta T}{\delta z}$), which ranges between 22 and 35℃/km in coalfields in Scotland, with a median value of 25℃/km (Farr et al., 2020), and on the effective heat conductivity of the rock (λ_{eff}).

$$q_G = \lambda_{eff} \frac{dT}{dz} \tag{5.4}$$

We calculate the mean effective thermal conductivity of the Carboniferous succession using the average of the heat conductivities of each formation given in and Busby (J. P. Busby, 2019), weighted on the formation thickness described in the Carrington-1 borehole (A. Monaghan, 2014). The apparent heat conductivity for the Upper Carboniferous Coal Measures and Clackmannan Group in Scotland varies between 2.2 W/(℃.m) and 5 W/(℃.m) (Banks, Withers, Cashmore, & Dimelow, 2013), with the conductivity of individual rocks varying from $\sim$1.5 W/(℃.m) for mudstone (K. E. Rollin, 1987) to 3.3 W/(℃.m) for sandstone (British Geological Survey, 2018; K. E. Rollin, 1987). Using λ_{eff} = 2.2 W/(℃.m) and $\frac{\delta T}{\delta z}$ = 25℃/km, we find that the geothermal heat flux through the overall sedimentary succession q_G averages 57 mW/m^2, with a minimum and maximum q_G = 1.5 W/(℃.m) × 22℃/km = 33 mW/m^2 and q_G = 5.0 W/(℃.m) × 35℃/km = 175 mW/m^2.

By multiplying the assumed geothermal heat flux (q_G) by the areal impact of heat extraction from a vertical BHE (A), we determine the amount of renewal geothermal heat (Q_G) and its relative contribution to the renewal of stored heat used by a BHE ($\%Q_G$) using Eqs. 5.5 and 5.6, respectively.

$$Q_G = A \times q_G \tag{5.5}$$

$$\%Q_G = \frac{Q_G}{G} \times 100 \tag{5.6}$$

Radiogenic Heat Production (RHP). The Earth's natural heat flow is broadly attributed to a contribution from the primordial heat inherited from the formation of Earth and from the natural decay of radioactive elements, typically of the isotopes of uranium (232, 235U), thorium (232Th) and potassium (40K) (Pollack & Chapman, 1977). Due to geochemical differentiation, partial melting and magma crystallisation processes, the upper crust is generally enriched in heat-producing (Beamish & Busby, 2016) and their distribution can provide an important control on the temperature distribution within the Earth's lithosphere (Sandiford & McLaren, 2006). A linear correlation between radiogenic heat production (RHP) and heat flow has been described in the literature and explained by the exponential decrease of heat production with depth within the crust (Lachenbruch, 1970). Although this relationship was verified for granite to low-grade metasedimentary sequences (Richardson & Oxburgh, 1979), no correlation has been identified for the Cornubian batholite in SW England (Wheildon, 1981). There, the surface heat flow pattern was suggested to be controlled by the complex 3D form of the batholite, enhanced by heat refraction caused by thermal conductivity contrasts, and reduced by the lateral heat flow caused by heat production contrasts (Sams & Thomas-Betts, 1988). A combined determination of the conductive heat flow and radiogenic heat production (RHP) can therefore better constrain the subsurface thermal field (Jaupart & Mareschal, 2013).

The MVS is located in a geologically stable part of Earth's crust, where the concentrations of K, Th and U elements are too low to generate significant radiogenic heat (Gillespie et al., 2013). We use the data provided in Table 5.1 to calculate the relative contribution of RHP ($\mu W/m^3$) to the subsurface heat flux in the MVS and its contribution to the renewal of stored heat used by a single BHE. We then compare results with the RHP calculated for the Cornubian granite to assess the importance of RHP (Beamish & Busby, 2016).

Atmospheric heat recharge. In addition to the geothermal heat flux, the temperature of the ground is largely controlled by the yearly average soil temperature, which depends on the air temperature and atmospheric radiations (Banks, 2008; Liang et al., 2019). In summer, the ground surface heats up as a result of intensified solar radiation and elevated temperature (Banks, 2008). However, due to the delayed response of the ground to a heat pulse at the surface, the ground is warmer than the air during the night/in winter and colder than the air during the day/in summer, down to a propagation depth that depends on the amplitude and duration of the fluctuating signal and the ground thermal diffusivity (Eskilson, 1987; Lesperance, Smerdon, & Beltrami, 2010). In the Midlothian area, the yearly average rate of solar insolation (i.e. the direct and diffuse shortwave radiations) is about $\sim$100 W/m^2 (Whitlock, Browne, & Chandler, 2000). With such irradiance ($\sim$1600 × geothermal flux), it is easy to suggest that solar recharge is the dominant control on the heat transmitted to the ground, and an almost infinite resource at the surface. However, this is erroneous, as prior to the heat being transmitted into stored heat in the ground, several factors need to be taken into account, such as the amount of backscattered solar radiation, the longwave radiation emitted by the ground or the surface heat losses due to evaporation and convective processes (Banks, 2008). Using the approach detailed in Supplementary Material 2, we estimate the amount of radiative thermal input to the ground using climate data collected at the meteorological station in Paisley, Glasgow, Scotland (source: Climate, Hydrological and Ecological Research Support System (CHESS) database) (Robinson et al., 2016, 2017). Data collected at this station are extensive and considered to be representative of both the study area and of temperate climates, where the use of GSHP systems presents a strong interest. It is important to note that this does not apply to BHE utilisation in colder regions with low geothermal heat flux, as GHE would extract heat from the ground more intensively and over longer periods (Emmi, Zarrella, De Carli, & Galgaro, 2015).

To overcome the high uncertainties linked to the complex surface energy balance calculations (and the various parametrical assumptions e.g. soil reflectivity, emissivity), we then quantify numerically the amplitude of the seasonal variations in surface heat flux required to reproduce the yearly change in soil temperature measured at 30 cm and 100 cm depth at Paisley, Glasgow (Met Office, 2006, 2019). The model consists of a 1D vertical section composed of 500 line elements representing a saturated porous medium with heat diffusivity α = 7.4 $\times$ 10^{-7} m^2/s, the initial temperature gradient of 25℃/km and surface temperature T_0 = 9℃ corresponding to the yearly average air temperature in the UK. The mean daily heat flux values (Q_s) are calculated using Eq. 5.7 for a series of signal amplitudes (A_s).

$$Q_s = -A_s \times sin(2\pi \frac{\Delta t}{\theta}) - q_G \tag{5.7}$$

where θ is the period of fluctuation (366 days), Δt the time increment (86400 s) and q_G = 0.057 W/m^2 the geothermal flux entering the model from below. For each scenario, surface temperatures are calculated for a period of 100 years to ensure stable conditions. The effect of heat extraction from a BHE using the best-fitting surface heat curve is then compared to a reference scenario with a constant surface heat flux boundary to quantify the contribution of a yearly fluctuating surface heat recharge on the thermal drawdown around the BHE.

5.4.2 Numerical analysis of heat mining

Quantifying the transient ground heat flux regime induced by BHEs is essential to determine the source of power provided by the system and get a better insight into the sustainability of heat extraction.19 Here, we use the OpenGeoSys (OGS) finite element modelling software (C. Chen et al., 2019; Kolditz et al., 2012) to simulate heat transfers in a homogeneous saturated porous medium without groundwater flow, whose properties are defined according to the analytical solution. Axial effects (i.e. heat flux from the volume of rock located above/below (Erol, Hashemi, & François, 2015)) induced by the operation of the 100 m long BHE are first described using 1D models, ignoring the effects of surface heat recharge. The 1D models consist of 1) a 100 m long model representing the BHE interval, situated between 10 and 110 m depth (i.e. no axial recharge) and 2) a 1000 m deep model allowing for axial heat flux. Two 3D diffusion models are then used to quantify the areal footprint of heat mining and quantify the radial heat fluxes. They consist of 1) a 100 m thick model over the BHE depth interval and 2) a 160 m thick allowing for both axial and radial heat fluxes. In the 3D models, the BHE is represented as a vertical line source embedded in the centre of a cylindrical volume with higher mesh resolution, which represents the predicted volume of rock required for heat extraction. The size of the domain (300 m x 300 m) was chosen to be sufficiently large to make sure that the thermal drawdown around the BHE does not interfere with the model lateral boundaries over the simulation period (Hein, Zhu, et al., 2016).

In all models, heat is extracted at a constant rate of G equally distributed along the BHE, with the effects of fluid circulation on the temperature distribution along the BHE walls being neglected. We use a surface heat flux boundary of -0.057 W/m^2 (i.e. equal to the geothermal heat flux) to ensure that the models maintain a natural subsurface heat balance before operation starts. The contribution of the surface boundary to the heat recharge of vertical BHEs has been discussed in the past. Whilst first-type surface temperature boundary conditions intrinsically prevent cooling to occur at the surface (Rivera et al., 2015a), Rivera et al. (2016) showed using a Cauchy surface boundary condition that the ground surface can supply 26-40% the total power demand for a single 100 m BHE; however, its contribution increases with time (Rivera et al., 2015b) and decreases as the BHE length increases (Bidarmaghz, Narsilio, Johnston, & Colls, 2016; Erol et al., 2015). By setting a heat flux boundary, we here allow for the propagation of ground cooling to the ground surface and therefore avoid overestimating the heat recharge from the atmosphere (i.e. worst-case scenario). Alternative scenarios accounting for the increase in the surface heat flux as the surface cools down during operation or displaying forced surface recharge (i.e. constant temperature boundary) are then presented to discuss the significance of the top boundary condition and assess the uncertainties in the estimates of the long-term potential of BHEs systems.

For each scenario, we calculate the amplitude of the diffusive axial heat flux q_{ax} (Eq. 5.8) from the 1D results and the radial heat flux q_{rn} (Eqs. 5.10 and 5.11) at the interfaces of the different volumes defined in the 3D models (W/m^2), as well as their relative contribution Q_{ax} and Q_{rad} (%) to the heat mined by the BHE (Eqs. 5.9 and 5.12), respectively.

$$q_{ax} = \frac{\frac{\Delta E_{OUT}}{\Delta t} - \frac{\Delta E_{v_{BHE}}}{\Delta t}}{2 \times S_{BHE}} \tag{5.8}$$

With ΔE_{BHE} and $\Delta E_{v_{OUT}}$ the energy change in the BHE interval and in the over/underlying rock volumes (J), respectively, for a considered time step Δt (s), and $S_{BHE} = \pi r^2$ (m^2) the surface area of the borehole (r = 16 m).

$$Q_{ax,t} = \frac{E_{v_{out,t_0}} - E_{v_{out,t}}}{E_{t_0} - E_t} \times 100(\%) \tag{5.9}$$

Where E_{t_0} and E_t are the initial energy content (i.e. at time t_0) and the total energy in the system at time t (s), respectively, and $E_{v_{out,t_0}}$, $E_{v_{out,t}}$, are the energy content in the volumes located above/below the BHE depth interval (v_{OUT}) at time t_0 and t, respectively.

$$q_{rn} = \frac{\frac{\Delta E_{v<r}}{\Delta t} - \frac{\Delta E_{v>r}}{\Delta t}}{S_r} \tag{5.10}$$

with v the volume of rock in the BHE depth interval located within a distance r < 2 m, between 2 m < r < 6 m, 6 m < r < 16 m or at r > 16 m from the BHE, as described later, and $S_r = 2\pi r h_{BHE}$ the area of the interface for the considered volume. For r = r_a (i.e. the radius of the area calculated analytically), the steady-state q_{rn} can be compared to the analytical solution q_{ra} given by Eq. 5.11.

$$q_{ra} = \frac{H_m}{2\pi r h_{BHE}} \tag{5.11}$$

With $H_m = G - Q_G$ the amount of heat to be mined by the BHE, neglecting the radiative recharge and RHP, and $2\pi r h_{BHE}$ the lateral area of the cylinder at a distance r from the BHE. Therefore, the relative contribution of each volume within a radius r from the BHE and after a production period t is:

$$Q_{rad,t} = \frac{E_{v<r,t_0} - E_{v<r,t}}{E_{t_0} - E_t} \times 100(\%) \tag{5.12}$$

5.5 Results

5.5.1 Subsurface heat balance

Here, we quantify analytically the volume of stored heat in the subsurface required to satisfy the typical heat demand of a single-family house in the UK and the natural heat sources which may balance this (i.e. the geothermal and radiative heat flux and RHP). This is a pre-requisite to the understanding of the long-term thermal footprint of heat extraction and the necessity of engineered heat recharge.

Heat in place

The yearly average gas consumption for a 3-bedroom house in the UK is $\sim$ 12,300 kWh, including 9,800 kWh for space heating and 2,500 kWh for hot water (OFGEM). Assuming a yearly average space heating and hot water usage time of 5.4 h/day (Morley, 2022) and 2 h/day, respectively, the peak heat requirement for such property amount H = 8,430 W (BEIS, 2019), of which G = 6,320 W would be extracted from the ground under a heat pump COP of 4 (Eq. 5.2), e.g. value used in the literature for 70 m - 150 m long BHEs (Hein, Kolditz, Görke, Bucher, & Shao, 2016; X. Wang et al., 2018), with the greater the COP and the higher the heat sourced from the ground. This represents a total energy requirement of Q = 1.00 $\times$ 10^{12} J over 30 years, which is equivalent to the extraction of G = 1,058 W from the ground on a yearly average (i.e. heat requirements equally distributed over 24h rather than as a peak heat load). If the overall volume of rock cools by ΔT = 5℃ over 30 years (H. Wang, Qi, Du, & Gu, 2010; Zhai, Cheng, & Wang, 2017), $\sim$ 80,500 m^3 of rock would be needed to provide those heat requirements from stored heat. For a 100 m-deep vertical BHE situated under the property with specific peak heat extraction rate of $\sim$ 60 W/m (yearly average q = 11 W/m), this represents a cooled sub-surface area $A \approx$ 804 m^2 (Eq. 5.3) with a radius of impact r_a = 16 m (Fig. 5.1), which is about four times the median garden size for a house in the UK (226 m^2) (Ons.gov.uk, 2020). For such heating requirements (e.g. 10 kW), two or three 80-110 m BHE are generally used (Tamas Vekony, 2023).

However, we consider multiple boreholes as a whole, ignoring interference issues and looking only at the overall subsurface heat balance. A longer BHE would also be able to access greater temperatures and reduce the area of impact but increase the drilling cost. Assuming a more reasonable specific peak heat extraction rate of 30-35 W/m, a single $\sim$180-210 m long BHE would be required to provide the necessary heat load to a single house, reducing the analytical thermal footprint to 380 - 450 m^2 after 30 years of operation (r_a < 12 m). A 360 m deep BHE would be required to constrain the heat plume to the average size of a house with gardens (r_a = 8 m and q = 18 W/m). A separation distance of 6 m, as recommended in the UK, would mean that the specific heat extraction rate is no more than 8 W/m, which would require a 700 m deep BHE. It is important to note that from an analytical perspective, those values also depend on the BHE inlet and outlet temperatures ΔT, with the greater the temperature contrasts at the heat pump/the permitted cooling and the smaller the volume of rock required.

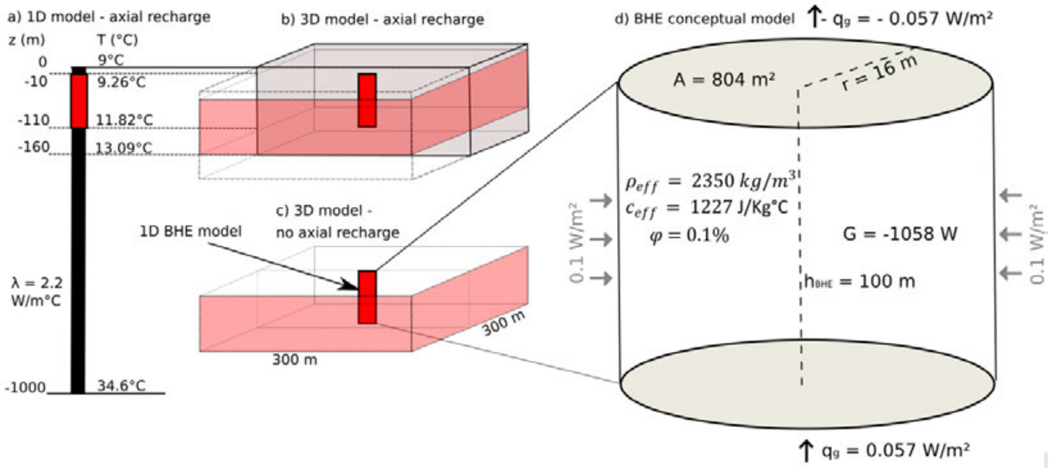

Figure 5.1: Conceptual sketches representing a) the 1D 1000 m long and b) 3D 160 m thick models with axial recharge, c) the 100 m thick 1D and 3D BHE models and d) the heat balance around the vertical BHE determined from analytical models considering ΔT = 5℃, G = 1,058 W and a heat pump COP = 4.0. All models assume an initial temperature gradient of 25℃/km and an effective thermal conductivity of λ_{eff} = 2.2 W/m^2. The 100 m and 160 m thick 3D models are composed of 235,000 and 376,000 prismatic elements, respectively. The radial heat flux q_{ra} = 0.1 W/m (Eq. 5.11) is calculated based on the heat balance for a 100 m long BHE and an area of 804 m^2 (r = 16 m) considering heat recharge from the geothermal flux only.

Heat recharge

In this section, we constrain the proportion of stored heat renewed via the geothermal flux, radiative flux and RHP on a yearly basis, considering the areal impact of a 100 m BHE over 30 years (A = 804 m^2).

Geothermal flux. Assuming $\frac{\delta T}{\delta z}$ = 25℃/km and λ_{eff} = 2.2 W/(℃.m), the average geothermal heat flux q_G in Midlothian is 0.057 W/m^2 (Eq. 5.4). Balancing heat availability (i.e. for an impact area A = 804 m^2) and heat extraction, such geothermal flux would provide up to $Q_G \approx$ 46 W of geothermal heat recharge to the BHE (Eq. 5.5), representing $\%Q_G \approx$ 4% of the yearly average heat demand (Eq. 5.6). Alternatively, a total area of $\sim$ 18,000 m^2 would be required to fully balance the energy extracted by a 100 m long BHE over a year, which is $\sim$ 80 times the median size for a house with a garden. Considering the minimum and maximum geothermal fluxes of 0.033 and 0.175 W/m^2, the minimum and maximum contribution of the geothermal heat to the recharge of a BHE over a 804 m^2 area would be 2.5% (27 W) and 13% (141 W).

Radiogenic Heat Production (RHP). Considering a total rock volume of 80,500 m^3 with an average RHP of 1.542 μ W/m^3 (Table 5.1), the total heat generated within a typical sedimentary section in the Midlothian Coalfield would equal 0.12 W, which represents $\sim$0.01% of the yearly average heat requirements G = 1,058 W. Granitic intrusions are considered as a better geothermal resource, with the higher heat flux observed above intrusions being often associated to the greater radionuclide concentration, and therefore a greater heat production. The RHP values calculated for the Cornubian granite average 3.8 μW/m^3 (Beamish & Busby, 2016). Using a maximum value of 6 μW/m^3, the total RHP in the 80,500 m^3 volume would be 0.483 W, which is 0.05% of the required heat load. This suggests although the presence of radiogenic elements can locally increase the geothermal heat flux, it does not contribute significantly to the stored heat renewal over the lifetime of a BHE system. More importantly, it suggests that the higher geothermal flux measured in granitic areas, and its capacity to recharge the system in heat, mostly results from the higher thermal conductivity of granite rather than from its radionuclide concentration (Wheildon, 1981). Higher residual temperatures linked to the intrusion of the magmatic body and the latent heat released from its cooling could also explain the higher geothermal gradient and heat flux observed in such areas.

Atmospheric heat recharge. The yearly average downward shortwave and longwave radiation measured in Paisley, Glasgow over the period 1998-2012 equal q_{sw} = 104 W/m^2 and q_{lw} = 321 W/m^2, respectively (Robinson et al., 2016, 2017). Part of those incoming radiations are reflected back to space by the Earth's surface, depending on the surface albedo α_{sw} (0.18) and emissivity (ε = 0.98) (Liang et al., 2019), as described in SM2 (Appendix A.4.2). The radiations absorbed by the land surface heat the ground and are then either radiated back to the atmosphere as longwave thermal radiation ($\sim$360 W/m^2), lost as latent heat via evapotranspiration q_{evap} ($\sim$ 35 W/m^2) or as sensible heat such as rising air currents q_{conv} ($\sim$18 W/m^2). Balancing the net surface radiation budget to the surface heat balance equation, we can quantify the surface imbalance and estimate the yearly average thermal input from the atmosphere to the ground (Eq. 5.13) (Jia, Liang, Jiang, Zhang, & Wang, 2018; Liang et al., 2019).

$$R_n = (1-\alpha_{sw}) \times q_{sw} + \varepsilon q_{lw} - \sigma \varepsilon T_s^4 = q_{evap} + q_{conv} + q_g + \Delta G \tag{5.13}$$

Although heat can be conducted to depth and temporarily stored in the ground during the summer, the ground tends to release this energy back to the atmosphere in winter as the air temperature and the incoming solar radiation are reduced. In a balanced Earth-atmosphere heat budget, this process allows the ground to maintain a relatively constant temperature over time (Banks, 2008; Shuttleworth, 2012). Assuming that no heat is extracted from the ground, the change in heat stored in the ground (ΔG) will therefore tend to zero over the long term, with the geothermal and radiative heat flux maintaining a natural balance. However, the results presented in Fig. A.31 suggest a large variability of ground surface heat balance calculated at Paisley, with an average loss of heat of ΔG = -5 ±2 W/m over 1998 – 2012 and heat inputs of up to 2 W/m calculated for individual years. This can be explained by the large uncertainties that affect these calculations, including uncertainties in the albedo and emissivity estimates, the use of mathematical approximations, errors in the meteorological data, but also by the bias generated by missing datasets. In order to overcome those uncertainties, we then quantify numerically the yearly change in stored heat (i.e radiative energy absorbed and released at the surface in summer and winter, respectively) using the 1D approach described in methods (Eq. 5.7). We use this to determine the amplitude of the seasonal fluctuations A_s of the surface heat flux Q_s required to reproduce the yearly change in ground temperature at 30 cm and 100 cm below ground level at Paisley, Glasgow (Met Office, 2006, 2019; Robinson et al., 2016, 2017). Using a Neumann surface boundary condition, we can reproduce the change in ground temperature for A_s = ± 8 W/m^2, accounting for the time lag between a change in the air temperature and the response of the ground surface to the heat pulse (Fig. 5.2). For a ground conductivity of 2.2 W/°C.m, the fluctuating surface temperature signal propagates downward with time, and decreases exponentially down to $\sim$ 15 m where the absolute temperature change over a year is < 0.1 °C. Below that penetration depth, the geothermal heat flux dominates, and the temperature profile increases slowly, according to the local geothermal gradient (Banks, 2008).

Considering the variation of the radiative heat flux between 0 and 8 W/m^2 over 6 months of the year and ignoring the heat losses in winter, the heat input from the atmosphere represents 2.5 W/m^2 over a yearly average. Although such heat input would induce continuous warming of the ground in a balanced system, it represents the maximum radiative recharge potential that would be permitted through the cooling of the ground surface under the operation of a BHE. Hence, a footprint area of 420 m^2 (r $\sim$ 11 m) would be sufficient for the solar heat input to balance the heat extracted from the ground (Fig. 5.3), which is almost half the impact area calculated for a scenario without solar recharge, but about twice the average size of a house with garden in the UK.

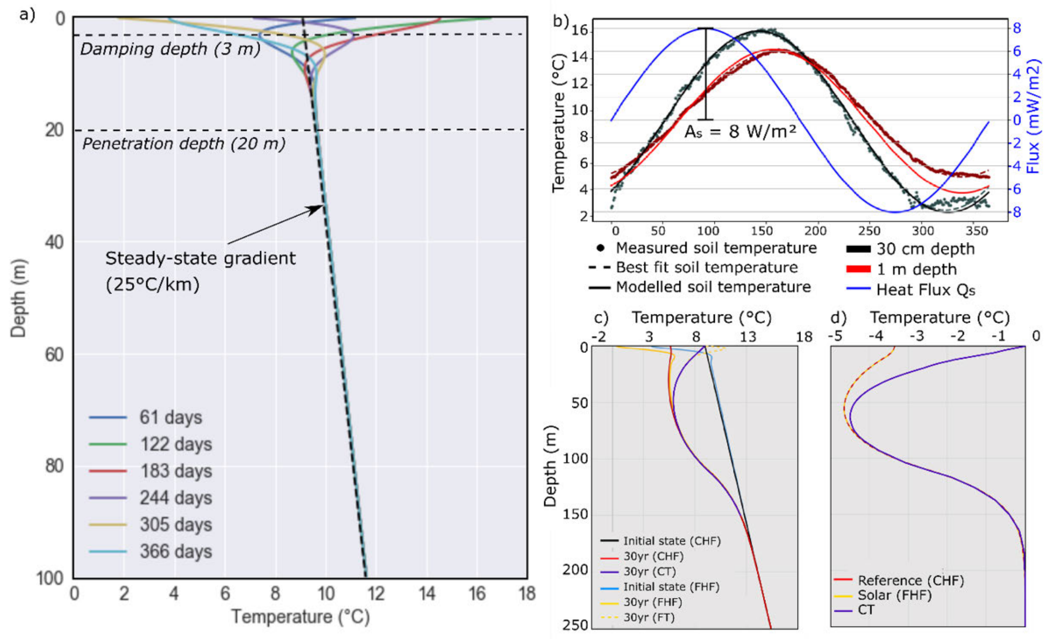

Figure 5.2: Effects of a time-varying surface heat flux boundary on the temperature profiles. a) Temperature profiles calculated at different times of the year for a balanced system (no production) with effective ground conductivity of 2.2 W/m^2. b) Comparison between the surface temperature obtained using a time-varying surface heat flux with A_s = $\pm$8 W/m^2 (blue curve) and the daily soil temperature data measured at z = 30 cm and z = 100 cm at Paisley in 2000 (Met Office, 2006, 2019). c) Temperature profiles and d) temperature drawdown after 30 years of production for constant and fluctuating surface temperature (CT and FT, respectively) and constant and fluctuating surface heat flux (CHF and FHF, respectively) boundary conditions.

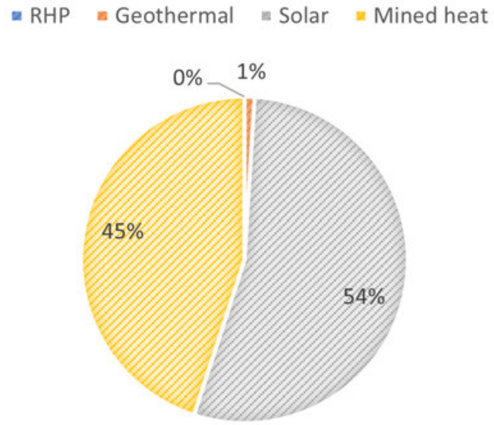

Figure 5.3: Pie chart showing the relative contribution of geothermal, solar energy and RHP in the renewal of the heat stored in the sub-surface, assuming a 226 m^2 area and a 100 m deep BHE.

5.5.2 Numerical analysis of heat mining

It is known that the production temperature of a BHE decreases exponentially as the thermal plume increases until reaching a quasi-steady-state condition (Banks, 2008; Beier, 2020; C. S. Brown, Cassidy, Egan, & Griffiths, 2021; Saadi & Gomri, 2017). To constrain the long-term dynamic and 3D transient mechanisms of heat mining from a shallow vertical BHE (h_{BHE} = 100 m), we here simulate numerically the continuous extraction of a heat load G = 1,058 W from a medium with effective thermal conductivity λ_{eff} = 2.2 W/(℃.m) for 30 years.

Axial heat flux

Fig. 5.4(a, c) shows the calculated temperature profiles after 1 and 30 years of heat extraction from the 1D 1000 m and 100 m long models, both having a fixed area of 804 m^2. Results from the 100 m model (dark blue line) confirm a uniform temperature decline of 5℃ along the BHE after 30 years, in accordance with the analytical solution. As heat extraction modifies the thermal field around the BHE, axial effects become more important (Erol et al., 2015). Using Eq. 5.9 we show that although axial recharge Q_{ax} is limited to 4% within the first year, $\sim$18% of the heat is mined via axial heat transfers after 30 years, reducing the thermal drawdown at the mid-BHE depth by 0.4℃ compared to a scenario with no axial recharge (Fig. 5.4c) (Bidarmaghz et al., 2016). Fig. 5.4(b, d) shows the temperature profiles extracted from the 3D numerical models at the BHE location (r = 0 m), at r = 6 m (i.e. minimum recommended separation distance between BHEs) and at r_a = 16 m, after 1 year and 30 years. In 3D, the temperature decline is not uniform around the BHE. Whilst a drawdown of 2.8℃ is observed at r = 0 m after 1 year, it is negligible at r = 16 m (Fig. 5.4b). After 30 years (Fig. 5.4d), the temperature at r = 16 m has declined by 0.78℃ and is 20% of the drawdown observed at the r = 0 m (ΔT = -4.1℃), which suggests the existence of a cone of thermal depression extending beyond the limits of the area predicted by the analytical solution. Although axial effects seem limited to both BHE ends within the whole duration of the simulation, with negligible effects on the temperature profile within the BHE interval, calculations confirm an increase of Q_{ax} from 4% to 18% after 1 and 30 years of production, respectively (see Fig. A.34).

Fig. 5.5 displays the temperature distribution along two horizontal profiles located at the surface and at the mid-BHE depth (i.e. z = -60 m) of the 3D 160 m deep model after 1 and 30 years of operation. In this model, we assume no surface recharge but allow for axial effects, as the BHE top is located at 10 m depth. Our results depict a funnel-shaped drawdown(Eskilson, 1987), where the temperature decline is the largest at the BHE location and quickly decreases with distance from it (Hein, Zhu, et al., 2016). Considering temperature decline threshold of 0.5℃, we calculate that the thermal footprint at z = -60 m extends up to $\sim$50 m^2 ($r \approx$ 4 m) after a year and $\sim$1660 m^2 ($r \approx$ 23 m) after 30 years (i.e. 144% of the analytical impact radius r_a = 16 m). Whilst no significant cooling is detected at the surface after a year, about 615 m^2 (r = 14 m) has cooled by ΔT > 0.5℃ after 30 years, with a maximum surface temperature drawdown

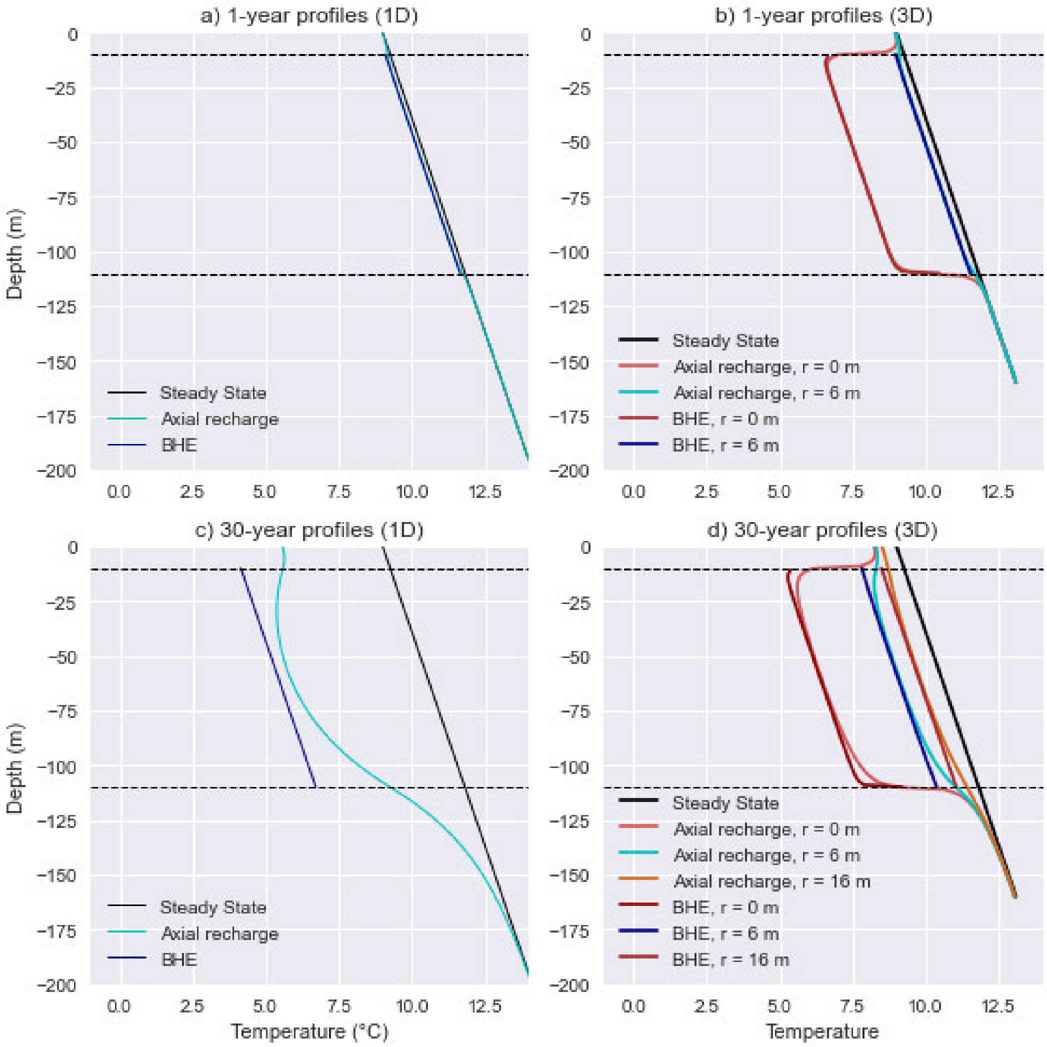

Figure 5.4: Temperature profile for the a) 1D and b) 3D models after 1 year of heat extraction, and for the c) 1D and d) 3D models after 30 years of heat extraction. The black profile corresponds to the initial temperature gradient of 25℃/km. Profiles from the 3D models are extracted at distances x = 0 m and x = 16 m from the BHE, which is the radius of the area for the corresponding 1D model (804 m^2). Profiles with axial recharge correspond to the 1D 1000-m long and 3D 160-m thick models while BHE profiles are 100-m long models ignoring the effects of head conduction from above/below the BHE.

of -0.8 ℃ measured above the BHE. Considering a 1 ℃ cooling threshold, the thermal footprint at the mid-BHE depth is reduced to ~310 m^2 ($r \approx$ 10 m) after 30 years. This is only 63% of the analytical impact radius r_a, but almost twice the minimum BHE spacing recommended by the MCS specifications for a 200 m BHE, with the temperature decline at r = 6 m reaching 0.3 ℃ and 1.5 ℃ after 1 and 30 years of operation, respectively (Fig. 5.5).

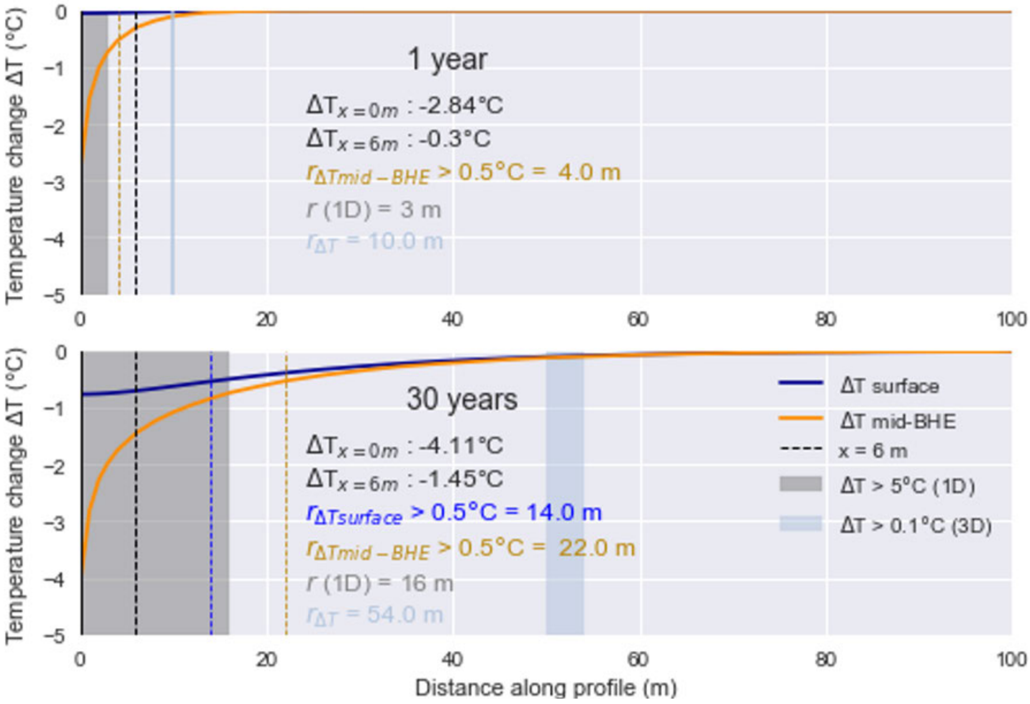

Figure 5.5: Horizontal profiles of temperature drawdown at the surface (solid blue) and at the mid-BHE depth (solid orange) after 1 year (upper panel) and 30 years (lower panel) of heat extraction from a 100 m BHE located at 10 m depth. The shaded grey area represents the impact volume predicted by the analytical models (with ΔT = 5 ℃) and the light blue shaded area is the actual distance from the BHE to which a temperature decline ΔT > 0.1 ℃ is observed in the 3D model. At r_a = 16 m, a cooling of -0.5 ℃ and -0.7 ℃ is measured at the surface and at the depth after 30 years. The area cooled by more than 0.1 ℃ detected both at depth and at the ground surface extends up to r = 54 m from the BHE after 30 years, in accordance with L. Rybach and Eugster (2010), which represents ~9,000 m^2. The blue and yellow dashed lines delineate the extent of the thermal drawdown for ΔT > 0.5 ℃ at the surface and at the mid-BHE depth, respectively. The dashed black line indicates the location of the recommended separation distance between BHEs in the current UK regulations.

Thermal footprint and radial heat mining

To constrain the thermal footprint, we quantify analytically and numerically the radial heat fluxes induced by the lateral temperature drawdown, and the proportion of heat mined within the finite volume of rocks situated at distances r < 2 m, 2 < r < 6 m, 6 m < r < 16 m and r > 16 m from the BHE to get insights into the origin of the heat extracted over time and the expansion rate of the thermal plume. As we have constrained that only 4% of the heat extracted annually is renewed by the geothermal flux, H_m = 1012 W would be mined from the source rock (Eq. 5.11), resulting in a steady-state radial heat flux (i.e. independent of the ground thermal conductivity) of q_{ra} = 0.1 W/m^2 on the outskirts of the 804 m^2 impact area at r_a = 16 m, which is almost twice the geothermal flux q_G (Fig. 5.1). A maximum geothermal heat recharge of 13% would only reduce q_{ra} to 0.09 W/m (H_m= 917 W), which confirm the key effect of lateral heat mining beyond the limit of the area selected for the analytical comparison. Using the numerical approach described in Methods, we find that when no axial recharge is allowed, $\sim$13% of the heat is mined from the area surrounding the borehole (r < 2 m) within the first year, with 94% of the energy being mined from the area at r < 16 m (Fig. A.34). After $\sim$4 years, most of the heat is sourced from the volume of rock located at r > 16 m, which represents 77% of the recharge after 30 years, with only 1% of the heat being sourced in the vicinity of the BHE (r < 2 m). At r = 2 m, r = 6m and r = 16 m, the radial heat fluxes q_{rn} approach $\sim$ 0.8 W/m^2, $\sim$0.3 W/m^2 and $\sim$0.09 W/m^2 after $\sim$10-30 years, respectively (Eq. 5.10). This corroborates with results from the analytical solution (Fig. 5.1), with the difference of 0.01 ℃ indicating that steady-state conditions at r = 16 m in the transient 3D model are not reached within 30 years.

The extent of the thermal footprint of the BHE predicted by the models to satisfy the BHE heat demand stipulated as a source term, is dependent on the geometry of the models and in particular, the location and type of boundary conditions assumed. Increased heat availability due to axial effects, which are particularly effective in the immediate vicinity of the BHE where the temperature contrasts are highest (see dashed and plain green curves from the 100 and 160 m deep models, Fig. 5.6a), reduces the heat which needs to be extracted in the perimeter of the model to satisfy the heat demand (see dotted and dashed pink curves, Fig. 5.6b). In the considered scenario, axial recharge reduces by 23% the rate of heat mining in the far field areas after 30 years, which reduces the areal footprint of heat extraction over the long term.

Fig. 5.7 shows the relationship between the extent of the thermal plume and the amplitude of the axial q_{ax} and radial fluxes q_{rn} after 1, 10, 30 and 100 years, extracted from the 160 m deep 3D model. In accordance with the time series presented in Fig. 5.6, it suggests that radial and axial heat fluxes in the vicinity of the borehole tend to approach a steady-state after $\sim$10 years after the start of production. The expansion rate of the thermal plume under heat extraction is the fastest in the initial years of production and decreases over time, with an average of 18 m^2/yr over the 30-year period (delineated based on a 1 ℃ cooling). Although

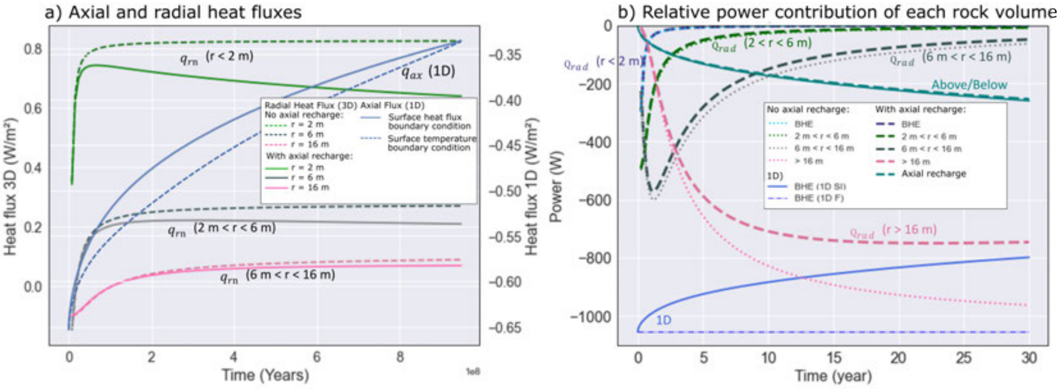

Figure 5.6: a) Axial heat flux q_{ax} calculated from the 1D modelling results using constant surface heat flux and constant surface temperature (Eq. 5.8) and radial heat fluxes q_{rn} at the volume interfaces from the 3D model (Eq. 5.10). b) Relative changes in power contributions showing the source of the heat mined by the BHE above/below (Qax) and at r < 2 m, 2 < r < 6 m, 6 < r < 16 m or r > 16 m from the BHE (Q_{rad}) in the 1D and 3D models, respectively, in scenarios with and without axial recharge (Eqs. 5.9 and 5.12). The blue line shows the amount of heat mined over time via axial effects in the 1D model (versus the heat mined from stored heat in the BHE interval as no radial heat recharge is allowed). After 3 years, most of the heat is mined from the far field area (r > 16 m).

a quasi-steady temperature can be reached at the borehole location, this does not indicate a balanced heat replenishment of the sub-surface, as the mining of heat in the far field area causes the continued expansion of the thermal plume (Banks, 2015). We find that lateral heat mining propagates away from the BHE, and downward axial heat fluxes propagate above the BHE, causing the cooling of the near-surface area just above the BHE top.

Engineered recharge requirements

Previous studies have shown that the irreversible cooling of the ground can be caused by yearly imbalances in heat extraction and injection from GSHP systems over long operational periods, in areas where the summer cooling needs are low. Cyclic production or artificial heat recharge during the non-heating season have been seen as solutions to mitigate the accumulation of cooling into the ground and achieve sustainable heat extraction (Ann Cruickshank & Baldwin, 2016; Cui, Diao, Gao, & Fang, 2015). Experimental studies have also shown that systems combining geothermal heat pumps and thermal solar collectors can establish a heat balance in the ground through the reinjection of excess heat not used for hot water heating (Trillat-Berdal et al., 2007), or via seasonal storage of industrial waste heat (Cui et al., 2015). In addition to solar thermal, photovoltaic, water-source heat-pump, heat boilers and CHP installations, the Midlothian area in Scotland is home to datacentres, waste incinerators and landfill gas infrastructures that represent potential sources of heat currently released into

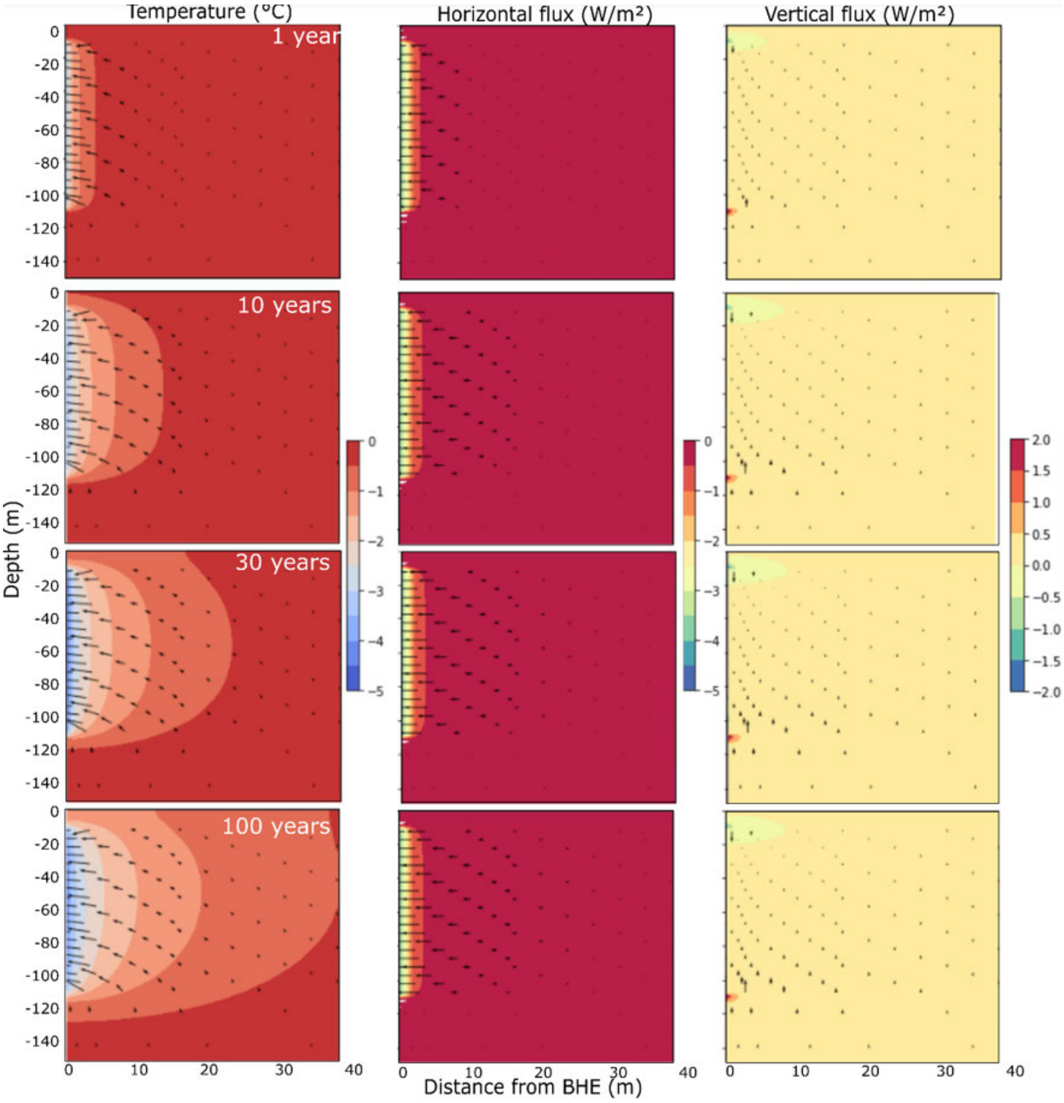

Figure 5.7: 2D vertical section in the central part of the 160 m thick 3D model showing the temperature distribution (1st column) and horizontal (2rd column, q_{rn}) and the vertical (2^{nd} column, q_{ax}) components of the heat fluxes after 1, 10, 30 and 100 years of heat extraction. The arrows in the 1^{st}, 2^{nd} and 3^{rd} columns represent the total, horizontal and vertical components of the heat flux, respectively. The scales for the horizontal and vertical flux are different to highlight the bi-directionality of the axial heat flux compared to the radial heat flux shown in this figure, with the maximum amplitude of the radial heat flux being more than twice the maximum amplitude of the axial heat flux.

the atmosphere (Fig. 5.8) (Survey, 2021). The storage of excess or industrial waste heat in shallow underground coal mines, located directly under a populated area, could therefore represent an efficient way to increase the sub-surface heat flux and ensure the sustainability of shallow geothermal systems (Fraser-Harris et al., 2022).

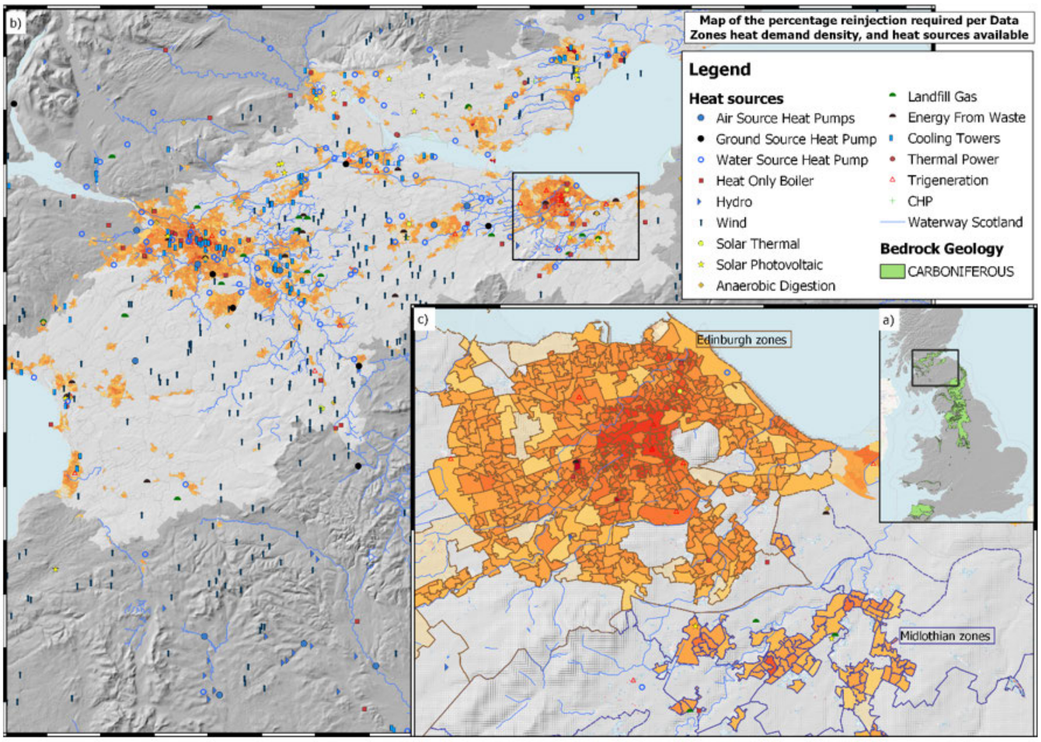

Figure 5.8: a) Regional view of the UK with the distribution of the Carboniferous deposits and outline of map b). b) Map of the Midland Valley of Scotland showing the percentage reinjection required in the data zone (see Scotland Heat map) and the heat sources available. c) Zoom over the Edinburgh and Midlothian data zones, outlines in brown and purple, respectively.

Given the limited contribution of atmospheric and geothermal heat recharge to the yearly renewal of stored heat, we use the 160 m deep 3D model developed in this study to determine the amount of periodic heat recharge that would be required to constrain the thermal plume within a required distance. A series of simulations considering the reinjection of 3 to 100% of the heat load extracted yearly are performed. The model results displayed in Fig. 5.9 depict the impact radius after 30 years of operation resulting from cyclical injection and production, considering cooling thresholds ΔT of 0.5℃ and 1℃ at the mid-BHE depth. These indicate that 10% and 50% of the heat load extracted would need to be reinjected yearly to constrain the thermal drawdown to an impact radius r = 6 m after 30 years, for ΔT > 1℃ and 0.5℃, respectively, i.e. 320 W and 1600 W reinjected during 3 summer months. Those results are in accordance with Bayer, de Paly, and Beck (2014) where a 6 m spacing between 78 m-deep BHE in an array with λ = 2.8 W/(℃.m) was shown to induce ground freezing after 15 years, whilst the reinjection of 50% of the extracted energy in summer significantly reduced ground cooling. Such power output could be provided through the installation of solar collectors, with the typical wattage of a premium solar panel reaching 300 W, which is about 30% of the yearly heating requirements of a single-family house in the UK (Now, 2021).

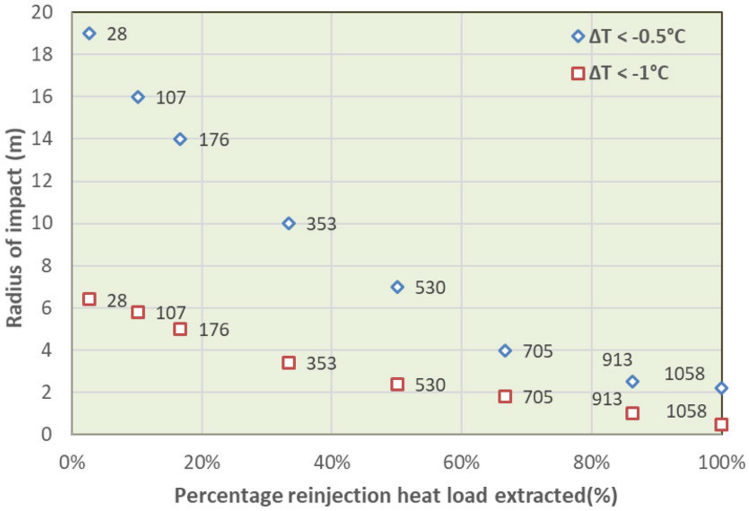

Figure 5.9: Relationship between the percentage of reinjection of the heat load extracted and the radius of impact of heat extraction from a 100 m BHE for λ = 2.2 W/(℃.m) after 30 years (for ΔT < -0.5℃). The labels correspond to the yearly heat load injected in W.

We analyse the implication of those results on the reinjection requirements in the MVS. There, the heat in place calculated for resources < 100 m depth using the properties given in Table 5.1 and a temperature decline ΔT = 0.2℃/yr (Eq. 5.1) averages 11.3 kWh/(m^2.yr), representing a total available heat of 6.63 $\times$ 10^{10} kWh/yr. Based on the heat demand given by the Scotland Heat Map (Survey, 2021), we find that although the overall total demand in the MVS is about half the heat available (i.e. $\sim$3.6 $\times$ 10^{10} kWh/yr), it is not distributed equally within the territory. As a result, the heat in place cannot meet the demand (i.e. where Q available / Q demand < 1) in 90% of the data zones (Fig. 5.8), which represents a heat deficit of 2.2 $\times$ 10^{10} kWh/yr (SM4, Appendix A.4.4).

We determine for each data zone the amount of reinjection that would be required to guarantee 30 years of sustainable heat extraction from the 100 m deep BHE and prevent interferences between users. To do so, we first calculate the number of BHEs that would be required to satisfy the demand in each data zone, assuming 100 m deep BHE and a heat capacity of 1,058 W/BHE. By dividing the data zone area by the number of required BHE, we obtain the area available for each BHE. Using the results described in Fig. 5.9, we then determine for each data zone the percentage of reinjection that would be required to constrain the radius of impact to the calculated area available for each BHE, considering a maximum temperature decline ΔT = 0.5℃ at the mid-BHE depth. Such threshold is treated as a compromise between a 1℃ cooling that would represent significant interference risks and a no-risk scenario that would assume a maximum temperature decline of 0.1℃ at the thermal footprint boundary. Results suggest that for a total heat demand of 3.6×10^{10} kWh/yr in the MVS, 1.64 $\times$ 10^{10} kWh/yr would need to be reinjected in areas of high demand, to constrain the thermal footprint around BHEs (SM4, Appendix A.4.4). This is less than the value of 2.2 $\times$ 10^{10} kWh/yr estimated analytically, given that a certain volume of ground is here allowed to cool around each BHE.

Fig. 5.10 indicates the distribution of the reinjection requirements per data zone in the MVS and suggests that for most systems in urban areas, the reinjection needs are only 30-40% of the heat load extracted, which is less than half the yearly average heat requirements. Whilst 7 regions located in Fife, Edinburgh and Glasgow would need full reinjection of the yearly average heat load extracted by the 100 m-deep BHEs, sustainable heat extraction is possible in rural areas, where vertical BHEs are more widely spaced. We however note that in a few areas where the heat in place is slightly higher than the heat demand, $\sim$10% reinjection of the heat load extracted is required to prevent interferences between users in the long term.

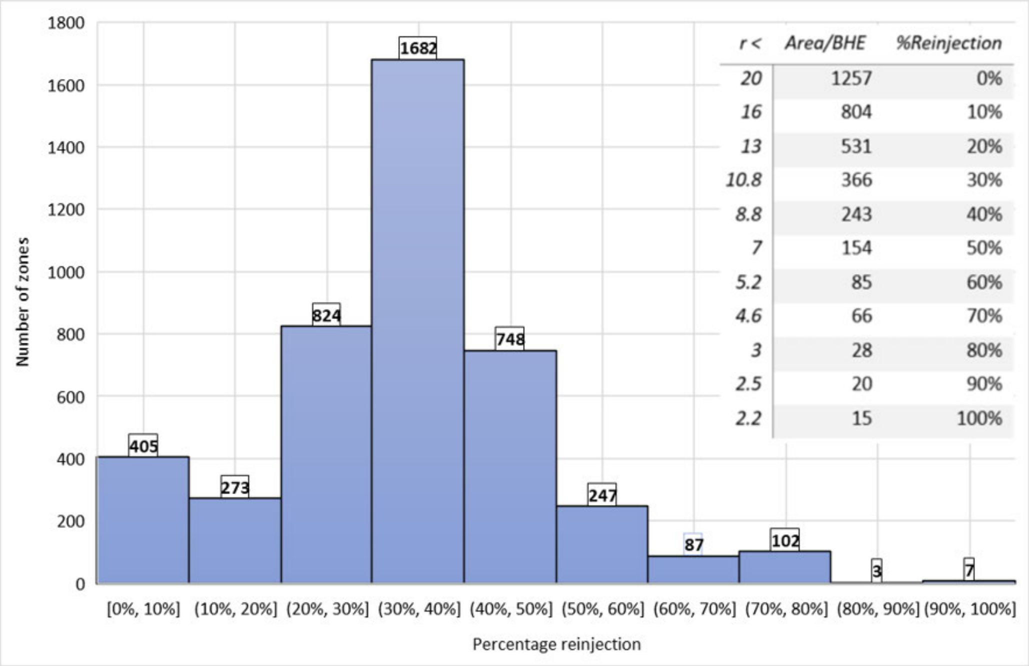

r <	*Area/BHE*	*%Reinjection*
20	1257	0%
16	804	10%
13	531	20%
10.8	366	30%
8.8	243	40%
7	154	50%
5.2	85	60%
4.6	66	70%
3	28	80%
2.5	20	90%
2.2	15	100%

Figure 5.10: Number of data zones in the Midland Valley of Scotland distributed as a function of the percentage reinjection required, calculated using the thermal footprint of a 100 m long BHE with an average consumption of 1,058 W (for ΔT > 0.5℃), accounting for the demand density and the heat available in the data zone (see Scotland Heat map).

5.6 Discussion

5.6.1 Effect of model parameters on dynamic heat recharge rate

The key considerations in BHE design are the length/depth and the thermal conductivity of the ground. Deeper BHEs typically have better performance but incur additional drilling costs. Here we use our model to evaluate the effect of different BHE designs on the thermal footprint assuming a rate of extraction which is necessary for the heat demand, rather than considering the operational performance.

BHE design: length, depth

Results detailed in SM3 (Appendix A.4.3) show that for a 40 m long borehole, axial recharge Q_{ax} increases from 18% to 40% after 30 years relative to the 100 m BHE, in accordance with the observations from Rivera et al. (2015b). However, this increased contribution relates to the larger footprint area (i.e. $\sim$2,000 m^2) necessary to match the volume of rock required to meet the demand (i.e. V = 80,400 m^3). Decreasing the BHE length by 60% (i.e. from 100 m to 40 m), increases the surface thermal footprint by 54% after 30 years, for ΔT > 0.5℃. At the mid-BHE depth, the thermal footprint increases by factors of 1.8 and 1.5 after 1 and 30 years, respectively. By controlling the yearly average specific heat extraction rate of the system (i.e. 30 W/m for a 40 m and 11 W/m for a 100 m BHE), the BHE length therefore represents an essential design criterion(Casasso & Sethi, 2014) in terms of its effect on the extent of the thermal footprint, especially in the initial years of production. Additional models show that decreasing the BHE depth from 10 to 2 m below ground level decreases the contribution from axial recharge Q_{ax} by 17% and 28% after 1 and 30 years, increasing the thermal drift at the surface by 94% and 62%, respectively. Although deeper BHEs prevent large cooling at the surface, this overall small contribution to the heat balance results in a limited effect on the temperature drawdown at the BHE and footprint area at depth.

Material heat conductivity

Whilst longer or deeper BHE generally achieve better performances, they require significant investment costs, and therefore improving the thermal conductivity of the medium around the heat exchanger is often seen as a more effective means to improve heat transfers and access the energy required over the long term (Dehkordi & Schincariol, 2013). High ground conductivity increases the efficiency of heat pump systems as it enhances heat transfer and reduces the depletion of heat at the borehole (C. Chen et al., 2019). The higher the thermal conductivity of the ground surrounding the BHE, the higher the specific heat extraction rate can be, with an increase from 25 to 70 W/m shown for a 150 m BHE with increasing rock thermal conductivity from 1.5 to 3 W/℃.m (L. Rybach, 2002), but the larger the areal impact of heat extraction. An appropriate estimate of the thermal conductivity is therefore essential to assess the long-term performances of a BHE system, the risk of interferences, and also the heat recharge rate from the geothermal heat flux (Stylianou et al., 2017).

Our results show that the increase in the contribution from the geothermal heat recharge with increasing rock conductivity is limited. Using numerical simulations, we can constrain the effect of rock thermal conductivity on the transient rates of expansion of the thermal plume after 30 years of operation for a 100 m BHE (SM5, Appendix A.4.5). This shows that for a given heat load, the areal impact of heat extraction increases linearly with ground thermal conductivity, as heat is mined further away from the BHE (Fig. 5.11). Low conductivity amplifies the amplitude of the radial heat fluxes as the temperature drop and contrasts around the BHE increase, which will reduce the heat pump efficiency and increase the electricity consumption (E) (Dehkordi & Schincariol, 2013; Hein, Zhu, et al., 2016). This highlights a challenging but necessary balancing act between the need to ensure BHE efficiency and to restrict the thermal footprint on the geological resource.

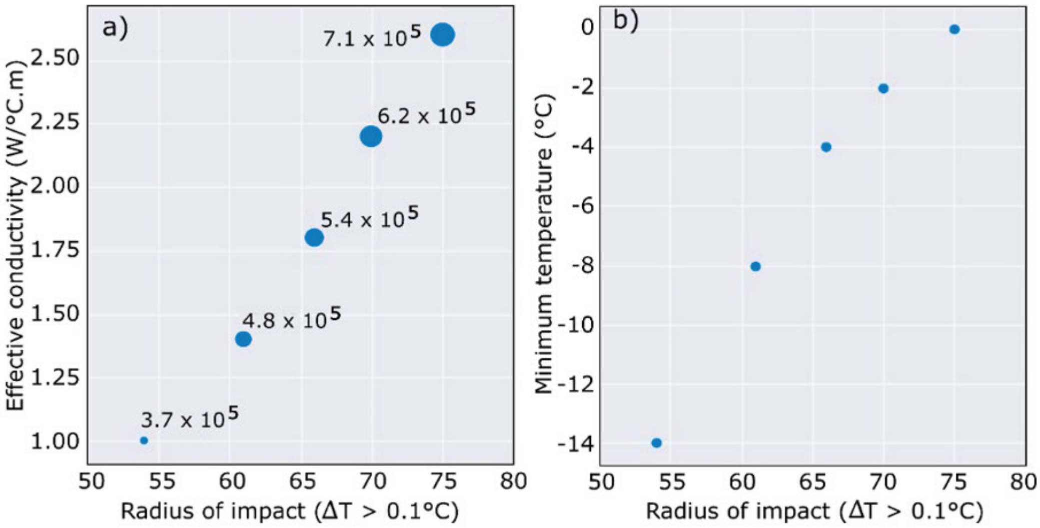

Figure 5.11: a) Relationship between the areal footprint of heat extraction (for $\Delta T > 0.1$ ℃) and the effective ground conductivity, with the labels representing the estimated volume of impact (m^3). b) Relationship between the areal footprint of heat extraction and the maximal temperature drawdown at the BHE. More details on the effects of the ground conductivity on the heat availability are given in SM5 (Appendix A.4.5).

5.6.2 Surface recharge and urban island effect (UHI)

In our reference model, we used a surface heat flux equal to the geothermal heat flux to calculate the worst-case amplitude and extent of the thermal drawdown induced by continuous heat extraction from a vertical BHE. This heat flux was calculated for a balanced system and does not account for the heat recharge from the atmosphere. Many studies consider that solar radiations and surface air temperature (SAT) keep the yearly average ground surface temperature (GST) nearly constant, arguing that the thermal imbalance caused by the operation of a BHE in heating mode increases the downward heat flux from the atmosphere. This is interpreted as being associated with an increase in solar heat recharge as the ground surface progressively cools down (Banks, 2008; Rivera et al., 2015b). For example, Rivera et al. (2015b) showed using a semi-analytical expression accounting for axial heat flux and heat exhaustion from storage, that the ground surface can provide up to 35% of the total power demand for a 100 m BHE (twice the contribution from the basal plane) over the long-term. Their approach assumed a constant temperature at the surface to simulate recharge from the atmosphere, thereby ignoring the possibility of ground cooling and freezing. Using a Cauchy-type surface boundary, where the heat flux is proportional to the difference between the GST and SAT, Rivera et al. (2016) alternatively showed that the heat transfers between the atmosphere and the ground surface have negligible effects for BHE > 50 m. Similarly, modelling results from Saadi and Gomri (2017) concluded that under the new surface heat balance generated by the operation of a BHE, seasonal effects are only relevant for short BHE depths and long operation periods. When cyclical production and injection are implemented, Bidarmaghz et al. (2016) confirmed using a time-depth varying ground temperature boundary condition that accounting for yearly variations in air temperature can promote heat recharge essentially for shallow and short BHE systems, and would allow shortening by 11% GHE systems.

In theory, the process of increasing atmospheric heat recharge to the ground is possible if the ground surface temperature is lower than the air temperature, which is the case in summer. Nevertheless, we showed that the renewal of the stored heat utilised by a 100 m BHE in the UK from the atmosphere cannot be achieved without the significant cooling of $\sim$420 m^2 of the ground surface. Given the limited surface imbalance within the first years of operation, the yearly average recharge potential of 2.5 W/m^2 calculated in this study (with a maximum of 8 W/m^2 in summer) could indeed only be achieved in the long-term and would require the subsurface to unsustainably cool by 5℃ over 30 years. This is effectively mining a resource that has long-term negative environmental impacts and making it unavailable for future generations. This suggests that although net incoming radiations are about three orders of magnitude higher than the geothermal heat flux (0.057 W/m^2), ignoring the complex processes occurring at the near surface can lead to an overestimation of the yearly average radiative heat input to the ground.

In contrast to vertical BHEs, shallow horizontal GSHP systems can directly benefit from this process and harness the radiative heat flux that penetrates and warms up the ground during the day and in summer, disturbing the heat balance and promoting downward heat flux from the surface. Using a constant surface temperature boundary to consider heat recharge from the atmosphere, Bortoloni, Bottarelli, and Su (2017) showed that the ground surface can contribute up to 98% to the energy balance of shallow horizontal ground heat exchangers, against 2% for the bottom heat flux.

Here, we simulate a series of 'best-case' scenarios to discuss the relationship between axial effects and atmospheric heat recharge, and the impact of radiative heat fluxes on the renewal of heat used by a vertical BHE. Based on Rivera et al. (2016) we first adjust the surface heat flux boundary of the 1D 1000 m long model accounting for the decrease in surface temperature calculated in the 'worst-case' simulation (SM6, Appendix A.4.6). The updated numerical results, which account for the increase in heat flux from the atmosphere, indicate a reduction of the temperature drawdown at the surface by only ~0.4℃ after 30 years, relative to a scenario without forced heat recharge, whilst the reduction in the thermal footprint is negligible. We then assess the effect of a forced surface heat recharge on the thermal drawdown after 30 years of operation, assuming a fixed surface temperature (T = 9℃). Our results indicate a reduction in the amplitude of the axial heat fluxes during the first 30 years, which can be explained by the reduced cooling above the BHE (Fig. 5.2c-d). After 30 years, Fig. 5.6 suggests that axial effects become more important and allow for more recharge than in a scenario with a surface heat flux boundary. However, the effects on the maximum thermal drawdown at the BHE and the extent of the thermal footprint are negligible. Similar conclusions are obtained when using a fluctuating surface heat flux boundary (A_s = -0.057 ±8 W/m^2) representing the seasonal variations in air temperature.

In urban areas, accelerated heat flux from the warmed basement caused by the 'urban heat island' (UHI) effect was shown to promote heat recharge to BHE, by increasing up to 3-4℃ the temperature of shallow aquifers compared to average rural groundwater temperatures (Allen, Milenic, & Sikora, 2003). Results from Rivera, Blum, and Bayer (2017) suggested that for shallow systems, this effect increases by up to 40% geothermal utilisation and can save about 4 m of borehole length. We here investigate numerically the UHI effects by setting a fixed surface temperature of 13℃ (4℃ higher than the yearly average surface temperature of 9℃). After 30 years of heat extraction, the simulation results indicate a reduction of the temperature drawdown at the mid-BHE depth by 0.8℃ compared to a scenario without UHI effect (1D analysis), with axial heat fluxes representing only 8% of the heat recharge, whilst the thermal footprint for ΔT > 0.5℃ at the mid-BHE depth is reduced by half after 30 years, i.e. from 22 m to 10 m (3D analysis).

Given the best and worst-case surface recharge scenario, this analysis confirms that the increasing contribution of the surface boundary to provide renewable heat to a 100 m vertical BHE is only significant for long operation periods, and the limited potential of radiative heat recharge (Banks, 2008; Erol et al., 2015; Eskilson, 1987; Y. Guo, Hu, Banks, & Liu, 2021; Saadi & Gomri, 2017; Spitler & Bernier, 2016). Forced ‘natural’ atmospheric heat cannot compensate for the heat extracted by a vertical BHE within the life span of a BHE, not only because a limited section of a 100 m BHE is located within the interval of influence of the surface heat flux, but because the amplitude the yearly fluctuations would require a large cooled area, which cannot be sustainable in densely populated areas. Ignoring the effects of climate warming or urban heat island (Rivera et al., 2015b; K. Zhu, Bayer, Grathwohl, & Blum, 2015), this effect is even more true as the BHE depth decreases and the BHE length increases, given the reduction in axial effects and the increase in the surface thermal drawdown (SM3, Appendix A.4.3).

5.6.3 Implications for Heat Regulation using an example from the MVS

This study has shown that sustainable BHE utilisation cannot be achieved in the long term under the current regulations of a minimum separation distance between BHEs of 6 m within the surficial area of a typical house with a garden in the UK unless reinjection is performed. The utilisation of a BHE in heat load only would lead over the long-term to thermal disturbances up to $\sim$40 times the UK median garden size and impact neighbouring properties. With the separation distance between BHEs being in practice often reduced to 4 - 5 m, there is an urgent need to review the current regulations of shallow geothermal utilisation (< 100 m depth) in urban areas. Licensing heat is essential to control production and interference between users, but it also provides a better regulatory framework to financial risks and therefore promotes investments (McClean & Pedersen, 2022). However, it cannot be made from generalised recommendations of the separation but needs to account for the area available for heat extraction. This depends on the resource in place but also on the distribution of the heat demand, the dynamic of heat recharge (i.e. ground heat conductivity, groundwater flow), the design of the GHE system (i.e. number of BHE system, ΔT) and on the permitted temperature decline. Hence, regulations must include directives on a management strategy including the minimum percentage reinjection that would be required to prevent the over-exploitation of the resource.

In the previous section, we showed that in most urban areas in the MVS, 30-40% reinjection is required to ensure sustainable utilisation of BHE systems. Solar-assisted ground heat exchanger systems were shown to be a valuable solution to provide such recharge to the ground during summer months, ensuring the long-term viability of shallow GHE systems in areas of high demand. Alternatively, ‘industrial waste’ heat sources have been of increasing interest for the potential to provide ‘recycled’ heat to local users or to renew the stored heat in depleted ground. A comparison of the local heat demand and industrial waste heat available for reinjection in the Edinburgh and Midlothian areas, where we calculate a total heat reinjection requirement of 4.0×10^9 kWh/yr, suggests that local waste heat sources could contribute up to $\sim$4% of this requirement, the exact power capacity of each heat source being uncertain (SM4, Appendix A.4.4). However, balancing heat availability and heat demand is challenging, as many industrial heat sources are located in areas of low heat demand (Fig. 5.8). On the other hand, Fig. 5.8 suggests that there is a large proportion of MVS where the demand density is smaller and the use of BHE can be effective (i.e. no reinjection requirements). Deducing the area required for heat utilisation by BHEs over 30 years in areas of low heat demand from the total heat in place (i.e. for ΔT = 0.5℃, r = 23 m), we find that 6% of the data zones could provide up to 4.9×10^{10} kWh/yr, which is almost three times the heat required for reinjection in areas of high demand in the MVS, i.e. 1.64×10^{10} kWh/yr (SM4, Appendix A.4.4). Although heat transport from one area to another is possible via the underlying groundwater flow, a thorough investigation of the regional hydrogeology would be required to understand if the excess heat from low-demand areas could naturally advect in the subsurface and provide thermal recharge to areas of high demand. Current research out of the scope of this study is being undertaken to understand how mine water in shallow interconnected collieries in the Midlothian Coalfield in the MVS can be used to convey heat reinjected from a datacentre to potential users located south of Edinburgh (Fraser-Harris et al., 2022).

This analysis shows the importance of diversifying the energy sources within an integrated heating system in cities. Given the limited potential of the shallow subsurface to provide sustainable heat over the long term in areas of high demand, there is a strong advantage in combining the use of industrial waste heat with BHE systems to store and access heat from the ground. This will require the development of district heating systems and increased communication between the different actors, such as local authorities, industries, investors, constructors, and heat licensing regulators.

5.7 Conclusions

This study defines the available heat for utilisation via a vertical BHE for a single-family house in Carboniferous sedimentary basins and identifies potentially critical issues surrounding the licensing of heat caused by a continuously expanding thermal footprint. The heat balance analysis showed that the natural heat recharge via geothermal, solar heat flux and RHP cannot compensate for more than 5% of the heat extracted annually by a 100 m long BHE within a radius of 16 m unless a significant ground surface cooling allows for the increase in radiative flux from the atmosphere. This energy imbalance has a major impact on the subsurface thermal footprint in the long term, as most of the stored heat is mined by the BHE via radial heat conduction. Numerical models showed that the areal impact of heat mining of a 10 m deep and 100 m long BHE (i.e. for ΔT > 0.1℃) extends up to ∼40 times the median size of a UK house with a garden (226 m^2) after 30 years, with a maximal surface temperature decline of 0.8℃ calculated at the surface and a radial flux of 0.1 W/m calculated at 16 m from the BHE. This shows that although quasi-steady-state temperatures can be reached at the BHE after a few years of production, this is not indicative of a non-evolving thermal plume.

By quantifying the areal extent of the heat resource accessed by BHEs rather than the system performance, we highlight the importance of setting new regulations on the use of shallow geothermal heat, using reinjection as a way to constrain the impact on the resource and between users. Careful site-specific geological characterisation (i.e thermal response tests for analysis of the site heat conductivity) and considerations of the rate of renewable heat, the density of heat demand and the presence of groundwater/mine-water flow paths must be considered when planning and licensing shallow < 100 m heat utilisation and designing BHEs. A series of models presented here using the example of the Midland Valley of Scotland demonstrated that a proper analysis of the ground properties and heating requirements allows determining the percentage reinjection required to constrain the thermal footprint of GHE utilisation. In areas where natural heat recharge cannot compensate for the heat mined, reinjecting the equivalent of at least 35% of the yearly average heat requirements was shown to constrain the thermal footprint of heat extraction within ΔT < 0.5℃, and limit interferences after 30 years in most urban areas. As the number of shallow geothermal systems is expected to increase, the injection of excess industrial waste or solar heat should be considered to ensure the sustainability of BHE systems in the long term. This will be essential to address the energy needs whilst avoiding depleting shallow geothermal resources over the operating lifetime of shallow vertical systems in urban areas.

5.8 Author Contributions

M.R., C.McD, A.F-H., S.G. and I.W defined the scope of the study. M.R. and C.McD developed the methodology and numerical approaches to address the research questions. C.McD updated the OpenGeoSys source code for calculations of energy change. M.R collected and processed the data, created the analytical and numerical models, ran the simulations, and wrote the python codes used for data analysis and figure generation. C.McD and A.F-H provided technical support for the creation of the numerical models and running the simulations. M.R, C.McD and A.F-H analysed, validated and interpreted the results. I.W, A.F-H and S.G provided literature resources and GIS data. M.R. was responsible for the manuscript writing and the preparation of the figures. C.McD, A.F-H., and S.G contributed to the drafting of the manuscript. All co-authors reviewed, approved and contributed to the final version of the manuscript.

5.9 Conflicts of interest

There are no conflicts to declare.

5.10 Acknowledgements

We thank NERC for providing funding for this research through an E4 DTP studentship (NE/S007407/1) and The Coal Authority for providing funding through a CASE partnership. We thank the British Geological Survey for providing borehole records and GIS data via the GeoIndex Database. The 3D mesh used in the simulations was generated using Gmsh (Geuzaine & Remacle, 2009) and figures were produced using Python (Matplotlib).

5.11 General chapter conclusion

This analysis, based on conductive heat transfer mechanisms only, suggests that sustainable heat extraction from a 200 m deep BHE can only be achieved if cyclical heat rejection is performed. Here, sustainable heat extraction is defined as the rate at which the heat load requirements for a single-family house can be met without cooling the subsurface by more than 0.1 °C over an area larger than the area of a typical house with a garden in the UK. The subsurface heat balance analysis for the Midlothian coalfield will be used as a reference for the study of the conductive and convective heat transfers in flooded mines in the following chapters.

Chapter 6

Numerical modelling of heat flow in flooded coal mines: Model development, parametrisation and sensitivity analysis

6.1 Chapter Overview

The data analysis presented in chapter 3 highlighted a linear relationship between the average temperature in mine shafts and the average depth of the measurements. However, the relationship between the average water level in time series and the corresponding average mine-water temperature (MWT) at a given site is less straightforward. The considered water level and temperature averages generally neglect the change in the state of the mine (e.g. from rebounding to pumped or discharging) and potential change in the depth of the measurements relative to the water level, which is often unknown. These factors might generate discrepancies within the dataset and degrade any potential observable correlations in the time series.

Temperature observations in mines are often limited to measurements in shafts, boreholes or discharge areas. The data set is generally inconsistent between the monitoring sites, and the lack of systematic data associated with the temperature measurements such as flow rate and probe depth, makes a thorough analysis of the effect of hydraulic conditions on the temperature difficult. Whilst the precise hydraulic and thermal properties are often unknown, the geometry and hydrogeology of abandoned flooded coal mines are complex and uncertain, and the undisturbed temperatures and geothermal gradient (i.e. not impacted by drilling or mining) are likely to be subject to both measurement and calculation errors. This makes it difficult to identify the source of heat and assess the rate at which heat can be extracted without depleting the resource.

Here, a generic model representing a flooded coal mine of simple geometry is developed to overcome those limitations. Numerical simulations are used to predict the MWT and its relationship with unknowns of interest (e.g. rock temperature distribution, heat mining rate) within the inter-connected parts of a mine, where measurements are not possible, for a known range of rock property values, pre-defined model geometry, hydraulic and thermal conditions. The sensitivity analysis consists of an update of the results published in the Proceedings for the World Geothermal Congress 2020+1 (see original published paper in Appendix A.5), and aims at validating results from the data/statistical analysis presented in Chapter 3. The reference porous model is moreover compared to a multi-element model, whilst different OGS processes are compared to characterise the best modelling approach and parameters to simulate (coupled) groundwater flow and heat transfer in flooded mines. The effect of free/forced convection in a porous system with high permeability contrasts and their effect on shaping the temperature profiles in the shafts is of particular interest. However, the effect of induced fractures above the mined area and the nature of the hydraulic recharge conditions are neglected and will be investigated in further detail in Chapter 8.

Key questions:

- What are the key controls on the temperature profiles measured in mine shafts?
- What are the key controls on the heat extraction/heat renewal rate?
- What are the key mechanisms of heat recharge/recovery?

Hypothesis

- The rock permeability, heat conductivity, pumping rate and recharging water temperature control the rate of heat extraction and recovery
- During production, heat is mainly transferred via advective mine water in tunnels and horizontal conduction in goaf
- Thermal balance can be reached for a low extraction rate, and the footprint area is mainly dependent on the thermal conductivity of the host rock.

6.2 Introduction

Abandoned legacy coal mine workings have been described as highly permeable 'anthropogenic aquifers' (Adams & Younger, 2001), from which important volume of water can be stored and extracted at relatively high rates (Banks et al., 2004). Mine waters filling the underground mining voids are generally hotter than natural groundwater at depths above 100-200 m depth, ranging from 12℃ to 21℃ (Gillespie et al., 2013). This represents a potential valuable low-temperature geothermal heat resource that can be accessed using ground-source heat pump systems to provide low-carbon heating or cooling to local users. Mine-water heat resources are largely available across the UK and have been of growing interest as they could contribute to reaching the Net-Zero carbon emission target set by the 2019 UK's Climate Change Act by 2050 (House of Commons Energy and Climate Committee, 2016). In Scotland, Todd et al. (2019) showed that about 7% of the heat requirement could be sustainably sourced from abandoned flooded mine workings lying just below populated areas without the need for artificial heat storage.

To date, there is no clear understanding of the key controls on MWT. Flooded coal mines are inherently complex systems formed of interconnected water-filled voids (i.e. roadways, shafts, drifts and galleries) embedded in a porous and fractured host rock. These characteristics are the result of a long mining history during which multiple coal seams have been worked over time. In the early times of mining ($16^{th} - 17^{th}$ Century), coal was mostly extracted from shallow mines using the pillar-and-stall method. In the early 18^{th} Century, the invention of the Newcomen steam engine enabled the pumping of water more efficiently, allowing access to deeper coal seams. From the 1950s, longwall mining was the main method of coal extraction in deep mines, and many mined areas were reworked using this method (P. Younger & Robins, 2002). The decline in coal demand led to the progressive closure of the underground mines from the 1960s, and the last underground colliery in the UK closed in 2015. In most cases, dewatering stopped following the abandonment of mines, leading to the progressive flooding of the underground workings (P. Younger & Adams, 1999). Whilst water is still rebounding in some coalfields, pumping has been reintroduced at a few locations by The Coal Authority for water level management and active/passive treatment purposes, to prevent the discharge of iron-rich mine water at the surface. Where rebound is completed, gravity outflows may occur and controlled discharges can be managed via the implementation of passive treatment sites.

The hydrodynamics of mines therefore depend on a combination of natural and anthropogenic processes that are likely to vary over time under the effect of water rebound, pumping, the nature of recharge (i.e. rainfall, reinjection) and discharging waters. As water is rebounding, new hydraulic connections can be created within a mine, between collieries or a network of collieries, connecting over large-scale hydrological units potentially previously isolated. Those are in return likely to promote the advection of heat at a large scale, modify the thermal state of mines, disturbing the purely diffusive pre-mining subsurface geothermal gradient and any potential thermal equilibrium acquired within portions of the collieries. Although a volumetric assessment of the mining voids is the first step to determining the initial heat potential of mine-water systems, characterising the mechanisms and source of heat recharge is essential to understanding the rate at which heat can be extracted without depleting mine-water heat reservoirs over the long-term, and therefore support the development of mine-water heating systems in the UK and worldwide. MWT observations in mines are however often limited to shafts or surface discharges, therefore not providing a full picture of the temperature distribution within the mines.

In this study, numerical modelling is used to investigate the relative effect of a series of controlled parameters on the observed mine-water temperature and the thermal footprint of heat extraction within the mine reservoir. The finite-element numerical modelling software OpenGeoSys (Kolditz, Görke, Shao, Wang, & Bauer, 2016) is used to simulate transient groundwater flow and heat transfers induced by pumping from a flooded coal mine with horizontal layers, for a range of rock properties, pumping scenarios and model geometries. Although the generic models used in this study are not calibrated on real data (i.e. conceptual representations of mines with simple geometry), transient analysis is used to get insights into the effects of pumping on both the thermal plume propagation and rate of heat extraction in the short-term and long-term. Different numerical modelling approaches are moreover compared to identify the key elements (i.e. mesh size, element type, properties, numerical parameters, slice thickness) required to optimise the simulation of groundwater flow and heat transfers in mines (e.g. computational time, stability).

6.3 Methods

6.3.1 Reference model set-up

Model geometry and meshing

The 800 m long and 300 m deep reference model represents a generic deep mine of simplified geometry. It is formed of an unstructured grid composed of 92,216 triangular elements and 46,401 nodes. The model consists of three saturated porous materials comprising a homogeneous host rock, two shafts, and three horizontal coal seams located at 100, 130 and 160 m depth (Fig. 6.1). The coal seams (i.e also referred to as mine workings, galleries or caved zone) are modelled as 2 m-thick 'goaf' horizons, assumed to have been extracted under the longwall mining approach, the main extraction method in deep mines. The two 180 m-deep mine shafts, that are connected to all three seams, are separated by a distance of 250 m in the central part of the model. The model neglects the extent of the collapse zone above the mined seams, which will be discussed in Chapter 8.

Material and fluid properties

Each material group is characterised by their own hydraulic and thermal properties (Table. 6.1). The thermal property values (i.e. heat capacity ρc, heat conductivity λ, density ρ) for the reference model are calculated based on the relative proportion of rock types for a typical Carboniferous succession in the Midland Valley of Scotland (MVS) (Table 2.1) and their harmonic mean property values (J. P. Busby, 2019; S. M. Watson & Westaway, 2020). Details of the data and methods are provided in Appendix A.1.

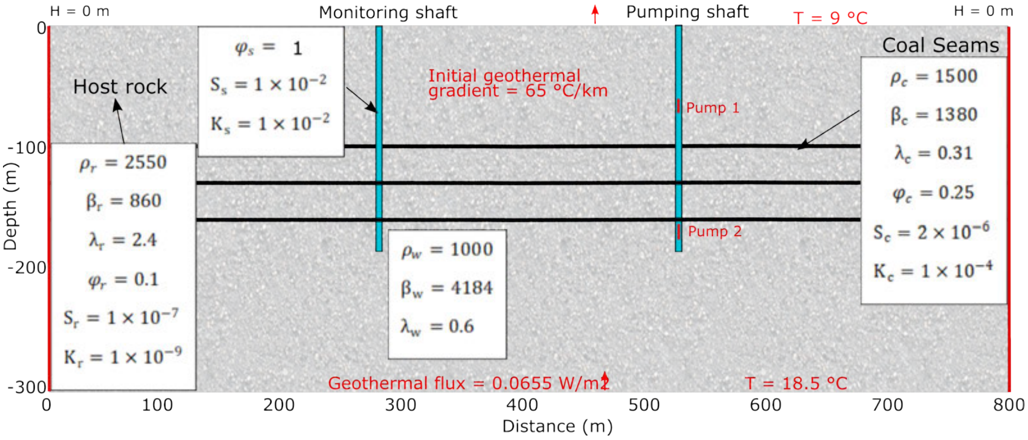

Figure 6.1: Sketch of the horizontal porous model showing the different materials and the thermal and hydraulic boundary conditions for the reference scenario. ρ, β, λ, ϕ, S and K correspond to the density, specific heat capacity, heat conductivity, porosity, storage and hydraulic conductivity, respectively. The subscripts r, s, c and w refer to the host rock, shaft, coal seams and water, respectively.

The hydraulic properties (i.e. storage S, hydraulic conductivity K and porosity ϕ) for the different porous materials are alternatively chosen to be in the order of magnitude of the values used in the literature (Table 6.1). In Raymond and Therrien (2008), the mine workings and host rock were attributed hydraulic conductivity values of $K_w = 2.3 \times 10^{-2}$ m.s^{-1} and $K_r = 4.5 \times 10^{-5}$ m.s^{-1}, and porosity values of $\phi_w = 25\%$ and $\phi_r = 5\%$, respectively. P. Guo et al. (2018) alternatively considered differences in the intact cap/base rock permeability k_r, the matrix permeability k_m and the fracture permeability in both a caved zone (i.e. where coal has been mined out) k_{c_f} and a fractured zone (i.e. above the caved zone) k_{f_f}, with $k_r = 1 \times 10^{-17}$ m^2, $k_m = 2 \times 10^{-16}$ m^2, $k_{c_f} = 2.5 \times 10^{-8}$ m^2 and $k_{f_f} = 1.3 \times 10^{-9}$ m^2. The hydraulic conductivity of the saturated rock strata around the mined voids was assumed to average 4 $\times$ 10^{-5} m.s^{-1} in Western Pennsylvania (1 $\times$ 10^{-6} m.s^{-1} for coal pillars; Aljoe and Hawkins (1994)) and to be in the range of 10^{-8} - 10^{-6} m.s^{-1} in the Durham Coalfield (Minett, 1987).

Parameter	Host rock	Seams	Shafts	Water
Slice thickness (m)	1	1	1	n
Hydraulic conductivity K (m.s^{-1})	1×10^{-7}	2×10^{-2}	1	n
Storage S	1×10^{-5}	2×10^{-4}	1	n
Porosity (%)	10	25	100	n
Heat conductivity λ (W°C^{-1}.m^{-1})	2.4	0.31	0.63	0.63
Heat capacity c (J.kg^{-1}.K^{-1})	860	1380	4184	4184
Density ρ (kg.m^{-3})	2550	1500	2550	1000
Kinematic viscosity μ (Pa.s)	n	n	n	1×10^{-3}

Table 6.1: Hydraulic and thermal properties for the reference mine model (no coupling).

In addition to the reference porous model, a multi-element model is developed. This model aims to investigate the possibility of representing shafts and in a second instance the roadways, as open pipes. There, 1D line elements representing the shafts are embedded in a 2D porous mesh. The properties of each material group are summarised in Table. 6.2.

Parameter	Host rock	Seams	Shafts
Dimension	2	2	1
Area (m)	100	100	28
Porosity (%)	10	25	100
Storage	1×10^{-5}	2×10^{-4}	1
Hydraulic conductivity (m.s^{-1})	1×10^{-7}	1×10^{-2}	1

Table 6.2: Material properties for the multi-element model.

Initial and boundary conditions

In the reference model, hydraulic recharge is controlled by constant heads of 0 m (Type-1 or Dirichlet boundaries) on the left and right boundaries, whilst no hydraulic recharge is permitted at the surface or bottom boundaries (i.e. no-flow). The system is initially saturated with water and the initial temperature distribution is controlled by a geothermal gradient of 30 °C/km with surface temperature $T_s = 9°C$, which corresponds to the yearly average surface temperature in UK Coalfields (Farr et al., 2020). The initial conditions in the domain (i.e. temperature and head distribution) are calculated using steady-state simulations (storage S = 0). This allows accounting for the heterogeneities caused by the low thermal conductivity and high permeability of the mined seams and getting an accurate estimate of the initial heat content of the system.

Pumping is simulated via a source-term Q = -0.01 m^3.s^{-1} distributed along the polyline representing Pump 1, located above the mining area in shaft 1 (Fig. 6.1). This shallow pumping scenario is assumed to best represent current conditions in UK mine shafts pumped for water management purposes. It is compared to deep pumping scenarios (Pump 2) which is considered to best represent the dewatering conditions during mining. During the pumping simulations, constant heat flux boundaries of 0.065 W/m^2 are set at the surface and bottom. The heat flux is calculated as a function of the geothermal gradient and of the harmonic mean vertical thermal conductivity of the complete modelled lithological succession, to maintain thermal equilibrium in a balanced system (Eq. 6.1).

$$q = \lambda \times \frac{\Delta T}{\Delta z} \tag{6.1}$$

where q (W.m^{-2}) is the heat flux, $\frac{\Delta T}{\Delta z}$ (C.m^{-1}) is the geothermal gradient, and λ (W/°C^{-1}.m^{-1}) is the harmonic mean vertical thermal conductivity of the geological succession. λ is calculated as the product of the relative thickness of the host rock h_r and mine workings h_m by their effective thermal conductivity λ_{eff_r} and λ_{eff_m}, respectively (Eq. 6.2).

$$\lambda = \frac{h_r}{H} \times \lambda_{eff_r} + \frac{h_m}{H} \times \lambda_{eff_m} \tag{6.2}$$

Where H is the total model thickness (m). λ_{eff} is in turn determined based on the relative proportion of water-filled voids and solid particles in each material (Eq. 6.3):

$$\lambda_{eff} = \phi \times \lambda_s + (\phi - 1) \times \lambda_w \tag{6.3}$$

where the subscripts s and w correspond to the solid material and mine-water, respectively. For the reference model with effective vertical heat conductivity λ = 2.2 W/°C^{-1}.m^{-1} (Table 6.1), this corresponds to a flux of -6.55 mW.m^{-2} and 6.55 mW.m^{-2} set at the surface and bottom boundaries, respectively.

Time control

Pumping is simulated using either steady-state or transient simulations for 732 days (i.e. about 2 years), which is the time required for the system to reach quasi-steady state conditions in the reference scenario. In the transient simulations, daily time steps (i.e. 86400 sec) are set to ensure numerical stability whilst providing a high-resolution time series. This is particularly relevant within the first days of pumping, where the relative change in temperature and water level close to the pump are the greatest.

6.3.2 Sensitivity analysis

Sensitivity analyses are generally used to investigate how uncertainties in model parameters affect the output values. Here, the aim is to understand the controlling effect of the thermal and hydraulic properties of rocks as well as the pumping depth on the MWT, thermal footprint and power output. The ranges of properties tested (Table 6.3) have been chosen according to values for the Carboniferous rocks encountered in UK Coalfields (Table 2.1) and on the hydraulic property values for mines given in the literature (see Chapter 2).

Parameter	Unit		Min	Max	Step
Geothermal gradient	℃.km^{-1}	$\frac{\Delta T}{\delta z}$	20	35	5
Rock heat conductivity	W.℃$^{-1}$.m^{-1}	λ_r	1.8	3.0	0.3
Rock density	kg.m^{-3}	ρ_r	2100	3000	300
Rock heat capacity	J.kg^{-1}.℃$^{-1}$	c_r	770	950	45
Rock storage		S_r	1.5×10^{-4}	1.5×10^{-6}	0.5×10^{-1}
Rock porosity	%	ϕ_r			
Rock hydraulic conductivity	m.s^{-1}	K_r	10^{-9}	10^{-5}	10^{-1}
Shaft storage		S_s	10^{-9}	10^{-9}	10^{-9}
Workings storage		S_m	7×10^{-1}	2×10^{-3}	0.5×10^{-1}
Workings hydraulic conductivity	m.s^{-1}	K_m	10^{-4}	10^{-1}	0.5×10^{-1}
Water heat conductivity	W.℃$^{-1}$.m^{-1}	λ_w	0.2	0.5	0.1
Pumping depth	m	P_z	52	142	30
Pumping rate	m^3.s^{-1}	Q	10^{-3}	10^{-1}	0.5×10^{-1}

Table 6.3: Range of values for each parameter tested in the sensitivity analysis.

For each scenario, the models calculate the average temperature in the shafts, the pumped temperature as well as the relative energy change within each material over the 2 years of pumping. In opposition to steady-state simulations, transient analysis allows the understanding of the temporal effect of pumping on the hydraulic and thermal state of the mine, that is the changes in the rate of heat extraction and temperature distribution before steady-state conditions are reached. As discussed later, this is particularly important when investigating the effect of heat conductivity, hydraulic conductivity, pumping rate and material storage.

The sensitivity index (SI) is a dimensionless parameter used to determine the relative effect of a change in the input parameter on the output values (Eq. 6.4). In this case, it provides a way to identify the rock property or parameter that has the most influence on the pumped temperature, average MWT in the pumping shaft, heat extraction rate or total power output.

$$SI = \frac{\%\Delta\theta_o}{\%\Delta\theta_i} \tag{6.4}$$

Where $\%\Delta\theta_o$ and $\%\Delta\theta$ are the percentage change in the output and input parameter values, respectively. Those are calculated according to Eq. 6.5.

$$\%\Delta\theta = \frac{v_2 - v_1}{v_1} \tag{6.5}$$

where v_1 and v_2 are the initial and new values, respectively. When relationships are non-linear, the average SI for the range of values tested at a given time step (i.e. at t = 24 and 732 days since the onset of pumping) is used to get insight into the relative effect of the considered property at that given time step.

The total heat output P_{total} and the relative power contribution from each material at each time step P_{rel} (i.e. goaf, host rock, shafts) are determined using Eqs. 6.6 and 6.7, respectively.

$$P_{total} = \frac{E_{t,t_f} - E_{t,t_i}}{t_{tot}} \tag{6.6}$$

$$P_{rel} = \frac{E_{m,t+1} - E_{m,t}}{\delta t} \tag{6.7}$$

With E_t the total energy in the model at the initial t_i or final t_f time step, and E_m the energy within a given material group at two successive time steps t and $t+1$. t_{tot} corresponds to the total duration of the simulation and δt is the time step length. P_{total} corresponds to the average heat output over the simulation period whilst P_{rel} provides an accurate time series or the change in heat extraction rate over the simulation period and within each material type.

6.3.3 Thermal conditions and geometrical analysis

The effects of the thermal conditions (i.e. heat flow/temperature boundary, reinjection temperature) and mine geometry (i.e. seam depth, seam spacing, shaft depth) are qualitatively analysed based on visual inspections of the temperature distribution in the model after 2 years of pumping (steady-state simulations), together with the calculation of the total heat output (Eq. 6.6). The heat recharge scenario includes:

- heat flow surface and bottom boundaries (reference scenario), and
- constant temperature boundaries

Investigating the effect of the mine structure implies repeating the meshing and set-up process for each model, given the characteristics shown in Fig. 6.2. In particular, the effect of the seam depth, seam thickness and shaft spacing on the temperature and heat extraction rate is determined. Only one seam is here considered to simplify the analysis.

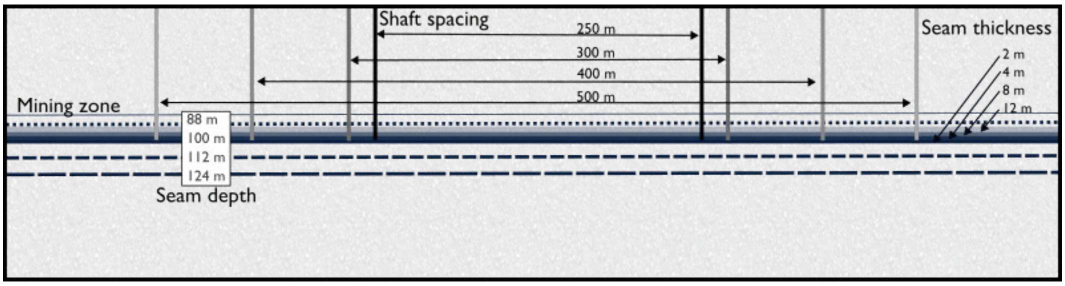

Figure 6.2: Sketch showing the various seam depths, seam thickness and shaft spacing tested to investigate the effect of the mine geometry on the temperature and power output. All depth, thickness and spacing values are in meters.

6.4 Results

6.4.1 Sensitivity analysis

A thorough review of the relationship between the material properties and the average MWT in the pumping shaft, pumped temperature, heat extraction rate and total average power output after 2 years of pumping is conducted. Comparison of the sensitivity index (Fig. 6.3) suggests that most parameters have a negligible effect on the steady-state outputs in a 2-year-pumping period. The greatest variations are observed for the geothermal gradient and seam hydraulic conductivity. Although not displayed in Fig. 6.3 due to the high SI values, the pumping depth is also a key contributor to the observed MWT (SI = -0.14) and power output (SI = -13).

Pumping depths

Temperature distribution in the pumping shaft induced by pumping are observed at depths of 52 m, 82 m, 112 m, 142 m and 158 m bgl. Results for the 2-year-long steady-state simulation depict shifts in temperature that are referred to as ‘steps’, formed at the pump location and the depth of the seam’s insets (Fig. 6.4.a). Heat convection cells are formed between the main inflow zones (the seams insets), and are expressed as constant temperature intervals that overprint the purely diffusive/linear pre-pumping geothermal gradient.

Pumping tends to drag cold water from the surface and warm water from the shaft bottom up to the pump location. In shallow pumping scenarios (i.e. pumping from above or within the mining area), this generates a positive thermal anomaly, where the temperature profiles depict warmer temperatures than those predicted by the pre-pumping undisturbed geothermal gradient. In those scenarios, the MWT modelled at the deepest seam inset equals the temperature predicted by the undisturbed geothermal gradient at that depth. On the contrary, a general cooling is observed along the shaft when water is pumped close to the shaft bottom (i.e. below the mining area, at P_z = 158 mbgl). In this scenario, the temperature at the shallowest inset approximately matches the temperature predicted by the geothermal gradient at that depth. Discrepancies between the pre-pumping geothermal gradient and the observed MWT at the other seams insets suggest the existence of a mixing of waters of different temperatures as they enter the shaft.

By comparing the temperature distribution to the power output, Fig. 6.4.b suggests that the up-flow of warm water induced by shallow pumping (< 125 mbgl) tends to promote heat recharge into the system. On the contrary, by dragging colder recharge water from the shallower layers down to the pump location, deep pumping enhances heat mining from the reservoir rock. Whilst the average MWT in the shaft decreases quasi-linearly with increasing pumping depth 6.4.c), the pumped temperature does not depict any clear correlation with the abstraction

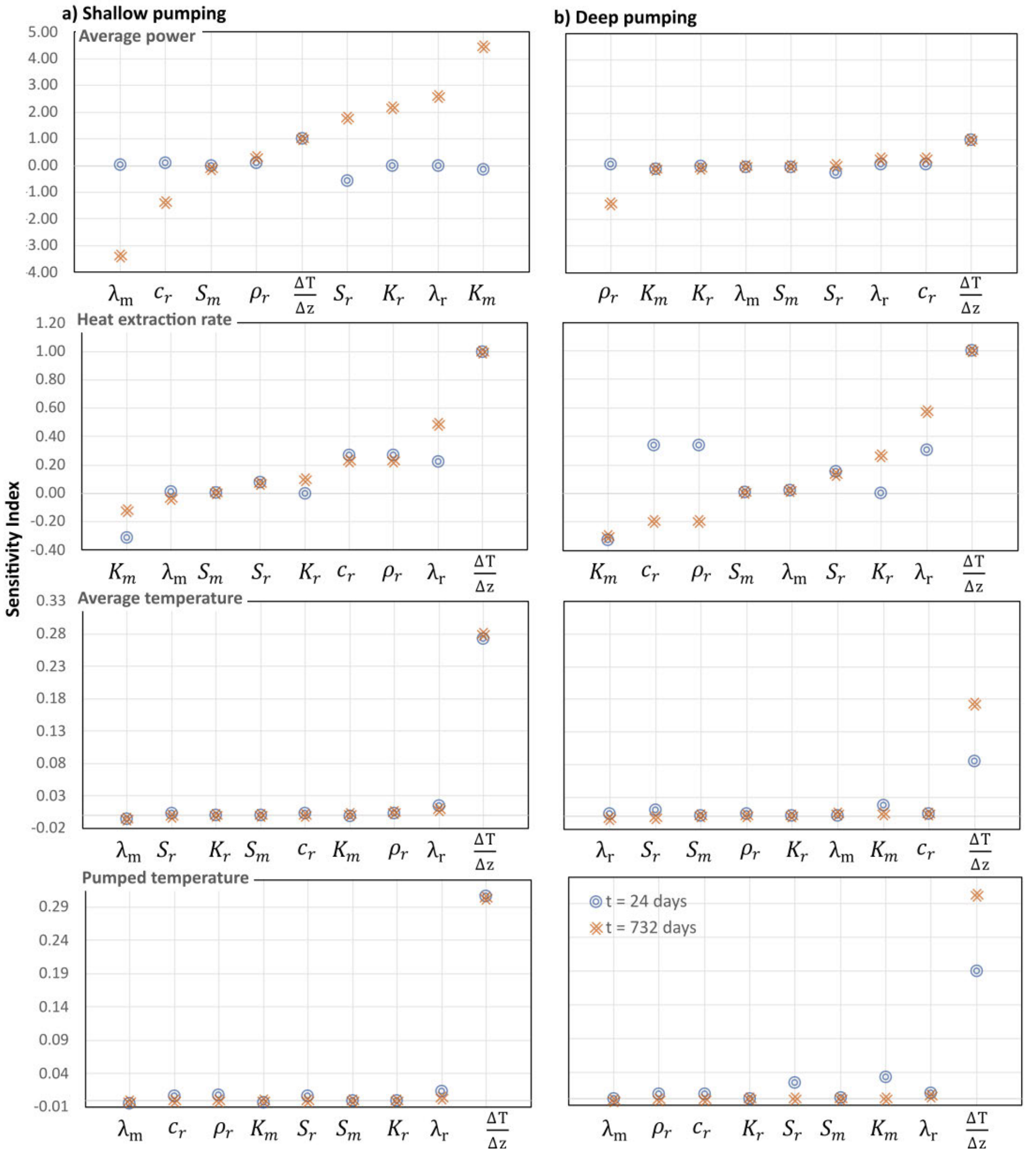

Figure 6.3: Sensitivity index of selected input parameters on the average power output, heat extraction rate, average pumping shaft temperature and pumped temperature for a shallow (a) and deep (b) pumping scenario. Values are determined from the horizontal layer model after 24 days (blue dots) and 2 years (orange dots) of pumping. The further away from 0 the value is, the larger the sensitivity of the output value to the input parameter. Positive and positive values suggest positive and negative correlations between the input and output parameters. On the x-axis, the input parameters include rock density ρ, specific heat capacity c_r, heat conductivity λ_r, hydraulic conductivity K_r and storage S_r, and the worked seam hydraulic conductivity K_m and storage S_m, and the geothermal gradient $\frac{\Delta T}{\Delta z}$ (see parameters units in Table 6.3).

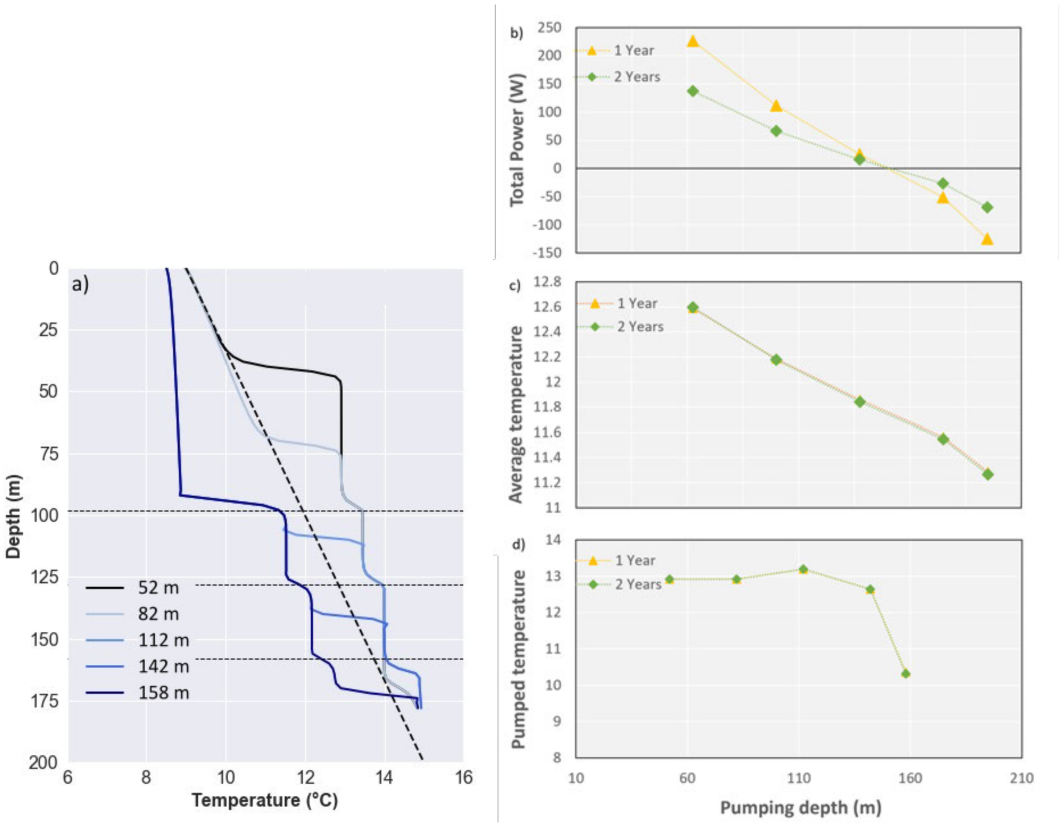

Figure 6.4: a) Temperature profiles in the pumping shaft, b) Total power output, c) Average temperature in the shaft (℃) and d) Pumped temperature (℃) for different pumping depths based on 1-year and 2-year-long steady-state simulations.

depth (Fig. 6.4.d). The pumped temperature slightly increases with increasing depth for depths < 125 m (i.e. above the mid seam), whilst it dramatically decreases for greater pumping depths. This suggests that the abstraction temperature highly depends on the location of the pump relative to the seams insets.

Geothermal gradient

The effect of the geothermal gradient, which defines the pre-pumping undisturbed temperature distribution within the reservoir model, on the changes in MWT, heat extraction rate and average power output after 2 years of pumping was then investigated. For each scenario, the surface and bottom heat flux boundary conditions are adjusted according to equation Eq. 6.1, assuming an initial constant surface temperature of 9℃ and a specific vertical mean heat conductivity of 2.2 W.$℃^{-1}$.m^{-1} (Table. 6.4).

Results suggest that the temperature, heat extraction rate and total power output are linearly correlated to the geothermal gradient (Fig. 6.5). Whilst the temperature increases with increasing gradient after both 24 days and 732 days (i.e. ~2 years) of pumping, the heat extraction rate changes are reversed with time. In the initial days of pumping, the larger the

Gradient (℃/km)	Heat flux (W/m^2)	Bottom temperature (℃)
20	0.0437	15
25	0.0546	16.5
30	0.0655	18
35	0.0764	19.5

Table 6.4: Heat flux and bottom temperature used for the different geothermal gradient scenarios. the heat flux was calculated assuming a heat conductivity of 2.2 W℃.m,

gradient and the faster the heat extraction rate (i.e. negative values), especially for shallow pumping scenarios. After 2 years, the larger the gradient and the faster the heat recharge rate (i.e. positive values), especially for shallow pumping scenarios. In this generic model, the mine water entering the shafts at the seams insets equals the temperature of the recharging water at the model boundaries, which is defined by the geothermal gradient, and no mixing of water occurs across different depths (i.e. no connections between the mined seams outside the shafts). As a result, the greater the geothermal gradient, the higher the average shaft temperature and pumped temperature for both shallow (52 mbgl) and deep (168 mbgl) pumping scenarios. This relationship however appears to be stronger for shallow pumping scenarios, where the temperature increases faster with increasing geothermal gradient. Over time, the pumped temperature becomes independent from the pumping depth, whilst the average temperature in the shaft remains higher for shallow pumping scenarios. In opposition to deep pumping scenarios, this prevents long-term heat depletion from the system, as suggested by the analysis of the total average power output.

Host rock heat conductivity

The heat conductivity defines the rate at which heat or cold propagates through the rock. Whilst this impacts the time at which steady-state conditions are reached, the rock heat conductivity has a negligible effect on the temperature distribution in the long term. Only limited increases and decreases in temperature are observed for an increase in the rock heat conductivity under shallow and deep pumping scenarios, respectively (Fig. 6.6). However, transient analysis suggests that the heat extraction rate and total heat output are highly sensitive to a change in rock heat conductivity. In the initial days of pumping, heat is mined at a greater rate for shallow pumping scenarios, with the higher the conductivity the higher the heat extraction rate. At t = 732 days, shallow pumping promotes heat recovery relative to deep pumping scenarios, with the higher the conductivity the higher the heat recharge rate. In the long-term, the greater the heat conductivity and the greater the total average heat recharge (for shallow pumping scenarios) or heat mining from the rock (for deep pumping scenarios).

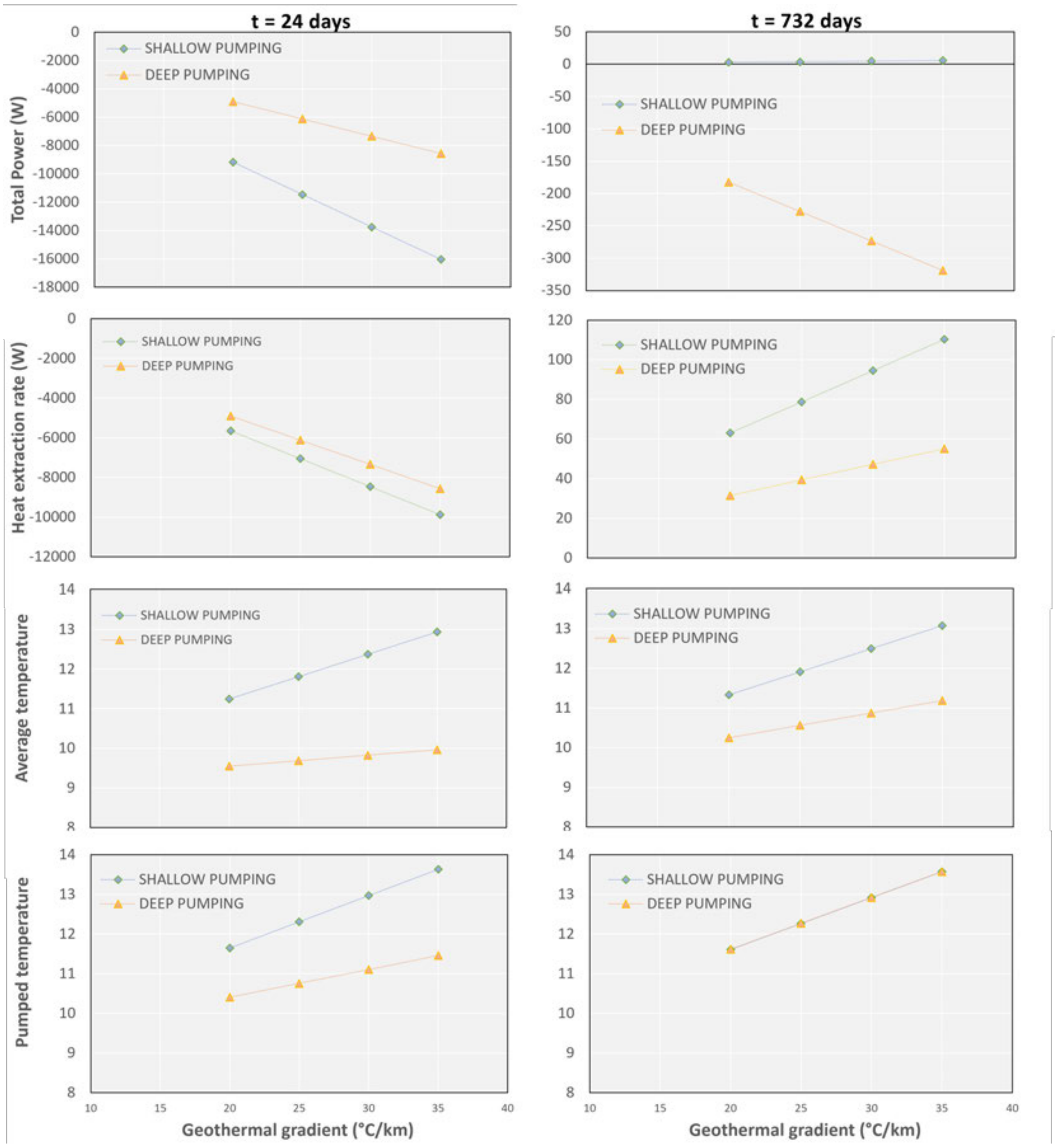

Figure 6.5: Relationship between undisturbed geothermal gradient and the total power output, heat extraction rate, average temperature (℃) in the pumping shaft and pumped temperature, after 24 and 732 days of pumping.

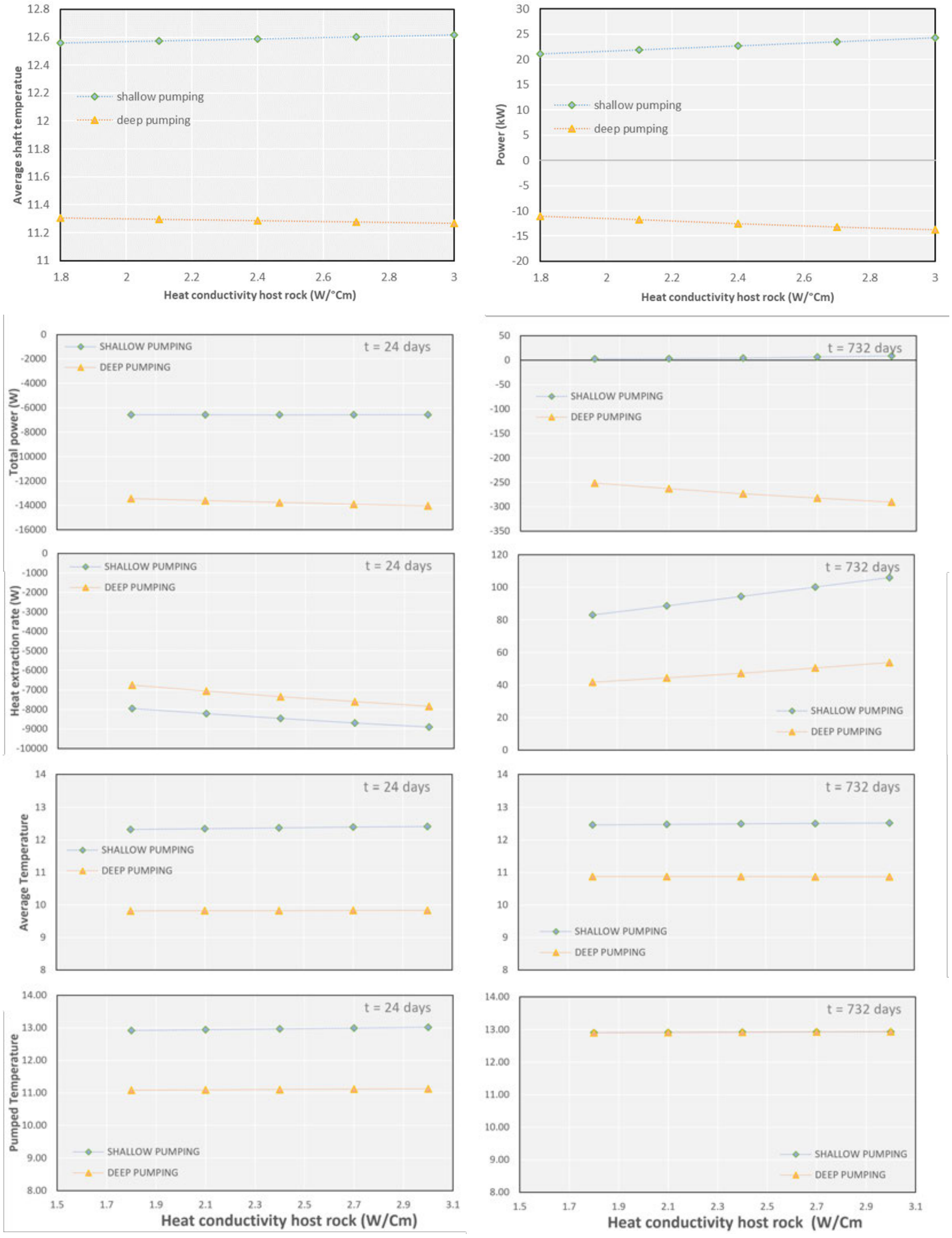

Figure 6.6: Relationship between the host rock heat conductivity and the average shaft temperature (℃) and power output for a 1-year-long steady-state simulation (upper panel). The four lower rows represent the effect of the host rock heat conductivity on the total power output, heat extraction rate, average pumped shaft MWT and pumped temperature (℃) after 24 days and 732 days of pumping (transient simulation).

Seam heat conductivity

Changes in the coal bed/worked seam heat conductivity (λ_m) can be used to assess the effect of different coal grades (i.e. how mature it is) on the rate of heat transfers within the mine. This has a particular interest when investigating the effect of trapped heat, i.e. the accumulation of heat below a low-conductivity layer.

Similarly to the host rock conductivity, results displayed in Fig. 6.7 suggest the limited effect of the seam heat conductivity on the observed MWT and heat extraction rate in the long term. However, the greater the seam conductivity, the greater the heat mining rate in the early stage of pumping. Overall, low seam conductivity tends to promote heat recovery in the system in shallow pumping scenarios.

Host rock heat capacity and density

The effects of the density and specific heat capacity, the product of which can be referred to as the volumetric heat capacity ρc, are here described together. Although there is no correlation between the two quantities, both properties influence the change in heat content and temperature in a similar way.

No significant changes in temperature and heat output are observed for a change in the host rock heat capacity (Fig. 6.8) and density (Fig. 6.9). In the early stage of pumping, increased ρc slightly increases the heat extraction rate for both deep and shallow pumping scenarios, that is the amount of heat mined per unit change in temperature. In the long-term, increased rock density and heat capacity both promote heat recovery in the system for shallow pumping scenarios, whilst it advocates heat mining in deep pumping scenarios, with the higher the ρc the higher the heat recharge/heat mining rate, respectively. This suggests that the rate of heat extraction and power output is mostly determined by the nature of the recharge (i.e. cold or warm water), with the larger the temperature contrasts between the inflowing water and the rock, the larger the amount of heat recharged/mined.

Seam hydraulic conductivity

A series of simulations have been run to quantify the relative change in MWT and power output for a change in the hydraulic conductivity of the mine workings K_m, under both deep and shallow pumping scenarios. In this analysis, K_m is used as a proxy for the goaf compaction level (i.e. how easy the flow can go through the porous material), whilst keeping a constant seam/caved zone thickness. The same hydraulic conductivity is attributed to all mined seams, allowing them to equally contribute to the inflow of water into the shaft. Further analysis is later conducted to investigate the effect of the different seam contributions to the hydraulic recharge to the shaft on the temperature profiles.

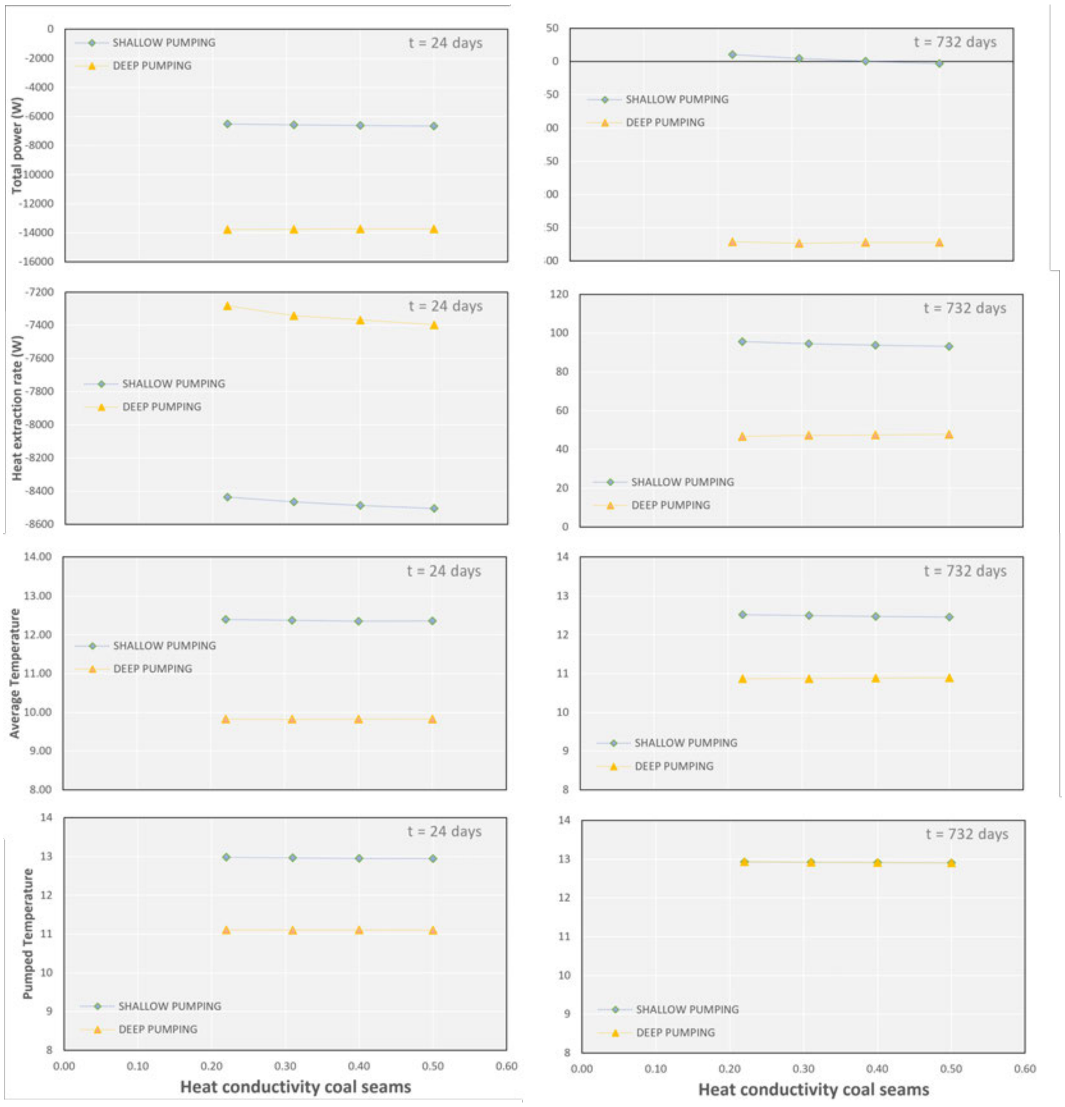

Figure 6.7: Relationship between the worked seam heat conductivity (W/℃.m) and the total power output, heat extraction rate, average MWT in the pumping shaft and pumped temperature (℃) after 24 days and 732 days of pumping (transient simulation).

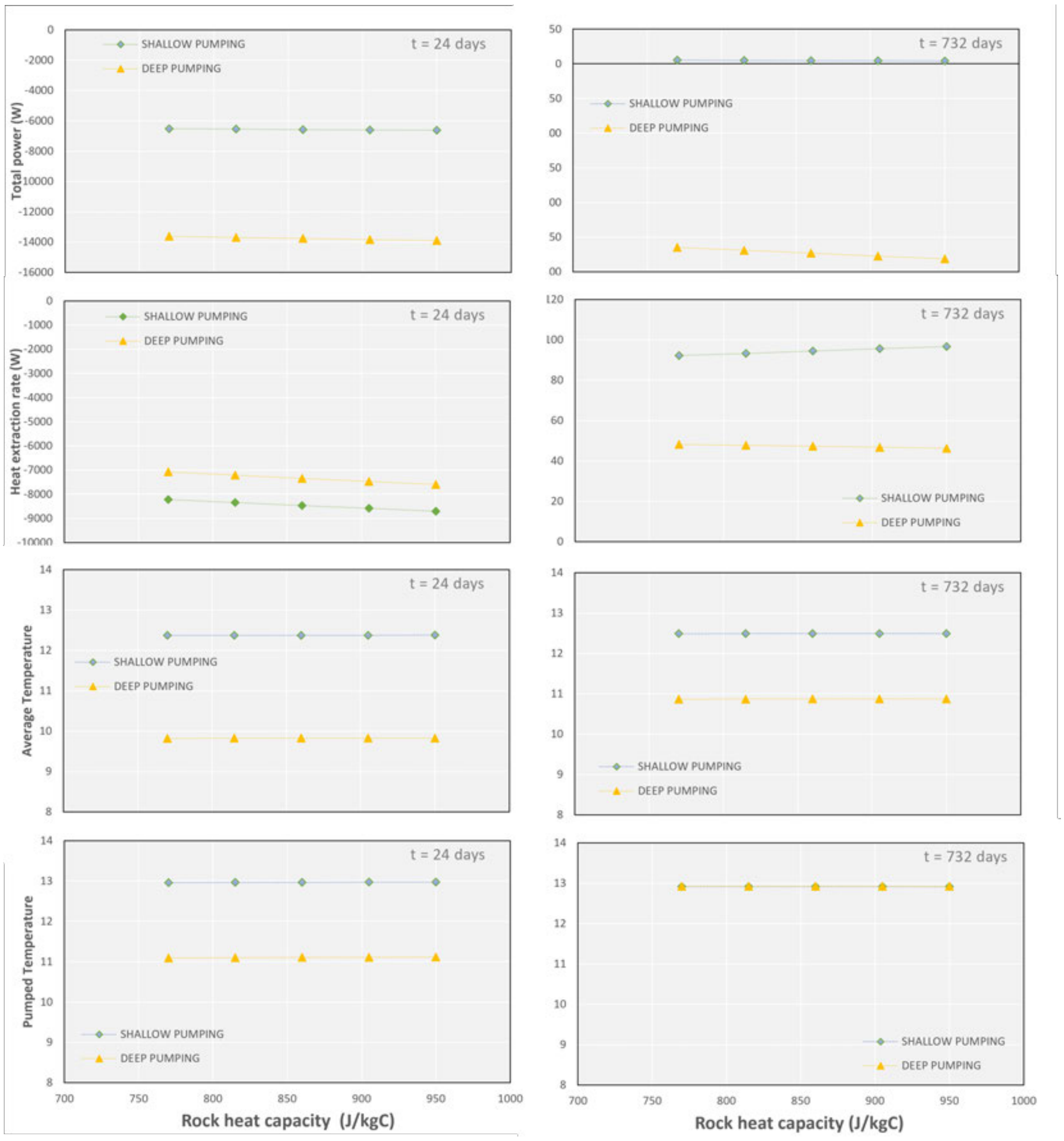

Figure 6.8: Relationship between the host rock heat capacity and the total power output, heat extraction rate, average MWT in the pumping shaft and pumped temperature (℃) after 24 days and 732 days of pumping (transient simulation).

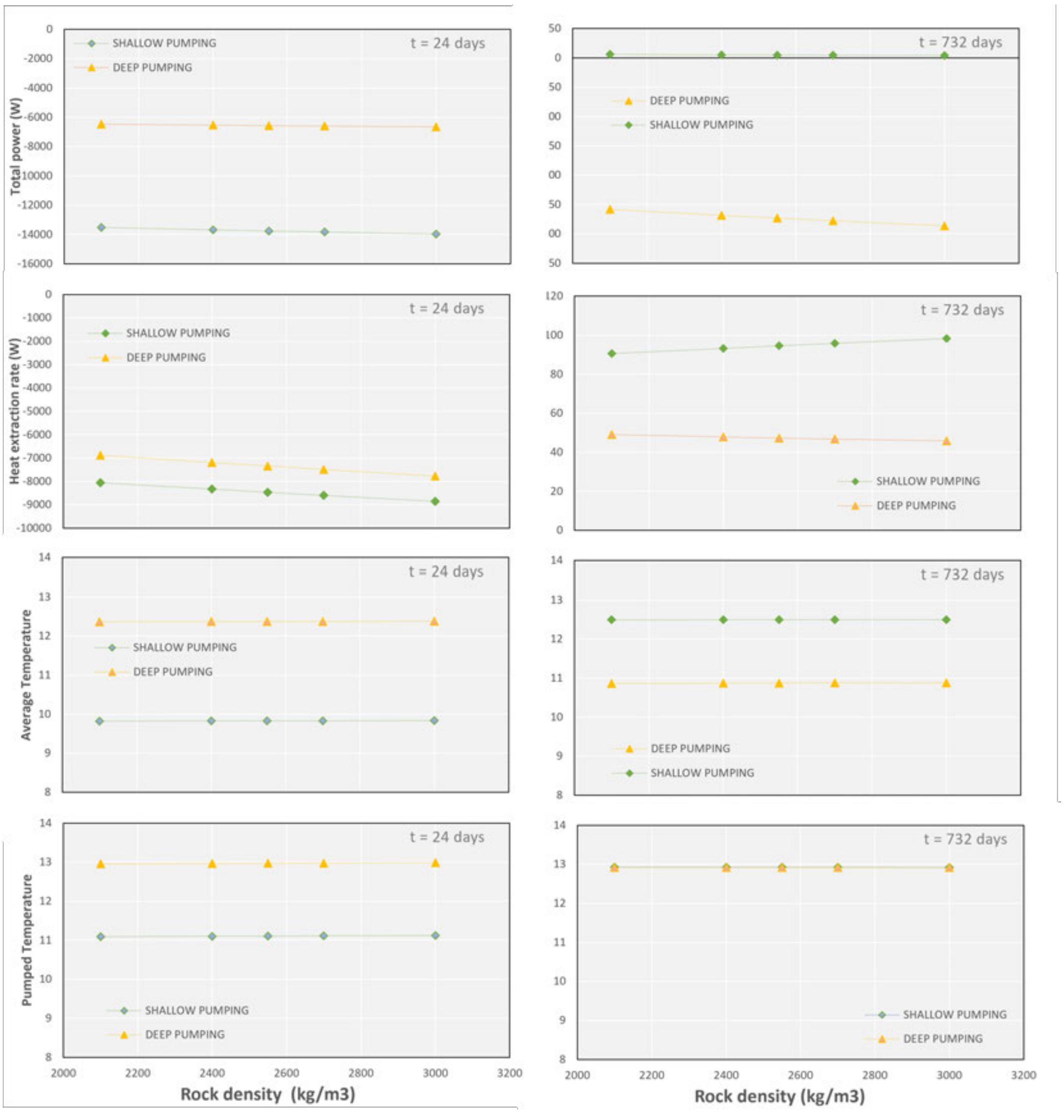

Figure 6.9: Relationship between the host rock density and the total power output, heat extraction rate, average MWT in the pumping shaft and pumped temperature (℃) after 24 days and 732 days of pumping (transient simulation).

Multiple challenges have been encountered, linked to the non-linearity of the relationship between K_w and the output parameters, and the larger instabilities created as the flow velocity increases (at high K_m) or is inhibited (for low K_m). Results are here presented for K_m ranging from 10^{-5} to 10^{-1} m/s for a 2-year-long pumping period. In accordance with Darcy's law, K_m was shown to have a negligible effect on the temperature distribution and heat output in the long term, despite the greater hydraulic drawdown observed for low-permeability scenarios (Fig. 6.10). It can however be noted that thermal steady-state is generally not reached within the two years of simulations in the low-permeability scenarios, suggesting that the slower/larger the hydraulic drawdown, the slower the thermal recovery.

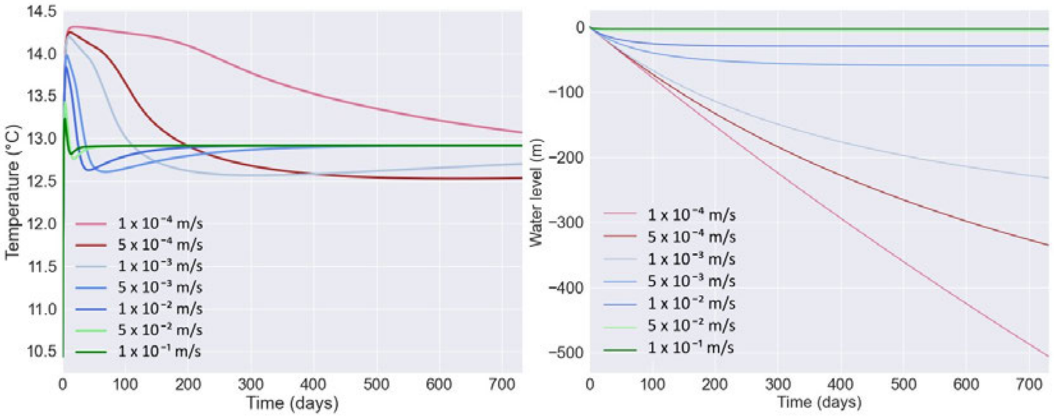

Figure 6.10: Time series of temperature and water level change for a range of seam hydraulic conductivity.

Consideration of the transient effect of pumping reveals that the temperature distribution in the pumping shaft at a given time highly depends on the hydraulic conductivity of the mine workings intersecting the shaft, with the greatest variability being observed in the initial stage of pumping (Fig. 6.11). However, the profiles tend to follow the same recovery pattern for all scenarios until the steady-state temperature is reached, with the higher the hydraulic conductivity the faster the return to equilibrium. For high seam permeability, the hydraulic flow is equally distributed among all the mined seams from the onset of production, creating regular shifts in temperature at each seam inset. For low seam permeability scenarios, most of the hydraulic flow is directed downward (in a case with deep pumping) or upward (shallow pumping) in the early stage of pumping, promoting forced vertical heat convection, with only one large shift observed at the pump location. Above the pump (shallow pumping) or the mined area (deep pumping), the temperature initially equals the surface temperature and progressively returns toward the pre-pumping linear geothermal gradient, suggesting the dominance of conductive heat transfers outside the mining area.

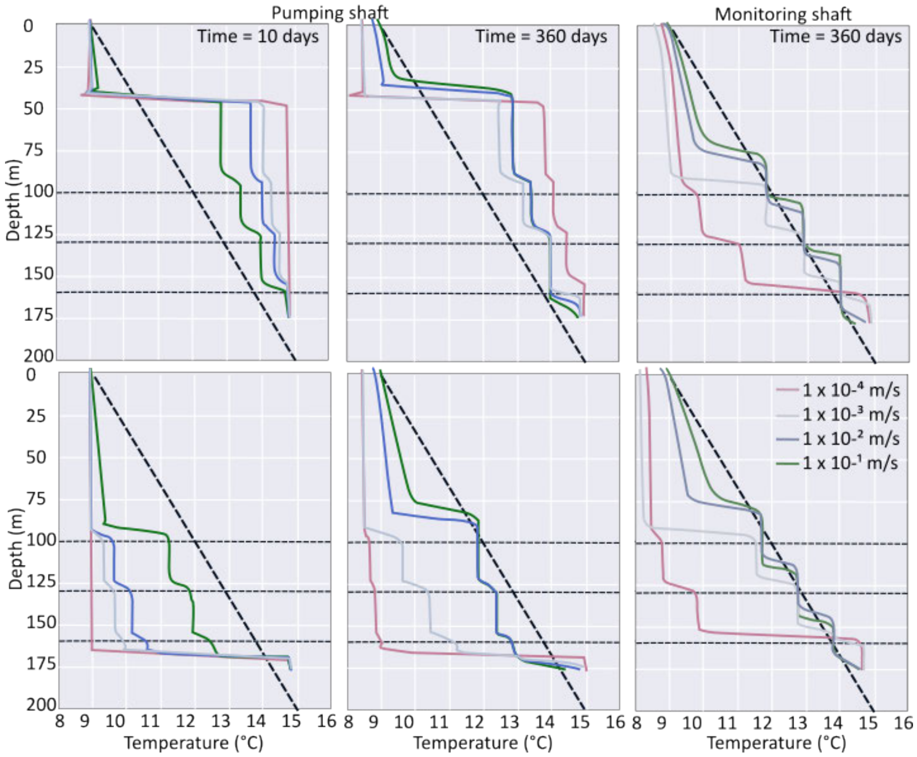

Figure 6.11: Temperature profiles in the pumping shaft after 10 days of pumping and in the pumping and monitoring shafts after 1 year of pumping, for different seam hydraulic conductivity. Profiles in the upper and lower panels are obtained for shallow and deep pumping scenarios, respectively. The different time steps allow comparing the effect of the hydraulic and thermal states of the mine on the apparent temperature in the shafts. After 1 year, thermal steady-state is reached in both shafts for the highest seam hydraulic conductivity scenario (i.e. 1×10^{-1} m/s), with all scenarios leading to this temperature distribution with increasing pumping duration.

In the monitoring shaft, a large shift in temperature is alternatively observed at the mid-seam in the early stage of pumping, and through the duration of pumping for low permeability seams (see Fig. A.48 in original published paper). As pumping continues and the system approaches steady-state, the temperature progressively re-equilibrates towards the pre-pumping geothermal gradient, with the larger the seam permeability the faster the return to equilibrium. The same temperature distribution is observed independently of the pumping depth, which is interpreted to result from the equal contribution of both lateral boundaries to the recharge, with no mixing occurring within the horizontal strata (Fig. 6.11).

Fig. 6.12 summarises the relationship between K_m and the average MWT in the pumping shaft, the pumped temperature and heat extraction rate at t = 24 days and t = 732 days since the start of pumping as well as the average heat output over this time period. This analysis confirms that these relationships are non-linear and vary as pumping progresses. At t = 24 days, the average MWT and pumped temperature decrease with increasing K_m under shallow pumping but increase under deep pumping conditions, until $K_m < 1 \times 10^{-2}$ m/s, with $T_{shallow} > T_{deep}$. As the system approaches steady-state, this trend is reversed and the average MWT in the shaft increases with increasing hydraulic conductivity for both shallow and deep pumping scenarios, with $T_{shallow} > T_{deep}$. Fig. 6.12h also confirms that steady-state is reached faster for high seam permeability cases, with the pumped temperature reaching a constant value of 13℃ in both shallow and deep scenarios for $K_m > 7 \times 10^{-3}$. In the long term, the average MWT in the pumping shaft is independent of the seam hydraulic conductivity and reaches a value of 12.7℃ for shallow pumping and 11.7℃ for deep pumping scenarios.

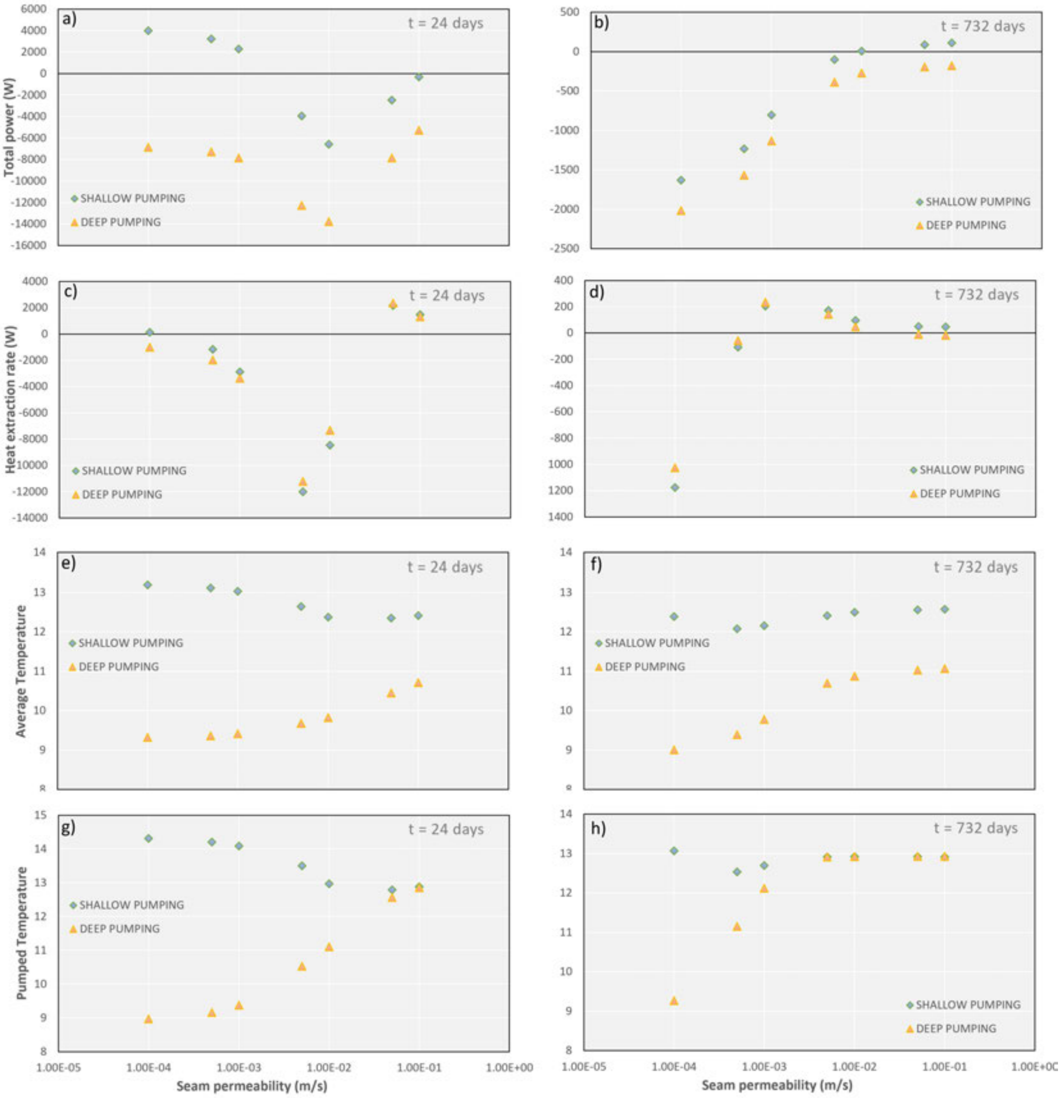

Figure 6.12: Relationship between the seam hydraulic conductivity and a-b) the total power output, c-d) the heat extraction rate, e-f) the average temperature in the pumping shaft and g-h) the pumped temperature (℃), after 24 and 732 days of pumping (transient simulation).

Looking into the heat output at t = 24 days indicates that the greater the seam hydraulic conductivity, the faster the heat mined, for seam hydraulic conductivity $K_m < 7 \times 10^{-3}$ m/s, whilst high seam hydraulic conductivity promotes thermal recovery in the system for both deep and shallow pumping scenarios (Fig. 6.12c). As pumping continues, this trend is also progressively reversed, with the heat mining rate decreasing/heat recovery being promoted as the hydraulic conductivity increases. At t = 732 days, the highest heat recovery rate is observed for K_m = 1×10^{-3} m/s. Above this threshold, the heat recovery rate slightly decreases. Overall, high seam permeability can after 2 years, either promote heat mining or thermal recovery depending on the depth of pumping and on the relative time since the onset of pumping (i.e. the equilibrium state). On the contrary, low seam permeability prevents efficient thermal recovery and sustainable heat extraction independently of the pumping depth (Fig. 6.12b). This suggests that the hydraulic recharge enabled via greater seam permeability has a key role in renewing the heat in mine-water systems. In the long term, a similar heat extraction rate and thermal equilibrium state can however be expected independently of the permeability value for a given pumping depth.

Host rock hydraulic conductivity

For the range of values tested, the host rock hydraulic conductivity has negligible control on the transient rates of thermal and hydraulic drawdown (Fig. 6.13). This can be explained by the fact that most of the flow occurs within the high-permeability seams, with the larger the rock-seam permeability contrasts, the larger the pressure drop required to generate flow in the host rock with lower hydraulic conductivity.

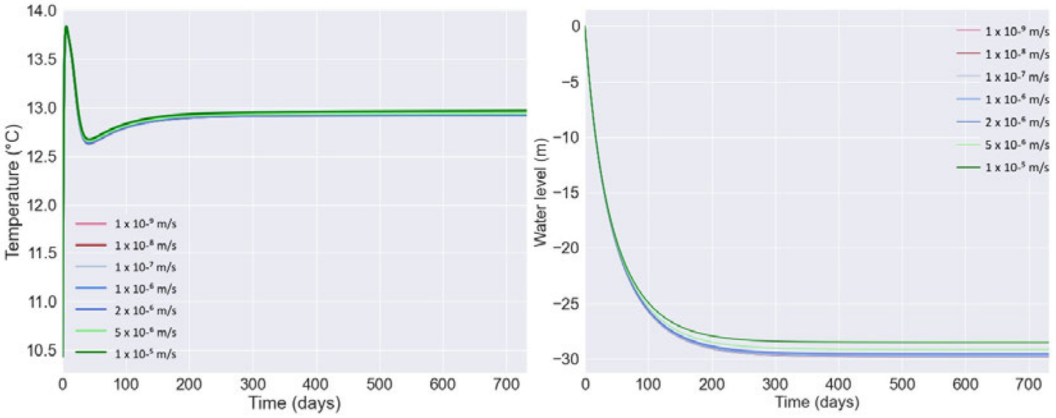

Figure 6.13: Time-series of temperature and water level change for different host rock hydraulic conductivity (shallow pumping scenarios).

As a result, the shaft profiles at a given time step depict similar temperature distributions within the mine area independently of the rock hydraulic conductivity (Fig. 6.14). The greatest discrepancies are observed above the shallowest seam, where the MWT increases with increasing K_r in both the pumping and monitoring shafts. At t = 360 days, thermal recovery above the mining area is almost complete for $K_r = 1 \times 10^{-5}$ m/s, the highest hydraulic conductivity value tested. This implication is important when considering the potential existence of a fractured zone in the mining area and suggests that the lateral hydraulic recharge plays a major role in renewing the heat from the system. This is discussed further in Chapter 8.

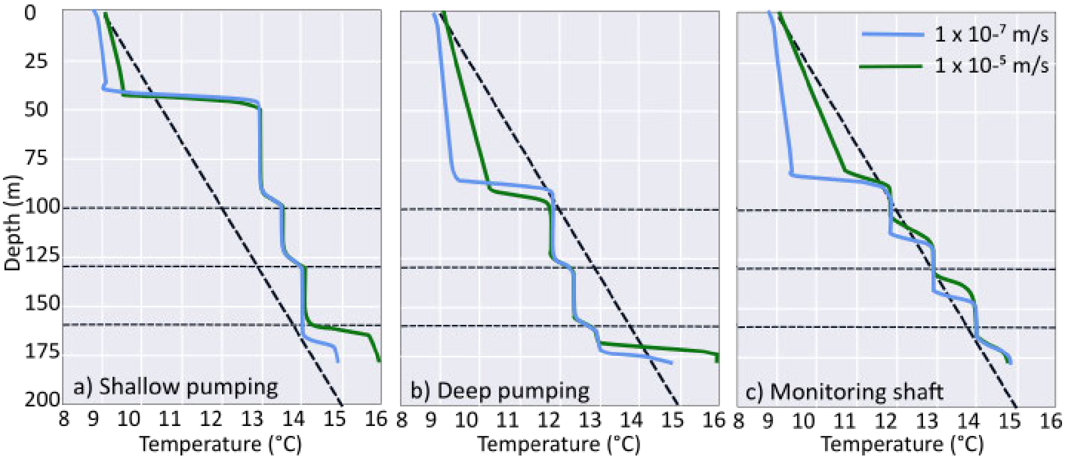

Figure 6.14: Temperature profiles in the pumping shafts for a) shallow and b) deep pumping scenarios, and c) in the monitoring shaft, for different host rock hydraulic conductivity.

Comparing results for deep and shallow pumping scenarios indicates that at t = 24 days, the deep pumping temperature is 2℃ lower than in shallow pumping scenarios, and reaches a similar temperature of 13℃ in the long term. At t = 732 days, the average shaft temperature remains higher for shallow pumping scenarios (12.5 ℃ against 11 ℃ for deep pumping) and slightly increases for $K_r > 1 \times 10^{-6}$ m/s in both cases. Whilst heat mining is observed for both deep and shallow pumping in the initial days of pumping (t = 24 days), with the heat mining rate being higher for shallow pumping scenarios, an increase in the rock hydraulic conductivity exponentially increases the heat recovery rate over time (Fig. 6.15). Results at t = 732 days confirm that steady-state conditions are reached faster for the high hydraulic conductivity scenarios ($K_r > 1 \times 10^{-6}$ m/s), where the heat recovery rate becomes independent from the pumping depth. Overall, the higher the rock permeability, the faster the host rock can replenish in heat, especially if pumping is performed from shallow depths (Fig. 6.15).

Materials storativity

The storativity represents the volume of water released by an aquifer per unit area of the aquifer and unit change in head. Because the storage is not involved in the determination of the steady hydraulic state of a system (see Chapter 4), it is essential to evaluate the changes in temperature and energy in the mine-water reservoir for a range of host rock, shaft and workings storage through transient analysis.

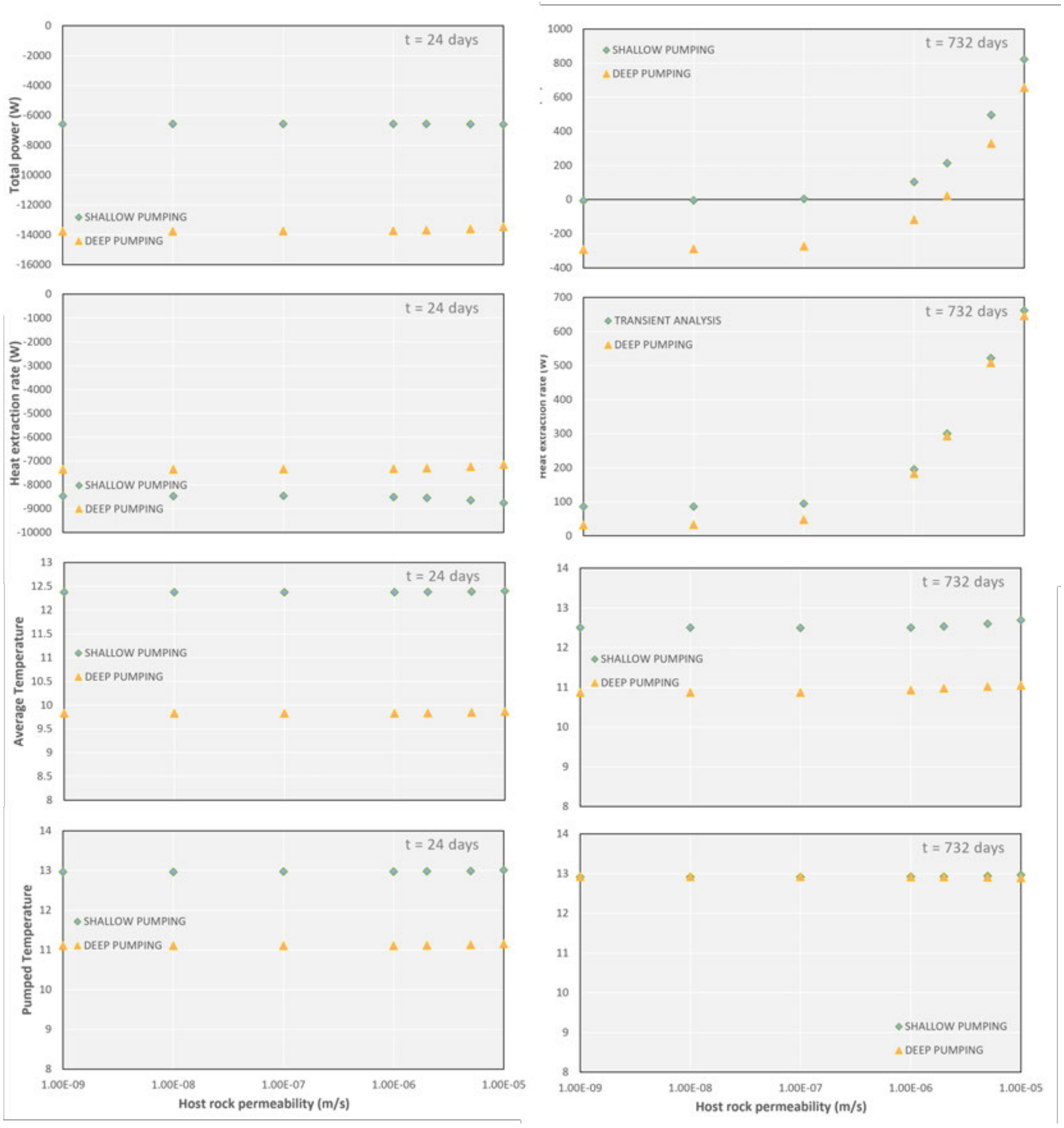

Figure 6.15: Relationship between the host rock hydraulic conductivity and the total power output, heat extraction rate, average MWT in the pumping shaft and pumped temperature (℃) after 24 days and 732 days of pumping (transient simulation).

Results suggest that the lower the storage, the quicker the hydraulic drawdown (Fig. 6.16). The head and the temperature at the pump location are particularly sensitive to the shaft storage and to a lower extent to the mine workings and host rock storage. High storage delays the time to reach the hydraulic steady-state, which in turn delays the pumped temperature to reach the thermal steady-state in a similar way to the hydraulic conductivity (Fig. 6.10). The temperature profiles however suggest that although low shaft storage promotes thermal recovery and a quick return to thermal equilibrium in the monitoring and pumping shafts, higher host rock and mine workings storage prevents extensive heat mining within the mining area in the early stage of pumping (Fig. 6.17).

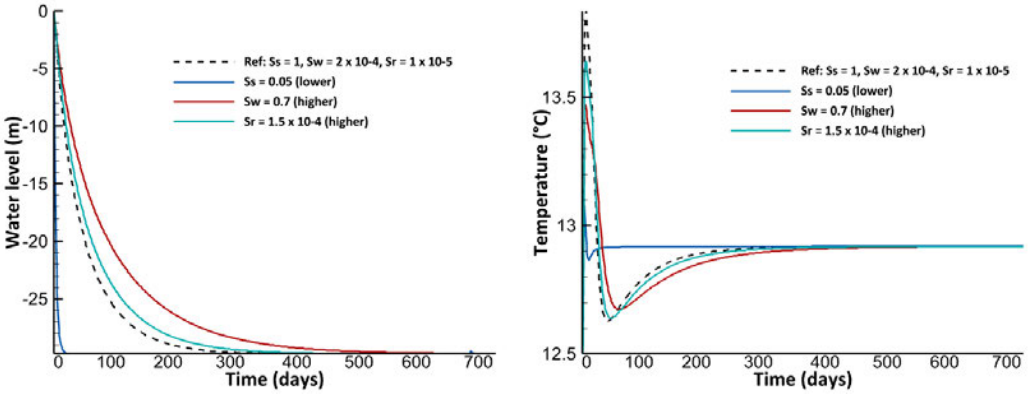

Figure 6.16: Time series of water level (left) and temperature change (right) for different host rock S_r, mine workings S_w and shaft storage S_s (shallow pumping scenario).

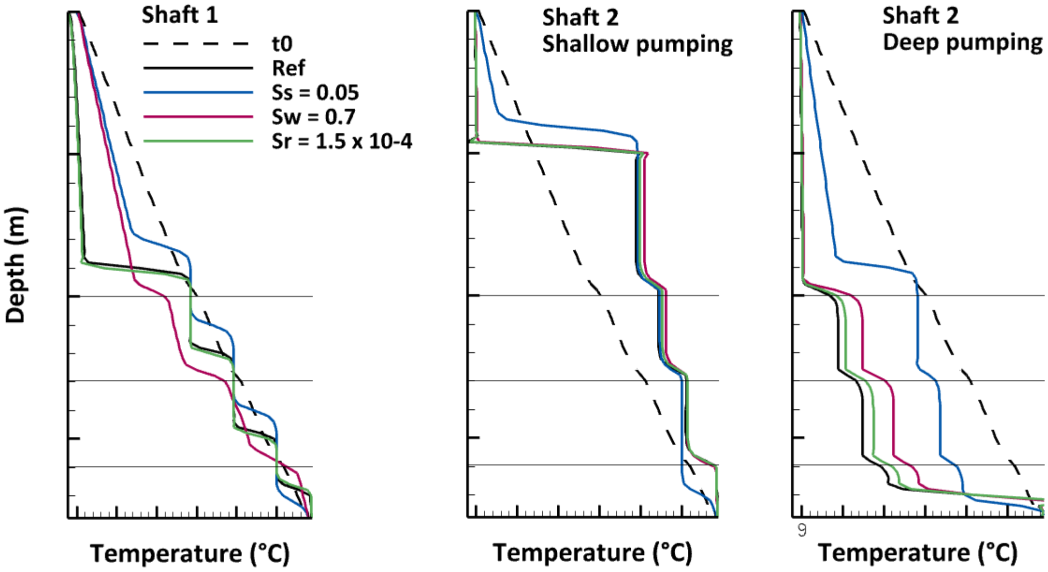

Figure 6.17: Temperature profiles in the monitoring shaft 1 and pumping shaft 2 after 24 days of pumping for deep and shallow pumping scenarios and different host rock S_r, mine workings S_w and shaft storage S_s.

In the long-term, the greater the mine workings storage, the faster the thermal recovery rate, but the total power output slightly reduces for high storage values (Fig. 6.18). The same observation can be made for the host rock storage, although the impact on the long-term average power output is negligible (Fig. 6.19). The relationship between the shaft storage and the heat extraction rate/power output is more complex due to the greater sensitivity of the system to a variation in the shaft storage (Fig. 6.20). However, it is possible to observe the overall increase in heat recharge rate after 2 years of pumping for $S_s > 0.1$ m^{-1}, whilst the total average power output reduces as S_s increases.

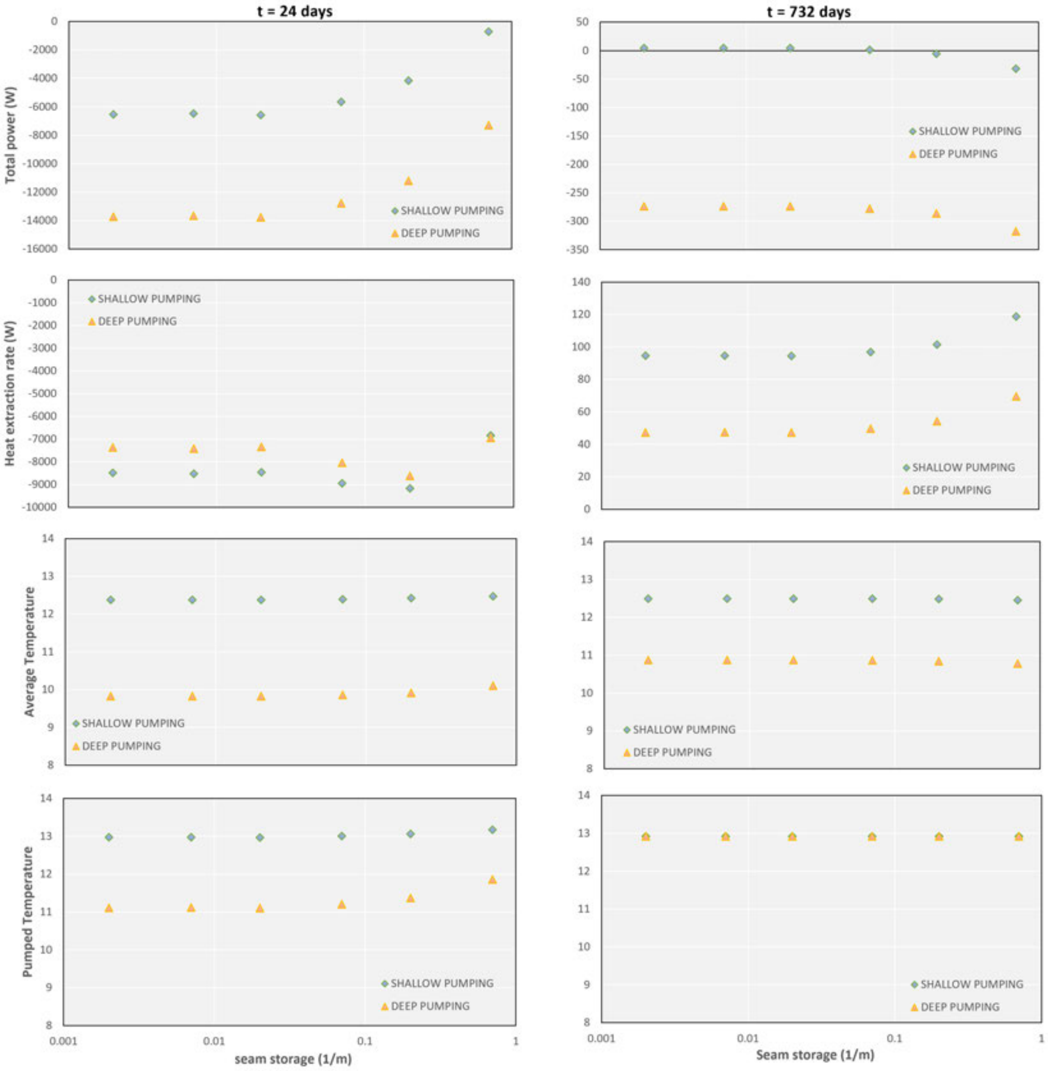

Figure 6.18: Relationship between the seam storage and the total power output, heat extraction rate, average MWT in the pumping shaft and pumped temperature (℃) after 24 days and 732 days of pumping (transient simulation).

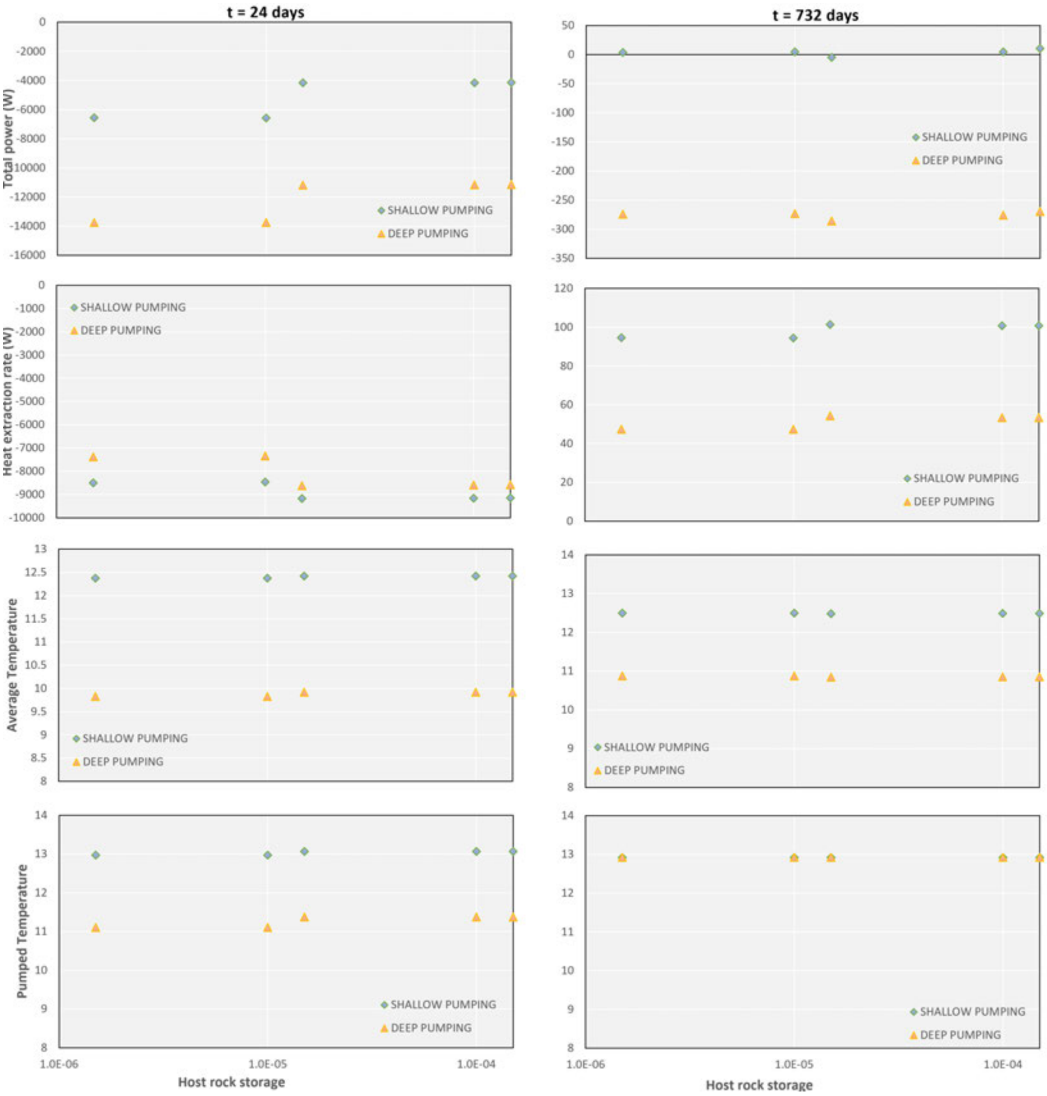

Figure 6.19: Relationship between the host rock storage and the total power output, heat extraction rate, average MWT in the pumping shaft and pumped temperature (℃) after 24 days and 732 days of pumping (transient simulation).

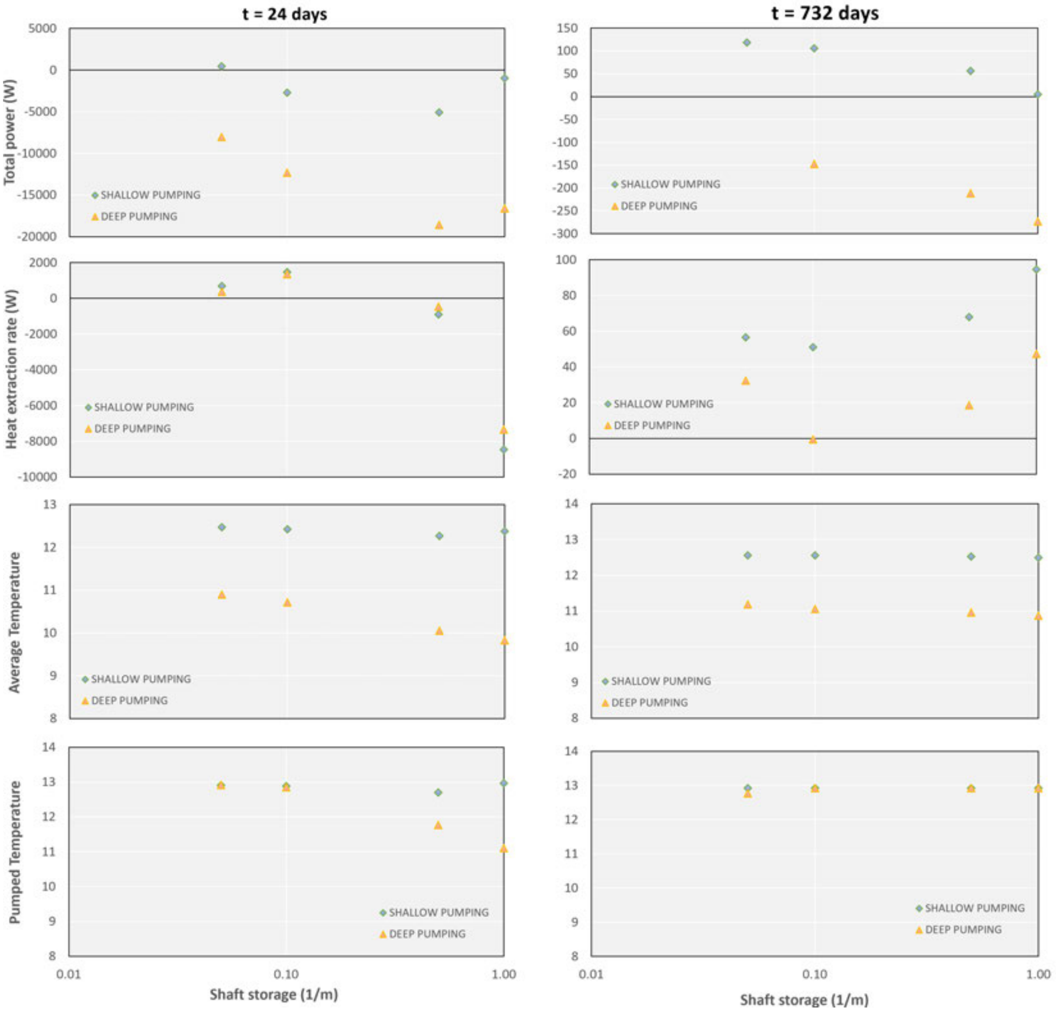

Figure 6.20: Relationship between the shaft storage and the total power output, heat extraction rate, average MWT in the pumping shaft and pumped temperature (℃) after 24 days and 732 days of pumping (transient simulation).

Pumping rate

The effect of the pumping rate Q is finally determined, keeping the material properties for the reference model constant. Results suggest that the pumping rate has a negligible effect on the steady-state temperature and average MWT in the pumping shaft. However, for $Q >$ 0.01 m^3.s^{-1}, the steady-state power output and heat extraction rate increase linearly with increasing flow rate Q (Fig. 6.21), suggesting that the higher the fluid velocity, the larger the heat mining rate. This is also expressed by a larger drawdown (according to Darcy's law) and a faster return to steady hydraulic conditions. As the pumping rate increases, the heat extraction rate for both deep and shallow pumping scenarios moreover tends to reach a similar value, whilst discrepancies of up to 50 W are calculated for Q = 0.001 m^3.s^{-1}.

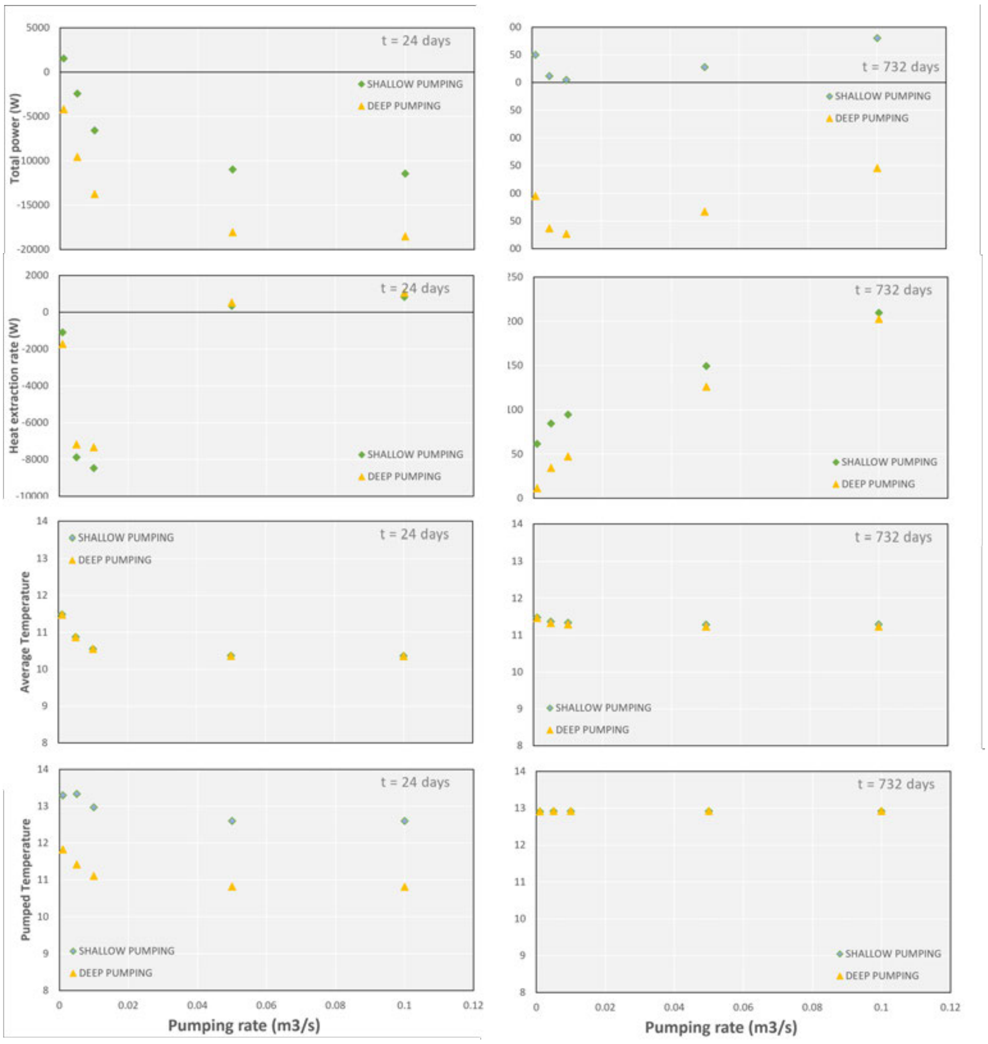

Figure 6.21: Relationship between the pumping rate and the total power output, heat extraction rate, average MWT in the pumping shaft and pumped temperature (℃) after 24 days and 732 days of pumping (transient simulation).

6.4.2 Relationship between pumped, reservoir and average shaft temperature

The transient changes in the pumped temperature and average MWT in the pumping shaft are compared against the temperatures predicted by the geothermal gradient at the pump depth and in the mining area (i.e. mid-seam depth) (Fig. 6.22), and for a range of geothermal gradient and seam hydraulic conductivity (Fig. 6.23).

The time series displayed in Fig. 6.22 suggests that in systems with horizontal layers, where no water mixing occurs outside the shaft, the pumped temperature (plain lines) re-equilibrates with the temperature predicted by the geothermal gradient at the mid-seam depth (dashed red line) when pumping occurs from above the shallowest seam (z_P = 52 mbgl) or below the deepest seam (z_P = 158 mbgl). This results in the pumped temperature being higher and lower than the temperature predicted by the geothermal gradient at the pump depth in shallow and deep pumping scenarios, respectively. When pumping is performed within the mining area, potential mixing results in a shift in the pumped temperature towards warmer (z_P = 110 mbgl) or cooler temperatures (z_P = 140 mbgl) relative to the average temperature at the mid-seam (dashed red line), and compared to the temperature predicted by the geothermal gradient at the corresponding pump depth.

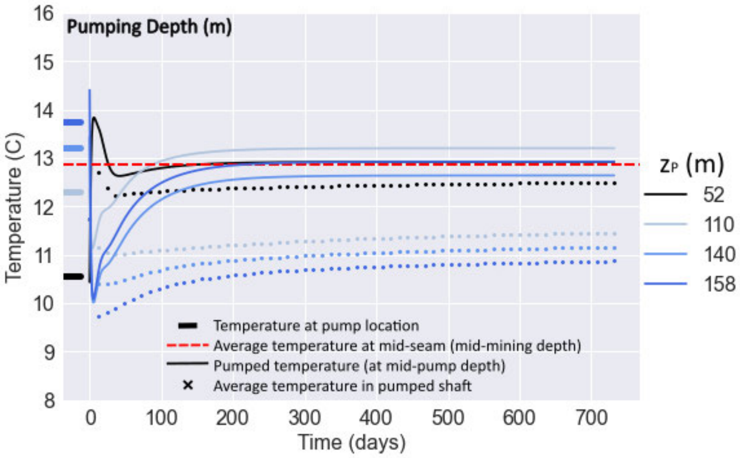

Figure 6.22: Transient change in the pumped temperature (plain lines) and average shaft temperature (crosses) over 732 days of pumping, for different pumping depths. The thick lines at t = 0 represent the temperature at the pump location. The horizontal dashed lines represent the temperature at the mid-seam, that is the average temperature in the mining area.

When looking at the results for a range of geothermal gradients, the pumped temperature is generally higher than the average temperature in the shaft (dots/crosses) for the corresponding scenario. This observation is particularly true for deep pumping scenarios (Fig. 6.23A), where the difference between the two temperature types is the greatest. The rate at which thermal equilibrium is reached will also depend on the seam permeability (Fig. 6.23B), with the smaller the permeability the slower the recovery. It is also possible to note that the sensitivity of the observed MWT to the seam permeability is higher for deep pumping scenarios.

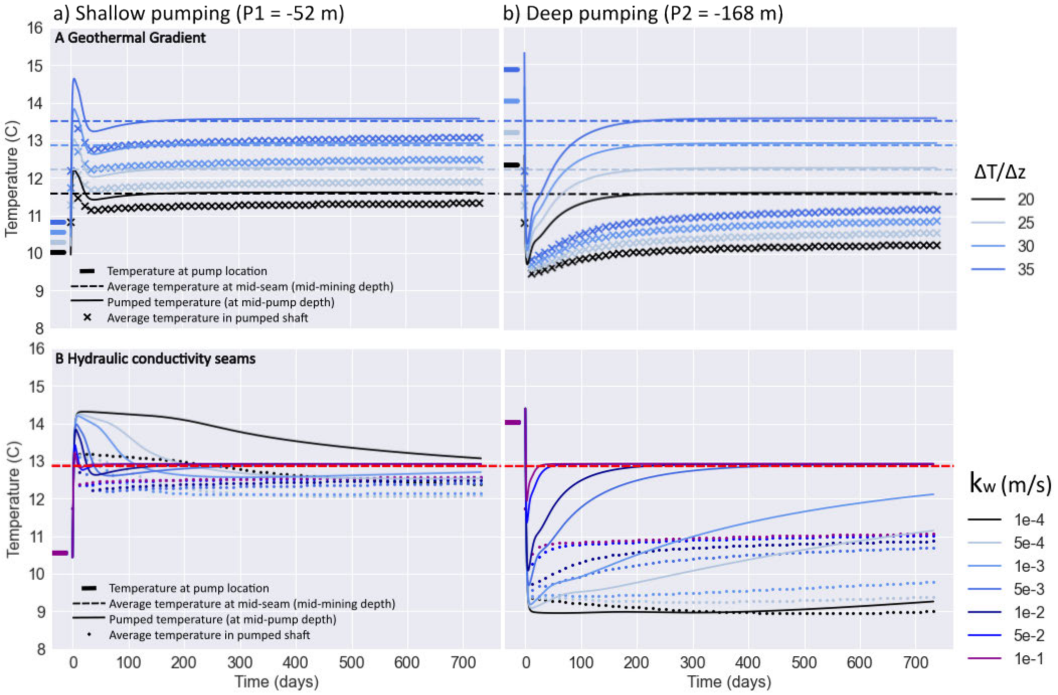

Figure 6.23: Transient change in the pumped temperature (plain lines) and average shaft temperature (crosses) over 732 days of pumping, for A) different geothermal gradients and B) seam hydraulic conductivity, and for the shallow (right) and deep (left) pumping scenarios. The thick lines at t = 0 day represent the temperature at the pump location. The horizontal dashed lines represent the temperature at the mid-seam, that is the average temperature in the mining area.

6.4.3 Effect of temperature boundary condition

Two scenarios involving the use of constant heat flux of -0.065 W.m^{-2} and constant surface temperatures of 9℃ are compared to investigate the effect of forced surface heat recharge on the rate of heat transfer and thermal state of the mine after 2 years of pumping. Results depict no differences in the temperature distribution in the mine, in the pumped temperature and the rate of heat extraction within the full duration of the simulations, whether pumping is performed from shallow or deep seams (Fig. 6.24). This suggests that the surface boundary has a limited contribution to the heat recharge in the system. The effect of the nature of hydraulic recharge is investigated further in Chapter 7 for a mine with dipping seams.

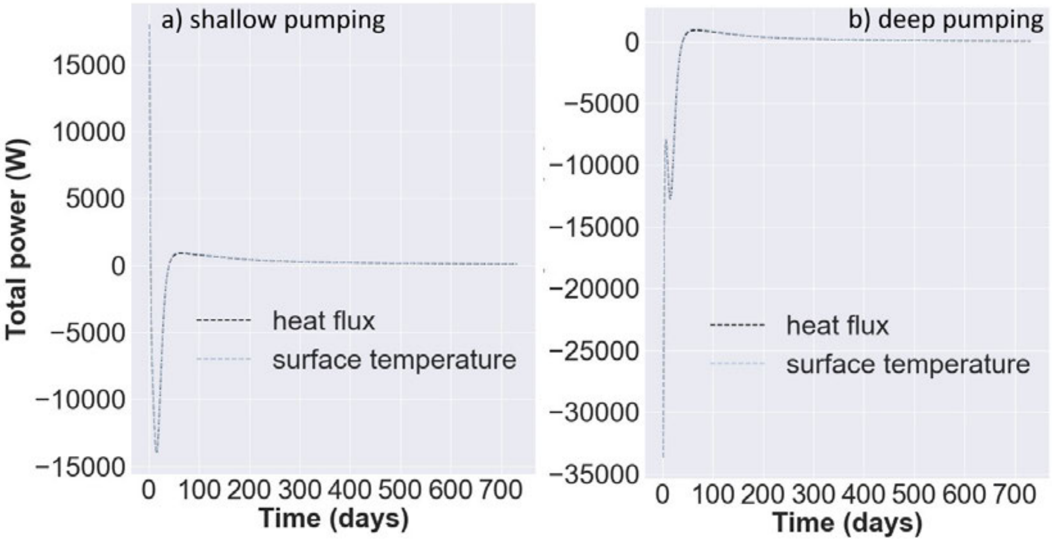

Figure 6.24: Rate of heat extraction for a) a shallow and b) a deep pumping scenario for scenarios with a constant surface temperature and surface heat flux. The model consists of the porous media model with horizontal seams.

6.4.4 Effect of seam depth, thickness and shaft spacing

New model meshes have been generated to investigate the relative effect of the seam depth, the shaft spacing and the seam thickness on the pumped temperature and heat output. The model considers one mined seam from which water is pumped and re-injected for 2 years, assuming constant heads at the pump equal to -1 m and 1 m, respectively.

Fig. 6.25 shows the percentage change in pumped temperature per relative change in the property values (i.e. sensitivity index). Results indicate that the temperature increases linearly with increasing shaft spacing and seam depth. The first correlation is interpreted to relate to the increased travel distance between the injection and production point, which promotes the heat recovery of water via increased heat transfer between the rock and water. The relationship with the seam depth is assumed to be directly linked to the effect of the geothermal gradient, where deeper seams access greater temperatures. On the other hand, the pumped temperature decreases exponentially with increasing seam thickness. This is assumed to relate to the increased volumetric flow rate in the galleries induced by higher gallery volume when considering constant head values at the pumps. The simulations are therefore repeated using source terms of -0.001 and 0.001 $m^3.s^{-1}$ to represent pumping and reinjection, which allow maintaining an absolute velocity of 2.37×10^{-4} m/s in the shafts and galleries. The updated results indicate a slight increase in pumped temperature per increasing seam thickness. This can be explained by the higher specific heat capacity of water, which is present in larger quantities as the seam thickness increases (i.e. larger increase in temperature per mass flow rate).

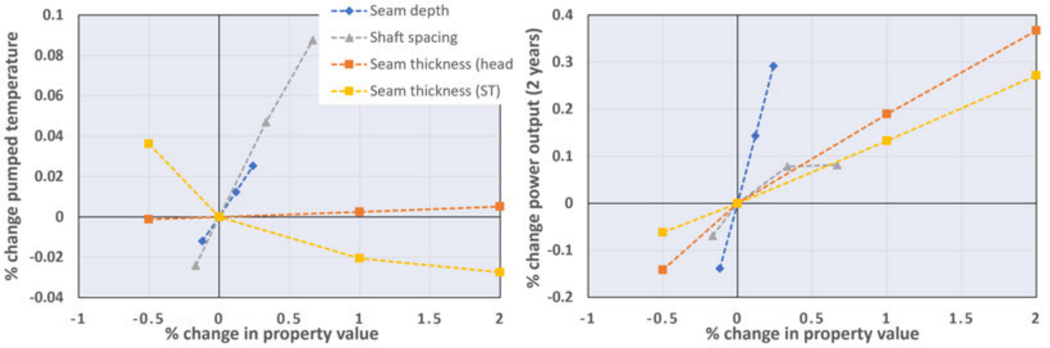

Figure 6.25: Relationship between a relative change in shaft spacing, seam depth and seam thickness, and the pumped temperature/power output (2-year long steady-state simulations).

The largest effect on the power output is observed for a change in seam depth, and to a lower extent to the seam thickness. The power output only increases by a maximum of 10% with increasing shaft spacing, whilst a decrease in shaft spacing below the reference value of 250 m has no significant effects on the power output. This non-linear relationship is here attributed to boundary effects, that increase as the shafts are getting closer to the lateral boundaries of the model.

6.4.5 Multi-element model

A multi-element model is finally developed to analyse the advantages/disadvantages of simulating heat transfers between shafts (and in a second instance roadways) modelled as 1D elements and the surrounding porous mesh, relative to the fully-saturated 2D porous media approach. The model is moreover expected to give insights into the preferred adjustments of the 2D porous media characteristics (e.g. shaft/host rock volume ratio), to assess the potential overestimation of the thermal drawdown that might be caused by the utilisation of an unscaled 2D porous model, and provide realistic assessments of the heat mining effect of pumping. This will be used as a reference to study the long-term thermal footprint of pumping on the thermal distribution in the mine-water reservoir (Chapter 7).

1D shafts The temperature distribution and heat output from the reference 2D porous media and a multi-element model with 1D shaft elements are compared, assuming a perpendicular thickness of 1 m (scenarios P1 and M1 in Table 6.5). After 2 years of deep pumping at a rate of -0.01 $m^3.s^{-1}$, results indicate that the steady temperature profiles and the extent of the thermal footprint calculated using both approaches are similar (Fig. 6.26). However, the power output is higher for the 2D porous model (i.e. -137 W, against -103 W for the multi-element model), with the thermal and hydraulic drawdown at the pump being slightly higher (i.e. -2.5 ℃ against -2.3℃ for the multi-element model) and smaller (i.e. -29.8 m against -30.7 m for the multi-element model), respectively. Considering the larger heat capacity of water, this slight discrepancy is here explained by the larger number of nodes in the porous media approach (4 triangular elements in the X-direction against 1 line element in the multi-element model) and therefore the larger heat gained from the 6 m-diameter shafts.

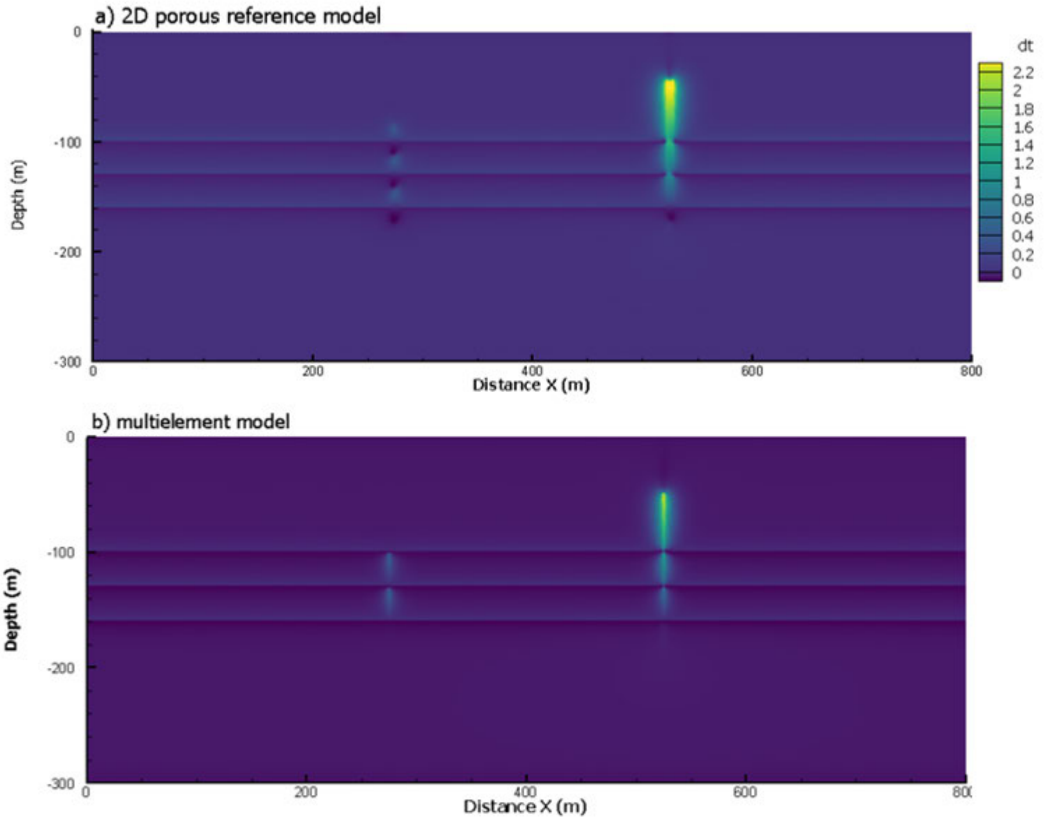

Figure 6.26: Comparison of the temperature distribution for a shallow pumping scenario using a) the 2D porous and b) the multi-element modelling approaches after 2 years of pumping (steady-state). In the multi-element model, the shafts are modelled as 1D elements. Both models depict a maximum hydraulic drawdown of 30 m and thermal drawdown of 2.2°C (considering a model perpendicular thickness A = 1 m and a pumping rate Q = -0.01 m^3/s).

1D shafts and roadways An alternative multi-element mesh is developed, implementing 1D roadway features at the location of the layers previously mined as goaf panels. To compare results with the reference 2D porous model, 1D roadways and shaft elements are modelled with an area A = 1 m and hydraulic conductivity of 1×10^{-2} m.s^{-1} and 1 m.s^{-1}, respectively. Results from the simulation using a deep pumping rate of -0.01 m^3.s^{-1} shows that this model tends to overestimate the hydraulic drawdown and underestimate the thermal drawdown at the shaft compared to the porous model P1, suggesting that heat transfers between the water in the roadways and the surrounding porous media are hindered (Fig. 6.27).

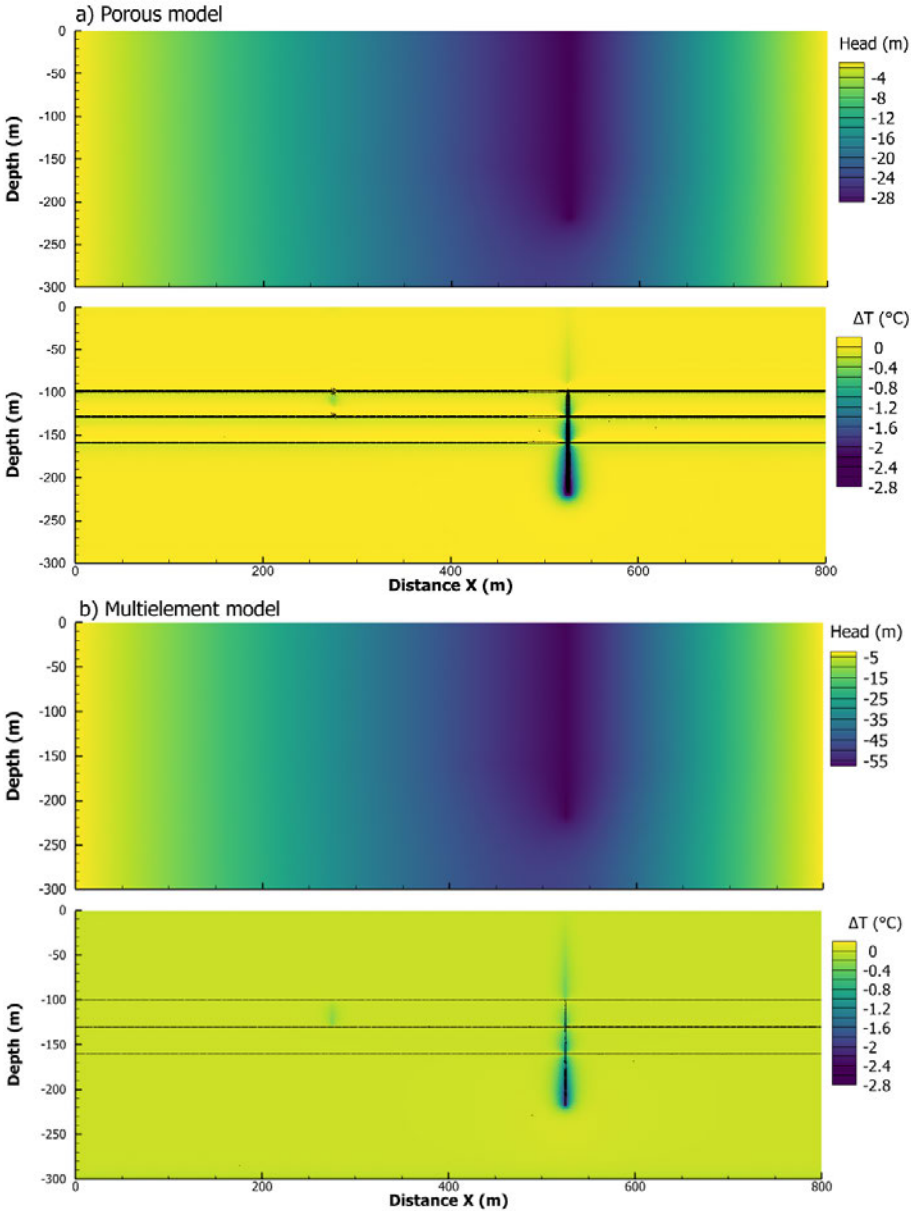

Figure 6.27: Thermal footprint induced by deep pumping from the porous and multi-element models (steady-state). In the multi-element model, both shafts and roadways are modelled as 1D elements. Flow vectors are drawn in black and suggest that most of the flow is concentrated in the roadways and the pumping shaft, which are the main flow pathways from the model hydraulic boundaries to the pump.

6.5 Discussion

6.5.1 Slice thickness, transmissivity and thermal footprint

The reference model presented in this study uses a slice thickness (i.e. model extent in the Y-direction perpendicular to the model plan) equal to 1 m (Model P1 in Table 6.5). Ignoring the true extent of the mine-water reservoir is acceptable when performing comparative analysis, provided the shorter computation time. However, this neglects the lateral extent of the mine workings relative to the shafts and roadways, which will both underestimate the initial heat potential of a given system and overestimate the rate of thermal drawdown induced by pumping. This becomes an issue when assessing the true heat capacity, the rate of extractable heat from a mine-water reservoir, and when quantifying the extent of the thermal plume over a given period.

Here, the impact of the slice thickness relative to the shaft/roadways on the thermal footprint and heat extraction rate is investigated. The hydraulic and thermal drawdown measured at the pump location and the heat output after 2 years of pumping from 2D porous models, calculated using steady-state simulations are compared. The characteristics of each model (e.g. slice perpendicular thickness A, material permeability) and the result outputs are summarised in Table 6.5 together with results for the multi-element models.

Model	A	A_s	K	K_s (m/s)	Q (m^3/s)	ΔH	ΔT	ΔE
P1	1	1	1×10^{-7}	1	-0.01	-29.8	2.5	137
P2	1	0.06	1×10^{-7}	1	-0.01	-31.4	2.5	89
P2b	1	0.06	1×10^{-7}	16.6	-0.01	-29.8	2.5	73
P3	100	100	1×10^{-7}	1	-0.01	-29.8	2.2	1.2×10^4
P3b	100	6	1×10^{-7}	1	-0.01	-31.4	2.5	8.9×10^3
P4	100	100	1×10^{-9}	1×10^{-2}	-0.01	-29.8	2.2	1.2×10^4
P4b	100	6	1×10^{-9}	1×10^{-2}	-0.01	-31.4	2.3	7.0×10^3
P5	100	100	1×10^{-7}	1	-1	-29.8	2.5	1.4×10^4
P5b	100	6	1×10^{-7}	1	-1	-31.4	2.5	8.9×10^3
M1	1	1	1×10^{-7}	1	-0.01	-30.7	2.3	103
M2	1	0.28	1×10^{-7}	1	-0.01	-32.3	2.3	112
M2b	1	0.28	1×10^{-7}	3.6	-0.01	-30.7	2.3	102
M3	100	28	1×10^{-7}	1	-0.01	-32.3	2.1	6.8×10^3
M4	100	28	1×10^{-9}	1×10^{-2}	-0.01	-32.3	2.1	6.8×10^3
M5	100	28	1×10^{-7}	1	-1	-32.3	2.3	1.0×10^4

Table 6.5: Change in hydraulic drawdown (ΔH), thermal drawdown (ΔT) and energy content (ΔE) for different slice perpendicular thickness (A), pumping rate (Q) and hydraulic conductivity (K) combinations.

Results show that the hydraulic drawdown at the pump after 2 years of pumping at a rate Q = -0.01 m^3/s can be scaled for an increase in the model perpendicular thickness by decreasing proportionally the hydraulic conductivity K of the media (Scenario P4) so that the material transmissivity T = Kh remains the same (see Table 6.1). However, this adjustment does not reproduce the temperature distribution in the mine whilst the heat output is almost two orders of magnitudes higher than in the reference model P1 (i.e. proportional to the volume increase). At steady-state, both the thermal drawdown at the pump and the extent of the thermal footprint are reduced compared to P1, which can be explained by the larger volume and increased heat availability in P4. Alternatively, increasing the pumping rate proportionally to the increase in the slice perpendicular thickness (P5, Q = -1 m^3/s) allows reproducing both the hydraulic and thermal state of model P1. As for model P3/P4, the heat output remains two orders of magnitude higher than for a slice thickness of 1 m.

In scenarios P3, P4 and P5, the area of both the reservoir and shafts is multiplied by 100, which is suspected to largely promote hydraulic recharge via the high permeability voids (i.e. the shafts), overestimate the surface area available for heat exchanges between the water in the shaft and the surrounding rock, and therefore the heat recharge/heat mining potential. In reality, the shaft diameter (e.g. 6 m) is much smaller than the width of a coal panel (> 40 m). The previous scenarios (P3, P4 and P5) are therefore adjusted for a shaft perpendicular thickness of 6 m (P3b, P4b and P5b). Comparing models P3/P3b show that the shaft dimensions have a key effect on the heat output from the reservoir. Whilst a smaller shaft area will reduce the heat output and increase both ΔT and ΔH, Model P2 and P2b suggest that the hydraulic drawdown can be adjusted for a reduction in the shaft area by increasing the shaft hydraulic conductivity.

In the multi-element model, scaling the shaft area (using A_S = 28 m^2, with $A_S = \pi(d/2)^2$ and d = 6 m) and hydraulic conductivity proportionally to the slice thickness has a negligible effect on the energy output (e.g. models M2/M2b) compared to the porous model (models P2/P2b). Unlike the porous model, the energy output does not increase proportionally to the increase in the slice thickness (e.g. Model M3/M4). However, scaling the pumping rate (M5) for an increase in the slice thickness to -1 m^3/s allows reproducing both the thermal and hydraulic drawdown of the reference model (Model M2) whilst increasing the heat output compared to a pumping rate of -0.01 m^3/s. Overall, model P2 with As = 0.06 m reproduces best the drawdown and heat recharge rate simulated by M3, which is assumed to replicate the shaft/mine workings volume ratio.

Overall, all the modelled scenarios result in similar steady-state temperature profiles (Fig. 6.28). Given the longer time required for calculations to be done with the multi-element model, the 2D porous model is considered to be a valid approach to investigate convective heat transport in flooded mines and will therefore used in chapter 7 to investigate the effect of dewatering on the thermal state of the mine.

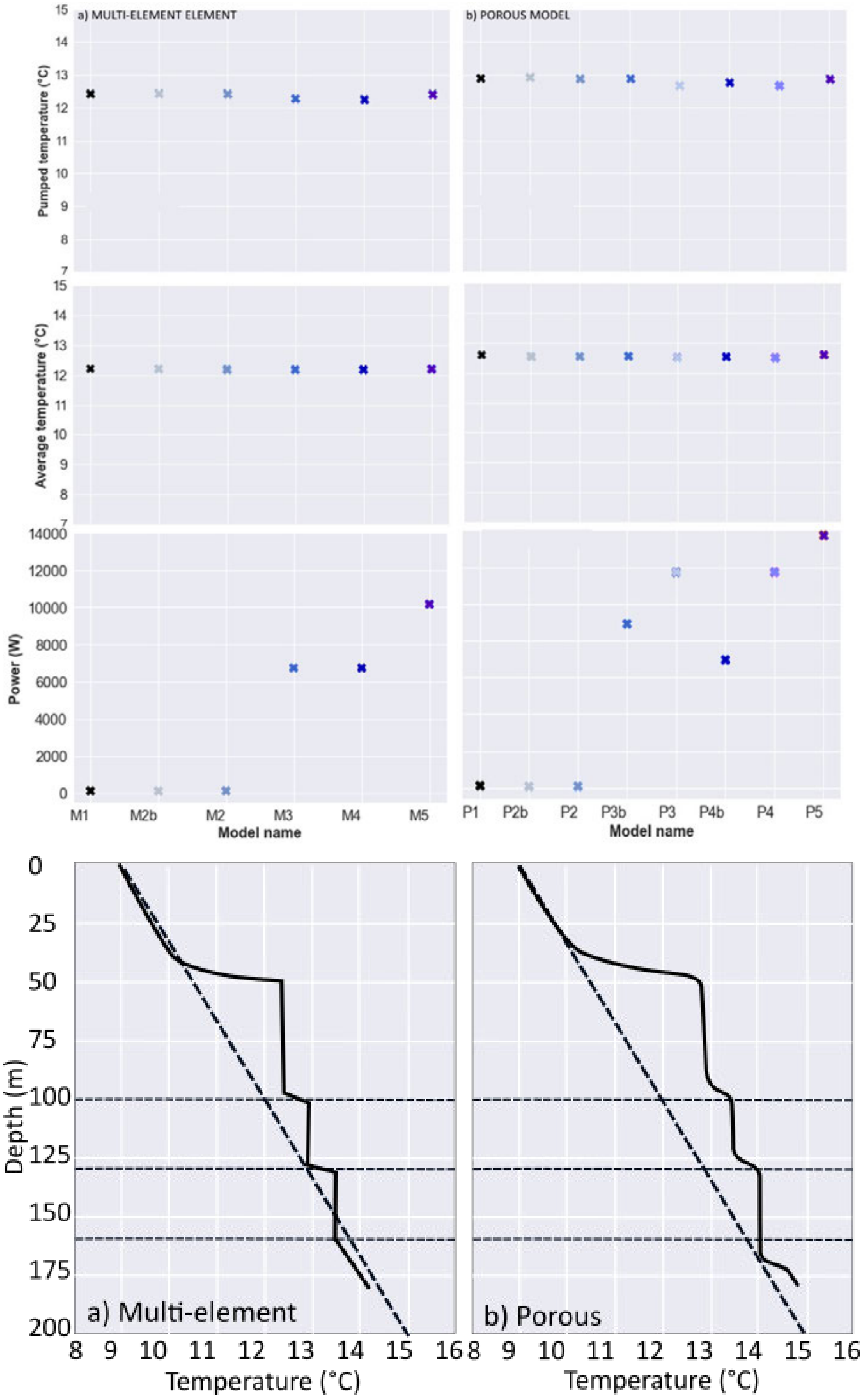

Figure 6.28: Comparison of the average temperature, pumped temperature, power output and temperature profiles in the pumping shaft for a shallow pumping scenario using a) the shaft-only multi-element modelling approaches and b) the 2D porous after 2 years of pumping (steady-state). Results suggest that the same steady-state temperature distribution is reached in the pumping shaft for all scenarios.

6.5.2 Steady-state and transient analysis

Steady-state simulations have been used as input to set the initial conditions of numerical models (i.e. initial head and temperature distribution) and predict the changes induced by a modification of the equilibrium state, and for different numerical parameters. Steady-state simulations significantly speed up the numerical analysis (up to 300 times compared to a two-year transient simulation) and are particularly relevant when linear relationships exist between the input properties and output parameters, independently of the simulation time. However, they are only indicative of the equilibrium state and therefore do not give insights into the short-term behaviour of a geothermal resource. When calculating the total heat output based on the final and initial energy in the system, this generally results in a lower value as the simulation time increases. This can be explained by the fact that steady simulations average the heat extraction rate, which tends to decrease over time and does not account for the change in the heat extraction and recharge dynamic.

Reservoir properties such as thermal conductivity or hydraulic conductivity have limited effect on the steady-state conditions, but considerably impact the short-term behaviour of heat transfers. Transient analysis therefore allows providing an insightful understanding of the non-linear temporal behaviour of pumping on the changes in the heat extraction rate and heat recharge dynamic over the short-term and as the system reaches a steady state. This is particularly relevant when analysing and comparing results to pumping test data, that are generally acquired over a short period.

6.5.3 Pump boundary conditions

During the model development process, water abstraction is either simulated as a constant head (Type 1 Dirichlet) corresponding to the top depth of the considered pump or as a hydraulic flow boundary (Type 2 Neumann) equally distributed along the pump polyline, determined so that the drawdown at the pump equals the top depth of the selected pump. For the liquid flow process, setting the pressure to 0 at the pump location permitted the drawdown to equal the pump depth. In the former case, the boundary modifies the flow velocity and the rate of hydraulic drawdown according to the permeability of the seam, whilst the latter case ensures similar hydraulic conditions between all permeability scenarios. Using a constant head boundary at the pump provides better control of the amplitude of the hydraulic drawdown, preventing it from reaching a depth greater than the pump. This is a convenient approach to analyse the effect of hydraulic properties on the thermal footprint independently of the hydraulic drawdown they induce. In transient analysis, it moreover ensures that hydraulic steady-state is reached within the initial time steps of the simulation, as it removes the effects of a progressive decline in the water level. This allows thermal equilibrium to be reached faster and to decrease the computational time. However, this also increases the fluid velocity in the initial time steps, which is more prone to generate instabilities, especially in scenarios where the permeability of the shaft and worked seams is high. This approach therefore appears to be more appropriate in steady-state analysis.

Here, the effects of simulating pumping as a fixed head boundary or as the equivalent source term on the rate of thermal drawdown are compared, considering the properties for the reference model (Fig. 6.1). For each scenario, steady-state simulations are used to determine the drawdown induced by a given pumping rate before simulating the steady-state hydraulic and thermal conditions induced by the corresponding head boundary. Transient simulations are then used to investigate the rate of temperature change for each scenario. Although the time to reach equilibrium is delayed compared to a scenario with a fixed head, using a source-term boundary at the pump ultimately results in similar steady-state temperature distribution in the pumping and monitoring shafts (providing the simulation time is sufficiently long) whilst improving the stability of the simulations (Fig. 6.29). It is therefore important to note that this differential rate of return to equilibrium will lead to discrepancies in the time-dependent relationship between e.g. the seam hydraulic conductivity and the average temperature in the shaft, at a given time step, depending on the boundary condition used (Fig. 6.30).

6.5.4 Model stability

Stability in the model is calculated for elements in the shafts and roadways, where the fluid velocity and the mesh resolution are the highest. In the reference mode, the highest horizontal velocity is observed in the mined coal seams, reaching 5×10^{-4} m/s to the left of the pumping shaft (flow toward the right) and 1×10^{-3} m/s to the right of the pumping shaft (flow toward the right). The highest vertical velocity is observed in the pumping shaft, where it reaches 1×10^{-2} m/s. Based on those values, the Courant, Neumann and Peclet numbers are calculated to determine the stability of the reference model using Eqs. 4.52, 4.53 and 4.54 (Table 6.6).

In the reference model, the volume of water extracted at each time step (86400 s) from each element representing the pump for Q = -0.01 $m^3.s^{-1}$ is 200 times the volume of the element, which is likely to create instabilities in the direct vicinity of the pump in the shaft. Reducing the pumping rate, the shaft permeability, the time step length, or increasing the pump length (i.e. reducing the volume of water extracted at each element) would be ways to reduce the risk of instabilities in the vicinity of the pump. Here, reducing Q to 0.001 $m^3.s^{-1}$, with a reduction of α to 0.2 and increasing the mesh size in the shaft to 2 m would allow reducing the Neumann (diffusion) instability within the high permeability voids, with Co = 4.8, Ne = 0.5 and Pe = 10 in the shaft and Co = 4.3, Ne = 0.9 and Pe = 20 in the seams. Despite the large instabilities created around the pump, the velocities are highly reduced with increasing distance from the abstraction nodes. Those are therefore relatively focused on the pump location and do not affect the reliability of the model at a large scale, where the flow velocities are highly reduced.

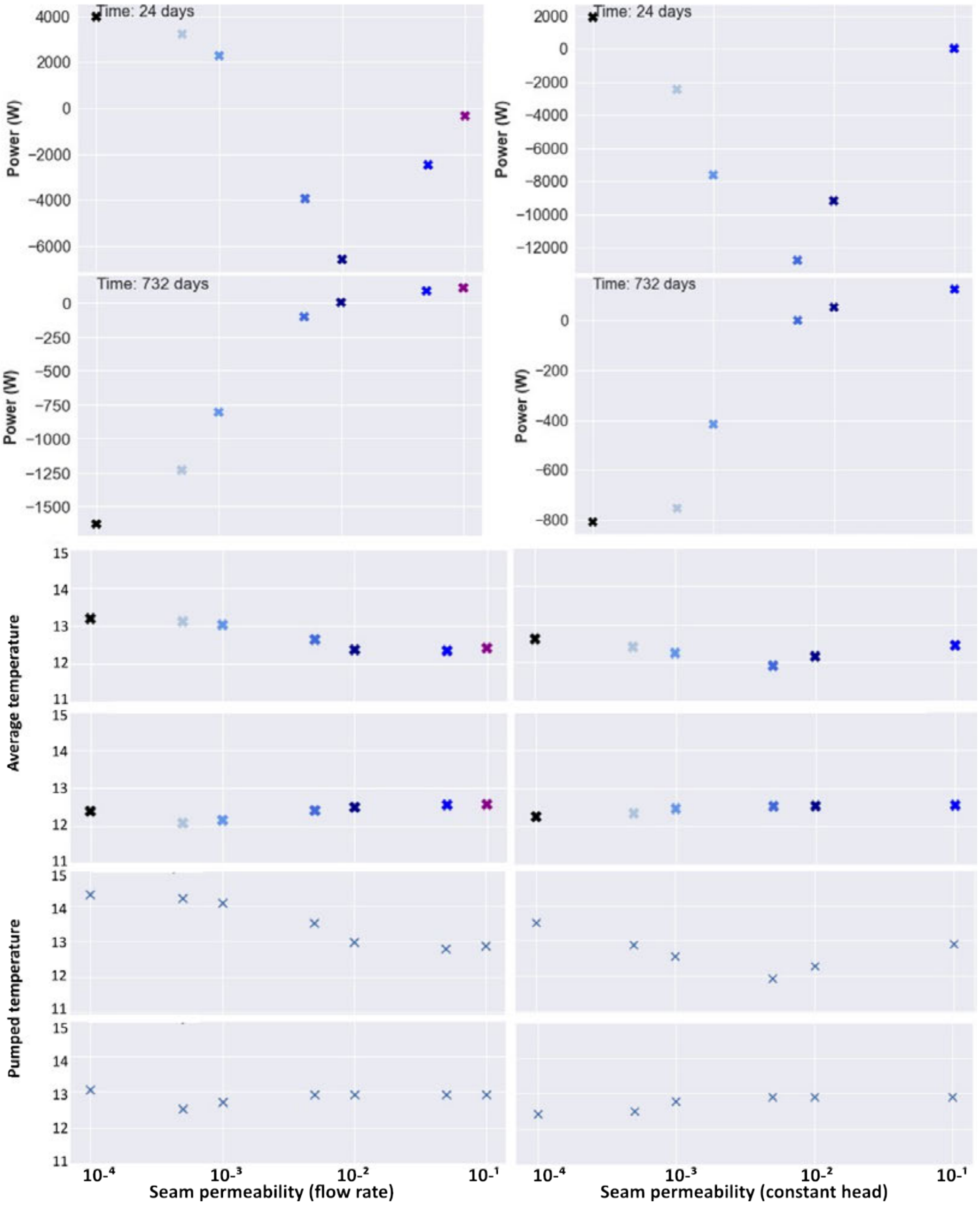

Figure 6.29: Comparison between the average temperature, pumped temperature and power output from the reference scenario resulting from using a) a flow boundary (Q variable) or b) a constant head boundary (H = -52 m) to simulate water abstraction, for different seam hydraulic conductivity (m/s).

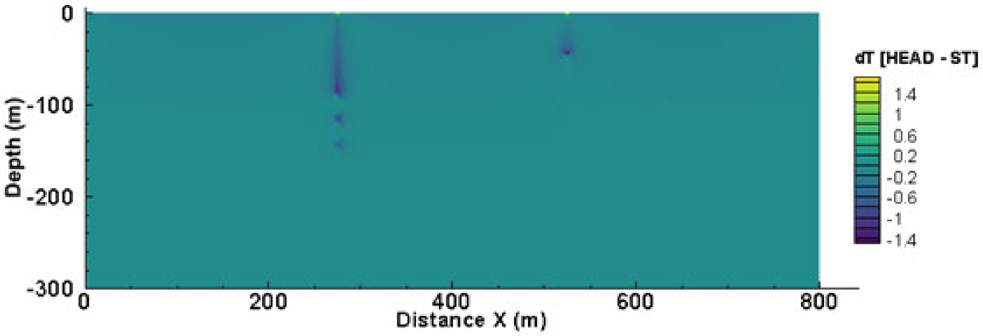

Figure 6.30: Difference in the steady temperature distribution between the two water abstraction simulation approaches (i.e. flow and head boundaries). Results suggest discrepancies of up to ± 1.4℃ concentrated in the top part of the monitoring and pumping shafts.

Parameters	shaft	seams
Thermal Conductivity Fluid	0.60	0.60
Thermal Conductivity Rock	2.4	0.31
Heat Capacity Fluid	4184	4184
Heat Capacity Rock	4184	1380
Density Fluid	1000	1000
Density Rock	1000	1500
Porosity	1	0.25
Thermal Conductivity Media	2.2	0.38
Heat Capacity Media	4184000	2598500
Thermal Diffusion Coefficient	1.4×10^7	1.5×10^7
Groundwater Flow Model		
Element size dx	1.5	1
Darcy Velocity	1.10×10^{-3}	5×10^{-4}
Advective Velocity	1.10×10^{-3}	2×10^{-3}
Dispersion coefficient	0.5	0.5
D (media)	1.43×10^{-7}	1.47×10^{-7}
D dispersion	5×10^{-4}	2.50×10^{-4}
Courant (advective front)	1728	86
Neumann (diffusion)	864	43
Peclet (combined)	2	8

Table 6.6: Stability criteria for the reference horizontal layers porous model, for Q = -0.01 $m^3.s^{-1}$ (see parameters units in Table 6.3).

6.5.5 Processes and coupling effects

In the sensitivity analysis, equations for a saturated media are used to solve for groundwater flow and heat transport, ignoring the effect of coupling. Free convective flow induced by salinity and temperature contrasts has been suggested to be a key process impacting the vertical transport of heat in mines (e.g. Hamm and Bazargan Sabet (2010)). Here, the effect of density and density-viscosity driven flow on the temperature distribution within the shafts are discussed, by implementing internal coupling between hydraulic flow and heat transport. This requires a modification of the process to LIQUID_FLOW (see Chapter 4) and an adjustment of the hydraulic conductivity values K to permeability k, according to Eq. 4.56. The resulting permeability sets equivalent to the two main hydraulic conductivity scenarios presented in this chapter are summarised in Table 6.7.

Parameter	Host rock	Workings	Shafts
k1 (m^2)	1 $\times 10^{-14}$	1 $\times 10^{-9}$	1 $\times 10^{-7}$
S1	1 $\times 10^{-12}$	2 $\times 10^{-11}$	1 $\times 10^{-7}$
k2 (m^2)	1 $\times 10^{-16}$	1 $\times 10^{-11}$	1 $\times 10^{-9}$
S2	1 $\times 10^{-14}$	2 $\times 10^{-13}$	1 $\times 10^{-9}$

Table 6.7: Host rock, seams and shaft permeability (m^2) and storage for the models used in the analysis of coupling.

A LIQUID_FLOW (LF) model is first developed without coupling to verify that the code correctly simulates both hydraulic and thermal processes. Shallow pumping (Q = -0.01 m^3.s^{-1}) from the 2D reference porous model is considered, assuming a slice thickness A = 1 m and the permeability set k1 (Table 6.7), with constant pressure gradients of 9180 Pa/m as lateral boundaries. This aims at reproducing results from the reference scenario P1 (Table 6.5).

Comparison of the results obtained using the GROUNDWATER_FLOW (GF) and LIQUID _FLOW (LF) processes confirm the equivalence between the hydraulic and thermal drawdowns calculated from both approaches. A negligible overestimation of the hydraulic drawdown is depicted in the LF results, which is suggested to be caused by the approximation of the gravitational constant of acceleration and the pressure gradient. The GF process also slightly underestimates the MWT in the mine workings and shafts (same results for deep and shallow pumping) and overestimates the temperature above the mining area between the shafts (Fig. 6.31).

The density and density-viscosity coupling is then implemented following the approach described in Chapter 4. Comparison of the head and temperature distributions after a 2-year steady simulation suggests an increase in the hydraulic drawdown by 6 m in the fully coupled model compared to the uncoupled liquid flow model, although the effect on the steady-state pumped and monitored temperature profiles is negligible (Fig. 6.32).

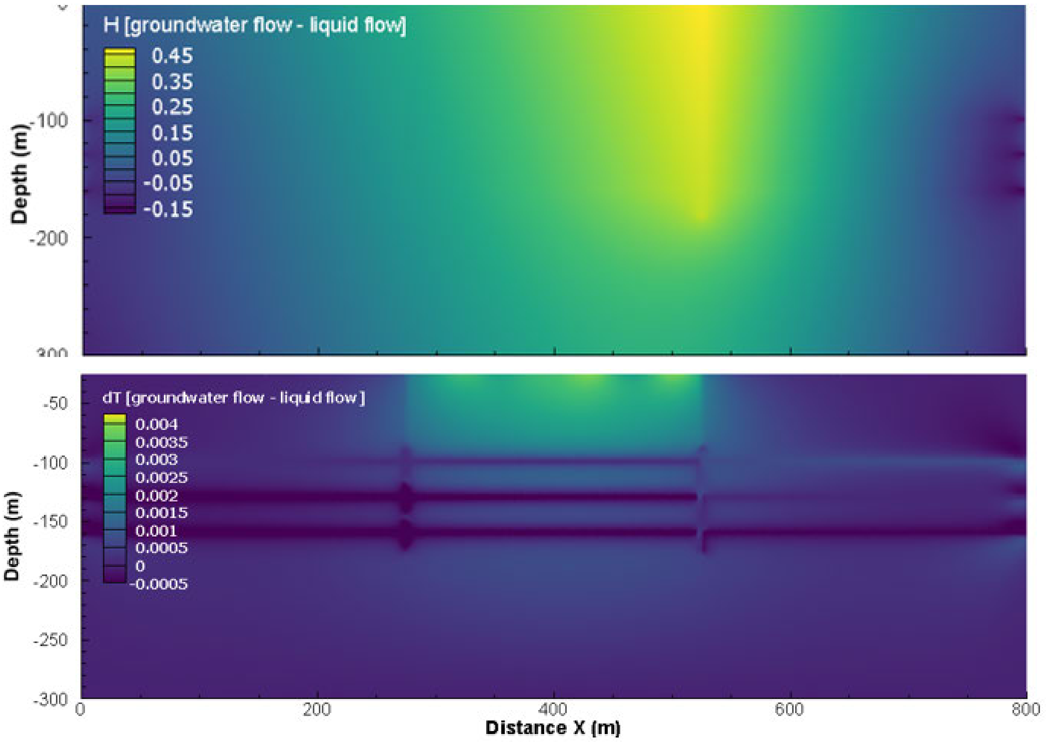

Figure 6.31: Difference between the steady-state hydraulic drawdown H (meters) and the thermal drawdown dT (℃) obtained from the GROUNDWATER_FLOW and equivalent LIQUID_FLOW model after 2 years of pumping, for a deep pumping scenario. The LIQUID_FLOW model underestimates by only 0.45 m the maximum hydraulic drawdown. This difference is partly attributed to approximations of the constant of gravitational acceleration and the water density. However, the difference in the temperature distribution induced by the choice of the process is negligible.

A series of fully coupled steady-state models are moreover developed to investigate the effect of different permeability contrasts on the temperature distribution in shafts. The steady-state pumped profiles are calculated for a series of host rock, mine workings and shaft permeability contrasts, assuming A = 100 m and Q = -1 $m^3.s^{-1}$ (Fig.6.33). Results suggest that the profiles depict dominant convective heat transfers when the shaft permeability k_s is high relative to the host rock k_r and seam permeability k_w. Whilst the MWT along the shaft is lower than the undisturbed geothermal gradient in most scenarios, high permeability contrasts between the host rock/mine workings and the shaft tends to promote warming in the mining area (e.g. $k_s = 1 \times 10^{-2}$ m^2, $k_r = 1 \times 10^{-14}$ m^2). Low host rock permeability relative to the shaft promotes convection above the mining area (e.g. $k_s = 1 \times 10^{-7}$ m^2, $k_r = 1 \times 10^{-16}$ m^2) whilst conduction tends to dominate the heat transfer processes when the shaft permeability decreases (e.g. $k_s < 1 \times 10^{-7}$ m^2). On the contrary, high mine workings permeability ($k_w = 1 \times 10^{-9}$ m^2) promotes cooling along the shaft.

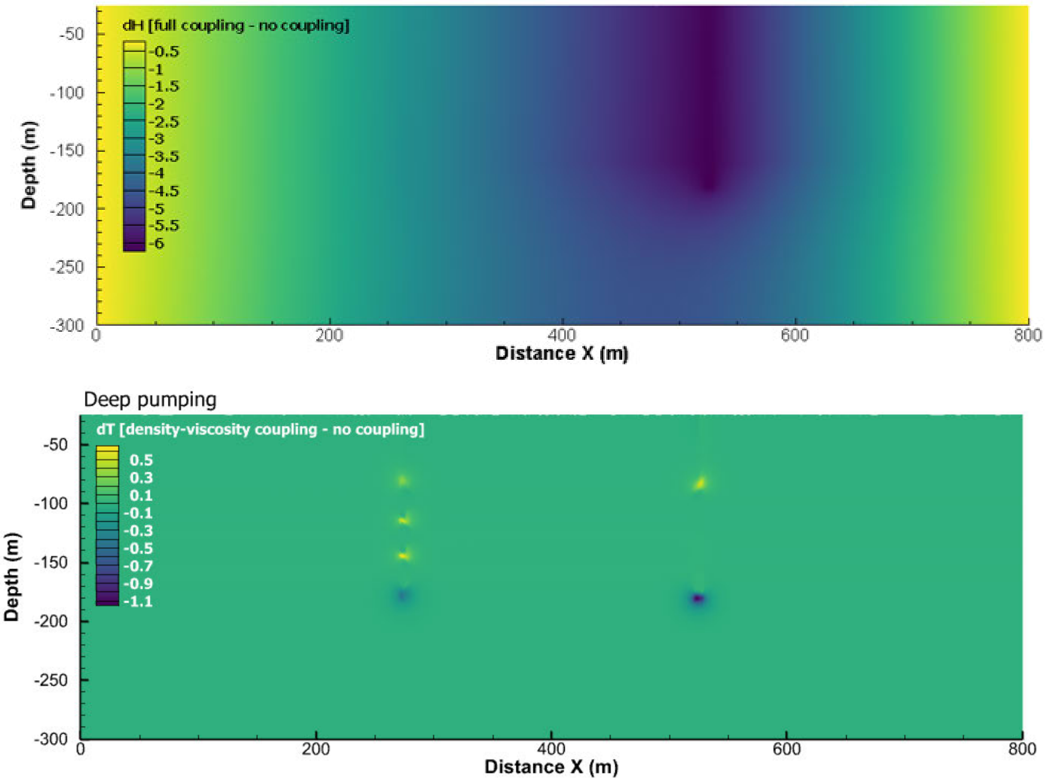

Figure 6.32: Difference in the steady-state head dH (m) and temperature distribution dT obtained from the fully coupled density-viscosity model and the uncoupled LIQUID_FLOW model, after 2 years of pumping for a deep pumping scenario. Neglecting coupling overestimates by up to 6 m the maximum hydraulic drawdown at the pump. However, coupling only induces warming and cooling of up 0.5 ℃ and -1.1 ℃ where the shafts intersect the shallower and the deep seams, respectively.

Those results suggest that the flow induced by temperature-related density-viscosity variations plays a key role in shaping the temperature profiles depending on the permeability contrasts, creating patterns typical of those observed in UK mine shafts (see chapter 3). However, the analysis under pumping conditions performed in this chapter does not allow a full investigation of the extent of 'free' natural convection. The limited impact of coupling on the temperature distribution in the reference model (Fig. 6.32) is here suggested to be caused by the effect of forced convection induced by pumping, which hinders natural density-driven flow in vertical shafts. Further analysis is conducted in chapter 7 to better understand the effect of density-related convective heat transfers, based on a series of steady-state simulations aiming at reproducing the conditions and temperature profiles in unpumped rebounding or discharging mines in the UK.

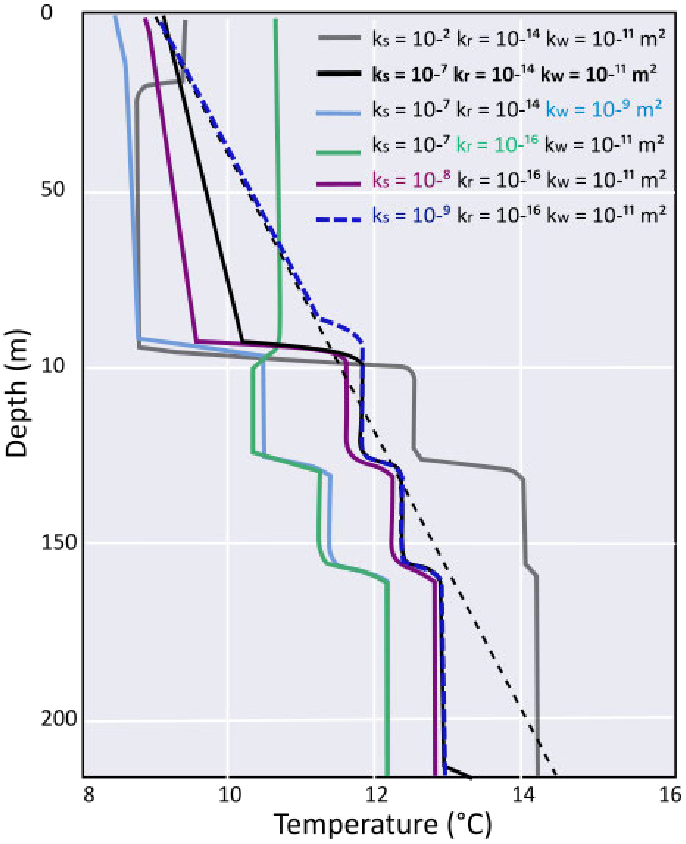

Figure 6.33: Steady-state temperature profiles in the pumping shaft for different permeability contrasts under fully coupled conditions, with k_s, k_r and k_w the permeability of the shaft, host rock and mined seams (m^2), respectively.

6.5.6 Uncertainties and limitations

In this analysis, mine workings are modelled as a goaf panel with a hydraulic conductivity of 1×10^{-4} m/s, which tends to promote porous/linear Darcy flow. However, pumping tests performed at the Glasgow UKGEOS Observatory showed that the hydraulic conductivity of roadways can reach values up to 10^6 m/s, whilst Wolkersdorfer (2008) showed that velocities of up to 1500 m/d can occur in mine workings. This suggests that non-linear or turbulent flow might develop in the open voids (i.e. roadways, shafts), making the use of Darcy's law inadequate. Provided open voids represent the preferential pathways for fluid flow in mines, this also means that in some places, mine water might not be in thermal equilibrium with the surrounding rock and therefore the local geothermal gradient. However, whilst the limited amount of data makes it challenging to verify this hypothesis, implementing numerical solutions for turbulent heat transfers and their interactions with other heat transfer processes, e.g. conductive transfers in porous media, is complex and has yet to be verified in OGS.

6.6 Conclusion

In this chapter, the effect of pumping on the temperature distribution in the shafts and heat output was investigated. Although the temperature ’steps’ observed in UK mine shafts are successfully reproduced by the models, those convection cells are present whether the shafts are pumped, monitored in pumped coalfields or rebounding coalfields. This suggests that in both naturally convective (i.e. groundwater flow in rebounding coalfields) and pumped (i.e. forced convection) systems, equilibrium has not been reached in most coalfields and therefore steady-state analysis might not allow understanding of the true hydraulic and thermal state of mines. Whilst HT coupling and the development of free convection cells might explain these temperature distribution patterns, this could also be caused by the flow and rebound of mine water in dipping layers, which is investigated in chapter 7. Results indicate that:

- Despite the predominance of convective flow and water mixing both in pumped and unpumped shafts, the geothermal gradient controls the temperature of the mine water entering the shaft at the seams insets. In the absence of mixing (i.e. inter-seam connectivity or flow across dipping layers), the average MWT in the mining area will therefore highly depend on the depth interval at which the shaft intersects the mined seams. Depending on the pumping depth, the geothermal gradient also impacts the rate of heat extraction from the mine. Results showed that shallow pumping promotes sustainable heat extraction, interpreted to result from the upflow of deep warm waters. However, deep pumping promotes heat mining from the system, with the higher the geothermal gradient and the higher the heat extraction rate (i.e. larger temperature contrasts between the shallow recharge water and the deep rocks).
- The permeability contrasts between the shaft, mined seams and surrounding host rock play a key role in determining the temperature distribution and heat extraction rate from mines. In particular, the hydraulic conductivity of the mined seams determines the relative contribution of each seam to the water recharge, with deeper seams allowing access to warmer waters.
- The shaft storage and host rock hydraulic conductivity have a large impact on the recovery rate above/outside the mining area
- The rock conductivity, and to a lesser extent the volumetric heat capacity, determine the rate of heat recharge/heat mining, which is in turn controlled by the temperature of recharging water. High rock conductivity under deep pumping scenarios will promote heat mining, but in shallow pumping scenarios, high conductivity will promote heat recharge. Low conductivity can retard heat mining in scenarios with cold surface water recharge, but increase the thermal sink at the pump or in the highly permeable layers.
- In the porous media approach, the shaft volume relative to the surrounding rock mass is of key importance to determine the rate of heat extraction from the porous host rock.

- At equilibrium, the temperature distribution in the monitoring shaft tends to follow the geothermal gradient, indicating the lack of influence of pumping and heat convection from the pumping shaft.

Chapter 7

Thermal footprint of heat extraction from dipping layers: understanding the effect of hydraulic recharge and mixing

7.1 Chapter Overview

In Chapter 6, the temperature profiles in the pumping and monitoring shafts were modelled for a range of rock properties and pumping scenarios assuming horizontal strata with simplified mine geometrical settings. For regularly spaced coal seams, results suggested that the geothermal gradient is one of the key controls on the temperature distribution in shafts, with the gradient being linearly correlated to the observed average mine-water temperature (MWT) in shafts. Both the pumping depth and the permeability contrasts between the mined seams and the surrounding rock were shown to create the greatest disturbances in the temperature profiles during transient analysis. However, additional controlling parameters were suggested to explain the divergences in the measured MWT within a same coalfield, as described in Chapter 3. Those hypothetical factors include:

1. the heterogeneities between mined coal seams. This means that each seam inset will contribute differently to the hydraulic and hence to the convective heat recharge to the shaft.
2. the strata dip. Although assuming horizontal layers is useful for sensitivity analysis, it might not be representative of reality. In the UK, most of the coal-bearing units are folded and tilted. If heat convection is the main heat transport process in the caved zones/roadways, the mixing of waters with different temperatures and across a large depth range might occur within the interconnected galleries before flowing into the shafts, which might add to the mixing of mine waters from different horizons. This

is likely to create more complex temperature patterns compared to a scenario with horizontal layers, and potentially cause a divergence between the data (i.e. observed temperature profiles in UK shafts) and the profiles simulated using numerical models in Chapter 6.

3. the nature/source of the hydraulic recharge. Dipping layers can promote surface recharge via rainfall infiltration along the outcropping mined layers, but also warmer water recharge from greater depths. Depending on the seam permeability and their connectivity to the pumping/monitoring shaft, this might highly impact the observed MWT in the shaft and the heat distribution within different parts of a mine/coalfield.
4. the hydraulic state of the mine. In the UK, a large number of mine-water blocks (MWB) are still rebounding and unpumped, whilst pumping might have been resumed recently in some of them for water level management purposes. This suggests that steady-state conditions might not be reached. In addition, thermal disturbances might remain following long periods of mining activities, dewatering and subsequent water rebound.

In this chapter, the effect of shallow and deep mine water recharge and the flow of water across the geothermal gradient on the mine-water temperature, heat extraction rate, and thermal footprint is assessed. The key characteristics of the temperature profiles in both pumped and rebounding coalfields are identified, for cases with dipping layers (Fig. 7.1). A combination of steady-state and transient simulations is used to simulate dewatering and the subsequent water rebound and heat recovery. The effect of induced fractures above the mined area is ignored in this study and will be investigated further in Chapter 8.

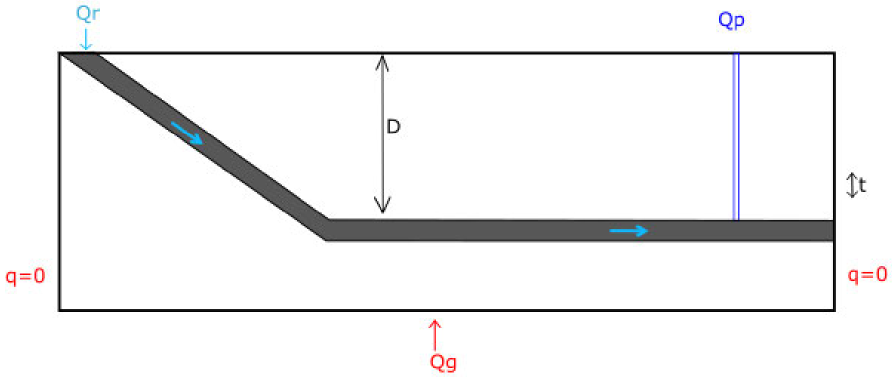

Figure 7.1: Conceptual model geometry and hydraulic recharge for the dipping seams model, with Q_r the hydraulic recharge, Q_p the pumping rate, Q_g the geothermal flux, D and t the seam depth and thickness, respectively, and $q = 0$ representing no-flow boundaries.

Key questions:

- What is the effect of the nature/source of recharging water on the sustainability of heat extraction?
- What is the effect of dipping layers on the extent of mixing and MWT?

- What is the extent of the thermal disturbances induced by mining and dewatering activities in rebounded/flooded collieries?

Hypothesis:

- The source of groundwater recharge determines the sustainability of heat extraction from mine-water reservoirs
- The geothermal gradient in the flooded mine reaches a state of "partial equilibrium" once flooding is completed
- The thermal disturbances caused by past mining activities have a limited effect on the heat potential assessment.

7.2 Introduction

Convective heat flow associated with the circulation of mine water within open voids (e.g. shaft, roadways) and mined layers (i.e. collapsed 'goaf' material) has been considered to dominate the transport of heat in flooded coal mines (Beamish & Busby, 2016). The network of underground galleries, tunnels and shafts left from mining activities indeed tend to form highly transmissive flow pathways that can connect laterally and vertically hydrogeological units previously isolated (P. Younger & Robins, 2002). Those create complex groundwater flow patterns, disturbing the purely diffusive heat flow and therefore the subsurface temperature distribution at the scale of the mine (Beamish & Busby, 2016). Depending on the depth of the seams insets and geothermal gradient (i.e. the inflow temperature), the hydraulic permeability of mining voids was shown to play a major role in shaping the temperature profiles in pumping shafts during transient analysis (Chapter 6). In addition to the seam heterogeneity, other factors were however suggested to explain the discrepancies between the temperature profiles observed in shafts at the scale of a mine-water block/coalfield (Chapter 3), and between the predicted and observed MWT in mine shafts (Chapter 6). This includes the effect of the hydraulic state of the mine, the nature of hydraulic recharge, and the mixing of mine waters with different temperatures, which might be caused by the geometry of the seams (e.g. dipping strata) or the presence of connections between mine workings (e.g. staple shafts).

Understanding the contribution of convective heat flow relative to conductive heat transfers is essential when assessing the long-term heat potential of mines. In particular, characterising the rate of heat transfer between the advective mine water and the surrounding host rock can provide a better understanding of the processes of heat mining/heat recovery and of the rate at which mine water can be pumped without depleting the system in heat. Furthermore, determining the time required for the rebounding mine water to equilibrate with the surrounding rock following the closure of a mine appears essential to accurately assess its heat potential before the start of geothermal operations.

Previous studies have used either numerical (P. Guo et al., 2018; Hamm & Bazargan Sabet, 2010; Raymond & Therrien, 2008; Renz et al., 2009) or analytical models (Ferket et al., 2011) to determine the initial heat capacity and the sustainability of heat extraction from flooded coal mines. Those generally assume the undisturbed geothermal gradient to be representative of the thermal state of the mine, with the mine water being in thermal equilibrium with the surrounding host rock (see Chapter 3). An analysis of temperature data collected in UK mines by Farr et al. (2020) showed that mine water generally re-equilibrates with the surrounding rock temperature. Although Farr et al. (2020) suggests that "older in situ strata temperature data could, with caution, be used to predict mean post-closure modern flooded temperatures in a coal mine", it is important to understand the extent of the disturbances caused by mining activities on the rock temperature. Most of the in-situ rock strata temperatures used to represent undisturbed conditions were indeed measured in active collieries, where it might be impacted by e.g. air conditioning, exothermic reactions or cold water infiltration (Farr et al., 2020).

A few authors have already suggested the existence of quasi-permanent rock thermal disturbances resulting from extensive periods of mining and dewatering Malolepszy (2003). During mining activities, water is pumped to allow access to deep parts of the mine and air ventilation is installed to guarantee the removal of gas and dust in the underground mine, minimise the stresses on the equipment and ensure safe conditions for the miners (R. Anderson & De Souza, 2017; Majolepszy, 1998). The forced circulation of water within the large interconnected mining voids combined with the inflow of cold air in the pumped sections of the mine was suggested to decrease the temperature in the galleries and disturb the virgin rock temperature in the long term (Tammemagi & Wheildon, 1974). Malolepszy (2003) showed based on rock temperature measurements taken during mining in the Nowa Ruda mine in Poland that about 10 years would be required for the rock mass surrounding the galleries to heat up back to its initial temperature following a 200-year-long mining period with a 8℃ cooling and a subsequent flooding period of 5 years. In the UK, a large range of MWT observed for recent borehole data (BGS UKGC) compared to historic in situ temperatures was interpreted as the effect of boreholes having not reached thermal equilibrium at the time of measurement, or being located either within or outside mining areas (Farr et al., 2020). The timescale between water rebound and thermal recovery is to date not well documented, and it is essential to understand how a slower rate of water rebound in some coalfields (e.g. South Yorkshire, where water is still rising) might affect the return to thermal equilibrium. A refined analysis at the scale of the coalfield or MWB was deemed necessary to characterise the temperature distribution within mines and understand if discrepancies between the MWT profiles in flooded mine shafts are due to a potential slow return to equilibrium (Farr et al., 2020).

This chapter focuses on the effects of the nature and rate of hydraulic recharge on the temperature distribution and heat extraction rate from mine-water reservoirs. For each scenario, the temperature profiles measured in the pumping and monitoring shafts for a mine with dipping strata are compared. The heat extraction rate from the different mining zones (i.e. goaf, mining area, host rock) is moreover calculated to get an insight into the long-term dynamic of heat recovery and the relative contribution of the natural heat flow and convective heat recharge, depending on the source and rate of hydraulic recharge. In addition, a preliminary assessment of the potential long-term disturbances caused by extended periods of dewatering during mining, followed by water rebound and heat recovery is made. In other words, the discrepancies between the undisturbed pre-mining temperature distribution and the post-recovery host rock temperature are evaluated to quantify the errors in the initial heat potential assessment induced by an uncorrected geothermal gradient.

7.3 Methods

7.3.1 Model set-up

The model represents a mine of simple geometry consisting of four porous materials: the host rock, the shafts, a soil layer, and the caved zone (i.e. the mined seams or galleries). The mesh is composed of 8,693 triangular elements ranging from 2 to 12 m in size, and 44,677 nodes. The 3 coal seams are distributed at regular depth intervals of 30 m and are dipping toward the right boundary at an angle of about 10° (Fig. 7.2). The two 140 m and 170 m deep shafts are located at x = 675 m and x = 900 m from the left boundary and are intersected by the 3 coal seams. Pumps 1 and 2 are located above (z = 50 mbgl) and below (z = 160 mbgl) the mined area in the downdip shaft 2 (x = 900 m). Pumps 3 and 4 are located in the updip shaft 1 (x = 675 m) at z = 60 mbgl and z = 130 mbgl depth, respectively. All mined seams reach the surface on the top left part of the model and terminate on the right boundary. The top right boundary is assumed to represent a confining impermeable boundary (no flow). When permitted, rainfall recharge is set at the unconfined section of the mine-water reservoir (top left) where a soil layer of lower permeability 1×10^{-4} m/s is defined to reduce the infiltration rate and downflow of cold water into the high-permeability mine workings.

The properties for each material group, chosen based on Chapter 6, are provided in Table. 7.1. A detailed description of the initial conditions, boundary conditions and time control can also be found in Chapter 6.

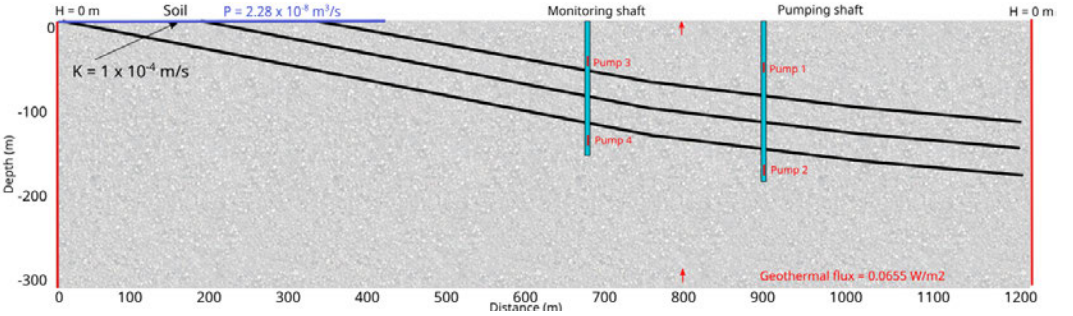

Figure 7.2: Dipping model sketch showing the different materials and boundary conditions for the reference scenario. Pumps 1, 2, 3 and 4 are located at depths of 50 mbgl, 160 mbgl, 60 mbgl and 130 mbgl, respectively.

Parameter	Host rock	Seams	Shafts	Soil	Water
Slice thickness (m)	1	1	0.06	1	n
Hydraulic conductivity (m/s)	1×10^{-7}	1×10^{-2}	1	1×10^{-4}	n
Storage	1×10^{-5}	2×10^{-4}	1	1×10^{-4}	n
Porosity (%)	10	25	100	15	n
Heat conductivity (W/(m℃))	2.4	0.31	0.63	2.4	0.63
Heat capacity (J/(kg℃))	860	1380	4184	860	4184
Density (kg/m^{-3})	2550	1500	2550	1900	1000
Kinematic viscosity (Pa.s)	n/a	n/a	n/a	n/a	1×10^{-3}

Table 7.1: Hydraulic and thermal properties for the dipping layers mine model (no coupling).

7.3.2 Hydraulic recharge and heat extraction rate

The steady-state temperature profiles and heat extraction rate in the pumping and monitoring shafts are calculated for 2-year-long simulations representing a series of pumping and hydraulic recharge scenarios. Constant head boundaries equal to the top pump depths are first used to reproduce the drawdown induced by pumping from pumps 1, 2, 3 and 4, assuming constant lateral head boundaries H = 0 m that allow for hydraulic recharge from both the surface and the deep end of the seams. Different boundary conditions, summarised in Table 7.2 are then employed to investigate the effect of the nature of hydraulic recharge on the temperature profiles, thermal footprint and rate of heat extraction over 2 years of pumping at a rate of -0.001 m^3/s from pump 1 (30 mbgl). Those include a combination of constant head boundaries (i.e. Type-1 Dirichlet) and flow boundaries (Type-2 Neumann). Rainfall recharge is modelled as a Neumann boundary condition, with a flow of 3.4786×10^{-8} m^3/s distributed along the top-left part of the surface boundary, which represents the unconfined section of the saturated mine-water reservoir. This value corresponds to the yearly average precipitations in the UK (1100 mm/yr) calculated over the 2000-2020 period (source: Met Office). Due to unstable results, the effect of water drainage from the overlying semi-confining aquifer using a Cauchy (Type-3) boundary is not presented in this chapter but implemented in Chapter 8.

	Left	Right	Surf. unconfined	Surf. confined	Comment
a	H = 0 m	3×10^{-8} m^3/s	NF	NF	
b	H = 0 m	3×10^{-8} m^3/s	3.4786×10^{-8} m^3/s	NF	Rainfall
c	H = 0 m	6×10^{-8} m^3/s	NF	NF	
d	H = 0 m	1.25×10^{-8} m^3/s	NF	NF	
e	H = 0 m	H = -10 m	NF	NF	
f	H = 0 m	H = 0 m	NF	NF	Ref. scenario
g	H = 0 m	H = 10 m	NF	NF	
h	H = 0 m	H = 20 m	NF	NF	
i	H = 0 m	NF	NF	NF	Shallow recharge
j	NF	H = 0 m	NF	NF	Deep recharge
k	NF	H = 0 m	3.4786×10^{-8} m^3/s	NF	Rainfall

Table 7.2: Hydraulic recharge scenarios for the dipping seam model (no coupling). H : head boundary (m), NF: No flow boundary.

7.3.3 Dewatering and heat recovery rate

A combination of steady-state and transient simulations is used to investigate the extent of the thermal disturbances induced by extensive dewatering periods, assuming pumping from the deep shaft 2, following water rebound. After calculating the steady-state head and temperature distribution for a 50-year mining/dewatering period, water rebound is simulated over a 50-year-long transient simulation period, allowing either shallow or deep recharge from the left or right boundary (Q = 3×10^{-8} m^3/s). For each scenario, the time required for the mine-water and rock temperature to return to a quasi-equilibrium is assessed, considering a threshold of relative temperature change between time steps of 0.1 ℃. The rock-fluid equilibrium state is determined by comparing the temperature in the shaft and galleries to the surrounding rock mass temperature at different recovery stages and fluid velocities (i.e.assuming linear Darcy flow in porous media). The relative difference in the heat content between the pre-pumping and post-recovery state of the mine reservoir is finally used to calculate the percentage error in assessing the initial heat potential when neglecting the mining history.

7.4 Results

7.4.1 Effect of pumping location

The temperature profiles induced by pumping above and below the mining area in both the updip and downdip shafts are first determined for a scenario with a constant head (H = 0 m) at the lateral boundaries (Fig. 7.3). In the early stage of pumping, shallow pumping (i.e. PUMP 1 (P1) for downdip shaft 2 and PUMP 3 (P3) for updip shaft 1) and deep pumping (i.e. PUMP 2 (P2) for downdip shaft 2 and PUMP 4 (P4) for updip shaft 1) respectively lead to general warming and cooling in the pumping shaft, producing temperature profiles similar to those observed in the horizontal layers model (see chapter. 6). When water is pumped from P3 and P4 (updip shaft 1), the temperature in the downdip monitoring shaft 2 depicts clear steps, with the temperature at each inset corresponding to the temperature predicted by the undisturbed geothermal gradient. On the contrary, when water is pumped from P1 and P2 (downdip shaft 2), the temperature between each seam in the updip monitoring shaft tends to follow a quasi-linear trend that suggests the reduced effect of convective flow.

After 2 years, the pumped temperature profiles depict general warming independently of the pumping shaft location, suggesting the predominance of deep warm water recharge (i.e. from the right boundary). In the shallow P1 (shaft 2) and P3 (shaft 1) pumped temperature profiles, the temperature at the deepest seam corresponds to the temperature predicted by the geothermal gradient at that depth. In the deep P2 (shaft 2) pumped profiles, this warming is more moderate, with the average temperature in the mining area returning towards the average temperature inferred from the undisturbed geothermal gradient (i.e. same temperature at the mid-seam). On the contrary, the deep P4 (shaft 1) profile depicts exacerbated warming. In the monitoring shafts, the temperature profiles highly depend on the relative location of the pumping shaft and the pumping depth. For downdip pumping (shaft 2), a general cooling is observed in the updip monitoring shaft 1, suggesting the predominance of shallow cold water recharge to this shaft. Pumping from the updip shaft 1 alternatively allows the temperature at the seams insets in the deep monitoring shaft 2 to re-equilibrate with the undisturbed geothermal gradient. Slight upward temperature shifts are visible in the mining area in shaft 2 after 2 years when shallow pumping from the updip shaft is implemented (profile P3).

The transient change in temperature over the 2 years of pumping (Fig. 7.4) confirms that pumping from the downdip shaft progressively reduces the average temperature in the updip shaft. On the contrary, pumping from the updip shaft allows both the pumping and downdip monitoring shafts to reach a quasi-steady temperature equal to or greater than the initial geothermal gradient, in accordance with the profiles displayed in Fig. 7.3.

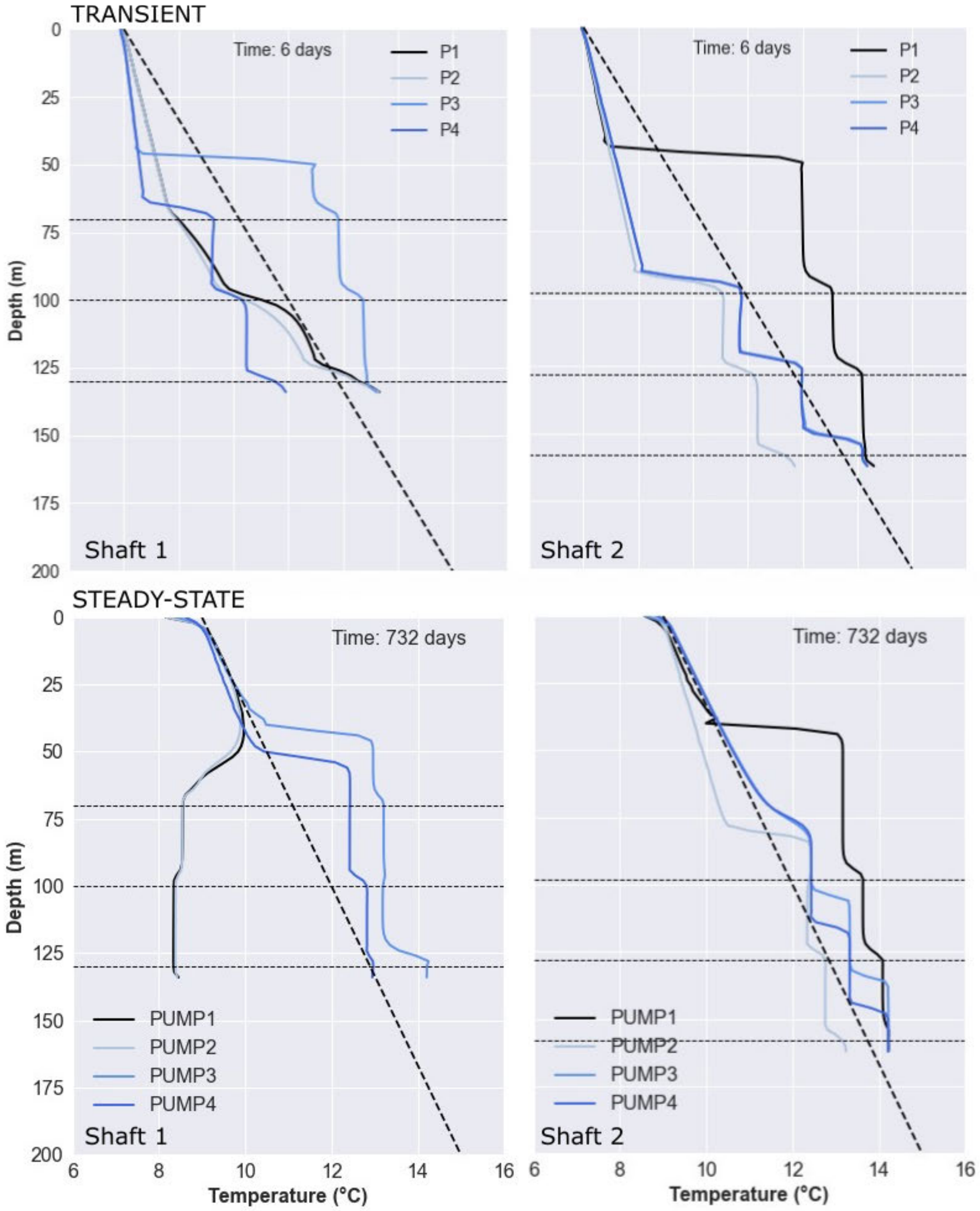

Figure 7.3: Transient temperature profiles in the pumping and monitoring shafts calculated after 6 days of pumping (upper plots) and steady-state profiles calculated after 2 years of pumping (lower plots), for different pumping depths. Pumps 1 and 2 are located in the downdip shaft 2 (profiles P3 and P4 there represent the monitoring profiles), and pumps 3 and 4 are located in the updip shaft 1 (profiles P1 and P2 there represent the monitoring profiles). Hydraulic recharge is permitted from both lateral boundaries via constant heads of 0 m. The differences between each profile are attributed to the effect of the pumping depth and the predominance of shallow (cold) recharge or deep (warm) recharge (see main text).

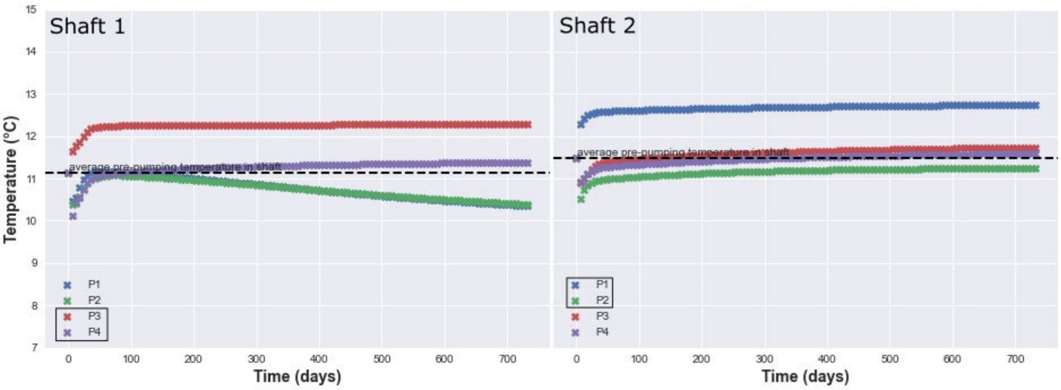

Figure 7.4: Yearly average temperature in shafts 1 (updip) and 2 (downdip) for each pumping depth scenario. Pumps 1 and 2 are located above and below the mining area in the deep shaft 2 (50 mbgl and 160 mbgl, respectively), and pumps 3 and 4 are located above and below the mining area in the updip shaft 1 (60 mbgl and 130 mbgl, respectively).

To better understand the cooling/warming effects of pumping, we calculate the thermal footprint induced by pumping after 2 years of pumping for each scenario. The velocity vectors (Fig. 7.5) confirm that for all scenarios, most of the flow occurs from the right boundary within the highly permeable galleries, promoting deep warm water recharge from adjacent systems/reservoirs towards the pumping shaft. When pumping is implemented in the updip shaft, this leads to general warming in both the pumping and monitoring shafts. On the contrary, pumping from the downdip shaft tends to drag colder water from the surface through the updip monitoring shaft 1. This flow is promoted within the deepest seam that outcrops near the left recharge boundary (Fig. 7.5). The flow in this shaft is however limited due to the lack of surface recharge (i.e. no rainfall). As a result, the temperature profile displays a limited 'convective cell' between the seams in the early stage of pumping, and a large cooling after 2 years of pumping (Figs. 7.3 and 7.4).

7.4.2 Effect of the nature of hydraulic recharge

Steady-state temperature profiles have been calculated to understand the effect of the nature of the hydraulic recharge on the temperature distribution in mine shafts, accounting for the depth of pumping (see Table. 7.2).

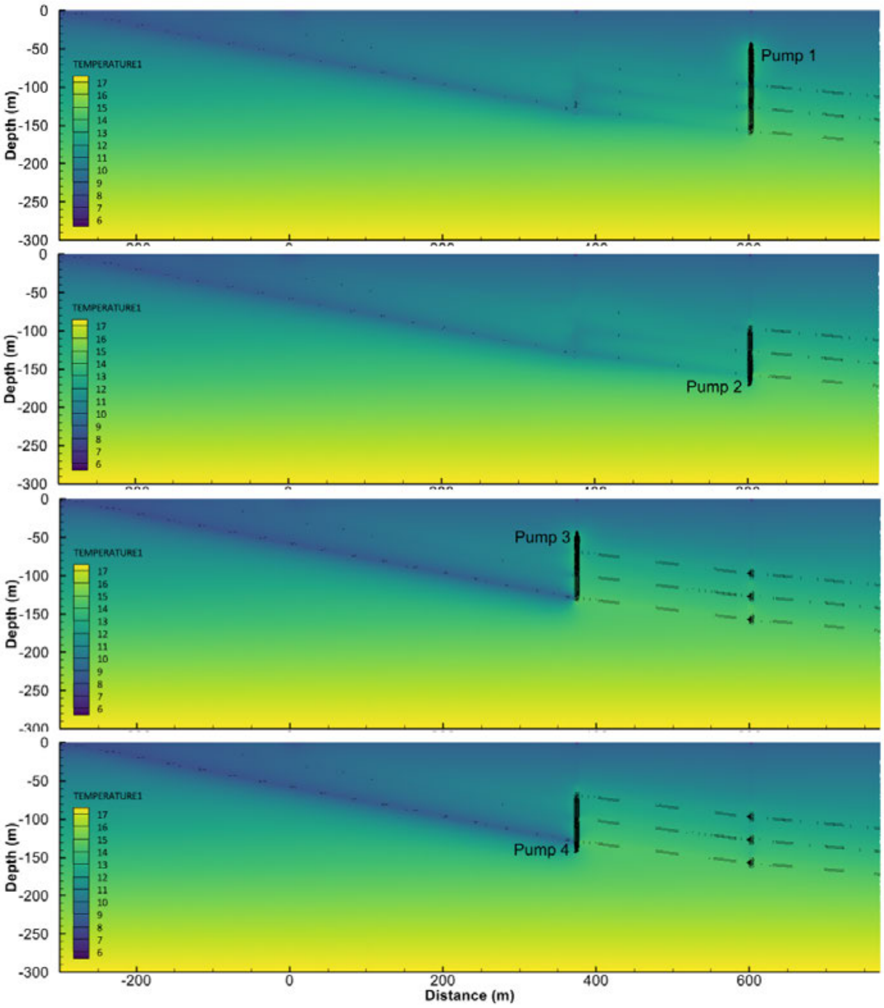

Figure 7.5: Temperature distribution after 2 years of pumping induced by pumping from pumps 1 and 2 (shaft 2) and pumps 3 and 4 (shaft 1).

Shallow pumping (Fig. 7.6) and deep pumping (Fig. 7.7) from the downdip shaft 2 both create two typical temperature distribution patterns, linked to the source of recharge water. As warm water recharge is permitted via a constant head value on the right model boundary, temperature 'steps' are created at each seam inset in shaft 2, similarly to the ones observed in the horizontal layers model (Chapter 6). In the shallow pumping scenario (P1, Fig. 7.6), the temperature profiles depict a general warming, with the temperature at each seam inset being slightly higher than the temperature predicted by the undisturbed geothermal gradient.

In the deep pumping scenario (P2, Fig. 7.7), this warming effect is less pronounced, with the average MWT in the mining area re-equilibrating with the temperature predicted by the undisturbed geothermal gradient at the mid seam. Alternatively, setting a flow boundary on the right and/or rainfall recharge at the top left boundary leads to a general cooling in the mining area independently of the pumping depth.

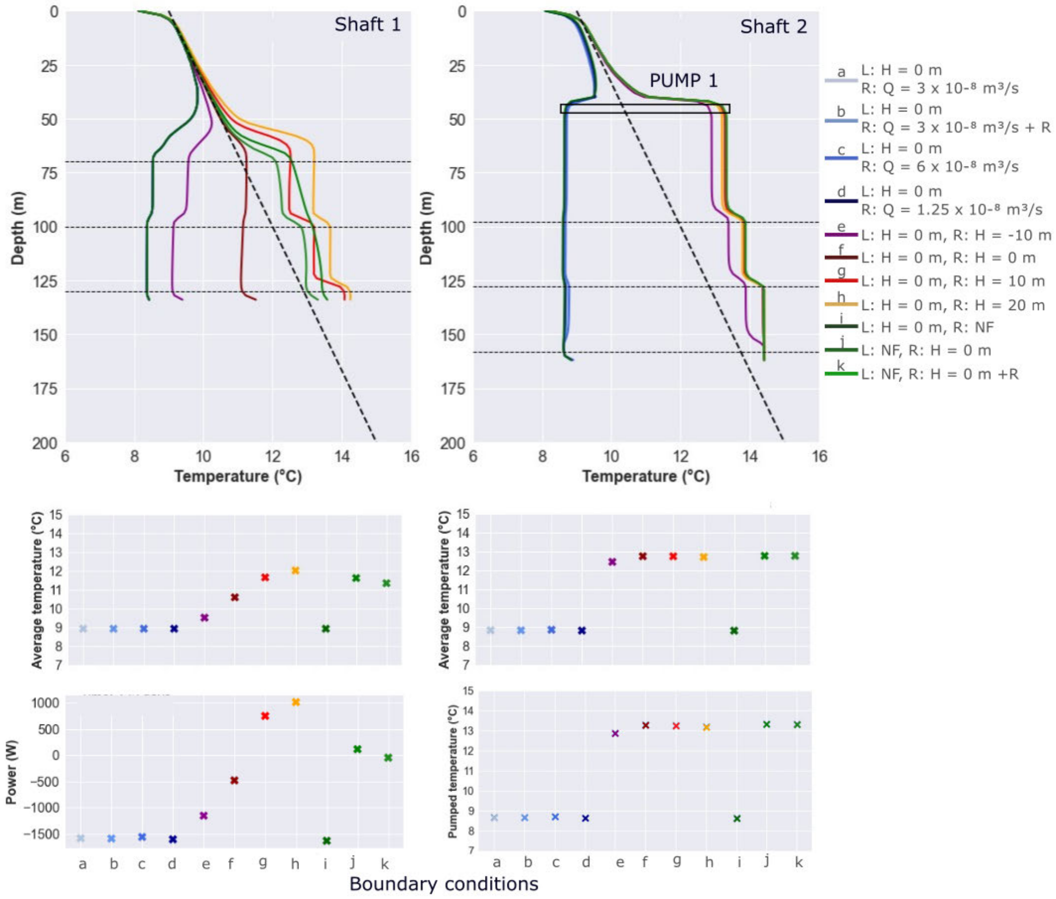

Figure 7.6: Steady-state temperature profiles in the pumping and monitoring shafts induced by pumping from pump 1 for different hydraulic recharge scenarios. The lower plots indicate the average temperature in each shaft, the power output and the pumped temperature for each scenario.

A larger variability in the temperature distribution is observed in the monitoring shaft 1 depending on the nature of recharge, which correlates well with the calculated total power output (Figs. 7.6 and 7.7). The larger the hydraulic gradient/flow from the right boundary, the greater the deep warm water recharge and the higher the average temperature in the updip shaft and the heat recharge to the system. Recharge from the left boundary alternatively promotes the inflow of colder water and therefore heat mining, with a reversed temperature gradient being observed in the monitoring shaft (i.e. lower temperature at the shaft bottom). However, the absence of deep recharge promotes cooling and heat mining to a greater extent than when allowing for rainfall recharge. This might be explained by the low topsoil permeability relative to the seam permeability.

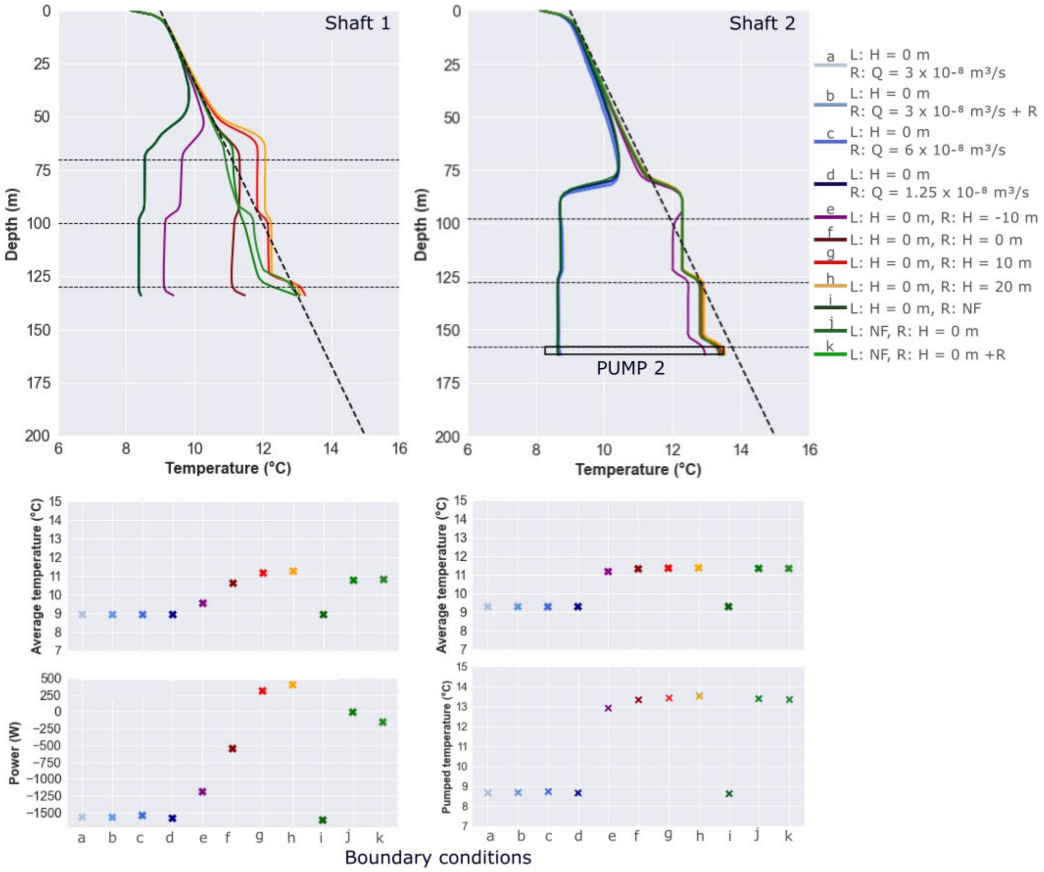

Figure 7.7: Steady-state temperature profiles in the pumping and monitoring shafts induced by pumping from pump 2 for different hydraulic recharge scenarios. The lower plots indicate the average temperature in each shaft, the power output and the pumped temperature for each scenario.

Similarly, the pumped temperature profiles generated from shallow pumping in the updip shaft 1 (P3, Fig. 7.8) are dependent on the nature of hydraulic recharge. Whilst a general cooling is depicted under the absence of deep recharge (i.e. no flow from the right boundary), the higher the gradient/recharge rate from the right boundary, the higher the average temperature in the mining area. A slight cooling is however generated in the lowest part of the pumping shaft when the regional flow is directed to the right. This deep cooling is interpreted to result from the enhanced hydraulic flow of cold water in the deepest seam relative to the two uppermost seams due to its closeness to the left head boundary at the surface, as noted earlier.

Deep pumping from the updip shaft 1 is characterised by two main temperature distribution patterns displaying clear steps at each inset (P4, Fig. 7.9). When deep recharge is dominant, the profiles depict a warming trend, with the temperature at the deep inset being equal to the temperature predicted by the undisturbed geothermal gradient. When shallow recharge is dominant (i.e. reduced flow from the right boundary, hydraulic gradient to the right or rainfall recharge), reversed steps are created, leading to cooler temperatures at the shaft bottom.

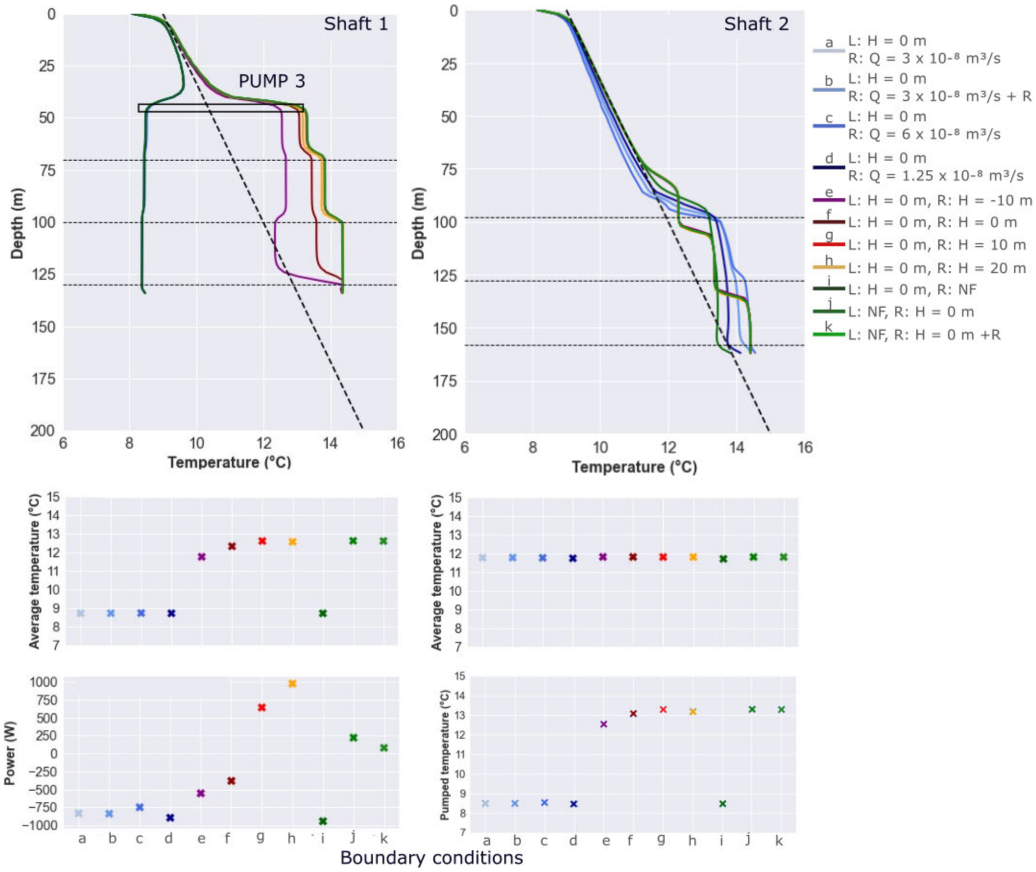

Figure 7.8: Steady-state temperature profiles in the pumping and monitoring shafts induced by pumping from pump 3 for different hydraulic recharge scenarios. The lower plots indicate the average temperature in each shaft, the power output and pumped temperature for each scenario.

In the deep monitoring shaft 2, the temperature profiles depict a slight warming for most hydraulic recharge scenarios. Whilst clear temperature steps are observed at each seam inset in scenarios with deep recharge, independently of the pumping depth, a reduction in the recharge contribution from the right boundary erases those temperature shifts. When P3 is active (shallow pumping from shaft 1), this is expressed by a relatively constant temperature distribution in the mining area (Fig. 7.8). When P4 is active (deep pumping from shaft 1), this reduced convection of heat from depth results in a return of the monitoring temperature profiles towards the undisturbed geothermal gradient (Fig. 7.9). As observed earlier, heat mining is largest for scenarios with no or limited deep recharge (HR = flow or no flow), but remains lower than in scenarios with downdip pumping (i.e. from P1 and P2).

Overall, the occurrence of deep warm water recharge is suggested to strongly slow down the cooling in the mining area, whilst allowing for shallow or surface water recharge is shown to promote cooling in the mining area (Fig. 7.10). Transient analysis results based on a series of different hydraulic gradients (i.e. head varying from - 10 m to 30 m on the right boundary)

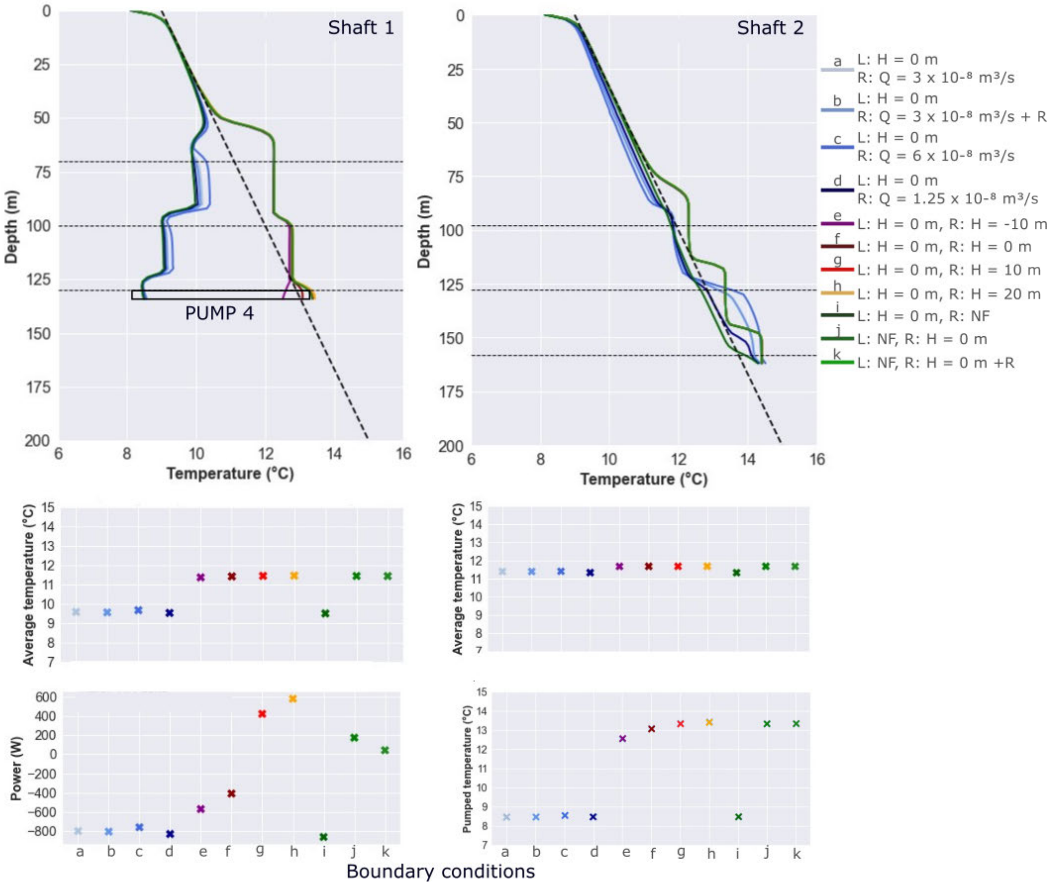

Figure 7.9: Steady-state temperature profiles in the pumping and monitoring shafts induced by pumping from pump 4 for different hydraulic recharge scenarios. The lower plots indicate the average temperature in each shaft, the power output and pumped temperature for each scenario.

moreover confirmed that the rate of hydraulic recharge due to varying regional flow velocity tends to control the temperature distribution in the shafts and the rate of return to equilibrium (see Appendix A.6). Comparison of the average temperature, pumped temperature and power output for different regional hydraulic gradients however suggests that there is a regional groundwater flow velocity at which the heat exchanges between the advecting mine-water and the rock is optimal (see Appendix A.6.1), i.e. H = 20 m. Further work would be required to understand the link between the infiltration rate of rainfall recharge, the water residence time and the heat recovery rate in mine-water reservoirs.

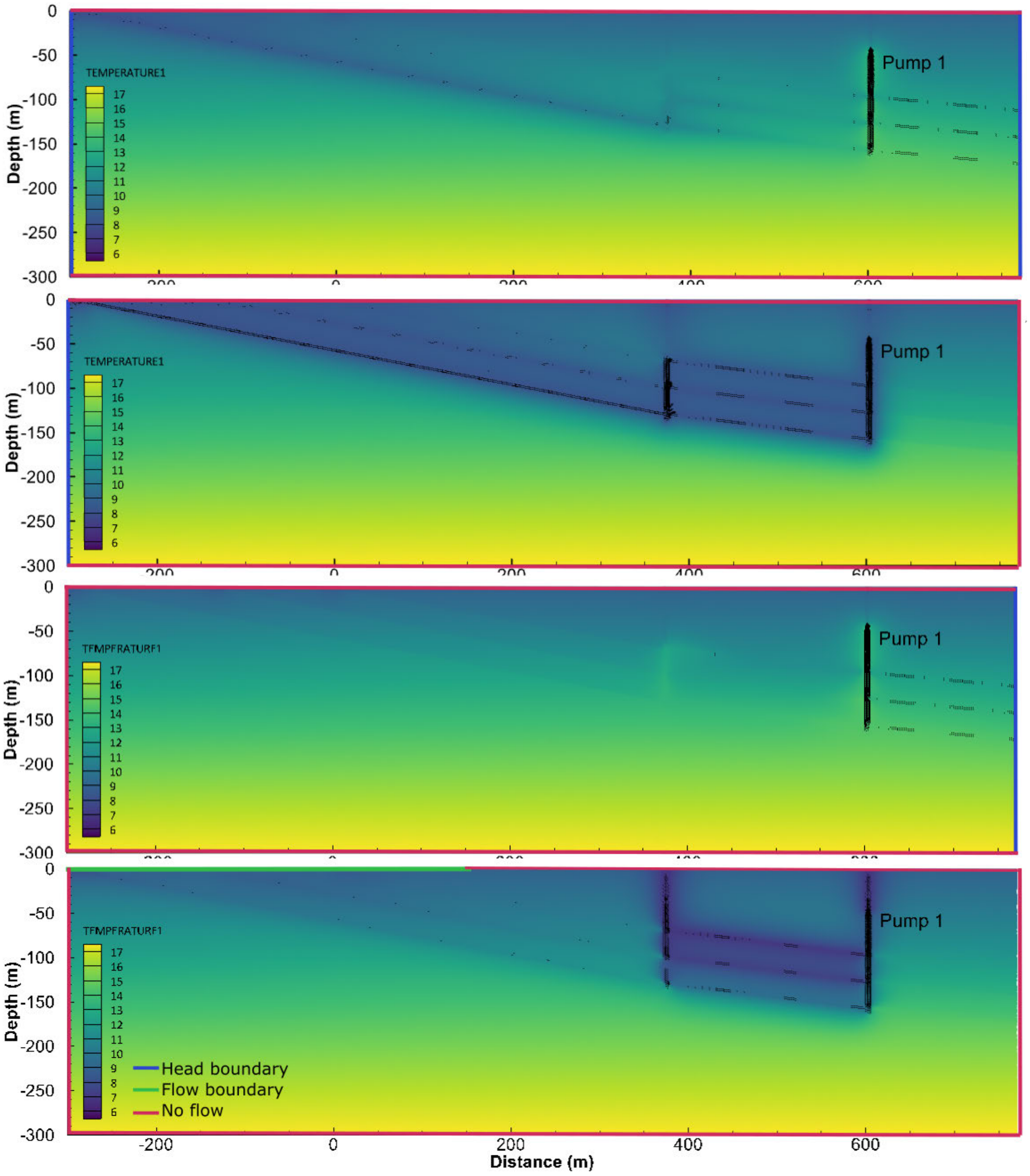

Figure 7.10: Temperature footprint induced by different sources of hydraulic recharge for shallow pumping from the downdip shaft (P1). This include from top to bottom: forced lateral hydraulic recharge, b) forced recharge from the left boundary (or shallow recharge), c) forced recharge from the right boundary (or deep recharge) and d) rainfall recharge.

7.4.3 Seam inset contribution

The previous scenarios considered that the mined seams have a similar permeability and therefore equally contribute to the flow to the shaft. As described in Chapter 6, the higher the permeability, the quicker the profiles return to equilibrium in the pumping shaft and the better the convective flow to the monitoring shaft. A preliminary analysis of the effect of heterogeneous seam permeabilities for the dipping seams model is available in Appendix

A.6.2. Here, the interest is to understand further the effect of various relative contributions from the mined seams to the hydraulic recharge on the observed MWT in the mining area. Shallow pumping (i.e. P1 and P3), implemented as a constant head boundary equal to the pump top depth, is used to understand the temperature distribution in shafts currently pumped for water management purposes (generally implemented at shallow depth to reduce the pumping costs). The effect of deep pumping is presented in more detail in the next section (i.e. deep dewatering scenarios).

Results show that the relative permeability of the seams intersected by the shaft controls the amplitude of the temperature shifts at each inset, and creates complex patterns depending on the equilibrium state of the system (Figs. 7.11 and 7.12). In general, the lower the seam permeability, the larger the thermal drawdown in the early stage of pumping. This is mostly observable in monitoring shaft 1 when P1 in shaft 2 operates. On the contrary, higher seam permeability creates better hydraulic connections between the shafts, which promotes deep warm recharge and therefore a faster return to thermal equilibrium (Fig. 7.11). The effect of seam permeability is more limited when P3 in shaft 1 operates, with only slight upward shifts in the temperature steps observed in shaft 2 as the seam permeability increases

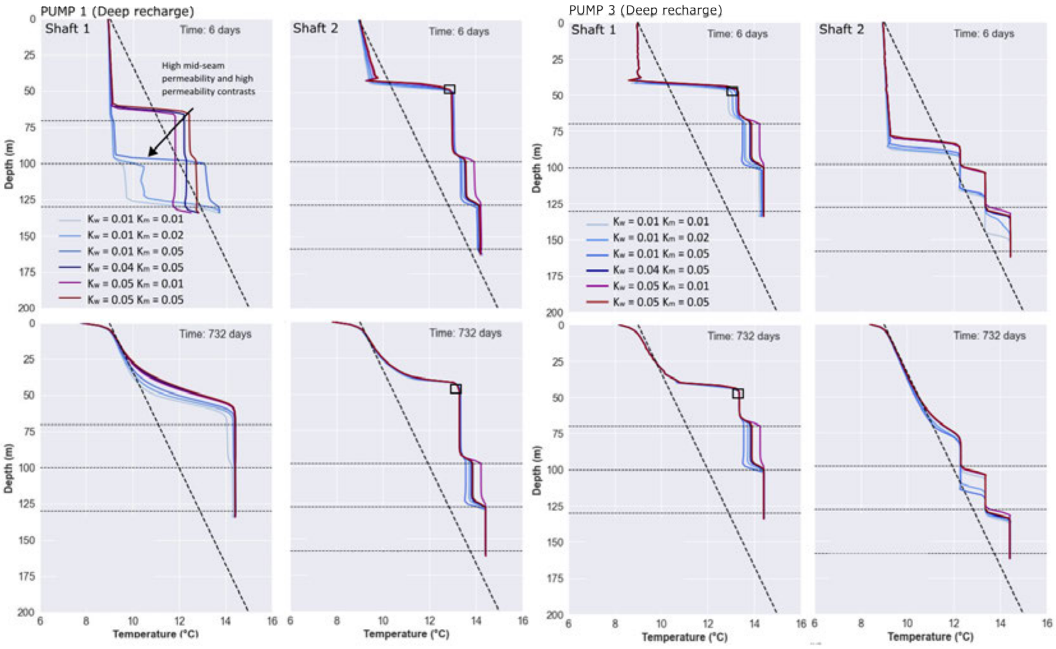

Figure 7.11: Temperature profiles in the pumping and monitoring shafts after 6 and 732 days of shallow pumping from pump 1 (left panel) and pump 3 (right panel) for different seam permeability contrasts, assuming deep water recharge. K_m and K_w represent the hydraulic conductivity (m/s) of the mid-seam and of the upper/lower mine workings, respectively. The large temperature shift in shaft 1 where K_w = 0.01 m/s and K_m = 0.05 m/s suggests that the high mid-seam permeability promotes thermal recovery in the early stage of pumping.

In scenarios where shallow surface recharge is dominant (Fig. 7.12), the dipping seams model exacerbates cooling in the mining area in the long term. Although warming is observed in the initial days of pumping in the pumping shaft, this general cooling trend is observed in the long term in both the pumping and monitoring shafts, especially for high seam permeability. This suggests the existence of short-circuiting between the water entering the system at the surface and the pump, which reduces the pumped temperature to the surface temperature of 9℃. For low seam permeability (i.e. mid seam K_w = 1 × 10^{-2} m/s), no extreme cooling is observed in monitoring shaft 2 within the simulation time. This is interpreted as the result of lower fluid velocities that increase the water residence time within the coal seams and allow the water to be warmed up by the surrounding rocks before mixing in the shaft.

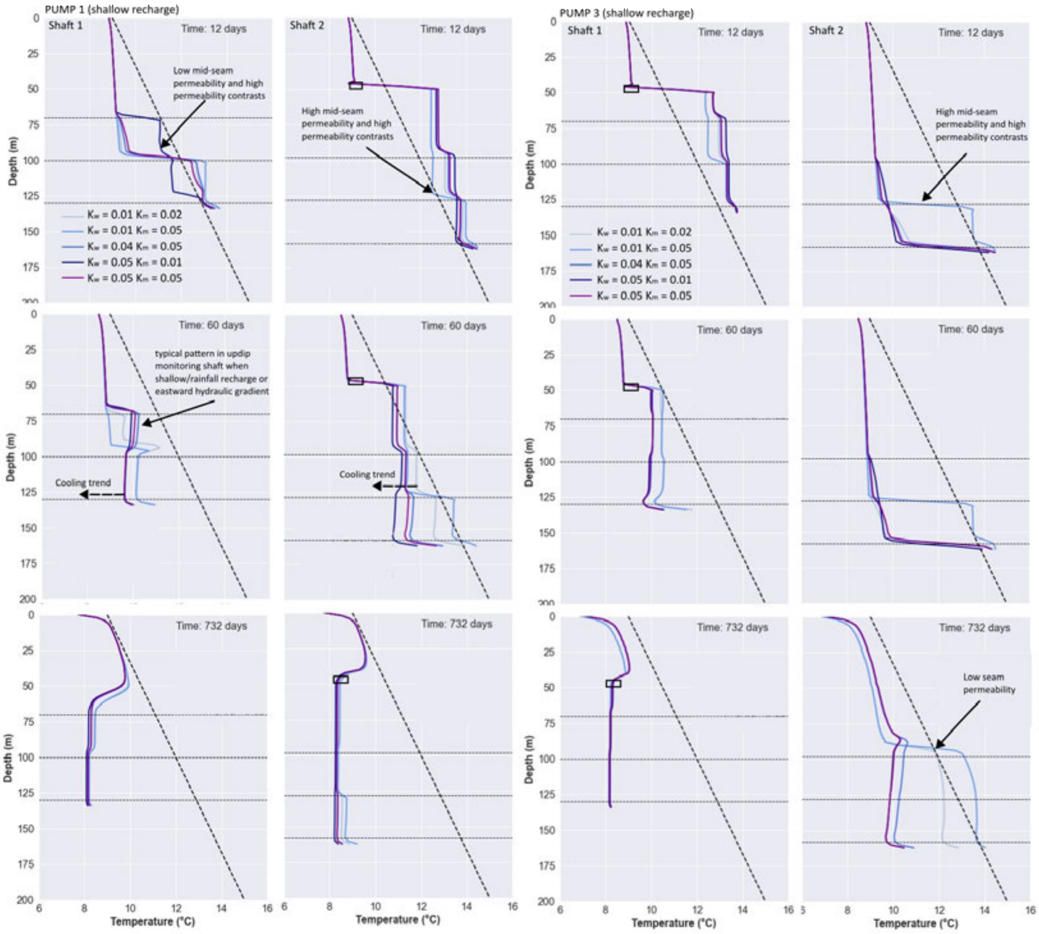

Figure 7.12: Temperature profiles in the pumping and monitoring shafts after 6 and 732 days of pumping from pump 1 (left panel) and pump 3 (right panel) for different seam permeability contrasts, assuming shallow water recharge. K_m and K_w represent the hydraulic conductivity (m/s) of the mid-seam and of the upper/lower seams, respectively. Low seam permeability prevents extreme cooling (i.e. thermal breakthrough) and promotes thermal recovery in the long-term in shaft 2, when pumping is performed from the updip shaft 1.

7.4.4 Long-term thermal disturbances

The dipping layer model is finally used to determine the extent of potential long-term thermal disturbances induced by dewatering during mining activities, for different hydraulic recharge scenarios. Those include 1) pumping at a rate of -0.0017 m^3/s with cold shallow recharge from the left boundary and b) pumping at a rate of -0.05 m^3/s with deep warm recharge from the right boundary. These values have been determined after a trial and error process, allowing pumping from the deep shaft (P2) to produce a drawdown of -160 m at the pump, according to the material properties defined in Table 7.1. Deep and shallow recharge are modelled as constant heads of 0 m on the right and left boundaries, respectively. The temperature distribution captured after 50 years of dewatering (transient simulations) confirms that deep pumping induces a general cooling along the shafts and dipping seams in scenarios where shallow recharge is dominant, of up to -7℃ (Fig. 7.13). The thermal disturbances induced by deep warm recharge are more subtle, with a slight warming of up to 2℃ observed along the seams between the pumping shaft 2 and the right recharge boundary.

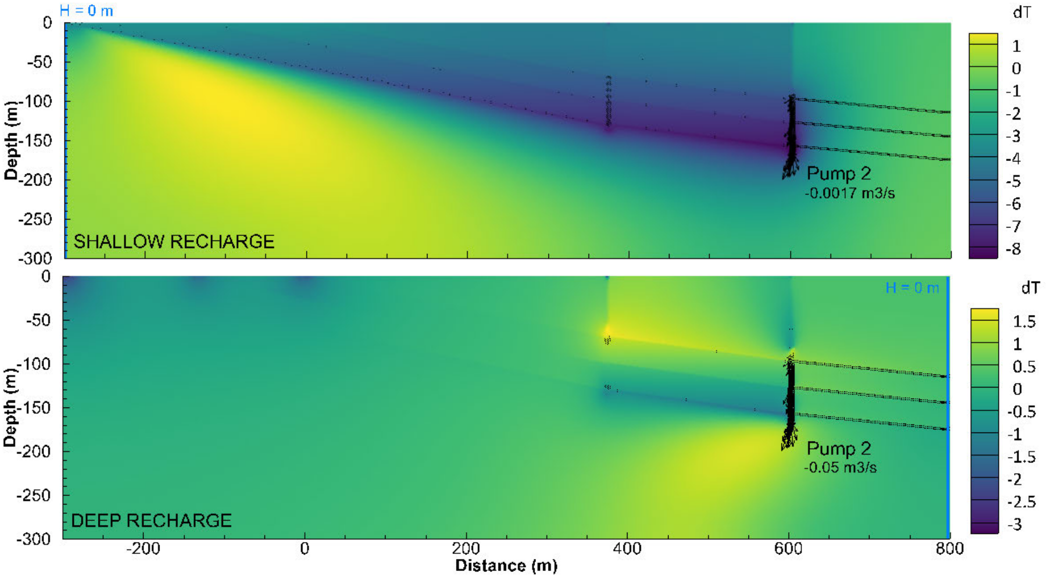

Figure 7.13: Thermal disturbances induced by 50 years of dewatering (steady-state simulations) for scenarios with surface and deep recharge. The porous model is characterised by a slice thickness of 1 m and a scaled shaft thickness of 0.06 m^2.

Water rebound is then simulated using the results from the dewatering scenarios as initial conditions, to investigate the potential residual disturbances following a period of flooding and thermal recovery. In the rebound scenarios, it is assumed that the permeability within and above the mined seams remains unchanged (i.e. neglecting the potential collapse of the roof above the seams). Water rebound is permitted via a hydraulic flow of 12 $\times$ 10^{-6} m^3/s distributed along the left and right boundaries, to represent shallow and deep water recharge, respectively. This value has been calculated to generate an average rebound rate of 20 m/yr in the deep recharge scenario, which is typical of the recovery rates observed in the Midlothian Coalfield in Scotland (Chapter 3). In the shallow recharge scenario, this flow rate induces a rebound of 2 mm/yr due to the lack of connection between the high permeability seams and the left boundary. In opposition to constant head boundaries, flow boundaries allow for a slower water rebound that best replicates the flooding rates observed in mines. As discussed in Chapter 6, determining the rate of hydraulic recharge and the hydraulic state of mines is essential when assessing the initial mine-water reservoir heat capacity, as thermal recovery might not be complete at the start of geothermal operations. Alternatively, a Cauchy boundary would allow setting the maximum rebound value and allow for a reduction of the inflow rate as the hydraulic gradient between the mine and the recharge boundary reduces (Chapter 4).

Fig. 7.14 shows the thermal footprint after a 50-year dewatering period and 50-year recovery. Although the model does not represent a specific case study, it suggests that residual thermal disturbances remain after at least 50 years following the start of the water rebound and thermal recovery period. However, after 50 years, the error in initial heat potential assessment equals 0.18% for a deep recharge scenario, and 0.27% for a shallow recharge scenario (Fig. 7.15). Assuming a smaller recharge rate (i.e. 7×10^{-6} m^3/s), it is moreover found that the discrepancies are reduced to 0.13% for a deep recharge scenario, and -0.10% for a shallow recharge scenario.

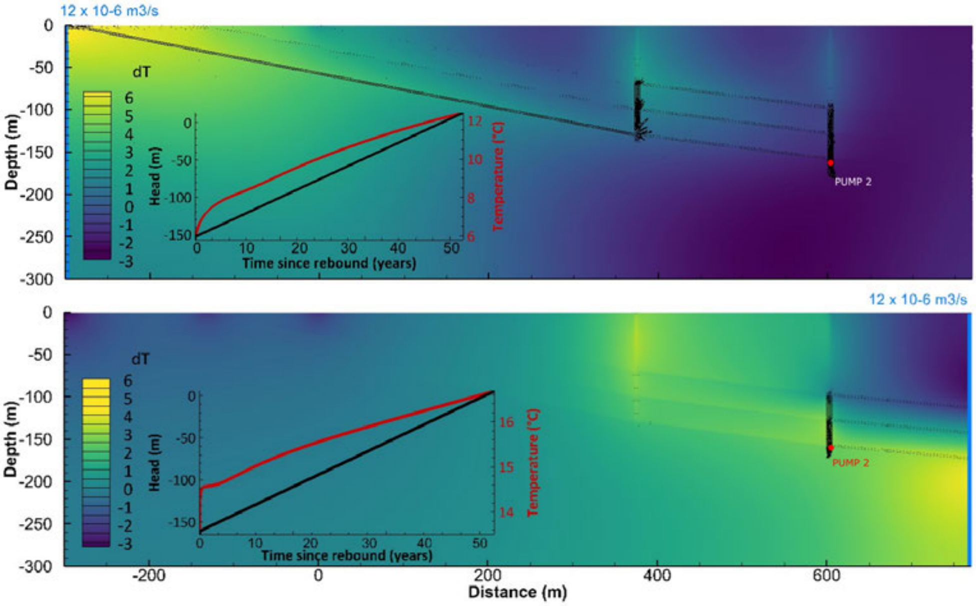

Figure 7.14: Residual thermal footprint in the mine relative to the pre-mining temperature distribution, following a 50-year dewatering period from pump 2 (deep shaft) and a 50-year rebound and thermal recovery period. The top figure assumed recharge from the left boundary (i.e. shallow cold water recharge) and the bottom figures consider deep recharge from the right boundary, at a rate of 12 $\times$ 10^{-6} m^3/s (flow rate equally distributed across the boundary). The time series of water rebound and temperature measured at the PUMP 2 monitoring point are provided in the bottom-left corner for each scenario.

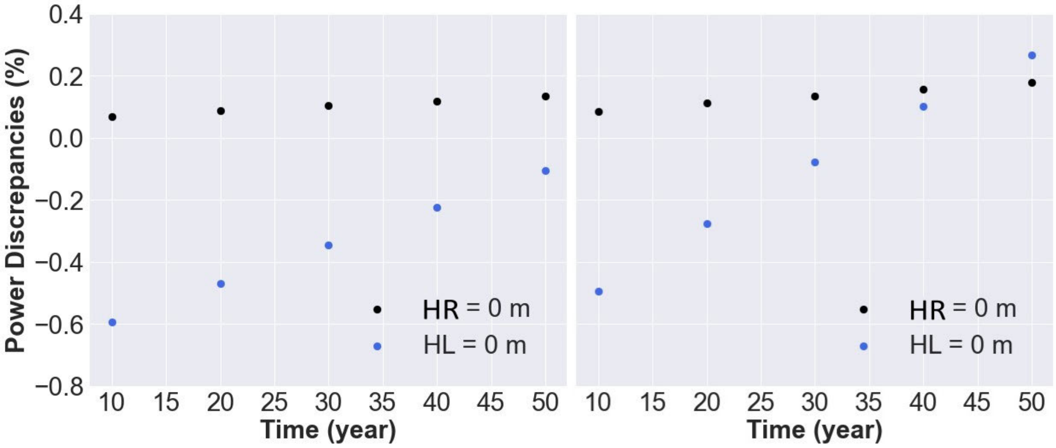

Figure 7.15: Percentage discrepancies between the post-recovery and pre-mining heat capacity of the mine-water reservoir, calculated for different recovery stages. Two scenarios are compared, for a hydraulic recharge rate of 7×10^{-6} m^3/s (left) and 12×10^{-6} m^3/s (right). HR and HL correspond to the head at the right and left boundaries, respectively.

7.5 Discussion

7.5.1 Effect of coupling during recovery (free convection)

In pumping scenarios, forced convection induced by water abstraction superimposes onto the density-driven convective flow in the mining area, explaining the limited coupling effect within this depth interval (Chapter 6). The effect of natural convection permitted via coupling becomes important outside the mining area, where it is suggested to explain the cooler/warmer temperatures observed in the lower/upper half of pumped (whether it is pumped from deep or shallow depths) and unpumped mine shafts, provided the permeability contrasts between the shaft, mine workings and surrounding rock and their area are well determined (Chapter 6).

Thermohaline stratification is a phenomenon commonly observed in mine shafts (Hamm & Bazargan Sabet, 2010), expressed by the layering of mine water as a result of temperature and salinity gradients. Those gradients generate density contrasts in the water column, creating buoyancy forces in large open voids and triggering natural heat convective flow that is thought to be beneficial to the heat recovery from geothermal systems (Bao et al., 2020; Bao & Liu, 2019a). In unpumped mine shafts, this effect is promoted by the inflow of mine waters from different depths (i.e. different temperatures and salinity) that favours the development of convective cells or layers with relatively uniform temperature and salinity, in between the seams insets where large temperature shifts are formed (Hamm & Bazargan Sabet, 2010).

Density-related effects are expected to play an essential role during water rebound in unpumped areas, where 'natural' effects would dominate (e.g. no turbulence induced by pumping). To explain the convective cells observed in monitoring shafts described in Chapter 3 (i.e. cooler/ warmer temperatures in the lower/top half of the shaft), rebound scenarios simulated in the previous section are here replicated assuming fully coupled processes (i.e. flow induced by temperature-related density-viscosity changes). Results for shaft 2 suggest that density effects promote the formation of convective cells and temperature steps during rebound, compared to a scenario without coupling, in cases where deep recharge dominates (Fig. 7.16). Surprisingly in the shallow water recharge scenario, a general warming is observed along the shaft, with a uniform temperature of 17℃ observed after 50 years, with no disturbances at the seams insets. This contrasts with the linear gradient observed in a scenario without coupling, which somewhat depicts cooler temperatures than the one predicted by the pre-pumping gradient below 100 mbgl.

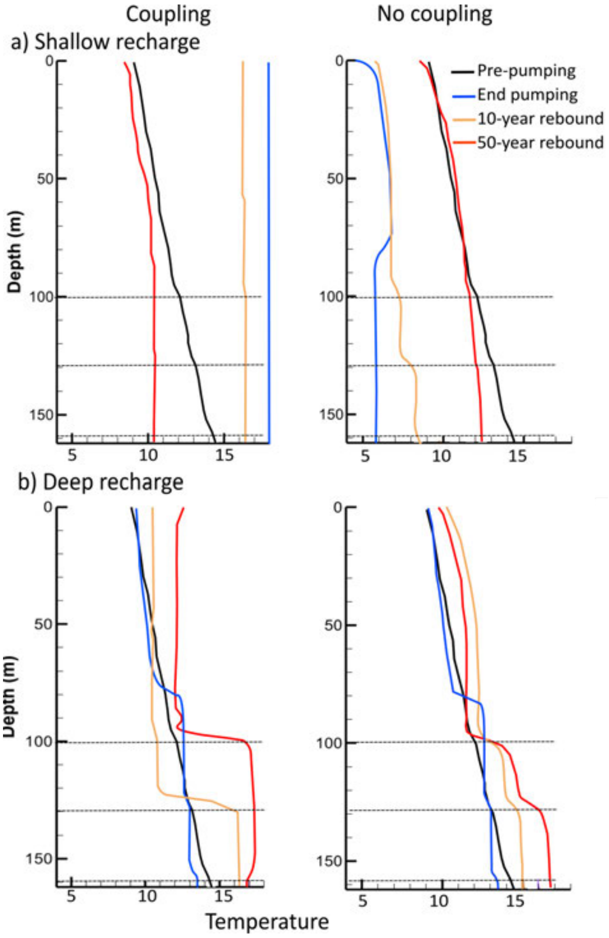

Figure 7.16: Temperature profiles in shaft 2 at the end of the dewatering period and after 10 and 50 years of rebound, for a) a shallow recharge scenario (HL = 0 m) and b) a deep recharge scenario. For both scenarios, temperature profiles obtained using coupling and no coupling between the hydraulic and thermal processes are compared.

7.5.2 Temperature versus heat flux boundary

There is an important debate in the literature about the choice of the surface and bottom temperature boundary conditions in numerical modelling. In this analysis, heat flux boundaries were used to prevent the overestimation of the heat recharge from the bottom boundary, or cooling at the surface. Here, the relative effect of the temperature boundary conditions on the thermal footprint, heat flow and power output are compared, assuming either constant surface and bottom temperature or surface and bottom heat flux boundaries. The constant temperature model considers a surface temperature of 9℃ and a bottom temperature of 18℃, which produce a geothermal gradient of 30°/km. Constant heads H = 0 m are set at the lateral boundaries, allowing for both deep and shallow hydraulic recharge to the mine. Those correspond to the initial conditions of the reference model presented in this study.

After running a pumping simulation for 2 years (with P1 extracting at a rate of -0.001 m^3/s in the deep shaft), results suggest the negligible impact of the temperature boundary conditions on the temperature distribution within the mine (Fig. 7.17). However, using constant temperature boundaries reduces by about 16% the heat mining rate from the system after 2 years (i.e. -395 W against -473 W for the heat flux boundary model). Using temperature boundaries tends to reduce the cooling at the surface, and increase the conductive heat flow that promotes recharge in the system.

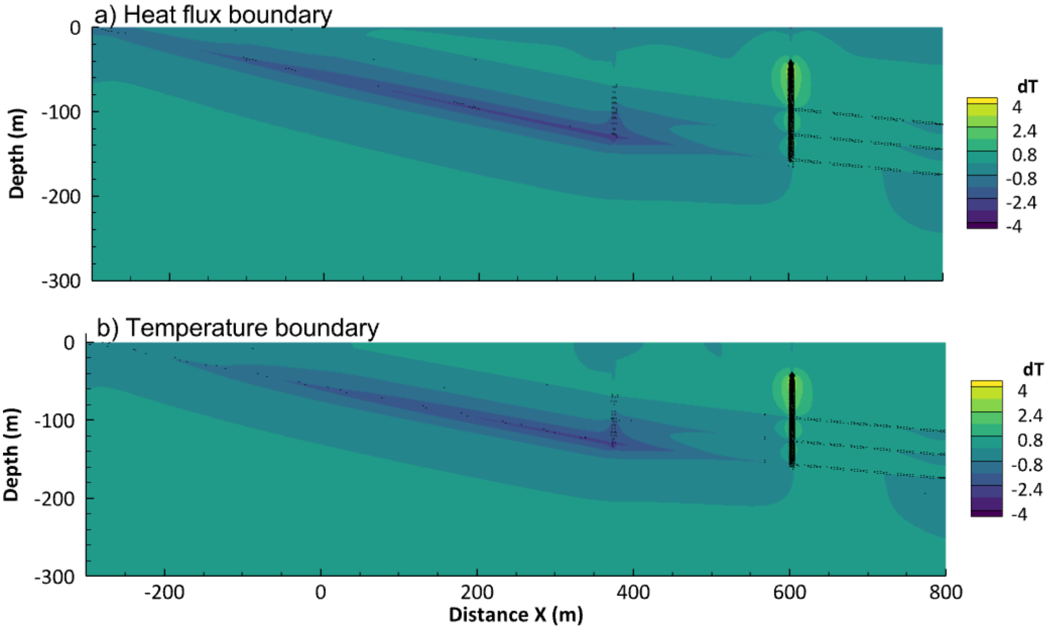

Figure 7.17: Comparison of the thermal footprint induced by pumping from pump 1 after 2 years of pumping using a) constant heat flux and b) constant temperature boundary conditions.

7.5.3 Heat flow and recovery mechanisms

Heat convection has been shown to represent the main means of transport of heat from the host rock to the shaft via the advecting mine water during pumping. Depending on the source of recharge (i.e. shallow subsurface or deep recharge), pumping can either promote heat mining or heat recovery within the system. To better understand the source of heat mined, the rate of energy change within each material (i.e. the seams, mining area, surrounding unaffected rock mass and the shafts) is calculated over the 2 years of pumping, for the different pumping depths and hydraulic recharge scenarios.

Based on the reference scenario (i.e. constant lateral head boundaries), results first indicate that deep pumping from the downdip shaft induces the largest depletion of heat, followed by shallow pumping from that shaft (Fig. 7.18). This is interpreted to result from the downflow of cold recharge water from shallow depths, across an extensive volume of mined seams, down to the deep part of the mine. In the initial days of pumping, most of the heat is sourced from the mine workings. Whilst the heat mining rate from the top and bottom seam decreases over time, the mid-seam is continuously depleted in heat over the simulation period. In the long term, the relative contribution from the rock surrounding the galleries (i.e. the mining area) increases, followed by the contribution from the host rock. When pumping from the updip shaft is implemented (P3 and P4), heat mining from the seams and host rock is exacerbated in the initial days of pumping. After 200 days, this trend is reversed and the heat extraction rate in all materials is reduced compared to the pumping scenarios in shaft 2 (P1 and P2), reaching a steady state that suggests that heat mining and heat recovery are balanced.

The heat extraction rate from the different material types in the mine also highly depends on the nature/source of hydraulic recharge Fig. (7.19). Under shallow pumping conditions (i.e. assuming pumping from P1 in shaft 2), shallow recharge (HL = 0 m) induces the largest depletion of heat by promoting the migration of a cold plume from the outcrop to the mining area (Fig. 7.10). Whilst heat mining from the seams is dominant in the initial 100 days of pumping, heat is mostly sourced from the surrounding unaffected host rock and in the mining area in the long term. On the contrary, deep recharge (HR = 0 m) allows the system to reach a sustainable heat recovery rate, by promoting heat convection via the mined seams, preventing heat mining from the host rock and the mining area. When both deep and shallow recharge is permitted (H = 0 m), the heat mining rate keeps increasing with time, with most of the heat being sourced from the mining area. Rainfall recharge alternatively leads to a continuous decline in the heat mining rate, interpreted to result from the low infiltration rate through the soil layer and the increased water residence time as it flows towards the pumping shaft.

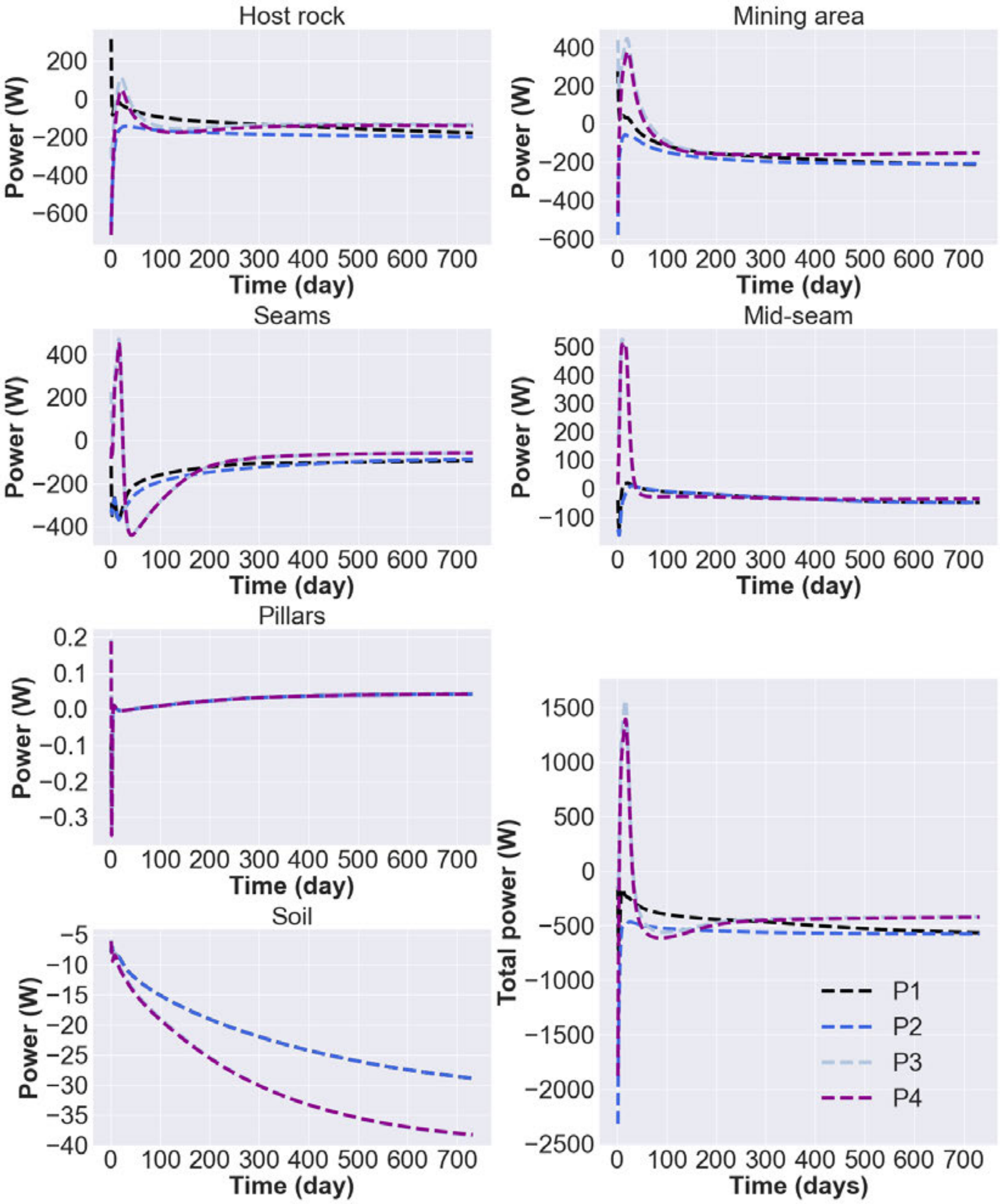

Figure 7.18: Rate of energy change (daily time steps) in each material group for the four pumping depths scenarios. Pumps 1 and 2 are located in shaft 2 and pumps 3 and 4 are located in shaft 1. Note the different y-axis scales for each plot.

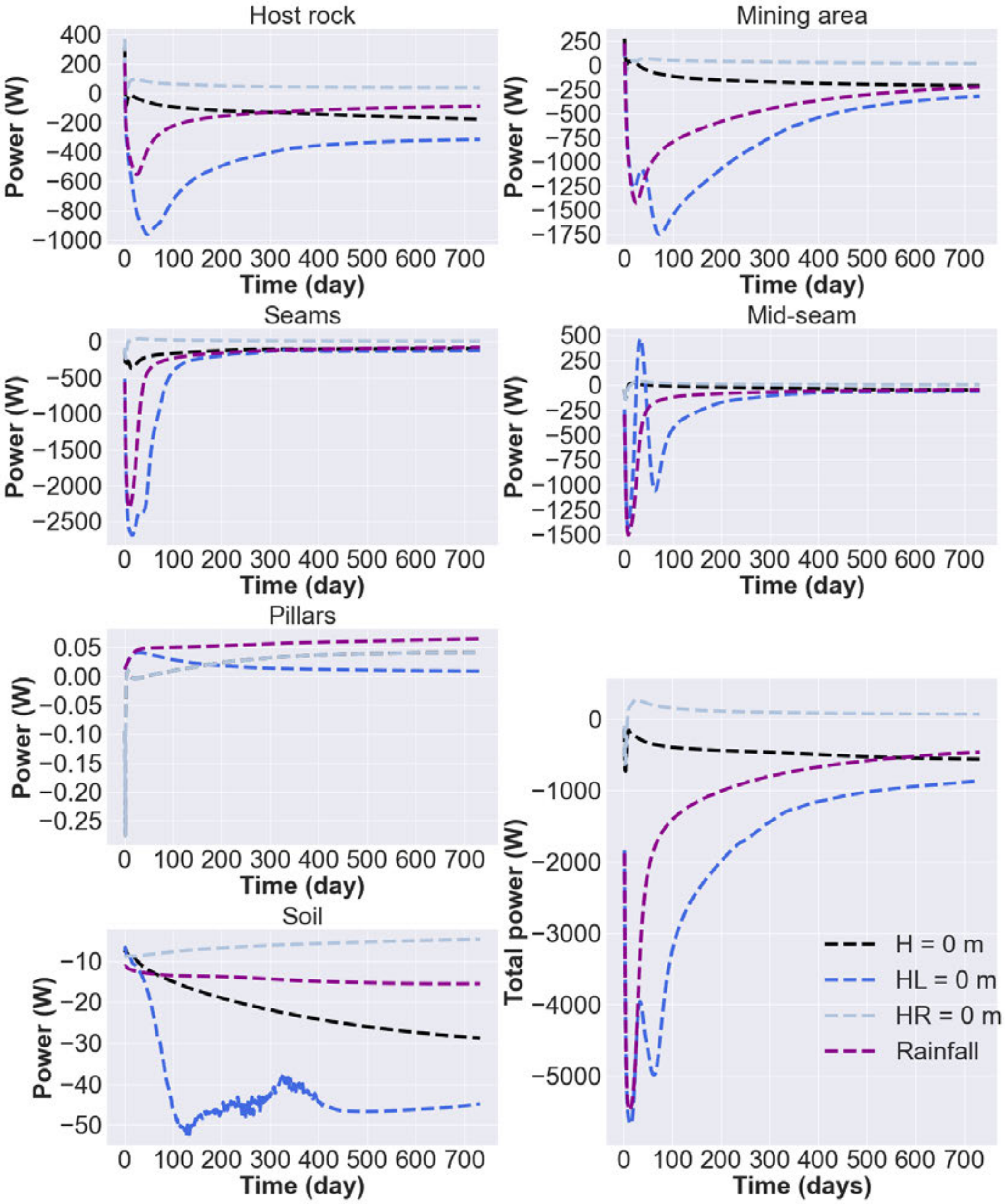

Figure 7.19: Rate of energy change (daily time steps) in each material group for the four hydraulic recharge scenarios. H = 0 m, HL = 0 m and HR = 0 m assume recharge from both lateral boundary, shallow recharge from the left boundary, and deep recharge from the right boundary, respectively. Note the different y-axis scales for each plot.

Results presented in Fig. 7.20 finally suggest that during water rebound (i.e. no pumping), thermal recovery is faster in a scenario with shallow hydraulic recharge, whilst the heat content in the deep recharge scenario remains relatively constant. This is interpreted to result from the fact that deep recharge allows for thermal balance to be reached in the system during pumping/dewatering. In the initial days of flooding, the mining area is the first to be recharged in heat, whilst the heat recharge to the host rock reaches a steady state after about 30 years.

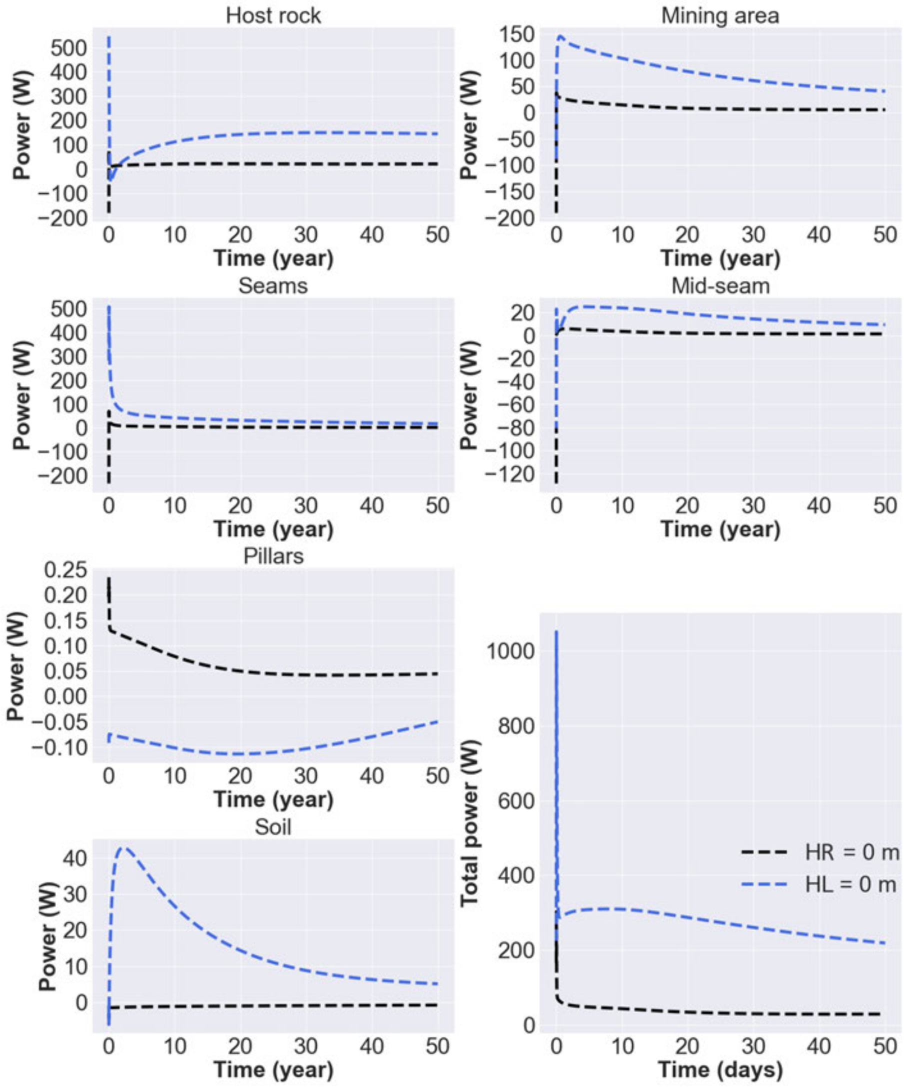

Figure 7.20: Rate of energy change (daily time steps) in each material during water rebound, for scenarios with deep (HR = 0 m) and shallow (HL = 0 m) water recharge. Note the different y-axis scale for each plot. The low heat recovery rate in the deep recharge scenario is interpreted to result from the balanced heat recharge reached during pumping.

7.6 Conclusion

This analysis suggests that the temperature in flooded shafts and heat mining/recovery rate highly depend on the nature of the recharging water and on the extent of water mixing associated with the mine geometry. Shallow pumping promotes heat recovery, especially if deep water recharge scenarios. The heat recovery rate is also impacted by the residence time of the pumped mine water as it flows towards the pumping shaft. This will depend in the short term on the regional flow and pumping rate, which are linked to the seam permeability. As discussed in Chapter 6, the seam permeability controls the transient behaviour of heat extraction and heat recovery, with low seam permeability promoting heat mining in a deep recharge scenario and heat recovery in a shallow water recharge scenario. In the long term, most of the heat mined through the operation of a mine-water pumping scheme is sourced from the fractured mined area and the surrounding host rock. Further analysis of the effect of the hydraulic properties of the damage zone surrounding the mined seams on the heat extraction rate is conducted in Chapter 8.

This analysis moreover suggests that the error in the heat potential assessment associated with the effect of past mining/dewatering activities is limited for recovered coalfields. However, the extent of the disturbances depends on the time since the flooding/recovery started. In addition, constant temperature boundaries tend to overestimate the extent of conductive heat recharge, and therefore a proper assessment of the undisturbed geothermal heat flux and boundary conditions is essential to determine the long-term rate of recoverable heat.

Chapter 8

Conceptualisation of heat transfers in flooded mine workings

8.1 Chapter Overview

Mines are complex systems, both geometrically and hydraulically, and simplifications are generally required to make numerical computation feasible. However, the current state of the mine galleries e.g. amount of collapsed material, connectivity of galleries, nature of the hydraulic recharge, or the hydraulic properties associated with different zones around mine workings, are often unknown. To date, no standardised modelling approach has been developed to assess the long-term heat recovery potential of flooded coal mines.

This chapter aims to characterise the key geometrical features controlling the heat extraction rate from mine-water systems and the level of simplification possible when assessing the long-term heat recovery rates, at the scale of the mine. It includes a review of the following issues:

- The extent of the geometrical simplification for mine-water reservoir modelling versus scale and timing of the analysis
- The source of heat and dominant heat recharge mechanisms under different hydraulic recharge scenarios
- The sustainability of heat supply (e.g. heat mining versus heat recharge rate and thermal footprint of heat extraction)

After performing a preliminary analysis of the effect of the geometry for a simple panel, a range of 3D models of the worked Dawdon High Main (E) Seam with different levels of complexity are developed. Those are compared to identify to what extent the rates of recoverable heat and thermal plume propagation are sensitive to the presence of specific mine features (e.g. roadways, pillars) and the rock properties (e.g. extent of the fractured zone, hydraulic conductivity contrasts). Please note that although the term 'permeability' is used to improve the flow of the text, this study only uses hydraulic conductivity values (m/s). In addition, the key heat recharge mechanisms for a series of hydraulic recharge scenarios are characterised. Results are used to suggest a conceptual tool for the estimation of the initial heat potential and recoverable heat from mines. In particular, the possibility of using a statistical depth distribution of the void percentage and the impact of the nature of hydraulic recharge on the long-term heat recovery potential is discussed (see Chapter 9).

This chapter was initially written for publication in the World Geothermal Congress proceedings 2023 before being withdrawn from the WGC program. Updated results have been presented instead at the Energy Geoscience Conference 1 in Aberdeen in May 2023, and the manuscript is being prepared for submission to the conference proceedings (Geological Society of London).

Hypothesis:

- An equivalent porous media approach can be used to reproduce heat transfers in interconnected roadways and pillar-and-stall mining areas
- The height of the fractured zone has a key impact on the long-term rate of heat extraction and recovery
- The nature of the hydraulic recharge controls the heat recharge rate

8.2 Introduction

Past studies involving numerical modelling of abandoned flooded coal mines have faced important difficulties arising from the complex geometry of mine workings and the necessity to solve simultaneously for heat transfer and groundwater flow (Ferket et al., 2011). Accurate representation of mine workings can be tedious, computationally expensive and prone to numerical instabilities. This results from the high permeability contrast between the mine galleries, shafts and the surrounding host rock. Different approaches have been used to assess the geothermal potential of flooded coal mines, with studies prior to 2016 being discussed in Loredo et al. (2016). Those include analytical (Lauwerier, 1955; Pruess & Bodvarsson, 1984) and semi-empirical Rodríguez and Díaz (2009) approaches also discussed in Loredo et al. (2017) as well as numerical methods. Those range from 1D heat transfers in mine tunnels (S. A. Ghoreishi-Madiseh et al., 2012) to more complex 2D/3D numerical models (Andrés et al., 2017; Ferket et al., 2011; P. Guo et al., 2018; Hamm & Bazargan Sabet, 2010; Malolepszy, 2003).

In the tunnel approach described by S. A. Ghoreishi-Madiseh et al. (2012), the tunnel dimensions were shown to determine the total recoverable heat from mines. Although heat is transferred in an open pipe through forced convection, the authors demonstrated that the thermal conductivity of the surrounding mine rock determines the sustainable rate of heat extraction in the long term. In a flooded mine with large open voids, the long-term heat extraction rate was shown to be less impacted by the rock permeability. Among hybrid approaches, Raymond and Therrien (2008) and Renz et al. (2009) used a combination of a 1D pipe network embedded in a 2D/3D mesh to simulate turbulent flow in the open mining voids (e.g. shafts, tunnels, roadways, galleries), and laminar Darcy flow in the surrounding porous media. Similarly, Ferket et al. (2011) developed a hybrid approach combining analytical and numerical methods to overcome the complexity of the mine geometry whilst accounting for the various nature of the flow (e.g. matrix, fracture and open pipe flow). Hamm and Bazargan Sabet (2010) and P. Guo et al. (2018) alternatively modelled mine-water reservoirs as a dual-porosity medium. In Hamm and Bazargan Sabet (2010), the reservoir was divided into a high water flow velocity regime (i.e. open galleries and vertical shafts) and a less permeable low-velocity regime i.e. (backfilled coal panels and intact rock masses) zone. In their model, Hamm and Bazargan Sabet (2010) showed that for permeability contrasts between the mine void K_{mine} and the rock $K_r < 1 \times 10^5$ m/s, the higher the K_{mine}, the smaller the decrease in extraction temperature. For low permeability, the cold water mainly flows within the lowermost galleries and is separated from the warm water above due to density effects. For higher contrasts, the higher the K_{mine}, the greater/quicker the decrease in extraction temperature. From permeability contrasts greater than 10^4 m/s, the mixing of warm and cold water occurs as a result of the establishment of free convection within the mine voids, leading to faster transport of cold water toward the extraction well (Renz et al., 2009). P. Guo et al. (2018) modelled in 3D a typical working face of a longwall panel, considering a caved zone or goaf (i.e. the collapsed overburden roof rock filling longwall panels), a fractured zone and a continuous zone (i.e. unaffected rock mass), with various porosity and permeability values. The authors showed that the height of the fractured zone above the panel highly influences the heat potential of the mine reservoir. High roof permeability in a typical working panel was also shown to be beneficial to heat transfers and increase the sustainability of heat production. Strong roof rocks were shown to be particularly beneficial as they tend to produce a wider distribution of fractures, influencing the temperature distribution and increasing the heat production from mines. On the contrary, high fracture permeability in the fractured zone was shown to reduce the production temperature. According to S. Ghoreishi-Madiseh et al. (2015), backfilled stopes, where conduction is the main heat transfer mechanism, also have great potential for sustainable geothermal heat production. Andrés et al. (2017) used a 2D model composed of 3 porous materials (i.e. the unaltered rock, the mined volume and the open voids) to calibrate the hydrogeological and thermal properties of the mine reservoir between the Barredo and Figaredo shafts in Spain, but did not consider the fractured zone. There, the heat capacity of mines and the rate at which heat can be extracted sustainably appear to highly depend on the volume of water-filled voids, the distribution of the permeability in the mine reservoir, the nature of hydraulic recharge and the thermal conductivity of the rock mass. Currently, there are however no standard modelling approaches to simulate the heat transfer/recharge mechanisms in mines (Renz et al., 2009).

Estimates of the geothermal potential of flooded mine (i.e. Heat in Place or HIP) are generally based on the volume of water available at a given depth (i.e. on its temperature) and on the local hydraulic condition (R. Anderson & De Souza, 2017). Jessop (1995) derived an estimate of the Nova Scotia mine in Canada using the product of the area mined in each seam and the average thickness, adjusted considering the coal seam dip angle and the roof subsidence after mining. When available, the authors also suggested the possibility of using the volume of extracted rock or total coal production to determine the initial void volume and scale it up by a factor accounting for backfilling and subsidence. Whilst Jessop (1995) used a constant factor of 25% independently of the type of mine workings, Malolepszy (2003) declared that this factor depends on the exploitation depth and the type of abandoned mine workings. Bazargan and Demollin (2008) alternatively argued that the volume of the water-filled void can be calculated by subtracting the volume of extracted rock V_{ext} by the backfilled volume cV_{back} and volume loss through subsidence V_{sub}, with c = 0.7 for caving and 0.85 for compacted sand. On the other hand, K. R. Whitworth (2002) and Banks et al. (2010) used dewatering and rebound rate data to get insight into the volume of inter-connected voids in UK mines. S. Chen et al. (2021) however highlighted that volumetric methods do not account for the dynamic convective and conductive heat recharge during production, which can be significant in mine systems. Based on the mine structure described in P. Guo et al. (2018) and the dynamic thermal energy recharge defined in Bao and Liu (2019a), the authors therefore developed a novel approach to calculate the total heat potential of mine-water reservoirs, accounting for both the structural differences between the shafts, galleries and stopes (i.e. for a longwall panel), and the dynamic heat re-supply. There, shafts and galleries were considered as cylinders with porosity/permeability of 1, whilst the water-bearing unit combining the caved and fractured zone was considered as an equivalent virtual cylindrical reservoir comprising both the volume of the caved and fractured zones (P. Guo et al., 2018).

Case-specific studies are subject to the nature and the amount of the data available, and many parameters such as the volume of mined coal, the extent of subsidence, the amount of collapsed material or the potential existence of obstructions to flow (e.g. closed dam) are often uncertain. Predictions of groundwater flow in mine strata are generally limited due to the uncertainties in the boundary conditions and the lack of pre-mining data. Few aquifer properties data are available from pumping tests for boreholes intercepting former mines, making it challenging to characterise the properties associated with the lateral and vertical interconnectivity of the different parts of the mines (Sherwood, 1997). In addition, the mining method used is not always known and mine plans are not always up-to-date nor accurate (B. J. Andrews et al., 2020). Many shallow pillar-and-stall workings were indeed reworked using the longwall mining approach, whilst some of them remain unknown or unmapped. Although keeping a record of the state of the mine at abandonment in the UK became a requirement under the 1870 Mines Inspection and Regulation Act (NRA, 1994), the acquisition of reliable data and maps only started with the nationalisation of the coal industry in 1947

(Richardson & Oxburgh, 1979), whilst keeping accurate and detailed records including the depth or any geological information became mandatory in 1972. Before then, mine plans only showed the extent of the mine workings. As a first step towards developing a conceptual standard approach for the assessment of the recoverable heat from mine-water reservoirs and its uncertainties, this study aims to:

- Determine the key features controlling the long-term heat extraction rate, looking into structural differences between pillar-and-stall and longwall workings,
- Assess the extent to which the geometry of mines can be simplified for large-scale and long-term heat potential assessments,
- Understand the effect of hydraulic recharge on the heat recovery rate and sustainability of heat extraction.

After performing a preliminary analysis on a simplified coal panel, a set of 2D and 3D numerical models for the Dawdon High Main seam (E) are developed to analyse both the relative importance of the different mine features and the effect of the hydrogeological settings on the thermal plume propagation and power output.

8.3 Preliminary study

The OpenGeoSys (OGS) finite-element numerical modelling software (Kolditz et al., 2012) is used to simulate groundwater flow and heat transfer in two models of simple geometries. The first model represents a horizontal coal panel worked using the pillar-and-stall approach (Fig. 8.1). This method was used in the early stage of mining (i.e. from the 13^{th} Century), consisting of leaving in place coal pillars between the worked zones to support the roof. Although it is thought that this would prevent the collapse of the roof following the abandonment of the mine, the current state of the working following water rebound and the amount of collapsed material remains unknown. The second model corresponds to a vertical section of a longwall panel (Fig. 8.2). This mining approach was used in the later stages of mining (i.e. mostly from 1950), as the implementation of the Newcomen engine permitted more efficient pumping and access to greater mining depths. There, coal was mined backwards and the roof was allowed to collapse, forming goaf materials where the porosity and permeability highly depend on the subsequent extent of subsidence and compaction (P. Younger & Robins, 2002). For both models, the rate of heat extraction and change in pumped temperature over 1 year of pumping/injection is investigated. An initial temperature gradient of 25.6℃/km with a surface temperature of 9℃ (i.e. panel temperature $\sim$14.2℃ at 200 m depth) is assumed. Detailed models are compared to equivalent simplified models (in 2D and 3D) to discriminate between key features controlling the large-scale heat potential and storage capacity of flooded mines.

8.3.1 Horizontal panel

The pillar and stall model P1 consists of 8 × 14 coal pillars, 10 m × 20 m in size and 10 m thick, in between which high-permeability porous material is left in place (Fig. 8.1a-b). Although coal seams in the UK are 1.5 m thick on average, a thicker model ensures numerical stability and allows a valid comparative study. An equivalent porous media representing a goaf panel with homogeneous material properties (P2) is developed in parallel to investigate the relative effect of panel heterogeneities on the long-term heat extraction rate. The equivalent hydraulic properties θ_{eq} (i.e. porosity, permeability, storage) are calculated considering the relative proportion of void and the corresponding properties for the pillars and stalls (Table 8.1), according to Equation 8.1.

$$\theta_{eq} = \theta_{pillars} \times \%V_{pillars} + \theta_{stalls} \times \%V_{stalls} \tag{8.1}$$

with the relative proportion of pillars $\%V_{pillars}$ and stalls $\%V_{stalls}$, such as:

$$V_{pillars} = \frac{V_{pillars}}{V_{total}} \tag{8.2}$$

and

$$V_{stalls} = \frac{V_{stalls}}{V_{total}} = 1 - \%V_{pillars} \tag{8.3}$$

In both models, water is pumped from near the bottom-left boundary and injected at a temperature of 10℃ near the top-right boundary.

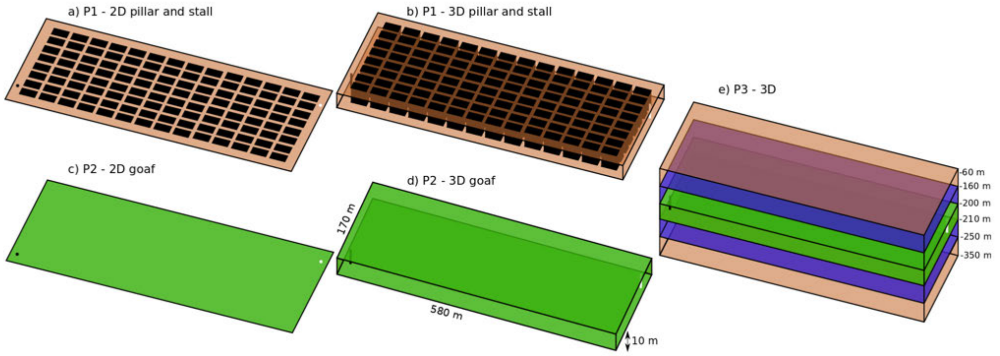

Figure 8.1: Conceptual representation of the numerical models of the horizontal panel. a) 2D and b) 3D pillar-and-stall models P1, c) 2D and d) 3D equivalent goaf panel P2, and e) embedded 3D equivalent goaf P3. The black and white dots/lines represent the pumping and injection locations, respectively

Properties	P1 Pillars	P1 Open voids	P2 Equivalent
L x W x h (m)	20 x 10 x 10	-	580 x 170 x 10
N	14 x 8	-	-
V_P (m^3) and (%)	2000 (23%)	762,000 (77%)	986,0000 (100%)
Φ (%)	5	75	59
c	1380	1380	1380
ρ	1500	1500	1500
λ	0.31	0.31	0.31
k	1×10^{-9}	1×10^{-2}	7.73×10^{-3}
S	1×10^{-5}	2×10^{-2}	1.55×10^{-2}

Table 8.1: Hydrogeological and thermal properties for the different materials in the horizontal pillar-and-stall models, with N the number of pillars, V_P the volume of pillars, Φ the porosity, c the heat capacity, ρ the rock density, λ the heat conductivity, k the permeability and S the storage.

8.3.2 Vertical section of longwall panel

2D vertical models of a typical longwall panel are used to investigate the effects of overlying/underlying rocks on the rate of heat recovery from the mine workings (Fig. 8.2). I first compare results from the horizontal goaf panel (P2) to an equivalent vertical model (D0) to assess the effects of the model geometry on the amount of extractable heat from goaf materials and calibrate the results. In the vertical 580 m $\times$ 350 m model D1 (Fig. 8.2b), the goaf material/caved zone is surrounded by a fractured/damaged zone and a continuous/unaffected host rock. The heat extraction rate for a range of thicknesses, porosities and permeabilities for the different zones is calculated to get insight into the key parameters controlling the long-term heat potential of mines. The models assume no-flow temperature boundaries to allow comparison with the models introduced in section 8.3.1. I then assess the validity of using an equivalent permeability for the whole mining area using model D2. This model consists of two materials, the equivalent mined zone, encompassing the caved and fractured zones, and the unaffected rock mass. Properties for the equivalent zone are attributed so as to represent the average porosity, permeability and heat conductivity, weighted to the relative thickness of the zone in model D1 (Table 8.2). The possibility and the advantages of using a 1D horizontal line element rather than porous media to represent open tunnels (D3) is finally discussed. There, the tunnel is located at about 200 m below the surface and is embedded in the continuous porous host rock.

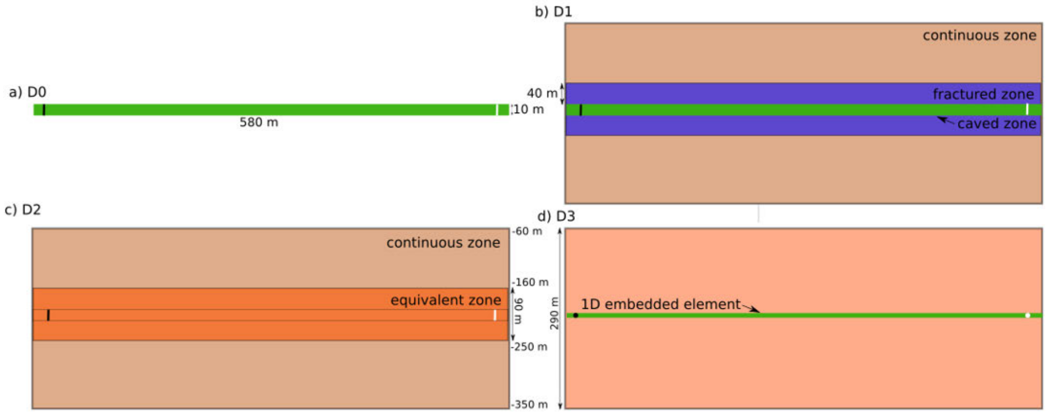

Figure 8.2: Conceptual representation of the 2D vertical models of a typical longwall mine working. a) goaf panel (D0), b) full vertical 2D section of model P3 (D1), c) equivalent mining zone model (D2) and d) multi-element tunnel model (D3).

Properties	D0 (a)	D1 (b)			D2 (c)	D3 (d)
Zone	Goaf	Caved	Fractured	Continuous	Eq.	Tunnel
h	10	10	80	200	90	1
V (m^3)	986,000	986,000	7,888,000	19,720,000	8,874,000	580
V (%)	3.4	3.4	27.6	69.0	31.0	-
Φ	59	59	15	5	20	1
V_{void}	582,700	582,700	1,183,200	986,000	1,765,900	-
c	1380	1380	860	860	918	1380
ρ	1500	1500	2400	2550	2300	1500
λ	0.31	0.31	2.4	2.4	2.2	0.31
k	7.73×10^{-3}	7.73×10^{-3}	5×10^{-4}	1×10^{-7}	1.3×10^{-3}	1
S	1.55×10^{-2}	1.55×10^{-2}	1×10^{-4}	1×10^{-5}	1.8×10^{-3}	1

Table 8.2: Hydrogeological and thermal properties for the different materials in the vertical longwall panel models, with h the layer thickness, V the zone volume, V_{void} the void volume in the zone, Φ the porosity, c the heat capacity, ρ the rock density, λ the heat conductivity, k the permeability and S the storage.

8.4 Dawdon Seam E model

8.4.1 Mining history

The Dawdon-Horden mine-water block (MWB) is situated in the East Durham Coalfield in North-East England (Fig. 8.3). In Dawdon, 6 main seams from the Carboniferous Pennine Coal Measures (CM) have been worked using both the pillar-and-stall (shallow workings) and longwall (deep workings) mining approaches (Table 8.3). A more detailed description of the geology of the coalfield is provided in Chapter 2.

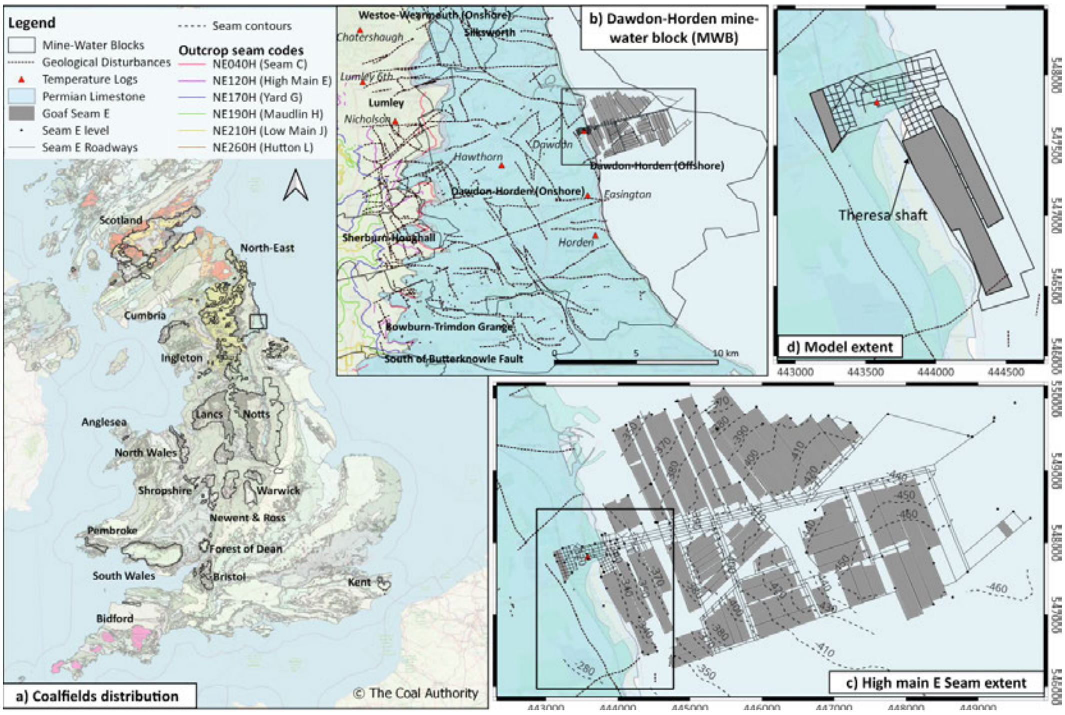

Figure 8.3: Map showing a) the coalfield distribution in the UK, b) the Dawdon-Horden mine-water block, c) the digitised Dawdon Seam E mine workings, including the roadways, panels and shafts, and d) the extent of the reference model.

Seam code	Ref letter	Name	Mean depth	Thickness	Area
NE120H	E	HIGH MAIN	-396	1.8	10298134
NE140H	F	MAIN	-381	1.2	472531
NE170H	G	YARD	-437	1.7	6707668
NE190H	H	MAUDLIN	-440	1.1	4352325
NE210H	J	LOW MAIN	-510	1.4 - 2.1	13071735
NE260H	L	HUTTON	-514	1.5	8482442

Table 8.3: Main seams worked in the Dawdon area and estimated average thickness and goaf area for each seam, calculated from digitised mine plans.

Mining and dewatering activities ceased in the area in 1993 with the abandonment of the Easington Colliery. Pumping for mine-water treatment purposes resumed at Horden in 2004 and Dawdon in 2008 (Bailey et al., 2013). As of 2022, mine water levels controlled via pumping at the Horden and Dawdon shafts appeared to have stabilised around 15 - 17 mBOD (source: The Coal Authority (TCA)). With the mine-water levels being maintained below the Permian piezometric surface throughout the block (Fig. A.20), reports undertaken by ESI and the Environmental Agency (EA) on behalf of TCA suggested that there is no leakage from the mine workings to the Magnesian Limestone aquifer (Streetly et al., 2009).

Since the onset of pumping, the mine water pumped at a rate of 100 - 150 L/s has maintained a constant temperature of about 20℃, offering new commercial opportunities for TCA to use this low-grade heat as a by-product of the treatment operations. In addition to providing energy to the treatment plant, the newly built Seaham Garden Village plans to provide 6 MW of heat from the Dawdon via a heat pump system (source: TCA). The development of such a system requires an important understanding of the source of heat controlling the temperature of the pumped mine water and the sustainability of mine-water heat utilisation. Here, the aim is to determine the key geometrical features and knowledge required when modelling and assessing the long-term sustainable heat extraction rate, at the scale of the mine.

8.4.2 Dawdon hydrogeological model

Details of the external and internal hydraulic connections within the Dawdon-Horden MWB are provided in Appendix A.2.5. Here, the pieces of information relevant to the development of the conceptual and numerical models for the Dawdon mine developed in this chapter are summarised (Fig. 8.4).

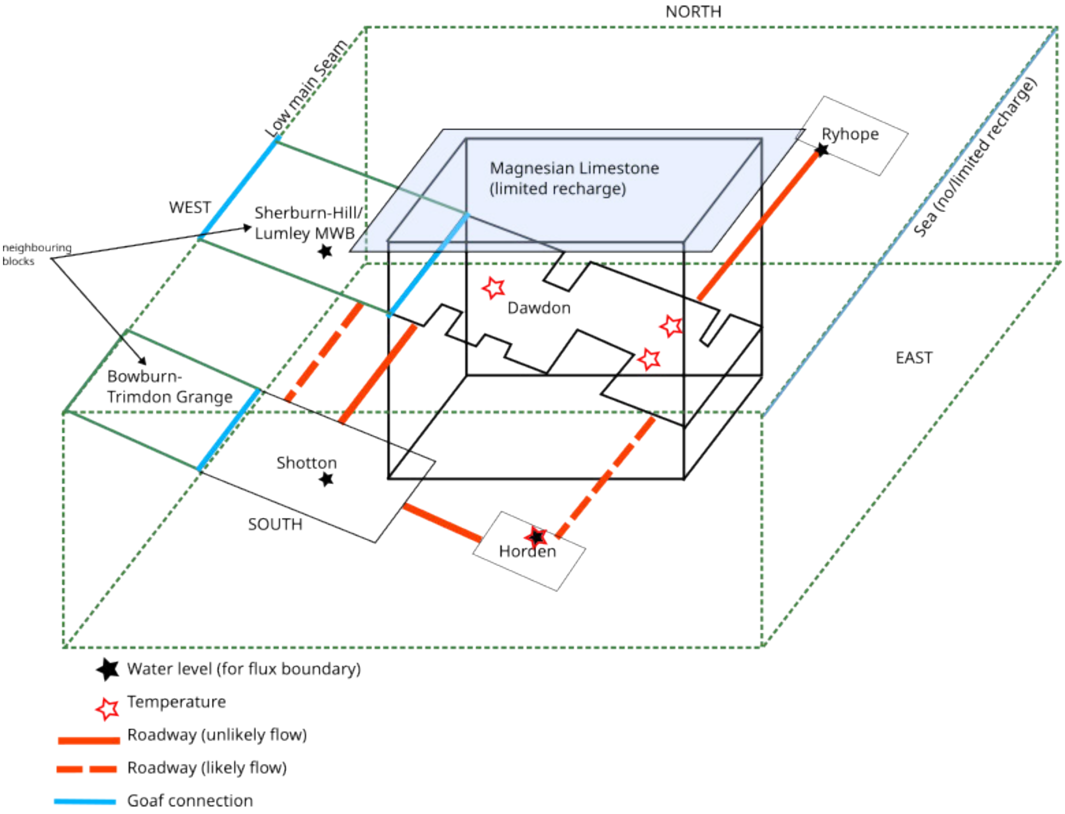

Figure 8.4: Conceptual sketch for the Dawdorn-Horden MWB hydraulic connections adapted from The Coal Authority conceptual model.

External connections.

The Dawdon-Horden MWB is bounded to the North by the Silksworth and Westoe-Wearmouth MWB, to which there is no recorded connection. The analysis of mine plans suggests that to the South, there is a direct roadway connection to the Bowburn-Trimdon Grange block via the Five Quarter (F) Seam (54 mAOD). A potential goaf connection between the two blocks exists in the Main (G) Seam (7 mAOD), but it is uncertain if it is actively contributing to the recharge to Dawdon. The Dawdon-Horden MWB is almost entirely concealed by the Permian Magnesian Limestone aquifer (IMC, 2001). There is however limited evidence of Permian inflows to the mines, suggesting that the recharge predominantly occurs via inflow from the adjacent Sherburn-Houghall and Lumley blocks, located to the West of Dawdon-Horden (IMC, 2001). Historically, a total recharge of 200 to 230 L/s was estimated for those three interconnected blocks (K. Whitworth, 2012). Whilst current pumping rates at Dawdon and Horden indicate a recharge of $\sim$100 - 140 L/s, this would suggest that $\sim$60 - 90 L/s is being discharged at Chatershaugh in the Lumley block (Farr et al., 2020; K. Whitworth, 2012). To the East, the Dawdon-Horden MWB is bounded by the North Sea, whilst the mine workings within the eastward dipping Coal Measures extend offshore up to approximately 10 km.

Internal connections

The Dawdon-Horden block is split into two sub-blocks by the WSW-ENE striking Ludworth Whin Dyke (Chapter 2). According to British Coal reports (British Coal, 1992), the Dawdon shaft is interconnected with the general body of mine workings via the Murton (Hawthorn) Colliery, and with the Easington (roadways in Low main J and Main F), Vane (connection in Low Main J) and Seaham (roadway in High Main E) collieries (Fig. 8.4). A dam in the roadway between the Horden Low Main (J) and Easington Main (F) seams (274 mBOD to 305 mBOD), initially built to withstand a head of 122 m on the north/Easington side, is assumed to be no longer active (i.e. same recovery rate observed at Easington and Horden), allowing the water to flow between the two sub-blocks (IMC, 2001). This is further evidenced by the control of the mine-water level at Easington via pumping at Horden.

Mine-water flow at Horden and Dawdon is mainly directed towards the Horden and Dawdon pumping shafts. Slightly higher water levels have been measured at Easington, located in between. Reports undertaken on behalf of TCA also suggested the connection of the Hawthorn colliery, located further west, to the coastal collieries, with the regional flow being directed from inland toward the coastal pumping stations (WYG, 2006). The relatively flat hydraulic gradients observed in recent years suggest that pumping at Dawdon and Horden has stabilised the water level across the MWB (WYG, 2006). Diurnal and tidal effects observed in the water levels monitored in coastal shafts were moreover interpreted to be a pressure response of the mine water in the undersea mine workings to the tides, given the absence of a known connection between workings and the sea floor (source: TCA).

Data limitations

Chemical analysis suggested mine water in Dawdon-Horden to be sourced from deep waters with long residence time. However, the water source and the extent of the catchment area available for hydraulic recharge to the pumping shafts is uncertain, making it difficult to assess the source of heat controlling the mine-water temperature. Other uncertainties in the conceptual model for the Dawdon-Horden MWB include the extent of the connections, interactions and leakage between the overlying Permian aquifer and the mine waters. In addition, there are only four mine-water monitoring sites in the Dawdon-Horden MWB. Two of them are also pumping sites, which limits the understanding of water levels outside of the immediate pumping zone, and three of them (Dawdon, Easington, and Hawthorn) are located to the north of Ludworth Whin Dyke. Only Hawthorn is located inland, with Dawdon, Horden and Easington being coastal collieries.

8.4.3 Numerical model development

Mine plan inventory and digitising. The workflow to generate the 3D geometry of the selected worked seam is described in the following (Fig. 8.5).

- STEP 1: Create 2D shapefiles of the worked coal seams of interest in the Dawdon mine, including a layer for the goaf panels, the interconnected roadways and the pumping/monitoring shafts
- STEP 2: Digitise seam levels and seam contours from the mine plans (source: TCA) in both the onshore and offshore parts of the coalfield. Seam depths are also available together with the depth of other geological boundaries (e.g. base Permian) from deep offshore oil and gas exploration boreholes (BGS GeoIndex database) and mine shaft logs (i.e. TCA seams insets files). For each data point/curve, the name, TCA code, depth and thickness of the seam are included in the layer's attribute table.
- STEP 3: Create a DEM from the seam levels and contour layers using the ArcGIS tool 'Topo to Raster' for each digitised layer.
- STEP 4: Use the 'Interpolate Shape' tool in ArcGIS to extract the depth value from the DEM at each workings polygon vertices and create 3D seam layers.
- STEP 5: Identify the drifts, roadways and shaft connections between the different layers
- STEP 6: Convert the different shapefiles into a geometry file using the different node coordinates, to be imported into the GMSH software (Geuzaine & Remacle, 2009) for the model mesh development.

Model geometry and meshing. Once the 3D geometry is available, a 120 m deep 3D planar model representing the High Main seam (E), one of the main coal seams worked in the area, is developed. The multi-element mesh consists of a combination of 1D, 2D and 3D elements, extending from 250 mbgl to 370 mbgl. To simplify the model and speed up the simulation,

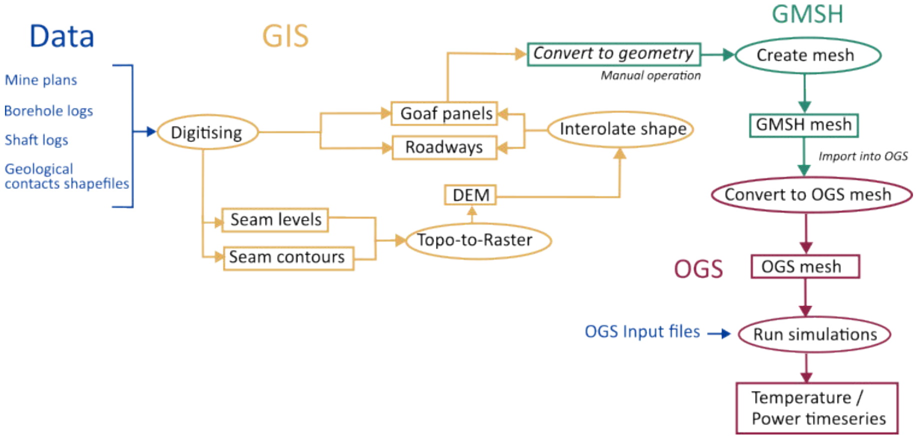

Figure 8.5: Dawdon Seam E model development workflow. ArcGIS, GMSH and OGS are the software used for the data analysis, mesh generation and simulations of heat transfer and groundwater flow in mines. The circled text represents the tools/processes used and the squared text represents the output files.

the 2 m-thick seam is represented as a 2D layer embedded in a homogeneous 3D mesh representing the surrounding damaged host rock at 330 mbgl (i.e. 80 m below the model top boundary). I thereby ignore the overlying/underlying seams and focus on the zone around the Theresa shaft, which consists of roadways, pillar-and-stall and goaf panels (Fig. 8.6).

The X, Y and Z coordinates of the workings polygons and roadways are first formatted and imported in GMSH to create the model mesh. Roadways consist of 1D elements embedded in a 2D triangular mesh representing the worked seam, that is itself integrated in the 3D mesh representing the surrounding porous rock. Overall, the model consists of a total of 61,793 and 386,442 elements, including 2,729 1D line elements, 45,801 2D triangular elements and 337,912 3D tetrahedron elements ranging from 6 m to 22 m in size. The hydraulic and thermal properties for each material are provided in Table 8.4.

	Roadway	Goaf	Pillar	Rock	Equivalent
ID zone	1	2	3	4	5/6
Dimensions	1D	2D	2D	3D	2D
Area (m^2)	28	1.6	1.6	1	1.6
Porosity (%)	1	0.25	0.05	0.1	7.3
Hydraulic conductivity (m/s)	1	2×10^{-2}	2×10^{-4}	1×10^{-6}	2.4×10^{-2}
Storage	1	1×10^{-2}	1×10^{-4}	1×10^{-5}	2.4×10^{-2}
Heat dispersion	3	8	8	8	8
Density (kg/m^3)	1500	1500	1500	2500	1500
Heat capacity (J/℃.kg)	1380	1380	1380	860	1380
Heat conductivity (W/℃.m)	0.31	0.31	0.31	2.4	0.31

Table 8.4: Rock properties for the different materials in detailed model and the equivalent porous model.

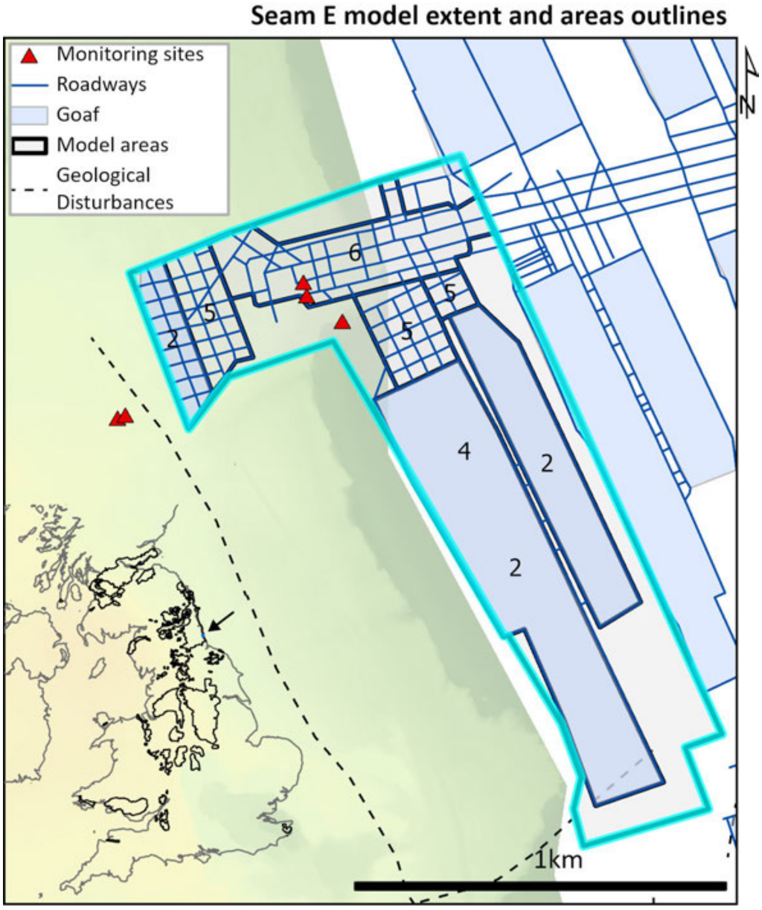

Figure 8.6: Area extent for the Seam E Model. Zones are as follows: 1: roadways; 2: goaf; 3: surrounding host rock; 4: unmined panel; 5: pillar-and-stall; 6: roadway area.

A series of 3 additional planar models with different levels of simplifications are then developed (Fig. 8.7).

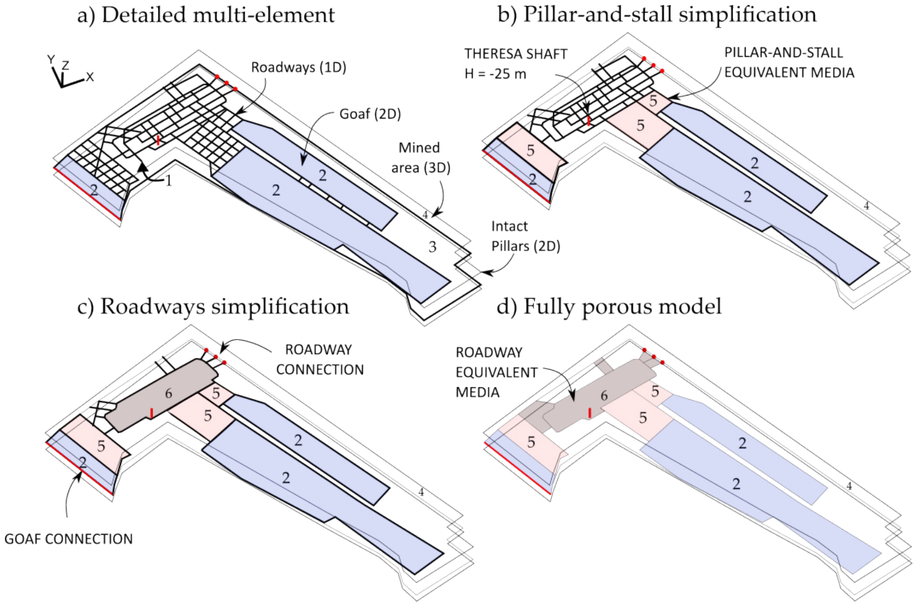

Figure 8.7: Diagram representing a) the detailed model, b) the equivalence pillar-and-stall model, c) the equivalent roadway model, d) the fully porous model. The model top boundary, seam E layer and bottom boundaries are located at 250, 330 and 370 mbgl, respectively.

For each equivalent porous model, selected pillar-and-stall and roadway areas around the pumping shafts are modelled as an equivalent porous zone to investigate the relative importance of the different mine geometrical features in controlling the thermal plume and heat extraction rate at different scales. Hydraulic properties for the equivalent porous zones are calculated based on the relative volume of roadways versus the volume of pillars in each zone using GIS analysis, and their corresponding hydraulic properties, according to Eq. 8.4.

$$\theta_{eq} = \overline{X}\% \times \theta_r + (1 - \overline{X}\%) \times \theta_p \tag{8.4}$$

with $\theta_e q$, θ_r and θ_p, the equivalent, roadway and pillar material property value, respectively, and $\overline{X}\% = \frac{Vroadway}{Vtotal}$ is the relative volume of open void in each zone.

The details of the measured length/volumes and results of the calculations for each zone are provided in (Table 8.5). I find that the proportion of open voids $\overline{X}\%$ for areas 5 and 6 averages 2.4%. This value is determined for a seam thickness of 1.6 m and does not account for the void space created in the overlying damaged zone. It is also one order of magnitude lower than the assumed goaf porosity of 25%. The resulting equivalent properties for each zone are provided in Table 8.4.

Zone	A	h	V	L_r	V_r	%	$\overline{X}$%
5 (1)	47,400	1.6	75840	1600	2011	2.65%	2.35%
5 (2)	46,142	1.6	73829	1600	2011	2.72%	2.35%
5 (3)	12,228	1.6	19566	780	330	1.69%	2.35%
6	133,000	1.6	212800	4200	5278	2.48%	2.48%

Table 8.5: Relative volume of roadways in zones 5 and 6 (Fig. 8.6). A the zone area (m), h the zone thickness (m), V the total zone volume ($A \times h$, m^3) and L_r the roadway length (m), determined from GIS analysis. The roadways/open void volume V_r (m^3) is calculated assuming a pipe area of 2 m^2. The void percentage % (i.e. equivalent porosity) in the considered zone corresponds to the ratio between the open void volume and the total zone volume ($\frac{V_r}{V} \times 100$), and $\overline{X}$% is the average void percentage for each zone type.

Recharge scenarios. The initial temperature and head distribution in the models are calculated via steady-state simulations, assuming a gradient of 30 C°/km and a constant head of -17 m. As the modeled layer extends from 250 mbgl to 370 mbgl, this corresponds to a top and bottom temperature of 16.74℃ and 20.34℃, respectively.

Due to the restricted extent of the model, a water level of -17 mBGL is considered outside the model boundary, allowing recharge into the model zone of the seam as water is pumped from the Theresa shaft. Pumping at Dawdon is assumed to maintain the water level at 25 mbgl at the Theresa shaft location throughout the 1-year simulation. A Cauchy (Type 3) boundary is used to simulate the inflow of water via:

- roadway connection $Q_r = c_r \times (H - H_b)$
- goaf connection $Q_g = c_g \times (H - H_b) \times A_n$

Where Q is the flow rate (m^3/s), c the transfer coefficient (i.e. conductance), A_n the node area, and H and H_b (m) the hydraulic heads inside and outside the model boundary, respectively. The subscripts g and r refer to the goaf and roadway, respectively.

For each planar model, the propagation rate of a thermal plume is calculated as it moves from the hydraulic recharge boundary to the pumping shaft, considering a temperature boundary of 9℃ at the active hydraulic recharge boundary. The extent of the thermal plume, steady-state pumping temperature and heat extraction rates are compared for all the planar models with different levels of simplification. This is done to investigate the possibility of modelling seams worked using both pillar-and-stalls and longwall mining approaches, and including roadways as equivalent porous media, and find an approach to best calculate the equivalent hydraulic parameters for such medium.

8.5 Results

8.5.1 Horizontal panel

Equivalent goaf material

The results from models P1 (pillars and stalls) and P2 (equivalent horizontal goaf panel) are compared to understand the effects of coal pillars on the rate of heat mining and the propagation rate of the thermal plume, for a simple worked panel (Fig. 8.1). Different hydraulic boundaries are tested, including a-b) no natural groundwater flow (i.e. impermeable boundaries), c-d) natural recharge from the right boundary (constant head H = 0 m) and e-f) regional flow/recharge from the top right boundary east (i.e. constant head H = 0 m). The recharge groundwater is assumed to enter the model at a temperature of 14.2°C, which corresponds to the initial layer temperature. For each scenario, I calculate the total average power output from each material after a 1 year-long steady-state simulation period, considering the injection of a 10°C fluid at a rate Q = 1 L/s and a pumping rate Q = -1 L/s. In addition, the transient changes in power contribution and temperature change at the monitoring point V1 are calculated over 2 years of production.

Results from the steady-state simulations suggest that the 2D goaf model (P2) provides an accurate estimate of the rate of heat mining compared to the reference pillar-and-stall model (P1) when no natural groundwater recharge is permitted (Table 8.6). Allowing for hydraulic recharge at the right and top boundaries leads to the goaf model to predict a higher end of values of heat extraction rate (-0.5 kW) relative to the reference model. After one year, the thermal plume induced by injection of a 10°C water is similar in both the pillar-and-stall and goaf models for the considered hydraulic recharge scenario (Fig. 8.8).

Power (kW)	P1	P2	P2 3D	D0
No recharge	-17.8	-17.8	-17.8	-20.2
Right recharge	-9.0	-9.5	-9.5	-20.2
Top-right recharge	-5.6	-6.2	-6.2	-

Table 8.6: Average heat extraction rate (kW) from the 170 x 580 x 10 m thick pillar-and-stall (P1), horizontal goaf (P2/P2 3D) and vertical goaf (D0) models calculated for a 1 year-long steady-state simulation period.

Transient analysis of the power contribution from the different materials moreover confirms that the greater the natural hydraulic recharge, the lower the heat depletion in the system (Fig. 8.9), suggesting that natural groundwater flow promotes heat recharge in the system. Temperature time series at V1 indicate that both the nature of the hydraulic recharge and the permeability distribution impact the propagation rate of the thermal plume. The greater the hydraulic recharge, the slower the rate of temperature decline, and therefore the longer the time to reach thermal steady-state. Although the goaf model P2 predicts a higher end of values

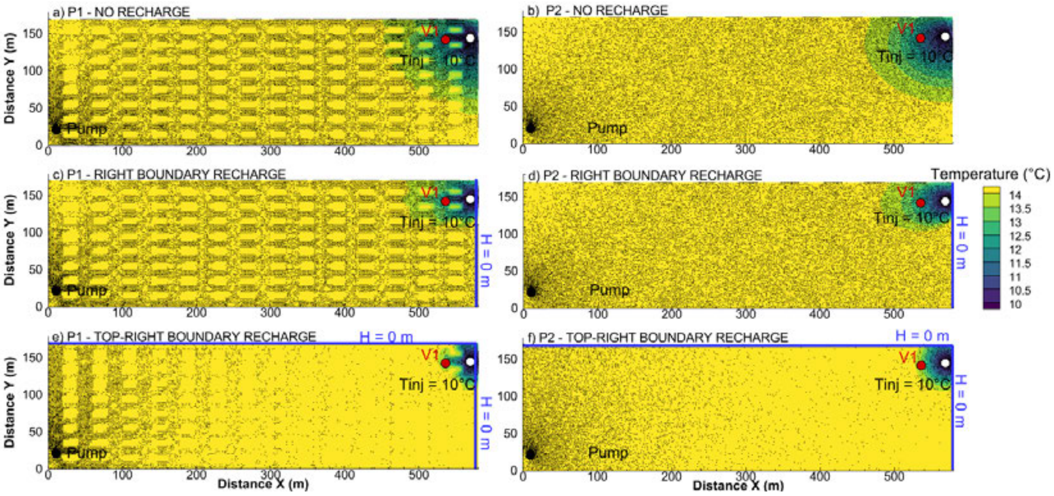

Figure 8.8: Steady-state temperature distribution after one year of pumping and injection of a 10 ℃ water in a 10 m thick pillar-and-stall panel (model P1, left) and equivalent goaf panel (model P2, right) for scenarios with no hydraulic recharge (a-b), recharge from the right boundary (c-d) and the top and right boundaries (e-f). The black arrows represent the flow vectors. Those are principally located in the stalls (voids) in the pillar-and-stall model. The flow concentration is the greatest around the pumping and injection wells.

for the heat mining effect of mine-water utilisation in transient analysis relative to P1, where the thermal plume propagates faster (i.e. within higher permeability material), similar steady-state temperatures are expected for scenarios with similar boundary conditions over time. This indicates that the groundwater recharge plays a major role in determining the sustainability of heat extraction from mine workings, although the rate of temperature change depends on the permeability of the mined materials.

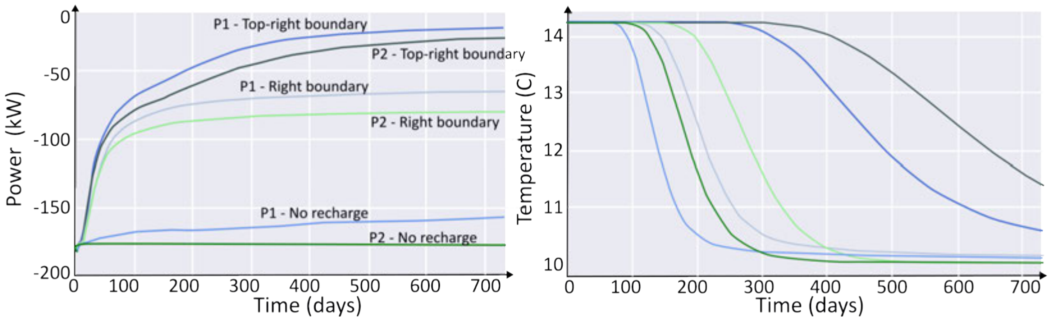

Figure 8.9: Time series of a) rate of extractable heat (i.e. power output at each time step) and b) temperature change at V1 over two years of production in the 2D vertical goaf models (D0) and the horizontal pillar-and-stall models (P1) and goaf model (P2), for scenarios with east, north-east recharge and no recharge (transient simulations).

Transposing 2D horizontal vs 2D vertical vs 3D

The temperature distribution and energy change in the 2D planar models (P1 and P2) are then compared to their 3D equivalent (P1 3D and P2 3D) and to the vertical section of the goaf panel (D0) after 1 year of production/injection (Fig. 8.1), for scenarios without groundwater recharge and recharge at the right boundary (steady-state simulations). This is done to investigate how accurately simple 2D vertical models can predict the energy change in a horizontal panel in OpenGeoSys.

Results suggest similar thermal plumes (Fig. 8.10) and power contribution (Table 8.6) between the goaf models P2 and P2 3D for all groundwater recharge scenarios, suggesting that faithful predictions of the production temperature and steady-state heat capacity can be made from the 2D goaf model. The vertical goaf model D0 however tends to predict a higher end of values for the rate of heat mining from the horizontal goaf panel P2 and be unresponsive to the nature of groundwater recharge, with a heat extraction rate of -20.2 kW calculated for both hydraulic recharge scenarios (Table 8.6). This might be explained by the fact that the propagation of the thermal plume is assumed to be homogeneous across the model in the axis perpendicular to the model plane, thereby not accounting for the circular shape of the plume around the injection point.

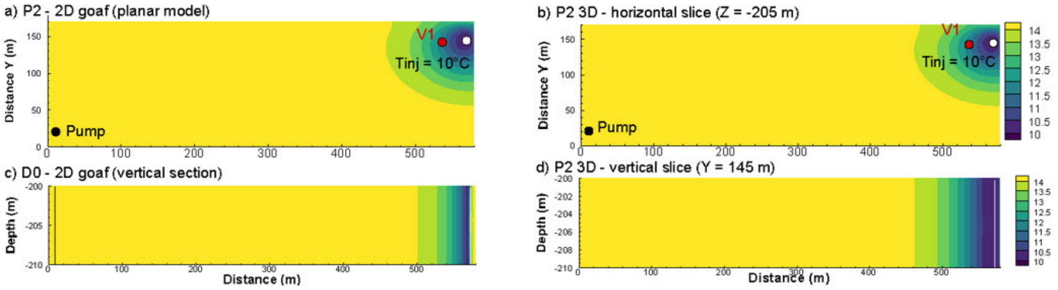

Figure 8.10: Temperature distribution after one year of pumping/injection (steady-state simulations) in the goaf material for a) the 10 m thick 2D horizontal goaf model P2, b) the 3D goaf model P2 3D (horizontal slice), c) the 2D vertical goaf model D0 and d) the 3D goaf model P2 3D (vertical slice), for a scenario without natural groundwater recharge (closed system).

Steady-state simulations of mine-water utilisation from the 2 m thick pillar-and-stall models P1 and P1 3D also result in comparable thermal plume distribution and heat extraction rate for a scenario without natural hydraulic recharge. Allowing groundwater recharge at the right boundary leads to larger discrepancies, with the 3D model predicting a higher end of values for the heat mining rate (Table 8.7). The higher uncertainties when considering recharge can be explained by the hydraulic imbalance caused by forced groundwater recharge and reinjection.

Power (kW)	P1	P1 3D
No recharge	-17.6	-17.6
Right recharge	-1.5	-7.8

Table 8.7: Rate of extractable heat (kW) from the 170 x 580 x 2 m thick pillar-and-stall models (P1 and P1 3D), calculated for a 1-year long steady-state simulation period.

Effects of overlying/underlying layers

Although 2D planar goaf models can faithfully reproduce the heat extraction rate simulated from the reference pillar-and-stall panel, they cannot account for the effects of rock layers located above/below the mine workings. Here, the results for the 2D vertical section of a goaf panel (D0) are compared to a full mine section (D1) and to their equivalent 3D models (P2 and P3) to assess the effect of the fractured zone permeability surrounding the mined coal seam (Fig. 8.2).

For a scenario without groundwater recharge, results indicate that the presence of underlying/overlying layers increases the rate of heat extraction by 1.4 - 1.5 kW. In both the 2D and equivalent 3D models, similar heat extraction rates are calculated (Table 8.8), suggesting that using a 2D vertical model with an appropriate slice thickness (i.e. width of the gallery/panel) can be used instead of a fully 3D model to assess the heat potential of a single panel with simple geometries (Fig. 8.11).

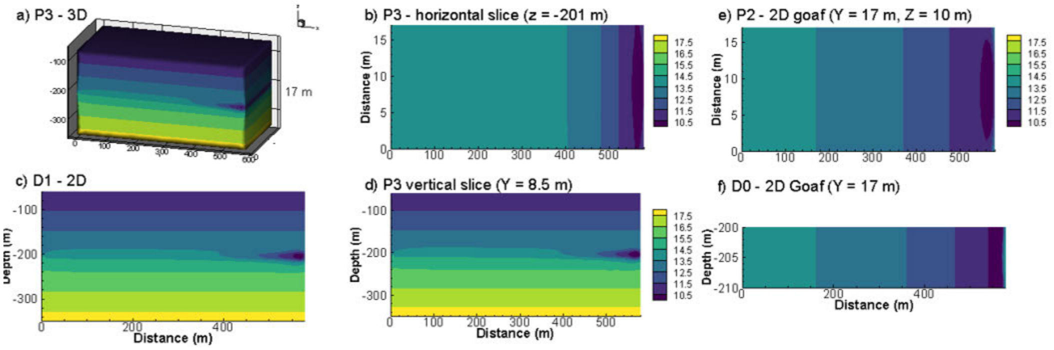

Figure 8.11: Temperature distribution after one year of pumping/injection from a 580 x 17 x 10 m goaf panel (steady-state simulations): a) 3D view of the embedded goaf panel (P3), b) horizontal slice within the caved zone (P3), c) 2D vertical mine model (D1) and d) vertical slice from the 3D model (P3), e) 2D horizontal goaf model and f) 2D vertical goaf model.

Power (kW)	D0	D1	P2	P3
No recharge	-16.5	-17.9	-16.3	-17.8

Table 8.8: Comparison of the rate of extractable heat (kW) from the 2D 17 x 580 x 10 m thick vertical goaf models (D0 and D1) and the 3D equivalent (P2 and P3), for a 1-year long steady-state simulation period (Q = 1 L/s) without natural groundwater recharge.

8.5.2 Vertical model

Permeability contrasts

Using model D1, I investigate the effects of the hydraulic conductivity and thickness of the caved and fractured/damaged zones on the thermal recovery rate in a typical mine working, considering heat injection and pumping at a rate Q = 1 L/s for 2 years. The power contribution of the mine systems is calculated for a range of caved zone hydraulic conductivity K_c and fractured zone hydraulic conductivity K_f. Results show that the heat extraction rate decreases with increasing K_f (for tested values ranging from 5 × 10^{-7} m/s to 5 × 10^{-4} m/s) and increases with increasing K_c (for tested values ranging from 5 × 10^{-4} to 2 × 10^{-1} m/s). Results reported in Fig. 8.12 reveal that for all the combinations tested, the heat extraction rate follows a similar trend depending on the contrasts in hydraulic conductivity K_f/K_c. The minimum rate of heat mining is achieved for K_f/K_c = 1 and depends on the thickness of the fractured zone; the thicker the fractured zone, the lower the power output. For high contrasts in hydraulic conductivity ($K_f/K_c > 1 \times 10^3$), the heat extraction rate reaches a maximum that mostly depends on the thickness/volume of the caved zone. In such a situation, the flow is indeed concentrated in the highly permeable material, the caved zone, with the transition between the two hydrogeological units (i.e. the caved and fractured zone) acting as a hydraulic boundary. This suggests that estimates of the power output of a longwall panel can be bounded based on estimates of the relative thicknesses and permeability contrasts between the two zones.

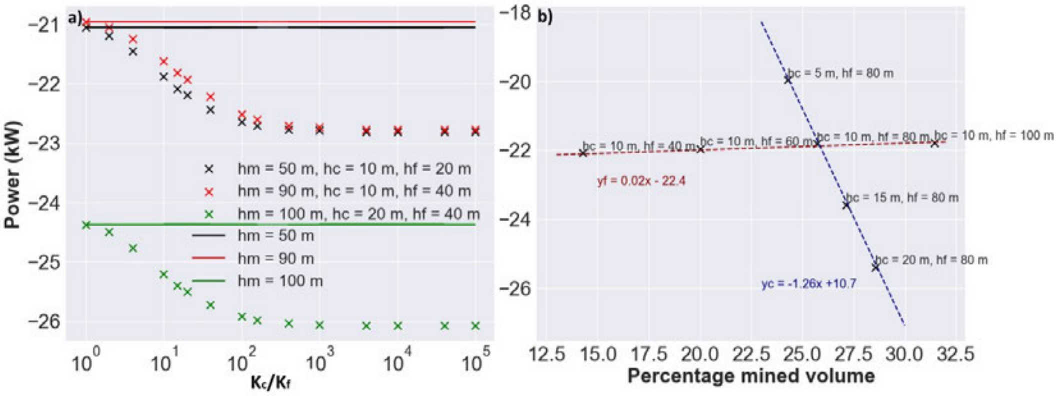

Figure 8.12: Steady-state heat mining rate from model D1 (Table 8.2) for a) a range of caved zone/fractured zone permeability contrasts and zone thicknesses and b) as a function of the percentage volume of the mined zone (right), with K_c and K_f the caved zone and fractured zone hydraulic conductivity and h_m, h_c and h_f the height of the mined area, caved zone and fractures zone, respectively. The horizontal lines represent the power output induced by the use of an equivalent hydraulic conductivity for the mined area (K_m = K_c = K_f) for different layer thicknesses. For K_m = 10^{-5} m/s to 10^{-1} m/s, the steady power output is independent of the equivalent mined area permeability.

Zone thickness and permeability distribution

I look in further detail at the relationship between the relative energy change over a year of pumping/injection and the thickness of the caved zone (i.e. 5, 10, 15, 20 m) and of the fractured zone (i.e. 20, 30, 40, 50 m), keeping the hydraulic conductivity values constant for each zone (see reference model in Table 8.2). Results suggest linear correlations between the heat extraction rate and both the caved zone (blue line) and fractured zone (red line) thicknesses (Fig. 8.12). These relationships are given as a function of the volume percentage of the mining area (i.e. caved and fractured zones) relative to the model volume. Whilst the heat extraction rate is highly sensitive to an increase in the volume of the highly permeable caved zone, this analysis confirms that an increase in the fractured zone thickness only slightly decreases the heat extraction rate.

Equivalent mining area

A series of models with an equivalent zone for the whole mining area (D2) rather than separate caved and fractured zones (D1) are finally used to understand the importance of considering the permeability contrasts around mine workings when assessing the long-term heat potential of flooded mines. In the equivalent zone, hydraulic properties are attributed so as to represent the average of the caved and fractured zone property values weighted to the relative volume of each zone (Table 8.9). Results indicate that a change in the equivalent zone permeability has little effect on the power output. Those are represented as quasi-straight lines in the left graph (Fig. 8.12). For all equivalent hydraulic conductivity values tested, the models tend to provide a similar heat extraction rate equal to the minimum power output calculated when considering permeability contrasts K_c/K_f, for a given mined area thickness. This suggests that whilst the permeability contrast between the caved and the surrounding fractured zone plays a major role in determining the rate of heat extraction, the total thickness of the mining area (i.e. the high-permeability caved and fractured zones) can provide an initial assessment of the minimum rate of heat extraction from the reservoir. Further tests to determine the permeability contrast between the two zones are however necessary to avoid underestimating the heat mining rate, especially if K_c/K_f is situated in the 10^0 - 10^2 range (Fig. 8.12).

Multi-element model

Short-circuiting is often considered the main production risk in mine water heat schemes. In opposition to flow in goaf material, where the lower permeability reduces the hydraulic velocities and enhances the heat mining from the rock, high-permeability channels between the injection and production wells (e.g. tunnels, roadways) can prevent efficient thermal recovery and result in the arrival of the cold water at the pump. Although it is considered to be adequate for large-scale analysis Hamm and Bazargan Sabet (2010); Renz et al. (2009), modelling the 3D open voids network using the equivalent porous media approach can be complex and

K_c (m/s)	K_f (m/s)	K_c/K_f	Eq 50 m (m/s)	Eq 90 m (m/s)	Eq 100 m (m/s)
5×10^{-4}	5×10^{-4}	1	5×10^{-4}	5×10^{-4}	5×10^{-4}
1×10^{-3}	5×10^{-4}	2	6×10^{-4}	5.56×10^{-4}	6×10^{-4}
2×10^{-3}	5×10^{-4}	4	8×10^{-4}	6.67×10^{-4}	8×10^{-4}
7.73×10^{-3}	5×10^{-4}	15	1.95×10^{-3}	1.30×10^{-3}	1.95×10^{-3}
1×10^{-2}	5×10^{-4}	20	2.40×10^{-3}	1.56×10^{-3}	2.40×10^{-3}
5×10^{-2}	5×10^{-4}	100	1.04×10^{-2}	6×10^{-3}	1.04×10^{-2}
8×10^{-2}	5×10^{-4}	160	1.64×10^{-2}	9.33×10^{-3}	1.64×10^{-2}
5×10^{-4}	5×10^{-5}	10	1.40×10^{-4}	1×10^{-4}	1.40×10^{-4}
2×10^{-3}	5×10^{-5}	40	4.40×10^{-4}	2.67×10^{-4}	4.40×10^{-4}
2×10^{-2}	5×10^{-5}	400	4.04×10^{-3}	2.27×10^{-3}	4.04×10^{-3}
2×10^{-2}	5×10^{-6}	4000	4×10^{-3}	2.23×10^{-3}	4×10^{-3}
2×10^{-1}	5×10^{-6}	40000	4×10^{-2}	2.22×10^{-2}	4×10^{-2}
5×10^{-4}	5×10^{-7}	1000	1×10^{-4}	5.60×10^{-5}	1×10^{-4}
5×10^{-3}	5×10^{-7}	10000	1×10^{-3}	5.56×10^{-4}	1×10^{-3}
5×10^{-2}	5×10^{-7}	100000	1×10^{-2}	5.56×10^{-3}	1×10^{-2}

Table 8.9: Hydraulic conductivity values used for the transient analysis of temperature and energy change in D1 over 2 years

geometrical simplifications are generally required Andrés et al. (2017). 1D elements have been used in the past to represent the open voids in flooded coal mines (i.e. shafts, tunnels), assuming linear flow defined by the Darcy law (Raymond, 2018) or turbulent pipe-flow (Adams & Younger, 2001; Renz et al., 2009).

Here, the heat distribution around a single roadway using the porous and multi-element approach is compared. The aim is to understand to what extent the multi-element approach can simplify the large-scale modelling of interconnected mining void networks and the computational efficiency of flow and heat transport modelling with OGS, relative to a porous media approach. The multi-element model consists of 1D line elements representing a tunnel having similar properties as the caved zone, embedded in a 2D porous media corresponding to the continuous zone (Table 8.2). In both models, the thermal plume and power output resulting from 732 days of pumping and injection of a 10℃ fluid are compared. The energy time series shows that over the long term, the multi-element model can faithfully calculate the power output obtained from the porous model, although discrepancies in the thermal plume can be observed in the continuous media around the tunnel (Fig. 8.13). The thermal plume is indeed more localised in the multi-element model than in the porous model, which can be explained by the smaller number of nodes involved in the tunnel material group relative to the caved zone in the porous model. The simulation output log for the multi-element model moreover indicates a computational time x 1.5 the one for the porous model. This suggests that although the use of 1D elements simplifies the model development, it increases the computational cost, which might represent a major limitation for large-scale mine modelling applications.

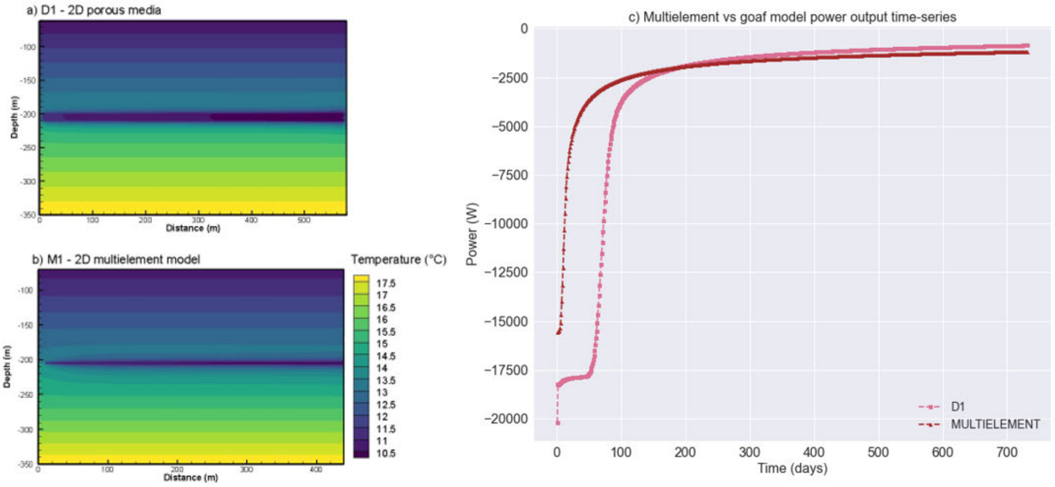

Figure 8.13: Temperature distribution in a) the porous (D1) and b) multi-element (M1) model (steady-state simulation). c) Time series of heat extraction rate in both models, considering a model area A = 170 m and a pumping/injection rate Q = -1 L/s (closed system).

8.5.3 Dawdon model

Based on the preliminary analysis, I then investigate the effect of geometrical simplifications on the sustainable heat extraction rate from mine-water reservoirs for more complex mine geometries, using the example of the Dawdon High Main Seam workings, NE England Coalfield. A combination of porous and multi-element models is used to find the optimal numerical approach to model flooded mine workings, i.e. an approach that optimises the model development/simulation time and provides relatively accurate estimates of the large-scale heat potential.

For each model described in section 8.4.3, I consider the inflow of a 9 ℃ groundwater at the boundary of the Dawdon seam E via a roadway connection (to the external section of the Dawdon mine model) or goaf connections (to neighbouring collieries). According to the mine plans NZ4247 (TCA data), unmined coal is separating the Dawdon seam E to the Seaham E seam on the West. However, the goaf connection is used here to investigate the potential effect of leakage through fractured boundaries between collieries. The inflow temperature is chosen to get a clear picture of the thermal plume induced by the arrival of colder water relative to the initial mined seam temperature, assuming that mine water and the surrounding rock are at equilibrium (19.11 ℃). This simulation does not aim at representing the real conditions, the relative contribution of different sources of water (i.e. surface rainfall recharge, deep recharge or drainage from the overlying aquifer) being uncertain. Further work beyond the scope of the study should be undertaken to assess the nature and rate of hydraulic recharge as well as the extent of mixing between the seams, to better predict the long-term effect of pumping on the temperature distribution in the colliery.

Following a 1-year transient simulation period, results indicate that the thermal plume induced by the inflow of colder water is similar for all four models for a given recharge scenario (Fig. 8.14), considering the properties detailed in Table 8.4. Visual inspections do however not provide quantitative information on the relative effect of the different geometrical simplification levels on the heat extraction rate. For each model, the relative energy change calculated within each material type, i.e. the goaf, roadway, pillars, and equivalent porous areas is compared.

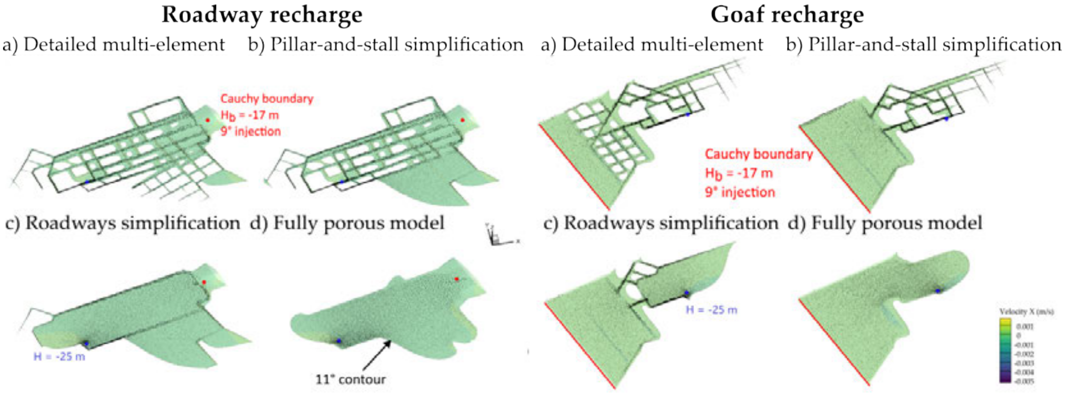

Figure 8.14: Comparison of the thermal plume (11 °C contours) in the Dawdon seam E models a, b, c and d, induced by the injection of a 9 °C water, assuming hydraulic recharge via roadway connections (left panel) and goaf connection (right panel).

The time series of energy change displayed in Fig. 8.15 show the relative power contribution from each material resulting from the inflow of colder water in the mine working due to pumping. The analysis suggests that in the long-term, most of the heat is sourced from the host rock, with the heat mining rate being higher when recharge is provided through roadway connections (i.e. -0.6 $\times$ 10^6 W, against -0.5 $\times$ 10^6 W for the goaf recharge scenario). A large proportion of heat is also recovered from the unmined pillars in the initial days of pumping, especially in the roadway recharge scenario. However, their relative contribution decreases as the model complexity decreases (i.e. model a to d). This is a reasonable observation, as the proportion of the material type 'pillar' reduces as the level of geometrical simplification increases and the pillars are merged with roadways to form the equivalent porous media zones 5 and 6 (Fig. 8.7). The contribution from the roadways and goaf material to the heat recovery is the greatest in the initial 100 days of pumping and becomes negligible in the long term. It moreover depends on the nature of hydraulic recharge, with the power contribution from the roadways in the early stage of pumping being higher in roadway recharge scenarios, and the goaf material being mostly sensitive to heat extraction in the goaf recharge scenarios.

Similarly, the relative contribution from the equivalent porous zones 5 and 6 depends on both the level of simplification and the nature of hydraulic recharge within the first 250 days of pumping. The most notable difference is the larger heat extraction rate from zone 5 (i.e. equivalent pillar-and-stall zone) in the goaf recharge scenario. This can be explained by the presence of zone 5 between the recharge zone (goaf boundary) and the pumping shaft.

Similarly, the heat extraction rate from zone 6 (equivalent roadway zone) is the greatest in the roadway recharge scenario, as this zone represents the main recharge pathway from the roadway connection to the pumping shaft. In the fully porous model d, the power output from the pillar-and-stalls equivalent zone (zone 5) is significantly larger than in the other models in the roadway recharge scenario, whilst the contribution from the roadway equivalent zone (zone 6) is the highest in the goaf recharge scenario.

For a given hydraulic recharge scenario, the models however suggest that the long-term heat extraction rate and pumping temperature are broadly similar irrespective of the complexity of the model geometry (see bottom panel in Fig. 8.15). This highlights a potential for simplification of the geometry of flooded mines in long-term modelling studies.

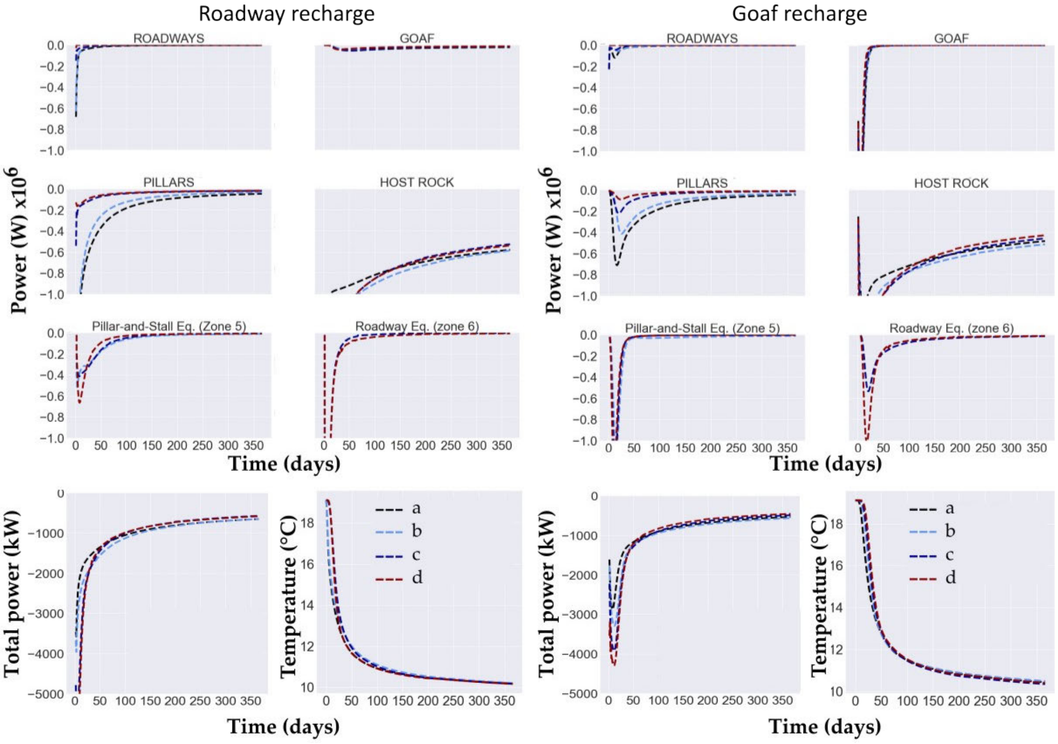

Figure 8.15: Time series of energy change induced by the injection of a 9°C water in the Dawdon Seam E models (a, b, c and d) with different levels of simplifications. The left and right panels depict the relative energy change in each material (roadways, goaf, pillars, etc), assuming hydraulic recharge via roadway connections and goaf connections, respectively.

A sensitivity analysis is then performed to compare the effect of the permeability of the equivalent porous zones on the power output and pumped temperature of each simplified model (b - d), against the outputs from the reference detailed model (a). Hydraulic conductivity values ranging from 2.4 $\times$ 10^{-3} m/s to 7.4 $\times$ 10^{-1} m/s are attributed to both zone 5 (simplified pillar-and-stall zone in models b and d) and zone 6 (simplified roadway zone in models c and d). The analysis detailed in Appendix A.7 suggests that the equivalent hydraulic conductivity of zones 5 and 6 has a negligible impact on the heat extraction rate from the different materials, or is in most cases limited to the short-term (i.e. within the 100-200 first days of pumping). In a roadway recharge scenario, the long-term heat recovery rate from the host rock is on the other hand highly sensitive to the equivalent hydraulic conductivity of the roadway zone (zone 6, Fig. A.59) and to a lower extent of the pillar-and-stall zone (zone 5, Fig. A.58). This, however, does not have a significant effect on the overall long-term heat recovery potential from the mine, with a similar power output being reached for each model independently of the equivalent zones permeability (Figs. A.60 and A.63).

To assess the simplified models in comparison to the reference model a, I then calculate the percentage difference in both the total power output and final pumped temperature (detailed in Fig. A.64) for each simplified model relative to the reference detailed model, under both hydraulic recharge scenarios (Fig. 8.16).

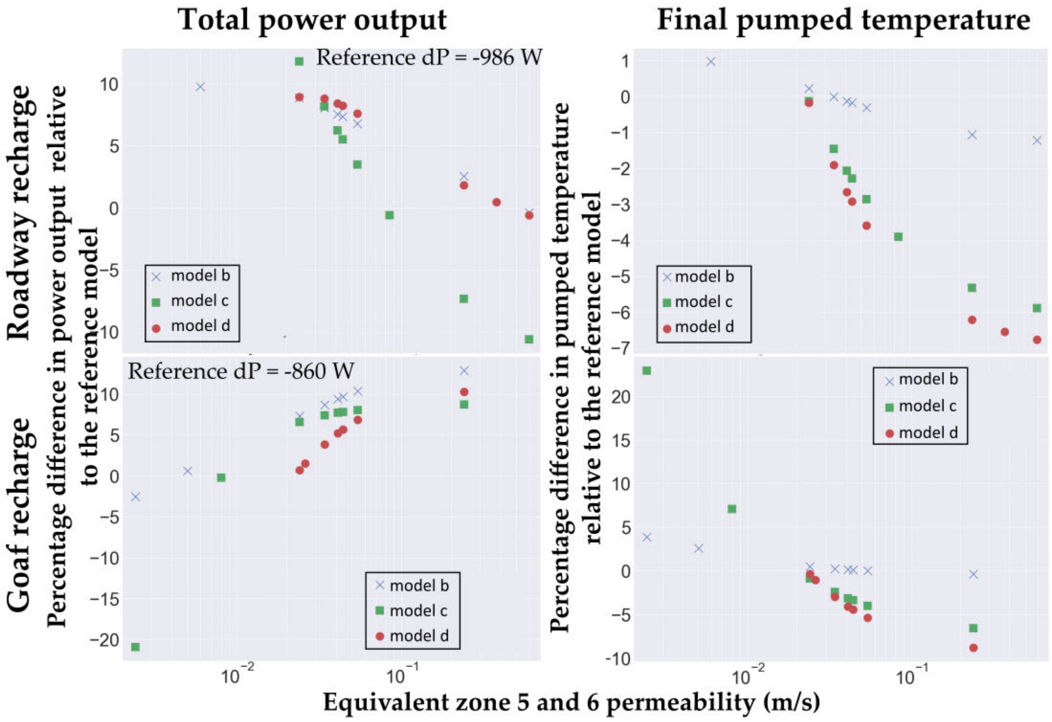

Figure 8.16: Sensitivity analysis of the steady-state power output and final pumped temperature to the equivalent porous zone hydraulic conductivity. The plots display the relative difference in power and temperature between the simplified models b (pillar-and-stall simplification via zone 5), c (roadway simplification via zone 6), and d (fully porous model) and the reference detailed model a, for both the roadway (top row) and goaf (bottom row) recharge scenarios.

Results suggest that the best-fit final pumped temperature (i.e. where the temperature difference between the reference and simplified models is zero) is obtained for all scenarios for an equivalent hydraulic conductivity of 2.4 × 10^{-2} m/s. For such an equivalent hydraulic conductivity, discrepancies in the power output between the simplified and the reference model of up to 7% are observed in the goaf recharge scenarios (for model b), whilst discrepancies of about 8% are observed for the roadway recharge scenarios. Overall, the relative difference in power output from the simplified models tends to increase with increasing permeability in the roadway recharge scenario and with decreasing permeability in a goaf recharge scenario. As a result, the best-fit power outputs are obtained for equivalent permeabilities ranging between 5×10^{-3} m/s (model b) and 2.4×10^{-2} m/s (model d) for the goaf recharge scenario and between 8.5×10^{-2} m/s (model c) and 0.6×10^{-1} m/s (model b and d) for the roadway recharge scenario. As mentioned before, this suggests that the fully porous model (model d) can provide a relatively good approximation of the long-term heat recovery potential of more complex models.

8.6 Discussion

8.6.1 Porosity and mined volume

The heat capacity of mines is generally assumed to be related to the amount of water-filled void, which can be calculated as follows:

$$V_{void} = N_w \times A \times h_w \times f$$

where N_w is the number of seams, A and h_w are the area and thickness of the worked seams, respectively, and f is a factor accounting for subsidence and compaction ($f < 1$). Jessop (1995) suggested that in both longwall and pillar-and-stall mining areas, the residual void volume is in the order of 25%, while Malolepszy (2003) considered that 5 - 40% of the initial volume of the mined space generally remains open, depending on the mining method employed. In pillar-and-stall workings, pillars and open spaces are generally left in place, and only small and local convergence of the roof/floor is expected. Debris resulting from roof falls are found on the floor and are assumed to be compensated by the creation of voids in the roof. For P. Younger and Robins (2002), 50% of mining voids are therefore likely to remain open if no collapse occurs. A recent study however suggested that collapsed pillar and stall workings in abandoned coal mines in the UK are highly heterogeneous and potentially clay-rich, as a result of the collapse process (B. J. Andrews et al., 2020). Although the overlying fractured zone could potentially enhance the flow pathway, the permeability of the collapsed material would progressively degrade over time. In longwall mining, the formation of goaf and the convergence of the roof/floor strata tend to fill the caved zone and reduce the void volume in the workings Vervoort (1988); Whittles, Lowndes, Kingman, Yates, and Jobling (2006). Over time, the permeability of the goaf material reduces as it is compacted by the overburden (Esterhuizen & Karacan, 2005, 2007). Gillespie et al. (2013) suggested that about 20% of the mine voids remain after subsidence above longwall panels, while P. Younger and Adams (1999) attributed to goaf a porosity of 30% after subsidence and fracturing. K. R. Whitworth (2002) considered that residual void volume in the longwall mining area represents 10% of the extracted height in areas of total extraction.

Results from this study showed that the minimum and maximum power output from a longwall mine working can be constrained based on estimates of the total thickness of the caved and fractured zones, considering an average permeability for the equivalent zone. However, the permeability contrasts between the two zones play a key role in determining the rate of heat extraction from the reservoir over the short term. Using model D1, I here discuss further the potential effect of the caved zone porosity on the heat potential of a mine-water system. Results from a series of steady-state simulations indicate that the initial heat capacity of the mine slightly increases with increasing caved zone porosity, as the heat capacity of the water ρc is higher than the volumetric rock heat capacity (Fig. 8.17). However, an increase in the porosity from 20% to 80% results in an increase in extractable power of less than 1 kW (i.e. -21.2 kW for ϕ = 20% and -22.1 kW for ϕ = 80%), which is limited compared to the effect of a change in the volume of the mined area (i.e. 5 kW for a percentage increase in mined volume of 5%; Fig. 8.12).

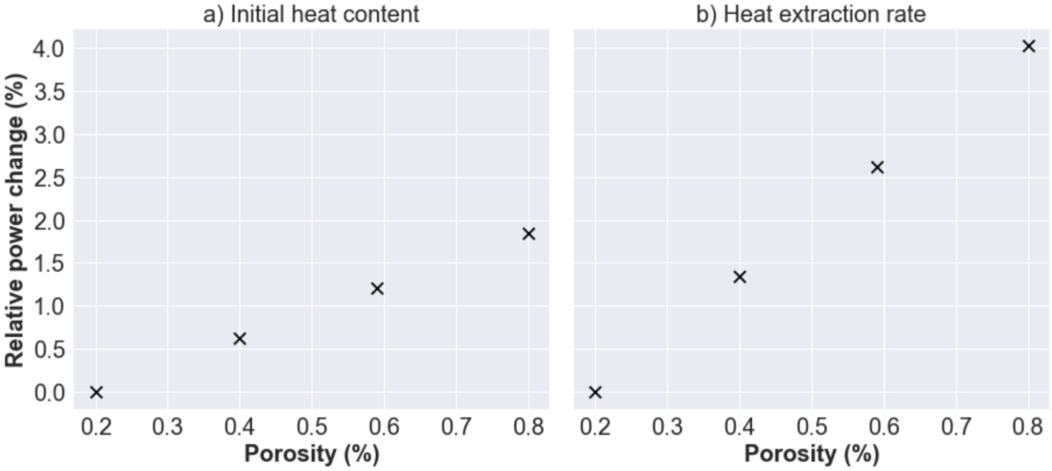

Figure 8.17: Relative change in a) the initial heat capacity and b) the rate of extractable heat from the vertical goaf model D1, for different caved zone porosity. The heat content and heat extraction rate both increase linearly with increasing caved zone porosity.

8.6.2 Heat mining versus production temperature

Fluid flow through the less-permeable fractured zone was demonstrated in this study to be the main mechanism of heat recovery in the long term, depending on the nature of hydraulic recharge (i.e. regional groundwater regime, reinjection). Whilst the volume of the mining area determines the maximum extractable heat, the permeability contrasts between the different mining zones (i.e. caved, fractured zones) and/or mine infrastructures (i.e. roadways, goaf) tend to control the heat extraction rate in the short-medium term. Although those properties also affect the rate at which the thermal plume propagates, temperature time series at the monitoring point V1 indicated that for all scenarios, similar production temperature is eventually reached over the long term, suggesting that the steady-state production temperature does not reflect the sustainable rate of heat extraction from mine-water reservoirs.

To better understand the short versus long-term relationship between the rate of temperature change and the rate of heat mining in a closed system (i.e. no natural groundwater recharge), I look further into the transient change in temperature at the observation point V1 (see section 8.5.2) for a range of hydraulic conductivity contrasts K_c/K_f ranging between 10^0 and 10^6 (Table 8.9). Results obtained for a 2-year-long pumping and heat injection period (at a rate Q = 1 L/s) show that:

- For K_f > 1×10^{-5} m/s - 1×10^{-4} m/s (K_c/K_f < 5×10^2 - 5×10^3), the higher the fractured zone hydraulic conductivity K_f, the smaller the decrease in temperature at V1. However, it increases/decreases the heat mining rate for a model area A = 1 m^2/A = 170 m^2, respectively. The trend in temperature change and heat mining rate is reversed at K_c/K_f = 5×10^2 - 5×10^3.
- For K_c > 5×10^{-3} m/s - 5×10^{-2} m/s (K_c/K_f > 1×10^1), the higher the caved zone hydraulic conductivity K_c, the greater the temperature decline at V1. However, it decreases/increases the heat mining rate for A = 1 m^2/A = 170 m^2, respectively. The trend in temperature change is reversed at K_c/K_f = 1×10^1 - 1×10^2. As K_c/K_f reaches 1, the extractable power reaches its maximum.

The temperature decline at V1 is limited for K_c/K_f = 1 and increases with increasing K_c/K_f, reaching a maximum of about -2°C for K_c/K_f > 100 – 1000, depending on the thickness of the 2D model slice (Fig. 8.18a). Fig. 8.18b shows that the heat extraction rate is positively correlated to the temperature decline at V1, as observed in Fig. 8.12. The heat extraction rate reduces with an increase in permeability contrasts, as a reduction of the permeability of the caved zone prevents mine-water flow. This confirms that the rate of heat extraction from mines is controlled by the permeability contrasts between the highly permeable mining features (i.e. tunnel) and the surrounding (fractured) zone. The permeability contrasts influence the

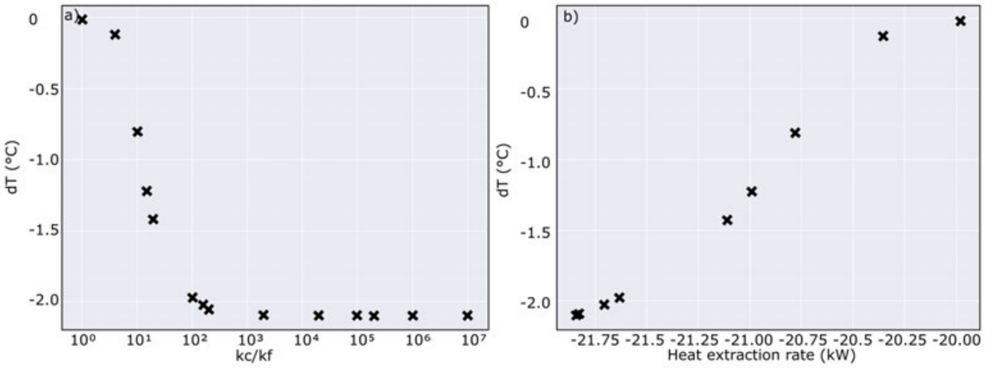

Figure 8.18: Temperature change at V1 as a function of a) the hydraulic conductivity contrasts K_c/K_f and b) the heat mining rate, for a model area A = 170 m after 2 years of pumping/injection at a rate Q = -1 L/s in a closed system (transient simulation).

rate at which hydraulic and thermal steady-states are reached in the system, suggesting the importance of using transient modelling to understand the short to medium-time scale dynamic behaviour of groundwater flow and heat extraction from mines. This is mostly relevant when results from short-term pumping tests are to be analysed.

In the Dawdon model, the divergence in the power output and pumped temperature between the detailed and simplified models is moreover higher in the goaf recharge scenario. This suggests that the nature of hydraulic recharge (i.e. source/temperature of water) and the recharge pathways (i.e. goaf or roadways) highly impact the dynamic of heat recharge and rate of heat recovery (i.e. water residence time, area available for fluid-rock interactions between the recharge and abstraction zone, groundwater flow velocities).

8.6.3 Model simplification, scale of analysis and equivalent porous media estimates uncertainties

When developing large-scale models, accounting for the detailed geometry and permeability contrasts in mines is time-consuming and highly uncertain, due to the many unknowns in the structure and hydrogeology of those systems. In this study, I compared models of the Dawdon High Main seam with different levels of simplifications to understand the extent to which the mine geometry can be simplified whilst allowing for a relatively accurate estimate of the long-term heat extraction potential.

In the reference Dawdon model, roadways have been modelled as 1D elements (i.e. open pipes) between unworked coal (pillars) or goaf panels rather than porous materials with different permeability/porosity values as in the preliminary analysis. After simplification of each pillar-and-stall and roadway zone, the results showed that most of the discrepancies between the detailed models and the simplified versions occur within the first 200 days of pumping, after which the heat extraction rate reaches a similar value in all material groups. This suggests that although the architecture of the mine tends to impact the propagation rate of the plume and rate of extractable heat in the vicinity of the borehole in the short term, most of the heat will be sourced from the surrounding goaf/fractured host rock in the long-term, where the exact connectivity of roadways will have less impact. Hence, the level of model complexity required highly depends on the mine extent and time scale of the analysis, with short-term models needing to be more geometrically complex. As mentioned previously, the nature of hydraulic recharge (i.e. the source and temperature of the water entering the seam) will be a determinant factor controlling the heat recovery rate, by either promoting recharge or mining of the host rock.

Estimating the relative proportion of void in each zone however highly depends on the accuracy of the mine plans and the method employed. In this analysis, I presented results for an estimated average void percentage of 2% (i.e. average of the ratio of open void within each equivalent permeability zone). Here, those results are compared to a void percentage of 4%, which represents the highest estimate based on the analysis of the mine plans, accounting for the roadways within and surrounding each mining area.

Results suggest that both temperatures and power fit best when considering the minimum estimates of 2% void. Assuming a 2% void ratio, the discrepancies in power output and monitoring temperatures in model b relative to the detailed model a reach -9.0% and 0.2% in a scenario with roadway recharge and -0.7% and 0.4% in a scenario with goaf recharge, respectively (Fig. 8.19). Assuming a 4% void ratio, the discrepancies in power output and monitoring temperatures in model b relative to the detailed model a reach 5.6% and 2.7% in a scenario with roadway recharge and 10.9% and 4% in a scenario with goaf recharge, which is about 10 times those observed in the 2% void ratio scenario. When considering equivalent porous zones with 4% voids, the pumped temperature significantly drops in models c and d relative to models a and b, suggesting an overvaluation of the hydraulic conductivity of zone 6 (i.e. short-circuiting).

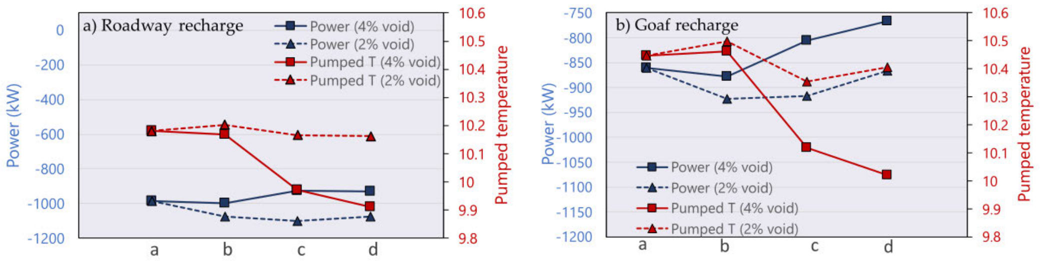

Figure 8.19: Comparison of the steady-state power output and pumped temperature (℃) for each model assuming equivalent porous zones with 2% and 4% voids, in scenarios with a) roadway recharge scenario and b) goaf recharge.

8.6.4 Models limitations and stability

The Courant (Eq. 4.52), Neumann (Eq. 4.53) and Peclet (Eq. 4.54) criteria described in Chapter 4 are used to assess the hydraulic and thermal stability of the detailed Dawdon model. This model assuming hydraulic recharge via roadway connection is chosen as it is assumed to be subject to the highest flow rates and therefore the highest risk of instabilities.

The thermal properties for the rock defined in Table 8.4 and for water (i.e. λ_w = 0.6 W/°C.m), ρ_w = 1000 kg/m^3 and c = 4184 J/°C.kg) are used to calculate the thermal diffusion coefficient D_m (Eq. 4.42). Considering a porosity ϕ = 1, the maximum Darcy velocity of 2.2 $\times$ 10^{-4} m/s calculated in the roadways equals the advective velocity v, so the dispersion $D = \alpha|v| + D_m$ = 6.6 $\times$ 10^{-4}. Using the model dispersion coefficient α = 3, the highest mesh resolution Δx = 6 m, and a time step length Δt of 86400 s, I find that C_o = 6.3, N_e = 3 and P_e = 2.

Although the Courant (spatial dispersivity) and Neumann (temporal dispersion) criteria are slightly above the expected values, the instabilities are concentrated within the roadways in the close vicinity of the pumping locations, which does not reduce the reliability of the model away from it where the velocities are largely reduced. Those spatial and temporal dispersions could be reduced by decreasing the length of the time steps or increasing the mesh density within the pumping shaft.

In this analysis, Darcy flow equations are used to solve for groundwater flow in both the porous materials representing the pillar-and-stall, goaf and surrounding fractured/porous rock. In some cases, roadways intersect the worked panels, and most of the flow will be concentrated along those open pipes, provided they connect the reinjection/recharge zone to the pumping borehole. This might lead to the development of turbulent flow and disturb the linearity of heat transfers between the fluid and surrounding rock, as highlighted by e.g. N. Burnside et al. (2016); Hamm and Bazargan Sabet (2010); Wolkersdorfer (2008). However, further work would be required to identify the impact of heat transfer in a non-linear/turbulent flow regime, via the implementation of e.g. Forchheimer equations.

8.7 Conclusion

This study lends insights into the complex link between the hydraulic properties and heat recovery potential from different mine features (i.e. roadway/tunnel, goaf, fractured area). Overall, it demonstrates that the importance of knowing the distribution of the mining voids in a mine working reduces as the time scale of the analysis increases, with the extent of damage zone around the galleries playing a key role in determining the long-term heat recovery rate. A conceptual model for the assessment of the long-term heat recovery potential from mine-water systems is discussed in Chapter 9, based on the following findings:

- Pillar-and-stall panels can be modelled as a porous goaf material with an equivalent permeability/porosity. In complex models, defining an equivalent porous media in the vicinity of the abstraction borehole, where the effect of local heterogeneities reduces over the long term, allows simplifying the modelling approach whilst providing a similar estimate of the rate of recoverable heat relative to more complex models. In the long term, most of the heat is sourced from the host rock, which controls the sustainable heat extraction rate, depending on the nature of hydraulic recharge. Discrepancies are greater in the short-term (i.e. pumping test time scale), where a proper assessment of the relative void volume and pathways between the inflow and pumping zones is essential.
- The thickness of the mined area and the caved zone guide the minimum and maximum recoverable heat from the mine-water reservoirs to an extent that depends on the initial heat content and the nature of hydraulic recharge. Although the proportion of open void determines the initial heat capacity of a mine (i.e. available water), the total volume of the mining area can be used to predict the minimum long-term heat recovery rate resulting from pumping/injection, assuming an equivalent permeability zone.
- The permeability contrasts between the highly permeable caved zone and the fractured zone control the heat extraction rate from mine-water reservoirs. Whilst high fractured zone permeability promotes heat recovery via increased fluid/rock interactions, high caved zone/tunnel permeability favours short-circuiting between the injection and pumping wells that favours heat mining. Using an equivalent hydraulic conductivity for the whole mining area $(K_c/K_f = 1)$ neglects potential short-circuiting effects and therefore provides the minimum rate of extractable heat from the system.
- Vertical models are essential to account for the effect of overlying and underlying layers, but require appropriate scaling for the mine extent perpendicular to the model plan to prevent overestimating the heat mining rate.
- The steady-state production temperature is not representative of the heat mining rate within mines, although the rate of temperature decline is positively correlated to the rate of heat mining. This mostly depends on the permeability of the material, the initial volume/heat capacity of the mine, and the regional hydraulic conditions.

Chapter 9

Discussion

9.1 Introduction

This chapter summarises the key findings of this study based on a comparative analysis of the results from the different chapters. Three research questions are discussed in sections 9.2, 9.3 and 9.4:

- What are the main heat sources controlling the mine-water temperature in flooded coal mines? (Chapters 3, 5 and 6)
- What are the main heat extraction/recovery mechanisms during pumping and water rebound? What is the impact of past mining activities on the thermal state and temperature distribution in mines? (Chapters 6 and 7)
- What are the key features controlling steady-state heat potential and long-term dynamic heat recovery in mines? (Chapter 8)

9.2 Temperature distribution in flooded shafts

The three hypotheses tested are:

- H6-1: The rock permeability, heat conductivity, pumping rate and recharging water temperature control the rate of heat extraction and recovery
- H6-2: During production, heat is mainly transferred via advective mine water in tunnels and horizontal conduction in goaf
- H6-3: Thermal balance can be reached for a low extraction rate, and the footprint area is mainly dependent on the thermal conductivity of the host rock.

9.2.1 Observed and modelled MWT

A combination of data and numerical analysis has been used to understand the key controls on the temperature measured in mine shafts accessing abandoned collieries in the UK. Results suggested an important variability in the temperature distribution in shafts attributed to the hydraulic state of the coalfield/MWB (Table 3.2), and the nature of hydraulic recharge (e.g. deep warm water recharge or shallow surface recharge).

Overall, a good linear correlation was found between the average profiling MWT and mean profiling depth. This linear relationship was the strongest for pumped shafts, with a gradient of 26℃/km. A lower gradient of 23.5℃/km was calculated for data collected in monitoring shafts, although Yorkshire shafts depict relatively cooler temperatures at greater depths, which could interpreted as a a slower return to thermal equilibrium or the effect of cold water recharge. In rebounding coalfields, where a larger range of temperature is observed at a given depth interval, a lower gradient of 17.2℃/km has been calculated. On the other hand, no clear correlation was observed for discharging shafts, whilst monitoring shafts in the pumped North-East, Nottinghamshire and Fife coalfields all depict an average temperature of around 14℃ independently of the measured depth range. An exception can be made for a set of temperature measurements in unpumped shafts in NE coalfields, that depict a gradient of 22.5℃/km (Fig. 3.30). The numerical approaches allowed attributing these relationships to the combined effect of the local geothermal gradient, the seam depths, the strata dip, the status of the coalfield and the nature of hydraulic recharge.

A comparison between the monitoring data and the modelling results is presented in Figs. 9.1 and 9.2, and is described in the following sections.

Pumped shafts

Active treatment schemes have been implemented at a few sites across the UK by The Coal Authority to prevent the discharge of mine water at the surface. These involve the implementation of pumping, generally from shallow depth to reduce the operating costs. Pumping water from the mine generally significantly alters the geothermal gradient (i.e. commonly reduces the apparent geothermal gradient in pumped shafts and encourages turbulent flow and water mixing in the shaft (i.e. forced heat convection), which can destroy density-related stratification in wells and reduce the water quality (N. Burnside et al., 2016; Hamm & Bazargan Sabet, 2010).

Temperature profiles measured in pumped shafts by The Coal Authority generally display greater temperatures in the upper part of the shaft, with temperature shifts observed at the inferred pumped depth, whilst the temperature below 200 - 300 m (i.e. in the bottom half of the shaft) is generally lower than predicted by the geothermal gradient. At the depth of the deepest seam or shaft bottom, the MWT tends to equal the temperature predicted by the local geothermal gradient. Numerical analysis showed that the pumping depth controls the temperature distribution in the pumping shaft. The flow of warmer temperature up to the pump location (in shallow pumping scenarios), and the temperature steps at the seam insets and at the bottom shaft temperature were all successfully reproduced through numerical modelling (Fig. 9.1). Modelling results revealed that at equilibrium, the shifts in the convective cells to temperatures higher or lower than the average temperature predicted by the geothermal gradient in the mining area highly depend on the dip of the strata, which allows the mixing of waters with greater or lower temperatures, and on the nature/source of hydraulic recharge. Before equilibrium, the seam permeability and the permeability contrasts between the caved zone and surrounding damaged zone tend to control the hydraulic flow and therefore, the rate at which the temperature returns to an equilibrium. Better fits were obtained when allowing coupling between the hydraulic and thermal processes, with uniform temperatures successfully modelled in the areas above and below the mining area. However, it is important to note that the models assume fully saturated media, and therefore the temperature above the pump, where partial dewatering might occur in reality, should be interpreted carefully.

Deep pumping (i.e. below the mining area) was also simulated to understand the effect of past dewatering activities on the temperature distribution and potential long-term disturbances of the rock temperature in active and recovering mines. In those scenarios, cooling is generally observed in the mining area interval as cold water is dragged from the surface to the pump.

Unpumped shafts

Depending on the extent of the connectivity between shafts via mined seams, pumping was found to influence the temperature distribution in local unpumped monitoring shafts. At steady-state, the modelled temperature profiles for a scenario with horizontal seams equally contributing to the flow (e.g. same permeability) depict regular temperature steps at the seams insets, that tend to follow the undisturbed geothermal gradient (Fig. 9.1). Although available unpumped temperature profiles from UK coalfields depict a relatively narrow range of temperature across the shaft depth interval (e.g. Langton, Nicholson, Hawthorn), the temperature at the seams insets shifts towards either higher or lower temperatures relative to the undisturbed gradient. This was interpreted to result from the effect of the nature of hydraulic recharge, on the hydraulic/thermal equilibrium state of the block at the time of acquisition or from the seam geometry (e.g. dipping layers). Those hypotheses were validated through numerical models, that showed that dipping seams are likely to impact the extent of deep versus cold shallow recharge and the extent of the mixing intervals in the monitoring shaft, which also depends on the depth of pumping in the pumped shaft it is connected to.

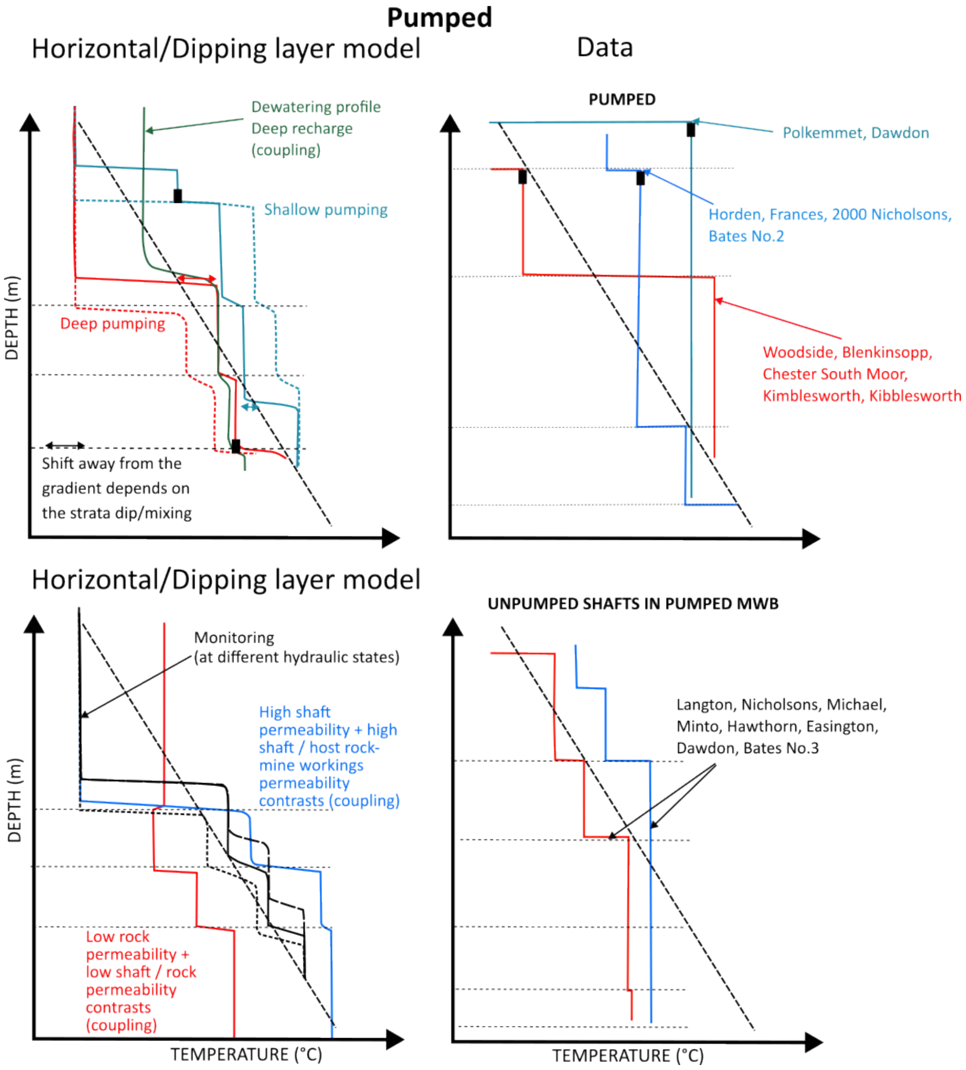

Figure 9.1: Comparison of the modelled and observed pumped temperature profiles and monitoring profiles in pumped coalfields in the UK (see description of the type of sites in Table 3.2 and the shafts/boreholes classification in Fig. A.8). The horizontal dashed lines and black squares represent the coal seam insets and pump depth, respectively.

Recovering shafts

In profiles acquired in unpumped/rebounding coalfields, temperature steps similar to those observed in shafts in pumped coalfields suggested the existence of other processes that forced heat convection. In recovering shafts, the temperature at each seam inset often follows the trend of the undisturbed geothermal gradient (e.g. Langton, Markham, Dawdon), whilst convective cells are formed between the seams insets. This observation can however not be generalised to all recovering shafts. In some cases, extensive warming (e.g. A Winning) or cooling (e.g. Williamthorpe) are observed, leading to warmer or cooler temperatures across the depth range of the profile. On the other hand, the average temperature in many recovering/discharging and recovered profiles (see blue profile on Fig. 9.2) tends to match the average temperature predicted by the geothermal gradient over that depth interval, despite the relatively uniform temperature distribution, suggesting the existence of thermal equilibrium.

The temperature steps observed in rebounding profiles were successfully reproduced numerically using density-viscosity coupling, suggesting the key control of free convective flow in rebounding and unpumped coalfields. Free or natural heat convection characterises the flow induced by water density and viscosity differences associated with salinity and temperature gradients (i.e. with deeper water being warmer and more saline). Those density-related effects are therefore expected to dominate the profiles in monitoring or rebounding areas, promoting the flow of warmer water towards shallower depth and the downflow of colder/denser waters down to the shaft bottom. This process called thermohaline stratification, is responsible for the formation of natural convection cells in large open voids (Bao et al., 2020) and has also been suggested to be a dominant heat transfer process in mines Hamm and Bazargan Sabet (2010). The nature of hydraulic recharge (i.e. hydraulic boundary conditions) tends to affect the rate at which the system returns to equilibrium, and therefore the temperature distribution in the pumping and monitoring shaft, which mostly differ at a given time for scenarios with hydraulic flux boundaries. Under coupling, the rebounding temperature profiles tend to be more sensitive to the relative position of the shaft along the strata dip. Given the scenarios modelled in Chapter 7, warming is observed in the shallow/updip monitoring shaft independently of the nature of recharge, and in the deep pumping shaft under deep recharge scenarios. On the other hand, cooling is observed in the deep pumping shaft when shallow recharge dominates, reproducing the temperature profiles observed in many rebounding coalfields (e.g. Barnsley, Morton, Bates).

Although Bao and Liu (2019b) suggested that the salinity contrasts have limited effects on the onset of thermohaline stratification, further work would be required to understand better the impact of the salinity-related density variations on the patterns of temperature distribution in both rebounding or discharging shafts. However, mass transport modelling is out of the scope of this study.

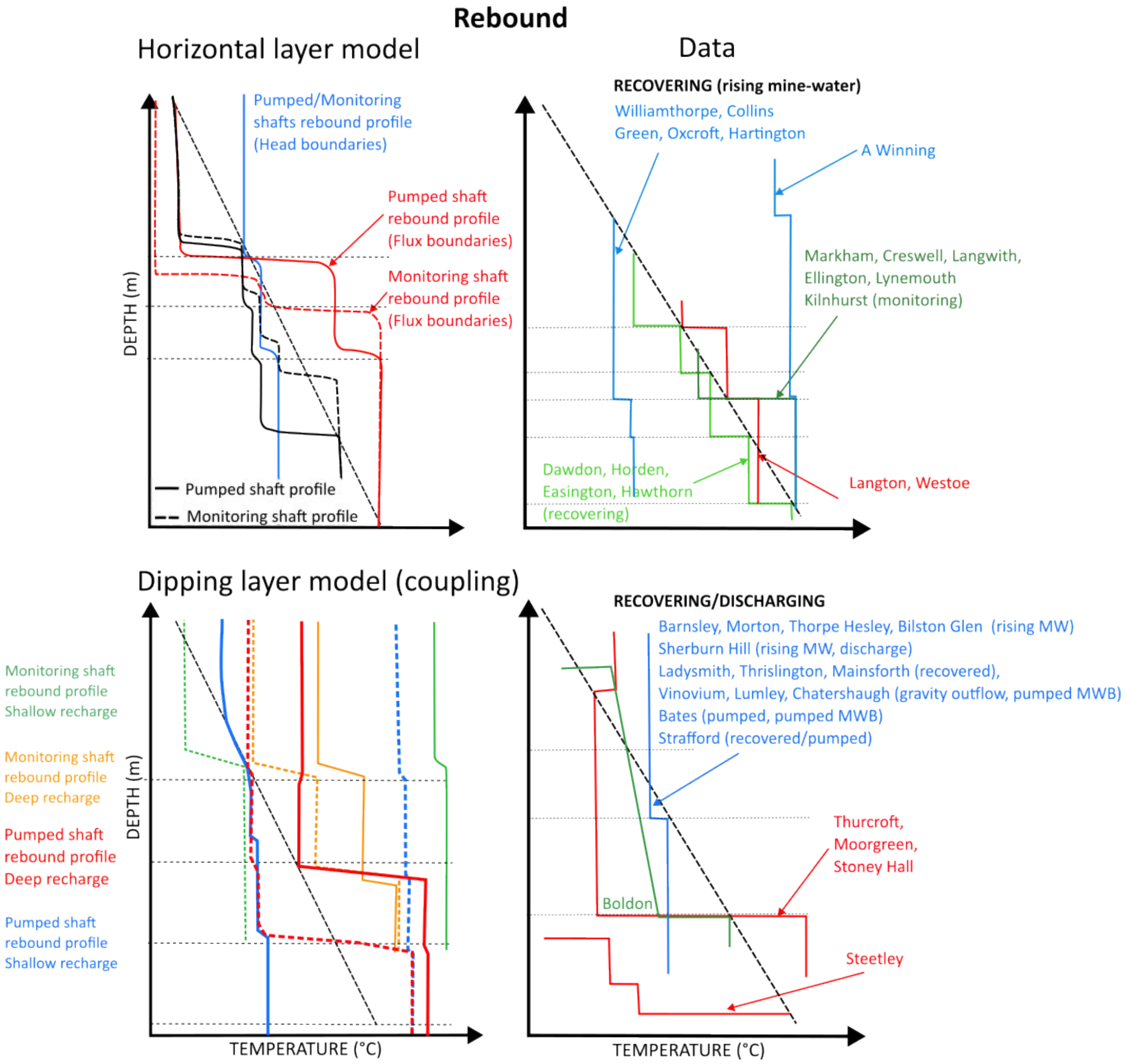

Figure 9.2: Comparison of the modelled and observed rebound temperature profiles in the UK (see description of the type of sites in Table 3.2 and the shafts/boreholes classification in Fig. A.8). The horizontal dashed lines represent the seams insets.

9.2.2 Parametric controls

Permeability effects

Results from the sensitivity analysis presented in Chapter 6 showed that the mine workings hydraulic conductivity K_w is a key control on the temperature distribution in mine shafts during transient analysis. The seam permeability determines the amplitude of the hydraulic drawdown and the rate at which the system reaches hydraulic and thermal steady-state, with the smaller K_w, the greater the decline in water level, and the slower the time to reach equilibrium. The seam permeability determines the hydraulic flow velocity, and therefore the rate at which heat is exchanged between the water and the surrounding rock and is conveyed to the shaft via the galleries. Depending on the temperature of the recharging water (i.e. natural groundwater regime or reinjection, e.g. P. Guo et al. (2018)) and the permeability of the fractured zone surrounding the galleries (Chapter 8), this heat exchange process will either mine or recharge the rock in heat, having either a beneficial or adverse effect on the sustainability of heat extraction. Whilst higher permeability will lead to heat mining in a scenario with cooler natural groundwater/thermal reinjection, lower permeability will prevent heat mining of the rock. In a scenario with warm natural groundwater recharge, higher permeability will promote heat replenishment, which will be hindered if the permeability of the rock is too low to allow groundwater flow.

Over the short term, the relationship between the average temperature in the shaft and the seam permeability highly depends on the duration since the onset of pumping (i.e. equilibrium state). Over time, the non-linearity of the relationship between permeability and temperature, i.e. with high-permeability systems reaching steady-state faster, leads to a reversal of the effect of the seam permeability on the average/pumped temperature and on the heat extraction rate (see Chapter 6). The time step at which this trend reversal occurs is linked to the overall heat available in the mine-water system (i.e. mine volume), the pumping depth and the flow rate. At steady-state, the models suggest that the effect of permeability for a given groundwater regime becomes negligible and the sustainable heat extraction is independent of the permeability unless coupling is implemented (Fig. 6.33).

Strata dip

Together with the seam permeability and the nature of hydraulic recharge, the mine geometry (e.g. strata/seam dip) and seam interconnectivity were shown to control the extent of water mixing and the temperature distribution within individual shafts. Where seams reach the surface, the infiltration of colder water at the outcrop could in some cases promote cooling in the pumped shaft or an updip/shallower monitoring shaft. On the contrary, deep warm water recharge would induce a general warming in shafts interconnected via mined galleries. This suggests that although shallow warming is observed in most coalfields (i.e. above 200-300 mbgl), either due to natural convection (i.e. density effects) or as the result of shallow pumping, (Farr et al., 2020) this is highly dependent on the geometry and hydrogeology of the block. Examples of general cooling have been identified in areas where recharge is inferred to occur from shallow mine workings in recovering coalfields (e.g. Williamthorpe, Collins Green, Oxcroft, Hartington).

Equilibrium state and mine status

Discrepancies between the observed and predicted geothermal gradient have been suggested to result from the unsteady hydraulic and thermal conditions within a particular coalfield area. Such conditions can result from a recent change in the groundwater regime or recharge dynamic (e.g. implementation of pumping, completion of water rebound, creation of new hydraulic connections as water is rebounding), leading to the new mixing of mine waters with different temperatures between interconnected shafts. The extensive sets of modelling scenarios simulated in this research can overall be used to get insight into the effect of the nature of hydraulic recharge in mines, which is often uncertain, on the temperature distribution in mine-water reservoirs. Here, the effect of the hydraulic settings in two different coalfields is discussed, based on a comparison between the observed temperature profiles and the profiles obtained from the generic models.

In the North-East England Coalfield (Fig. 9.3), the deep mine workings are suggested to be partially or totally concealed by the Permian strata. Assuming that no drainage occurs from the shallow mine workings to the deep mine workings, deep hydraulic recharge is expected to dominate the recharge to the shaft. Modelling results suggested that the temperature profiles and pumped temperature can reach a quasi-steady state, with values averaging the temperature predicted by the geothermal gradient over the depth range of the mine workings. In Dawdon, the mined seams are found between 381 and 514 mbgl (Table 8.3). Assuming a gradient of 30℃/km with a surface temperature of 9℃ (Farr et al., 2020), this represents an average of 22℃ (i.e. between 20.43℃ and 24.42℃) and correlates well with the temperature pumped at Dawdon since 2008. It is important to note that a potential cooling due to surface water drainage associated with an increase in the pumping rate is not to be excluded (Farr et al., 2020). However, further modelling work including a geological model of the Dawdon-Horden area would be required to validate this hypothesis.

The Midlothian Coalfield in Scotland alternatively consists of a syncline, with both limbs outcropping at the surface (Fig. 9.4). The literature suggests that no connection exists between the workings in the Coal Measures and Limestone Coal Formation (LCS). Although no connection was identified between the shallow and deep workings from the LCS, this is more uncertain and a potential limited drainage from the Roslin Colliery into the Bilston Glen mine has been suggested (Bamforth, 2014). On the contrary, connections via the Great Seam (502 mbgl) were inferred from the same water rebound rate observed in Bilston Glen and Easthouses colliery, each situated on one side of the syncline (Fig. 3.16). Water rebound

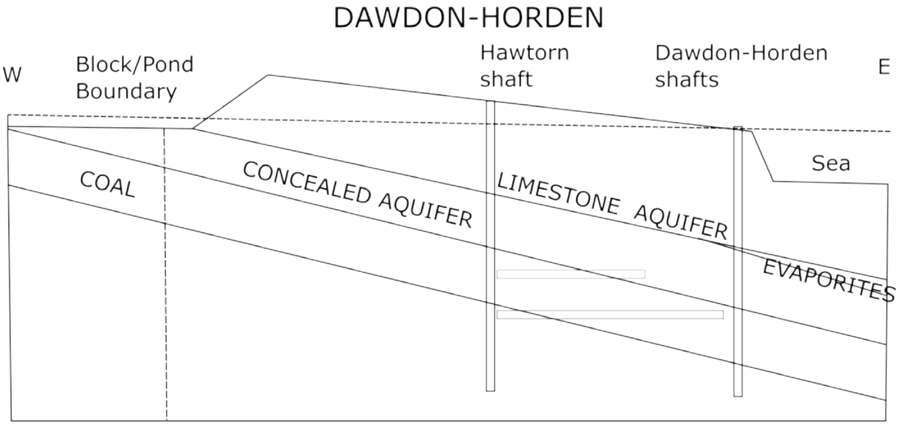

Figure 9.3: Conceptual sketch of the structure of the Dawdon-Horden mine-water block, NE England Coalfield (Ian Watson)

has been completed in the coalfield in 2020. There, the profile depicts a uniform temperature distribution with an average of 14℃ in Easthouses and 19℃ in Bilston Glen. Assuming a gradient of 24℃/km with a surface temperature of 7℃ (Farr et al., 2020), the temperature at the Great Seam would average 19℃, which correlates well with the average profiling temperature in Bilston Glen. The comparison with the modelling results (Fig. 9.2) moreover suggests a good fit with the shallow recharge scenario in the dipping layer model, which could advocate potential drainage of shallow recharge water to Bilston Glen via Easthouses, where the temperature is lower.

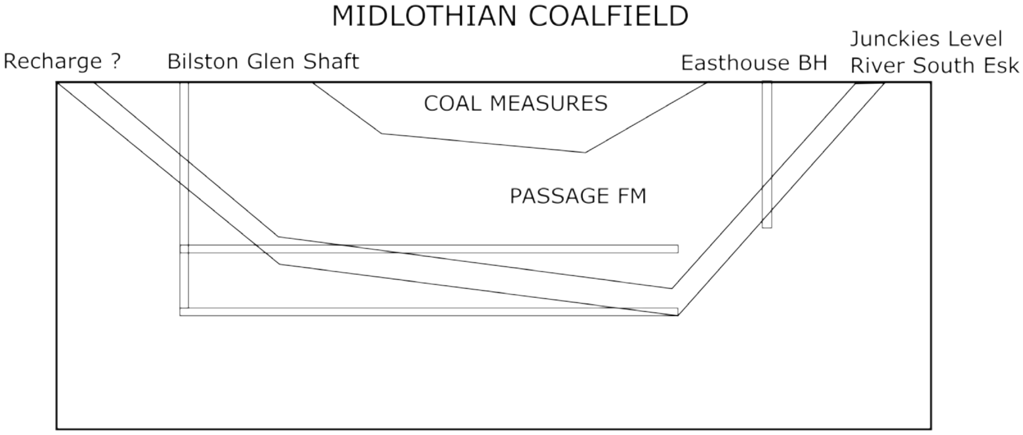

Figure 9.4: Conceptual sketch of the Midlothian Coalfield structure in Scotland (I. Watson)

9.3 Resource assessment

The three hypotheses tested are:

- H7-1: The source of groundwater recharge determines the sustainability of heat extraction from mine-water reservoirs
- H7-2: The geothermal gradient in the flooded mine reaches a state of "partial equilibrium" once flooding is completed
- H7-3: The thermal disturbances caused by past mining activities have a limited effect on the heat potential assessment.

9.3.1 Heat sources contribution

Estimating the relative contribution of natural heat sources is challenging, as the hydrogeology of mine-water reservoirs is highly impacted by the anthropogenic effects of mining. Groundwater flow within mine workings and convective heat recharge via advecting mine water was shown to be one of the key controls on the temperature profiles in mines and dominate the heat transfers in mine-water reservoirs and shafts (see Chapter 6), in agreement with S. M. Watson et al. (2019); Westaway and Younger (2016). Depending on the mine geometry, the design of the pumping operations (e.g. pumping-reinjection), affects the extent of mixing and the conductive heat exchanges between the rock mass and the mine water, which plays a key role in controlling the MWT over the long-term. Although conductive heat exchanges are slow relative to convective heat transfers, this suggests that an accurate estimate of the relative contribution of the undisturbed geothermal gradient and other heat-producing sources is necessary to determine the conductive heat flux and the long-term heat balance in the system.

In Chapter 5, the subsurface heat balance in the Midlothian Coalfield in Scotland was calculated for a 100 m deep borehole heat exchanger, based on the yearly heating requirements for a single-family house. The heat recharge potential from diverse natural and anthropogenic heat sources was determined. Results showed the key importance of the geothermal gradient relative to radiogenic heat production or solar heat recharge, in an environment where groundwater flow is neglected. In the mining environment, exothermic reactions such as pyrite oxidation were suggested to represent an additional source of heat (Banks, 2008), able to generate 0.5°C/L of water (Farr et al., 2016). Although past studies suggested that such reactions would mostly occur during mining activities as the rock entered into contact with oxygen, new reactions could be triggered by chemical changes resulting from the modification of the reservoir hydrodynamic during geothermal operations. However, further estimates of the contribution of such a process, which involves chemical and mass transport/reactive modelling are out of the scope of this work.

Additional phenomena occurring during the mining operations were suggested to have disturbed the rock temperature in the long term, such as instantaneous fires, air conditioning, or the effect of cold water circulation in open mining voids during dewatering activities. Based on the results presented in Chapter 7, it is however expected that the long-term footprint of such phenomenon on the rock temperature is limited, and becomes negligible following water rebound and recovery, as the water temperature re-equilibrates with the surrounding rock.

Although it does not represent a source of heat strictly speaking, the presence of low-conductivity layers is finally suggested to play a key role in controlling the conductive heat flux and the recharge potential in mines over the long term, as they favour the accumulation and storage of heat. Thermal blanketing due to the presence of insulating layers was shown to have the potential to cause local and regional ‘hotspots’ (Farr et al., 2020). However, further site-specific analysis would be required to quantify the relative contribution of this phenomenon in controlling the temperature in mines relative to the effect of local groundwater flow.

9.3.2 Static heat potential assessment

A key issue when assessing the heat potential of mine-water reservoirs is to know if the calculated local geothermal gradient (e.g. Farr et al. (2020)) is representative of the pre-mining undisturbed geothermal gradients, and how potential discrepancies are likely to affect the estimates of the geothermal flux recharging the mine in heat. Determining the undisturbed conductive geothermal heat flow in mines is however challenging. Most of the temperature data available have been measured in active collieries or in flooded mine shafts, where convective heat flow, turbulent mixing in open voids and the hydraulic dynamic of the system can thermally disturb the temperature of the surrounding host rock (see Chapter 7). It is therefore essential to understand the implication of such processes acting for decades (e.g. during dewatering), identify the rate at which the system is returning to equilibrium following water rebound as well as the potential effect that permanent disturbances of the host rock temperature can have on the heat capacity of mines.

Results from Chapter 8 suggested that most of the heat is sourced from the host rock in the long term, where conductive heat transfers dominate. Characterising the potential residual thermal footprint and disturbances of the conductive heat flux following extensive periods of mining and dewatering, and the subsequent water rebound was therefore interpreted to be essential to understanding the heat recharge rate in mines. Due to the uncertainty in the nature and reliability of the data, the potential long-term disturbances resulting from dewatering a mine with dipping seams were simulated numerically for a 50-year dewatering period and a 50-year rebound/recovery period (Chapter 7). The results suggested that after 50 years of recovery, the apparent temperature profiles can underestimate or overestimate by up to -0.6% to 0.3% the heat flux in mines (i.e. compared to the pre-mining undisturbed gradient), depending on the nature of the recharge.

On the other hand, shallow subsurface temperatures in the UK were shown to record the effect of paleo-climate (Westaway & Younger, 2016). Recent climate warming since the last glaciation has been shown to progressively warm up the ground down to 100s meters below the surface, which often leads to an underestimation of the geothermal gradient and therefore of the heat flux used to assess a geothermal resource potential (Gillespie et al., 2013). Corrections of the geothermal heat flux for paleo-climate effects have been performed in the UK, but are highly dependent on the geographical location and the data available (S. M. Watson & Westaway, 2020; S. M. Watson et al., 2019). In general, the temperature is assumed to equal the yearly average air surface temperature at about 10-20 mbgl, which is below the depth of influence of the daily variations in air temperature, depending on the ground heat conductivity. However, anthropogenic sources of heat in cities were shown to cause additional near-surface temperature disturbances. This phenomenon, the Urban Heat Island effect (see Chapter 5) was suggested to increase the surface heat flux, and represent a significant additional source of heat recharge to shallow geothermal systems (Allen et al., 2003; Rivera et al., 2017; Westaway & Younger, 2016).

9.3.3 Heat mining rate and dynamic heat recharge mechanisms

The sustainability of a heat resource does not only depend on the size of the resource in place and the relative contribution of heat sources to the heat recharge but also on the rate and scale of advective versus conductive heat transfers in the subsurface. Different processes might alter over different timescales and spatial scales (e.g. coalfield, MWB, borehole scale) the temperature profiles. On one hand, it is essential to understand the thermal footprint of those processes on the observed temperature gradient and heat flux to better quantify the resource in place (e.g. effects of past dewatering activities, Urban Heat Island effect). On the other hand, quantifying the rate of subsurface heat transfer can provide better insights into the resources available in the long term, the thermal footprint of heat extraction and the potential time required for the system to recover in heat when operations stop.

The heat flow in mines has been largely attributed to the effect of ’free’ density-driven heat convection (N. Burnside et al., 2016). In unobstructed vertical mine shafts, water bodies form density-related stratification resulting from salinity and temperature gradients Hamm and Bazargan Sabet (2010). The mixing of cold surface meteoric water and deeper/warmer saline water entering the shaft from different levels create buoyancy forces and form ’convection cells’, with better-quality water generally settling above poorer-quality ones after long periods of abandonment (C. Nuttall et al., 2002; C. A. Nuttall & Younger, 2004; Wolkersdorfer, 2008). This process was suggested to fix the temperature along unpumped shafts close to the average of the temperatures at the top and bottom, resulting in a lower apparent temperature gradient and creating temperature anomalies where the water is warmer than the predicted temperature at shallow depth (Krige & Schonland, 1939). This study showed that although this statement is valid in most coalfields, anomalies where the average shaft temperature is lower or higher than predicted by the geothermal gradient also result from differences in the nature of hydraulic recharge and the extent of mixing resulting from the dipping seams. The presence of several galleries intersecting the shaft at different levels induces local water mixing and allows the establishment of higher temperatures at the bottom of the shaft (Hamm & Bazargan Sabet, 2010).

In pumped coalfields, the numerical sensitivity analysis (Chapter 8) showed that the relationship between the pumped MWT and the heat output from the mine highly depends on the geothermal gradient (Fig. 6.5). For deep pumping scenarios, an increase in the geothermal gradient (assuming the same surface temperature) promotes heat mining from the rock, with the greater the pumped temperature and the greater the heat mined. In shallow pumping scenarios, the linear correlation between the geothermal gradient, MWT and heat output is even stronger, with the greater the gradient (and pumped temperature) and the greater the heat recharge to the system (Fig. 9.5). This is interpreted to result from the upward flow of deep warm water to the near-surface, whereas the pulling of cold water down to a deeper pump is interpreted to promote the mining of heat from the rock surrounding the shaft. For a given geothermal gradient, the pumped temperature however mostly depends on the position of the pump relative to the seams insets. In a scenario with horizontal layers, the maximum pumped temperature was calculated for a pump situated just above the deepest seam in the mine area, which was also shown to favour the depletion of the system in heat (Fig. 6.4), highlighting the necessity of a balancing act between ensuring sustainable heat extraction (i.e. limiting heat mining from the reservoir rock) and a high COP (i.e. high temperature at the heat pump).

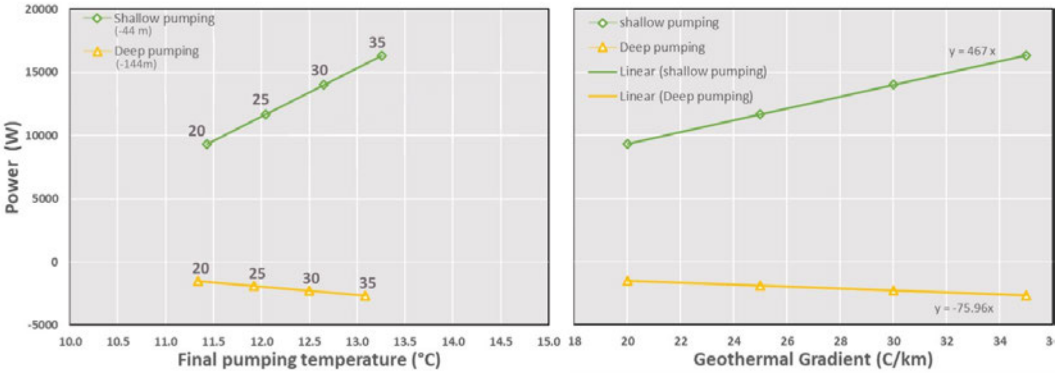

Figure 9.5: Relationship between the power output, the final pumping temperature, and the geothermal gradient, for different pumping depths. The labels on the left graph indicate the geothermal gradient in ℃/km. Results are based on the sensitivity analysis presented in Chapter 6, assuming a constant surface temperature of 9℃. They show that under a shallow pumping scenario, the heat recharge rate and pumped temperature increase with increasing geothermal gradient. Under a deep pumping scenario, the heat mining rate and the pumped temperature both increase, but at a smaller rate.

As pumping disturbs the initial equilibrium between the mine water and the rock mass, heat exchanges are induced between the advecting mine water in the high-permeability seams, roadways and shaft, and the surrounding fractured and undisturbed rock mass. In the horizontal layers model, vertical heat exchanges in the mining area were suggested to be limited, as the temperature of the recharging mine water flowing towards the shaft equals the temperature predicted by the geothermal gradient. In the dipping layer model, the mine water alternatively flows across a larger depth range before entering the shaft, which is likely to promote heat exchanges with the surrounding rock. Although heat conduction is assumed to be limited relative to convective heat transfers, heat will be mined from or transmitted to the surrounding rock mass where the advecting MWT in the roadways, galleries or shaft is cooler or warmer than the rock, respectively. The temperature in the shaft will therefore result from the complex combination of conductive heat exchanges and convective mixing in the galleries.

The numerical analysis showed that in the short period following the onset of pumping, the greatest hydraulic and thermal changes are observed in the high permeability voids (e.g. open roadways, un-collapsed panels, drifts), where the flow velocity is the highest. As most of the heat is conveyed via the mine water through the highly transmissive seams or roadways, the permeability of those elements tends to control the rate of heat exchange between the rock and advecting mine water and determines the proportion of mine water that flows into the shaft at a given temperature (Fig. 6.12), depending on the pumping depth and source of hydraulic recharge. This observation can be made following any change in the hydraulic conditions and hydrodynamics of mine-water reservoirs, such as the onset of water rebound, or the development of new hydraulic connections. Greater permeability enhances thermal recharge to the mine water in the shaft for shallow pumping and deep hydraulic recharge scenarios and promotes heat mining for deep pumping and cold hydraulic recharge scenarios (Figs. 7.6 to 7.12). Low permeability seams tend to inhibit the hydraulic flow, leading to reversed observations.

As the operational time increases and a hydraulic equilibrium is reached in the interconnected open voids, the heat extraction rate from the roadways and galleries decreases whilst the relative contribution from the goaf material and surrounding rock mass to the heat recharge, where conductive heat transfer dominates (i.e. low velocity), progressively increases. This is interpreted to result from the slower propagation of the thermal plume via conduction relative to the hydraulic/convective processes. As the system reaches thermal steady-state (i.e. steady-pumped temperature) the rate of heat exchanges between the mine-water and the rock mass depends on the flow rate (water residence time), the temperature of recharging water (Fig. 7.19), and the thermal and hydraulic properties (e.g. heat conductivity, permeability) of the damaged/porous zone surrounding the open voids/galleries (Fig. 8.12), in accordance with the observations from S. A. Ghoreishi-Madiseh et al. (2012). Whilst higher damaged zone permeability promotes the heat exchange rates, low heat conductivity layers tend to hinder heat transfers, but increase the long-term heat extraction or storage potential (e.g. Fig. 6.6). In large-scale heat potential assessment, an accurate characterisation of the petrophysical properties of the mining area and the hydraulic boundary conditions, including the volumetric flow rate, is therefore essential. Those determine the dynamic convective recharge available in a pumped system and therefore the sustainable heat extraction rate from mine-water reservoirs.

Although the models developed in this study represent ideal scenarios that are useful to understand the general behaviour of mine-water systems, it is important to keep in mind that in the long term, any heterogeneity or change in the hydrological conditions (e.g. new connections between collieries or mine-water blocks) will modify the flow and heat transfers and disturb the equilibrium state of the system.

9.4 Mine geometry and conceptual tool development

The three hypotheses tested are:

- H8-1: An equivalent porous media approach can be used to reproduce heat transfers in interconnected roadways and pillar-and-stall mining areas
- H8-2: The height of the fractured zone has a key impact on the long-term rate of heat extraction and recovery
- H8-3: The nature of the hydraulic recharge controls the heat recharge rate

Based on the research results, a conceptual model for the assessment of the long-term heat recovery potential from mine-water systems is suggested in Fig. 9.6.

9.4.1 Mine reservoir properties

One of the key elements to account for is the permeability (m^2) or hydraulic conductivity (m/s), and the relative thickness of the caved and fractures zones (K_r, K_f and h_r, h_f, respectively). In the caved zone, an equivalent permeability can be determined based on the proportion of open voids, pillars and/or goaf %V relative to the total volume of the worked coal panel in the considered area. Because of its lower permeability, the fractured zone plays a major role in determining the long-term heat extraction rate. Past studies however demonstrated that the geothermal potential of mines depends more on the height of the fractured zone than on the fracture permeability (P. Guo et al., 2018), which was confirmed in this analysis. Results from Chapter 8 showed that assuming an average permeability (K_{eq}) for the full thickness of damaged area above a mined seam (with volume $h \times A$) can provide a first assessment of the minimum amount of heat available over the long-term, depending on the rate of volumetric recharge Q and the temperature of recharging water T_r.

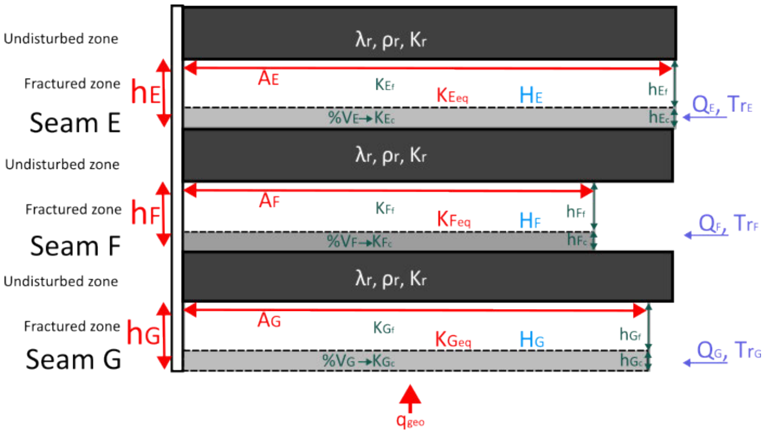

Figure 9.6: Suggested conceptual model to assess the long-term pumped temperature and heat extraction rate from a multi-layered mine-water reservoir. A represent the workings area, h the thickness, Q the flow rate, T_r the recharge water temperature. Subscripts *E*, *F*, *G* correspond to seam codes and subscripts *c*, *f* and *eq* represent the caved, fractured and equivalent zones. In the long-term, the sustainable rate of heat extraction is suggested to depend on the worked seams volume (i.e. $A \times h_c$, on the nature of hydraulic recharge (Q, T_r), and on the permeability contrasts between the caved and fractures zones, with K_{eq} the equivalent permeability of the caved zone calculated from the percentage void volume $\%V$. The minimum extractable power can be approximated using the total mined area volume ($h \times A$) independently of the equivalent hydraulic conductivity .

The petro-physical properties in the surrounding undisturbed rock mass are also of interest, as it holds the greatest amount of heat in the mine (with H = $\rho_r cV$). Although the models presented in this study represent simplified homogeneous systems, the layering of the sedimentary structure in real geological systems is likely to create heterogeneities in the vertical temperature gradient and the rate of heat exchange. Whilst competent sandstone rocks can promote the transfer of heat, especially if fractured, low-conductivity (λ_r) shale layers can act as an insulating seal rock, where heat can accumulate and be stored/released at a slower rate, increasing the long-term heat potential of the system.

9.4.2 Scale of simplifications

When modelling work is performed, a balance must be found between the time scale of the study, the spatial extent of the study area and the level of geometrical details needed to get reliable estimates of the parameters of interest. Geometrical simplifications can provide a first assessment of the heat accessed by a heat pump system and of the potential interference risk between different users accessing the same resource. In this research, a porous media approach was suggested to have the potential to accurately reproduce the overall thermal footprint and the heat mining rate of the system in the long term, independently of the type of mine workings.

The suggested conceptual modelling approach is based on calculating the relative proportion of open or high-permeability mining voids within predefined worked areas in a given seam and using it to derive the equivalent porous material properties of the layer (e.g. permeability, porosity). Determining the total extent of interconnected mine workings and the volume of water-filling voids can provide an initial assessment of the heat capacity of the mine-water reservoir. However, accounting for the dynamic conductive and convective heat exchanges during the lifetime of a system is essential to accurately determine the rate of extractable heat (Chu et al., 2021). The properties and thickness/volume of the damaged zone above a worked seam were shown to have a key role in determining the long-term heat extraction rate from mine-water reservoirs (Fig. 8.12), promoting conductive heat exchanges between the rock and circulating mine-water. Different approaches have been discussed in the literature to assess the height of the fractured zone. Whilst P. Guo et al. (2018) showed that it highly depends on the roof strength, additional constraints could be obtained from boreholes log analysis, when available (see Dawdon example in Appendix A.8). Based on this observation, the conceptual model presented in Fig. 9.6 suggests the vertical division of the model into two main layers consisting of the mining zone (i.e. combining the caved and fractured zones) and the overlying unaffected rock mass. Although this approach is likely to underestimate the overall heat potential of the mine (Fig. 8.12), it allows for simplifying the model development process in cases where several overlying seams are to be modelled. For each layer, considering the temperature of the recharging mine water in the corresponding depth interval and the relative contribution of each layer to the flow can provide insights into the convective heat recharge potential. Based on those parameters, numerical models constrained with appropriate hydraulic and thermal boundaries could finally be used to determine the sustainable rate of heat extraction from the system. Although 3D models best represent the system volume and heat capacity, the analysis presented in Chapter 8 suggests that those can be scaled in 2D and account for the extent of the reservoir in the direction perpendicular to the model plan.

Whilst longwall panels can be easily considered as a porous goaf material, pillar-and-stall workings are more complex, and calculations of the equivalent permeability, porosity and thermal properties will depend on the relative dimensions of the pillars and the amount of collapse in the stalls (Chapter 8). In areas dominated by roadway networks, the conversion to an equivalent porous material is more challenging. Uncertainties in the estimates of the thermal breakthrough/heat extraction rate due to inaccurate assumptions become more significant if the area represents the main flow path between the recharge and the pumping zone. An example of this is if the injection and pumping shafts are connected via a dense network of roadways/open galleries in a mine, which increases the short-circuiting risk. In the long-term and if no change in the hydraulic condition changes (i.e. the source of recharge water, reinjection temperature, pumping rate), the error is expected to reduce, as the heat is increasingly mined from the rock mass located above/below the open voids.

Chapter 10

General conclusion

This study successfully highlighted the key heat sources and parameters that need to be considered when evaluating the long-term sustainable heat extraction potential from flooded coal mines and provides an understanding of the key heat recharge mechanisms. The results showed the key role that the geothermal gradient, the geometry of the mine workings and the extent of mixing in collieries exert in controlling the temperature distribution in mines. With the extent of the fracture zone being a major control on the long-term heat extraction rate, simplification of the mine geometry to an equivalent porous media was shown to be a possible approach when large-scale analyses are involved, provided the hydraulic boundaries are well constrained. Convective heat transport by the recharge water was suggested to be an essential source of heat renewal, whilst conductive heat transfers through the lower permeability materials surrounding the open voids were shown to dominate the long-term heat transfer processes. Ensuring the sustainability of such a system therefore depends on a thorough investigation of the main flow paths, to avoid short-circuiting effects between a reinjection and pumping zone, but also of the volume and characteristics of the damaged zone available for heat exchange.

10.1 Data and limitations

Although this analysis describes generic processes of groundwater flow and heat transfers in mines, the results characterise ideal scenarios that are not entirely representative of reality. A key limitation of the models developed is that they do not account for the complex interactions between processes of different nature, such as the coupling between turbulent flow in shafts and laminar, conduction-dominated flow in the surrounding porous materials, or the effect of de-saturation of the mining voids.

In addition, the lack of data within the different sections of a mine, at the scale of the worked seam, colliery or interconnected mines within a coalfield, makes it difficult to develop a reliable model and validate the results. With the growing interest in mine-water heat resources, the increasing amount of research on the hydrogeology of mine-water reservoirs and data collected in real-scale laboratories (e.g. UKGEOS Observatory), there are promising opportunities to improve the understanding of those systems. It is hoped that the Glasgow Geothermal Energy Research Field Site will contribute to significantly reducing subsurface and geoscientific uncertainties and risks, but also raise awareness and stimulate the market for this low-carbon energy source (A. Monaghan et al., 2017).

10.2 Outlook and recommendations for future practice

Sustainable utilisation of mine water heat resources characterises the ability to maintain a constant pumping temperature over the long term, whilst ensuring a balance between the heat extracted and replenished within the system. This study showed that this depends on the complex interaction between the mine geometry, the hydraulic settings and the design of the heat recovery system. This section summarises the key lessons learned from the data and numerical analysis, which are used to provide recommendations for future practice.

10.2.1 Conceptual model development

Access to geothermal resources is commonly limited by the flow rate that can be sustained without depleting the system in water (i.e. reservoir depressurisation) and heat (i.e. thermal breakthrough). In Chapter 7, numerical models showed that the source and temperature of the recharging mine water is a key control on the heat recovery potential of pumped mines.

Developing a thorough hydraulic conceptual model of the mine is essential to characterise the source of recharge, the system hydraulic boundaries, the flow direction and the hydrogeological properties of the reservoir (e.g. geometry, thermal and hydraulic properties) before the development of mine water heating schemes. This can be done through the review of diverse data sources including but not limited to mining plans, geological maps, hydrogeological and mining reports, borehole logs, dewatering history and/or pumping data, rainfall data and water level measurements. Based on the available information, the conceptual model can be used to identify key interconnections between overlapping mine workings, different sections of the mine or surrounding mines and hydrogeological units likely to represent flow paths to the pumping site. Pumping tests (without re-injection) can moreover provide information on the available volumetric recharge, hydraulic properties, and the interconnectivity of the system, based on the analysis of the hydraulic drawdown.

In addition, Chapter 3 showed that the thermal state of the mine can be defined based on the local geothermal gradient and the depths of the seams intersecting the shaft. In a system at hydraulic and thermal equilibrium, the mine temperature is expected to represent the average of the temperatures of mine waters flowing from the different seams insets. Although the mixing of waters with different temperatures can occur in systems with dipping seams, temperature logs can be used to identify the key seams contributing to the hydraulic recharge. This is expressed by temperature shifts with different amplitudes at the depth of the seams insets, which can also provide insights into the temperature of the recharging mine water. Any temperature log acquired during the pumping test can provide additional information on the most productive (i.e. permeable) seams and insights into potential thermal breakthroughs.

10.2.2 Fractures zone characterisation

Chapter 8 showed that the power output of a longwall panel can be bounded based on estimates of the relative thicknesses and the permeability contrasts between the caved zone and the overlying fractured zone. Whilst the total thickness of the mining area (i.e. the high-permeability caved and fractured zones) can provide an initial assessment of the minimum heat extraction rate from the reservoir, the heat mining rate generally increases with the caved zone permeability. On the other hand, the fractured zone permeability was suggested to enhance heat recharge by promoting heat exchanges between the recharge mine water and the surrounding rock.

Previous research has shown that the thickness of the fractured zone above collapsed mine workings is a function of the nature of the roof/host rock, the width/thickness of the underlying mined area and the residual voids after subsidence, collapse and compaction (Adhikary & Guo, 2015; Booth, 2002; Esterhuizen & Karacan, 2007; Mucho et al., 2000). Miao, Cui, Xu, et al. (2011) showed that the height of the fractured zone above longwall panels can be determined based on the mining height and the stratum structure (thickness and strength), whilst P. Guo et al. (2018); W. Guo, Zhao, Lou, and Wang (2019); W. Zhu, Chen, Zhou, Shen, and Xu (2019) showed that pillar failure due to underlying longwall panel extraction depends on the pillar width/height ratio. However, fracturing above mine workings is not always beneficial to the development of permeability, as the presence of highly heterogeneous and clay-rich materials can reduce the water capacity of mines during the collapse process above pillar and stall (B. J. Andrews et al., 2020).

Based on the results from those studies, it is recommended that a thorough geological and structural investigation of the mine is conducted at the pre-feasibility stage. This can be done by mapping the type (i.e. pillar and stalls, total extraction area) and extent of mine workings reported in mine plans, the thickness of the mined seams (i.e. from geological logs or mining reports), and the characteristics of the overlying roof geology. This information can be combined to analytically approximate the thickness of the fractured zone above mine workings.

A combination of short-term and long-term pumping experiments using different flow rates could moreover be employed to get insights into the permeability distribution around the caved zone. Those pumping tests should be designed to allow discriminating between the permeability of the main flow paths (i.e. highly permeable roadways promoting short-term and high-velocity flow) and the lower-permeability fractured zone (i.e. lower velocity favouring heat exchanges over a larger time scale).

10.2.3 Design of the pumping (and injection) system

In addition to developing new mine-water heating systems, using heat as a by-product of mine-water treatment activities has been of growing interest to The Coal Authority. Mine-water heating systems represent a means to turn the liability of legacy mine workings into an opportunity to offset the costs of mine-water treatment schemes (Loredo et al., 2016). In abstraction-only scenarios, Chapter 6 showed that the pumping depth relative to the mined seams depth plays a major role in determining the pumping temperature and the heat recovery/mining rate from mine water reservoirs in the long term. Whilst shallow pumping can reduce the operational costs, results showed that such design can favour heat recovery within mine systems, by promoting the flow of warmer water from greater depth. This represents a double advantage for the development of mine-water heating systems.

In scenarios where the water recharge cannot balance the water abstracted for heat utilization, re-injection of water depleted in heat (in heating mode) is required to maintain sufficient pressure in the mine water reservoirs. In such a situation, pumping tests with re-injection of cold water can be performed prior to the development of the large-scale scheme to identify any potential short-circuiting (i.e. system interconnectivity) and get insight into sustainable pumping rate. Re-injecting in the deeper seam is recommended to optimize the heat recharge (heat exchanges between the warmer host rock and the water).

10.2.4 Heat storage and licensing issues

Chapter 4 showed that where groundwater flow is limited (i.e. dominated by geothermal and solar heat flux and conductive heat recharge), subsurface heat extraction systems cannot be operated sustainably in the long term without depleting the subsurface in heat. Whilst groundwater/mine-water flow can enhance heat recovery in the subsurface (Chapters 6 and 7), mines are increasingly considered for their heat storage potential. Heat storage in mines and/or cyclical utilisation is viewed as a way to periodically recharge the system in heat and promote the long-term heat utilisation of mine-water heat resources. Fraser-Harris et al. (2022) alternatively described a Geobattery system where heat injected from facilities with high cooling demand (e.g. data centres, gyms) could be transported to heat demand areas via the high-permeability network of galleries.

Based on results from Chapters 4 to 8, it is recommended that heat licensing should be primarily based on a good understanding of the hydrogeological constraints and natural systems dynamics. Heat storage should be employed to balance the heating requirements, and ensure the thermal footprint of heat extraction for a given abstraction rate does not expand over time and adversely impact neighbouring schemes. To do so, constant communication between users and industrial developers should be promoted to optimise the utilisation of the heat resource and prevent interferences in the long term.

10.2.5 Continuous monitoring

Chapter 3 highlighted the lack of consistency and relatively poor quality of the data set in UK coalfields. To better characterise the subsurface and optimise the operation of mine water heating systems, continuous monitoring of the temperature, water level and chemistry at the pumping and neighbouring observation points should be implemented in mine water heating schemes. In view of the increasing number of mine water systems within a single mine water block, understanding the potential interactions between those is essential and can only be achieved via the centralisation and sharing of data.

10.3 Further work

A few assumptions have been made during the model development presented in this research work. The impacts of simplifications of the real processes on the modelling results are discussed in this section and should be considered for future research work.

10.3.1 Groundwater and heat transfer coupling

The conceptual model introduced in this research is based on the understanding of key processes based on numerical results and on the analysis of data that are often poorly constrained. Further work should include a validation of the conceptual tool presented in Chapter 9 based on the acquisition of appropriate geological, petrophysical, hydrological and thermal data, and the development of a numerical model for a specific case study. Additional modelling work should focus on understanding the implications of implementing more complex equations for groundwater flow and heat transfer and understanding the contribution of those processes to the temperature distribution and heat recovery from mines. This includes the effect of long-term dewatering, using unsaturated flow equations (i.e. Richard’s flow), or the implementation of equations for turbulent flow.

10.3.2 Data digitising

With the improvement of machine learning techniques, developing methods to improve the digitising of mine plans and automatise the calculations of volume, heat in place and heat recovery rate from mines could accelerate projects from the pre-feasibility stage and largely benefit the development of mine-water heat projects at large scale. Given the site-specificity of mines, ensuring sustainable utilisation of mine-water heat resources cannot be done without a deep understanding of the local behaviour of mine-water reservoirs. Hence, defining the extent of the heat accessible by a given scheme is essential to assess the possibility of multiple users accessing the resource and/or the amount of recharge required to prevent interference. It is therefore crucial to use the knowledge being acquired to inform and guide the development of a regulatory framework for heat licensing. This is essential to reduce the geological and financial risks and ensure that the resources are well-managed in the long term.

10.3.3 Chemical modelling

No chemical modelling was undertaken as part of this research. However, pyrite oxidation is an exothermic chemical reaction that was suggested in previous research to release a substantial amount of heat in mines. Further modelling work should therefore consider the implementation of chemical processes to understand better the contribution of pyrite oxidation on the heat production rate during the operation of a mine water heating system. This can be accompanied by an analysis of the clogging risks due to the precipitation of iron oxide, and its effect on the sustainability of the geothermal infrastructures.

10.3.4 Anisotropic fractures zone and fault modelling

In the models developed in this study, the permeability within the fractured zone above the mine working was assumed to be isotropic. In reality, fractures develop above the collapsed mine working in a preferential vertical direction depending on e.g. the roof strength and panel width, which is likely to affect the flow of mine water and the convection of heat. Future research should integrate this complexity and include anisotropic fracture modelling in the fractured zone to characterise the fluid flow and quantify both the heat extraction rate and heat recovery potential from mines.

Similarly, faults have a key impact on fluid flow in Carboniferous deposits. Those can promote water circulation in the direction parallel to the fault plane. However, the analysis of mine plans shows that most workings are stopped at the intersection with faults, suggesting that the offset of the stratigraphy (e.g. normal faulting) is likely to prevent flow across the fault. B. Andrews et al. (2020) moreover showed that in exposed fluvial–deltaic lithologies at Spireslack Surface Coal Mine, Scotland, the highest-fracture-density part of the network often has the lowest open fracture connectivity as a result of cementation occurring during ongoing deformation. This suggests a thorough understanding of the fracturing process and faulting history is essential to identifying whether faults/fractures are open to heat convection in mine water reservoirs.

Appendix A

Appendix

A.1 Chapter 2: Volumetric assessment

A.1.1 Geological properties

Rock type distribution

Data from the Carrington-1 well is used to generate a typical stratigraphic sequence and temperature profile for the Scottish coalfields, based on the relative thickness of the Carboniferous formations (Fig. A.1). A. Monaghan (2014) reported total thicknesses of about 1200, 350 and 240 m for the UCMS, MCMS and LCMS, respectively, and of 600, 550 and 240 m for the ULCS, LSC and LLCS, respectively (Table A.1). In the Carrington-1 well, situated in the central part of the coalfield, the total thickness for the Coal Measures, PGP, ULCS, LSC and LLCS are about 250, 205, 165, 175 and 100 m, respectively. Carboniferous strata from the WLO and GUL formations are expected to extend further down by at least 500 m (A. Monaghan, 2014).

Abbreviation	Formation name
CMS	Coal Measures
UCMS	Upper Coal Measures
MCMS	Middle Coal Measures
LMCS	Lower Coal Measures
PGP	Passage Formation
ULCS	Upper Limestone Coal Formation
LCS	Limestone Coal Formation
LLC	Lower Limestone Coal Formation
WLO	West Lothian Oil Shale
GUL	Gullane Formation
ART	Arthur's Seat Volcanic Formation

Table A.1: Carboniferous formations names and abbreviations.

A 70 m thick interval from the Clyde Plateau Volcanic Formation, which represents a volcanic sequence within the Gullane Formation, has been crossed by the Midlothian-1 well, situated further west. Thermal modelling around the Midlothian–Leven Syncline however suggested that up to 1.9 km of Carboniferous strata have been uplifted and eroded (Vincent et al., 2010). Thus, most of the post-Carboniferous sediment rocks (>1.3 km of sedimentary cover) would have been removed in this area.

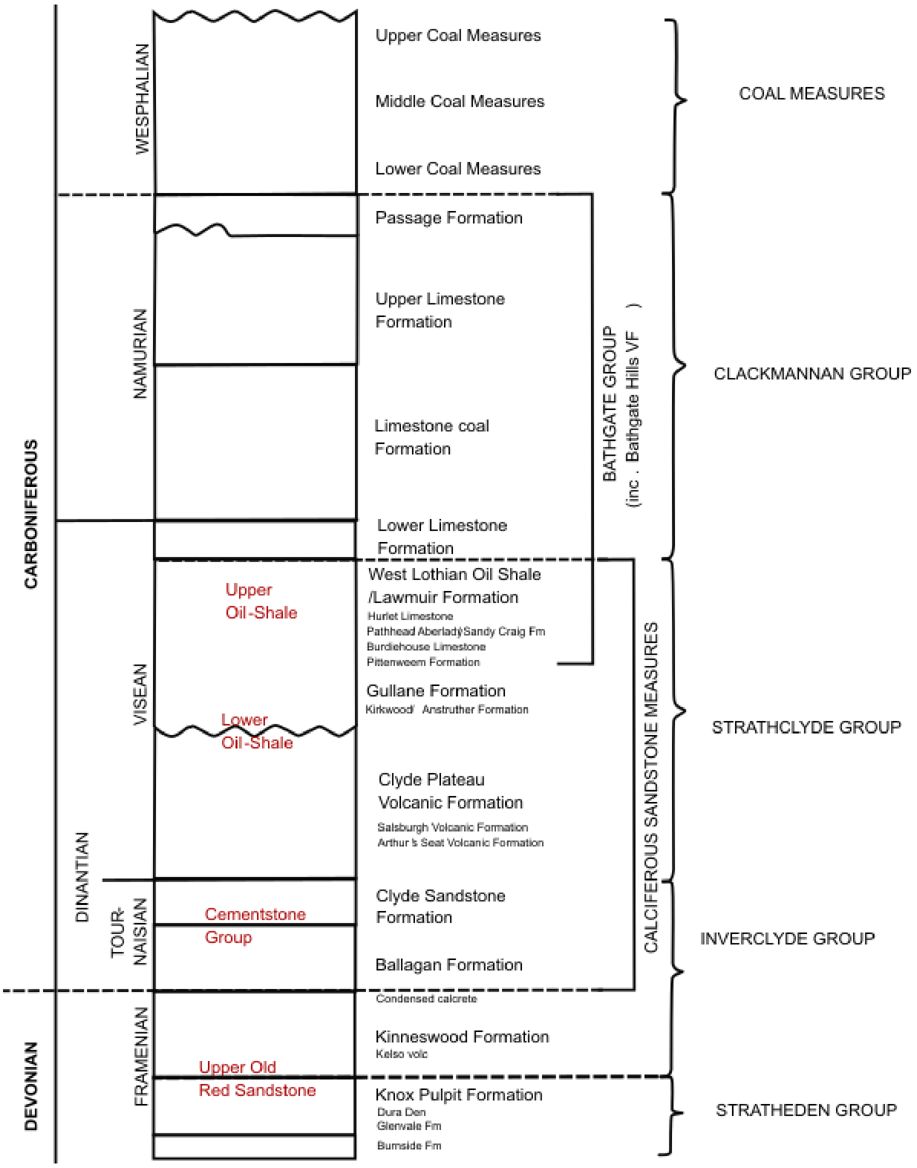

Figure A.1: Stratigraphical column showing the historical (in red) and modern (in black) classifications of the Devono-Carboniferous Formations in the UK.

The model created based on the Carrington-1 borehole is composed of 10000 1D line elements of 0.1 m in length. Thicknesses for the different formations were normalised to a 1000 m vertical section. The temperature at the surface is 7.4°C, which corresponds to the mean surface annual air temperature in the Lothian area between 1980 and 2019 (Farr et al., 2020) and the bottom temperature is 27.8 m (i.e. BHT measured in the Inverclyde Formations in the Spilmersford BH, Fig. A.2). According to the temperatures measured in boreholes in the Lothian Coalfield, the predicted temperatures in the LCS and the GUL are of ∼19.2°C and ∼26.5°C, respectively. In the model, those formations are located at average depths of 400 m and 882 m, respectively. To calculate a representative temperature distribution, each formation in the model is attributed thermal conductivity values calculated by J. P. Busby (2019). The harmonic mean heat capacity, density and Radiogenic Heat Production (RHP) values (Table A.2) were determined from the proportion of rock type in each formation (Table A.3) and their corresponding heat capacity, density RHP values taken from the literature (Table. 3.1). A detail of all the heat capacity, density and heat conductivity measurements for the different lithologies and/or formations in the Carboniferous succession found in the literature is also provided in Tables A.4 and A.5.

Fm	h	$\hat{h}$	$\sum h$	λ	RHP (μW/m3)	RHP (W)
UCMS/MCMS*	130	69	69	2.02	1.71275	1.176E-04
LCMS	250	132	201	1.91	1.8121	3.636E-04
PGP	205	108	309	2.91	1.01825	3.145E-04
ULCS	165	87	396	2.25	1.641	6.498E-04
LCS	175	92	488	2.24	1.2986	6.342E-04
LLCS	100	53	541	1.88	1.8235	9.868E-04
WLO	492	260	801	4.36	1.8235	1.461E-03
GUL	307	162	963	4.36	1.8121	1.745E-03
ART	70	37	1000	2.2	0.54	5.400E-04

Table A.2: Model properties and source terms. The thickness of each formation is based on the Carrington-1 and Midlothian-1 wells (A. Monaghan, 2014). CMS, MCMS and LMCS are the Upper, Middle and Lower Coal Measures, respectively; PGP: Passage Formation; ULCS, LCS and LLCs are the Upper Limestone, Limestone Coal and Lower Limestone Coal formations; WLO: West Lothian Oil Shale; GUL: Gullane Formation; ART: Arthur's Seat Volcanic Formation. The average thermal conductivity for the formations of the Carboniferous succession of the MVS (J. P. Busby, 2019) were estimated from the Maryhill, Hurlet House, Clachie Bridge, Barnhill, Kipperoch (Oxburgh, 1982), Boreland (E. Anderson, 1940) and Glenrothes (Brereton et al., 1988) borehole logs and samples from the Pennine Coal Measures (J. P. Busby, 2019), with the values for WLO and GUL taken from the Lawmuir Formation and values for ART taken from the Clyde Volcanic Plateau Formation. RHP values for each formation are based on data given in Table 3.1. h, $\hat{h}$, $\sum h$ and λ are the thickness, normalised thickness, cumulative thickness and heat conductivity (W/°C m), respectively.

Fig. A.3 displays the resulting temperature profile for the Carboniferous succession, with and without the effect of RHP.

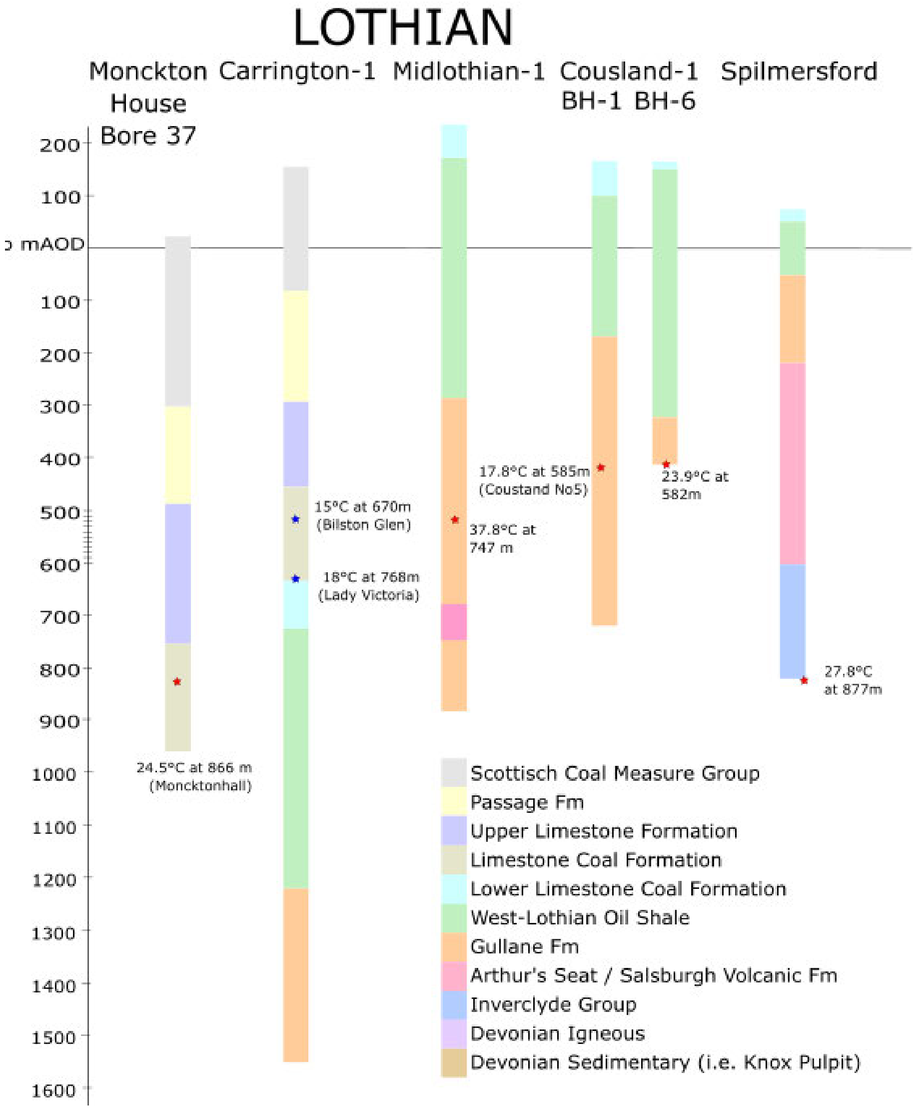

Figure A.2: Simplified geological logs and temperature measurements for boreholes in the Midland Valley of Scotland. Geological logs are from the BGS GeoIndex database. Temperature measurements are from Burley et al. (1984).

Statistical distribution rock types

Refined statistical analysis is performed by calculating the percentage of rock type for each lithostratigraphic formation, for boreholes and shafts where the thickness/depth of the Carboniferous formations is known (A. Monaghan, 2014). Those are summarised in Table A.6 and the statistical rock type distribution for each log are displayed in Figs A.4 and A.5. Based on the proportion of each rock type in each formation (Table. A.3) and their corresponding heat conductivity, capacity, density and RHP values (Table 3.1), the harmonic means of each parameter is calculated for each borehole and integrated into the **Borehole properties** Table of the database (Fig. 3.4).

Lithology	UCMS/MCMS	LCMS	PGP	ULCS	LCS	LLCS
Thickness (m)	130	330	210	165	175	85
% Sandstone	21	29	50	40	27	16
% Siltstone	8	5	0	0	14	17
% Seatrock	4	3	30	10	1	0
% Mudstone	25	45	15	40	49	57
% Limestone	24	0	3	5	1	8
% Ironstone	15	14	0	0	1	1
% Coal	3	3	2	4	1	1
% Dolerite	0	1	0	1	6	0

Table A.3: Percentage of lithologies for the different Carboniferous formations of the Midland Valley of Scotland recorded in existing boreholes. Data are based on the analysis of geological cores and samples from the Glasgow Observatory (Geothermal Energy Research Field Site), published by Vincent et al. (2010) and Entwisle (2019) and from borehole logs available in the BGS GeoIndex Database. Data for the Upper (UCMS), Middle (MCMS) and Lower Coal Measures (LCMS) are calculated from the Penine CM. Data for the Passage Formation (PGP) and Upper Limestone Coal (ULCS) are calculated from the Mackies Mill and Monckton House B37 LOGS (BGS GeoIndex Database) and data for the Limestone Coal (LSC) and underlying lower Limestone Coal were determined from the Maryhill Borehole. Additional rock percentages are given in the BGS Open Report OR19019 (Entwisle, 2019) and in Vincent et al. (2010). The thickness of each formation was determined from the Carrington-1 borehole.

Hydrogeology

Table A.7 provides a summary of the hydraulic characteristics of the aquifers extensively and not extensively mined for coal in the UK, as well as igneous volcanic aquifer (B. O Dochartaigh E et al., 2015). In addition, the typical porosity and hydraulic conductivity values for each rock type are given in Table A.8. Those are used to calculate the harmonic mean values for each geological log available in the database. Table A.9 summarised the past typical dewatering rates in active UK mines.

Lithology	λ (W/m/K)	Reference	c	ρ	α
Open Hole	0.59	(1)	4185	1000	0.141
Clay	1.11	(8)	860 (3)	1900 (3)	0.334
Coal	0.40	(7)	1300 (3)	1350 (3)	0.228
Fireclay	0.59	(2)**			
Ironstone	2.85	(1)	880	2760	1.173
Coal Measures irnst	2.35*	*(2)			
Lst	2.85	(10)	880 (3)	2760 (3)	1.173
Lower Carb. lst	3.14	(6)			
Namurian Millstone Grit lst	3.75	(6)			
Mudstone	1.41,	(9)	770 (4)	2600 (4)	0.704
Coal Measures mdst	1.49, 1.85*	(6); *(2)			
Siltstone	1.84	(1)	910	2680	0.754
Coal Measures slst	2.22, 2.23	(6); *(2)			
Sand/Gravel	0.77	(8)	860 (3)	1900 (4)	1.984
Sandstone	4.54	(9)	930 (4)	2460 (5)	1.984
Coal Measures sdst	3.31, 3.58*	(6); *(2)			
Upper Old Red sdst	3.26	(6)			
Seatrock	2.42	(1)	860	2680	1.050
Shale	1.3	(2)**			
Silurian slates	3.33	(6)			
Dolerite	1.81	(1)	858	2870	0.735
Basalt	1.8	(6)			
Tuff	2.15	(2)			
Hercynian granites	3.3	(6)			

Table A.4: Thermal conductivity λ, heat capacity c, density ρ and thermal diffusivity coefficients α for specific lithologies found in the MVS succession. *representative values for the Scottish Middle Coal Measured estimated from 5 boreholes in England. ** averages from the Boreland (Anderson, 1940) and Glenrothes (Gebski et al., 1987) boreholes. (1) Watson (2020), (2) Busby (2019), (2), (3), Wapled and Waples (2004), (4) Robertson (1988), (5) Westaway and Younger (2016), (6) Rollin (1987), (7) Herrin and Deming (1996), (8) Gale (2004), (9) Monro (1984), (10) England et al. (1980). lst: limestone; sdst: sandstone; mdst: mudstone; slst: siltstone; irnst: ironstone.

a) Lithology	Banks (2008)
Coal Measures Sandstone	3.31
Coal Measures Siltstone	2.22
Coal Measures Mudstone	1.49
Namurian Millstone Grit Limestone	3.75
Lower Carboniferous limestone	3.14
b) Formation	Busby (2019)
Scottish Coal Measures	2.02
Passage Formation	2.9
Upper Limestone Formation	2.25
Limestone Coal Formation	2.24
Lower limestone Formation	1.88
Lawmuir formation	4.36
Kirkwood Fm	2.1
Clyde Plateau Volcanic Formation	2.2
Clyde Sandstone Formation	4.19
Ballagan Formation	3.14
Kinnesswood formation	3.66

Table A.5: a) Thermal conductivity for specific lithologies found in the MVS, estimated based on laboratory measurements made on water-saturated samples extracted from boreholes (Rollin, 1987 in Banks, 2008). b) Average thermal conductivity for the formations of the Carboniferous succession of the MVS (from Busby, 2019).

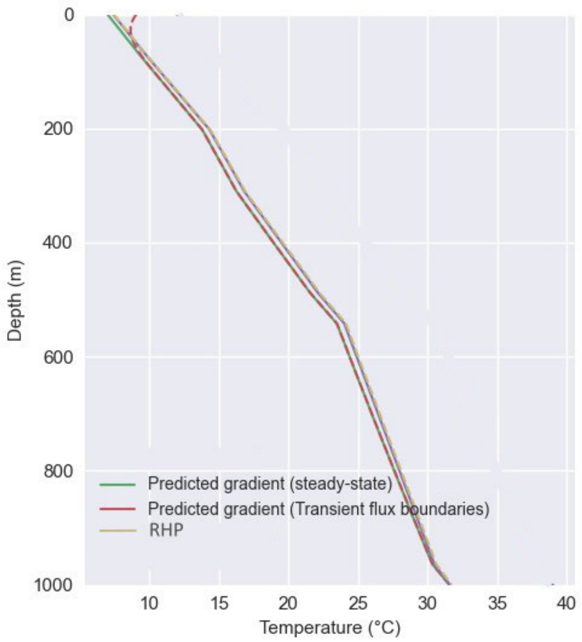

Figure A.3: Typical temperature profile generated for a 1000 m thick Carboniferous sedimentary succession in Scottish coalfield.

LOG	MCMS	LCMS	PGP	USLC	LCS	LSLC	WLO
Monckton House	-	0-330	330-521	521-790	790-	-	-
Mackies Mill	-	-330	330-521	521-790	790-	-	-
Bates No3	-	x	-	-	-	-	-
Chatershaugh	x	-	-	-	-	-	-
Easington	x	-	-	-	-	-	-
Hawthorn	x	-	-	-	-	-	- -
Eldon	-133	133-	-	-	-	-	-
Houghton	-62	62-	-	-	-	-	-
Ladysmith	-	x	-	-	-	-	-
Lady Victoria	-	-	-	-	x	-	-
Lumley 6th	-51	51-	-	-	-	-	-
Maryhill	-	-	-	-	x	x	-
Pumpherston	-	-	-	-	-	-	0-65
Salsburgh	-	-	-	-332	332-526	526-632	632-1113
Spilmersford	-	-	-	-	-	0-22	22-128

Table A.6: Depth range of the Carboniferous formations (Fm) in borehole logs from the GeoIndex database, including the Middle and Lower Scottish Coal Measures (MCMS and LCMS), the Passage Formation (PGP), the Upper Scottish Limestone Coal (USLC), the Limestone Coal Formation (LCS), the Lower Scottish Limestone Coal (LSLC), The West Lothian Oil-Shale Formation (WLO), the Gullane Formation (GUL), the Arthur's Seat Volcanic Formation (ART) and the Inverclyde Group (INV).

Aquifer	Extensively mined	Not extensively mined	Igneous volcanic
Flow type	Fracture/mine voids	Fracture/intergranular	Fracture
Productivity	Moderate	Moderate/High for Passage Fm	Low
Path length	1 - 10 km	1 - 10 km	0.1 - 1 km
Flow depth	100s m	100s m	10s - 100s m
Groundwater age	Month to millennia	Years to millennia	Month to decades
Chemical type	Moderate/highly mineralised (high Fe), often anoxic	Moderately mineralised, anoxic	Weakly/moderately mineralised, oxic, Ca-HCO3 dominated
Overlying strata	Low-k, thick in valleys	Low-k, thick	Thin or absent
Porosity (%)		12-17	
K (m/d)		3×10^{-4} - 0.1	
T (m^2/d)	10-1000	10-1000	
C_p (m^3/(d.m))	48 - 132	48 - 132	
Yield (m^3/d)	1987 - 3279	131 - 418	

Table A.7: Summary of the Carboniferous aquifer properties extracted from the Open Report OR15028 (Dochartaigh et al., 2015), with K the matrix hydraulic conductivity, T the transmissivity and Cp the specific capacity

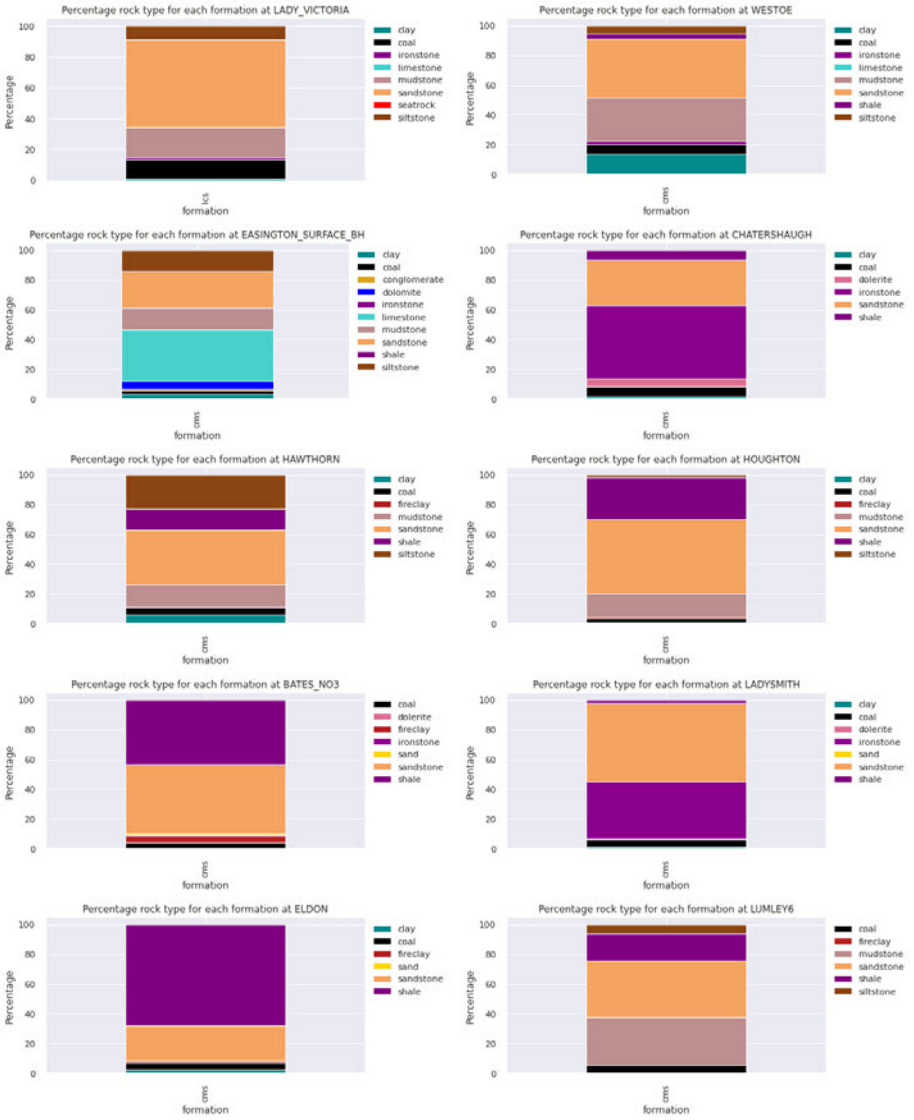

Figure A.4: Rock Percentage for the a) Limestone Coal (Lady Victoria), b) undifferentiated Coal Measures (Westoe), c) Middle Coal Measures (Easington, Chatershaugh, Hawthorn, Houghton), Lower Coal Measures (Bates, Ladysmith, Eldon, Lumley-6)

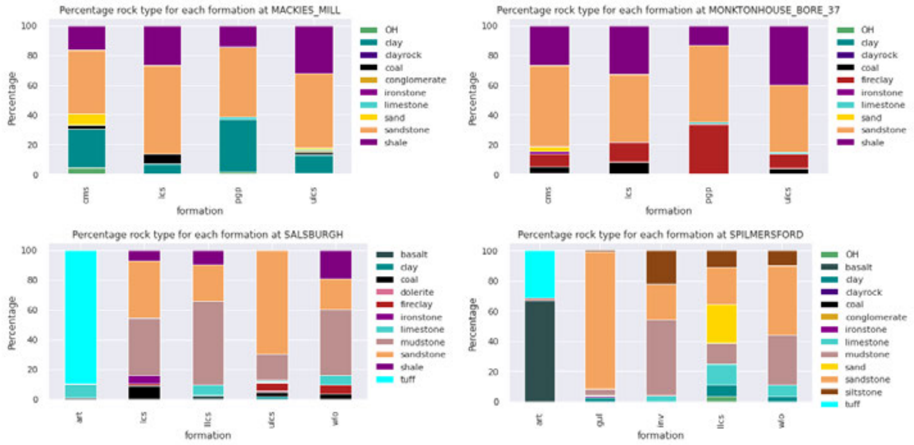

Figure A.5: Rock Percentage for the different Carboniferous formations

Lithology	Porosity (%)	Specific Yield (%)	Hydraulic conductivity (m/s)
Clay	30-60	1-10	10×10^{-12} - 10×10^{-8}
Silt	35-50	5-30	10×10^{-9} - 10×10^{-5}
Sands	25-50	10-30	10×10^{-7} - 10×10^{-3}
Gravel	20-40	10-25	10×10^{-4} - 10×10^{-1}
Sandstone	5-30	5-25	10×10^{-9} - 10×10^{-4}
Crystalline rocks	<1	<1	10×10^{-13} - 10×10^{-5}
Silicate rocks	0.1**		depends on
Schist/Gneiss	<0.05*		degree of fracturing
Basalt	<1-50	<1-30	10×10^{-13} - 10×10^{-2}

Table A.8: Typical porosity, specific yield and hydraulic conductivity for different lithologies. * Olofsson (2002) cites an effective kinematic porosity of crystalline rock aquifers. ** Domenico and Schwartz (1990) cite values as low as 0.1% for porosity and 0.0005% for effective porosity in granites (Banks, 2008).

Formation	Colliery	Flow rate (L/s)	Depth (m)
MCMS	Bothwell Colliery	230	396
LCMS	Polkemmet Colliery, West Lothian Frances Colliery, Fife	75 120	
LSC / SCM	Falkirk District Blindwells Colliery, East Lothian	30-55 315	
LSC	Prestongrange Colliery Kilsyth Colliery Twechar Colliery Monktonhall Colliery, Midlothian Blindwells Colliery, East Lothian	40-75 (140 h/week) 150 13 (12h/day) 35 ?	165-225 206 317

Table A.9: Historical mine dewatering rates (Gillespie et al., 2013). MCMS: Scottish Middle Coal Measures Formation; LCMS: Scottish Lower Coal Measures Formation; LSC: Limestone Coal Formation and SCM: Scottish Coal Measures

A.1.2 Void space estimates

Among the different volumetric assessment methods described in the main text, Banks et al. (2010) developed an approach based on the modelling of a mine-water rebound in the abandoned Siersza coal mine, Upper Silesian Coal Basin in Poland. To quantify the rate at which water is likely to rise within the mine complex in the absence of post-closure monitoring data, several parameters and mine characteristics have been considered, including:

- The mining history and geometry, including the location of faults, roads and shafts, the delineation of hydraulic connections between mine workings (Farr et al., 2016)
- The geology of the basin (i.e. deposits and mined layers, chemistry)
- The regional hydrogeology (i.e. average seasonal precipitations, temperature, groundwater recharge, surface runoff and evapotranspiration, calculated as a percentage of the annual average rainfall, discharge zones, hydraulic barriers, effective porosity and reservoir hydraulic conductivity), together with the dewatering history and the mine water inflows during operation (considering the influence of drifts/dewatering pumping station at specific mining levels). As the early stage of the flooding was considered (i.e. the lower part of the mine), the mine was assumed to be a single aquifer system, answering the need for a simple conceptual hydrological model upon which to base mathematical model. Those data were used to estimate the total amount of water pumped out from each mine level every year, divide this water into natural water inflow to the mine and water introduced to the mine by artificial processes (backfilling water), and finally estimate the flooding level prior closure of the mine.

In Banks et al. (2010), the void space in mines was divided into four types:

1. Void space in workings V_z (Rogoż 1974; Rogoż et al. 1999), determined based on geometric and geotechnical calculations.

   $$V_z = \frac{(cA_zM_z)}{cos\alpha} \tag{A.1}$$

   With A_z the area of the worked seam, M_z the exploited thickness of the seam, α the dip of the seam and c the available porosity in mine void (i.e. water capacity coefficient in Malolepszy et al. (2005), depends on the depth of exploitation and the type of abandonment of mine workings):

   - $c = 0.485 \exp -0.00205H$ for controlled collapse to goaf
   - $c = 0.275 \exp -0.0003675H$ for hydraulic backfilling of workings with sand slurry
   - $c = \frac{P-S}{100}; S = \frac{40-19P^0.2}{100}$ for dry backfilling of workings

   With H the depth of seam below ground (m), P the porosity of backfill (%), p the pressure exerted by rock overburden on the seam (MPa), S the pressure-dependent decrease in porosity (

2. Void space in tunnels, drifts and galleries V_k (Rogoż et al., 1999)

$$V_k = LA_k c_k$$

With L the length of the tunnel (m), A_k the cross-sectional area of the tunnel (m^2) and c_k a correction factor to take account of the decrease in void due to compression or backfilling.

- c_k = 0.9 to 1.0 for open tunnels in massive rock
- c_k = 0.6 for tunnels in compressible rocks (e.g., Orzesze mudstones)
- c_k =0.1 to 0.2 for infilled shafts and tunnels

3. Voids in fractures induced above workings Vszc (Rogoż et al., 1999)

$$V_s z^c = V_p(1-a-c)$$

if $(1-a-c) < 0$, then $V_s z^c = 0$

With V_p the volume of seam extracted, a a factor accounting for the loss in volume due to subsidence at the surface (a = 0.6 to 1.0) and c a factor to account for the proportion of void space available for filling with water.

V_k and $V_s z^c$ are numerically negligible in the overall void budget.

4. Void space in pores in dewatered sandstone strata V_g (based on assumptions)

$$V_g = U_p F_d J_0 \delta Z$$

with $F_d = 1.15 \times A$

With U_p the proportion of overburden which is water-bearing, ΔZ the depth interval under consideration (m), J_0 the proportion of open voids pace (i.e. specific yield) and A the area underlain by workings. An amount of resaturable porosity of 2.5% has been assumed in Rogoż et al. (1999), but this represents one of the most uncertain parameters.

Variable volume mine water filling models, with head-dependent and head-independent inflows, have been applied to simulate the progressive flooding of the Siersza Mine. Results showed that void space represented by resaturable porosity is essential in the mine water filling model where the mine host rock is substantially porous. Comparing simulation results with water level data measured during flooding moreover allows correcting for void volumes in the different reservoir parts of the model.

A.1.3 Heat potential assessment

In a porous rock, the total energy (J) stored can be calculated as follows:

$$E = V\rho_m c_m T$$

where

$$\rho_m c_m = \phi\rho_w c_w + (1-\phi)\rho_r c_r$$

represents the volumetric heat capacity of the solid materials and pore water, with ρ the density and c the specific heat capacity. Accounting for the time t of the heat exchanges and the difference between the recharging water and host rock temperature, the power extracted can be determined as follows:

$$P = \frac{V\phi\rho c}{t}(T_{inj} - T_{system})$$

Based on those equations and assuming the energy lost by the rock equals the energy gained by the water, the cooling rate of the reservoir rock under production due to the reinjection of fluid can be expressed by:

$$T_r = \frac{Q_w\rho_w c_w}{V_r\rho_r c_r}\delta T_w = \frac{Q_p\rho_p c_p T_p - Q_i\rho_i c_i T_i}{V_r\rho_r c_r}$$

with the subscripts *p* and *i* referring to the produced and injected water temperature.

Raymond and Therrien (2008) developed a resource estimation methodology for abandoned flooded coal mines based on an estimate of the geothermal heat flux. This method can be summarised as follows:

1. Site characterisation (geological context, presence of intrusions, topography, temperature, precipitation, hydrology)
2. Characterisation of the mine workings (type, depth, interconnections between mine shafts, underground roads and workings, state of the mine after abandonment, water levels)
3. Definition of the rock thermal properties (e.g. bulk thermal conductivity and specific heat capacity c). In the following equation, c is calculated as the weighted average of the heat capacity of the main mineral phases. The water c_w and mineral c_s specific heat capacities are from Somerton (1992) and Waples and Waples (2004a), the solid density ρ_s is estimated from the inferred mineralogy and the bulk density ρ_b is calculated from

the porosity-weighted average of solid and water densities.

$$c = \frac{\rho_s c_s (1-\phi) + \rho_w c_w \phi}{\rho_b}$$

4. Determination of the heat flux (product of the geothermal gradient estimated from temperature profile and the thermal conductivity).
5. Energy resources assessment: estimation of the total geothermal energy content from the sum of the energy associated with each flooded underground section E_r

   $$E_r = Vz\alpha\rho_w c_w$$

   with V the volume of water in a mine section, z its average depth, α the measured geothermal gradient. It is assumed that the heat exchanger return temperature is equal to the ground surface temperature above the considered mine section. Moreover, the volume of void is calculated as the product of the area of the excavated section by its average thickness and a correction factor of 0.25 accounting for subsidence, pillars and backfill in the workings (Jossop et al., 1995))
6. Realisation of a long-term pumping test in a mine shaft. This aims at defining the hydraulic properties of the host rock and mine workings (hydraulic conductivity and specific storage coefficient), the impact of geochemistry on the system performances and the rate $E_h p$ at which geothermal energy can be extracted using heat pumps

   $$E_{hp} = Q(T_p - T_r)\rho_w c_w$$

   with Q the average flow rate, T_p water temperature and T_r the exchanger return temperature
7. Development of 3D numerical models for groundwater flow and heat transfer simulations

A.1.4 Case study: The Midlothian coalfield

Mining history

Carboniferous Coal Measures, located at shallow depths in the central part of the Mid-Leven syncline, have been mined from the Polton and Whitehill collieries using the early-mining pillar-and-stall approach. Coal beds from the Limestone Coal Formation have both been mined from shallow workings on the edge of the syncline (i.e. Roslin, Ramsay, Burghlee on the western limb and Lingerwood, Bryan, Newbattle, Arniston on the eastern limb of the syncline) from the late 1800s/early 1900s, and by deep mines located in the deeper parts of the syncline (i.e. Bilston Glen, Lady Victoria, Easthouses) from the second half the 1900s. Most of the deep mines have been worked using longwall mining extraction methods. The depth of the deepest mined seams for each mine is summarised in Table A.10.

Colliery	Seam code	Panel	Seam name	Depth	Formation
Arniston	SC940L	6FFH	NORTH	-576	Limestone Coal
Bilston Glen	SC940L	6LIZ	NORTH	-734	Limestone Coal
Burghlee	SC670L	7ZQP	GREAT	-473	Limestone Coal
Easthouses	SC670L	6CXM	GREAT	-613	Limestone Coal
Lady Victoria	SC940L	6CXT	NORTH	763	Limestone Coal
Lingewood	SC900L	6F63	LOWER KALEBLADES	-540	Limestone Coal
Newbattle	SC670L	6CXO	GREAT	-610	Limestone Coal
Polton	SC400L	6CYF		-38	Coal Measures
Ramsay	SC740L	6ERU	GILLESPIE	-513	Limestone Coal
Roslin	SC880L	7ZP6	CRAIGIE	-620	Limestone Coal
Whitehill	SC400L	6FEF	SPLINT	-30	Coal Measures

Table A.10: Deepest worked seams for the main collieries in the Midlothian Coalfield

Consultancy reports ordered by The Coal Authority (TCA) suggest that no hydraulic connections exist between the shallow mines from the Coal Measures and the mines accessing the deep seams in the Limestone Coal Formation (Fig. 3.16). Moreover, no clear connections have been identified between the set of interconnected collieries on the western side of the coalfield (i.e. Ramsay, Roslin, Burghlee) and the deep mines (i.e. Bilston Glen) accessing the same coal beds in the Limestone Coal Formation, although potential limited drainage from the Roslin Colliery into the Bilston Glen mine has been suggested (Bamforth, 2014). Burghlee's old panels are located about 40 m above Bilston Glen workings in the Great seam and are separated by 330 m in the Craigie seam.

Drainage of water from the Eldin Adit at Elginhaugh (i.e. Eldin Day Level at 48 m) to the river North Esk has been reported following the flooding of the shallow mines in the Coal Measures, while water was still rebounding in the deep part of the syncline. The water rebound in Bilston Glen was completed by 2020 (source: Coal Authority). Similar rebound rates of 20 m/yr measured at the Bilston Glen and Easthouses shafts suggested roadway connections between those mines through the Great seam (-502 m). On the eastern side of the syncline, the Easthouses, Lady Victoria and Lingerwood mines are interconnected at different levels through goaf, shafts and roadways connections, mostly within the Parrot and Great seams. This includes a roadway connection between the Lingerwood Dicken Shaft and the Lady Victoria Shaft, an incline connection between the Easthouses Great Seam and the Lady Victoria Splint Seam, and a goaf connection between Lady Victoria and Lingerwood Parrot Seam. Those are accessed by the Easthouses pumping pit, Bryan's pit and Easthouses inclines that connect both to the Great and Parrot/Splint seams. In addition, the Eastwood Great seam connects to both the Lady Victoria Splint and Parrot seams by two steep drifts. The Eastwood pumping shaft connects the Parrot seam (shaft bottom) to the Great Seam from Easthouses.

During mining activities, most of the workings located in the Limestone Coal Group were dewatered via shallow drainage adits. Discharge levels include the Old Fordel/Junkies Day Level portal (35-37 mAOD), the Bryan's adit (50 mAOD) and the Burghlee Day Level (110 mAOD).

The decant location for the Junkies Level is at about 44 mAOD in the Easthouses incline C, which accesses the interconnected Lingerwood, Lady Victoria, Easthouses and Bilston Glen mines via the deep Great seam. Recent reports suggest that the Junkies adit only drains the northern area and/or the shallow parts of the Easthouses, Lingerwood and Lady Victoria workings in the Upper limestone, Limestone Coal, Lower Limestone Groups, and potentially from the Lower Coal Measures. Although the Easthouses shaft was suggested to drain deep waters to the Junkies Level (26 mBOD), chemical analysis supported a shallow source and low residential time for the water discharged at Junkies. This water was therefore interpreted to originate from rainwater infiltration into shallow workings in the Coal Measures or from the drainage of water from workings separated from the Lingerwood, Lady-Victoria and Easthouses workings in the same Limestone Measures, at greater depth or to the South.

The Bryan's adit was designed to drain deep mining units of the Lady Victoria and Lingerwood mines via gravity drainage from the overlying shallow workings to the Ochre Burn. The decant level for the Bryan's discharge is located in the Bryan's shaft (54.28 mAOD) that connects to the Lingerwood Parrot seam and Easthouses Great seam. At the time of writing, no discharge from the Bryan's adit has been observed and most of the discharge from the Parrot Seam is assumed to occur at Junkies via shallow levels.

Both the Burghlee and Roslin adits drain water from the shallow workings in the Limestone sequence on the west (reported as filled) to the Bilston Burn and Kill Burn watercourses, respectively.

Water has been reported as stabilised in the Arniston mine, which connects to the Lingerwood mine through roadway in the Great seam, and discharge at Vogrie.

The Bilston Glen shaft on the western limb of the syncline drains the deep Coal Measures and Limestone Coal workings, interconnected to the Elginhaugh mining block. The increased $CaCO_3$ alkalinity (but low Mg/Ca content) compared to water at Elginhaugh and Junkies indicates a longer residential time in the deep limestone formations. However, recharge in Bilston Glen is attributed to surface water/rainfall infiltration, similar to the deep mines on the eastern limb of the syncline. The high sodium chloride content of the water at Bilston Glen was moreover suggested to characterise saline connate groundwater dated from the limestone deposition.

Data availability

GIS data from TCA include the location of coalfields and mine-water bloc (MWB), monitoring temperature locations, discharge areas and information related to mine plans. This includes the location of the underground workings, shallow workings, probable workings, outcrop location, roadways, mine shafts, the area/thickness of the worked coal seam and the dip of the layer. Those can be used to estimate the volume of mined coal (Fig. A.6).

Volumetric heat assessment

The total volume of galleries in the Bilston Glen Colliery is calculated using Eq. A.1 after correcting the GIS shapefiles provided TCA (Fig. A.7). Those corrections involved attributing each 'unnamed' polygon with the proper colliery name, seam name and seam code to allow calculations of the total worked seam areas via GIS processing. For each mined seam in the Bilston Glen colliery, the total mined volume is calculated by summing the product of each worked panel area by its thickness, and scaling it by the panel dip rate and a factor accounting for the residual void volume. Here, a scaling factor of 0.25% that is assumed to be independent of the mining method is used (Jessop, 1995). Results summarised in Table (A.11) indicate a total mined volume of V_m = 0.106 km^3, which represents a total void volume V_v of around 0.027 km^3 after scaling for residual porosity. Overall, the projected mine area at the surface is 305,785 m^2 and the depth range of the seams is 900 m, which represents a total subsurface volume V of 0.275 km^3.

Seam code	Volume (m^3)	Scaled volume (m^3)
SC940L	26649243	6662311
SC930L	34658871	8664718
SC880L	328256	82064
SC820L	3606786	901696
SC711L	16584847	4146212
SC670L	24401631	6100407

Table A.11: Volumetric assessment for the Bilston Glen Colliery, Midlothian Coalfield, Scotland, showing the total area and void volume per worked seam.

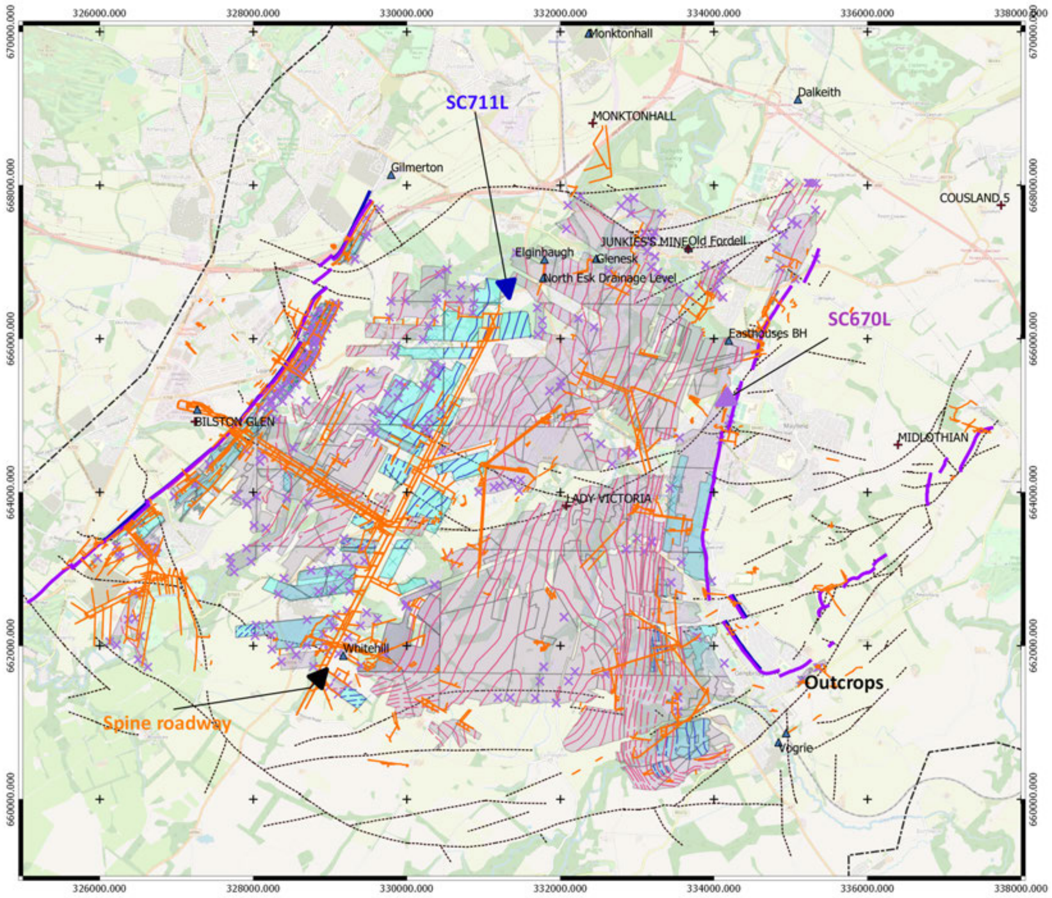

Figure A.6: Distribution of the mine workings, seam outcrops and roadways in the Midlothian coalfield. The map displays the seam levels, fault lines, monitoring sites, temperature sites and discharge zones. All GIS data are provided by TCA under an academic license. The boreholes with historic temperature measurements are from Burley et al. (1984)

.

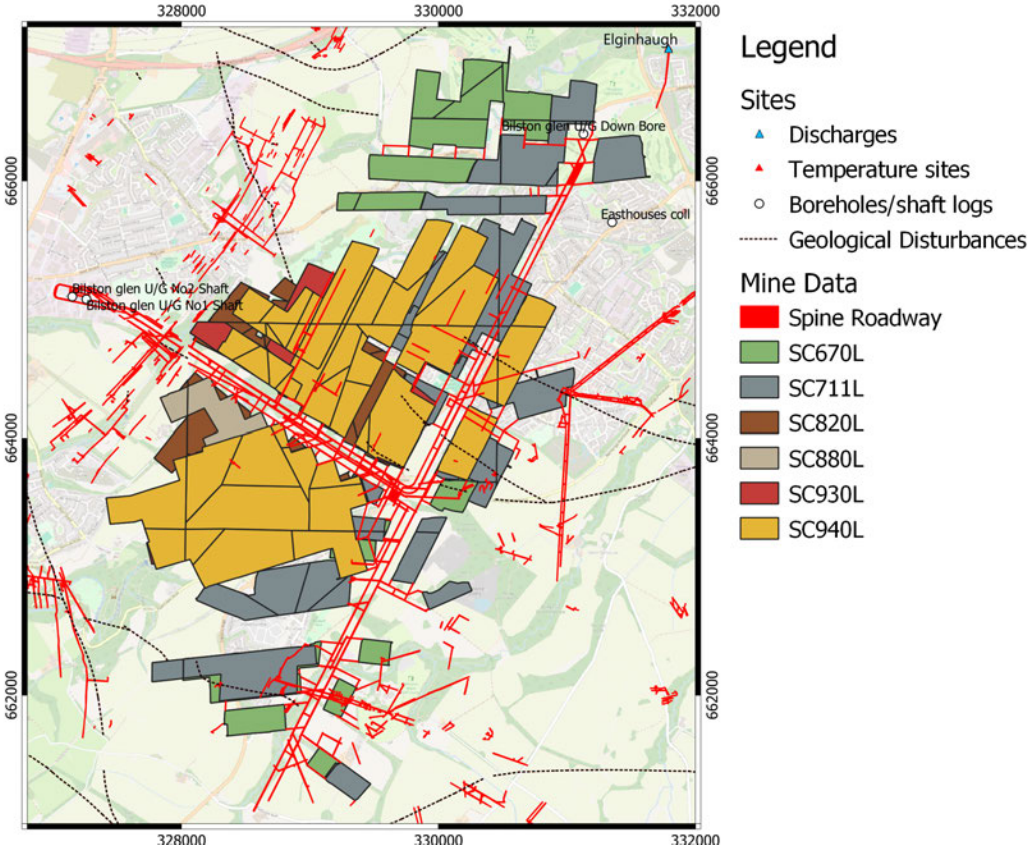

Figure A.7: Distribution of the mine workings, seam outcrops and roadways in the Bilston Glen colliery. The map displays the geological disturbances, monitoring sites, temperature sites and discharge zones. All GIS data are provided by TCA under an academic license. The geological borehole data are from the BGS GeoIndex Database

.

Based on the volumetric assessment, the subsurface heat content and potential heat recharge availability can be estimated. Those include:

- **Radiogenic heat production (RHP).** A quantification of the radiogenic heat production is conducted based on the geological section at the Carrington-1 borehole. Using the RHP value for the LCS of 6.324×10^{-4} (Table 2.1) and the total estimated volume of the mine V (i.e. 0.275 km^3), the total radiogenic heat produced by the Carboniferous formation (LCS) in the Bilston Glen area amounts to 0.174 W.
- **Solar recharge.** Using the equations described in Banks (2008), Receveur et al. (submitted) estimated the amount of energy transferred to the ground from the atmosphere based on meteorological data and soil temperatures measured at Paisley, near Glasgow in Scotland. Results suggested that although the net incoming radiations are about three orders of magnitude higher than the geothermal heat flux (0.057 W/m^2), the average thermal input to the ground from the atmosphere is negligible. In the long term, no atmospheric/solar heat is stored unless the near-surface temperature is significantly reduced. All the thermal energy entering the ground from the surface is naturally lost, with the energy coming out at the surface balancing the geothermal heat flux. Therefore, heat recharge from the surface does not access mines at hundreds of meters below ground.
- **Exothermic pyrite oxidation reaction.** The potential heat generated from pyrite oxidation is assumed to be negligible in flooded mines. Whilst the residual heat released during mining activities has been suggested to have negligible long-term effects on the host rock temperature (see main text), further work would be required to analyse the effect of pumping on the trigger of additional reactions.
- **Hydraulic recharge.** Based on the knowledge of the hydraulic connections between the different collieries in the Midlothian Sycline and the surrounding aquifers, it would be possible to calculate the rate of volumetric recharge to the Bilston Glen mine. Due to limited time, this has not been conducted in this research, but current modelling work is currently being undertaken as part of the Galleries2Calories project (Fraser-Harris et al., 2022) and would allow quantifying the rate of convective heat recharge to Bilston Glen.

A.2 Chapter 3: Data analysis

A.2.1 Geological borehole and monitoring sites

Tables A.12 and A.13 list the geological boreholes integrated in the geodatabase. Fig. A.8 summarised the different sites monitored by TCA for temperature and water level, classified by coalfield and type of site.

BOREHOLE NAME	LOCATION	COALFIELD	BGS Ref
Auchennidy	AUCHENNIDY	Lothian	NT26SW81
No.3 Shaft	BATES	North East	NZ38SW24
No.2 shaft	BILSTON GLEN	Lothian	NT26NE82
Boreland Bore	BORELAND	Fife	NT39SW44
CAMERON 1/79 Bore	CAMERON	Fife	NT39NW380
No1 shaft	CHATERSHAUGH	North East (Lumley)	NZ35SW92
Clachie-Bridge	CLACHIE-BRIDGE	Central Scotland	NS68SW1
Castlereagh Shaft	DAWDON	North East (DH)	
Theresa shaft	DAWDON	North East (DH)	NZ44NW37
SURFACE BH	EASINGTON	North East (DH)	NZ44SW212
North Pit	EASINGTON	North East (DH)	NZ44SW4/1
South shaft	EASINGTON	North East (DH)	
Easthouses 1/54 Bore	EASTHOUSES	Lothian	NT36NW58
Brockwell Borehole	ELDON	North East (SB)	
Frances Colliery	FRANCES	Fife	NT39SW102
Glenroth	GLENROTH	Fife	NO20SE
Hallside Bore	HALLSIDE	Central Scotland	NS65NE66
Hawthorn Shaft	HAWTHORN	North East (DH)	NZ34NE47
Downover Borehole Horden	HORDEN	North East (DH)	NZ44SW2415
North Pit	HORDEN	North East (DH)	
Houghton Colliery No2 Area	HOUGHTON	North East (Lumley)	NZ35SE35
Hurlet	HURLET	Central Scotland	NS56SW333
Lady Victoria No 6/77 Bore	LADY VICTORIA	Lothian	NT36NW269
Ladysmith Shaft	LADYSMITH	North East (SB)	
Lochhead Bore	LOCHHEAD	Fife	NT39NW136
Lumley 6th Pit	LUMLEY6	North East (Lumley)	NZ35SW27
Mackies Mill Bore	MACKIES_MILL	Fife	NT39NW16
Maryhill borehole	MARYHILL	Central Scotland	NS56NE1755
Monkton House Bore 37	MONKTONHALL	Lothian	NT37SW43
Shaft No1	MONKTONHALL	Lothian	NT37SW62
No.5 Mine B/H	MONKTONHALL	Lothian	NT36NW245
Pumpherston No1 Oil Bore	PUMPHERSTON	Central Scotland	NT06ME227
Bore No4 (temperature)	QUEENSLIE	Central Scotland	NS66NW326

Table A.12: List of geological boreholes used in the database development (part 1). DH: Dawdon-Horden mine-water block; SB: South of Butterknowle.

BOREHOLE NAME	LOCATION	COALFIELD	BGS Ref
Queenslie No3 Bore	QUEENSLIE	Central Scotland	NS66SE50
Lower Dysart B/H	RANDOLPH	Fife	
Rashiehill Bore	RASHIEHILL	Central Scotland	NS87SW22
Salsburgh No1A well	SALSBURGH	Central Scotland	NS84SW81
Seafield Colliery No2/70	SEAFIELD	Fife	NT38NW10
MAIN BORE	SHERIFFALL	Lothian	NT36NW47
South Hetton	SOUTH HETTON	North East (DH)	
Spilmersford BH	SPILMERSFORD	Lothian	NT46NE73
THORNTON BRIDGE	THORNTON BRIDGE	Fife	NT29NE69
THORNTON FARM	THORNTON FARM	Fife	NT29NE68
Thrislington	THRISLINGSTON	North East (SB)	NZ33SW62
Wellsgreen No1/1979 Bore	WELLSGREEN	Fife	NT39NW381
Crown Shaft	WESTOE	North East (WW)	NZ36NE82
Yard Seam BH	WHITBURN	North East (WW)	NZ46SW202
Banhill BH	BARNHILL		
Boreland BH	BORELAND	Fife	
Glenroth	GLENROTH	Central Scotland	
Kipperock	KIPPEROCK		
Acresford 6	ACRESFORD	South Derbyshire	SK31SW65
Barony 1/74 U/G	BARONY	Ayrshire	NS51NW174
Barony 1/78 U/G	BARONY	Ayrshire	NS51NW178
Barony 3/78	BARONY	Ayrshire	NS52SW58
Boomhill Farm (13/33)	BROOMHILL FARM	North East (H)	NU20SW16
Cross-Hands By Pass M7	CROSS_HANDS	South Wales	SN51SE74B
North Pit	DEEP NAVIGATION	South Wales	ST19NW19
Deerplay Collier 3A	DEERPLAY	Lancashire	SD82NE22
Betty Shaft	ELLINGTON	North East (EL)	NZ29SE53
Hauxley Shaft	HAUXLEY	North East (H)	NU20SE38
Furnace Pit	MOIRA	South Derbyshire	SK31NW249
Monckton 1	MONCKTON	Yorkshire	SE31SE128
New Murton	NEW MURTON	North East	NT94NE14
Oxcroft Shaft 2	OXCROFT	Nottinghamshire	SK47SE7
Parkside Farm	PARKSIDE	Lancashire	SJ69SW18
Portobello Bar	PORTOBELLO	Lancashire	SK07SW3
Hartington Drift	RENISHAW PARK	Nottinghamshire	SK47NW31
Seaton Delaval Coll. U/G	SEATON	North East (B)	NZ37NW13
Silverdale 48 U/G	SILVERDALE	Staffordshire	SJ84NW229

Table A.13: List of geological boreholes used in the database development (part 2). WW: Westoe-Wearmouth; EL: Ellington-Lynemouth; SB: South of Butterknowle; H: Hauxley, B: Bates.

Coalfield	Site	Type of site
Ayrshire	Cairnhill, Coalburn, Glenburn, Kames	Discharge
	Pennyvennie	Monitoring Shaft
Central Scotland	Blairingone, Cuthill Top, Douglas, Kingshill, Mains of Blairingon, Pool Farm, Wilsontown	Discharge
	Auchengeich, Tollcross Burn, Mosside, Rigside, Whitrigg, Riddochhill	Monitoring BH/Shaft
	Polkemmet	Pumped BH
Cumbria	Ewanrigg	Discharge
Fife	Balgonie Muirespot, Balgonie Dalginch (Thornton), Cameron, Cowdenbeath, Fordell No.2, Fordell No.5, Fordell Vengeance, Fordell Venerable Shaft, Lochhead, Middlefield, Muirebridge Chemiss, Randolph	Monitoring BH/Shaft
	Fordell Day Level, Fordell Upper Discharge, Kinglassie Discharge, Lathallan Mill, Leven 4 BH, Minto, Pitfirrane, Star Road	Discharge
	Frances, Michael	Pumped Shaft
Lancashire	Bridgewate, Blackclough, Broadclough, Carr and Craggs, Fennyfield, Haydock Sough, Jowkin Wood, Old Meadows	Cascade
	Collins Green No.1-4, Deerplay Waterloose, Duke's Level	Monitoring BH/Shaft
	Aspull Sough, Clough Foot, Deerplay, Downbrook, Hockery Brook, Pemberton, Summersales	Pumped Shaft/BH/Discharges
Lothian	Blindwells BH, Elginhaugh, Joppa Day Level	Discharge
	Bilston Glen, Blindwells, Easthouses, Muirpark, Niddire, Old Fordel, Riggonhead, Seton BHs, Wallyford Great	Monitoring BH/Shaft
	Blindwells, Monktonhall	Pumped BH
North East	Bates, Acomb, Broken Banks, Carking How, Chatershaugh, Chirm, East Edmonsley, Kimblesworth, Lumley, Stony Heap, Vivonium	Cascade
	Algernon, Bates No.2 , Boldon, Broomhill, Easington, East Chevington, East Holywell, Eldon, Ellington, Fishburn, Freeman Road, Hastings, Hauxley, Hawthorn, Kimblesworth Busty BH, Ladysmith, Maidens Hall, Mainsforth, Millwood, Moor Lane, Morpeth Moor, New Moor, Nicholson, Pegswood, Seaton Delaval, Sherburn Hill, Silksworth, Thrislingston, Tyneside North, Wearmouth Glassworks, Westoe	Monitoring Shaft/BH
	Allerdean Mill, Bates No.3, Blenkinsopp, Chester South Moor, Dawdon, Horden, Kibblesworth, Kimblesworth, Lambley, Saltburn, Whittle, Lynemouth, Whitburn	Pumped Shaft/BH/Discharge
North Wales	Hawarden	Monitoring Shaft
Nottinghamshire	Boythorpe, Morton	Discharge
	Babbington, Creswell, Hartington, Langton, Langwith, Markham, Moorgreen, Newstead, Oakwood, Oxcroft, Pinxton, Radford, Stoney Hall, Williamthorpe, A Winning	Monitoring BH/Shaft
	Fender, Woodside	Pumped Adit/Shaft
South Derbyshire	Cadley Hill, Moira, Netherseal, Oakthorpe, Rawdon, Saltersford	Monitoring BH
South Wales	Abercwmboi, Abersychan, Betws, Blackvein, Blaenavon, Cefn Hengoed, Craig Fawr, Crumlin Navigation, Dinas, Greens Level, Gwynfi, Morlais, Penywaun, Sunningdale, Tan Y Garn, Tower Shaft 4, Whitworth, Six Bells (Vivian) Cascade, Glyncastle	Discharge/Cascade
	Blaenavon Vivian BH, Cefn Coed Shaft - Blaenant, Craig yr Aber, Cross Hands, Cymmer, Duffryn Rhondda, Nant Llesg, Ogmore Vale, Pontlottyn, Rhondda, Tram Road	Monitoring BH/Shaft
	Lindsay, Mountain Gate, Six Bells (Vivian) BH, Taff Merthyr, Ynysarwed	Pumped BH/Shaft/Discharge
Staffordshire	Cannock Wood, Silverdale	Cascade
	Cannock Wood BH, Leacroft, Littleton, Wandon BH, West Cannock	Monitoring BH
	Cannock Wood BH, Silverdale	Pumped BH/Shaft
Yorkshire	Silkstone, Strafford, Sheephouse, Woolley	Discharge/Cascade
	Barnsley, Claywheels Lane, Crofton, Deepcar, Kilnhurst, Kimberworth, Kimberworth Park East, Kiveton, Monckton Coke Works, New Stubbin, Steetley, Thorpe Hesley, Thurcroft	Monitoring BH/Shaft
	Bullhouse, Caphouse, Strafford, Woolley, Sheephouse BH, Sheephouse	Pumped BH/Shaft/Adit

Figure A.8: Summary of the TCA temperature monitoring sites and site status classified by coalfield.

A.2.2 Rock type categories

To simplify the calculation of the harmonic mean thermal properties for each digitised log, rock types have been grouped by categories. Those are summarised in Table A.14.

Categories	Rock types
No core	No Core (inc. Open Hole)
Coal	Coal (inc. Cannel, Blackstone, Ribs, BBI, CBI, Waste)
Ironstone	Ironstone
Igneous	Basalt, Lava, Dolerite, Tuff, Agglomerate, Dyke (pegmatitic, teschenite, trachyte)
Coarse rock	Sandstone (inc. Chert), Conglomerate (inc. Breccia, gravel)
Fine Rock	Siltstone, Clayrock, Seatrock, Shale (inc. Fakes, blaes), Mudtone (inc. Marl, slate)
Carbonate	Limestone (inc. Calcite, cemenstone), Dolomite
Mud	Clay (inc. Seatearth, Seatclay), Fireclay
Sand	Sand (Soil)

Table A.14: Modified rock names and rock type categories.

A.2.3 Database table

This section displays samples of all the geodatabase entities (i.e. tables) developed in this study. This database has been created for the purpose of this research and to data sharing agreements (i.e. TCA data being accessed via an academic license), it is to date not available publicly.

Rock	Heat Conductivity	Heat Conductivity 2	Heat Capacity	Density	rhoc	Heat Diffusivity	RHP
OH	0.59	NaN	4185	1000	4185000	1.409800e-07	0.000000e+00
coal	0.40	0.31	1300	1350	1755000	2.279200e-07	5.000000e-07
ironstone	2.85	2.35	880	2760	2428800	1.173420e-06	7.000000e-07
limestone	2.85	3.05	880	2760	2428800	1.173420e-06	2.066000e-06
mudstone	1.41	1.92	770	2600	2002000	7.042960e-07	1.392000e-06
siltstone	1.84	2.26	910	2680	2438800	7.544690e-07	1.392000e-06
sandstone	4.54	3.96	930	2460	2287800	1.984440e-06	8.960000e-07
seatrock	2.42	NaN	860	2680	2304800	1.049980e-06	1.900000e-06
dolerite	1.81	1.90	858	2870	2462460	7.350370e-07	5.400000e-07
basalt	2.00	2.44	840	3000	2520000	7.936510e-07	5.400000e-07
clay	1.11	2.42	860	2380	2046800	5.423100e-07	1.900000e-06
clayrock	1.05	NaN	920	2450	2254000	4.658390e-07	1.900000e-06
conglomerate	NaN	2.63	930	2460	2287800	1.149580e-06	8.960000e-07
fireclay	NaN	0.59	860	2380	2046800	2.882550e-07	1.900000e-06
sand	0.77	NaN	860	1900	1634000	4.712360e-07	1.700000e-06
shale	NaN	1.50	390	2600	1014000	1.479290e-06	2.900000e-06
tuff	2.35	2.15	200	1500	300000	7.833330e-06	3.200000e-06
dolomite	4.29	NaN	920	2850	2622000	1.636160e-06	2.066000e-06

Figure A.9: Sample of the **Rock property** table.

REFERENCE GEOL LOG	ID GLOG	BOREHOLE NAME	LOCATION	COALFIELD	MWB	HEIGHT (mAOD)	BH DEPTH (mBGL)	BGS Ref	Easting	Northing
AUCHENNIDY	1	AUCHENNIDY	AUCHENNIDY	Lothian	Scotland - Lothian	166.0	461.8000	NT26SW81	324964.0	661241.0
BATES_NO3	2	No.3 Shaft	BATES	North East	Bates	6.0	301.6000	NZ38SW24	430496.0	582255.0
BILSTON_GLEN_2	3	No.2 shaft	BILSTON GLEN	Lothian	Scotland - Lothian	137.0	732.8192	NT26NE82	327260.0	665080.0
BORELAND	4	Boreland Bore	BORELAND	Fife	Scotland - East Fife	61.0	1006.7000	NT39SW44	330394.0	694222.0
CAMERON	5	CAMERON 1/79 Bore (LOG) / Dysart Main Borehole...	CAMERON	Fife	Scotland - East Fife	41.7	1258.1000	NT39NW380	334566.0	699006.0
...	...	...	...	...	...	...	...	...	...	...
PARKSIDE	66	A3/10/2 PARKSIDE FARM	PARKSIDE	Lancashire	Lancashire	35.0	178.3100	SJ69SW18	360900.0	394880.0
PORTOBELLO	67	PORTBELLO BAR	PORTOBELLO	Lancashire	Lancashire	452.6	205.4300	SK07SW3	403280.0	371380.0
RENISHAW	68	RENISHAW PARK COLLIERY HARTINGTON DRIFT	RENISHAW	Nottinghamshire	Hartington-Creswell-Langwith	-95.0	94.4900	SK47NW31	443412.0	375673.0
SEATON	69	SEATON DELAVAL COLLIERY U/G	SEATON	North East	Bates	-132.0	174.3500	NZ37NW13	430320.0	576320.0
SILVERDALE	70	SILVERDALE 48UGBH	SILVERDALE	Staffordshire	Staffordshire	-390.0	98.4500	SJ84NW229	382370.0	345945.0

REFERENCE GEOL LOG	TRUE	TEMPERATURE BOREHOLE	HISTORIC TEMPERATURE DATA TYPE	HISTORIC DEPTH MEASUREMENT	HISTORIC TEMPERATURE	GRADIENT	HEAT FLUX	Farr et al (2020)	TEMPERATURE DATA SOURCE
AUCHENNIDY	Y	AUCHENNIDY	BHT	459.0	18.0	19.6	NaN	19.0	Burley & Gale (1981)
BATES_NO3	N	WHITEY BAY	BHT	1052.0	32.2	21.1	NaN	36.0	Burley & Gale (1981)
BILSTON_GLEN_2	Y	BILSTON GLEN	MWT	670.0	15.0	8.7	NaN	19.0	Burley & Gale (1981)
BORELAND	Y	BORELAND	EQM	1007.0	29.8	20.2	54.0	14.0	Oxburgh (1982)
CAMERON	N	WINDYGATE	BHT	1298.0	30.0	16.1	NaN	14.0	Burley & Gale (1981)
...	...	...	...	...	...	...	...	...	...
PARKSIDE	N	PARSIDE_COLL	VST	698.0	24.2	19.2	NaN	NaN	Burley & Gale (1981)
PORTOBELLO	N	NaN	NaN	NaN	NaN	NaN	NaN	NaN	Burley & Gale (1981)
RENISHAW	N	DOLSOVER	VST	610.0	27.1	28.0	NaN	34.0	Burley & Gale (1981)
SEATON	Y	SEATON	BHT	1052.0	32.2	21.1	NaN	36.0	Burley & Gale (1981)
SILVERDALE	Y	SILVERDALE	VST	537.0	20.4	20.1	NaN	NaN	Burley & Gale (1981)

Figure A.10: Sample of the **Geological Borehole** or **GLOG** table, that summarises the characteristics of the geological logs listed in Tables A.12 and A.13. Each entry is linked to the corresponding geological log via the *REFERENCE GEOL LOG* attribute (i.e. the filename).

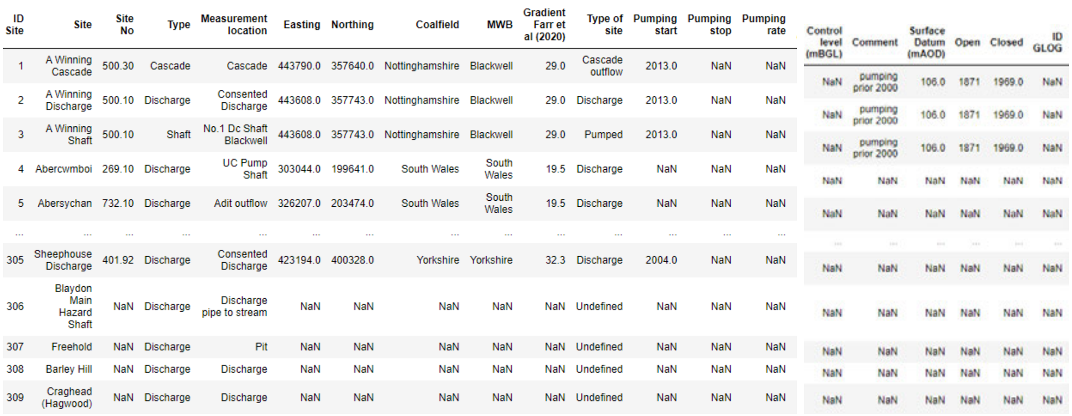

ID Site	Site	Site No	Type	Measurement location	Easting	Northing	Coalfield	MWB	Gradient Farr et al (2020)	Type of site	Pumping start	Pumping stop	Pumping rate
1	A Winning Cascade	500.30	Cascade	Cascade	443790.0	357640.0	Nottinghamshire	Blackwell	29.0	Cascade outflow	2013.0	NaN	NaN
2	A Winning Discharge	500.10	Discharge	Consented Discharge	443608.0	357743.0	Nottinghamshire	Blackwell	29.0	Discharge	2013.0	NaN	NaN
3	A Winning Shaft	500.10	Shaft	No.1 Dc Shaft Blackwell	443608.0	357743.0	Nottinghamshire	Blackwell	29.0	Pumped	2013.0	NaN	NaN
4	Abercwmboi	269.10	Discharge	UC Pump Shaft	303044.0	199641.0	South Wales	South Wales	19.5	Discharge	NaN	NaN	NaN
5	Abersychan	732.10	Discharge	Adit outflow	326207.0	203474.0	South Wales	South Wales	19.5	Discharge	NaN	NaN	NaN
...	...	...	...	...	...	...	...	...	...	...	...	...	...
305	Sheephouse Discharge	401.92	Discharge	Consented Discharge	423194.0	400328.0	Yorkshire	Yorkshire	32.3	Discharge	2004.0	NaN	NaN
306	Blaydon Main Hazard Shaft	NaN	Discharge	Discharge pipe to stream	NaN	NaN	NaN	NaN	NaN	Undefined	NaN	NaN	NaN
307	Freehold	NaN	Discharge	Pit	NaN	NaN	NaN	NaN	NaN	Undefined	NaN	NaN	NaN
308	Barley Hill	NaN	Discharge	Discharge	NaN	NaN	NaN	NaN	NaN	Undefined	NaN	NaN	NaN
309	Craghead (Hagwood)	NaN	Discharge	Discharge	NaN	NaN	NaN	NaN	NaN	Undefined	NaN	NaN	NaN

ID Site	Control level (mBGL)	Comment	Surface Datum (mAOD)	Open	Closed	ID GLOG
1	NaN	pumping prior 2000	106.0	1871	1969.0	NaN
2	NaN	pumping prior 2000	106.0	1871	1969.0	NaN
3	NaN	pumping prior 2000	106.0	1871	1969.0	NaN
4	NaN	NaN	NaN	NaN	NaN	NaN
5	NaN	NaN	NaN	NaN	NaN	NaN
...	...	...	...	...	...	...
305	NaN	NaN	NaN	NaN	NaN	NaN
306	NaN	NaN	NaN	NaN	NaN	NaN
307	NaN	NaN	NaN	NaN	NaN	NaN
308	NaN	NaN	NaN	NaN	NaN	NaN
309	NaN	NaN	NaN	NaN	NaN	NaN

Figure A.11: Sample of the **Site** table, that summarises the characteristics of the TCA monitoring sites.

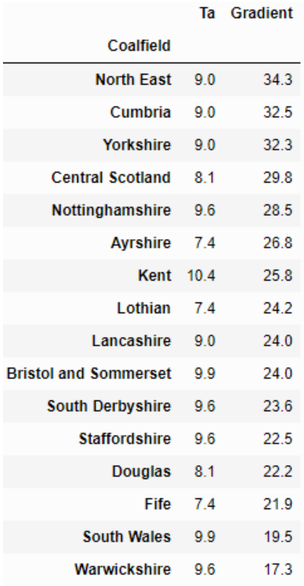

	Ta	Gradient
Coalfield		
North East	9.0	34.3
Cumbria	9.0	32.5
Yorkshire	9.0	32.3
Central Scotland	8.1	29.8
Nottinghamshire	9.6	28.5
Ayrshire	7.4	26.8
Kent	10.4	25.8
Lothian	7.4	24.2
Lancashire	9.0	24.0
Bristol and Sommerset	9.9	24.0
South Derbyshire	9.6	23.6
Staffordshire	9.6	22.5
Douglas	8.1	22.2
Fife	7.4	21.9
South Wales	9.9	19.5
Warwickshire	9.6	17.3

Figure A.12: Sample of the **Geothermal gradient Farr et al. (2020)** table. The average surface temperature and equilibrium geothermal gradient calculated by Farr et al. (2020) at the scale of the MWB.

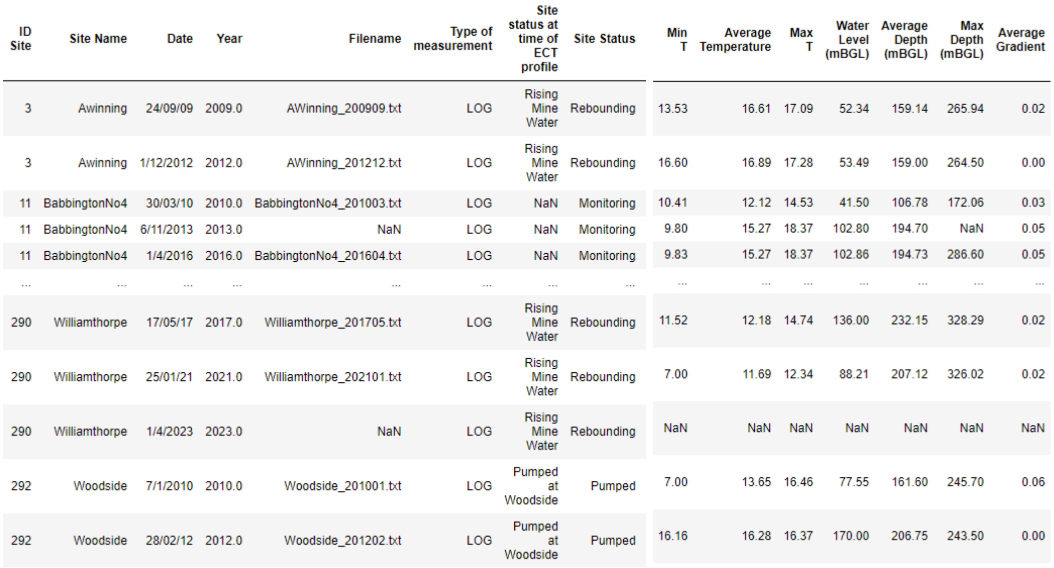

ID Site	Site Name	Date	Year	Filename	Type of measurement	Site status at time of ECT profile	Site Status	Min T	Average Temperature	Max T	Water Level (mBGL)	Average Depth (mBGL)	Max Depth (mBGL)	Average Gradient
3	Awinning	24/09/09	2009.0	AWinning_200909.txt	LOG	Rising Mine Water	Rebounding	13.53	16.61	17.09	52.34	159.14	265.94	0.02
3	Awinning	1/12/2012	2012.0	AWinning_201212.txt	LOG	Rising Mine Water	Rebounding	16.60	16.89	17.28	53.49	159.00	264.50	0.00
11	BabbingtonNo4	30/03/10	2010.0	BabbingtonNo4_201003.txt	LOG	NaN	Monitoring	10.41	12.12	14.53	41.50	106.78	172.06	0.03
11	BabbingtonNo4	6/11/2013	2013.0	NaN	LOG	NaN	Monitoring	9.80	15.27	18.37	102.80	194.70	NaN	0.05
11	BabbingtonNo4	1/4/2016	2016.0	BabbingtonNo4_201604.txt	LOG	NaN	Monitoring	9.83	15.27	18.37	102.86	194.73	286.60	0.05
...	...	...	...	...	...	...	...	...	...	...	...	...	...	...
290	Williamthorpe	17/05/17	2017.0	Williamthorpe_201705.txt	LOG	Rising Mine Water	Rebounding	11.52	12.18	14.74	136.00	232.15	328.29	0.02
290	Williamthorpe	25/01/21	2021.0	Williamthorpe_202101.txt	LOG	Rising Mine Water	Rebounding	7.00	11.69	12.34	88.21	207.12	326.02	0.02
290	Williamthorpe	1/4/2023	2023.0	NaN	LOG	Rising Mine Water	Rebounding	NaN	NaN	NaN	NaN	NaN	NaN	NaN
292	Woodside	7/1/2010	2010.0	Woodside_201001.txt	LOG	Pumped at Woodside	Pumped	7.00	13.65	16.46	77.55	161.60	245.70	0.06
292	Woodside	28/02/12	2012.0	Woodside_201202.txt	LOG	Pumped at Woodside	Pumped	16.16	16.28	16.37	170.00	206.75	243.50	0.00

Figure A.13: Sample of the **Temperature LOG** table, that describes the characteristics of all the temperature profiles acquired by TCA.

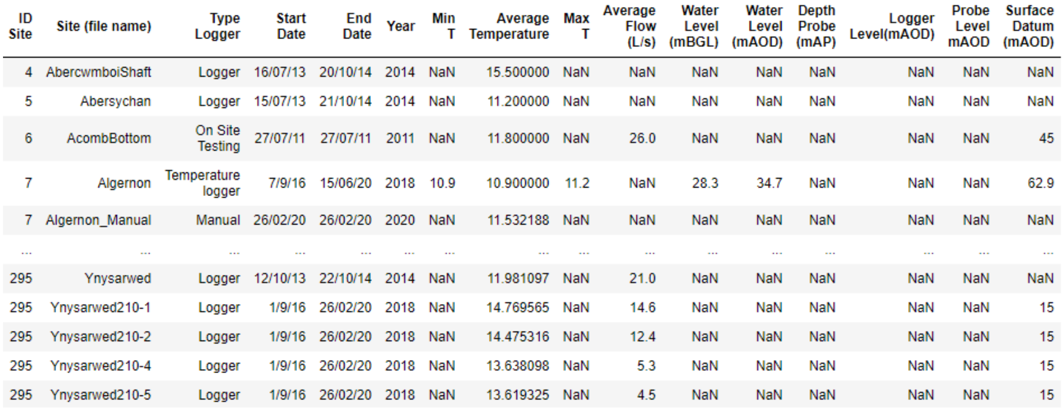

ID Site	Site (file name)	Type Logger	Start Date	End Date	Year	Min T	Average Temperature	Max T	Average Flow (L/s)	Water Level (mBGL)	Water Level (mAOD)	Depth Probe (mAP)	Logger Level(mAOD)	Probe Level mAOD	Surface Datum (mAOD)
4	AbercwmboiShaft	Logger	16/07/13	20/10/14	2014	NaN	15.500000	NaN	NaN	NaN	NaN	NaN	NaN	NaN	NaN
5	Abersychan	Logger	15/07/13	21/10/14	2014	NaN	11.200000	NaN	NaN	NaN	NaN	NaN	NaN	NaN	NaN
6	AcombBottom	On Site Testing	27/07/11	27/07/11	2011	NaN	11.800000	NaN	26.0	NaN	NaN	NaN	NaN	NaN	45
7	Algernon	Temperature logger	7/9/16	15/06/20	2018	10.9	10.900000	11.2	NaN	28.3	34.7	NaN	NaN	NaN	62.9
7	Algernon_Manual	Manual	26/02/20	26/02/20	2020	NaN	11.532188	NaN	NaN	NaN	NaN	NaN	NaN	NaN	NaN
...	...	...	...	...	...	...	...	...	...	...	...	...	...	...	...
295	Ynysarwed	Logger	12/10/13	22/10/14	2014	NaN	11.981097	NaN	21.0	NaN	NaN	NaN	NaN	NaN	NaN
295	Ynysarwed210-1	Logger	1/9/16	26/02/20	2018	NaN	14.769565	NaN	14.6	NaN	NaN	NaN	NaN	NaN	15
295	Ynysarwed210-2	Logger	1/9/16	26/02/20	2018	NaN	14.475316	NaN	12.4	NaN	NaN	NaN	NaN	NaN	15
295	Ynysarwed210-4	Logger	1/9/16	26/02/20	2018	NaN	13.638098	NaN	5.3	NaN	NaN	NaN	NaN	NaN	15
295	Ynysarwed210-5	Logger	1/9/16	26/02/20	2018	NaN	13.619325	NaN	4.5	NaN	NaN	NaN	NaN	NaN	15

Figure A.14: Sample of the **Temperature time series** table, that describes the characteristics of all the temperature and water level time series acquired by TCA.

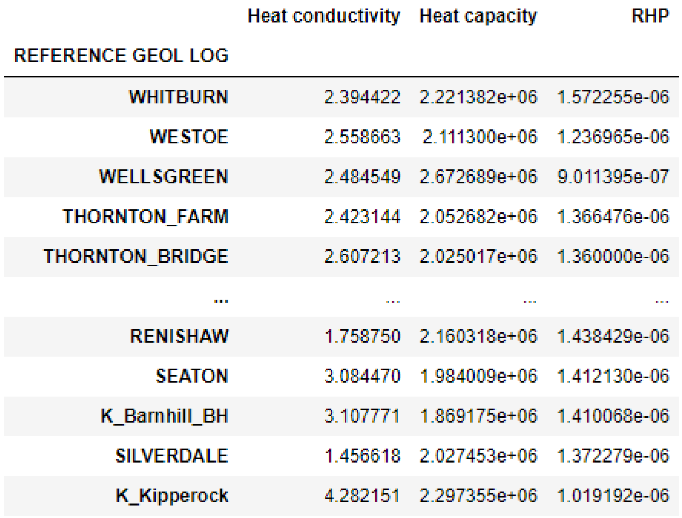

	Heat conductivity	Heat capacity	RHP
REFERENCE GEOL LOG			
WHITBURN	2.394422	2.221382e+06	1.572255e-06
WESTOE	2.558663	2.111300e+06	1.236965e-06
WELLSGREEN	2.484549	2.672689e+06	9.011395e-07
THORNTON_FARM	2.423144	2.052682e+06	1.366476e-06
THORNTON_BRIDGE	2.607213	2.025017e+06	1.360000e-06
...	...	...	...
RENISHAW	1.758750	2.160318e+06	1.438429e-06
SEATON	3.084470	1.984009e+06	1.412130e-06
K_Barnhill_BH	3.107771	1.869175e+06	1.410068e-06
SILVERDALE	1.456618	2.027453e+06	1.372279e-06
K_Kipperock	4.282151	2.297355e+06	1.019192e-06

Figure A.15: Effective heat conductivity, heat capacity and RHP for each borehole (**Borehole properties** table), calculated based on the rock type percentage determined from the digitised geological logs and on the corresponding rock properties. The table is linked to the **GLOG** table and corresponding geological log via the *REFERENCE GEOL LOG* attribute, whilst each rock type from the geological log is linked to its corresponding properties via the *Rock type* attribute from the **Rock property** table.

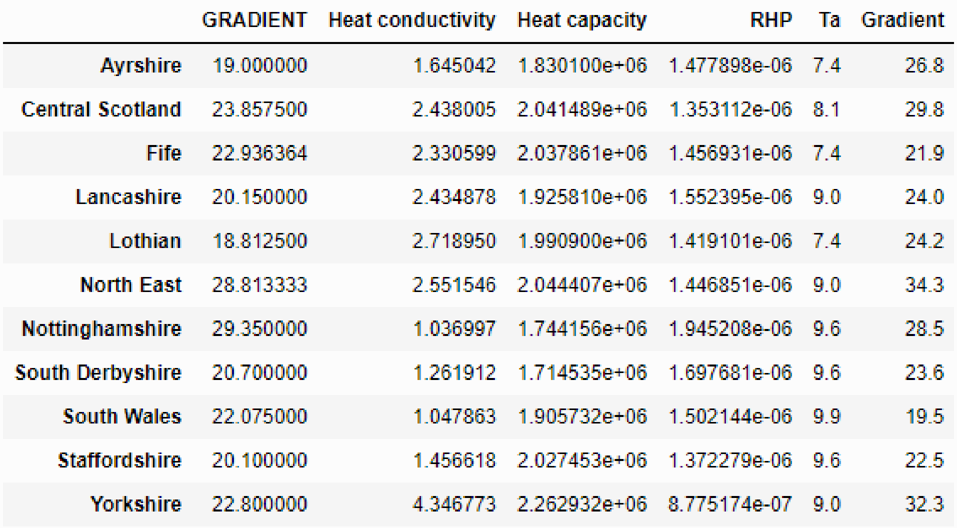

	GRADIENT	Heat conductivity	Heat capacity	RHP	Ta	Gradient
Ayrshire	19.000000	1.645042	1.830100e+06	1.477898e-06	7.4	26.8
Central Scotland	23.857500	2.438005	2.041489e+06	1.353112e-06	8.1	29.8
Fife	22.936364	2.330599	2.037861e+06	1.456931e-06	7.4	21.9
Lancashire	20.150000	2.434878	1.925810e+06	1.552395e-06	9.0	24.0
Lothian	18.812500	2.718950	1.990900e+06	1.419101e-06	7.4	24.2
North East	28.813333	2.551546	2.044407e+06	1.446851e-06	9.0	34.3
Nottinghamshire	29.350000	1.036997	1.744156e+06	1.945208e-06	9.6	28.5
South Derbyshire	20.700000	1.261912	1.714535e+06	1.697681e-06	9.6	23.6
South Wales	22.075000	1.047863	1.905732e+06	1.502144e-06	9.9	19.5
Staffordshire	20.100000	1.456618	2.027453e+06	1.372279e-06	9.6	22.5
Yorkshire	22.800000	4.346773	2.262932e+06	8.775174e-07	9.0	32.3

Figure A.16: Effective heat conductivity, heat capacity and RHP averaged at the scale of the MWB together with the corresponding undisturbed temperature gradient calculated by Farr et al. (2020). The table is linked to the **Temperature gradient** and **GLOG** tables via the *Coalfield* attribute.

A.2.4 Additional correlation analysis

This section displays the correlation analyses between the rock properties and the geothermal gradient at the borehole scale (Fig. A.17) and the MWB scale (Fig. A.18), as well as between the mine-water temperature and flow rate at the MWB scale (Fig. A.19).

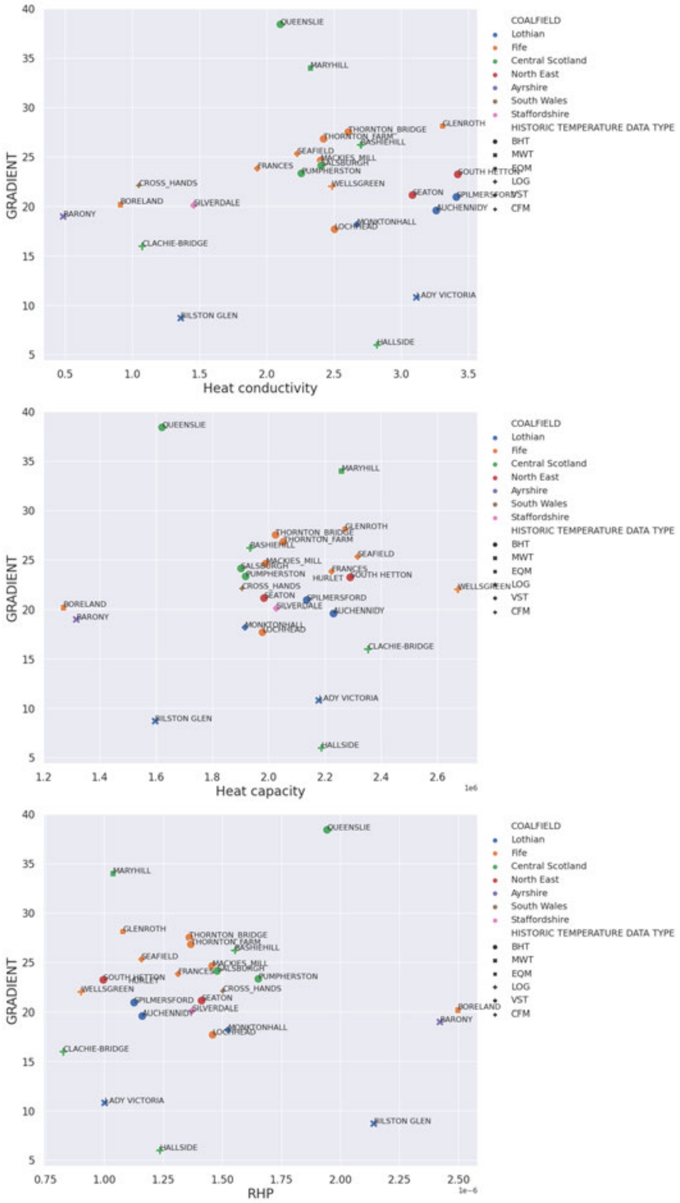

Figure A.17: Relationship between the harmonic mean heat conductivity, heat capacity and RHP for each geological borehole and the historic temperature gradient for the corresponding or neighbouring borehole (Burley et al., 1984), classified by coalfield.

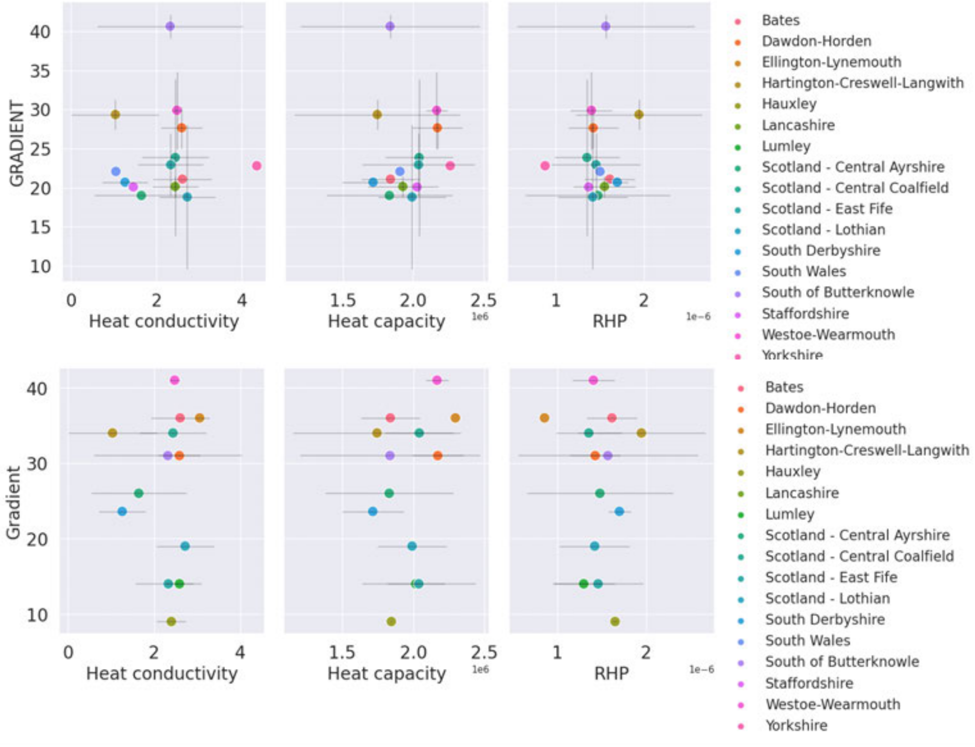

Figure A.18: Relationship between the harmonic mean heat conductivity, heat capacity and RHP values calculated for each geological borehole, and the geothermal gradient from Burley et al. (1984) and Farr et al. (2020). Here, values are averaged at the scale of the MWB to reduce the scattering effect of single acquisitions whilst increasing the number of data points compared to a coalfield scale average.

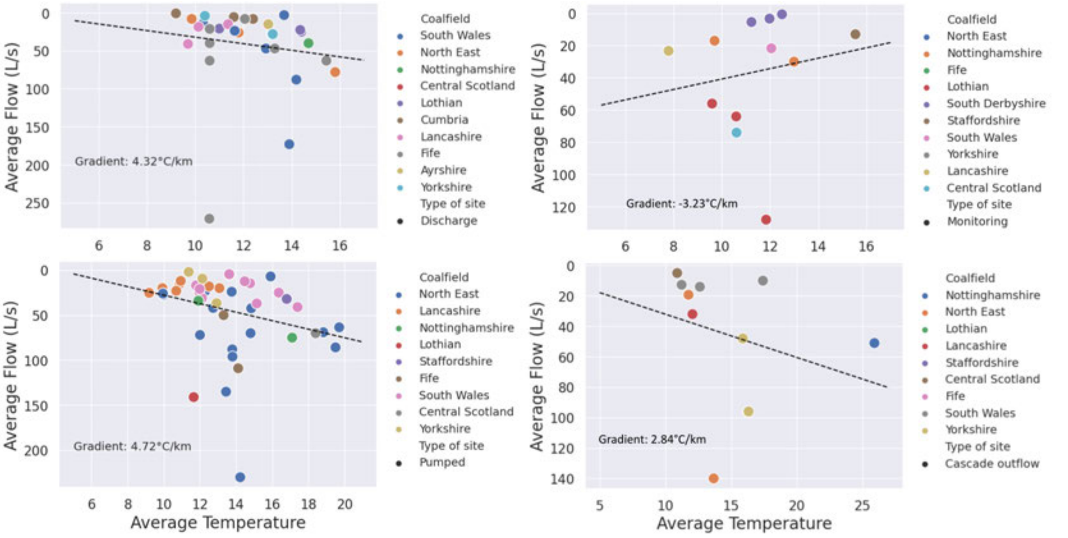

Figure A.19: Relationship between the average flow and the average monitored temperature at monitoring sites, averaged at the MWB scale.

A.2.5 Conceptual model for the Dawdon-Horden MWB

Mining history

The Dawdon-Horden mine-water block (MWB) is situated in the East Durham Coalfield in North-East England, in the UK (Fig. 8.3). Approximately 36% of the block is located offshore, where coal has been worked underneath both the seabed and the Permian strata (see chapter 2). Based on digitised mine plans obtained from TCA through an academic license, the block is found to extend over 251 km^2, including 160 km^2 of onshore mine workings and about 90 km^2 of offshore mine workings. The total inland volume of the galleries is estimated to be 1.8 and 5.0 $\times$ 10^7 m^3 (Coal Authority data). Coal mine workings are present within at least 16 seams between the Ryhope Five Quarter (C) and Bottom Busty (Q2) seams. In Dawdon, 6 main seams have been worked using both the pillar-and-stall (shallow workings) and longwall (deep workings) mining approaches (Table 8.3).

Mining activities started in the Dawdon, Horden and Easington collieries in 1900, and in Hawthorn in 1960. Following the nationalisation of the coal industry in 1947, 16 collieries were operated within the Dawdon-Horden mining block. The entire block was dewatered at a rate of about 650 L/s. Older shallow workings located near the River Wear (i.e. Lumley and Sherburn-Houghall) were also pumped by British Coal to prevent the overflow of water to deeper mines. The Horden, Dawdon and Hawthorn (Murton) collieries closed in 1986, 1991 and 1992, respectively.

The mining and dewatering activities ceased in the Dawdon-Horden mining block in 1991/1992 when the Easington colliery last closed (abandonment in 1993). Following the abandonment of the Easington colliery in 1993, shallow pumping at Lumley 6th was maintained by TCA until 2008. The cessation of pumping in the Lumley block ultimately led to the rebound of water in all blocks in the area (Fig. A.20).

Pumping resumed at Horden in 2004, when a temporary active mine-water treatment plant started operating to gain control of the rising mine water levels, and prevent the occurrence of unwanted surface discharge and the contamination of the overlying Permian Magnesian Limestone (major drinking water supply) by saline mine water. Previous investigations have shown that to mitigate the risk of contamination of the Permian aquifer, mine-water levels along the coast require control at about 16 mBOD at Dawdon and 10 mBOD at Horden (Streetly et al., 2009). From 2006, about 100 L/s of mine water was abstracted from the Horden shaft and reached 120 L/s at its peak before Dawdon became operational. In 2008, the main pumping and active mine-water treatment site was moved to Dawdon, designed to continually treat about 100 L/s of the mine water recharging the MWB (WYG, 2006). In Horden, the temporary active plant was replaced by a passive treatment site (i.e. lagoons and reed beds system) in 2011 as a result of the change in mine-water chemistry. Both active and passive treatment systems are used to reduce the concentration of iron and other adverse elements in the mine

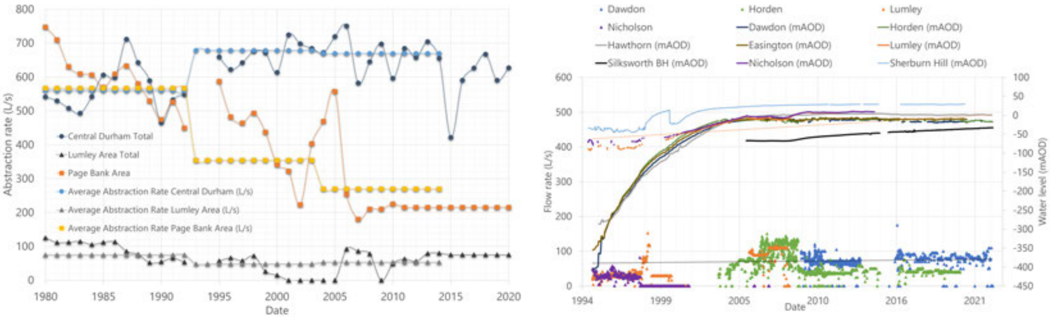

Figure A.20: Historic flow rate (L/s) and water levels (mAOD) in the Durham block. The Dawdon-Horden, Silksworth and Wearmouth MWB are located in the concealed part of the coalfield, whilst Chatershaugh, Lumley 6^{th}, Nicholson, Boldon and Chester South Moor blocks are located in the exposed section. The average water level in the concealed coalfield (Thrislington, Mainsforth, Stony Hall) between 1999 and 2008 was 79 mAOD, against 108 mAOD for the exposed coalfield (Ladysmith, Woodhouse No1 shaft, Vivonium, Page Bank, Whitworth) (source: ESI report for The Coal Authority, Streetly et al. (2009)).

water before discharging the treated water to the sea (Bailey et al., 2013). Although Horden has the hydraulic capacity to treat 50 L/s, a maximum of 40 L/s is abstracted to prevent the deterioration of the water quality. As of 2022, mine water levels controlled by abstraction at the Horden and Dawdon shafts appear to have stabilised around 15 mBOD. With the mine-water levels being maintained below the Permian groundwater piezometric surface throughout the block, it is assumed that there is no leakage from the mine workings to the Permian Limestone aquifer (Fig. A.20).

Hydrogeological conceptual model

This section summarises the conceptual model for the Dawdon-Horden MWB. It is based on the review of consultancy and EA reports undertaken on behalf of The Coal Authority (British Coal, 1992; IMC, 2001; Streetly et al., 2009; Villasenor, 2019; WYG, 2006).

External connections. The block is bounded to the North by the Silksworth and Westoe-Wearmouth MWB, to which there is no recorded connection. There, water levels are below the one recorded in Dawdon-Horden. To the South, there is a direct roadway connection in the Five Quarter (F) Seam (54 mAOD) and potential goaf connections in Main (G) Seam (7 mAOD) to the Bowburn-Trimdon Grange block. However, the degree of goaf connection is uncertain and the absence of water level measurements in the Bowburn-Trimdon Grange block makes it impossible to determine the nature of the connections (i.e. whether they are located within the flooded zones or on an overflow/perched water level) and actively contributing to the recharge to Horden-Dawdon. The Dawdon-Horden MWB is almost entirely concealed by the Permian Magnesian Limestone and limited evidence of Permian inflows to the mines suggests that recharge predominantly occurs via inflow from the adjacent Sherburn-Houghall and Lumley blocks, that bound Dawdon-Horden to the West. The external connections to those blocks include:

- Two dams connecting the Thornley Hutton (L) Seam at 77 mBOD to the Sherburn Hill Low Main (J) Seam at 45 mBOD. Initially built to withstand a head of 105 m (60 mAOD), the rise in water level at Sherburn Hill in the 1990s caused one of those dams to fail with a head of 59 m (13.6 mAOD). Although it has been reported to be leaking small flows of water, it is unknown if the dams have failed completely or if there is a partial restriction to the flow.
- Goaf and/or roadway connections in the Maudlin (H) Seam (134 mBOD and 158 mBOD) between Lumley and Eppleton-Houghton-Elemore, but it is unclear if water flow is restricted via this connection.

In both Sherburn Hill and Lumley, the water levels are similar or higher than the ones at Hawthorn. Historically, those three interconnected blocks were collectively called the East of Wear block, with an estimated total recharge of 200 to 230 L/s. Whilst current pumping rates at Dawdon and Horden indicate a recharge of $\sim$100-140 L/s, this would suggest that $\sim$60-90 L/s is being discharged at Chatershaugh (Lumley block).

To the East, the Dawdon-Horden MWB is bounded by the North Sea coast, whilst the mine working within the eastward dipping Coal Measures extend offshore up to approximately 10 km. Based on a pumping test, Pastor (2007) suggested that 90%, 9% and 1% of the water pumped originates from the mine water, the Magnesian Limestone Aquifer and the seawater, respectively. In mine workings beneath the North Sea, Pastor (2007) reports historical inflow rates of over 8.6 ML/day, which are above the current average pumping rate of 100 L/s (Appendix E – Coal Measures Hydrogeology - EA Report, Streetly et al. (2009)).

Internal connections Since the closure of the mines and the cessation of pumping in 1993 at Easington, mine-water levels have been continuously monitored by TCA at four mine shafts within the block (i.e. Dawdon, Horden, Easington and Hawthorn). Monitoring initially allowed predicting the rate of mine-water rebound and anticipating timings for mine-water levels to rise above the aquifer water level and associated pollution risks. Since the implementation of pumping in 2004, continuous loggers have been measuring both the water level and MWT at the four monitoring sites. Data suggested good connectivity between Dawdon, Easington and Horden, despite the existence of the E-W trending Ludworth Whin Dyke splitting the Horden-Dawdon MWB into two sub-blocks.

To the north of the Ludworth Whin Dyke are the Dawdon and Easington collieries, the Murton (Hawthorn) colliery that effectively merges with South Hetton, Eppleton and Elemore, the Haswell Colliery, and the merged Seaham/Vane Tempest collieries that a dam separates from Ryhope. Reports suggested that the Dawdon shaft is interconnected with the general body of mine workings via the Murton Colliery, and with the Easington (roadways in Low Main J and Main F), Vane (connection in Low Main J) and Seaham (roadway in High Main E) collieries. Roadway connections between Easington and Murton in the Main seam E are also likely to allow for the flow of water between the two collieries. Roadway and goaf connections between Murton and Seaham in the Main (F) and High Main (E) seams have also been reported. The High Main seam in Murton was worked from South Hetton Colliery where a whin dyke was proven by a borehole.

In the southern section of the dyke, a dam with unknown flow status divides the collieries into west and east areas. On the eastern side are the merged Horden/Blackhall collieries, linked to Castle Eden via goaf connections with Blackhall. On the western side are the Shotton, Wheatley Hill and Thornley collieries, linked to Cassop Vale via a goaf connection to Thornley. An open roadway between the Ludworth and Thornley collieries connects workings on the north and south of the Ludworth Whin Dyke. Dammed roadways between the north and south collieries may also contain drainage pipes allowing the flow of water between different sub-blocs (e.g. Sherburn Hill – Thornley, Horden – Easington).

British Coal reported a dam in the roadway between the Horden Low Main (J) and Easington Main (F) seams (274 mBOD to 305 mBOD), initially built to withstand a head of 122 m on the north/Easington side, which is assumed to be no longer active (i.e. same recovery rate observed at Easington and Horden), allowing the water to flow between the two sub-blocks. This is further evidenced by the control of the mine-water level at Easington via pumping at Horden. In addition, 2 dammed drifts between the Shotton and Haswell Hutton (L) seams connect the northern and southern sub-blocks through the Ludworth Whin Dyke. British Coal (1992) suggested that a build-up of water on the south side might have caused the failure of the dams, initially designed to withstand a head of 436 m on the north/Haswell side. Additional internal connections include a roadway connection between Horden Main (F) at 177 mBOD and Shotton Low Main (J) at 242 mBOD (south of Ludworth Whin Dyke, east and west sections), and between Thornley and Cassop Vale Hutton (L2) Seam through the filled mine Cassop Vale No.1 Shaft. Cassop/Cassop Vale only have recorded workings in the Main (G) and Five Quarter (F) Seams, although the No.1 Shaft was sunk to the Hutton seam. However, the mine-water level data does not cover the south-west section of the Ludworth Whin Dyke and it is therefore unknown if the flow paths from the Ryhope Colliery and the Thornley-Shotton area are restrictive to Dawdon and Horden.

Mine-water flow at Horden and Dawdon is mainly directed towards the Horden and Dawdon pumping shafts. Slightly higher water levels have been measured at Easington, located in between. Reports also suggested the connection of the Hawthorn colliery, located further west, to the coastal collieries, with the regional flow being directed from inland toward the coastal pumping stations. The relatively flat hydraulic gradients observed in recent years suggest that pumping at Dawdon and Horden has stabilised the water level across the MWB. Diurnal and spring-neap cycles tidal effects observed in the water levels monitored in coastal shafts were moreover interpreted as a pressure response of the undersea mine workings to the tides, given the absence of known connections between workings and the sea floor.

Magnesian Limestone aquifer The Coal Measures are almost entirely concealed by the overlying Permian Magnesian Limestone aquifer, which is itself overlain by Permo-Triassic sandstones. Till deposits above the outcropping Magnesian Limestone have been suggested to protect the aquifer from surface pollutants and limit the recharge to the aquifer (EA report 6886R2). The Carboniferous/Permian boundary is however considered ‘leaky’ due to the presence of minor sandstone aquifers within the Coal Measures that subcrop against the unconformity, creating natural pathways within the rock.

Large hydraulic gradients between the mine workings and the overlying Permian aquifer caused by dewatering have been suggested to represent a potential source of recharge during mining. Similarly, the head difference between the seabed and the offshore mine workings has been suggested to result in a small inflow of hypersaline water from overlying Permian evaporite beds, located undersea between the Coal Measures and the Permian Magnesian Limestone. The reduction of the vertical hydraulic gradients as mine water rebounded ultimately led to the reduction of leakage from the Permian strata. As the mine-water level is now maintained a few meters below both the Permian aquifer and sea level, it is expected that the inflow into onshore and offshore workings is minimal (Fig. A.21). Leakage via open or backfilled mine shafts has alternatively been suggested to create connections between the flooded mine workings and the overlying Magnesian aquifer.

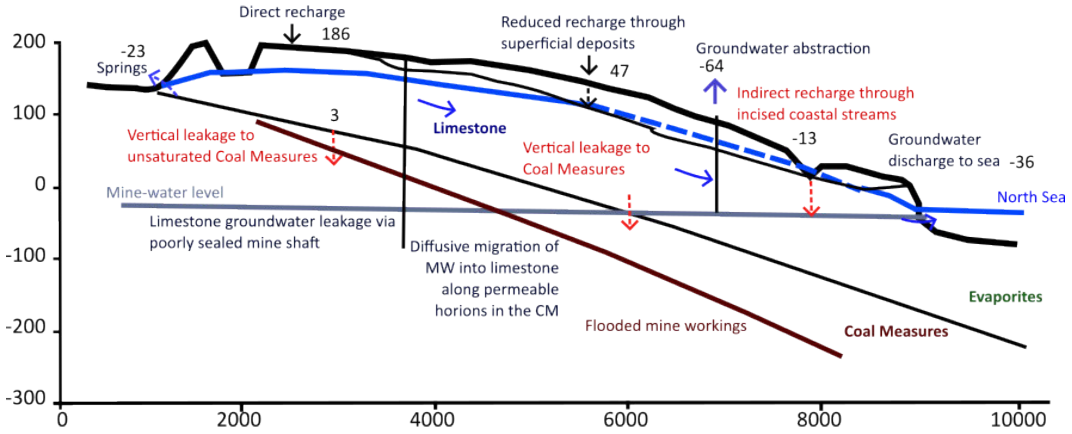

Figure A.21: Groundwater balance for the Magnesian Limestone Aquifer, adapted from the ESI Report 6886 R2 for the EA (Streetly et al., 2009).

Temperature profiles

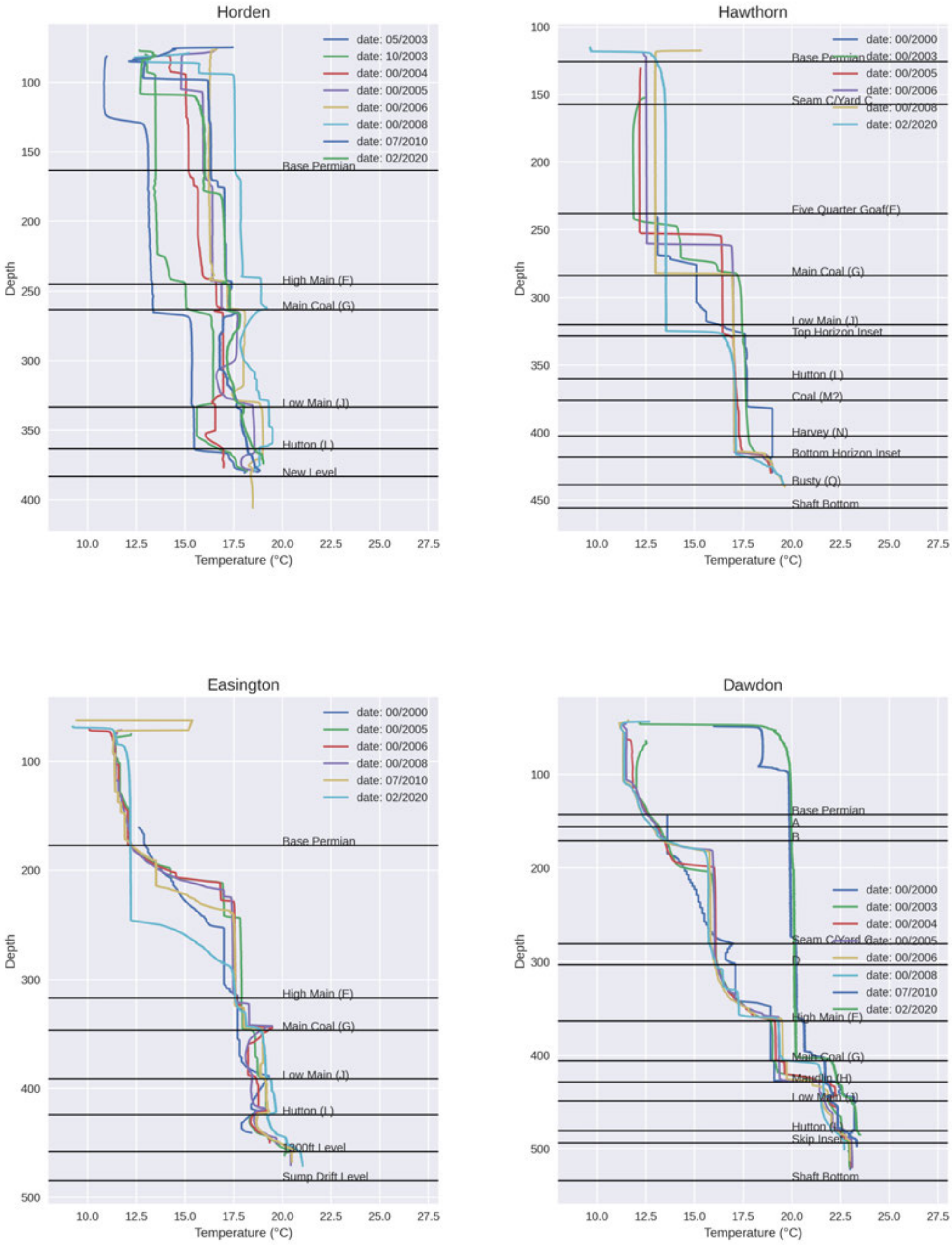

Figure A.22: Temperature profiles for the Horden, Hawthorn, Easington and Dawdon shafts at different acquisition time. The horizontal black lines are the seams intersected by each shaft (source: TCA).

Loggers have been continuously measuring the mine-water temperature alongside the water level in a few shafts located in the Dawdon-Horden and neighbouring mine-water blocks, including the Dawdon and Horden pumping shafts and the Easington and Hawthorn monitoring shafts. The time series of temperature measured at the logger depths in shafts only provides limited information on the actual MWT at greater depth. Conveniently, in Dawdon-Horden, repeated ECT profiles (electrical conductivity and temperature) have also been acquired by TCA during surveys in 2000, Sept/Dec 2003, 2004, 2005, 2006, 2008, 2010 and 2020 in order to get further insight into the seasonal and long-term effects of pumping. The profiling temperatures, made available by TCA under an academic license agreement, are described in this section to get a first insight into the temperature and hydraulic conditions in the Dawdon-Horden MWB (Fig. A.22).

Dawdon The Dawdon Theresa Shaft is 6.1 m in diameter and capped down to 1.3 mBGL, with a total reported depth from abandonment plans of 531.9 mBGL. Surveys of the Theresa shaft were carried out in 2020, 2010, 2008, 2006, 2005, 2004, 2003, 2000. ECT profiles and CCTV recordings indicate a decrease in the depth to the bottom of the shaft interpreted as the result of a sequential collapse and filling by debris as well as sedimentation from the shaft water column, down to 497.4 mBGL in 2010 and 487.75 mBGL in 2020 (10 m infill per 10 years).

In Dawdon, the mine-water level peaked in 2008 at 40.33 mBGL. A water level rise of about 96 m was measured between the pre-pumping conditions in 2000 and the 2020 survey, where it reached 45 mBGL (against 47.45 mBGL in 2010). Since the implementation of pumping in December 2009, the water level has varied between 37 and 52 mBGL.

Between 2000 and 2008, the principal area of change in conductivity (and to a lesser extent in temperature) is observed above the High Main (E) inset, also visible on CCTV, suggesting that mine water is moving through the Dawdon shaft at the High Main inset and the insets above. Although little temperature change is observed within this period (pre-pumping), the increase in EC observed at shallow depth between 2000 and 2004 is interpreted as the effect of rising mine water before the onset of pumping at Horden in 2004. Between 2004 and 2008, a gradual decrease in EC correlates with the onset of pumping at Dawdon, where only one gradual step change is observed at 110-173 mBGL. The 2010 and 2020 EC profiles (post-pumping) suggest relatively stable conditions compared to the 2000 - 2008 surveys. There, only two main stratification units are observed, with a large step change in electrical conductivity visible at 401.8 mBGL between the High Main seam E (360.2 mBGL) and the underlying Maudlin seam H (425.7 mBGL) insets. However, the 2010 survey also indicates a step change at 91.5 5mBGL which is not visible in 2020 but coincides with the pump intake located at 100 mBGL.

In 2020, the shaft temperature profile showed the water temperature to be in the range of 18.2 to 23.5℃ and consistently increases with depth with no change around the pump intake level. A comparison of the temperature profiles suggests that pumping increases the MWT in the shaft, removing some of the step changes so that water temperature is fairly consistent down to approximately 400 m.

Horden The Horden South shaft is 6.1 m in diameter and capped to 2.1 mBGL, with a total reported depth from abandonment plans of 406 mBGL. Surveys were carried out in 2020, 2010, 2008, 2006, 2005, 2004, 2003 and 2000. ECT profiles and CCTV recordings indicate a decrease in the depth to the bottom of the shaft interpreted as the result of the large backfilling by debris and sedimentation over 14 years of surveys, down to 406 mBGL in 2008, 380 mBGL in 2010 and 378 mBGL in 2020. There is no clear image of the seam insets due to the large amount of debris.

Following a pumping test carried out in December 2003, full-scale pumping started in Horden in 2004 to control the water level of the region. In 2004, the water level was at 81.15 mBGL and has since then been held between 74 and 80 mBGL (e.g. 74.7 mBGL in 2010 and 77.32 mBGL in 2020). In 2009 pumping started in Dawdon, reducing the reliance on Horden as the sole pumping shaft to maintain the water level in the region and decreasing the abstraction rate from 100 L/s to 40 L/s on average. The water level in Horden is also subjected to tidal variations by a few metres. There are two pumps in Horden Shaft both with a maximum capacity of about 80 L/sec depending on head. The north pump intake is at approximately 112 mBGL (49 m below ordnance datum (BOD)) and the south pump intake is at about 107 mBGL (44 m BOD).

Stratified units are characterised by rapid changes in temperature and EC and are generally observed at the shaft inset levels. In 2020, water quality changes have been inferred at:

- 108-110 mBGL (ECT change at the pump intake)
- 179 mBGL (unknown horizon between BOP and High Main)
- 244 mBGL (High Main)
- 263 mBGL (Five Quarter Seam Inset at 265.7mBGL)

Those stratification levels have been relatively stable throughout the years, with the major change occurring at the Five Quarter Seam Inset in 2020. Before pumping, the highest conductivities were limited to the bottom of the shaft around the Hutton Seam inset. In the initial years of pumping at rates of 35 – 50 L/sec (i.e. 2003 ECT profile), stratification observed at the Low Main Seam J inset suggested that the flow was principally from this horizon, that connects Horden to Easington. However, the EC and temperature change at that depth are largely reduced in the 2010 and 2020 profiles. As the abstraction rate is increased to 60-75 L/sec, later ECT profiles suggest a significant increase in the flow from the deeper Hutton (L), Main (G) and High Main (E) horizon, but also the deterioration of the water quality resulting from the mixing of deeper and more saline waters within the shaft. The largest increases in

EC were observed between the Five Quarter Seam inset (265.7mBGL) and Hutton Seam insets (368.1mBGL) (i.e. × 5-6) and above the High Main Seam inset (244.7mBGL) (× 2-3 in 2004 compared to pre-pumping conditions). A decrease in conductivity was however then measured between 2008 and 2010, interpreted as the result of the decrease in pumping rate at Horden as Dawdon started operating, followed by a new increase in EC between 2010 and 2020.

The 2020 temperature profile depicts the general increase in temperature from 17 ℃ to 19 ℃ despite a slight drop in temperature at the Five Quarter Seam below which the temperature increases linearly down to the shaft bottom. Comparison with pre-pumping profiles (i.e. September 2003) suggests that the temperature has overall increased by 2℃, whilst broadly retaining the depth of the step changes. Although the 2010 and 2020 are relatively similar (i.e. show less than 0.5℃ difference throughout the shaft profiles), a greater variability in the temperature is observed for the period 2004-2009 when Horden was the only active pumping shaft in the block. This suggests that the temperature of the Horden shaft can remain stable over extended periods of pumping. The EC tends to be more sensitive to a change in water quality than the temperature. I interpret this as the effect of the lower permeability of the insets, that prevents the advection of warmer water (i.e. conduction dominant processes), whilst still favouring the transport of solute.

Easington The Easington shaft is 6.1 m in diameter and capped to 1 mBGL, with a total reported depth from abandonment plans of 485 mBGL. Surveys were carried out in 2020, 2010, 2008, 2006, 2005 and 2000. The 2020 survey indicates a shaft depth of 471 mBGL as it was intentionally filled with debris to this point. The good visibility during this survey allowed identifying a couple of seam insets, including the Low Main seam inset at 342 mBGL.

ECT profiles suggest an increase in the flow at the Main Coal (G) horizon and a decrease in the flow at the High Main (E) seam between 2000 and 2005, interpreted as the result of the onset of pumping at Horden. The mine water level in the Easington mining system has remained relatively stable between 2005 and 2020 (where it reached 69.5 mBGL), with fluctuations of only 5 m that confirm the control of pumping at Horden and Dawdon on the water level in Easington.

In 2020, four key changes in water quality were observed at 247 mBGL, 280 mBGL, 342.6 mBGL (Main Coal Seam inset) and 360 mBGL (below the step change at Main Coal Seam inset), consistent with the step changes observed in the previous surveys. Over time, the EC profiles depict a gradual decrease and increase in conductivity above and below the Main Coal, respectively. The temperature increases from 11/12℃ to 17/18℃ between the Base of Permian and the High Main Inset and reaches a maximum of 21.0℃ at the shaft bottom. The 2020 profile depicts no substantial change in the shaft temperature between 2010 and 2020, although the temperature has decreased in the middle portion of the shaft (Base of Permian to High Main Seam inset) compared to the previous years.

Hawthorn The Hawthorn shaft is a modern shaft sunk specifically for coal clearance from several adjacent collieries via two main horizon tunnels. It is 6.1 m in diameter and sealed with a 1.2 m concrete cap, with a total reported depth from abandonment plans of 456 mBGL. Surveys were carried out in 2020, 2008, 2006, 2005, 2003 and 2000. The 2010 and 2020 surveys indicate that the shaft terminates at 443 mBGL as it was intentionally filled with debris to this point.

The water level in the Hawthorn shaft has increased by about 113 m over the 20 years of surveys; with the largest rise (i.e. 88.5 m) occurring in the years before pumping (2000 to 2003). Since 2006, the water level has remained relatively stable with less than 5 m of fluctuation, due to the ongoing pumping at Horden and Dawdon (i.e. 118 mBGL in 2020).

Pumping at Horden has had the greatest impact on the Hawthorn shaft, with the flow induced at both horizon tunnels being visible in the 2020 ECT logs and resulting in three stratified units. Those two step changes, that imply a change in the water quality, occur at:

- 324.5 mBGL (Between Low Main (J) and Top Horizon (K) Seam insets); both EC and temperature changes
- 415.7 mBGL (Bottom Horizon Inset)

For all depths, the conductivity has decreased sequentially over the years, whilst the step at the Bottom Horizon inset has been multiplied by 8 between 2000 and 2020. The EC data moreover indicates a step between the Five Quarter Seam and Main Coal Seam in all profiles, whose depth increased over time. This is interpreted as a result of pumping from Dawdon and Horden and the reduction of the inflow of deep saline water in the shaft. Pumping also lowered the base of the clean surface water layer that had previously been rising by about 10 metres from 123 to 133 metres BOD, inferring a flow down the shaft.

Although the 2020 profile does not indicate a significant change in the water temperature for the upper and lower portions of the profile, the temperature around the Main Coal Seam inset has decreased by at least 3℃ compared to the previous surveys. In 2020, the shaft temperature profile showed the water temperature to be in the range of 11.7 to 19.6℃.

A.3 Chapter 4: Numerical methods

A.3.1 Dimensionless parameters

The relative contribution of diffusive and advective heat transfers is generally expressed using dimensionless parameters.

The **Nusselt number** represents the ratio of convective to conductive heat transfer across a boundary. It represents the observable dynamic of heat flow at the macroscopic level. The convective term includes the heat advected and diffused by a fluid in motion whilst the conductive term includes the heat transported under the same conditions but for a hypothetically motionless fluid. Pure conduction happens when Nu = 0. Laminar flow occurs for 0 < Nu < 10, whilst active convection and turbulent flows are described for 10 < Nu > 100 and Nu > 100, respectively (Roy & Roy, 2020).

$$Nu = \frac{h_c L}{\lambda}$$

with h_c the convective heat transfer coefficient (W/(℃.m^2)), L the characteristic length or distance between a boundary and the point of interest (m) and λ the heat conductivity of the fluid (W/(℃.m)).

The **Peclet number** defines the ratio between the rate of advection to the rate of diffusion at the microscopic level (Squires, 2005). It is defined as:

$$Pe = Re \times Pr = \frac{q_{conv}}{q_{cond}} = \frac{\rho c v L}{\lambda} = \frac{\rho c v(T_s - T_f)}{\frac{\lambda(T_s - T_f}{L}} = \frac{vL}{\alpha}$$

with α the thermal diffusivity $\alpha = \frac{\lambda}{\rho c}$ and v the flow velocity. Conduction is dominant if Pe <1 and convection is dominant if Pe > 1. Alternatively, the Peclet number can be described as the product between the Reynolds number Re and the Prandtl number. The Reynolds number, described earlier, is a dimensionless parameter that predicts fluid flow patterns by measuring the ratio between inertial forces to viscous forces (e.g. transition between laminar and turbulent flow).

The **Prandt number** represents the ratio of the momentum diffusivity ψ (i.e. convection) to the thermal diffusivity α (m^2/s) (i.e. conduction) for a fluid for a given temperature and pressure conditions (Rapp, 2017). There, thermal diffusivity dominates if Pr < 1.

$$Pr = \frac{\psi}{\alpha} = \frac{c\mu}{\lambda}$$

with μ (Pa.s) the dynamic viscosity of the fluid, c the specific heat (J/(℃.kg)) and λ the heat conductivity (W/(° C.m)).

The **Rayleigh number** is used to characterise the heat transport associated with a fluid's flow regime (Cengel, Turner, & Smith, 2001). It is defined as:

$$Ra = Pr \times Gr = \frac{\psi}{\alpha} \times \frac{B}{\mu}$$

with Gr the Grashof number that describes the relationship between buoyancy B and viscosity μ within a fluid, and the Pr the Prandtl number. Low Ra denotes laminar flow whilst Ra values in a higher range denote turbulent flow. Below a certain critical value, there is no fluid motion and heat is mostly transferred by conduction.

A.3.2 OpenGeoSys

Numerical file

Table A.15 describes the characteristics of the numerical parameters used for the simulation of groundwater flow and heat transfer in chapters 6 and 7. More information about each parameter can be found in the OpenGeoSys manual (Kolditz et al., 2008).

Process	method	error tolerance	max iteration	θ	precond	storage
Groundwater flow	2 6	1×10^{-12}	20 000	1	100	4
Heat transport	2 6	1×10^{-12}	10 000	1	1	2
Liquid flow	2	6	1e-14	1000	100	4
Heat transport	2	6	1e-14	5000	100	4

Table A.15: Numerical parameters for groundwater flow and heat transport model and the coupled heat transport and liquid flow model (Kolditz et al., 2008).

Cauchy boundary condition

The Cauchy boundary has been implemented in OGS for a point, polyline and surface, to simulate the water flux through a model boundary based on the difference in head between the inside and outside model boundaries, based on a transfer coefficient called conductance. The CAUCHY condition is activated in the SOURCE_TERM input file by specifying "CAUCHY" under the 'DIS_TYPE', followed by the conductance λ_c and the head value (m) in the external part of the model, e.g. CAUCHY 0.01 0.0. In the case of the polyline and surface, the area assigned to each node as a portion of the surface is distributed similarly to the CONSTANT_NEUMANN approach and is weighted according to the area that the node represents in the mesh. In this example, the flux through the polyline node or surface node into or out of the model domain (m3/s) is:

$$\lambda_c \times (0.0 - H) \times A_n$$

with H the model head (m) and A_n the node area (calculated internally). For a point, the code assumes that the area represented by the node is 1.0, and the user should include the area in the transfer coefficient. For a node, the flux into or out of the model domain (m^3/s) is therefore:

$$\lambda_c \times (0.0 - H)$$

Within the NUMERICS file, a non-linear iteration step needs to be included as the CAUCHY condition is evaluated as a function of the difference in the head external to the model and the model boundary head. There, the non-linear solver is characterised by the following method, error tolerance, maximum iterations and relaxation: NEWTON 1×10^{-4}, 2×10^{-10}, 100 and 0, respectively.

Flow in unsaturated aquifers

In a reference saturated/confined aquifer flow, a linear relationship is assumed between the relative permeability and the saturation (case 2 in OGS), so that

$$k_{rel}^{y} = 1 - S^{y}$$

Relative permeability using the van Genuchten model (1980) can be implemented in OGS to simulate unsaturated/multiphase flow (case 4 in OGS), defined as follows:

$$S_{eff} = \frac{S^{y} - S_{r}^{y}}{S_{max}^{y} - S_{r}^{y}}$$

$$k_{rel}^{l} = S_{eff}^{1/2}[1 - (1 - S_{eff}^{1/m})^{m}]^{2}$$

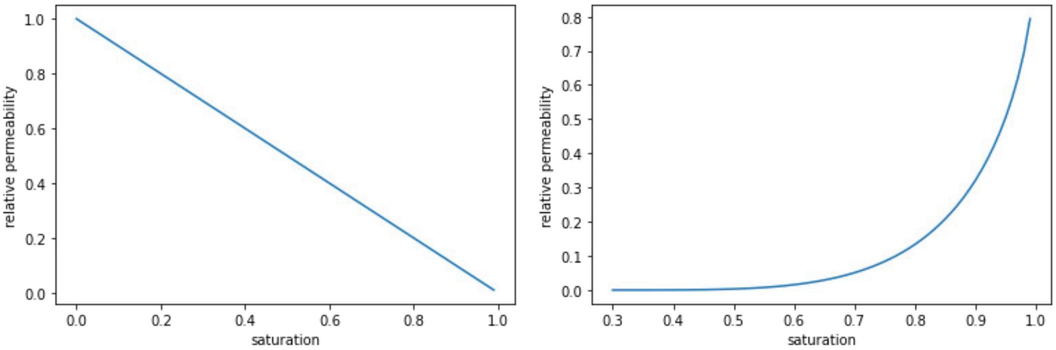

Figure A.23: Relationship between the relative permeability and the saturation for a linear (left) and non-linear (right) scenario.

Alternatively, unsaturated flow can be implemented in OGS using Richard's flow equations, which depend on the aquifer saturation and the definition of relative permeability curves.

Forchheimer analytical solution

In OGS, the Forcheimer equations can be activated via two functions, namely cases 4 and 5, to simulate non-linear flow.

Case 4 is based on the definition of two Forchheimer coefficients, as follows:

$$k_{rel} = \frac{1.0}{a_1 + a_2 \times v} \tag{A.2}$$

With a_1 and a_2 the Forchheimer constants (1/m) and v the average linear velocity ($v = \frac{q}{\mu}$, with q the specific discharge or Darcy flux in m/s and μ the porosity).

In case 5, only one Forchheimer coefficient is defined, as follows:

$$k_{rel} = \frac{1.0}{1 + a_2 \times v \times k_0} \tag{A.3}$$

With $a_1 = \frac{1}{k_0}$, k_0 being the initial permeability.

For both functions, the effect of the Forchheimer constants on the relationship between the relative permeability and the flow velocity is compared analytically, as described in Eqs. A.2 and A.3 (Figs A.24 and A.25, respectively).

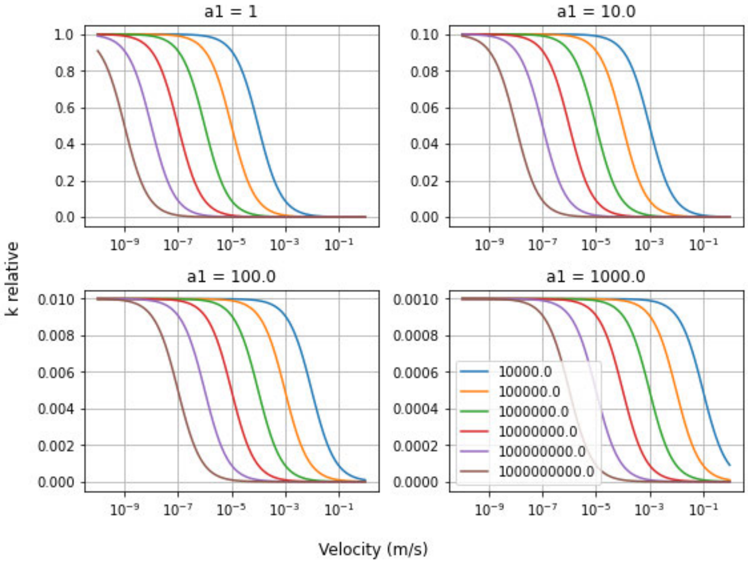

Figure A.24: Analytical results for the Forchheimer solution (case 4) showing the relationship between the relative permeability k and the velocity, for different Forchheimer constants a_1 and a_2.

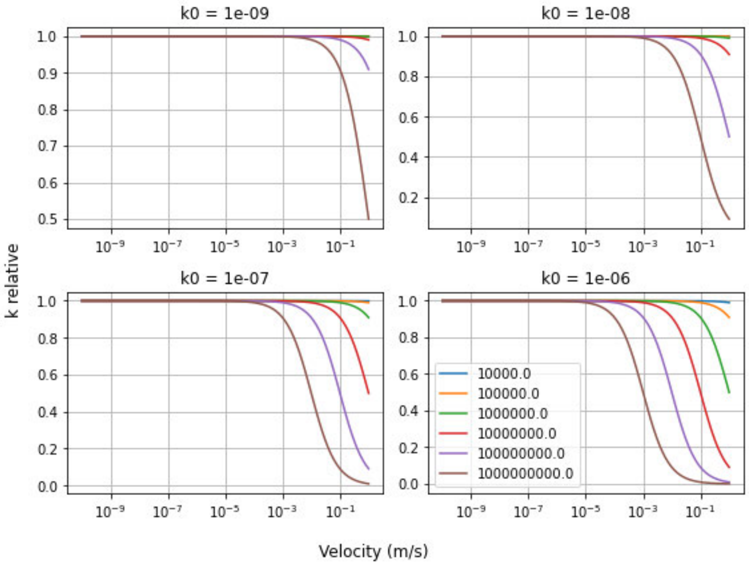

Figure A.25: Analytical results for the Forchheimer solution (case 5) showing the relationship between the relative permeability k and the velocity, for different reference permeability k_0 and Forchheimer constant a_2.

A.4 Chapter 5: Heat balance for a single vertical BHE in the UK

A.4.1 Supplementary Material 1: Properties for the rocks in the MVS

The study area is located in the Midlothian area, southeast of Edinburgh in the Midland Valley of Scotland (MVS) (Fig. A.26).

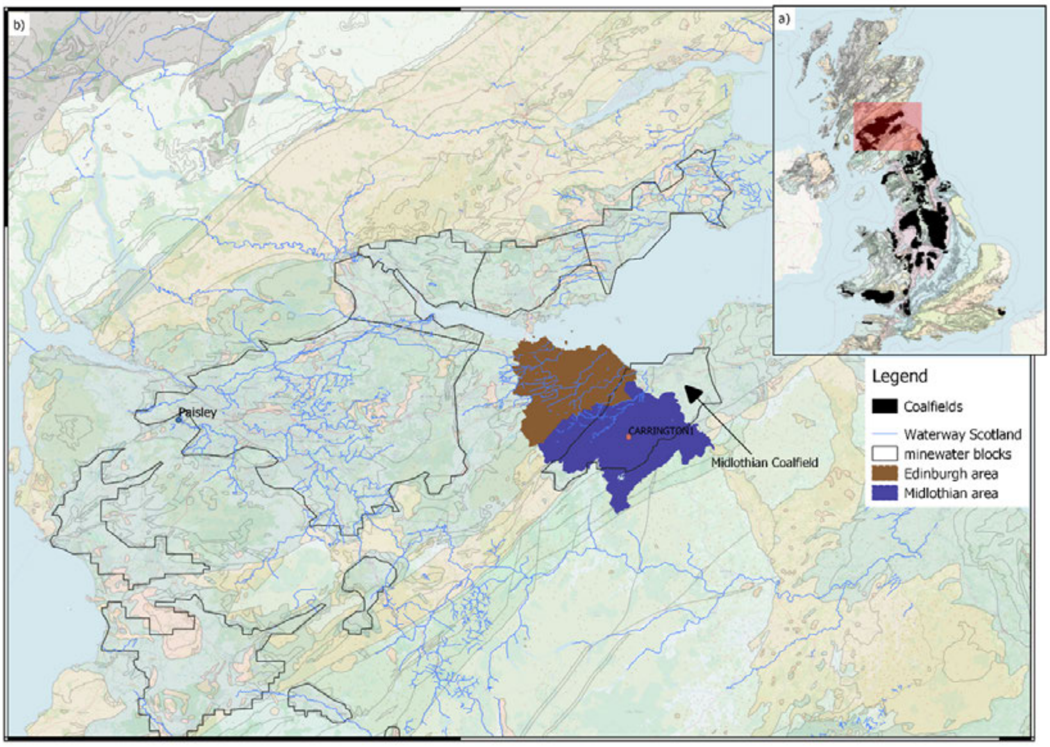

Figure A.26: Geological map showing the extent of the coalfields a) in the UK and b) in the Midland Valley of Scotland, together with the location of the Edinburgh and Midlothian counties, the Midlothian coalfield, of the Paisley meteorological station and the Carrigton-1 borehole.

We calculate the harmonic mean density, heat capacity and radiogenic heat production (RHP) for each Carboniferous formation based on the percentage of rock type in each formation, determined from geological logs available in the BGS GeoIndex Database, and the values for each rock type (Table 1). The density and heat capacity values are from S. M. Watson and Westaway (2020), and the RHP values are from Hasterok et al. (2018); Osimobi et al. (2018); Vilà et al. (2010), as reported in Table A.27. The average effective subsurface heat capacity, conductivity, density and RHP are finally calculated by calculating the cross product of the harmonic means for each formation by the formation thickness h_f, as described for the Carrington-1 borehole (A. Monaghan, 2014).

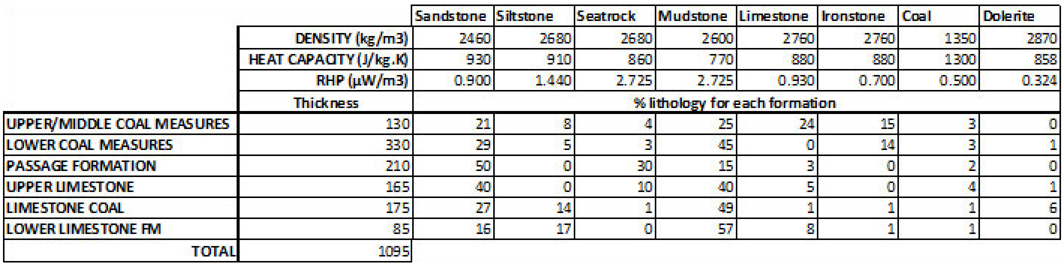

		Sandstone	Siltstone	Seatrock	Mudstone	Limestone	Ironstone	Coal	Dolerite
	DENSITY (kg/m3)	2460	2680	2680	2600	2760	2760	1350	2870
	HEAT CAPACITY (J/kg.K)	930	910	860	770	880	880	1300	858
	RHP (µW/m3)	0.900	1.440	2.725	2.725	0.930	0.700	0.500	0.324
	Thickness	% lithology for each formation							
UPPER/MIDDLE COAL MEASURES	130	21	8	4	25	24	15	3	0
LOWER COAL MEASURES	330	29	5	3	45	0	14	3	1
PASSAGE FORMATION	210	50	0	30	15	3	0	2	0
UPPER LIMESTONE	165	40	0	10	40	5	0	4	1
LIMESTONE COAL	175	27	14	1	49	1	1	1	6
LOWER LIMESTONE FM	85	16	17	0	57	8	1	1	0
TOTAL	1095								

Figure A.27: Summary of the percentage of lithologies for each Carboniferous formation and the thermal and radiogenic properties for each lithology. The thickness for each formation was determined from the Carrington-1 borehole (A. Monaghan, 2014). The percentage lithologies are determined from geological logs available in the BGS GeoIndex Database. The density and heat capacity values are from S. M. Watson and Westaway (2020), and the RHP values are from Hasterok et al. (2018); Osimobi et al. (2018); Vilà et al. (2010).

The average effective subsurface thermal conductivity was calculated based on the values for each formation λ given in J. P. Busby (2019) and the thickness of the formations intersected by the Carrington-1 borehole, as followed: $\lambda_{eff} = \sum \frac{h_f}{h} \times \lambda$, with h the total thickness of the stratigraphic column. Assuming a rock porosity ϕ = 10% and knowing that $\lambda_{eff} = (1-\phi)\lambda_r + \phi\lambda_w$, with λ_w = 0.6 W/°C.m, the heat conductivity of the dry rock used as input parameter to the numerical models is λ_r = 2.4 W/°C.m.

A.4.2 Supplementary Material 2: Quantification of the solar heat flux

We estimate analytically the yearly average thermal input from the atmosphere to the ground using meteorological and soil temperature data measured in Paisley, Glasgow. There, the yearly average downward direct and diffuse shortwave solar radiations received on a horizontal plane on the ground, and the downwelling longwave thermal radiations from the atmosphere calculated over the period 1998-2012, equal q_{sw} = 104 W/m^2 and $q_{l}w$ = 321 W/m^2, respectively (Robinson et al., 2016, 2017). A part of the incoming shortwave radiations are however reflected back to space by the Earth's surface depending on the surface albedo, whilst the emissivity will determine together with the land surface temperature the amount of longwave radiations absorbed or backscattered to the atmosphere (Liang et al., 2019). The shortwave and longwave radiative energy absorbed by the land surface will indeed heat the ground and is then either radiated back to the atmosphere as longwave thermal radiation (which is then absorbed by the clouds), lost as latent heat via evapotranspiration q_{evap} or via sensible heat through convective processes q_{conv}, i.e. rising air currents (Banks, 2008). This surface energy budget can therefore be expressed in terms of net incoming radiations, which corresponds to the sum of the absorbed downward shortwave and longwave radiations from the atmosphere q_{sw} and q_{lw}, respectively, minus the longwave upwelling radiations emitted from the Earth back to the atmosphere (Banks, 2008; Liang et al., 2019).

$$R_n = (1-\alpha_{sw})q_{sw} + \varepsilon q_{lw} - \sigma\varepsilon T_S^4 \tag{A.4}$$

With α_{sw} the surface albedo, ε the emissivity of the ground, σ = 5.669 × 10^{-8} W/m^{2}K^4 the Stefan-Boltzmann constant and T_s (K) the daily averaged land surface temperature (Jia et al., 2018).

Heat can be conducted to depth and temporarily stored in the ground as shortwave radiations warm up the ground during the day/in summer. However, the absence of incoming solar radiations and the net loss of longwave radiations during the night/in winter will tend to release this heat back into the atmosphere and cool down the Earth's surface, as the air temperature is lower than the ground temperature. This ensures that the heat budget at the Earth's surface-atmosphere interface is balanced on a yearly average (i.e. incoming radiations equal the outgoing radiations) and that the average near-surface temperature is stable over time (Banks, 2008; Shuttleworth, 2012). Assuming a balanced system and ignoring the advection of heat via infiltration, the energy gained at the ground surface through the incoming net surface radiations R_n will therefore be lost in the long-term through latent heat flux (i.e. evapotranspiration q_{evap}) or sensible heat flux (i.e. convective losses q_{conv}), so that:

$$R_n = q_{evap} + q_{conv} + q_g \tag{A.5}$$

$$q_{evap} = EV \times \frac{L_v}{86400} \tag{A.6}$$

$$q_{conv} = h \times (T_a - T_s) \tag{A.7}$$

where, h = 5.7 + 3.8u if u < 4.88 and h = 7.2$u^{0.78}$ if u >4.88).

EV is the evaporation rate (mm/day), L_v is the latent heat of vaporization of water (2.257 MJ/kg), T_a and T_s are the air and soil temperatures (Kelvin), u the wind velocity (m/s), q_g the soil/geothermal heat flux and ΔG is the change in stored heat in the ground per square metre or soil heat flux Mihalakakou, Santamouris, Lewis, and Asimakopoulos (1996); Saadi and Gomri (2017). Assuming that no heat is extracted from the ground and neglecting the effects of climate warming, the change in heat stored in the ground ΔG will therefore tend to zero in the long term, with the geothermal and radiative heat flux maintaining a natural balance with the surface heat flux (Banks, 2008). Recent studies however showed an increase in longwave incoming radiations of 0.2-0.3 W/m^2 linked to climate warming (Liang et al., 2019).

Using Landsat-8 images acquired on 18 September 2020 over the Midlothian area in Scotland (Fig. A.28), we calculated surface albedo and emissivity values of α_{sw} = 0.16 (i.e. 16% of the shortwave radiations are reflected back to the atmosphere) and ε = 0.98, respectively. At Paisley, the yearly average downward shortwave and longwave radiations calculated over the period 1998-2012 using available meteorological data in this area (Fig. A.29) are about q_{sw} = 104 W/m^2 and q_{lw} = 320 W/m^2, respectively (Fig. A.30).

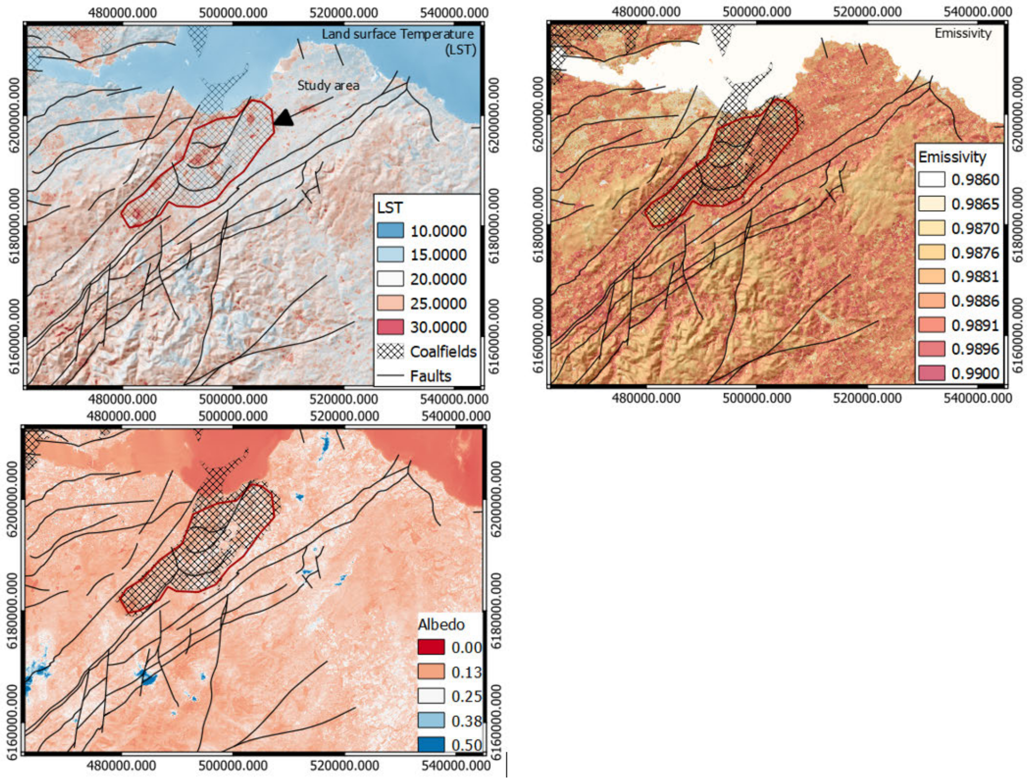

Figure A.28: a) Land Surface Temperature, b) emissivity and c) albedo map calculated from Landsat-8 images dated from the 18/09/2020 (source: https://earthexplorer.usgs.gov/).

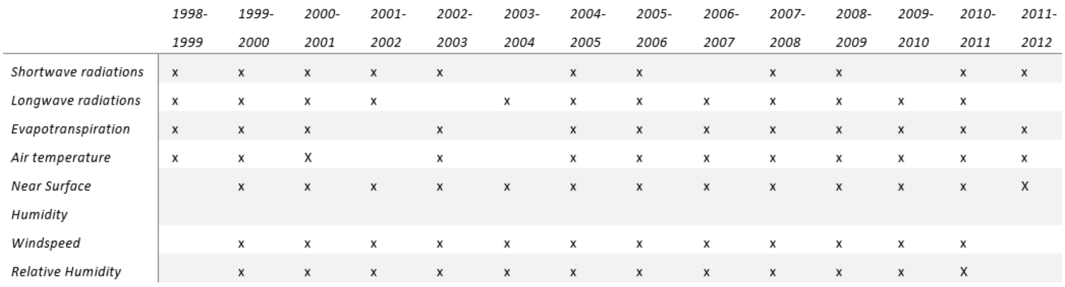

	1998-1999	1999-2000	2000-2001	2001-2002	2002-2003	2003-2004	2004-2005	2005-2006	2006-2007	2007-2008	2008-2009	2009-2010	2010-2011	2011-2012
Shortwave radiations	x	x	x	x	x		x	x		x	x		x	x
Longwave radiations	x	x	x	x		x	x	x	x	x	x	x	x	
Evapotranspiration	x	x	x		x		x	x	x	x	x	x	x	x
Air temperature	x	x	X		x		x	x	x	x	x	x	x	x
Near Surface Humidity		x	x	x	x	x	x	x	x	x	x	x	x	X
Windspeed		x	x	x	x	x	x	x	x	x	x	x	x	
Relative Humidity		x	x	x	x	x	x	x	x	x	x	x	X	

Figure A.29: List of available data collected from the CHESS database (Robinson et al., 2017).

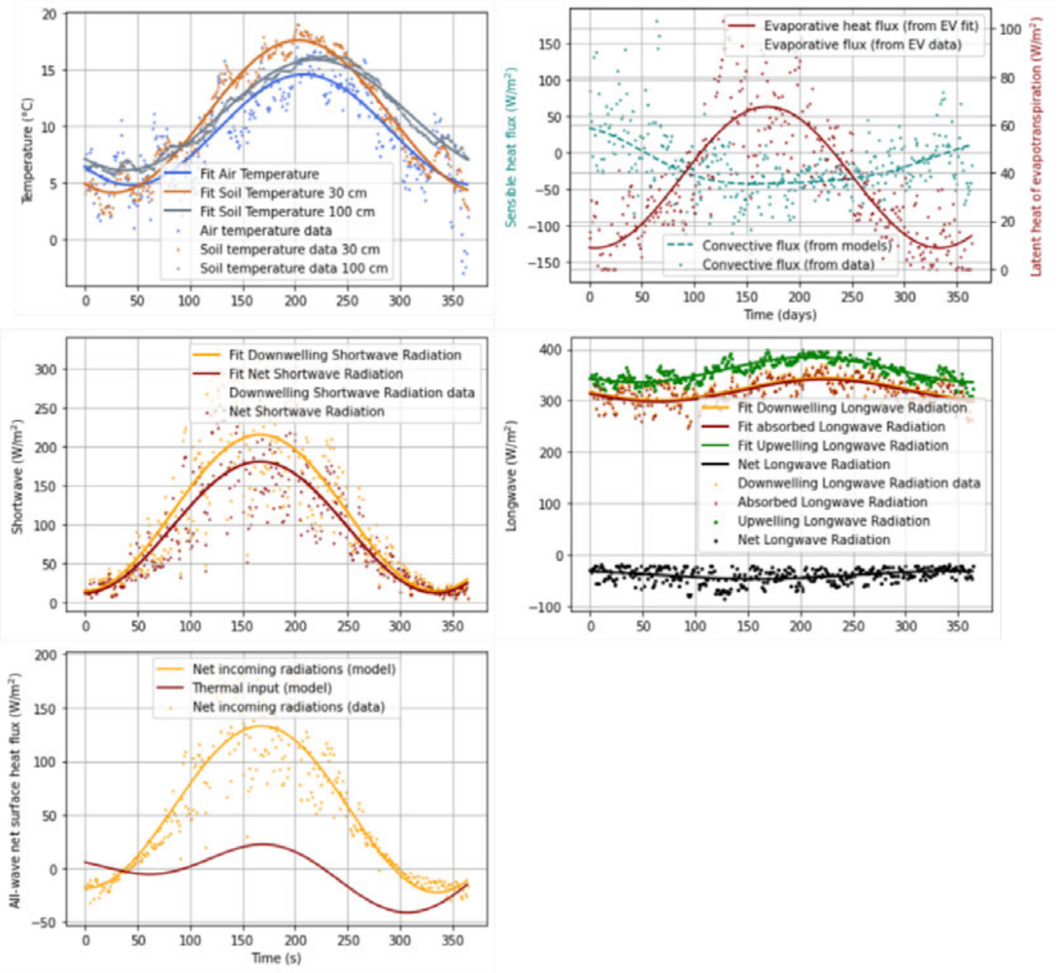

Figure A.30: Annual variations in a) Air and soil temperature, b) wind speed, c) downwelling shortwave and d) downwelling and reflected longwave radiations, e) relative humidity and evapotranspiration, f) latent heat of evaporation and g) calculated heat flux and thermal input to the ground at Paisley (Met Office, 2006, 2019; Robinson et al., 2016, 2017).

Fig. A.31 summarizes the net radiative surface heat budget for the MVS together with estimates of the yearly average convective heat losses and latent heat of evaporation. Using those equations and the data available from the Paisley station (Fig. A.30), results suggest a net all-wave Earth's surface radiative imbalance R_n of $\sim$48 W/m^2 (Fig. A.31). We moreover show that convective (i.e. wind velocity) and evaporative heat losses account for $\sim$30% and $\sim$70% of the net all-wave radiations R_n, respectively. Results suggest a large variability of ground surface heat balance over the years, with a yearly average thermal loss from the ground of ΔG= -5 $\pm$ 2 W/m^2 calculated for the period 1998 – 2012, using a ground emissivity of 0.98 and an albedo of [0.16 – 0.18]. Given the uncertainty in the ground emissivity and albedo, we show that the surface heat input and output are relatively well balanced (ΔG = 0 $\pm$ 2 W/m^2) for ε = 0.98 and α = 0.17, with years having a positive thermal input to the ground (i.e. when the net incoming radiations > evaporative and convective heat losses, e.g. heat inputs of up to 2 W/m^2 calculated for 2005) and years having net thermal losses.

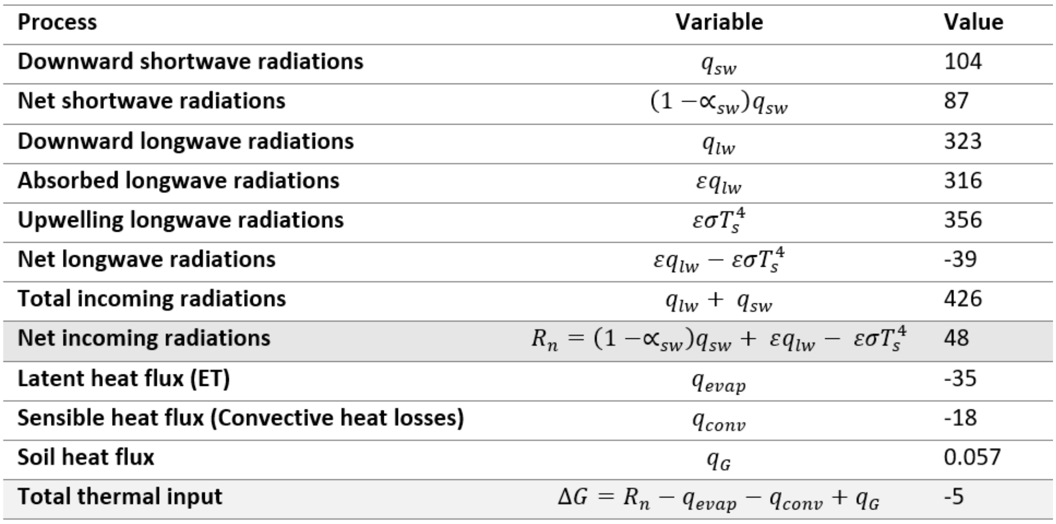

Process	Variable	Value
Downward shortwave radiations	q_{sw}	104
Net shortwave radiations	$(1-\propto_{sw})q_{sw}$	87
Downward longwave radiations	q_{lw}	323
Absorbed longwave radiations	εq_{lw}	316
Upwelling longwave radiations	$\varepsilon\sigma T_s^4$	356
Net longwave radiations	$\varepsilon q_{lw} - \varepsilon\sigma T_s^4$	-39
Total incoming radiations	$q_{lw} + q_{sw}$	426
Net incoming radiations	$R_n = (1-\propto_{sw})q_{sw} + \varepsilon q_{lw} - \varepsilon\sigma T_s^4$	48
Latent heat flux (ET)	q_{evap}	-35
Sensible heat flux (Convective heat losses)	q_{conv}	-18
Soil heat flux	q_G	0.057
Total thermal input	$\Delta G = R_n - q_{evap} - q_{conv} + q_G$	-5

Figure A.31: list of properties and values for the surface heat balance. The yearly average shortwave and longwave radiations, evapotranspiration and relative humidity data were obtained from the CHESS Explorer (Met Office, 2006, 2019; Robinson et al., 2016, 2017) over the period 1998-2012 at Paisley, Glasgow, Scotland.

Although net incoming radiations are here about three orders of magnitude higher than the geothermal heat flux (0.057 W/m^2), this analysis suggests that the average thermal input to the ground from the atmosphere is negligible. In the long term in a balanced system, all the thermal energy entering the ground from the surface will naturally be lost, with the energy coming out at the surface balancing the geothermal heat flux. Although this analysis neglects the existence of heat advection and highly depends on the choice of parameters (i.e. emissivity, albedo), it shows that ignoring the complex processes occurring at the near-surface together with the seasonal variations of the solar heat flux tends to overestimate the actual heat input to the ground on a yearly average.

A.4.3 Supplementary Material 3: Effects of borehole depth, length and model area

Analytical solutions

Fig. A.32 represents the areal impact of heat extraction for different BHE lengths together with the predicted geothermal and solar heat recharge, from an analytical perspective (Fig. A.33).

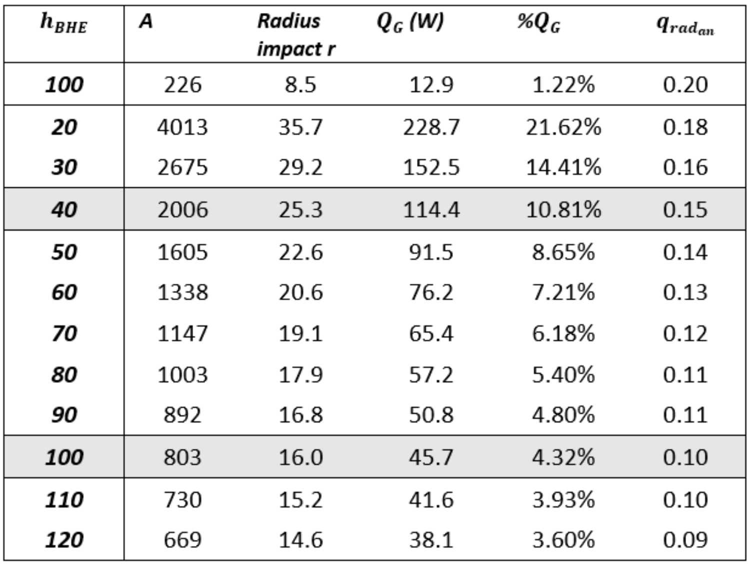

h_{BHE}	A	Radius impact r	Q_G (W)	$\%Q_G$	$q_{rad_{an}}$
100	226	8.5	12.9	1.22%	0.20
20	4013	35.7	228.7	21.62%	0.18
30	2675	29.2	152.5	14.41%	0.16
40	2006	25.3	114.4	10.81%	0.15
50	1605	22.6	91.5	8.65%	0.14
60	1338	20.6	76.2	7.21%	0.13
70	1147	19.1	65.4	6.18%	0.12
80	1003	17.9	57.2	5.40%	0.11
90	892	16.8	50.8	4.80%	0.11
100	803	16.0	45.7	4.32%	0.10
110	730	15.2	41.6	3.93%	0.10
120	669	14.6	38.1	3.60%	0.09

Figure A.32: Analytical solutions for the areal impact, geothermal heat recharge and radial heat flux for different borehole lengths.

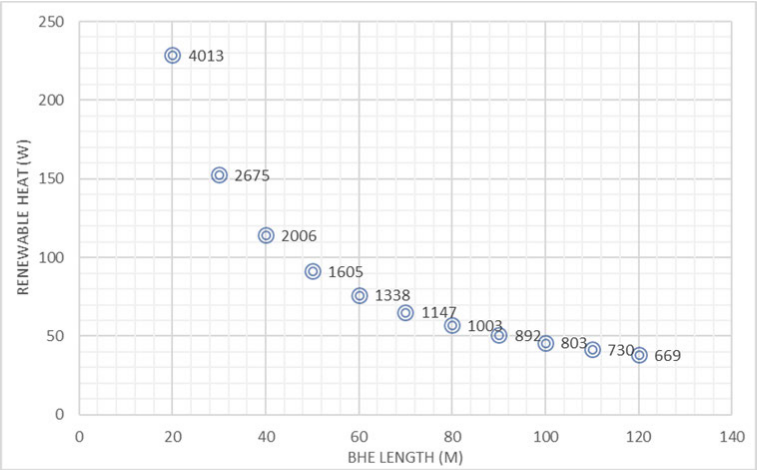

Figure A.33: Relationship between BHE length and the renewable geothermal heat over the areal impact of heat extraction (m^2) calculated analytically (see labels), considering a total impact volume of 80,400 m^3.

Numerical solutions for Axial/Radial Heat flux (constant geothermal heat flux)

We calculate numerically the change in relative contributions from axial and radial heat recharge for different BHE depths (2 m and 10 m) and lengths (40 m and 100 m). Results are summarized in Fig. A.34 together with the measured thermal footprint at the mid-BHE depth and at the surface for a scenario with axial heat recharge.

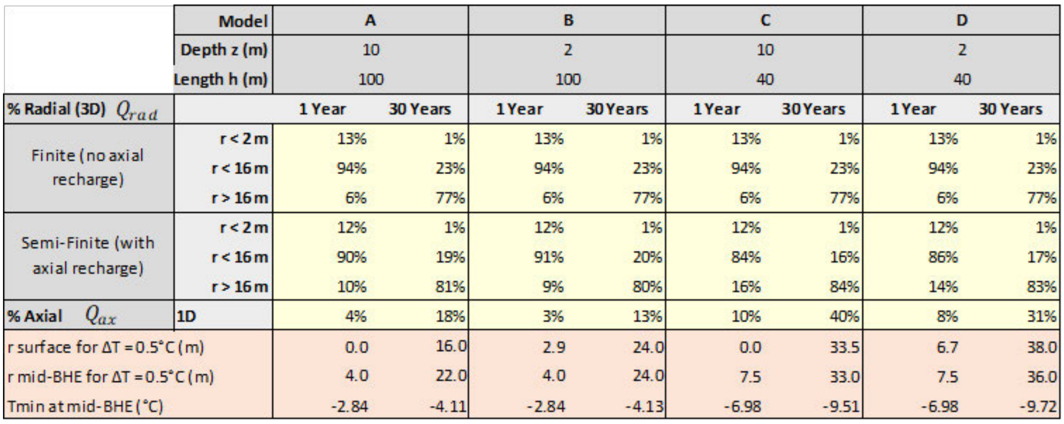

	Model	A		B		C		D	
	Depth z (m)	10		2		10		2	
	Length h (m)	100		100		40		40	
% Radial (3D) Q_{rad}		1 Year	30 Years	1 Year	30 Years	1 Year	30 Years	1 Year	30 Years
Finite (no axial recharge)	r < 2 m	13%	1%	13%	1%	13%	1%	13%	1%
	r < 16 m	94%	23%	94%	23%	94%	23%	94%	23%
	r > 16 m	6%	77%	6%	77%	6%	77%	6%	77%
Semi-Finite (with axial recharge)	r < 2 m	12%	1%	12%	1%	12%	1%	12%	1%
	r < 16 m	90%	19%	91%	20%	84%	16%	86%	17%
	r > 16 m	10%	81%	9%	80%	16%	84%	14%	83%
% Axial Q_{ax}	1D	4%	18%	3%	13%	10%	40%	8%	31%
r surface for ΔT = 0.5°C (m)		0.0	16.0	2.9	24.0	0.0	33.5	6.7	38.0
r mid-BHE for ΔT = 0.5°C (m)		4.0	22.0	4.0	24.0	7.5	33.0	7.5	36.0
Tmin at mid-BHE (°C)		-2.84	-4.11	-2.84	-4.13	-6.98	-9.51	-6.98	-9.72

Figure A.34: Results from the 1D and 3D numerical models showing the relative proportion of heat mining within 2 m, 16 m, and >16 m away from the BHE, for scenarios with and without axial heat recharge and for different BHE length and/or depths. The last lines indicate the thermal footprint area (for ΔT = 0.5℃) at the surface and/or at depth after 1 and 30 years of heat extraction.

Comparing the results for the two BHE lengths reveals a greater thermal drawdown at the BHE location that leads to ground freezing and a reduction of the heat available in the volume at r < 16 m for a 40 m BHE. This suggests that a larger amount of heat will be mined at a greater distance from the BHE in the long term for short BHEs, explaining the larger footprint area. However, the BHE depth has no impact on the maximal thermal drawdown at the BHE (Fig. A.36).

For the 40 m BHE, increasing the BHE depth increases the potential of axial recharge from 31% to 40% after 30 years, which slightly decreases the radial recharge within r < 16 m (Fig. A.36). For a short BHE, the large axial effects permitted by a greater separation distance between the BHE and the ground surface allows reducing the footprint area compared to a shallower BHE over the long-term (i.e. for ΔT > 0.5℃ at the mid-BHE depth, the radius of impact is r = 33 m for a 10 m deep BHE and 36 m for a 2 m deep BHE).

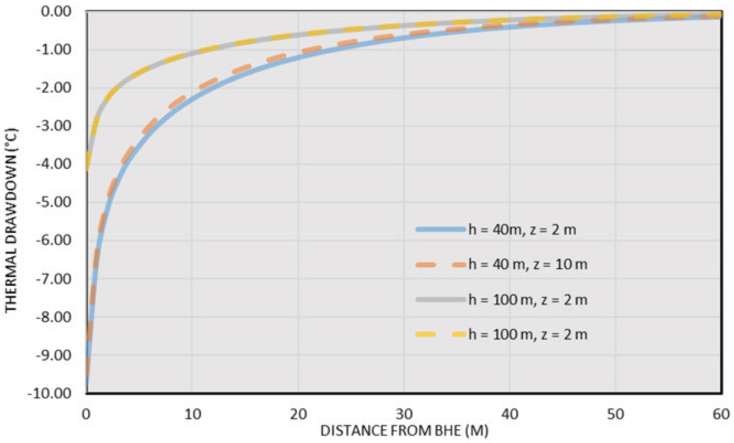

Figure A.35: Horizontal profiles showing the thermal drawdown after 30 years at the mid-BHE depths for a 40 m and 100 m long BHE.

For the 100 m BHE, increasing the BHE depth increases axial recharge from 13% to 18% only, whilst the decrease in the amount of radial recharge within r < 16 m is less pronounced than for a shorter BHE after 1 year. However, a longer BHE significantly reduces the thermal footprint of heat extraction for the same heat load. After 30 years, the radius of the footprint area for ΔT > 0.5℃ at the mid-BHE depth is indeed equal to 22 m for a 10 m deep BHE and to 24 m for a 2 m BHE This also suggest that the longer the BHE the smaller the importance of axial effects in the long-term.

A.4.4 Supplementary Material 4: Artificial heat recharge

Fig. A.37 summarizes the calculations performed to determine the percentage reinjection in all the data zones in the Midland Valley of Scotland, as described in the main text, and more specifically in Edinburgh and the Midlothian area (Fig. A.26).

We look in further detail into the demand in reinjection needs in Edinburgh and in the Midlothian area, where the total heat demand is about 6.1 × 109 kWh/yr (Fig. A.38). Although the total heat available calculated analytically reaches 7.0 × 10^9 kWh/yr, the demand is not distributed uniformly across the area, with the average population density being 1884 inhabitants per km^2 in the centre of Edinburgh against 268 in the Midlothian. Comparing availability to the demand in each data zone in the MVS, we find a cumulated deficit of 4.2 × 10^9 kWh/yr in some areas and an excess heat availability of 5.0 × 10^9 kWh/yr in others. In Edinburgh more specifically, the heat in place < 100 m depth cannot meet the demand in 95% of the data zones, where a deficit of 3.9 × 10^9 kWh/yr is calculated. Following the same method as in the regional analysis described in the main text, i.e. accounting for the maximum area available for each BHE and ignoring the UHI effect, we show that in total, 2.9 × 10^9 kWh/yr would need to be reinjected into Edinburgh's ground to constrain the areal impact of heat extraction within a maximum drawdown of 0.5℃ (i.e. 54% of the total heat demand), with

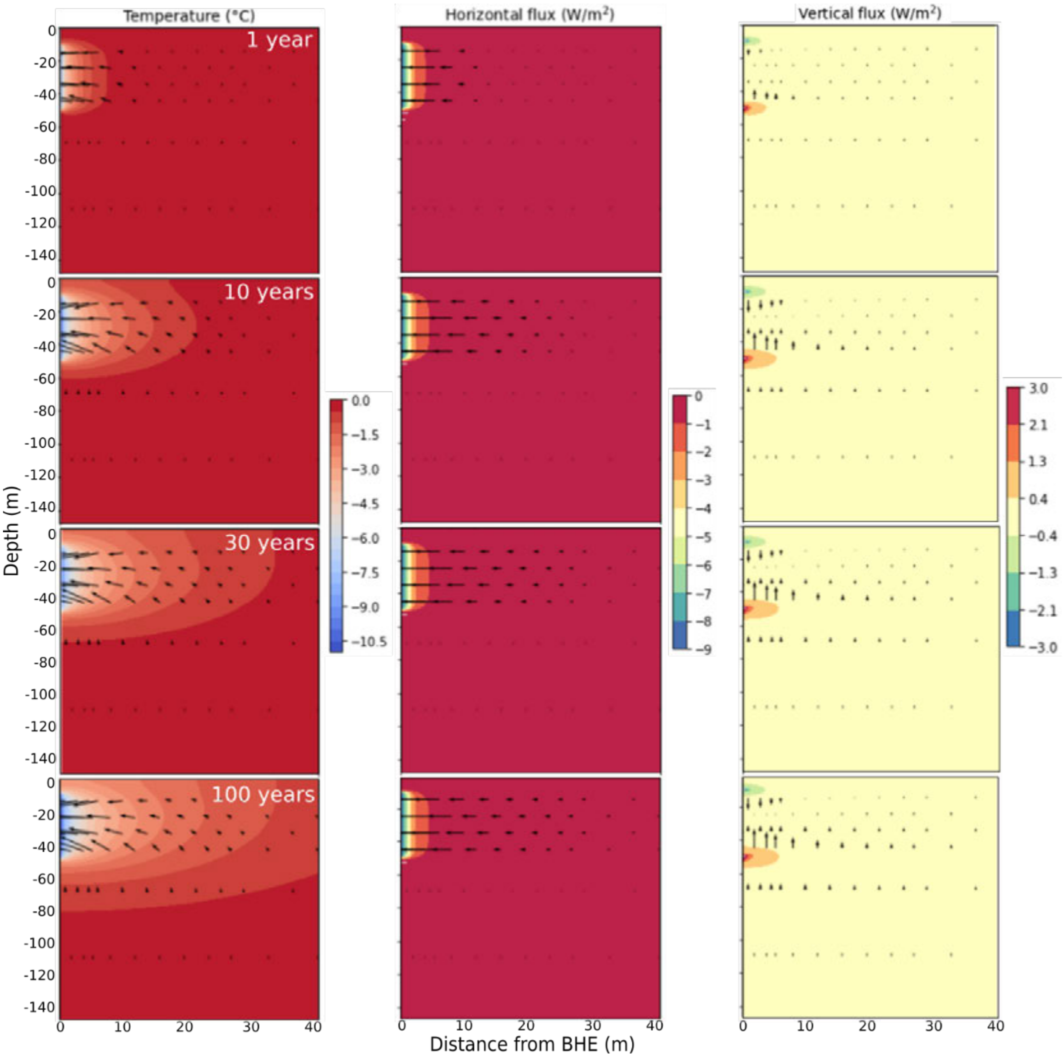

Figure A.36: 2D vertical section in the central part of the 160-m thick 3D model showing the temperature distribution (1st column) and the radial ($q_{rad_{num}}$), 2nd column) and axial/vertical (q_{ax}, 3rd column) heat fluxes after 1, 10, 30 and 100 years of heat extraction, for a 40 m long BHE. The arrows in the 1st, 2nd and 3rd columns represent the total, horizontal and vertical components of the heat flux, respectively.

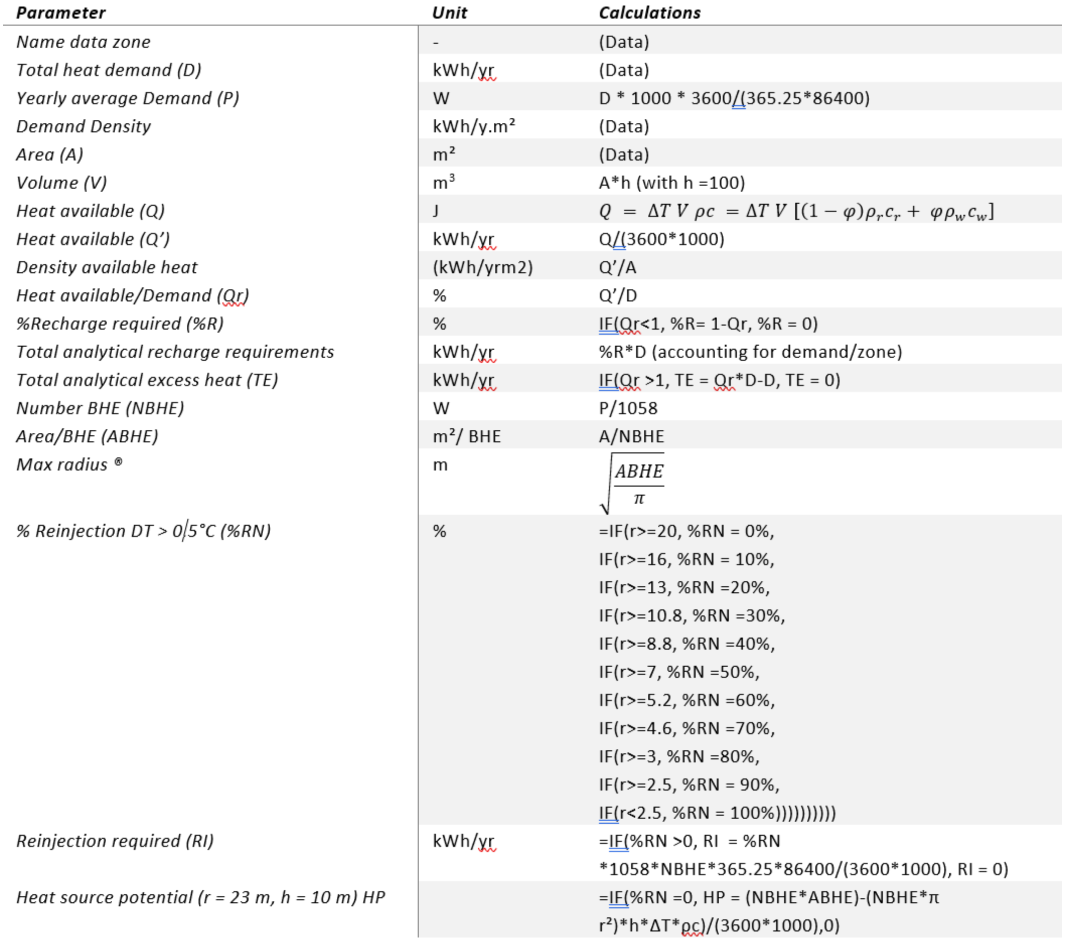

Parameter	*Unit*	*Calculations*
Name data zone	-	(Data)
Total heat demand (D)	kWh/yr	(Data)
Yearly average Demand (P)	W	D * 1000 * 3600/(365.25*86400)
Demand Density	kWh/y.m²	(Data)
Area (A)	m²	(Data)
Volume (V)	m³	A*h (with h =100)
Heat available (Q)	J	$Q = \Delta T\ V\ \rho c = \Delta T\ V\ [(1-\varphi)\rho_r c_r + \varphi \rho_w c_w]$
Heat available (Q')	kWh/yr	Q/(3600*1000)
Density available heat	(kWh/yrm2)	Q'/A
Heat available/Demand (Qr)	%	Q'/D
%Recharge required (%R)	%	IF(Qr<1, %R= 1-Qr, %R = 0)
Total analytical recharge requirements	kWh/yr	%R*D (accounting for demand/zone)
Total analytical excess heat (TE)	kWh/yr	IF(Qr >1, TE = Qr*D-D, TE = 0)
Number BHE (NBHE)	W	P/1058
Area/BHE (ABHE)	m²/ BHE	A/NBHE
Max radius ®	m	$\sqrt{\frac{ABHE}{\pi}}$

% Reinjection DT > 0|5°C (%RN)	%	=IF(r>=20, %RN = 0%,
		IF(r>=16, %RN = 10%,
		IF(r>=13, %RN =20%,
		IF(r>=10.8, %RN =30%,
		IF(r>=8.8, %RN =40%,
		IF(r>=7, %RN =50%,
		IF(r>=5.2, %RN =60%,
		IF(r>=4.6, %RN =70%,
		IF(r>=3, %RN =80%,
		IF(r>=2.5, %RN = 90%,
		IF(r<2.5, %RN = 100%))))))))))

Reinjection required (RI)	kWh/yr	=IF(%RN >0, RI = %RN *1058*NBHE*365.25*86400/(3600*1000), RI = 0)
Heat source potential (r = 23 m, h = 10 m) HP		=IF(%RN =0, HP = (NBHE*ABHE)-(NBHE*π r²)*h*ΔT*ρc)/(3600*1000),0)

Figure A.37: Parameter calculated to determine the percentage reinjection for a given zone, with unit and equation details.

only 2.1 × 10^8 kWh/yr of excess heat available in lower demand areas. In the Midlothian area, the reinjection needs are lower, with a requirement of only 1.1 × 10^9 kWh/yr, whilst 3.5 × 10^9 kWh/yr of excess heat is available. As a result, the Midlothian area would be able to meet its own reinjection needs and also provide up to 3.2 × 10^9 kWh/yr to surrounding regions, i.e. available for utilization in Edinburgh. The main issue with heat is that it cannot be transferred efficiently. In such a scenario, heat transport via groundwater flow or the network of flooded underground coal mine workings underlying the area is limited.

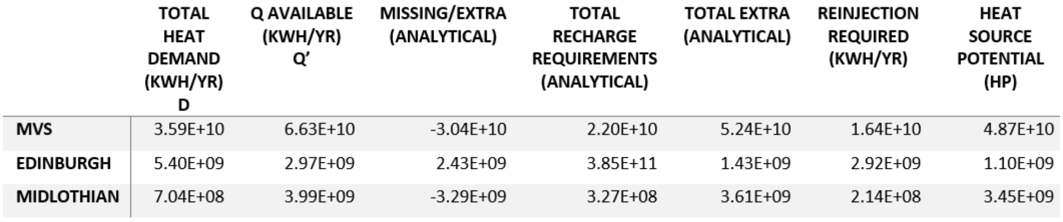

	TOTAL HEAT DEMAND (KWH/YR) D	Q AVAILABLE (KWH/YR) Q'	MISSING/EXTRA (ANALYTICAL)	TOTAL RECHARGE REQUIREMENTS (ANALYTICAL)	TOTAL EXTRA (ANALYTICAL)	REINJECTION REQUIRED (KWH/YR)	HEAT SOURCE POTENTIAL (HP)
MVS	3.59E+10	6.63E+10	-3.04E+10	2.20E+10	5.24E+10	1.64E+10	4.87E+10
EDINBURGH	5.40E+09	2.97E+09	2.43E+09	3.85E+11	1.43E+09	2.92E+09	1.10E+09
MIDLOTHIAN	7.04E+08	3.99E+09	-3.29E+09	3.27E+08	3.61E+09	2.14E+08	3.45E+09

Figure A.38: Analytical and numerical calculations of the percentage reinjection and heat source potential for the MVS, Edinburgh and Midlothian areas.

In addition to the heat resources available in areas with low demand, we investigate the potential and available artificial sources of heat in the MVS, especially within the Edinburgh and Midlothian areas. Fig. 5.8 in the main text shows the distribution of the percentage reinjection areas together with the location of the heat sources available for heat reinjection into the ground. Overall, the heat sources in Edinburgh comprise 1 potential large (i.e. 1 MW) water-source heat pump, 4 small-medium (i.e. 45 kW – 1 MW, or 523 kW in average) heat boilers (3 actual and one potential), one small-medium hydro system under construction, one operating micro (< 45 kW) solar thermal plant, an operating large energy from waste plant, 7 trigeneration plants (including one actual large, 4 potential large and 2 potential small-medium systems), 2 operating CHP plant (1 large, 1 small-medium in addition to 1 potential large) located where the demand is the highest, and 1 large active landfill gas plant. In the Midlothian, 2 potential solar photovoltaic (1 small-medium and 1 micro), 1 potentially large water-source heat pump and 3 operational large landfill gas systems could provide additional heat. In total, the actual and potential heat sources in Edinburgh and the Midlothian would represent about 18 MW (12,300 kW), which is a yearly average of 1.6 × 10^8 kWh/yr. This represents 4% of the heat reinjection requirements calculated for the Edinburgh and Midlothian areas. This can be added to the excess heat available in areas of low heat demands, which represents ∼90% of the reinjection needs in areas of high demand in Edinburgh and the Midlothian area.

This analysis shows that shallow heat resources < 100 m cannot provide the required heat demand in densely populated areas such as Edinburgh unless reinjection is performed. Groundwater flow would allow increasing advective heat recharge from areas with lower demand to a limited extent. As the transport of heat is challenging, solar-assisted systems could represent a valuable solution to recharge the ground in heat in areas of high demand and ensure the long-term viability of shallow vertical GHE systems. Assuming 4.5 peak sun hours per day, solar panels can provide up to 1.8 kWh of energy per day, which represents 660 kWh/yr, in addition to 18 MW potentially available from industrial activities in the area. Alternatively, greater geothermal potential could be accessed from the implementation of deep BHE arrays that would reduce the issues of interference between multiple users. As for the utilization of industrial waste or recyclable heat, the utilization of deep resources would however require the development of district heating systems and increased communication between the different actors, i.e. industries, heat licensing regulators, municipalities, constructors, etc. This highlights the importance of diversifying the energy sources within an integrated heating system in cities. The licensing of heat cannot be made from generalized rules but needs to account for the distribution of the heat demand, and the ground heat conductivity, and will need to account for the dynamic of heat recharge (i.e. delineation of a zone depending on groundwater flow) and the design of the GHE system. In that sense, the property of heat must be different from the property of the land, and regulations must include directives on a management strategy including the minimum percentage reinjection that would be required to prevent the overexploitation of the resource. This study provides a specific example of the approach that could be implemented, for the Midland Valley of Scotland, UK.

A.4.5 Supplementary Material 5: Effect of rock conductivity

The analysis of the relative effect of the rock conductivity on the footprint area over a 30-year production period was performed on the 40 m long BHE model (no axial recharge allowed) to optimize the simulation time (Fig. A.39, Fig A.40 and Fig. A.41).

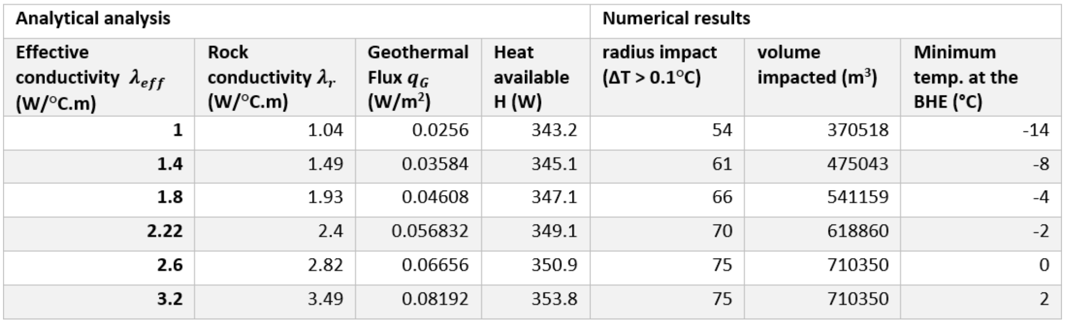

Analytical analysis				**Numerical results**		
Effective conductivity λ_{eff} (W/°C.m)	**Rock conductivity λ_r (W/°C.m)**	**Geothermal Flux q_G (W/m^2)**	**Heat available H (W)**	**radius impact (ΔT > 0.1°C)**	**volume impacted (m^3)**	**Minimum temp. at the BHE (°C)**
1	1.04	0.0256	343.2	54	370518	-14
1.4	1.49	0.03584	345.1	61	475043	-8
1.8	1.93	0.04608	347.1	66	541159	-4
2.22	2.4	0.056832	349.1	70	618860	-2
2.6	2.82	0.06656	350.9	75	710350	0
3.2	3.49	0.08192	353.8	75	710350	2

Figure A.39: Summary of available heat calculated analytically and of the areal impact and maximum temperature drawdown at the borehole calculated numerically for different ground conductivity (40-m BHE model).

$$q_G = \lambda_{eff} \times \frac{\Delta T}{\Delta z} \tag{A.8}$$

$$H = q_G \times A \tag{A.9}$$

where q_G and H are the geothermal flux (W/m^2) and the total available geothermal power available for heat recharge (W), with λ_{eff} = $\lambda_r \times$ 0.9 + 0.6 $\times$ 0.1 W/℃.m, $\frac{\Delta T}{\Delta z}$ = 0.0256℃/m, and A = 188 m^2,

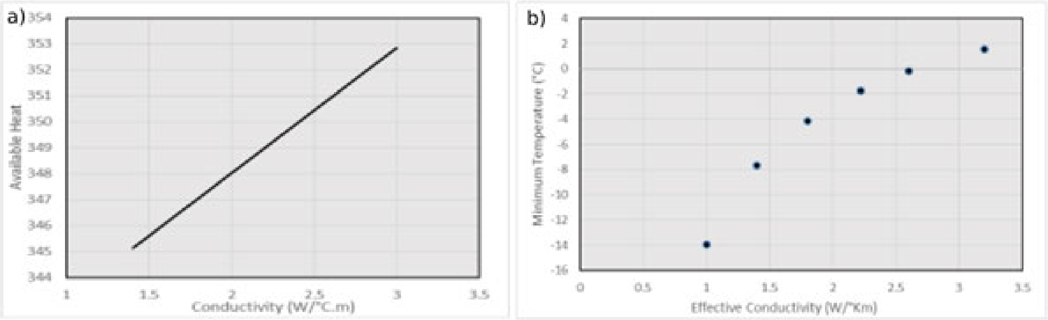

Figure A.40: Relationship between the ground conductivity and a) the amount of renewable (available) heat and b) the maximal temperature drawdown at the borehole.

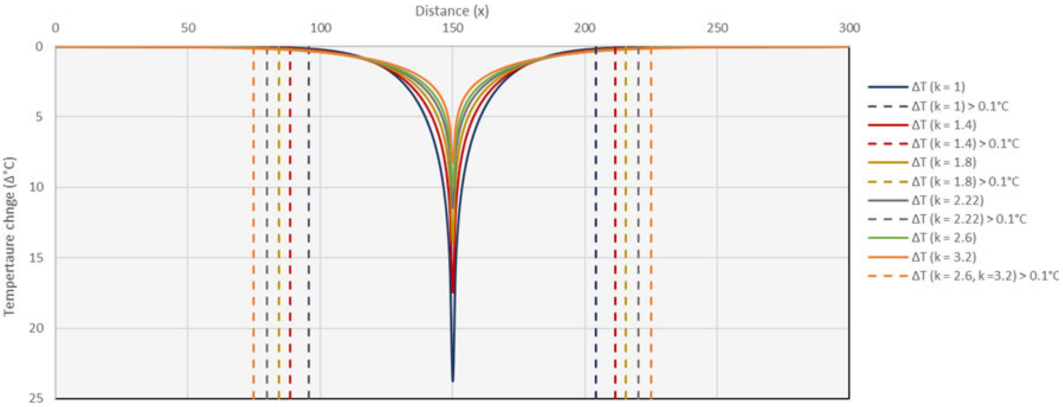

Figure A.41: Horizontal profiles showing the thermal drawdown after 30 years at the mid-borehole depths for different ground heat conductivity.

A.4.6 Supplementary Material 6: Surface boundary conditions

Fig. A.42 shows the temperature profiles obtained from the 1D 1000 m deep model due to heat extraction from a 100 m long BHE at 10 – 110 m depth, as well as the induced vertical/axial heat fluxes (without radial heat transfers) for different surface boundary conditions.

Heat mining near the surface is expected to induce an increase in the downward surface heat flux from the atmosphere to the ground (Banks, 2008). We therefore use results from the 30-year-long simulation from the 1D 1000-m long model to predict the heat flux induced an increase in the temperature contrast between the ground surface (i.e. using the average air temperature of 9℃) and the borehole top (i.e. located at 10 mbgl). A new 30-year-long heat extraction simulation is then performed using the predicted increasing surface heat flux as an upper boundary condition. Results displayed in Fig. A.43 suggest that using an increasing

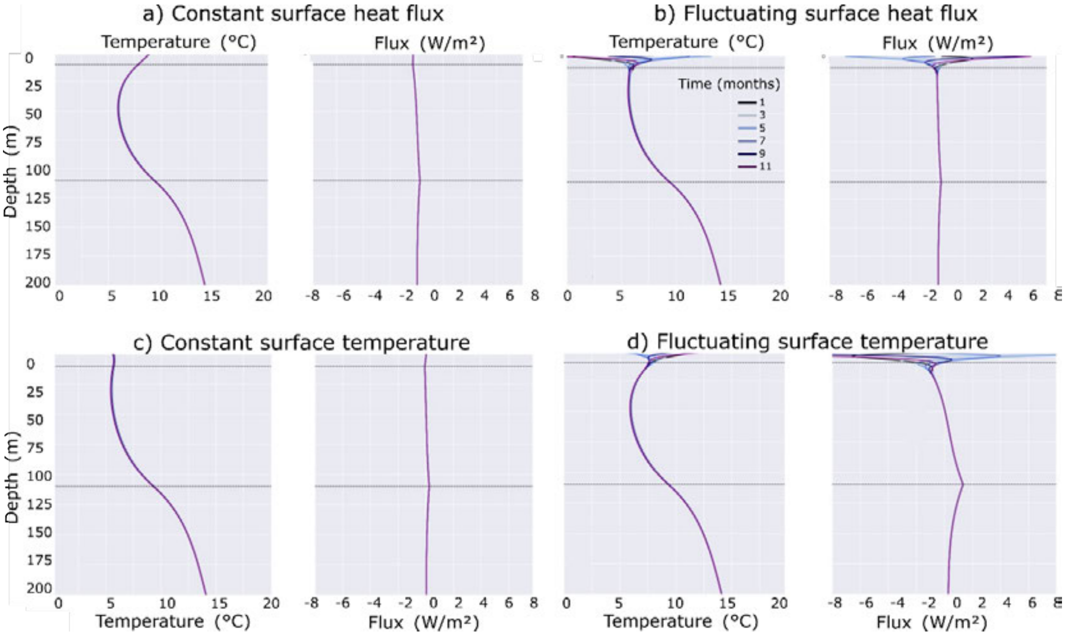

Figure A.42: Temperature profiles and axial heat flux calculated over 30 years of heat extraction from the 1000 m long 1D models for (a) a constant surface heat flux, (b) a fluctuating surface heat flux, (c) a constant surface temperature and (d) a fluctuating surface temperature. The profiles show the temperature in months 1, 3, 5, 7, 9, and 11 of the 30th year.

surface heat-flux boundary rather than a constant heat flux of -0.057 W/m^2 permits additional recharge to the borehole. There, the overall energy drop is reduced by 3% compared to a scenario with no increase in surface heat flux. The temperature drop at the surface is however only reduced by 0.5℃.

A.4.7 Supplementary Material 7: Thermal recovery for different surface boundary conditions

In terms of ground thermal recovery, Piotrowska-Woroniak (2021) has shown based on the analysis of ground temperature data measured every year for 4 years in eastern Poland, that the ground temperature (either at the surface or in the BHE) never fully returns to the pre-extraction temperature after the heating seasons. Similar observations were made by Signorelli et al. (2005) despite using a seasonally fluctuating ground surface temperature and constant bottom heat flux boundary. The authors showed that thermal recovery for a single BHE is the strongest at the beginning and levels off with time, and is almost total (i.e. ~0.1℃ cooler) after about the same amount of time as the heat extraction period (i.e. 30 years). In the 3D reference model described in this study (i.e. scenario with geothermal recharge only), we confirm that following a 30-year production period, the ground temperature at the BHE location is still about 0.1℃ cooler than the initial temperature after 100 years of recovery (Fig. A.44). However, time series of temperature recovery calculated from the 1D models (i.e. no radial

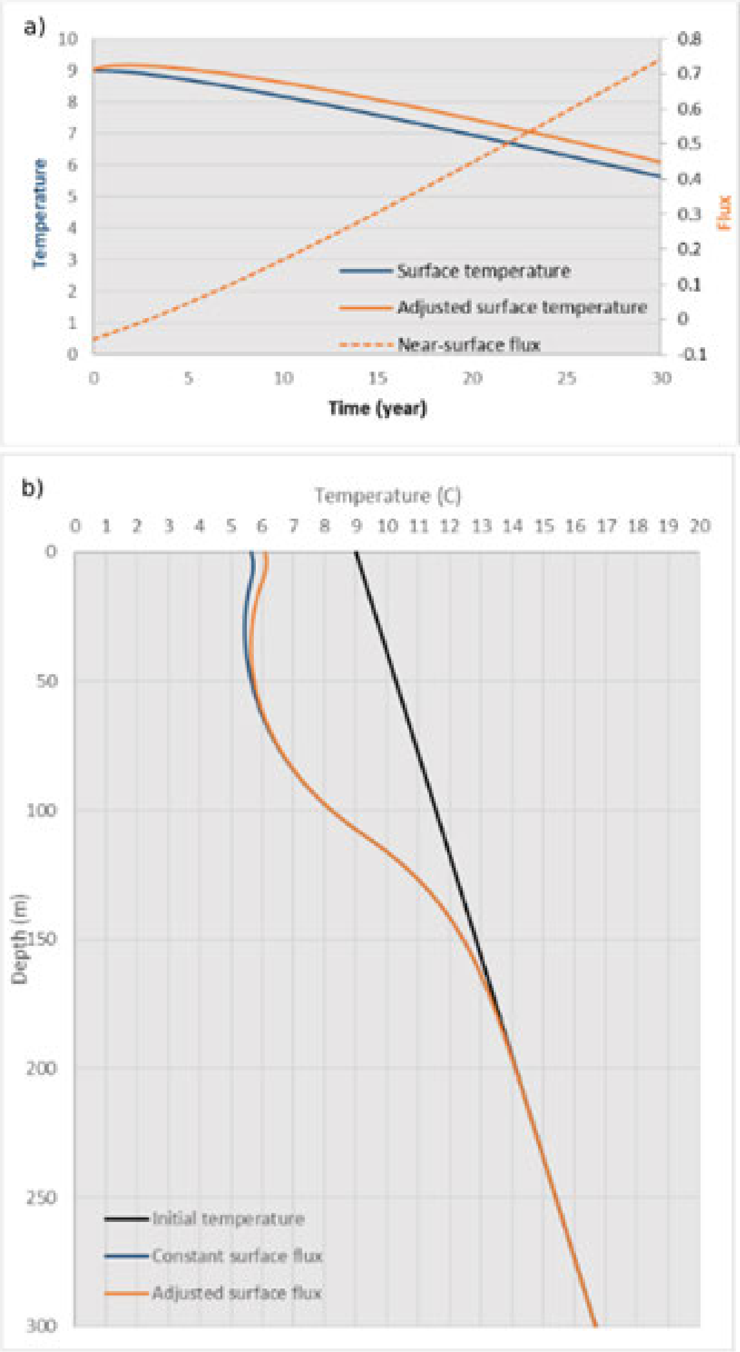

Figure A.43: a) Time series of surface temperature and heat flux and b) 30-year temperature profiles of heat extraction from a 100-m BHE for scenarios with constant surface heat flux and heat flux adjusted for cooling of the ground surface.

heat transfers) indicate that constant temperature boundaries allow increasing the thermal recovery rate at the BHE by two, while a fluctuating surface heat flux boundary only improves recovery by ∼0.2℃ after 100 years (A.4.1). This suggests that although the increase in the surface/axial heat flux from the atmosphere can only contribute to a maximum of ∼8% of the BHE requirements during production (A.4.1), they can benefit thermal recovery when heat extraction stops (Fig. A.45).

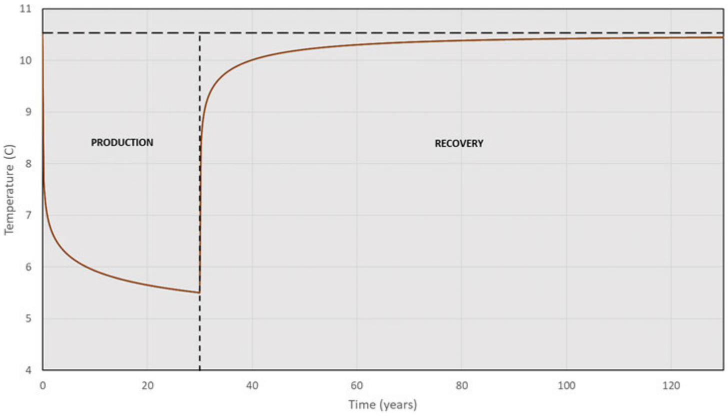

Figure A.44: Temperature change at the mid-BHE location in the 3D 160 m thick model over 30 years of heat extraction and 100 years of recovery (geothermal heat recharge only).

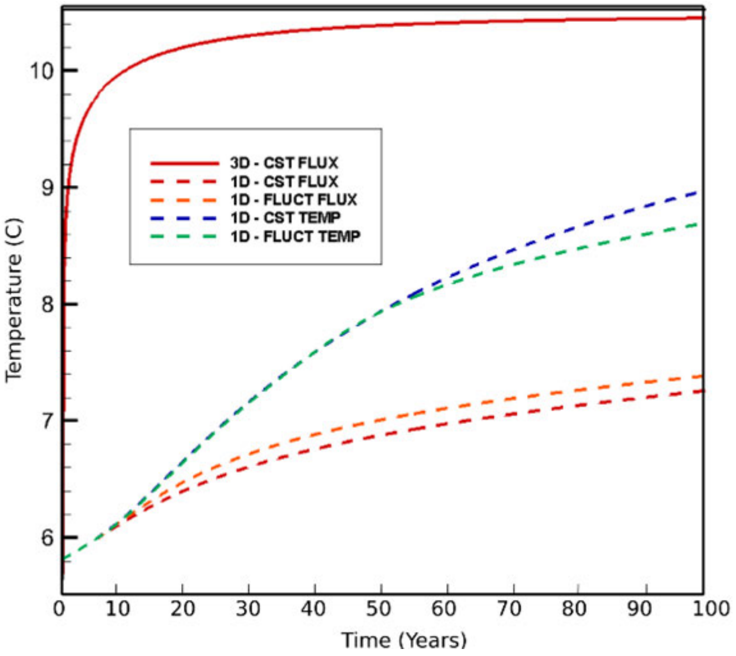

Figure A.45: Time series of temperature recovery measured at the mid-BHE in the 3D 160 m thick model after 30 years of heat extraction for different surface boundary conditions.

A.5 Chapter 6: WGC2020 paper

Key Controls on Mine-water Temperature in Flooded Mine Shafts: Insights from Temperature Profiles and Numerical Modelling

Proceedings World Geothermal Congress 2020+1 Reykjavik, Iceland, April - October 2021

Mylène RECEVEUR, Christopher MCDERMOTT, Andrew FRASER-HARRIS, Stuart GILFILLAN and Ian WATSON

University of Edinburgh, Grant Institute, James Hutton Road, EH9 3FE Edinburgh

Keywords: Mine-Water Heat, Coal Mines, Temperature Profiles, Numerical Modelling, OpenGeoSys,

A.5.1 Abstract

Heat demand for domestic and industrial space heating represents more than 30% of the energy consumption in the UK. Most of this energy is currently supplied by natural gas, contributing up to 19% of the carbon footprint of the country in 2017. To reach Net-Zero carbon emissions by 2050, the UK Government is looking at new approaches to decarbonize residential heating. Among them, using mine water from abandoned legacy mine workings as a new low-carbon heat source has been of growing interest. Using open-loop ground-source heat pump systems, heat energy can be harnessed from the 12-20 °C water stored in the large underground voids inherited from past mining activities. Although the temperature of the water is expected to increase with depth according to the local geothermal gradient, temperature measurements in former mine shafts in the UK revealed the lack of correlation between the depth of the measurements and the mine-water temperature. The aim of this study is therefore to assess the key parameters controlling the temperature profiles in mine shafts to understand if those can be used to calibrate mine models aiming at assessing their long-term geothermal potential. We use the finite-element modelling software OpenGeoSys to simulate groundwater flow and heat transfers in a 2D porous media representing a mine of simple geometry.

We first analyse the effects of a 500-day pumping period followed by mine-water recovery on the temperature distribution in a pumping shaft for different hydraulic boundary conditions. We then investigate the effects of the material properties, the mine geometry and the pumping scenario on the modelled temperature profiles. Time series of energy changes in the system are also calculated to get insights into the relationships between the observed mine-water temperature and the actual heat potential of the mine.

Preliminary results indicate that the hydraulic conductivity of the worked coal seams intersected by the shaft and the nature of the hydraulic recharge governs the observed temperature profile and the mechanism of heat recovery in the mine. During pumping, the temperature of the shaft also depends on the pumping depth and on the temperature of the mine water flowing at the seam insets, as predicted by the geothermal gradient. However, the limited effect of the mined volume and seams inter-connectivity reduces the potential for using temperature profiles as calibration tools for the geometry of mine models. Likewise, time series of energy change suggest that steady pumped temperatures cannot give an overall understanding of the long-term potential of the mine. Although the mine-water temperature re-equilibrates with the surrounding rock within sim20 years following the cessation of pumping, post-recovery profiles moreover indicate the existence of long-term perturbations of the temperature gradient around the shaft. Those are attributed to the effects of heat convection within highly permeable voids during prolonged dewatering periods and water rebound. Further analysis is being undertaken to assess the thermal footprint of long-term mining on the observed temperature distribution in flooded coal mines.

A.5.2 Introduction

Mine water from abandoned legacy coal mines constitutes a low-temperature geothermal heat source that can be used for hot water or space heating. This low-carbon resource largely available across the UK has been of growing interest as it could contribute to reaching the Net-Zero carbon emission target set by the 2019 UK's Climate Change Act by 2050 (House of Commons Energy and Climate Committee, 2016). In Scotland, Todd et al. (2019) showed that about 7% of the heat requirements could be sustainably sourced from abandoned flooded mine workings lying just below populated areas without the need for artificial heat storage.

Underground coal mines have been described as highly permeable 'anthropogenic aquifers' (Adams and Younger, 2001), from which important volumes of water can be stored and extracted at relatively high rates (Banks et al., 2004). These characteristics are the result of a long mining history during which different mining approaches have been employed. In the early times of mining (16-17th Century), coal was mostly extracted from shallow mines using the pillar-and-stall method. In the early 18th Century, the invention of the Newcomen steam engine enabled pumping water more efficiently, allowing access to deeper coal seams. From the 1950s, longwall mining was the main method of extraction of coal in deep mines, and many mined areas were reworked using this method (Younger et al., 2002). The decline in demand for coal led to the progressive closure of the underground mines from the 1960s. In 1992, only 50 collieries were left open in the UK and the last one closed in 2015. Following their abandonment and the cessation of dewatering, most of the underground collieries were left to progressively flood as water rebounded back to natural levels, filling the complex network of voids inherited from the mining activities (Younger and Adams, 1999). A compilation of mine-water temperatures in the UK showed that mine waters are generally hotter than natural groundwater, ranging from 12℃ to 30℃ (Gillespie, 2013). Using open-loop ground source heat pump systems, mine water can be pumped from the mine and used for hot water or space heating, with the cooled water disposed of either through treatment and surface disposal or re-injection to another coal seam through boreholes or shafts (Banks et al., 2004). Such a system has been implemented in Dawdon, North-East England, where a 20℃ water is abstracted from the mine before being discharged to the sea (Bailey, 2013).

To promote the development of heat extraction schemes, The Coal Authority (i.e. TCA, responsible for the legacy of UK coal mines) wishes to get a better understanding of the geothermal resources in mines. To that end, Farr et al. (2020) provided a mapping and synthesis of the temperature of Britain's coalfields at the scale of the Mine-Water Block (MWB) by comparing equilibrium temperatures to recent mine-water temperatures measured by TCA. Their results indicated a good correlation between historic in-situ coal strata temperatures acquired during mining and more recent mine-water temperatures from un-pumped shafts, collected in the BGS UK Geothermal Catalogue (Burley et al., 1984; Rollin, 1987). This was suggested to indicate that mine water from flooded workings has reached an approximate temperature equilibrium with the surroundings (Farr et al., 2020). A comparison between equilibrium temperatures and temperatures from pumping shafts/boreholes moreover showed that pumping tends to significantly alter the calculated geothermal gradient. Although pumped temperatures tend to be higher than equilibrium temperature at shallow depth in most MWB, deeper data (300-500 m) in pumped coalfields indicates cooler temperatures than in the equilibrium coalfields. This was interpreted to result from the mixing between deep warm water and colder surface water in the shaft.

The lack of data in mine galleries however makes it difficult to know whether such effects are localized in the shaft or spread within the hydraulically connected parts of a mine or network of mine (Farr et al., 2020). Being able to extrapolate the measured data from shafts and boreholes is critical to be able to estimate the heat potential of mines. The aim of this study is therefore to investigate the key controls on the temperature profiles measured in shafts and to get a better understanding of the relationship between equilibrium and pumped mine-water temperatures. Using numerical modelling, we analyze the effects of different host rock thermal and hydraulic properties, the geometry of the mine galleries, the hydraulic recharge and the pumping scenario on the observed temperature profiles during pumping activities and recovery/flooding. In addition, we investigate the relationship between the temperature profiles and the energy change in the mine system to get a better understanding of how measured temperatures in shafts can be used to gain insights into the mine heat potential.

We finally discuss the potential effect of past mining activities on the observed temperature in shafts and in the galleries to assess if historical in-situ strata temperatures can be used to estimate post-closure temperatures in coal mines (Farr et al., 2020). This study does not aim at matching modelling results with real data, which will be the aim of future work.

A.5.3 Methods

We use the finite-element modelling software OpenGeoSys to simulate groundwater flow and heat transfers in a 2D porous medium representing a mine of simple geometry. The reference mine consists of three worked coal seams located at 100, 130 and 160 m depth. They are interconnected via two open shafts separated by a distance of 100 m and embedded in a homogeneous host rock, whose properties have been attributed accordingly to the geology of the Coal Measures in UK Coalfields.

Material	ϕ	K	ρ	c	λ	μ
Host rock	10	1×10^{-7}	2650	950	3.14	-
Seams	25	1×10^{-2}	1500	1380	0.31	-
Shaft	100	1	1000	4680	0.6	-
Water	-	-	1000	4680	0.6	0.003

Table A.16: Petro-physical, thermal and hydraulic properties for the 2D reference mine model, with ϕ (%), K (m/s), ρ (kg/m^3), c (J/℃.kg) and λ (W/℃.m) the porosity, hydraulic conductivity, density, specific heat capacity, heat conductivity of the material and μ (Pa.s) the water viscosity.

We first analyze the effects of pumping and recovery under different hydraulic conditions on the temperature profile in the production shaft. The impact of a westward regional hydraulic gradient is assessed using constant heads of 0 m on the eastern boundary and of 10, 20, 50 and 80 m on the western boundary. Additionally, we study the effects of a westward hydraulic flow of 1.3×10-8 m3/s using Neumann lateral boundary conditions. This hydraulic flow corresponds to the flow required to maintain a hydraulic gradient of 10 m between the lateral boundaries of the model. For each scenario, we assume a geothermal flux of 0.085 W/m², calculated for a temperature gradient of 30℃/km and a mean effective heat conductivity of 2.82 W/m℃. We investigate the effects of the geothermal gradient, the host rock properties (i.e. heat conductivity, heat capacity, hydraulic conductivity), the seam properties (i.e. porosity, hydraulic conductivity), the mine geometry (see Fig. A.46), the volume of mined rock and the pumping scenario (i.e. production rate, pumping depth) on the temperature profile. For each scenario, the overall change in energy content of the system is moreover calculated to gain insights into the relationships between the observed mine-water temperature and the heat potential of the mine. Initial steady-state conditions are calculated for each of them before simulating dewatering to account for possible shifts in the initial energy content of the flooded mine.

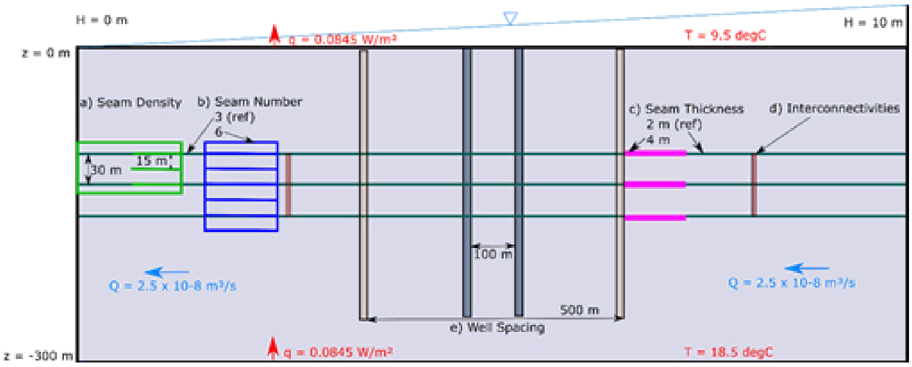

Figure A.46: Sketch of the 2D mine model with different geometrical features and boundary conditions.

A.5.4 Results

Fig. A.47) shows temperature data extracted from a vertical profile in the pumping shaft, after 500 days of pumping/dewatering at a rate of 0.05 m3/s. This production period was chosen in accordance with the time required for thermal and hydraulic steady-state to be reached in the shaft in the reference model (Table A.16). In the scenarios with constant head boundaries and a seam productivity of 1×10^{-2} m/s, pumping results in a decline in head down to the depth of the lowest seam (i.e. about -160 m) at the shaft location. Scenarios with a lower seam permeability induced a greater drawdown at the shaft location due to lower hydraulic recharge (i.e. up to -1600 m for a hydraulic conductivity of 1×10^{-5} m/s). A similar observation was made for models with hydraulic flux boundaries, where the head was lowered down to -800 m due to the reduced availability of water recharge. In all the production scenarios (Fig. A.47a-e), temperature offsets are visible in the profiles where the shaft intersects the mined seams. This suggests that the high permeability of the worked seams creates zones of higher productivity from where inflows of water into the shaft are enhanced. Profiles for the host rock heat conductivity, heat capacity and hydraulic conductivity, the hydraulic gradient, the seam and host rock porosity and the pumping rate are not displayed here due to their limited or absence of impact on the temperature profile.

Fig. A.48 moreover compares the temperature distribution at different time steps and for different borehole geometries in the pumping and monitoring shaft.

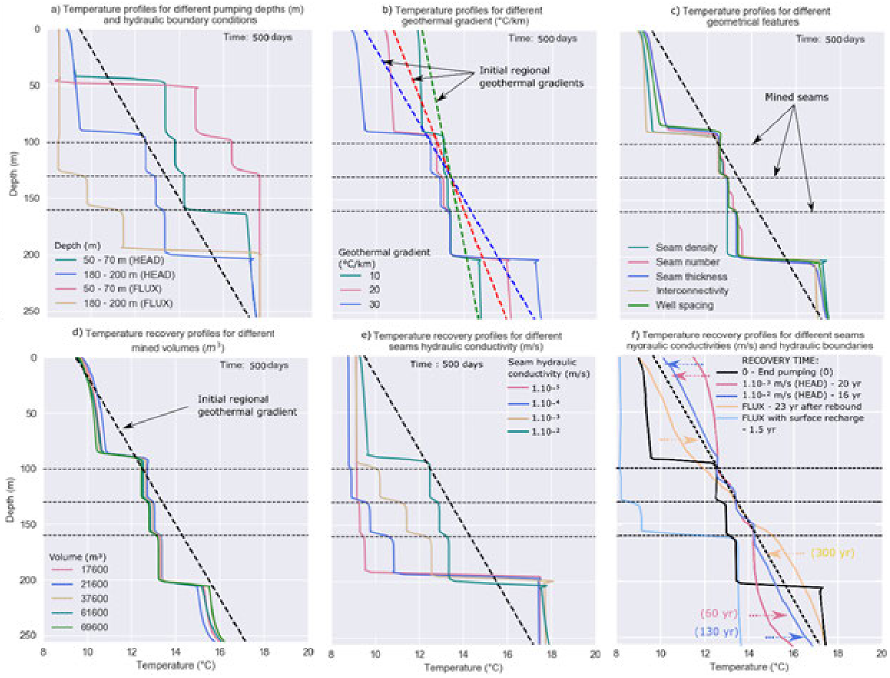

Figure A.47: Temperature profiles obtained after 500 days of pumping for a) pumping depths of 60 m and 190 m under constant head and hydraulic flux boundary conditions, with different b) geothermal gradients, c) geometrical features, d) mined volume and e) seams hydraulic conductivity under constant head boundaries. f) Temperature profile obtained after flooding and heat recovery. The arrows indicate the direction of temperature recovery for each scenario.

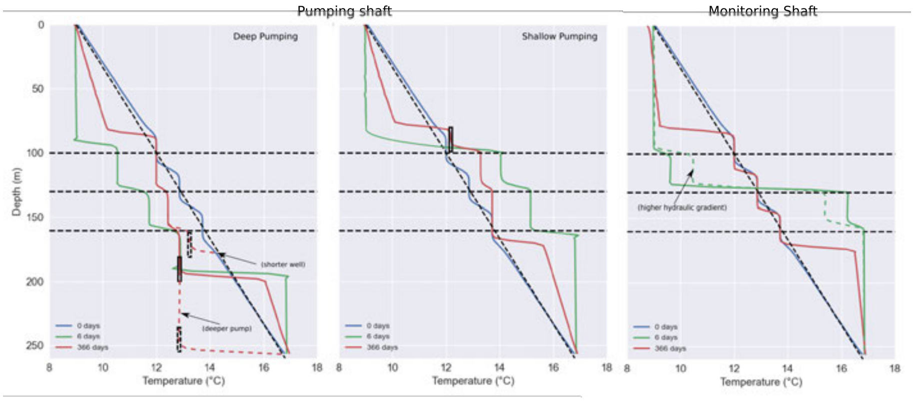

Figure A.48: Comparison of the temperature profiles in the pumping and monitoring shafts for different pumping depths and shaft geometry at t = 0, t = 6 and t = 366 days of pumping.

Boundary Conditions

Hydraulic Flux and Head Gradients: Temperature profiles displayed in Fig. A.47a suggest that the choice of a Dirichlet or Neumann hydraulic boundaries tends to considerably impact the temperature profiles during pumping activities. In models with constant head boundaries, the average temperature in the shaft is highly controlled by the temperature at the shallowest seam when water is pumped from below the mined area, resulting in cooling in the mined interval. Conversely, the temperature in the shaft increases relative to the initial temperature gradient when pumping is performed from above the mined seam, as the average temperature is controlled by the inflow at the deepest seam. A flow rate of -1.3×10-8 m3/s chosen to maintain the head gradient of 10 m across the model tends to favour cooling at the well location when the pump is located below the seams and favor warming when the pump is located above the worked seams. The nature and extent of hydraulic recharge could therefore explain a large range of temperatures observed at the same depth interval (Farr et al., 2020).

Further analysis of the effect of the regional hydraulic gradient on the measured temperature profile is performed, based on hydraulic heads of 10, 20, 50 and 80 m at the eastern boundary. For each scenario, new initial steady-state conditions are calculated before starting pumping simulations. Results (not displayed here) after 500 days of pumping indicate that an increase in the hydraulic gradients only slightly decreases the temperature in the mined area, suggesting that a high regional hydraulic flow rate through the highly conductive seams tends to reduce the amount of heat recharge to the well during pumping.

Geothermal Gradient: We then assess the effect of the geothermal gradient on the temperature profiles resulting from a 500-day long pumping period. Geothermal gradients of 10, 20 and 30℃/km are set so that the temperature at 130 m depth (i.e. mid-seam depth) is 13.15℃. Results displayed in Fig. A.47b show that for a pumping depth of 180 – 200 m, an increase in the geothermal gradient increases the amplitude of the temperature drops at the seams insets, so that the temperature at the shallowest seam matches the temperature predicted by the initial gradient. In those scenarios, the average temperature in the mined interval is linearly correlated to the surface temperature, which decreases as the geothermal gradient increases. This shows that the shallow part of the geothermal gradient can highly affect the observed temperature in the shaft.

Geometry

Fig. A.47c shows the temperature profiles for models with different geometries (Fig. A.46). These include a) a decrease in the seam spacing from 30 m to 15 m, b) an increase in the number of seams from 3 to 6, c) an increase in the seam thickness from 2 to 4 m, d) the addition of two staple shafts connecting the seams and e) an increase in the well spacing from 100 to 500 m. In those scenarios, the relatively high hydraulic conductivity of the mined seams (of 1×10-2 m/s,) relative to the surrounding rock (of 1×10^{-7} m/s) allows 'steps' to be visible at each intersection with the shaft. Results suggest that the depth range spanned by the mined seams (i.e. seam density, number of seams) has the largest influence on the average temperature in the mined area, in accordance with Banks et al. (2004). The deeper the seams, the higher the temperature of the water available for mixing in the shaft.

We also investigate the impact of the volume of the mine on the temperature profiles. In this series of models, we assume six areas of intensive mining or collapsed material with 25% porosity. The effective density, conductivity and heat capacity have been attributed accordingly to the relative proportion of mined seam/host rock in those areas (Table A.16) so as to maintain a geothermal flux of 0.085 W/m^2. Results displayed in Fig. A.47d suggest that the volume of mined rock controls the average temperature in the shaft. Above the pump location, the average temperature decreases with increasing mined volume while below the deepest seam, the temperature increases with increasing mined volume, with a temperature difference of up to 0.5℃ between the two end-members scenarios. One of the possible reasons for the observed decrease in the average temperature with increasing void volume could be explained by the lower heat conductivity of the water that fills the pores. This has been observed to a much smaller extent when performing a sensitivity analysis for the host rock heat conductivity.

Intrinsic rock Properties

Host rock hydraulic Conductivity K_r: We investigate the effect of different host rock permeability $K_r = 1 \times 10^{-8}$ m/s, 1×10^{-7} m/s (reference model), 1×10^{-6} m/s and 1×10^{-5} m/s) on the temperature profile after 500 days of pumping for a seam hydraulic conductivity $K_s = 1 \times 10^{-2}$ m/s. Results (not displayed here) indicate that the permeability of the host rock does not affect the observed temperature in the mined interval. The greatest perturbations are observed above the shallowest seam, where the higher the host rock permeability and the higher the temperature. This suggests that higher rock permeability enhances hydraulic recharge throughout the whole depth range of the well/shaft, allowing an inflow of heat that restricts the temperature drop away from the geothermal gradient. This improved recharge is confirmed by a slight reduction in the drop in head from -160 to -155 m at the pump location when increasing the permeability from 1 × 10^{-7} to 1 × 10^{-5} m/s. Although casings in the shafts/wells would prevent this hydraulic recharge from occurring, further analysis presented in the following section confirms that increasing the rock permeability favours heat recharge to the system.

Seam hydraulic conductivity K_s: Several authors suggested the importance of the effects of permeability contrasts between the mining voids and the host rock on the temperature distribution in mines (i.e. Renz et al., 2009). To verify this hypothesis, we here perform a sensitivity analysis on the effect of the hydraulic conductivity of the coal seams on the temperature profiles. Using hydraulic conductivities K_s of 1 × 10^{-5} m/s, 1 × 10^{-4} m/s, 1 × 10^{-3} m/s and 1 × 10^{-2} m/s (reference model) for Kr 1 × 10^{-7}7 m/s, we show that the productivity of the seams largely impacts the measured temperature profile in the mined interval, where the higher the permeability the higher the average shaft temperature (Fig. A.47e). Those moreover highly control the drop in head at the pump location, ranging from -160 m for K_s = 1 × 10^{-2} m/s to –1600 m for Ks = 1 × 10^{-5} m/s, for a pumping rate of 0.05 m^3/s. Further analysis showed that for the same contrasts in hydraulic conductivity evaluated (i.e. 10^3, 10^4, 10^5), the temperature profiles can be highly different depending on the absolute seam permeability. The temperature profiles measured in shafts therefore mostly depend on the absolute permeability of the host rock and the seams rather than on the permeability contrasts. Both tend to control the hydraulic flux and the extent of convective heat recharge that governs the pattern of the temperature profile during pumping.

Seam Porosity: In mines, the amount of void space is expected to depend on the mining approach (i.e. pillar-and-stall or longwall mining) and the volume of coal extracted. However, following the closure of a mine, subsidence, collapse and fracturing of the roof together with the backfilling of the galleries tend to alter the initial void volume (Younger and Adams, 1999). Several methods have been deployed in the past to derive estimates of the residual porosity in mine workings (see Fig. A.49). The reference model presented in this study considers the seams and the shafts as a porous medium of porosity ϕ = 25% (i.e. the amount of residual void in a fully mined coal panel) and 100% (i.e. open voids), respectively. To account for the uncertainty in the residual volume of void in mine galleries, we investigate the impact of different seam porosity (i.e. 15%, 25%, 50%, 55% and 75%) on the temperature profile.

Results (not displayed here) show that the seam porosity does not affect the observed temperatures in the shaft. In opposition to the seam permeability, the porosity does not improve the seam-shaft interconnectivity nor control the hydraulic flow rate in the galleries but only informs on the volume of water stored in the mine. The relatively small change in void volume induced by a change in seam porosity at the scale of the mine would explain the limited impact on the heat flow in mines and the measured temperature profiles. Further analysis (Fig. A.50) however shows that the volume of water does affect the energy content in the mine system.

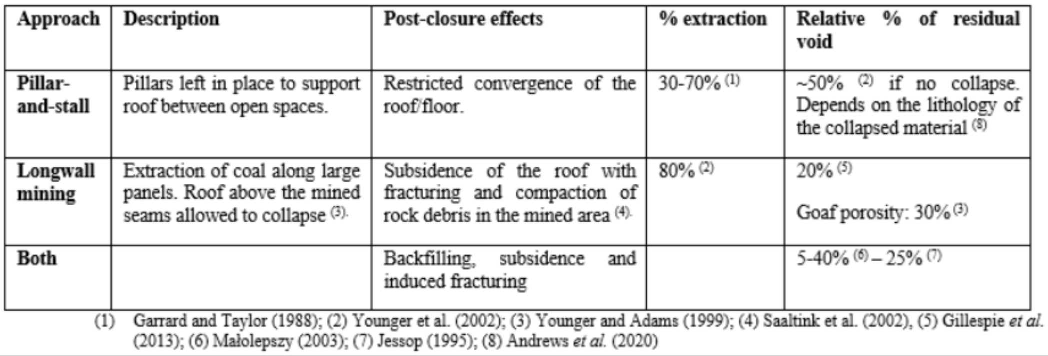

Approach	Description	Post-closure effects	% extraction	Relative % of residual void
Pillar-and-stall	Pillars left in place to support roof between open spaces.	Restricted convergence of the roof/floor.	30-70% (1)	~50% (2) if no collapse. Depends on the lithology of the collapsed material (8)
Longwall mining	Extraction of coal along large panels. Roof above the mined seams allowed to collapse (3).	Subsidence of the roof with fracturing and compaction of rock debris in the mined area (4).	80% (2)	20% (5) Goaf porosity: 30% (3)
Both		Backfilling, subsidence and induced fracturing		5-40% (6) – 25% (7)

(1) Garrard and Taylor (1988); (2) Younger et al. (2002); (3) Younger and Adams (1999); (4) Saaltink et al. (2002), (5) Gillespie *et al.* (2013); (6) Malolepszy (2003); (7) Jessop (1995); (8) Andrews *et al.* (2020)

Figure A.49: Summary of the characteristics and expected residual void volume in coal mines following their closure, depending on the mining approach.

Production Scenario

Pumping rate Farr et al. (2020) suggested that variations in the average profile temperature observed at Horden over time might be caused by changes in the pumping rate. To verify this hypothesis, we simulate the temperature profile in the pumping shaft after 500 days of pumping at rates of 0.01, 0.05 (reference model), 0.1, 0.2 and 0.5 m^3/s. Results (not displayed here) show that the pumping rate does not affect the temperature in the mining area. Above and below the mined seams, slightly cooler and warmer temperatures are modelled for higher pumping rates. This suggests that as the production rate increases, colder water is dragged from above and warmer water is accessed from depth, without significantly changing the average temperature. However, further investigation is required to evaluate the potential effects of a change in the balance between extracted mine water and natural recharge on the temperature profile.

Pumping depth We finally look at the impact of the pumping depth on the temperature profiles. Pumps located at 50-70 and 180-200 m depth are set in a series of two models with constant head and constant flux boundary conditions. The resulting profiles are shown in Fig. A.47a and indicate that the location of the pump defines the boundary between a zone of cooler temperature above it and a zone of warm temperature below. This has been predicted by i.e. Banks et al. (2004) and Nuttall and Younger (2004) as a result of cold water dragged from above and warmer water pulled from below.

A.5.5 Discussion

Temperature Profiles and Energy Content

In the previous section, we analyzed the effects of pumping from a flooded mine with highly permeable layers on the temperature profile observed in the pumping shaft. We showed that in addition to the geothermal heat flow, the advection of heat via highly conductive mined seams tends to control the mine-water temperature (i.e. Burnside et al., 2016). In parallel, we calculated the time series of energy change in the mine for each scenario to get better insights into the effects of the rock properties, the production scenario and the hydraulic/geothermal conditions on the energy content of the mine and its relationship to the observed temperature. Results displayed in Fig. A.50 indicate the followings:

Hydraulic gradient: The initial energy content in the mine decreases linearly with an increasing hydraulic gradient (Fig. A.50a), in accordance with the temperature observations. Time series of energy change during pumping indicates a rapid drop and a subsequent increase in energy in the initial stage of production, mostly observed for high hydraulic gradients (i.e. H = 50 m and H = 80 m). After 500 days of pumping, where the energy reaches a constant rate of decline, the higher the regional head gradient and the higher the energy losses in the system. This could suggest that although convective heat flow is essential to recharge a mine system in heat, high regional flow rates tend to ‘wash away’ the geothermal heat arriving from depth, decreasing the initial heat potential of the mine and its recharge rate during production.

Geothermal gradient: In the modelled scenarios, an increase in the geothermal gradient causes the upper part of the temperature profile to shift toward lower temperatures (Fig. A.47b) and both the surface and the average temperature in the shaft decreases. Energy time series (not displayed here) show that both the initial energy content and the energy drop after 500 days of pumping are linearly correlated to the temperature gradient. This suggests that although a higher geothermal gradient increases the heat potential of the mine, the geothermal flux is not sufficient to recharge the system during pumping. The absence of heat recharge at the surface, especially for high-temperature gradients where the surface temperature is lower, favours faster temperature decline.

Pumping depth and hydraulic boundaries: Pumping from shallow depths (i.e. -60 m, above the seams) drag hot water from depth and increases the temperature in the shaft up to the near-surface (Fig. A.47a). This permits to the system to maintain a high energy content relative to deeper production, independently of the hydraulic boundary (Fig. A.50b). While a quasi-steady-state situation is reached after about 200 days following the start of pumping in a system with constant head boundaries, the use of Neumann lateral boundary conditions causes the energy in the system to drop linearly after 50 days when pumping is at 180 – 200 m depth. In opposition to constant head boundaries that force water recharge into the system, deep pumping with hydraulic flux boundaries prevents from the convection of heat

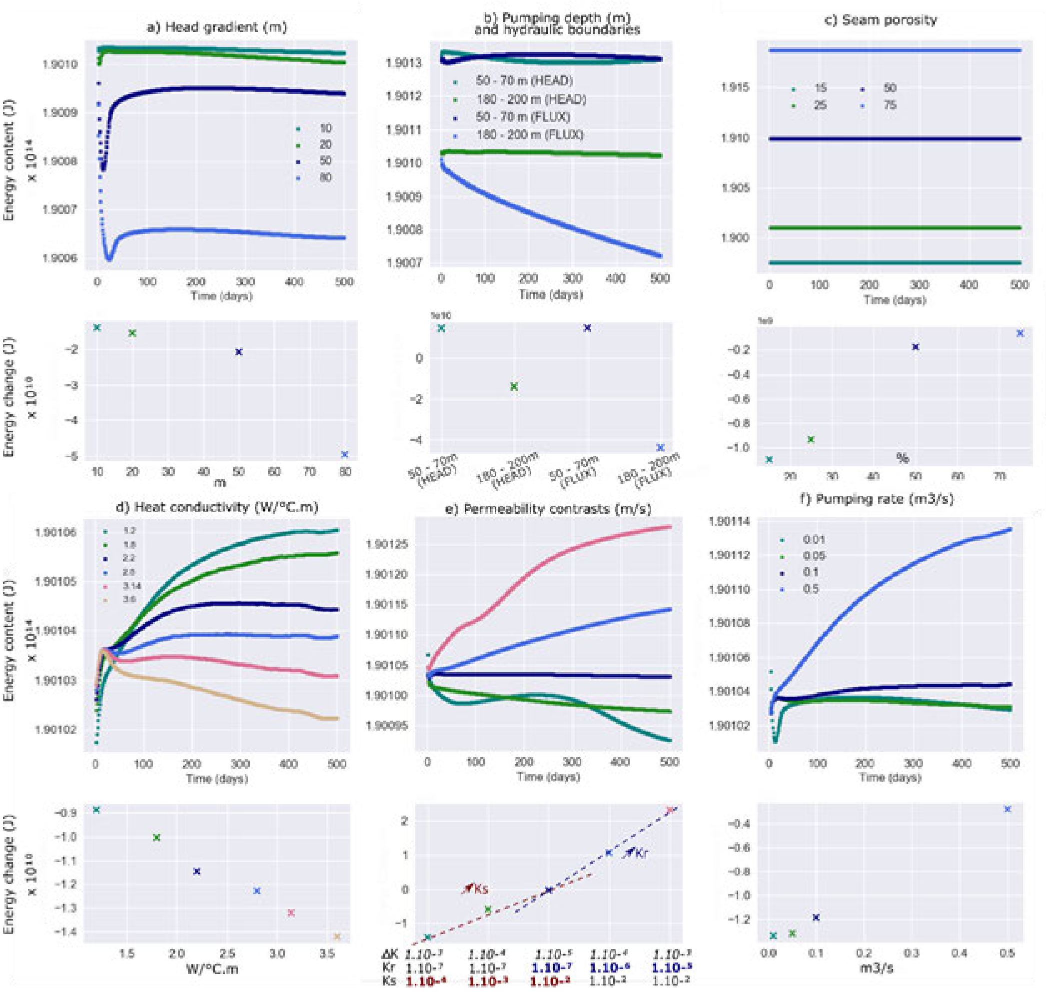

Figure A.50: Time series of energy change and overall energy change in the mine after 500 days of pumping observed for different values of a) head gradient, b) pumping depth (m) and hydraulic boundaries, e) seam porosity, d) host rock heat conductivity, e) seam and host rock hydraulic conductivity (see labels on lower panel x-axis for conductivity values in the time series using the corresponding dot colour) and e) pumping rate.

into the system, which might explain the faster energy drop. This effect is also observed in the temperature profiles (Fig. A.47a), where the average temperature for scenarios with head boundaries is higher than for scenarios with hydraulic flux boundaries at the corresponding pumping depth.

Seam porosity and mined volume: An increase in the seams porosity increases linearly the initial energy content in the mine and tends to reduce the overall energy drop in the system after 500 days of pumping (Fig. A.50c). Similar observations are made for the mined volume, for which the initial energy content also increases linearly with the volume of mined rock. This can be the higher specific heat capacity of water contained in higher quantity in both scenarios, relative to the host rock (Table A.16). Although the temperature above the pump decreases with increasing mined volume (Fig. A.47d), high void volumes ($> 4 \times 10^4$ m^3/s) also tend to favour heat recharge compared to lower void volumes. We suggest this reduction in energy drop to be linked to the low heat conductivity of the water, whose effect is described in the following.

Host rock heat conductivity: Although the rock heat conductivity does not have any influence on the temperature profile in the shaft, the higher the host rock heat conductivity the quicker the energy drop in the system (Fig. A.50d). This happens despite the higher geothermal flux set to maintain the geothermal gradient of 0.03℃/km through the model. A high effective thermal conductivity would therefore favor heat depletion in the mine system under pumping conditions while maintaining a constant temperature at the shaft. This is in accordance with the heat diffusion equation, where an increase in heat conductivity λ for the same temperature gradient $\frac{\Delta x}{\Delta z}$ generates a higher heat flux q (Fig. A.51).

Host rock and seam hydraulic conductivity: The initial energy content of the mine increases exponentially relative to the permeability of the seams and of the host rock, suggesting that promoting water flow through the rock improves the heat potential of the mine reservoir. Moreover, both tend to reduce the energy drop after 500 years of pumping, showing that enhanced fluid-rock interactions also favour heat recharge into the system. Although the seam productivity highly affects the temperature profiles in the shaft, a higher host rock permeability promotes quicker heat recharge to the mine system, as suggested by the slopes of the trends presented in Fig. A.50e. This effect is also likely to be responsible for the warmer temperatures observed above and below the mined area for higher rock permeability. Heat recharge in mines during pumping is therefore highly promoted by the combined effect of the seams and host rock permeability on heat convection (Fig. A.51).

Pumping rate: Although the pumping rate does not significantly alter the steady-state temperature in the shaft, increasing the production rate increases linearly the energy in the mine after 500 days of pumping (Fig. A.50f). This phenomenon might be explained by the effects of abstracting warm water from deeper seams as the head is lowered (i.e. -150 m for 0.05 m^3/s to -1500 m for 0.5 m^3/s after 500 days). However, the effect of the upwelling of warm water into the model might be overestimated in cases where hydraulic recharge is limited and the medium becomes unsaturated with water.

Specific heat capacity c and density ρ: Those parameters tend to increase the initial heat capacity of the mine without impacting the temperature profile in the shaft (see Fig. A.51).

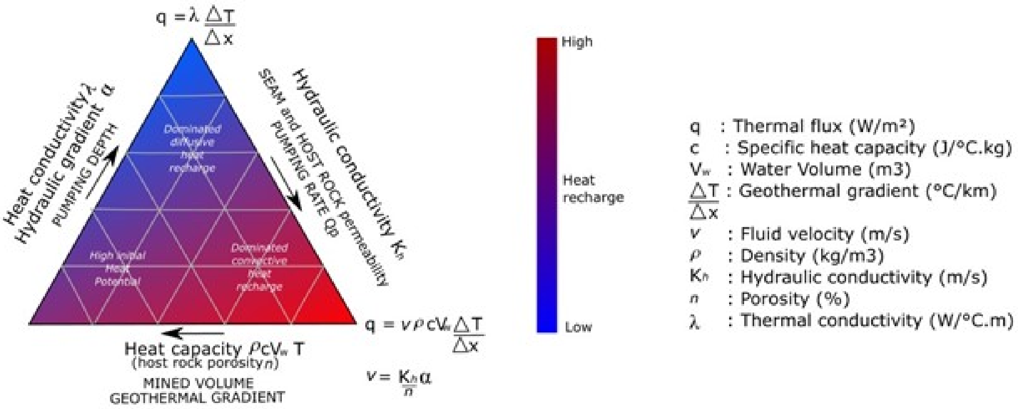

Figure A.51: Conceptual diagram showing the relationship between the parameters evaluated in this study and the expected amount of heat recharge within the mine system. Parameters in capital letters correspond to those having an impact on the temperature profiles (Fig. A.47).

Long-Term Perturbations of the Geothermal Gradient

Previous studies of the heat potential of flooded coal mines often considered the undisturbed geothermal gradient as the main contributor to the thermal state of the mine. However, Gillespie et al. (2013) pointed out the lack of correlation between the temperature of the mine water measured in abandoned un-pumped mine shafts in the UK and the depth of the measurements. To explain those discrepancies, some authors suggested the existence of other sources of heat controlling the mine water temperature, such as heat production from pyrite oxidation (Farr et al., 2016) or the effects of free density-related water convection within the large open mining voids (i.e. Nuttall and Younger, 2004; Renz et al., 2009; Hamm and Bazargan Sabet, 2010). Beamish and Busby (2016) interpreted those observations as the effect of heat advection through the artificial large-scale transmissive pathways that would indicate that the geothermal gradients in mines may not represent purely conductive heat flows (Bailey et al., 2016). However, only a few authors recognized the potential effect of extensive periods of mining with deep pumping and air-cooling on the virgin rock temperature in flooded mines (i.e. Malolepszy, 2003).

We simulate water rebound and heat recovery under different hydraulic boundary conditions and seam productivity, based on the modeling outputs for a 500-day pumping period. Although those models underestimate the mining periods and the effect of air cooling in the galleries before flooding, the objective is here to get an insight into the relative time necessary for the temperature in the mine to return to equilibrium. Scenarios with hydraulic flux boundary conditions assume a total recharge of 2.5×10^{-5} m^3/s from both lateral boundaries. This was done to ensure a water rebound in the same time scale as for a scenario with constant head boundaries. Fig. A.52 summarizes for each model the time for water rebound to be completed (i.e. head measured at the pump location) and the time for temperature in the shaft to reach a new equilibrium. Those were estimated based on a graphic analysis of the head and temperature time series measured at -50 m and -180 m depth at the shaft location.

Recovery profiles displayed in Fig. A.47f represent the temperature in the production shaft after the water rebound is completed and as thermal equilibrium approaches. Results show that in a case with constant head boundaries, the geothermal gradient remains lower than the pre-pumping steady-state temperature gradient. When pumping stops, the mixing of warm deep water and colder surface water in the shaft fixes the temperature in the shaft around the average temperature in the mined area. Once the flooding is completed, the temperature profile in the shaft slowly re-equilibrates with the temperature of the surrounding rock. However, the effects of convective heat flux at the intersection between the shafts and the mined seams together with the perturbations of the rock temperature induced by earlier pumping activities maintain a temperature anomaly in the shaft. Above the mined area, temperatures tend to be higher than the initial steady-state temperatures after recovery, while they remain lower than the pre-pumping temperatures below the deepest seam. The presence of productive seams favours a quicker water rebound and steady rate of heat recovery, although the projected time to return to the initial undisturbed temperatures is extended.

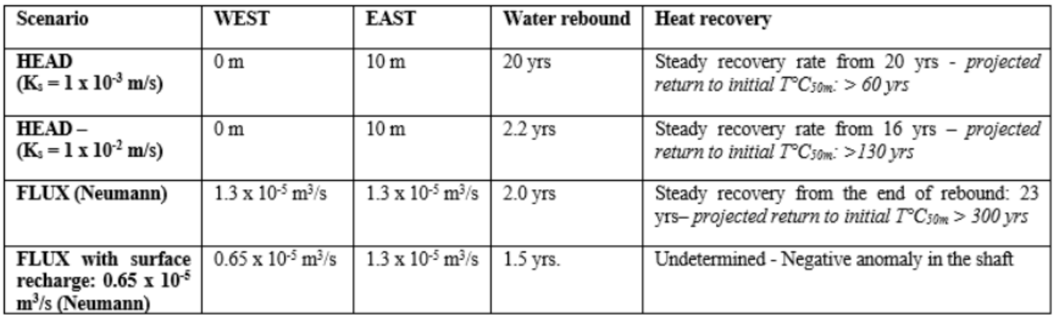

Scenario	**WEST**	**EAST**	**Water rebound**	**Heat recovery**
HEAD **($K_s = 1 \times 10^{-3}$ m/s)**	0 m	10 m	20 yrs	Steady recovery rate from 20 yrs - *projected return to initial T°C_{50m}: > 60 yrs*
HEAD – **($K_s = 1 \times 10^{-2}$ m/s)**	0 m	10 m	2.2 yrs	Steady recovery rate from 16 yrs – *projected return to initial T°C_{50m}: >130 yrs*
FLUX (Neumann)	1.3×10^{-5} m^3/s	1.3×10^{-5} m^3/s	2.0 yrs	Steady recovery from the end of rebound: 23 yrs– *projected return to initial T°C_{50m} > 300 yrs*
FLUX with surface recharge: 0.65×10^{-5} m^3/s (Neumann)	0.65×10^{-5} m^3/s	1.3×10^{-5} m^3/s	1.5 yrs.	Undetermined - Negative anomaly in the shaft

Figure A.52: Water rebound and heat recovery time obtained for different seam permeability and boundary conditions. Times are given relative to the cessation of pumping (t0) unless otherwise specified.

In a scenario with hydraulic flow, the reversed effect is observed. After water rebound and heat recovery, the temperature profile in the shaft displays lower temperatures in the upper part of the profile while temperatures remain higher than the pre-pumping geothermal gradient in the lower part. Time series analysis shows that this effect results from the nature of the hydraulic recharge during flooding. In opposition to water rebound in models with constant head boundaries that tend to promote diffusive heat recovery, the high hydraulic flow induced during water rebound in this case reproduces the offsets at the seams location similar to those observed during pumping. Instead of mixing water into the shaft, the upwelling of warm thermal waters from below the mine will heat up the base while the recharging water from shallower and colder seams will cool the upper part of the model. Heat convection will tend to superimpose onto the diffusive heat gradient during flooding. As the rebound is completed, the temperature profile is smoothed but conserves the temperature anomalies induced during recovery. Water recharge at the top of the model (light blue profile in Fig. A.47f) finally shows that infiltration of cold surface rainwater can highly reduce the temperature in the shaft.

A.5.6 Conclusion

We have performed a sensitivity analysis on the controls on the temperature profiles observed in mine shafts under pumping conditions and during recovery. Results indicated that the hydraulic conductivity of the worked coal seams intersected by the pumping shaft and the nature of the hydraulic recharge governs the temperature distribution in the shaft. During pumping, the offsets in temperature created at the seams insets moreover highly depend on the pumping depth and the temperature of the mine water predicted by the undisturbed geothermal gradient. Although the observed temperature profiles in pumping mine shafts can be an indicator of the hydraulic state of a mine, they only give a limited insight into the overall volume of mined rock, reducing their potential as a calibration tool for the geometry of mine models. A comparison between the steady-state temperature profiles and the energy change in the mine at the end of the pumping period moreover showed that observed temperature can only give limited insights into the heat potential of the mine over the long-term.

Simulation of water rebound and heat recovery moreover suggested that although the mine-water temperature tends to reequilibrate with the surrounding rocks within 20 years following the cessation of pumping, the observed temperature gradient in the shaft remains affected by the past dewatering activities. Modelling results indeed showed that dewatering of highly permeable mining voids tends to disturb the virgin rock temperature around the shaft and galleries. The effects of forced convective heat flow would superimpose onto the purely diffusive geothermal gradient and create new thermal equilibrium conditions. Post-recovery temperature profiles moreover suggested that the nature and the extent of hydraulic recharge during water rebound also control the mechanisms of heat recovery and the residual temperature anomaly in the mine. After the cessation of pumping, constant head boundaries favoured mixing in the shaft and diffusive heat transfers, resulting in a decrease in the geothermal gradient relative to the pre-pumping conditions. On the contrary, hydraulic flow boundaries promoted the advection of cold water at shallow depths and of warmer water in the deeper galleries, resulting in a near-surface cooling relative to the initial undisturbed geothermal gradient.

Although the models presented in this study might overestimate the advective flow in unmined parts of the collieries during mining activities, the short dewatering period (500 days) might underestimate the extent of the perturbations away from the shaft. Considering a real mining history, more time could be required for flooded mines to reach thermal equilibrium after flooding is completed, suggesting that some mines in the UK might not have reached equilibrium yet. Moreover, additional cooling of the rock might be induced by prolonged periods of air ventilation in the galleries and has not been considered in this study. Further modelling work accounting for more realistic geometry and dewatering history is therefore currently undertaken to assess the extent of the perturbations caused by past mining activities on the temperature distribution within mines. This is essential to get a better understanding of the heat potential of flooded mines.

A.5.7 Acknowledgments

Funding for this research was provided by NERC through an E4 DTP studentship (NE/ S007407/1).

A.5.8 References

Adams, R. and Younger, P. A Strategy For Modeling Ground Water Rebound In Abandoned Deep Mine Systems, Groundwater, 39(2), (2001), 249-261. doi: 10.1111/ j.1745-6584.2001. tb02306.x.

Andrews, B.J., Cumberbatch, Z.A., Shipton, Z.K. and Lord, R.: Collapse processes in abandoned pillar and stall coal mines: Implications for shallow mine geothermal energy. Geothermics, 88, (2020). doi: 10.1016/j.geothermics.2020.101904.

Bailey, M.T, Moorhouse, A.M.L and Watson, I.A., Heat extraction from hypersaline mine water at the Dawdon mine water treatment site', In Tibbett, M., Fourie, A.B., and Digby, C. (eds), Proceedings, 18th International Seminar on Mine Closure, Australian Centre for Geomechanics, Cornwall (2013), 559-570. doi: 10.36487/ACG_rep/1352_47_Bailey

Bailey, M.T, Gandy, C.J., Watson, I.A., Wyatt, L.M., and Jarvis, A.P.: Heat recovery potential of mine water treatment systems in Great Britain, International Journal of Coal Geology, 164, (2016) 77–84. doi: 10.1016/j.coal.2016.03.007.

Banks, D., Skarphagen, H., Wiltshire, R. and Jessop, C.: Heat pumps as a tool for energy recovery from mining wastes, Energy, Waste and the Environment: a Geochemical Perspective, R. Gieré, P. Stille. Geological Society London Special Publications, 236, (2004), 499-513. doi:10.1144/GSL.SP.2004.236.01.27.

Beamish, D. and Busby, J., The Cornubian geothermal province: heat production and flow in SW England: estimates from boreholes and airborne gamma-ray measurements, Geothermal Energy, 4(1), (2016), 4 pp. doi: 10.1186/s40517-016-0046-8

Burley, A.J., Edmunds, W.M., and Gale, I.N., Catalogue of geothermal data for the land area of the United Kingdom, Second Revision (1984), Investigation of the geothermal potential of the UK, British Geological Survey, Keyworth.

Burnside, N.M., Banks, D., Boyce, A.J., Sustainability of thermal energy production at the flooded mine workings of the former Caphouse Colliery, Yorkshire, United Kingdom, International Journal of Coal Geology, 164, (2016), 85-91.

Farr, G., Sadasivam, S., Manju, Watson, I.A., Thomas, H. R. and Tucker, D., Low enthalpy heat recovery potential from coal mine discharges in the South Wales Coalfield, International Journal of Coal Geology, 164, (2016), 92-103.

Farr, G., Busby, J., Wyatt, L.,Crooks, J., Schofield, D.I. and Holden, A.: The temperature of Britain's coalfields, Quarterly Journal of Engineering Geology and Hydrogeology, (2020). Geological Society of London. doi:10.1144/qjegh2020-109.

Garrard, G.F., Taylor, R.K.: Collapse mechanisms of shallow coal-mine workings from field measurements, Engineering Geology of Underground Movements, 5, (1988), 181-192. Geological Society London, Engineering Geology Special Publications.

Gillespie, M., Crane, E., and Barron, H.: Study into the Potential for Deep Geothermal Energy in Scotland, British Geological Survey Commissioned Report, CR/12/131, 2, (2013), 129 pp.

Hamm, V., and Bazargan Sabet, Modelling of fluid flow and heat transfer to assess the geothermal potential of a flooded coal mine in Lorraine, France, Geothermics, 39, (2010), 177-186. House of Commons Energy and Climate Committee, 2020 Renewable Heat and Transport Targets, 2(55), (2016). doi: 10.1016/j.vetpar.2006.11.008.

Jessop, A.: Geothermal energy from old mines at Springhill, Nova Scotia, Canada, (1995), 6 pp. Małolepszy, Z.: Low Temperature, Man-Made Geothermal Reservoirs in Abandoned Workings of Underground Mines, Proceedings, 28th Workshop on Geothermal Reservoir Engineering, Stanford University, Stanford, CA (2003).

Nuttall, C.A., Adams, R., and Younger,P.L., Integrated hydraulic-hydrogeochemical assessment of flooded deep mine voids by test pumping at the Deerplay (Lancashire) and Frances (Fife) Collieries, Mine Water Hydrogeology and Geochemistry, 198, (2004), 315-326

Renz, A., Rühaak, W., Schätzl, P., Diersch, H.J.G., Numerical Modeling of Geothermal Use of Mine Water: Challenges and Examples, Mine Water and the Environment, 28, (2009), 2-14.

Rollin, K.E., Catalogue of geothermal data for the land area of the United Kingdom, Third Revision (1987), Investigation of the Geothermal Potential of the UK, British Geological Survey, Keyworth.

Saaltink, M.W., Domenech,C., Ayora,C. and Carrera,J.: Modelling the oxidation of sulphides in an unsaturated soil, Mine Water Hydrogeology and Geochemistry, 198, (2002), 187-204. Geological Society, London, Special Publications.

Todd, F., McDermott, C., Harris, A. F., Bond, A., and Gilfillan, S.: Coupled hydraulic and mechanical model of surface uplift due to mine water rebound: implications for mine water heating and cooling schemes, Scottish Journal of Geology, 55, (2019), 124-133. doi: 10.1144/sjg2018-028.

Younger, P.L. and Adams, R. Predicting Mine Water Rebound, Environmental Agency Research and development Technical report W179 (1999). United Kingdom. 109 pp.

Younger, P. L., Banwart, S. A., and Hedin, R. S.: Mine water: hydrology, pollution, remediation, Environmental Pollution, 5, (2002), 442 pp.

A.6 Chapter 7: Thermal footprint

A.6.1 Regional hydraulic gradient

A series of transient analyses have been conducted to investigate the effect of the regional groundwater flow velocity on the rate of return to thermal equilibrium in the pumping shaft. This analysis is conducted by setting heads of -10, 0, 10, 20 and 30 m on the right boundary H_R and a constant head of 0 m on the left boundary H_L. Apart from the first scenario (H_R = -10 m) that defines a regional flow toward the right boundary ('eastward'), the regional hydraulic gradient toward the left boundary ('westward') increases with increasing H_R, which is expected to promote the flow of deep warm water.

The temperature profiles, average shaft temperature, pumped temperature and power output after 6 days and 732 days are displayed in Fig. A.53. Results suggest that the largest discrepancies between the temperature profiles are in the initial days of pumping, whilst the effect of the regional hydraulic gradient on the temperature profile becomes negligible after 2 years of pumping. Comparison between all the data outputs for the westward hydraulic gradient scenarios however suggests that the optimal power output and pumped temperature is reached for H_R = 15-20 m. At H_R = 30 m, the average shaft temperature and heat output largely drop. Although the eastward flow tends to have the greatest heat output, its effect on the pumped and average shaft temperature is limited compared to the lowest westward hydraulic gradients. This suggests that there is a regional flow velocity at which the heat exchanges between the advecting mine water and the rock are optimal.

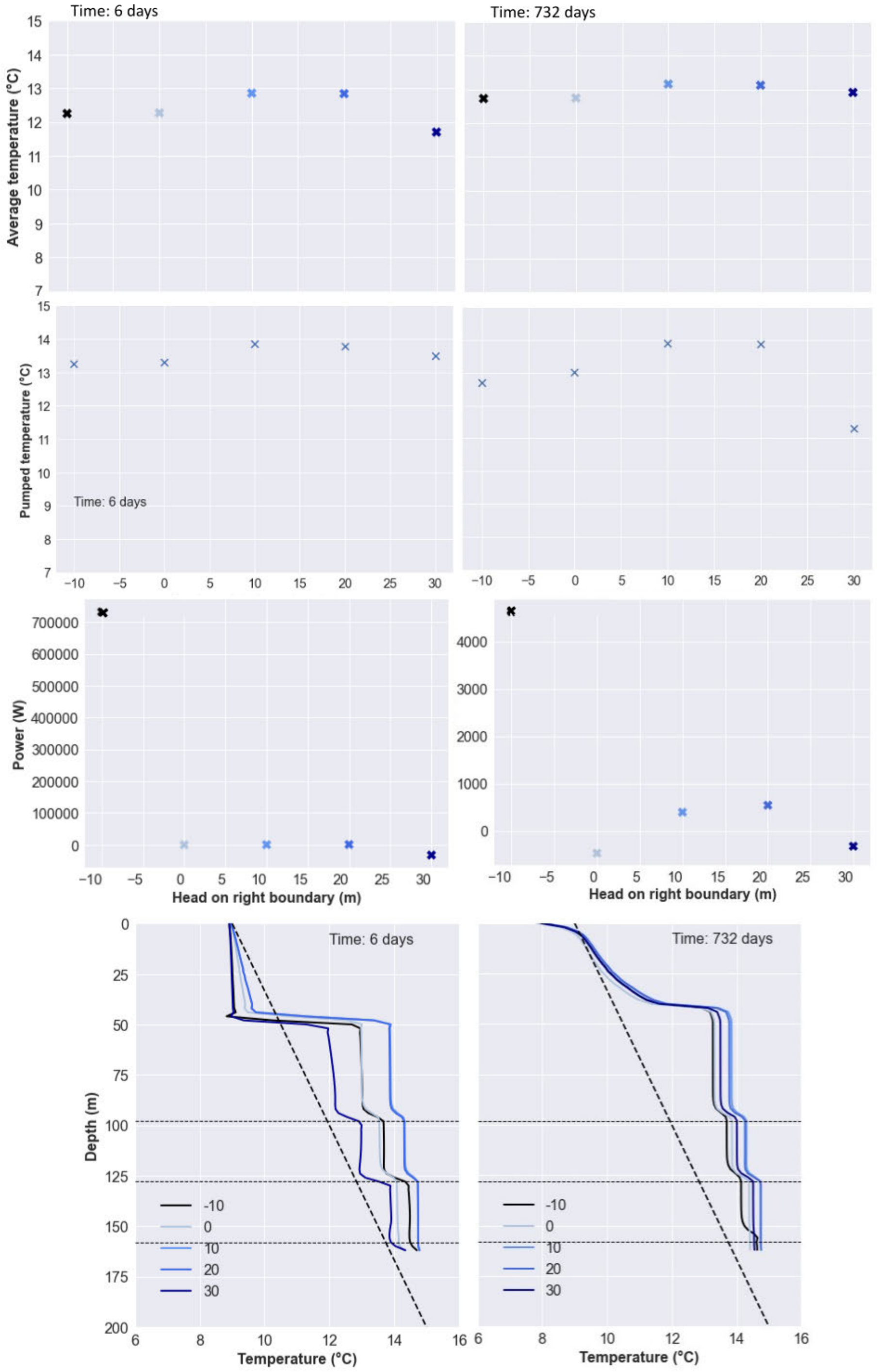

Figure A.53: Rate of energy change (daily time steps) in each material group for the four hydraulic recharge scenarios.

A.6.2 Seam permeability

The temperature profiles in the pumping and monitoring shaft are compared for models with homogeneous and heterogeneous seam permeabilities (Figs. A.54 and A.55). A pumping rate of -0.001 m^3/s is used for all pumping scenarios, ensuring better hydraulic and thermal stability in the temperature profiles compared to the use of a constant head boundary at the pump, with this latter approach generally underestimating the time to return to an equilibrium state (see discussion chapter 6).

Results for the homogeneous seams model suggest equivalent shifts in temperature at each seam inset in the pumped shafts, which are explained by the equal contribution of each seam to the flow. Higher seam permeability moreover tends to promote hydraulic flow to the monitoring shaft and promote convective heat transfers. On the contrary, the presence of seams with different hydraulic conductivity results in the variation in the amplitude of the temperature shifts at the seams insets, with the larger the hydraulic conductivity, the larger the temperature shift (Fig. A.55).

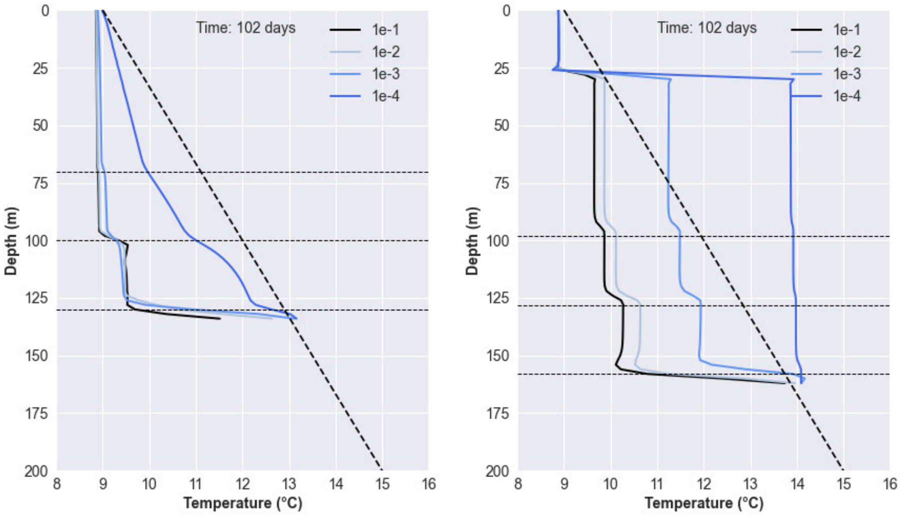

Figure A.54: Temperature profiles in the monitoring and pumping shafts after 102 days of pumping for different seam permeability (homogeneous system), considering shallow pumping from shaft 2 (PUMP 1) and shallow surface recharge. A pumping rate of -0.001 m^3/s is considered, which tends to mitigate the effect of heat convection in the monitoring shaft (i.e. reduced flow) and the formation of temperature steps.

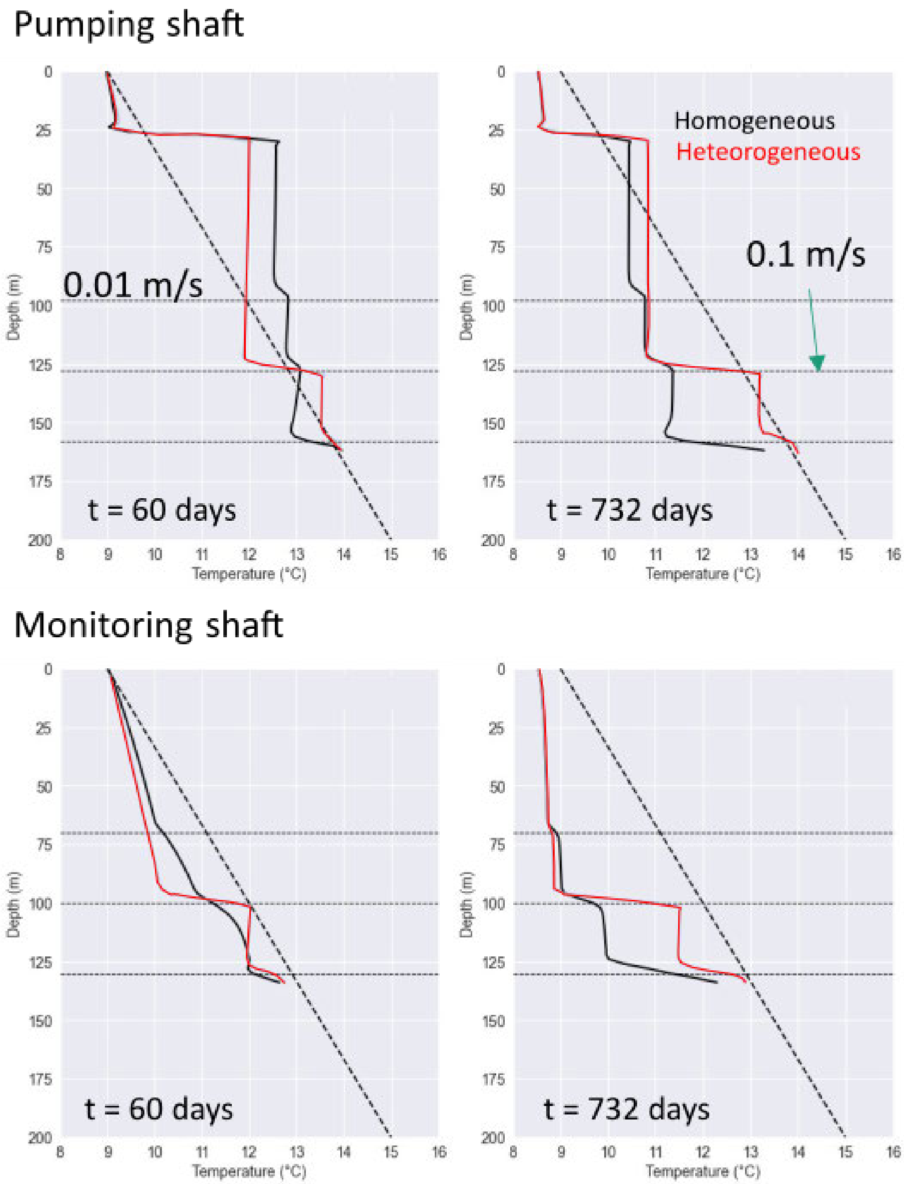

Figure A.55: Temperature profiles in the pumping and monitoring shafts after 6 and 732 days of pumping for different seam permeability contrasts (heterogeneous system), considering shallow pumping from shaft 2 (PUMP 1) and shallow surface recharge. A pumping rate of -0.001 m^3/s is used, which tends to mitigate the effect of heat convection in the monitoring shaft (i.e. reduced flow) and the formation of temperature steps.

A.6.3 Model dimensions

In chapter 6, the model slice thickness was interpreted to largely impact the assessment of the heat potential of mines and the residual footprint of mining and dewatering activities following water rebound. Results confirmed that appropriate scaling of the size of each mining fature is required to calculate the absolute heat output. Here, the thermal footprint induced by dewatering from the porous and multi-element dipping layer models are compared (Fig. A.56).

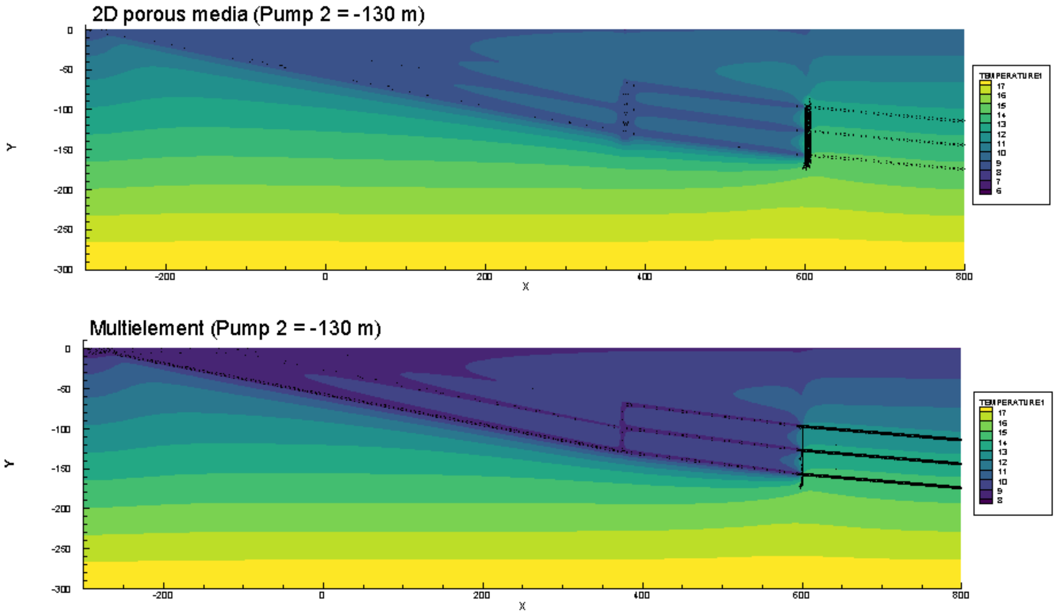

Figure A.56: Temperature footprint induced by 50 years of pumping from the porous and multi-element and dipping seams model, assuming A = 1 m.

Results show that the error induced by the choice of the slice thickness (100 m or 1 m) for the dewatering simulations is limited in the porous model, as long as the pumping rate and relative volume/area of the different mining structures (i.e. shaft, galleries) is properly accounted for and scaled proportionally to a change in the slice thickness (Fig. A.57). The discrepancies are larger for the multi-element model where the shaft/roadway volume remains the same independently of the slice thickness. This results in more heat being mined from the model with a thickness A = 1 m, and therefore induces relatively larger thermal disturbances.

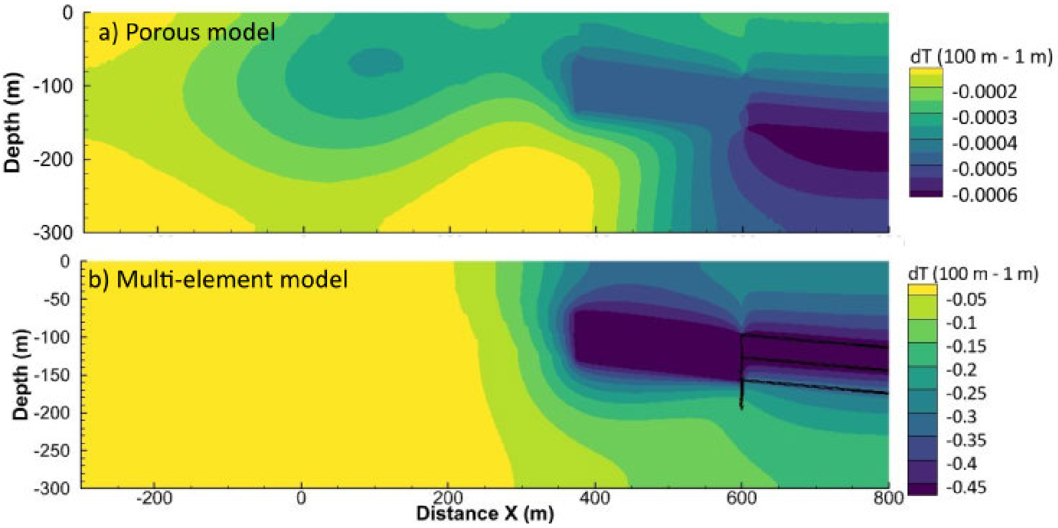

Figure A.57: Thermal discrepancies induced by 50 days of dewatering (steady-state simulations) from a 1 m and 100 m thick porous (a) and multi-element model (b). The shaft area for the 1 m and 100 m thick porous and multi-element models are a) 0.06 m^2 and 6 m^2, and b) 0.28 m^2 and 28 m^2, respectively. A pumping rate of -0.05 m^3/s and -5 m^3/s are used for the 1 m and 100 m thick models, respectively.

A.7 Chapter 8: Conceptual model

Figures A.58 to A.64 show the detailed results of the sensitivity of the power output and pumped temperature of the simplified models to the permeability of zones 5 and 6. This analysis was conducted for all three simplified models (b c and d, see main text) and for both the goaf and roadway hydraulic recharge scenarios.

Results suggest that the equivalent permeability of zones 5 and 6 has negligible or limited effect on the heat extraction rate from the different materials. Short-term effects (i.e. within the 100-200 first days of pumping) are particularly visible in model c in the goaf recharge scenarios (Fig. A.62), where the heat extraction rate from the goaf, intact pillars and host rock is sensitive to the permeability of the equivalent roadway zone 6. To a lower extent, the power contribution from the intact pillars is sensitive to the equivalent permeability of the pillar-and-stall zone 5 (model b, Fig. A.61) in a goaf recharge scenario, whilst the power contribution from the goaf panels is slightly sensitive to the equivalent permeability of both zones 5 and 6 in the roadway recharge scenario (Figs A.58 and A.59). Whilst the permeability of the equivalent pillar-and-stall zone 5 and equivalent roadway zone 6 only impact the heat extraction rate from the host rock in the short term in a goaf recharge scenario (Figs. A.61 and A.62), they tend to have a significant impact on the long-term heat recovery rate from the host rock in the roadway recharge scenarios (see zone 6 in model c, Fig. A.59 and zone 5 in model b, Fig. A.58). In model d (fully porous model, Figs. A.60 and A.63), the long-term heat extraction rate is independent from the permeability of the equivalent zones 5 and 6.

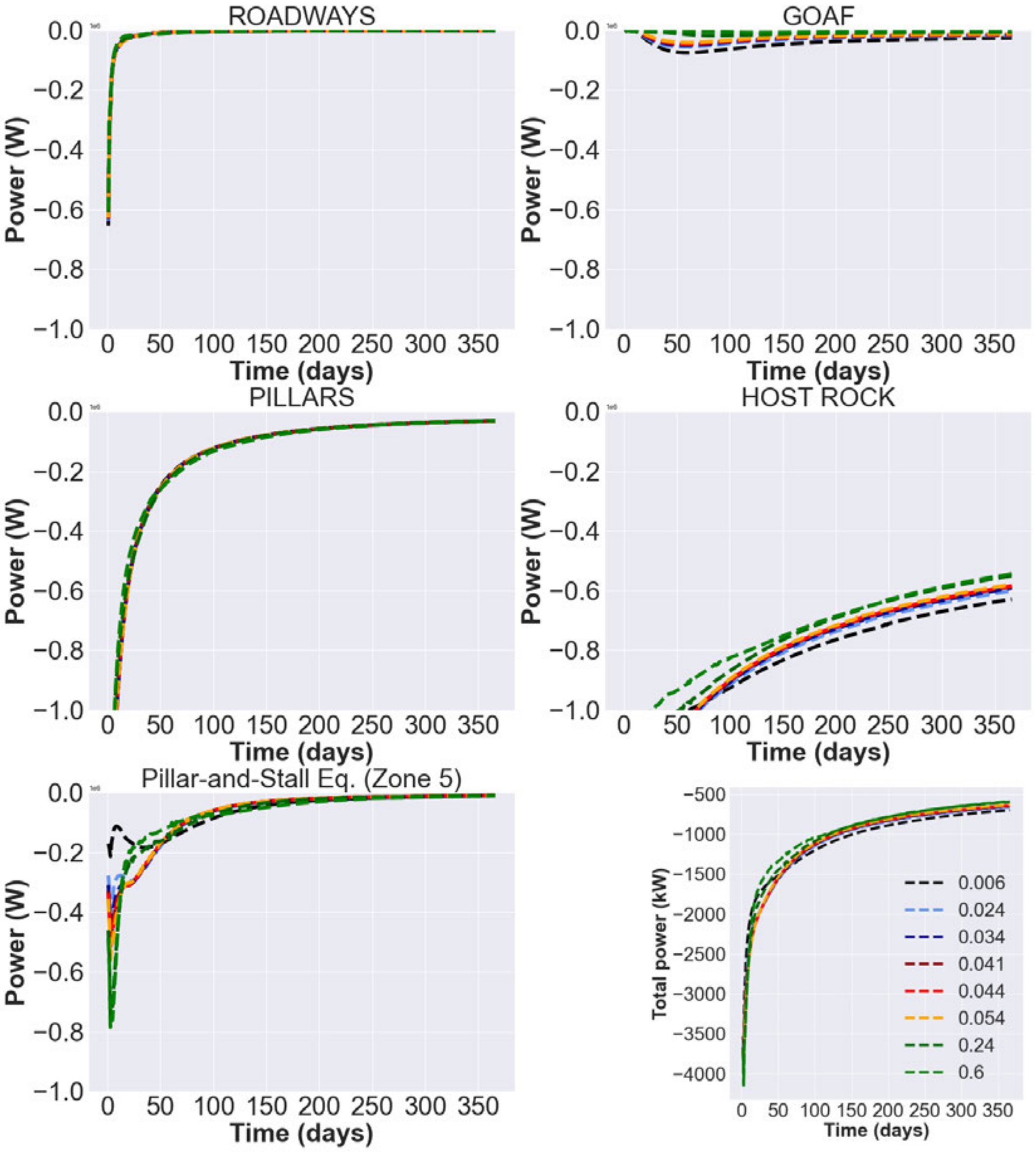

Figure A.58: Sensitivity analysis showing the relative power contribution of each material in model b (pillar-and-stall zone simplification) for the roadway recharge scenario, for different zone 5 hydraulic conductivity (m/s).

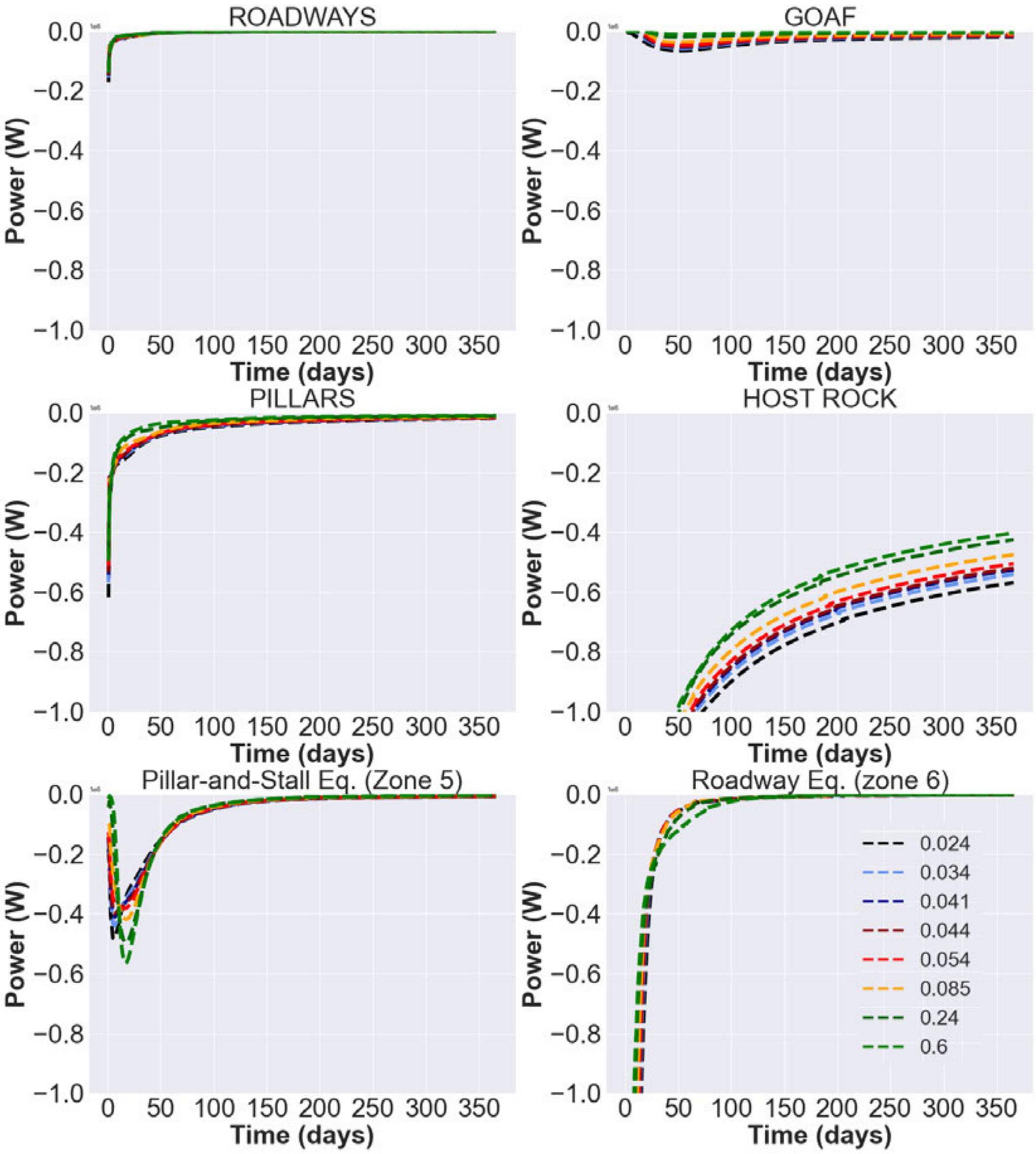

Figure A.59: Sensitivity analysis showing the relative power contribution of each material in model c (roadway zone simplification) for the roadway recharge scenario, for different zone 6 hydraulic conductivity (m/s).

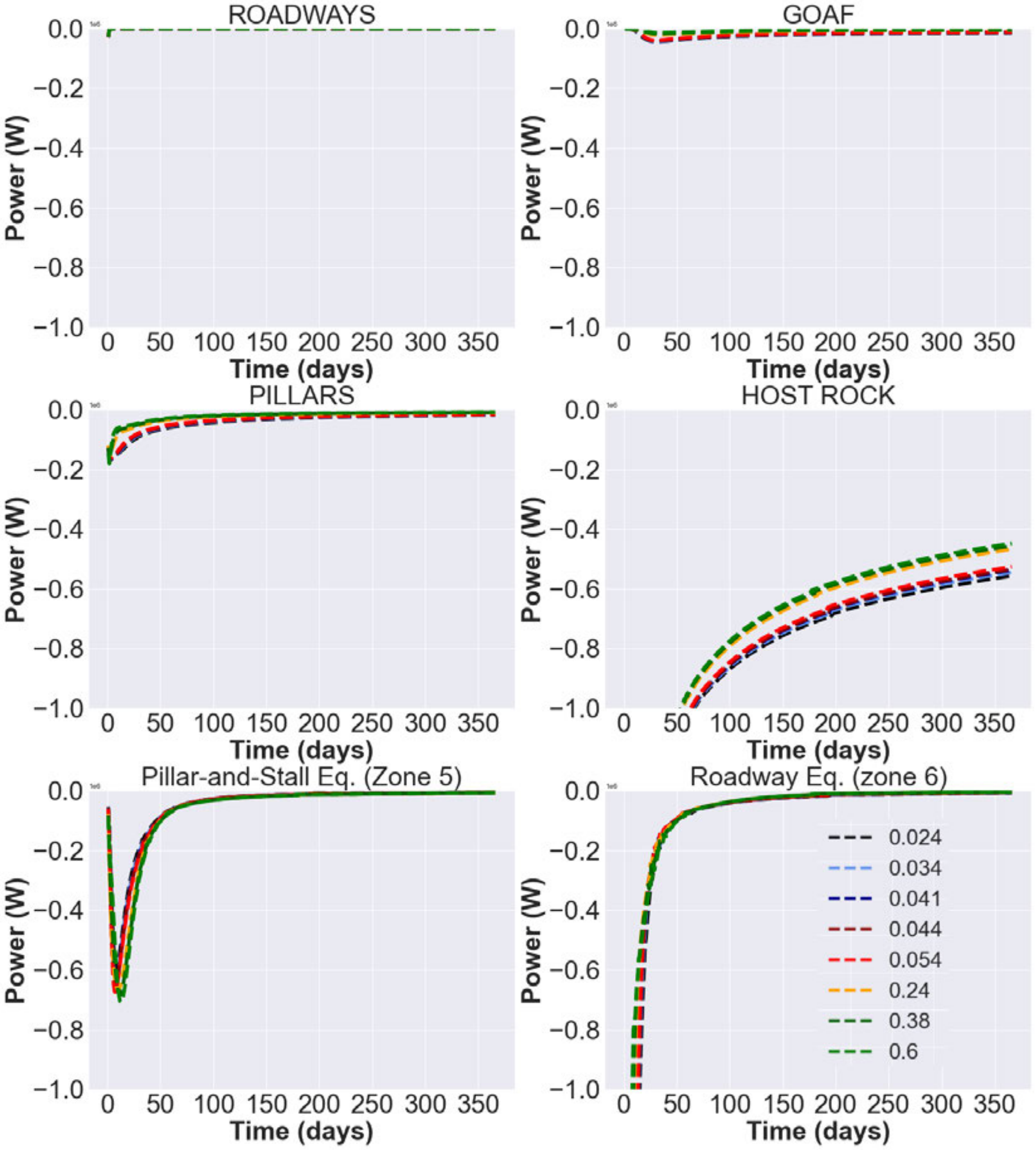

Figure A.60: Sensitivity analysis showing the relative power contribution of each material in model d (pillar-and-stall and roadway zones simplification) for the roadway recharge scenario, for different zone 5 and 6 hydraulic conductivity (m/s).

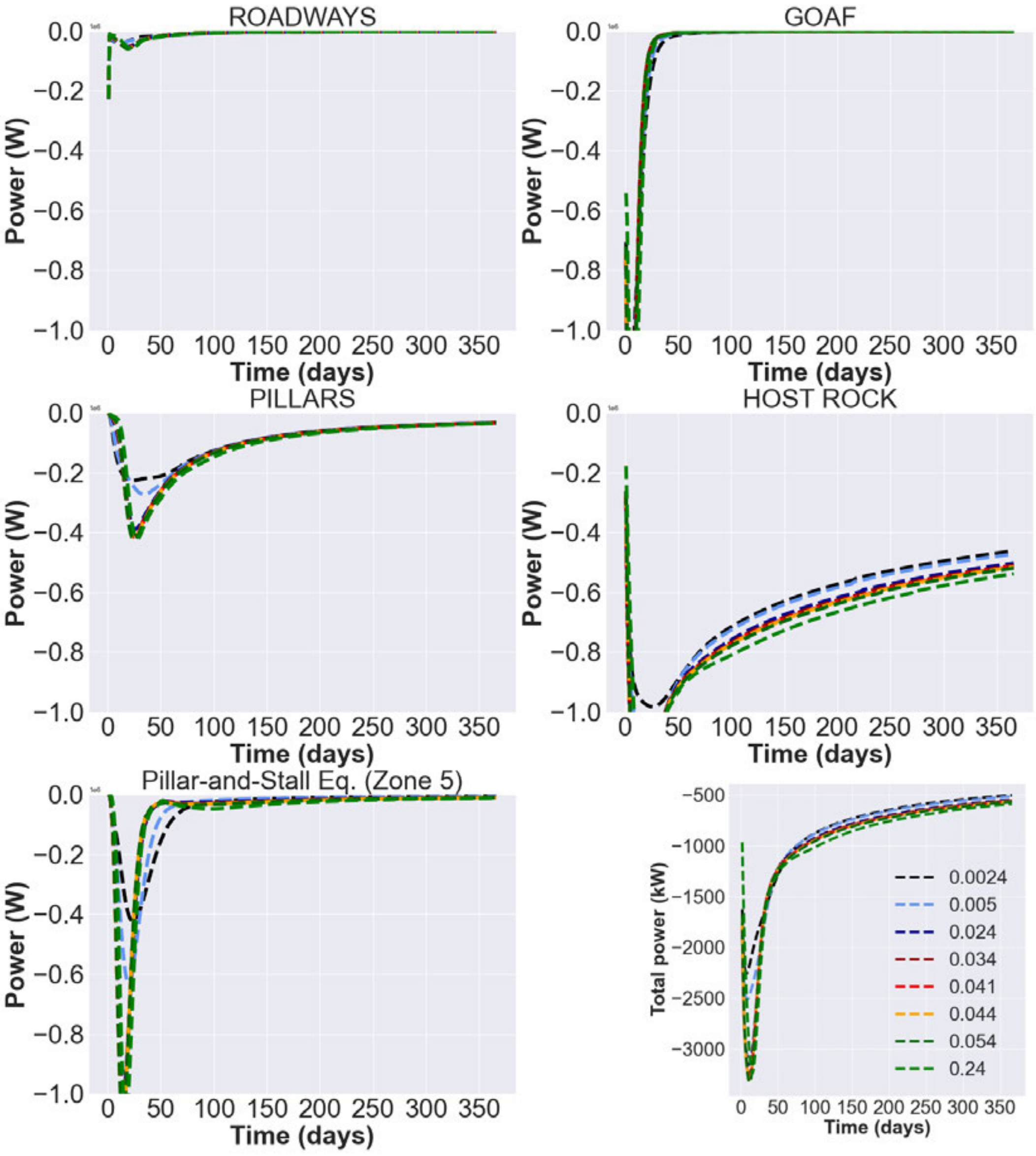

Figure A.61: Sensitivity analysis showing the relative power contribution of each material in model b (pillar-and-stall zone simplification) for the goaf recharge scenario, for different zone 5 hydraulic conductivity (m/s).

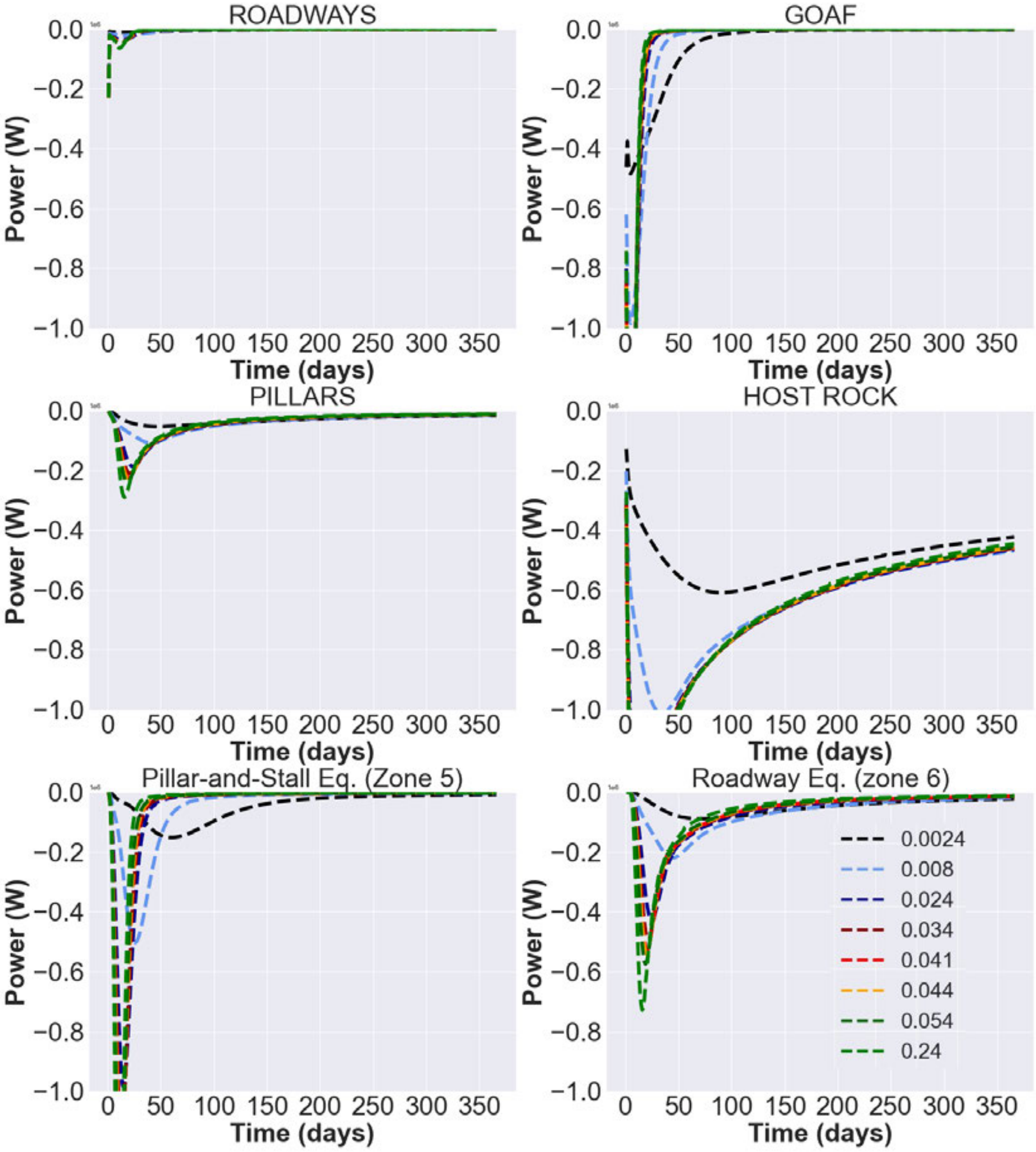

Figure A.62: Sensitivity analysis showing the relative power contribution of each material in model c (roadway zone simplification) for the goaf recharge scenario, for different zone 6 hydraulic conductivity (m/s).

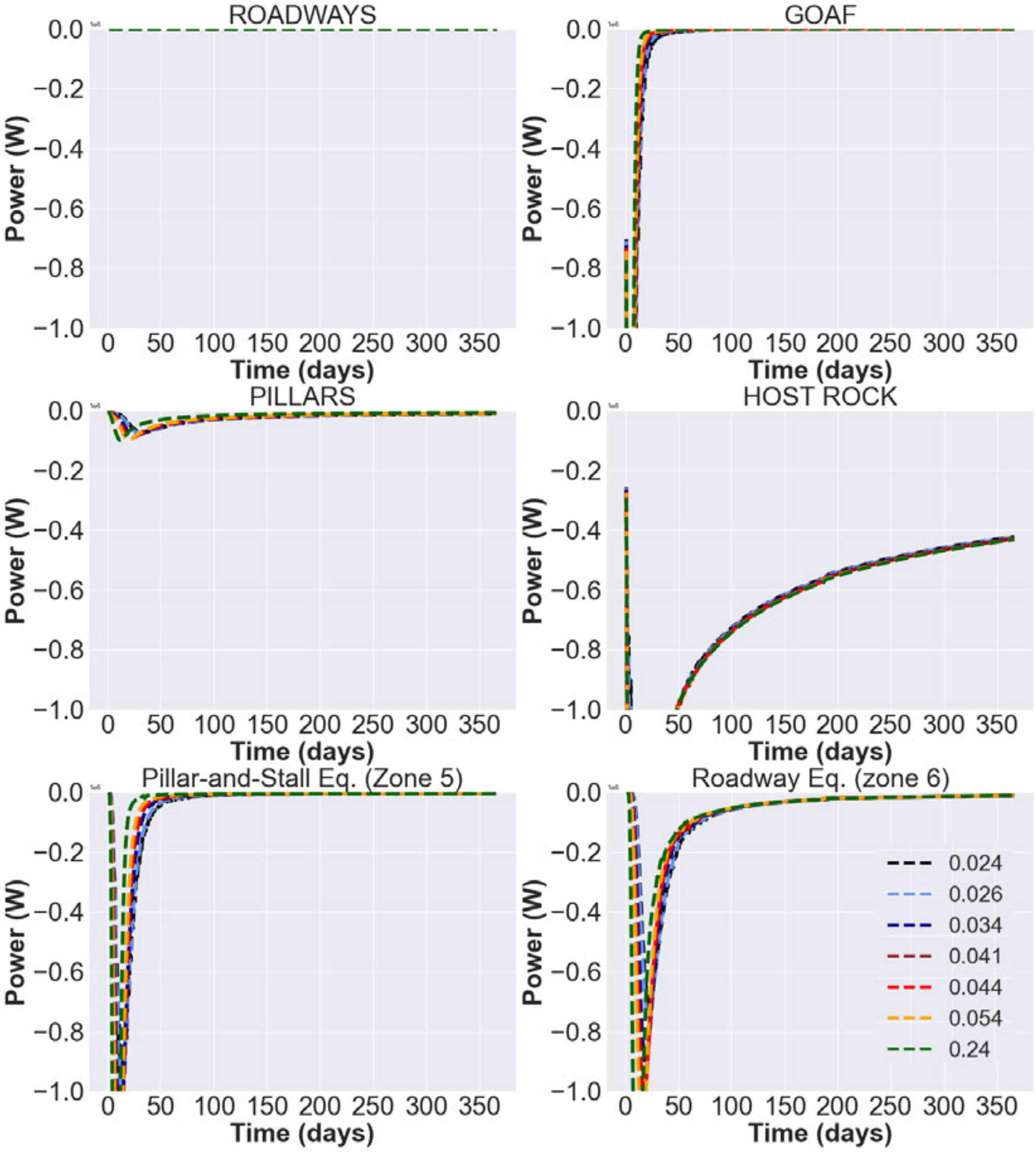

Figure A.63: Sensitivity analysis showing the relative power contribution of each material in model d (pillar-and-stall and roadway zones simplification) for the goaf recharge scenario, for different zone 5 and 6 hydraulic conductivity (m/s).

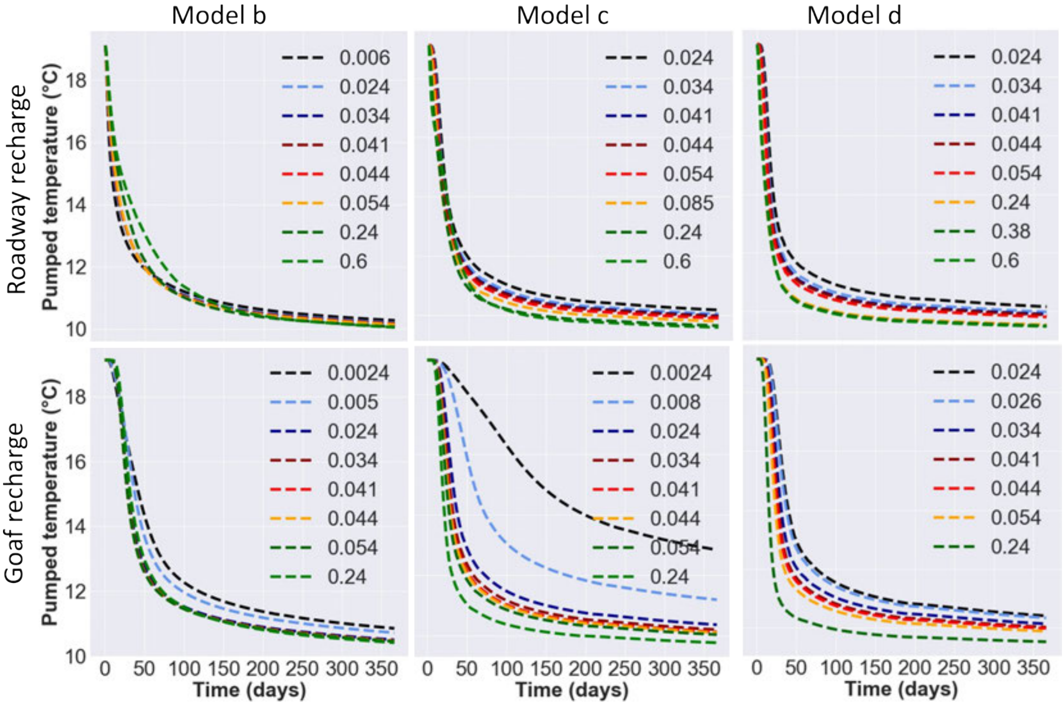

Figure A.64: Pumped temperature in the simplified models b, c and d for the roadway (upper panels) and goaf (lower panels) recharge scenarios, for different equivalent zones 5 and 6 hydraulic conductivity (m/s).

A.8 Chapter 9: Discussion

Fig. A.65 provides a preliminary analysis of the estimates of the heat potential of the Dawdon mine, based on the estimated volume and temperature in the caved and fractured zones. This analysis needs to be refined and should be verified against numerical models and compared to the conceptual approach developed in this research work.

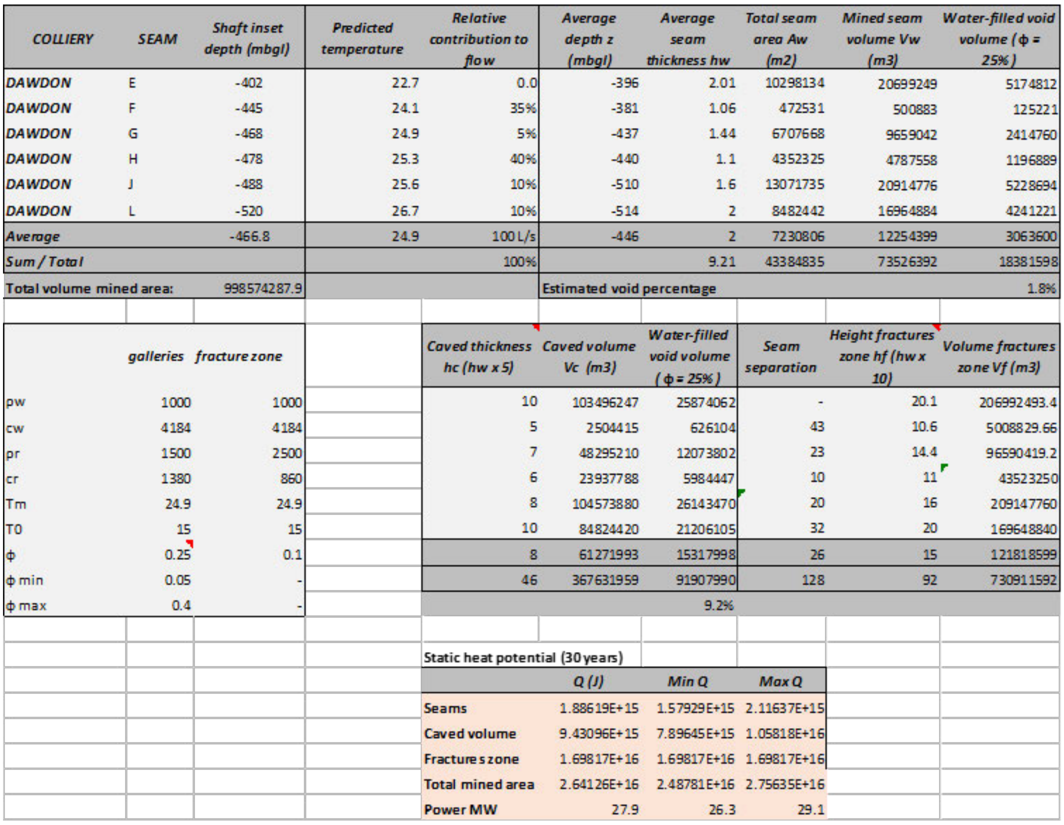

COLLIERY	SEAM	Shaft inset depth (mbgl)	Predicted temperature	Relative contribution to flow	Average depth z (mbgl)	Average seam thickness hw	Total seam area Aw (m2)	Mined seam volume Vw (m3)	Water-filled void volume (ϕ = 25%)
DAWDON	E	-402	22.7	0.0	-396	2.01	10298134	20699249	5174812
DAWDON	F	-445	24.1	35%	-381	1.06	472531	500883	125221
DAWDON	G	-468	24.9	5%	-437	1.44	6707668	9659042	2414760
DAWDON	H	-478	25.3	40%	-440	1.1	4352325	4787558	1196889
DAWDON	J	-488	25.6	10%	-510	1.6	13071735	20914776	5228694
DAWDON	L	-520	26.7	10%	-514	2	8482442	16964884	4241221
Average		-466.8	24.9	100 L/s	-446	2	7230806	12254399	3063600
Sum / Total				100%		9.21	43384835	73526392	18381598
Total volume mined area:		998574287.9			Estimated void percentage				1.8%

	galleries	fracture zone	Caved thickness hc (hw x 5)	Caved volume Vc (m3)	Water-filled void volume (ϕ = 25%)	Seam separation	Height fractures zone hf (hw x 10)	Volume fractures zone Vf (m3)
pw	1000	1000	10	103496247	25874062	-	20.1	206992493.4
cw	4184	4184	5	2504415	626104	43	10.6	5008829.66
pr	1500	2500	7	48295210	12073802	23	14.4	96590419.2
cr	1380	860	6	23937788	5984447	10	11	43523250
Tm	24.9	24.9	8	104573880	26143470	20	16	209147760
T0	15	15	10	84824420	21206105	32	20	169648840
ϕ	0.25	0.1	8	61271993	15317998	26	15	121818599
ϕ min	0.05	-	46	367631959	91907990	128	92	730911592
ϕ max	0.4	-			9.2%			

Static heat potential (30 years)

	Q (J)	Min Q	Max Q
Seams	1.88619E+15	1.57929E+15	2.11637E+15
Caved volume	9.43096E+15	7.89645E+15	1.05818E+16
Fractures zone	1.69817E+16	1.69817E+16	1.69817E+16
Total mined area	2.64126E+16	2.48781E+16	2.75635E+16
Power MW	27.9	26.3	29.1

Figure A.65: Heat in place estimated for the Dawdon mines, NE England, used as a preliminary analysis for the potential future validation of the conceptual tool presented in chapter 8.

Bibliography

Abesser, C., Schofield, D., Busby, J., Bonsor, H., & Ward, R. (2018). Who owns geothermal heat? [Science briefing paper]. *British Geological Survey*, 7.

Adams, R., & Parkin, G. (2002). Development of a coupled surface-groundwater-pipe network model for the sustainable management of karstic groundwater. *Environmental Geology*, *42*(5), 513–517. Retrieved from `https://doi.org/10.1007/s00254-001-0513-8` doi: 10.1007/s00254-001-0513-8

Adams, R., & Younger, P. (2001). A strategy for modeling ground water rebound in abandoned deep mine systems. *Ground Water*, *39*(2), 249–261. Retrieved from `http://doi.wiley.com/10.1111/j.1745-6584.2001.tb02306.x` doi: 10.1111/j.1745-6584.2001.tb02306.x

Adhikary, D. P., & Guo, H. (2015). Modelling of longwall mining-induced strata permeability change. *Rock Mechanics and Rock Engineering*, *48*(1), 345–359. Retrieved from `http://link.springer.com/10.1007/s00603-014-0551-7` doi: 10.1007/s00603-014-0551-7

Agemar, T., Weber, J., & Moeck, I. S. (2018). Assessment and public reporting of geothermal resources in germany: Review and outlook. *Energies*, *11*(2), 332.

Aljoe, W. W., & Hawkins, J. W. (1994). Application of aquifer testing in surface and underground coal mines. In *International Mine Water Association Proceedings.*

Allen, A., Milenic, D., & Sikora, P. (2003). Shallow gravel aquifers and the urban ‘heat island’ effect: a source of low enthalpy geothermal energy. *Geothermics*, *32*(4), 569–578. Retrieved 2023-09-06, from `https://www.sciencedirect.com/science/article/pii/S0375650503000634` doi: 10.1016/S0375-6505(03)00063-4

Anderson, E. (1940). The loss of heat by conduction from the Earth’s crust in Britain. In *Proceedings of the Royal Society, Edinburgh* (Vol. 60, pp. 192–209).

Anderson, R., & De Souza, E. (2017). Heat stress management in underground mines. *International Journal of Mining Science and Technology*, *27*(4), 651–655. Retrieved from `https://linkinghub.elsevier.com/retrieve/pii/S2095268617303580` doi: 10.1016/j.ijmst.2017.05.020

Andrews, B., Shipton, Z., Lord, R., & McKay, L. (2020, 01). The role of pre-existing jointing on damage zone evolution and faulting style of thin competent layers in mechanically stratified sequences: a case study from the limestone coal formation at spireslack surface coal mine.
doi: 10.5194/se-2019-202

Andrews, B. J., Cumberpatch, Z. A., Shipton, Z. K., & Lord, R. (2020). Collapse processes in abandoned pillar and stall coal mines: Implications for shallow mine geothermal energy. *Geothermics*, *88*, 101904. Retrieved from `https://www.sciencedirect.com/science/article/pii/S0375650520301966` doi: 10.1016/j.geothermics.2020.101904

Andrés, C., Ordóñez, A., & Álvarez, R. (2017). Hydraulic and thermal modelling of an underground mining reservoir. *Mine Water and the Environment*, *36*(1), 24–33. Retrieved from `http://link.springer.com/10.1007/s10230-015-0365-1` doi: 10.1007/s10230-015-0365-1

Angelotti, A., Alberti, L., La Licata, I., & Antelmi, M. (2014). Energy performance and thermal impact of a borehole heat exchanger in a sandy aquifer: Influence of the groundwater velocity. *Energy Conversion and Management*, *77*, 700–708. Retrieved from `https://linkinghub.elsevier.com/retrieve/pii/S0196890413006535` doi: 10.1016/j.enconman.2013.10.018

Ann Cruickshank, C., & Baldwin, C. (2016). Chapter 15 - sensible thermal energy storage: Diurnal and seasonal. In T. M. Letcher (Ed.), *Storing Energy* (pp. 291–311). Elsevier. Retrieved from `https://www.sciencedirect.com/science/article/pii/B9780128034408000154` doi: 10.1016/B978-0-12-803440-8.00015-4

Athresh, A. P., Al-Habaibeh, A., & Parker, K. (2016). The design and evaluation of an open loop ground source heat pump operating in an ochre-rich coal mine water environment. *International Journal of Coal Geology*, *164*, 69–76. Retrieved from `https://linkinghub.elsevier.com/retrieve/pii/S0166516216301604` doi: 10.1016/j.coal.2016.04.015

Baier, J., Polak, M., Sindelar, M., & Uhlik, J. (2011). Numerical modeling as a basic tool for evaluation of using mine water as a heat source. *WIT Transactions on Ecology and the Environment*, *143*, 73–84.

Bailey, M., Gandy, C., Watson, I., Wyatt, L., & Jarvis, A. (2016). Heat recovery potential of mine water treatment systems in great britain. *International Journal of Coal Geology*, *164*, 77–84. Retrieved from `https://linkinghub.elsevier.com/retrieve/pii/S0166516216300490` doi: 10.1016/j.coal.2016.03.007

Bailey, M., Moorhouse, A., & Watson, I. (2013). Heat extraction from hypersaline mine water at the dawdon mine water treatment site. In M. Tibbett, A. Fourie, & C. Digby (Eds.), *Proceedings of the Eighth International Seminar on Mine Closure, Cornwall, UK* (pp. 559–570). Australian Centre for Geomechanics. Retrieved from `https://papers.acg.uwa.edu.au/p/1352_47_Bailey/` doi: 10.36487/ACG_rep/1352_47_Bailey

Ball, D. (1999). *An overview of groundwater in scotland* [Technical book WD/99/44]. British Geological Survey.

Bamforth, S. (2014). *Bilston glen.* (Scoping Study prepared for the Coal Authority No. 47068917). URS Infrastructure & Environment UK Limited.

Banks, D. (2008). *An introduction to Thermogeology: Ground Source Heating and Cooling*. Blackwell Publishing, Ltd. Retrieved from `http://doi.wiley.com/10.1002/9781444302677` doi: 10.1002/9781444302677

Banks, D. (2012). *An introduction to Thermogeology: Ground Source Heating and Cooling* (2nd ed.). John Wiley & Sons, Ltd.

Banks, D. (2015). A review of the importance of regional groundwater advection for ground heat exchange. *Environmental Earth Sciences*, *73*(6), 2555–2565. Retrieved from `https://doi.org/10.1007/s12665-014-3377-4` doi: 10.1007/s12665-014-3377-4

Banks, D. (2016). Making the red one green – renewable heat from abandoned flooded mines. In *36th Annual Groundwater Conference of the International Association of Hydrogeologists: Sustaining Ireland's Water Future: The Role of Groundwater* (pp. 1–9).

Banks, D., Athresh, A., Al-Habaibeh, A., & Burnside, N. (2019). Water from abandoned mines as a heat source: practical experiences of open- and closed-loop strategies, United Kingdom. *Sustainable Water Resources Management*, *5*(1), 29–50. Retrieved from `http://link.springer.com/10.1007/s40899-017-0094-7` doi: 10.1007/s40899-017-0094-7

Banks, D., Fraga Pumar, A., & Watson, I. (2009). The operational performance of scottish minewater-based ground source heat pump systems. *Quarterly Journal of Engineering Geology and Hydrogeology*, *42*(3), 347–357. Retrieved from `http://qjegh.lyellcollection.org/lookup/doi/10.1144/1470-9236/08-081` doi: 10.1144/1470-9236/08-081

Banks, D., Frolik, A., Gzyl, G., & Rogoż, M. (2010). Modeling and monitoring of mine water rebound in an abandoned coal mine complex: Siersza Mine, Upper Silesian Coal Basin, Poland. *Hydrogeology Journal*, *18*, 519–534. doi: 10.1007/s10040-009-0534-z

Banks, D., Skarphagen, H., Wiltshire, R., & Jessop, C. (2004). Heat pumps as a tool for energy recovery from mining wastes. *Geological Society, London, Special Publications*, *236*(1), 499–513. Retrieved from `http://sp.lyellcollection.org/lookup/doi/10.1144/GSL.SP.2004.236.01.27` doi: 10.1144/GSL.SP.2004.236.01.27

Banks, D., Steven, J., Black, A., & Naismith, J. (2022). Conceptual modelling of two large-scale mine water geothermal energy schemes: Felling, Gateshead, UK. *International Journal of Environmental Research and Public Health*, *19*(3), 1643. Retrieved from `https://www.ncbi.nlm.nih.gov/pmc/articles/PMC8834720/` doi: 10.3390/ijerph19031643

Banks, D., Withers, J. G., Cashmore, G., & Dimelow, C. (2013). An overview of the results of 61 in situ thermal response tests in the UK. *Quarterly Journal of Engineering Geology and Hydrogeology*, *46*(3), 281–291. Retrieved from `https://www.lyellcollection.org/doi/10.1144/qjegh2013-017` doi: 10.1144/qjegh2013-017

Banks, D., Younger, P., Arnesen, R., Iversen, E., & Banks, S. (1997). Mine-water chemistry: the good, the bad and the ugly. *Environmental Geology*, *32*(3), 157–174. Retrieved from `http://link.springer.com/10.1007/s002540050204` doi: 10.1007/s002540050204

Bao, T., Cao, H., Qin, Y., Jiang, G., & Liu, Z. L. (2020). Critical insights into thermohaline stratification for geothermal energy recovery from flooded mines with mine water. *Journal of Cleaner Production*, *273*. Retrieved from `https://www.sciencedirect.com/science/article/pii/S0959652620330341` doi: 10.1016/j.jclepro.2020.122989

Bao, T., & Liu, Z. L. (2019a). Geothermal energy from flooded mines: Modeling of transient energy recovery with thermohaline stratification. *Energy Conversion and Management*, *199*. Retrieved from `https://linkinghub.elsevier.com/retrieve/pii/S0196890419309628` doi: 10.1016/j.enconman.2019.111956

Bao, T., & Liu, Z. L. (2019b). Thermohaline stratification modeling in mine water via double-diffusive convection for geothermal energy recovery from flooded mines. *Applied Energy*, *237*, 566–580. Retrieved from `https://www.sciencedirect.com/science/article/pii/S0306261919300480` doi: 10.1016/j.apenergy.2019.01.049

Batchelor, G. K. (1967). *An introduction to fluid dynamics.* Cambridge University Press.

Bayer, P., de Paly, M., & Beck, M. (2014). Strategic optimization of borehole heat exchanger field for seasonal geothermal heating and cooling. *Applied Energy*, *136*, 445–453. Retrieved from `https://linkinghub.elsevier.com/retrieve/pii/S0306261914009763` doi: 10.1016/j.apenergy.2014.09.029

Bazargan, B., & Demollin, E. (2008). Geothermal use of deep flooded mines. In *Post-mining Proceedings, nancy, france* (pp. 1–11).

Beamish, D., & Busby, J. (2016). The Cornubian geothermal province: heat production and flow in SW England: estimates from boreholes and airborne gamma-ray measurements. *Geothermal Energy*, *4*(1), 4. Retrieved from `http://geothermal-energy-journal.springeropen.com/articles/10.1186/s40517-016-0046-8` doi: 10.1186/s40517-016-0046-8

Beier, R. A. (2020). Thermal response tests on deep borehole heat exchangers with geothermal gradient. *Applied Thermal Engineering*, *178*. Retrieved from `https://www.sciencedirect.com/science/article/pii/S1359431120306992` doi: 10.1016/j.applthermaleng.2020.115447

BEIS. (2019). *BEIS 2019 ECUK – end uses database - energy consumption in the UK*. Retrieved from `https://www.gov.uk/government/statistics/energy-consumption-in-the-uk`

Beltrami, H., Matharoo, G. S., & Smerdon, J. E. (2015). Impact of borehole depths on reconstructed estimates of ground surface temperature histories and energy storage: Uncertainties on the shallow subsurface. *Journal of Geophysical Research: Earth Surface*, *120*(5), 763–778. Retrieved from `http://doi.wiley.com/10.1002/2014JF003382` doi: 10.1002/2014JF003382

Benfield, A. E., & Lenox-Conyngham, G. P. (1939). Terrestrial heat flow in great britain. *Proceedings of the Royal Society of London. Series A. Mathematical and Physical Sciences*, *173*(955), 428–450. Retrieved 2024-05-26, from `https://royalsocietypublishing.org/doi/10.1098/rspa.1939.0157` (Publisher: Royal Society) doi: 10.1098/rspa.1939.0157

Benton, M., Cook, E., & Turner, P. (2003). *Carboniferous and Permian igneous rocks of Great Britain: north of the Variscan front* (No. 27). Joint nature conservation committee, Geological conservation review series. ISBN: 978-1-86107-497-3.

Bidarmaghz, A., Narsilio, G. A., Johnston, I. W., & Colls, S. (2016). The importance of surface air temperature fluctuations on long-term performance of vertical ground heat exchangers. *Geomechanics for Energy and the Environment*, *6*, 35–44. Retrieved from `https://www.sciencedirect.com/science/article/pii/S2352380816300089` doi: https://doi.org/10.1016/j.gete.2016.02.003

Bluck, B. J. (2002). The Midland Valley terrane. In N. H. Trewin (Ed.), *The Geology of Scotland.* Geological Society of London. Retrieved from `https://doi.org/10.1144/GOS4P.5` doi: 10.1144/GOS4P.5

Blum, P., Campillo, G., & Kölbel, T. (2011). Techno-economic and spatial analysis of vertical ground source heat pump systems in germany. *Energy*, *36*(5), 3002–3011. Retrieved from `https://www.sciencedirect.com/science/article/pii/S036054421100140X` doi: 10.1016/j.energy.2011.02.044

Booth, C. (2002). The effects of longwall coal mining on overlying aquifers. In *Mine Water Hydrogeology and Geochemistry* (Younger, El & Robins, N.S. ed., p. 198). Geological Society, London, Special Publications.

Bordier, C., & Zimmer, D. (2000). Drainage equations and non-Darcian modelling in coarse porous media or geosynthetic materials. *Journal of Hydrology*, *228*(3), 174–187. Retrieved from `https://www.sciencedirect.com/science/article/pii/S0022169400001517` doi: 10.1016/S0022-1694(00)00151-7

Bortoloni, M., Bottarelli, M., & Su, Y. (2017). A study on the effect of ground surface boundary conditions in modelling shallow ground heat exchangers. *Applied Thermal Engineering*, *111*, 1371–1377. doi: 10.1016/J.APPLTHERMALENG.2016.05.063

Brabham, P., Manju, M., Thomas, H., Farr, G., Francis, R., Sahid, R., & Sadasivam, S. (2020). The potential use of mine water for a district heating scheme at Caerau, Upper Llynfi valley, South Wales, UK. *Quarterly Journal of Engineering Geology and Hydrogeology*, *53*(1), 145–158. Retrieved from `https://www.lyellcollection.org/doi/full/10.1144/qjegh2018-213` doi: 10.1144/qjegh2018-213

Brereton, R., Browne, M. a. E., Cripps, A. C., Gebski, J. S., Bird, M., Halley, D. N., ... Gebski, J. S. (1988). *Glenrothes borehole: geological well completion book. Investigation of the geothermal potential of the UK*. Retrieved from `https://www.osti.gov/etdeweb/biblio/6374149`

Bridger, D. W., & Allen, D. M. (2014). Influence of geologic layering on heat transport and storage in an aquifer thermal energy storage system. *Hydrogeology Journal*, *22*(1), 233–250. Retrieved from `http://link.springer.com/10.1007/s10040-013-1049-1` doi: 10.1007/s10040-013-1049-1

British Coal. (1992). *Report on mine water pumping and water problems in the northumberland and durham coalfield area*. British Coal Report.

British Geological Survey. (2018). *Ground source heat pump GeoReports; example report Keyworth* [Report GR_999999/1]. British Geological Survey. Retrieved from `http://shop.bgs.ac.uk/GeoReports/examples/S005.pdf`

Brown, C. S., Cassidy, N. J., Egan, S. S., & Griffiths, D. (2021). Numerical modelling of deep coaxial borehole heat exchangers in the cheshire basin, UK. *Computers & Geosciences*, *152*. Retrieved from `https://www.sciencedirect.com/science/article/pii/S0098300421000601` doi: 10.1016/j.cageo.2021.104752

Brown, G. O. (2012). The history of the darcy-weisbach equation for pipe flow resistance. *Environmental and Water Resources History, American Society of Civil Engineers*, 34–43. Retrieved from `https://ascelibrary.org/doi/10.1061/40650%282003%294` doi: 10.1061/40650(2003)4

Browne, M., Dean, M., Hall, H., McAdam, A., Monro, S., & Chisholm, J. (1999). *A lithostratigraphical framework for the Carboniferous rocks of the Midland Valley of Scotland* (Research book No. RR/99/07). British Geological Survey.

Bullard, E. C., & Niblett, E. R. (1951). Terrestrial heat flow in england. *Geophysical Journal International*, *6*, 222–238. Retrieved 2024-05-26, from `https://onlinelibrary.wiley.com/doi/abs/10.1111/j.1365-246X.1951.tb03007.x` (_eprint: https://onlinelibrary.wiley.com/doi/pdf/10.1111/j.1365-246X.1951.tb03007.x) doi: 10.1111/j.1365-246X.1951.tb03007.x

Burley, A., Edmunds, W., M., & Gale, I. (1984). *Catalogue of geothermal data for the land area of the United Kingdom* (2nd ed.). British Geological Survey.

Burnside, N., Banks, D., & Boyce, A. (2016). Sustainability of thermal energy production at the flooded mine workings of the former Caphouse Colliery, Yorkshire, United Kingdom. *International Journal of Coal Geology*, *164*, 85–91. Retrieved from `https://linkinghub.elsevier.com/retrieve/pii/S0166516216300489` doi: 10.1016/j.coal.2016.03.006

Burnside, N. M., Banks, D., Boyce, A. J., & Athresh, A. (2016). Hydrochemistry and stable isotopes as tools for understanding the sustainability of minewater geothermal energy production from a 'standing column' heat pump system: Markham Colliery, Bolsover, Derbyshire, UK. *International Journal of Coal Geology*, *165*, 223–230. Retrieved from `https://www.sciencedirect.com/science/article/pii/S0166516216304943` doi: 10.1016/j.coal.2016.08.021

Burrell, R., & Whitworth, K. (2000). The influence of minewater recovery on surface gas and water discharges in the yorkshire coalfield. In *International Mine Water Association Proceedings.*

Busby, J. (2010). Geothermal Prospects in the United Kingdom. In *Proceedings world Geothermal Congress 2010, Bali, Indonesia* (p. 7).

Busby, J. (2015). UK shallow ground temperatures for ground coupled heat exchangers. *Quarterly Journal of Engineering Geology and Hydrogeology*, *48*(3), 248–260. Retrieved from `https://qjegh.lyellcollection.org/content/48/3-4/248` (Technical note) doi: 10.1144/qjegh2015-077

Busby, J., Kingdon, A., & Williams, J. (2011). The measured shallow temperature field in Britain. *Quarterly Journal of Engineering Geology and Hydrogeology*, *44*(3), 373–387. Retrieved from `http://qjegh.lyellcollection.org/lookup/doi/10.1144/1470-9236/10-049` doi: 10.1144/1470-9236/10-049

Busby, J., & Terrington, R. (2017). Assessment of the resource base for engineered geothermal systems in great britain. *Geothermal Energy*, *5*(1), 7. Retrieved from `http://geothermal-energy-journal.springeropen.com/articles/10.1186/s40517-017-0066-z` doi: 10.1186/s40517-017-0066-z

Busby, J. P. (2019). *Thermal conductivity and subsurface temperature data pertaining to the Glasgow Geothermal Energy Research Field Site (GGERFS)*. British Geological Survey, Nottingham, UK. Retrieved from `http://nora.nerc.ac.uk/id/eprint/523450/`

Calcagno, P., Baujard, C., Guillou-Frottier, L., Dagallier, A., & Genter, A. (2014). Estimation of the deep geothermal potential within the Tertiary Limagne basin (French Massif Central): An integrated 3D geological and thermal approach. *Geothermics*, *51*, 496–508. Retrieved from `https://www.sciencedirect.com/science/article/pii/S0375650514000194` doi: 10.1016/j.geothermics.2014.02.002

Cameron, I., & Stephenson, D. (1985). *British regional geology: The midland valley of scotland.* British Geological Survey.

Capozza, A., Zarrella, A., & De Carli, M. (2015). Long-term analysis of two GSHP systems using valiyeard numerical models and proposals to optimize the operating parameters. *Energy and Buildings*, *93*, 50–64. Retrieved from `https://www.sciencedirect.com/science/article/pii/S0378778815000997` doi: 10.1016/j.enbuild.2015.02.005

Casasso, A., & Sethi, R. (2014). Sensitivity analysis on the performance of a ground source heat pump equipped with a double u-pipe borehole heat exchanger. *Energy Procedia*, *59*, 301–308. Retrieved from `https://www.sciencedirect.com/science/article/pii/S1876610214017482` doi: 10.1016/j.egypro.2014.10.381

Cengel, Y., Turner, R., & Smith, R. (2001). Fundamentals of thermal-fluid sciences. *Applied Mechanics Reviews*, *54*(6), 110–112. Retrieved from `https://asmedigitalcollection.asme.org/appliedmechanicsreviews/article/54/6/B110/458195/Fundamentals-of-Thermal-Fluid-Sciences` doi: 10.1115/1.1421126

Cermak, V. (1982). *Thermal conductivity and specific heat of minerals and rocks. in: Angeneister, landolt-burnstein zahlenwerte and funktionen aus naturwissenschaften und technik, neue serie, physikalishe eigenschaften der gesteine. springer verlag, berlin, heidelberg and new york, v/1a, 305-343.*

Chen, C., Shao, H., Naumov, D., Kong, Y., Tu, K., & Kolditz, O. (2019). Numerical investigation on the performance, sustainability, and efficiency of the deep borehole heat exchanger system for building heating. *Geothermal Energy*, *7*(1), 18. Retrieved from `https://geothermal-energy-journal.springeropen.com/articles/10.1186/s40517-019-0133-8` doi: 10.1186/s40517-019-0133-8

Chen, S., Cai, W., Witte, F., Wang, X., Wang, F., Kolditz, O., & Shao, H. (2021). Long-term thermal imbalance in large borehole heat exchangers array – a numerical study based on the leicester project. *Energy and Buildings*, *231*. Retrieved from `https://www.sciencedirect.com/science/article/pii/S0378778820322842` doi: 10.1016/j.enbuild.2020.110518

Cherubini, Y., Cacace, M., Scheck-Wenderoth, M., & Noack, V. (2014). Influence of major fault zones on 3-d coupled fluid and heat transport for the brandenburg region (ne german basin). *Geothermal Energy Science*, *2*, 1-20. Retrieved from `https://api.semanticscholar.org/CorpusID:55915880`

Chiasson, A. D., Rees, S. J., & Spitler, J. D. (2000). *A preliminary assessment of the effects of groundwater flow on closed-loop ground source heat pump systems*. Retrieved from `https://www.osti.gov/biblio/20104801-preliminary-assessment-effects-groundwater-flow-closed-loop-ground-source-heat-pump-systems`

Chu, Z., Dong, K., Gao, P., Wang, Y., & Sun, Q. (2021). Mine-oriented low-enthalpy geothermal exploitation: A review from spatio-temporal perspective. *Energy Conversion and Management*, *237*. Retrieved from `https://www.sciencedirect.com/science/article/pii/S0196890421002995` doi: 10.1016/j.enconman.2021.114123

Clean growth - transforming heating. (2018).

Coal Authority. (2018). *A-winning mine water treatment scheme.* Retrieved from `https://www.gov.uk/government/case-studies/a-winning-mine-water-treatment-scheme`

Cui, P., Diao, N., Gao, C., & Fang, Z. (2015). Thermal investigation of in-series vertical ground heat exchangers for industrial waste heat storage. *Geothermics*, *57*, 205–212. Retrieved from `https://www.sciencedirect.com/science/article/pii/S0375650515000693` doi: 10.1016/j.geothermics.2015.06.003

Dacquay, C., Lohrenz, E., & Fujii, H. (2021). Ground heat exchanger thermal imbalance prevention using dynamic long-term ground temperature predictions. *International Journal of Green Energy*, *0*(0), 1–9. Retrieved from `https://doi.org/10.1080/15435075.2021.1977651` doi: 10.1080/15435075.2021.1977651

Dean, M. T., Browne, M. A. E., Waters, C. N., & Powell, J. H. (2011). *A lithostratigraphical framework for the carboniferous successions of northern great britain (onshore)* (M. C. Akhurst et al., Eds.). British Geological Survey.

De Carli, M., Fiorenzato, S., & Zarrella, A. (2015). Performance of heat pumps with direct expansion in vertical ground heat exchangers in heating mode. *Energy Conversion and Management*, *95*, 120–130. Retrieved from `https://www.sciencedirect.com/science/article/pii/S019689041500093X` doi: 10.1016/j.enconman.2015.01.080

Dehkordi, S. E., & Schincariol, R. (2013). Effect of thermal-hydrogeological and borehole heat exchanger properties on performance and impact of vertical closed-loop geothermal heat pump systems. *Hydrogeology Journal*. doi: 10.1007/s10040-013-1060-6

Dehkordi, S. E., Schincariol, R. A., & Olofsson, B. (2015). Impact of groundwater flow and energy load on multiple borehole heat exchangers. *Groundwater*, *53*(4), 558–571. Retrieved from `https://ngwa.booklibrary.wiley.com/doi/abs/10.1111/gwat.12256` doi: 10.1111/gwat.12256

Department of Energy and Climate Change. (2011). *MCS 022: GROUND HEAT EXCHANGER LOOK-UP TABLES*. Microgeneration Installation Standards.

Dethlefsen, F., Beyer, C., Feeser, V., & Köber, R. (2016). Parameterizability of processes in subsurface energy and mass storage: Supported by a review of processes, codes, parameters, and a regional example: Schleswig-holstein, germany. *Environmental Earth Sciences*, *75*(10), 885. Retrieved from `http://link.springer.com/10.1007/s12665-016-5626-1` doi: 10.1007/s12665-016-5626-1

Diersch, H.-J. (2005). *FEFLOW finite element subsurface flow and transport simulation system, reference manual* (WASY ed.). Institute for Water Resources Planning and Systems Research.

Diersch, H.-J., Rühaak, W., Schätzl, P., Bauer, D., & Heidemann, W. (2010). Numerical modelling of solar heat storage using large arrays of borehole heat exchangers. In *Proceedings World Geothermal Congress 2010, Bali, Indonesia.*

Dochartaigh, O., Macdonald, B., Fitzsimons, A., M, & Ward, R. (2015). *Scotland's aquifers and groundwater bodies* (Geological Survey Open Report No. OR/15/028).

Donnelly, L. (2020). *Chapter 17 Mining-induced fault reactivation in the UK*. Geological Society of London. Retrieved from `https://doi.org/10.1144/EGSP29.17` doi: 10.1144/EGSP29.17

Downing, R., & Gray, D. (1986). Geothermal resources of the united kingdom. *Journal of the Geological Society*, *143*, 499–507.

Díaz Noriega, R., Fernández, P., & Alvarez, L. (2020). *The challenges of sustainable use of abandoned underground flooded mines as geothermal resources.*

Edmonds, C. (2018). Five decades of settlement and subsidence. *Quarterly Journal of Engineering Geology and Hydrogeology*, *51*(4), 403–416. Retrieved from `https://www.lyellcollection.org/doi/full/10.1144/qjegh2018-089` doi: 10.1144/qjegh2018-089

Emmi, G., Zarrella, A., De Carli, M., & Galgaro, A. (2015). An analysis of solar assisted ground source heat pumps in cold climates. *Energy Conversion and Management*, *106*, 660–675. Retrieved from `https://www.sciencedirect.com/science/article/pii/S0196890415009371` doi: 10.1016/j.enconman.2015.10.016

England, P. C., Oxburgh, E. R., & Richardson, S. W. (1980). Heat refraction and heat production in and around granite plutons in north-east england. *Geophysical Journal International*, *62*(2), 439–455. Retrieved from `https://doi.org/10.1111/j.1365-246X.1980.tb04866.x` doi: 10.1111/j.1365-246X.1980.tb04866.x

Entwisle, D. C. (2019). *Engineering geology and geotechnical summary of central Glasgow in the vicinity of the UK Geoenergy Observatories field sites.* British Geological Survey, Nottingham, UK. Retrieved from `http://nora.nerc.ac.uk/id/eprint/523601/`

Erol, S., Hashemi, M. A., & François, B. (2015). Analytical solution of discontinuous heat extraction for sustainability and recovery aspects of borehole heat exchangers. *International Journal of Thermal Sciences*, *88*, 47–58. Retrieved from `https://linkinghub.elsevier.com/retrieve/pii/S1290072914002658` doi: 10.1016/j.ijthermalsci.2014.09.007

Eskilson, P. (1987). *Thermal analysis of heat extraction boreholes* [phdthesis]. Retrieved from `https://portal.research.lu.se/portal/en/publications/thermal-analysis-of-heat-extraction-boreholes(9a2a5bc5-d845-4599-8232-42a92b35825a).html` (ISBN: 9789179002985)

Esterhuizen, G., & Karacan, C. (2005). Development of numerical models to investigate permeability changes and gas emission around longwall mining panel. In *Proceedings of the 40th U.S. Symposium on Rock Mechanics, Alexandria, VA: American Rock Mechanics Association* (p. 1 - 13).

Esterhuizen, G., & Karacan, C. (2007). A methodology for determining gob permeability distributions and its application to reservoir modeling of coal mine longwalls. In *SME Annual Meeting and Exhibit, Denver, Colorado: Society for Mining, Metallurgy, and Exploration* (p. 1 - 6).

Fand, R. M., Kim, B. Y. K., Lam, A. C. C., & Phan, R. T. (1987). Resistance to the flow of fluids through simple and complex porous media whose matrices are composed of randomly packed spheres. *Journal of Fluids Engineering*, *109*(3), 268–273. Retrieved from `https://doi.org/10.1115/1.3242658` doi: 10.1115/1.3242658

Farr, G., Busby, J., Wyatt, L., Crooks, J., Schofield, D., & Holden, A. (2020). The temperature of Britain's coalfields. *Quarterly Journal of Engineering Geology and Hydrogeology*. Retrieved from `https://qjegh.lyellcollection.org/content/early/2020/09/14/qjegh2020-109` doi: 10.1144/qjegh2020-109

Farr, G., Sadasivam, S., Manju, Watson, I., Thomas, H., & Tucker, D. (2016). Low enthalpy heat recovery potential from coal mine discharges in the south wales coalfield. *International Journal of Coal Geology*, *164*, 92–103. Retrieved from `https://linkinghub.elsevier.com/retrieve/pii/S0166516216302002` doi: 10.1016/j.coal.2016.05.008

Farr, G., & Tucker, D. (2015). Mine water as an energy source for heat pumps: A case study from the south wales coalfield. *Presentation to the South West Regional Group of the Geological Society*. Retrieved from `https://nora.nerc.ac.uk/id/eprint/510965/1/FarrTucker%20SEREN%20for%20NORA.pdf`

Ferket, H., Laenen, B., & Van Tongeren, P. (2011). Transforming flooded coal mines to large-scale geothermal and heat storage reservoirs: what can we expect? In *International mine water association proceedings: Mine water - managing the challenges, aachen, germany* (pp. 171–175).

Forster, I., & Enever, J. (1992). Hydrogeological response of overburden strata to underground mining, central coast NSW. *NSW Office of Energy, Sydney, Australia*.

Forsyth, I., Hall, I., & McMIlan, A. (1996). *Geology of the Airdrie District. memoir of the British Geological Survey Sheet 31 (Scotland)*. The Stationery Office, London, for the British Geological Survey,.

Fraser-Harris, A., McDermott, C. I., Receveur, M., Mouli-Castillo, J., Todd, F., Cartwright-Taylor, A., … Parsons, M. (2022). The geobattery concept: A geothermal circular heat network for the sustainable development of near surface low enthalpy geothermal energy to decarbonise heating. *Earth Science, Systems and Society, Frontiers*, *0*. Retrieved from `https://www.escubed.org/articles/10.3389/esss.2022.10047/full` doi: 10.3389/esss.2022.10047

Frey, M., Van der Vaart, J., Bär, K., Bossennec, C., Calcagno, P., Dezayes, C., & Sass, I. (2023). Techno-economic assessment of geothermal resources in the variscan basement of the northern upper rhine graben. *Natural Resources Research*, *32*(1), 213–234.

Furlong, K. P., & Chapman, D. S. (1987). Crustal heterogeneities and the thermal structure of the continental crust. *Geophysical Research Letters*, *14*(3), 314–317. Retrieved from `https://booklibrary.wiley.com/doi/abs/10.1029/GL014i003p00314` doi: 10.1029/GL014i003p00314

Garcia-Gil, A., Mejias Moreno, M., Garrido Schneider, E., Marazuela, M. A., Abesser, C., Mateo Lazaro, J., & Sanchez Navarro, J. A. (2020). Nested shallow geothermal systems. *Sustainability, Multidisciplinary Digital Publishing Institute*, *12*, 1 – 12. Retrieved from `https://www.mdpi.com/2071-1050/12/12/5152` doi: 10.3390/su12125152

Garrard, G., & Taylor, R. (1988). Collapse mechanisms of shallow coal-mine workings from field measurements. *Geological Society, London, Engineering Geology Special Publications*, *5*(1), 181–192.

Gateshead Council. (2021). *Gateshead council district energy scheme benefits.* Retrieved from `https://www.gateshead.gov.uk/article/2994/District-Energy-Scheme-benefits`

Gatliff, R., Kemp, S., Merriman, R., Quinn, M., Baily, H., & Ritchie, J. (1996). *Patterns of uplift on the north west margin - integrated studies of clay maturity, geothermal gradients and interval velocities.* [Technical Report WB/96/14C.]. British Geological Survey.

Gee, D., Bateson, L., Sowter, A., Grebby, S., Novellino, A., Cigna, F., ... Wyatt, L. (2017). Ground motion in areas of abandoned mining: Application of the intermittent SBAS (ISBAS) to the northumberland and durham coalfield, UK. *Geosciences*, *7*(3), 85. Retrieved from `https://www.mdpi.com/2076-3263/7/3/85` doi: 10.3390/geosciences7030085

Geuzaine, C., & Remacle, J.-F. (2009). Gmsh: a three-dimensional finite element mesh generator with built-in pre- and post-processing facilities. *International Journal for Numerical Methods in Engineering*.

Ghoreishi-Madiseh, S., Hassani, F., & Abbasy, F. (2015). Numerical and experimental study of geothermal heat extraction from backfilled mine stopes. *Applied Thermal Engineering*, *90*, 1119–1130. Retrieved from `https://linkinghub.elsevier.com/retrieve/pii/S1359431114010217` doi: 10.1016/j.applthermaleng.2014.11.023

Ghoreishi-Madiseh, S., Hassani, F., Mohammadian, A., & Radziszewski, P. (2013). A transient natural convection heat transfer model for geothermal borehole heat exchangers. *Journal of Renewable and Sustainable Energy*, *5*(4).

Ghoreishi-Madiseh, S. A., Ghomshei, M. M., Hassani, F. P., & Abbasy, F. (2012). Sustainable heat extraction from abandoned mine tunnels: A numerical model. *J. Renewable Sustainable Energy*, 17.

Gillespie, M., Crane, E., & Barron, H. (2013). *Study into the potential for deep geothermal energy in scotland - volume 2* (No. AEC/001/11). Scottish Government.

Gosnold, W., Majorowicz, J., Klenner, R., & Hauck, S. (2011). Implications of post-glacial warming for northern hemisphere heat flow. *GRC Transactions*, *35*. Retrieved from `https://www.osti.gov/biblio/1137033` (GRC1029332)

Guo, P., He, M., Zheng, L., & Zhang, N. (2017). A geothermal recycling system for cooling and heating in deep mines. *Applied Thermal Engineering*, *116*, 833–839. Retrieved from `https://linkinghub.elsevier.com/retrieve/pii/S1359431116325121` doi: 10.1016/j.applthermaleng.2017.01.116

Guo, P., Zheng, L., Sun, X., He, M., Wang, Y., & Shang, J. (2018). Sustainability evaluation model of geothermal resources in abandoned coal mine. *Applied Thermal Engineering*, *144*, 804–811. Retrieved from `https://linkinghub.elsevier.com/retrieve/pii/S1359431117364888` doi: 10.1016/j.applthermaleng.2018.06.070

Guo, W., Zhao, G., Lou, G., & Wang, S. (2019). Height of fractured zone inside overlying strata under high-intensity mining in china. *International Journal of Mining Science and Technology*, *29*(1), 45-49. Retrieved from `https://www.sciencedirect.com/science/article/pii/S2095268618306530` (Special issue on ground control in mining in 2018) doi: https://doi.org/10.1016/j.ijmst.2018.11.012

Guo, Y., Hu, X., Banks, J., & Liu, W. (2021). Considering buried depth for vertical borehole heat exchangers in a borehole field with groundwater flow—an extended solution. *Energy and Buildings*, *235*. Retrieved from `https://www.sciencedirect.com/science/article/pii/S0378778821000062` doi: 10.1016/j.enbuild.2021.110722

Hall, T. (1981). *King Coal: mines, coal and Britain's industrial future*. Penguin.

Hamm, V., & Bazargan Sabet, B. (2010). Modelling of fluid flow and heat transfer to assess the geothermal potential of a flooded coal mine in lorraine, france. *Geothermics*, *39*(2), 177–186. Retrieved from `http://www.sciencedirect.com/science/article/pii/S037565051000012X` doi: 10.1016/j.geothermics.2010.03.004

Hannon, M. J. (2015). Raising the temperature of the UK heat pump market: Learning lessons from finland. *Energy Policy*, *85*, 369–375. Retrieved from `https://www.sciencedirect.com/science/article/pii/S0301421515002347` doi: 10.1016/j.enpol.2015.06.016

Hasterok, D., Gard, M., & Webb, J. (2018). On the radiogenic heat production of metamorphic, igneous, and sedimentary rocks. *Geoscience Frontiers*, *9*(6), 1777–1794. Retrieved from `https://www.sciencedirect.com/science/article/pii/S1674987117301937` doi: 10.1016/j.gsf.2017.10.012

He, M., Sousa, L., Elsworth, D., & Jr, E. (2011). *CO2 storage in Carboniferous Formations and abandoned coal mines.* doi: 10.13140/2.1.1630.8009

Hein, P., Kolditz, O., Görke, U.-J., Bucher, A., & Shao, H. (2016). A numerical study on the sustainability and efficiency of borehole heat exchanger coupled ground source heat pump systems. *Applied Thermal Engineering*, *100*, 421–433. Retrieved from `https://linkinghub.elsevier.com/retrieve/pii/S135943111630182X` doi: 10.1016/j.applthermaleng.2016.02.039

Hein, P., Zhu, K., Bucher, A., Kolditz, O., Pang, Z., & Shao, H. (2016). Quantification of exploitable shallow geothermal energy by using borehole heat exchanger coupled ground source heat pump systems. *Energy Conversion and Management*, *127*, 80–89. doi: 10.1016/J.ENCONMAN.2016.08.097

Heinze, T., & Pastore, N. (2023). Velocity-dependent heat transfer controls temperature in fracture networks. *Nature Communications*, *14*(1), 362. Retrieved from `https://www.nature.com/articles/s41467-023-36034-w` doi: 10.1038/s41467-023-36034-w

Herrin, J. M., & Deming, D. (1996). Thermal conductivity of u.s. coals. *Journal of Geophysical Research: Solid Earth*, *101*, 25381–25386. (_eprint: https://onlinelibrary.wiley.com/doi/pdf/10.1029/96JB01884) doi: 10.1029/96JB01884

Hillis, R., Thomson, K., & Underhill, J. (1994). Quantification of tertiary erosion in the inner moray firth using sonic velocity data from the chalk and the kimmeridge clay. *Marine and Petroleum Geology*, *11*(3), 283–293. Retrieved from `https://linkinghub.elsevier.com/retrieve/pii/0264817294900507` doi: 10.1016/0264-8172(94)90050-7

Hoek, E., & Bray, J. D. (1981). *Rock slope engineering: Third edition.* CRC Press.

Hu, J. (2017). An improved analytical model for vertical borehole ground heat exchanger with multiple-layer substrates and groundwater flow. *Applied Energy*, *202*, 537–549. Retrieved from `https://www.sciencedirect.com/science/article/pii/S0306261917307006` doi: 10.1016/j.apenergy.2017.05.152

IMC. (2001). *Report on minewater recovery in northumberland south of the stakeford dyke for the coal authority.* [Report number 7207/3.]. IMC Consulting Engineers.

Jaeger, J. C. (1965). Application of the theory of heat conduction to geothermal measurements. In *American geophysical union (AGU): Terrestrial Heat Flow* (pp. 7–23). Retrieved from `https://booklibrary.wiley.com/doi/abs/10.1029/GM008p0007` doi: 10.1029/GM008p0007

Jardón, S., Ordóñez, A., Alvarez, R., Cienfuegos, P., & Loredo, J. (2013). Mine water for energy and water supply in the central coal basin of asturias (spain). *Mine Water and the Environment*, *32*(2), 139.

Jaupart, C., & Mareschal, J.-C. (2013). Radiogenic heat production, thermal regime and evolution of continental crust. *Tectonophysics*, *609*, 524–534. Retrieved from `https://www.sciencedirect.com/science/article/pii/S004019511200769X` doi: 10.1016/j.tecto.2012.12.001

Jessop. (1995). Geothermal energy from old mines at springhill nova scotia, canada. In *Proceedings World Geothermal Congress 1995, Springhill, Canada.*

Jia, A., Liang, S., Jiang, B., Zhang, X., & Wang, G. (2018). Comprehensive assessment of global surface net radiation products and uncertainty analysis. *Journal of Geophysical Research: Atmospheres*, *123*(4), 1970–1989. Retrieved from `https://onlinelibrary.wiley.com/doi/abs/10.1002/2017JD027903` doi: 10.1002/2017JD027903

Kim, A. G., & Chaiken, R. F. (1993). *Fires in abandoned coal mines and waste banks*. U.S. Department of the Interior, Bureau of Mines.

Kolditz, O. (2002). Finite element method. In O. Kolditz (Ed.), *Computational methods in environmental fluid mechanics* (pp. 129–172). Springer. Retrieved from `https://doi.org/10.1007/978-3-662-04761-3_7` doi: 10.1007/978-3-662-04761-3_7

Kolditz, O., Bauer, S., Bilke, L., Böttcher, N., Delfs, J. O., Fischer, T., ... Zehner, B. (2012). OpenGeoSys: an open-source initiative for numerical simulation of thermo-hydro-mechanical/chemical (THM/c) processes in porous media. *Environmental Earth Sciences*, *67*(2), 589–599. Retrieved from `http://link.springer.com/10.1007/s12665-012-1546-x` doi: 10.1007/s12665-012-1546-x

Kolditz, O., Beinhorn, M., Xie, M., Kalbacher, T., Bauer, S., Wang, W., ... Delfs, J.-O. (2008). GeoSys/RockFlow version 4.5.10(WW) open source software design proposal. *Zentrum fur Angewandte Geowissenschaften Lehrstuhl fur GeoSystemForschung Universitat Tubingen*.

Kolditz, O., Görke, U.-J., Shao, H., Wang, W., & Bauer, S. (Eds.). (2016). *Thermo-hydro-mechanical-chemical processes in fractured porous media: Modelling and benchmarking: Benchmarking initiatives*. Springer International Publishing. Retrieved from `http://link.springer.com/10.1007/978-3-319-29224-3` doi: 10.1007/978-3-319-29224-3

Kresic, N. (2010). Chapter 5 - modeling. In N. Kresic & Z. Stevanovic (Eds.), *Groundwater hydrology of springs* (pp. 165–230). Butterworth-Heinemann. Retrieved 2024-02-25, from `https://www.sciencedirect.com/science/article/pii/B9781856175029000050` doi: 10.1016/B978-1-85617-502-9.00005-0

Krige, L. J., & Schonland, B. F. J. (1939). Borehole temperatures in the transvaal and orange free state. *Proceedings of the Royal Society of London. Series A. Mathematical and Physical Sciences*, *173*(955), 450–474. Retrieved from `https://royalsocietypublishing.org/doi/abs/10.1098/rspa.1939.0158` doi: 10.1098/rspa.1939.0158

Kruse, N., & Younger, P. (2009). Development of thermodynamically-based models for simulation of hydrogeochemical processes coupled to channel flow processes in abandoned underground mines. *Applied Geochemistry*, *24*(7), 1301–1311. Retrieved from `https://linkinghub.elsevier.com/retrieve/pii/S0883292709001000` doi: 10.1016/j.apgeochem.2009.04.003

Kschischang, F. R. (2017). The complementary error function.

Lachenbruch, A. H. (1970). Crustal temperature and heat production: Implications of the linear heat-flow relation. *Journal of Geophysical Research (1896-1977)*, *75*(17), 3291–3300. Retrieved from `https://booklibrary.wiley.com/doi/abs/10.1029/JB075i017p03291` doi: 10.1029/JB075i017p03291

Lapidus, L., & Amundson, N. R. (1952). Mathematics of adsorption in beds. The effect of longitudinal diffusion in ion exchange and chromatographic columns. *The Journal of Physical Chemistry*, *56*(8), 984–988.

Lauwerier, H. A. (1955). The transport of heat in an oil layer caused by the injection of hot fluid. *Applied Scientific Research, Section A*, *5*(2), 145–150. Retrieved from `https://doi.org/10.1007/BF03184614` doi: 10.1007/BF03184614

Lazzari, S., Priarone, A., & Zanchini, E. (2010). Long-term performance of BHE (borehole heat exchanger) fields with negligible groundwater movement. *Energy*, *35*(12), 4966–4974. Retrieved from `https://econpapers.repec.org/article/eeeenergy/v_3a35_3ay_3a2010_3ai_3a12_3ap_3a4966-4974.htm` (Publisher: Elsevier)

Lenci, A., Zeighami, F., & Di Federico, V. (2022). Effective forchheimer coefficient for layered porous media. *Transport in Porous Media*, *144*(2), 459–480. Retrieved from `https://doi.org/10.1007/s11242-022-01815-2` doi: 10.1007/s11242-022-01815-2

Lesperance, M., Smerdon, J. E., & Beltrami, H. (2010). Propagation of linear surface air temperature trends into the terrestrial subsurface. *Journal of Geophysical Research: Atmospheres*, *115*. Retrieved from `https://agupubs.booklibrary.wiley.com/doi/abs/10.1029/2010JD014377` doi: 10.1029/2010JD014377

Liang, S., Wang, D., He, T., & Yu, Y. (2019). Remote sensing of earth's energy budget: synthesis and review. *International Journal of Digital Earth*, *12*(7), 737–780. Retrieved from `https://doi.org/10.1080/17538947.2019.1597189` doi: 10.1080/17538947.2019.1597189

Loredo, C., Banks, D., & Roqueñí, N. (2017). Evaluation of analytical models for heat transfer in mine tunnels. *Geothermics*, *69*, 153–164. Retrieved from `http://www.sciencedirect.com/science/article/pii/S0375650517301955` doi: 10.1016/j.geothermics.2017.06.001

Loredo, C., Roqueñí, N., & Ordóñez, A. (2016). Modelling flow and heat transfer in flooded mines for geothermal energy use: A review. *International Journal of Coal Geology*, *164*, 115–122. Retrieved from `http://www.sciencedirect.com/science/article/pii/S0166516216301525` doi: 10.1016/j.coal.2016.04.013

Lund, J. W., & Boyd, T. L. (2016). Direct utilization of geothermal energy 2015 worldwide review. *Geothermics*, *60*, 66–93. Retrieved from `https://www.sciencedirect.com/science/article/pii/S037565051500156X` doi: 10.1016/j.geothermics.2015.11.004

Luo, J. (2014). *Experimental measurements and numerical modeling of a ground source heat pump system* (Unpublished doctoral dissertation). Der Naturwissenschaftlichen Fakultät der Friedrich-Alexander-Universität Erlangen-Nürnberg.

Luo, J., Zhang, Y., & Rohn, J. (2020). Analysis of thermal performance and drilling costs of borehole heat exchanger (BHE) in a river deposited area. *Renewable Energy*, *151*, 392–402. Retrieved from `https://www.sciencedirect.com/science/article/pii/S0960148119317008` doi: 10.1016/j.renene.2019.11.019

Lyu, Z., Song, X., Li, G., Hu, X., Shi, Y., & Xu, Z. (2017). Numerical analysis of characteristics of a single u-tube downhole heat exchanger in the borehole for geothermal wells. *Energy*, *125*, 186–196. Retrieved from `https://linkinghub.elsevier.com/retrieve/pii/S0360544217303080` doi: 10.1016/j.energy.2017.02.125

MacDonald, A., M, Robins, N., Ball, D., F, & O Dochartaigh, B., E. (2005). *An overview of groundwater in scotland*. British Geological Survey.

Majolepszy, Z. (1998). Modelling of geothermal resources witffin abandoned coal mines, upper silesia, poland. *Geothermal Training Programme, United Nations University*, 217-238.

Majorowicz, J., Gosnold, W., Gray, D., Safanda, J., Klenner, R., & Unsworth, M. (2012). Implications of post-glacial warming for northern alberta heat flow— correcting for the underestimate of the geothermal potential. In *Transactions - geothermal resources council* (Vol. 36).

Malolepszy, Z. (2003). Low temperature, man-made geothermal reservoirs in abandoned workings of underground mines. In *Stanford Geothermal Workshop.*

Malolepszy, Z., Demollin-Schneiders, E., & Bowers, D. (2005). Potential use of geothermal mine waters in Europe. In *Proceedings world Geothermal Congress 2005, Antalya, Turkey.*

Manju. (2014). Vertical, horizontal array or mine water source for heat pumps: Wales case studies. In *Ground source heat pump association technical seminar.* Retrieved from `https://www.gshp.org.uk/DeMontfort/Seren-Manju.pdf`

Manners, G. (1991). The future of coal-mining in britain. In P. Pearson (Ed.), *Prospects for british coal* (pp. 41–59). Palgrave Macmillan UK, London. Retrieved from `https://doi.org/10.1007/978-1-349-11508-2_3` doi: 10.1007/978-1-349-11508-2_3

Mareschal, J.-C., & Jaupart, C. (2013). Radiogenic heat production, thermal regime and evolution of continental crust. *Tectonophysics*, *609*, 524–534. Retrieved 2021-10-04, from `https://www.sciencedirect.com/science/article/pii/S004019511200769X` doi: 10.1016/j.tecto.2012.12.001

Marsily, D., & G. (1986). *Quantitative hydrogeology*. Academic Press, Inc., Orlando, FL.

McClean, A., & Pedersen, O. W. (2022). Who owns the heat? the scope for geothermal heat to contribute to net zero. *Journal of Environmental Law*, *34*(2), 343–351. Retrieved from `https://doi.org/10.1093/jel/eqab038` doi: 10.1093/jel/eqab038

Met Office. (2006). *MIDAS: UK soil temperature data. NCAS British Atmospheric Data Centre.* Retrieved from `https://catalogue.ceda.ac.uk/uuid/8dc05f6ecc6065a5d10fc7b8829589ec?jump=related-docs-anchor`

Met Office. (2019). *MIDAS open: UK soil temperature data, v201908. centre for environmental data analysis, 30 october 2019. doi:10.5285/9972bc173ef94068b2070d4b26f849a7.* Retrieved from `http://dx.doi.org/10.5285/9972bc173ef94068b2070d4b26f849a7`

Miao, X., Cui, X., Xu, J., et al. (2011). The height of fractured water-conducting zone in undermined rock strata. *Engineering Geology*, *120*(1-4), 32–39.

Mihalakakou, G., Santamouris, M., Lewis, J., & Asimakopoulos, D. (1996). On the application of the energy balance equation to predicted ground temperature profiles. *Pergamon*.

Minett, S. T. (1987). *The hydrogeology of parts of the Northumberland and Durham Coalfield related to opencast mining operations* (Unpublished doctoral dissertation). University of Newcastle upon Tyne.

Monaghan, A. (2014). *The Carboniferous shales of the Midland Valley of Scotland: geology and resource estimation.* British Geological Survey for Department of Energy and Climate Change, London, UK. Retrieved from `https://assets.publishing.service.gov.uk/government/uploads/system/uploads/attachment_data/file/360472/BGS_DECC_MVS_2014_MAIN_bookLOWRES.pdf`

Monaghan, A., Dochartaigh, B., Fordyce, F. ., Loveless, S., Entwisle, D., Quinn, M., . . . Mosca, I. (2017). *UKGEOS - Glasgow Geothermal Energy Research Field Site (GGERFS): Initial summary of the geological platform* (Open Report No. OR/17/006). British Geological Survey.

Monaghan, A., & Parrish, R. (2006). Geochronology of Carboniferous–Permian magmatism in the Midland Valley of Scotland: implications for regional tectonomagmatic evolution and the numerical time scale. *Journal of the Geological Society*, *163*(1), 15–28. Retrieved from `http://jgs.lyellcollection.org/lookup/doi/10.1144/0016-764904-142` doi: 10.1144/0016-764904-142

Monaghan, A. A., Starcher, V., Barron, H. F., Shorter, K., Walker-Verkuil, K., Elsome, J., . . . Callaghan, E. (2021). Drilling into mines for heat: geological synthesis of the UK Geoenergy Observatory in Glasgow and implications for mine water heat resources. *Quarterly Journal of Engineering Geology and Hydrogeology*, *55*(1). Retrieved 2024-02-05, from `https://doi.org/10.1144/qjegh2021-033` doi: 10.1144/qjegh2021-033

Morchio, S., & Fossa, M. (2019). Thermal modeling of deep borehole heat exchangers for geothermal applications in densely populated urban areas. *Thermal Science and Engineering Progress*, *13*. Retrieved from `https://www.sciencedirect.com/science/article/pii/S2451904919301544` doi: 10.1016/j.tsep.2019.100363

Morley, E. (2022). Research reveals average number of hours brits leave the heating on. *Landlordnews (online)*. Retrieved from `https://www.landlordnews.co.uk/average-number-of-hours-brits-leave-the-heating-on/`

Mucho, T. P., Diamond, W. P., Garcia, F., Byars, J., & Cario, S. (2000). Implications of recent NIOSH tracer gas studies on bleeder and gob gas ventilation design. In *The Society of Mining Engineers Annual Meeting, Feb. 28-mar. 1, Salt Lake City, UT.* Retrieved from `https://www.semanticscholar.org/paper/Implications-Of-Recent-NIOSH-Tracer-Gas-Studies-On-Mucho-Diamond/c968a6c386dfc0cd683005d0994ce1020cdeb8c5`

Murchison, D. G., & Raymond, A. C. (1989). Igneous activity and organic maturation in the Midland Valley of Scotland. *International Journal of Coal Geology*, *14*(1), 47–82. Retrieved from `https://www.sciencedirect.com/science/article/pii/0166516289900785` doi: 10.1016/0166-5162(89)90078-5

Neumann, E.-R., Wilson, M., Heeremans, M., Spencer, E. A., Obst, K., Timmerman, M. J., & Kirstein, L. (2004). Carboniferous-Permian rifting and magmatism in southern Scandinavia, the North Sea and northern Germany: a review. *Geological Society, London, Special Publications*, *223*(1), 11–40. Retrieved from `https://sp.lyellcollection.org/content/223/1/11` doi: 10.1144/GSL.SP.2004.223.01.02

Ngoyo Mandemvo, D. D., Comeau, F.-A., Raymond, J., Grasby, S. E., & Terlaky, V. (2023). Geothermal Potential of Closed Underground Mines: Resource Assessment Study of the Con Mine, Northwest Territories, Canada. *Natural Resources Research*, *32*, 1579–1593. Retrieved from `https://ui.adsabs.harvard.edu/abs/2023NRR....32.1579N` doi: 10.1007/s11053-023-10214-3

Now, L. (2021). How much power (watts) does a solar panel produce? *Lumen Now (online)*.

Nuttall, C., Adams, R., & Younger, P. (2002). Integrated hydraulic-hydrogeochemical assessment of flooded deep mine voids by test pumping at the Deerplay (Lancashire) and Frances (Fife) collieries. In *Mine Water Hydrogeology and Geochemistry* (Younger & Robins ed., Vol. 198, pp. 315–326). Geological Society, London, Special Publications.

Nuttall, C. A., & Younger, P. L. (2004). Hydrochemical stratification in flooded underground mines: an overlooked pitfall. *Journal of Contaminant Hydrology*, *69*(1), 101–114. Retrieved from `https://www.sciencedirect.com/science/article/pii/S0169772203001529` doi: 10.1016/S0169-7722(03)00152-9

O Dochartaigh, B. (2009). *A scoping study into shallow thermogeological resources beneath Glasgow and the surrounding area.* [Internal Report IR/09/024]. British Geological Survey.

O Dochartaigh, B., E, MacDonald, A., M, Fitzsimons, V., & Ward, R. (2015). *Scotland's aquifers and groundwater bodies* [Report OR/15/028]. British Geological Survey.

O Dochartaigh, B. E., Smedley, P. L., MacDonald, A. M., Darling, W. G., & Homoncik, S. (2011). *Baseline scotland: groundwater chemistry of the Carboniferous sedimentary aquifers of the Midland Valley* [Report]. British Geological Survey. Retrieved from `http://www.bgs.ac.uk`

Ogata, A., & Banks, R. (1961). A solution of the differential equation of longitudinal dispersion in porous media. *Geological Survey Professional Paper*.

Ons.gov.uk. (2020). *One in eight british households has no garden.* Retrieved from `https://www.ons.gov.uk/economy/environmentalaccounts/articles/oneineightbritishhouseholdshasnogarden/2020-05-14`

Ordóñez, A., Jardón, S., Álvarez, R., Andrés, C., & Pendás, F. (2012). Hydrogeological definition and applicability of abandoned coal mines as water reservoirs. *Journal of Environmental Monitoring*, *14*(8), 2127. Retrieved from `http://xlink.rsc.org/?DOI=c2em11036a` doi: 10.1039/c2em11036a

Osimobi, J. C., Avwiri, G. O., & Agbalagba, E. O. (2018). Radiometric and radiogenic heat evaluation of natural radioactivity in soil around solid minerals mining environment in south-eastern nigeria. *Environmental Processes*, *5*(4), 859–877. Retrieved from `http://link.springer.com/10.1007/s40710-018-0336-1` doi: 10.1007/s40710-018-0336-1

Ovalle-Villamil, W., & Sasanakul, I. (2019). Investigation of Non-Darcy flow for fine grained materials. *Geotechnical and Geological Engineering*, *37*(1), 413–429. Retrieved from `https://doi.org/10.1007/s10706-018-0620-x` doi: 10.1007/s10706-018-0620-x

Oxburgh, E. (1982). *Compilation of heat flow data measured by the oxford university heat flow group under contract to the department of energy.* Unpublished document submitted to J D Garnish, ETSU, Harwell.

O'Neill, H. S. (2016). Heat-producing elements (HPEs). In P. Bobrowsky & B. Marker (Eds.), *Encyclopedia of Engineering Geology* (pp. 1–6). Springer International Publishing. Retrieved from `http://link.springer.com/10.1007/978-3-319-39193-9_265-1` doi: 10.1007/978-3-319-39193-9_265-1

Piotrowska-Woroniak, J. (2021). Assessment of ground regeneration around borehole heat exchangers between heating seasons in cold climates: A case study in bialystok (NE Poland). *Energies*, *14*(16). Retrieved from `https://www.mdpi.com/1996-1073/14/16/4793` doi: 10.3390/en14164793

Pollack, H. N., & Chapman, D. S. (1977). On the regional variation of heat flow, geotherms, and lithospheric thickness. *Tectonophysics*, *38*(3), 279–296. Retrieved from `https://www.sciencedirect.com/science/article/pii/0040195177902153` doi: 10.1016/0040-1951(77)90215-3

Pruess, K., & Bodvarsson, G. (1984). Thermal Effects of Reinjection in Geothermal Reservoirs With Major Vertical Fractures. *Journal of Petroleum Technology*, *36*(09), 1567-1578. Retrieved from `https://doi.org/10.2118/12099-PA` doi: 10.2118/12099-PA

Rapp, B. E. (2017). *Chapter 9 - fluids* (B. E. Rapp, Ed.). Elsevier. Retrieved from `https://www.sciencedirect.com/science/article/pii/B9781455731411500095` doi: 10.1016/B978-1-4557-3141-1.50009-5

Raymond, J. (2018). Colloquium 2016: Assessment of subsurface thermal conductivity for geothermal applications. *Canadian Geotechnical Journal*, *55*(9), 1209–1229. Retrieved from `http://www.nrcresearchpress.com/doi/10.1139/cgj-2017-0447` doi: 10.1139/cgj-2017-0447

Raymond, J., Comeau, F., Malo, M., & Blessent, D. (2017). The geothermal open laboratory: a free space to measure thermal and hydraulic properties of geological materials. In *IGCP636 2017 Annual Meeting.*

Raymond, J., Sirois, C., Nasr, M., & Malo, M. (2017). Evaluating the geothermal heat pump potential from a thermostratigraphic assessment of rock samples in the st. lawrence lowlands, canada. *Environmental Earth Sciences*, *76*, 83. doi: 10.1007/s12665-017-6398-y

Raymond, J., & Therrien, R. (2008). Low-temperature geothermal potential of the flooded Gaspé Mines, Québec, Canada. *Geothermics*, *37*(2), 189–210. Retrieved from `https://linkinghub.elsevier.com/retrieve/pii/S0375650507000818` doi: 10.1016/j.geothermics.2007.10.001

Raymond, J., & Therrien, R. (2010). Geothermal energy and mines. *Geothermics*, *5*, Environmental Society of The Canadian Institute of Mining.

Read, W., Browne, M., & Stephenson, B. (2002). The geology of scotland. *Geological Society*, 251–300.

Rees, S. J. (2016). Chapter 1 - an introduction to ground-source heat pump technology. In S. J. Rees (Ed.), *Advances in ground-source heat pump systems* (pp. 1–25). Woodhead Publishing. Retrieved from `https://www.sciencedirect.com/science/article/pii/B9780081003114000017` doi: 10.1016/B978-0-08-100311-4.00001-7

Reilly, T. E., & Harbaugh, A. W. (2004). Guidelines for evaluating ground-water flow models. *Scientific Investigations Report*. Retrieved from `https://pubs.usgs.gov/publication/sir20045038` (Number: 2004-5038) doi: 10.3133/sir20045038

Renz, A., Rühaak, W., Schätzl, P., & Diersch, H.-J. G. (2009). Numerical modeling of geothermal use of mine water: Challenges and examples. *Mine Water and the Environment*, *28*(1), 2–14. Retrieved from `http://link.springer.com/10.1007/s10230-008-0063-3` doi: 10.1007/s10230-008-0063-3

Richardson, S. W., & Oxburgh, E. R. (1979). The heat flow field in mainland UK. *Nature*, *282*(5739), 565–567. Retrieved from `http://www.nature.com/articles/282565a0` doi: 10.1038/282565a0

Rippon, J., Read, W., & Park, R. (1996). *The ochil fault and the kincardine basin: key structures in the tectonic evolution of the midland valley of scotland* (Vol. 153) (No. 4). Retrieved from `http://jgs.lyellcollection.org/lookup/doi/10.1144/gsjgs.153.4.0573` doi: 10.1144/gsjgs.153.4.0573

Rippon, J. H. (2002). *Coal.* The Geological Society London. Retrieved from `https://pubs.geoscienceworld.org/gsl/books/book/1524/chapter/107228653/Coal` doi: 10.1144/GOS4P.17

Rivera, J. A., Blum, P., & Bayer, P. (2015a). Analytical simulation of groundwater flow and land surface effects on thermal plumes of borehole heat exchangers. *Applied Energy*, *146*, 421–433. Retrieved from `https://linkinghub.elsevier.com/retrieve/pii/S0306261915002123` doi: 10.1016/j.apenergy.2015.02.035

Rivera, J. A., Blum, P., & Bayer, P. (2015b). Ground energy balance for borehole heat exchangers: Vertical fluxes, groundwater and storage. *Renewable Energy*, *83*, 1341–1351. Retrieved from `https://linkinghub.elsevier.com/retrieve/pii/S0960148115300148` doi: 10.1016/j.renene.2015.05.051

Rivera, J. A., Blum, P., & Bayer, P. (2016). A finite line source model with Cauchy-type top boundary conditions for simulating near surface effects on borehole heat exchangers. *Energy*, *98*, 50–63. Retrieved from `https://www.sciencedirect.com/science/article/pii/S0360544215017740` doi: 10.1016/j.energy.2015.12.129

Rivera, J. A., Blum, P., & Bayer, P. (2017). Increased ground temperatures in urban areas: Estimation of the technical geothermal potential. *Renewable Energy*, *103*, 388–400. Retrieved from `https://www.sciencedirect.com/science/article/pii/S0960148116309673` doi: 10.1016/j.renene.2016.11.005

Robertson, E. (1988). *Thermal properties of rocks.*

Robins, N. (1990). *Hydrogeology of Scotland.* [Report]. British Geological Survey.

Robins, N., Davies, J., & Dumpleton, S. (2008). Groundwater flow in the South Wales coalfield: historical data informing 3D modelling. *Quarterly Journal of Engineering Geology and Hydrogeology*, *41*(4), 477–486. Retrieved from `https://doi.org/10.1144/1470-9236/07-055` doi: 10.1144/1470-9236/07-055

Robinson, E., Blyth, E., Clark, D., Comyn-Platt, E., Finch, J., & Rudd, A. (2016). Climate hydrology and ecology research support system potential evapotranspiration dataset for great britain (1961-2015). *NERC Environmental Information Data Centre. [CHESS-PE].* Retrieved from `https://doi.org/10.5285/8baf805d-39ce-4dac-b224-c926ada353b7`

Robinson, E., Blyth, E., Clark, D., Comyn-Platt, E., Finch, J., & Rudd, A. (2017). Climate hydrology and ecology research support system meteorology dataset for Great Britain (1961-2015). *NERC Environmental Information Data Centre. [CHESS-met] v1.2*. Retrieved from .`https://doi.org/10.5285/b745e7b1-626c-4ccc-ac27-56582e77b900`

Rodríguez, R., & Díaz, M. B. (2009). Analysis of the utilization of mine galleries as geothermal heat exchangers by means a semi-empirical prediction method. *Renewable Energy*, *34*(7), 1716–1725. Retrieved from `https://linkinghub.elsevier.com/retrieve/pii/S096014810900007X` doi: 10.1016/j.renene.2008.12.036

Rollin, K. (1982). *A review of data relating to hot dry rock and selection of targets for detailed study. book in series: Investigation of the geothermal potential of the UK.* British Geological Survey.

Rollin, K. E. (1987). *Catalogue of geothermal data for the land area of the United Kingdom. third revision: April 1987. investigation of the geothermal potential of the UK.* British Geological Survey. Retrieved from `https://www.osti.gov/etdeweb/biblio/6705656`

Roy, U., & Roy, P. K. (2020). *Chapter 7 - advances in heat intensification techniques in shell and tube heat exchanger* (L. Pekař, Ed.). Academic Press. Retrieved from `https://www.sciencedirect.com/science/article/pii/B9780128194225000074` doi: 10.1016/B978-0-12-819422-5.00007-4

Ryan, A., & Euler, D. S. (2017). Heat stress management in underground mines. *International Journal of Mining Science and Technology*, *27*(4), 651–655. Retrieved from `https://www.sciencedirect.com/science/article/pii/S2095268617303580` doi: 10.1016/j.ijmst.2017.05.020

Rybach, K., Hokrick, L., & Eugester, W. (1988). Vertical earth heat probe measurements and prospects in switzerland. *Communication and Proceedings*, 67–372.

Rybach, L. (1976). Radioactive heat production in rocks and its relation to other petrophysical parameters. *Thermal and Radioactive Properties*, *114*, 309–317.

Rybach, L. (2002). Design and performace of borehole heat exchange heat pump systems. *Twenty-Seventh Workshop on Geothermal Reservoir Engineering*, 9.

Rybach, L., & Eugster, W. J. (2010). Sustainability aspects of geothermal heat pump operation, with experience from switzerland. *Geothermics*, *39*(4), 365 – 369. Retrieved from `http://www.sciencedirect.com/science/article/pii/S0375650510000441` doi: https://doi.org/10.1016/j.geothermics.2010.08.002

Rybach, L., Megel, T., & Eugster, W. (2000). At what scale are geothermal resources renewable ? In *Proceedings world Geothermal Congress 2000, Tohoku, Japan* (pp. 867–872).

Saadi, M. S., & Gomri, R. (2017). Investigation of dynamic heat transfer process through coaxial heat exchangers in the ground. *International Journal of Hydrogen Energy*, *42*(28), 18014–18027. Retrieved from `https://linkinghub.elsevier.com/retrieve/pii/S0360319917310510` doi: 10.1016/j.ijhydene.2017.03.106

Sams, M. S., & Thomas-Betts, A. (1988). 3D numerical modelling of the conductive heat flow of SW england. *Geophysical Journal International*, *92*(2), 323–334. Retrieved from `https://doi.org/10.1111/j.1365-246X.1988.tb01143.x` doi: 10.1111/j.1365-246X.1988.tb01143.x

Sandiford, M., & McLaren, S. (2006). Thermo-mechanical controls on heat production distributions and the long-term evolution of the continents. *Cambridge University Press.* Retrieved from `https://www.semanticscholar.org/paper/Thermo-mechanical-controls-on-heat-production-and-Sandiford-McLaren/718ff10eec1946774a50b9ccfbd158fe2e0fb95d`

Schulte, D. O., Welsch, B., Boockmeyer, A., Rühaak, W., Bär, K., Bauer, S., & Sass, I. (2016). Modeling insulated borehole heat exchangers. *Environmental Earth Sciences*, *75*(10), 910. Retrieved 2023-09-12, from `https://doi.org/10.1007/s12665-016-5638-x` doi: 10.1007/s12665-016-5638-x

Shen, H. H., Cheng, A. H., Wang, K.-H., Teng, M. H., & Liu, C. C. (2002). *Environmental fluid mechanics: theories and applications.* ASCE Publications.

Sherwood, J. (1997). *Modelling minewater flow and quality changes after coalfield closure.* [phdthesis]. Newcastle University.

Shuttleworth, W. J. (2012). *Terrestrial hydrometeorology.* John Wiley & Sons.

Signorelli, S., Kohl, T., & Rybach, L. (2005). Sustainability of production from Borehole Heat Exchanger fields. In *Proceedings World Geothermal Congress 2005, Antalya, Turkey.*

Singh, R., Ngah, S., & Atkins, A. (1985). Applicability of current groundwater theories for the prediction of water inflows to surface mining excavations. In *International Mine Water Association Proceedings.*

Singh, R. V. K. (2013). Spontaneous heating and fire in coal mines. *Procedia Engineering*, *62*, 78–90. doi: 10.1016/j.proeng.2013.08.046

Smedley, P. L. (1986). The relationship between calc-alkaline volcanism and within-plate continental rift volcanism: evidence from scottish palaeozoic lavas. *Earth and Planetary Science Letters*, *77*(1), 113–128. Retrieved from `https://www.sciencedirect.com/science/article/pii/0012821X86901378` doi: 10.1016/0012-821X(86)90137-8

Smith, D. C., & Elmore, A. (2018). The observed effects of changes in groundwater flow on a borehole heat exchanger of a large scale ground coupled heat pump system. *Geothermics*, *74*, 240–246. doi: 10.1016/J.GEOTHERMICS.2018.03.008

Snow, D. T. (1968). Rock fracture spacings, openings, and porosities. *Journal of the Soil Mechanics and Foundations Division*, *94*(1), 73–91. Retrieved from `https://ascelibrary.org/doi/10.1061/JSFEAQ.0001097` doi: 10.1061/JSFEAQ.0001097

Spitler, J. D., & Bernier, M. (2016). Chapter 2 - vertical borehole ground heat exchanger design methods. In S. J. Rees (Ed.), *Advances in ground-source heat pump systems* (pp. 29–61). Woodhead Publishing. Retrieved from `https://www.sciencedirect.com/science/article/pii/B9780081003114000029` doi: 10.1016/B978-0-08-100311-4.00002-9

Squires, T. (2005). Microfluidics: Fluid physics at the nanoliter scale. *Reviews of modern physics. The American Physical Society.*, *77*, 50.

Stark, C. (2019). *Net zero: The UK's contribution to stopping global warming*. Committee on Climate Change.

Stephenson, D., Loughlin, S., Millward, D., Waters, C., & Williamson, I. (2003). *Carboniferous and permian igneous rocks of great britain north of the variscan front* (Vol. 27).

Stephenson, D. J. (1979). *Rockfill in hydraulic engineering*. Elsevier.

Stone, P., Millward, D., Young, B., Merritt, J., Clarke, S., McCormac, M., & Lawrence, D. (2010). *Northern England British Regional Geology* (5th ed.). British Geological Survey. Retrieved from `https://webapps.bgs.ac.uk/Memoirs/docs/B06817.html`

Streetly, H., Buss, S., & Brown, L. (2009). *Northumbrian magnesian limestone aquifer hydrogeological conceptual model.* [Final Report 6886 R2]. ESI soil & groundwater.

Stumm, W., & Morgan, J. J. (2012). *Aquatic chemistry: Chemical equilibria and rates in natural waters*. John Wiley & Sons.

Stylianou, I. I., Florides, G., Tassou, S., Tsiolakis, E., & Christodoulides, P. (2017). Methodology for estimating the ground heat absorption rate of ground heat exchangers. *Energy*, *127*, 258–270. Retrieved from `https://linkinghub.elsevier.com/retrieve/pii/S0360544217304450` doi: 10.1016/j.energy.2017.03.070

Survey, O. (Ed.). (2021). *Scotland heat map* (OS Licence number 100024655 ed.). Scottish Government. Retrieved from `https://heatmap.data.gov.scot/custom/heatmap/`

Szczepiński, J. (2019). The significance of groundwater flow modeling study for simulation of opencast mine dewatering, flooding, and the environmental impact. *Water*, *11*(4), 848. Retrieved from `https://www.mdpi.com/2073-4441/11/4/848` doi: 10.3390/w11040848

Sáez Blázquez, C., Farfán Martín, A., Martín Nieto, I., Carrasco García, P., Sánchez Pérez, L. S., & González-Aguilera, D. (2017). Efficiency analysis of the main components of a vertical closed-loop system in a borehole heat exchanger. *Energies*, *10*(2), 201. Retrieved from `https://www.mdpi.com/1996-1073/10/2/201` doi: 10.3390/en10020201

Tamas Vekony, A. (2023). What is a ground source heat pump? *Greenmatch (online article)*. Retrieved from `https://www.greenmatch.co.uk/heat-pump/ground-source-heat-pumps-in-the-uk/ground-source-heat-pump-borehole`

Tammemagi, H. Y., & Wheildon, J. (1974). Terrestrial heat flow and heat generation in South-West England. *Geophysical Journal of the Royal Astronomical Society*, *38*(1), 83-94. doi: https://doi.org/10.1111/j.1365-246X.1974.tb04110.x

Thomas, D. J. (2017). Abandoned coal mine geothermal for future wide scale heat networks. *Fuel*, *189*, 445. Retrieved from `https://www.sciencedirect.com/science/article/pii/S0016236116310778` doi: 10.1016/j.fuel.2016.10.115

Timmerman, M. J. (2004). Timing, geodynamic setting and character of permo-carboniferous magmatism in the foreland of the variscan orogen, NW europe. *Geological Society, London, Special Publications*, *223*(1), 41–74. Retrieved from `https://sp.lyellcollection.org/content/223/1/41` doi: 10.1144/GSL.SP.2004.223.01.03

Todd, F. (2023). *Modelling the thermal, hydraulic and mechanical controlling processes on the stability of shallow mine water heat systems* (phdthesis). University of Edinburgh.

Todd, F., McDermott, C., Harris, A. F., Bond, A., & Gilfillan, S. (2019). Coupled hydraulic and mechanical model of surface uplift due to mine water rebound: implications for mine water heating and cooling schemes. *Scottish Journal of Geology*, sjg2018–028. Retrieved from `http://sjg.lyellcollection.org/lookup/doi/10.1144/sjg2018-028` doi: 10.1144/sjg2018-028

Trenberth, K. E., Fasullo, J. T., & Kiehl, J. (2009). Earth's global energy budget. *Bulletin of the American Meteorological Society*, *90*(3), 311–324. Retrieved from `https://journals.ametsoc.org/view/journals/bams/90/3/2008bams2634_1.xml` doi: 10.1175/2008BAMS2634.1

Trillat-Berdal, V., Souyri, B., & Achard, G. (2007). Coupling of geothermal heat pumps with thermal solar collectors. *Applied Thermal Engineering*, *27*(10), 1750–1755. Retrieved from `https://linkinghub.elsevier.com/retrieve/pii/S1359431106002559` doi: 10.1016/j.applthermaleng.2006.07.022

Tsagarakis, K. P. (2020). Shallow geothermal energy under the microscope: Social, economic, and institutional aspects (K. P. Tsagarakis, Trans.). *Renewable energy*, *v. 147*, pp. 2801–2808. doi: 10.1016/j.renene.2019.01.004

Turner, G. (2012). Water and gas emissions from disused mines. *Nottinghamshire County Council, Report to Communities and the Environment Standing Committee*.

Uhlík, J., & Baier, J. (2012). Model evaluation of thermal energy potential of hydrogeological structures with flooded mines. *Mine Water and the Environment*, *31*(3), 179.

Underhill, J., Monaghan, A., & Browne, M. (2008). Controls on structural styles, basin development and petroleum prospectivity in the midland valley of scotland. *Marine and Petroleum Geology*, *25*(10), 1000–1022. Retrieved from `https://linkinghub.elsevier.com/retrieve/pii/S0264817208000044` doi: 10.1016/j.marpetgeo.2007.12.002

Upton, B., Stephenson, D., Smedley, P., Wallis, S., & Fitton, J. (2004). Carboniferous and permian magmatism in scotland. *Geological Society, London, Special Publications*, *223*(1), 195–218. Retrieved from `http://sp.lyellcollection.org/lookup/doi/10.1144/GSL.SP.2004.223.01.09` doi: 10.1144/GSL.SP.2004.223.01.09

VDI. (2012). *Thermische nutzung des untergrundes (guideline for thermal use of the underground)*. Verein Deutscher Ingenieure (VDI) - Gesellschaft Energietechnik.

Verhoeven, R., Willems, E., Harcouët-Menou, V., De Boever, E., Hiddes, L., Op't Veld, P., & Demollin, E. (2014). Minewater 2.0 project in heerlen the netherlands: transformation of a geothermal mine water pilot project into a full scale hybrid sustainable energy infrastructure for heating and cooling. *Energy Procedia*, *46*, 58–67.

Vervoort, A. (1988). Influence of longwall support on the occurrence of roof cavities. *International Journal of Mining and Geological Engineering*, *6*(4), 313–326. Retrieved from `https://doi.org/10.1007/BF00880929` doi: 10.1007/BF00880929

Vienken, T., Schelenz, S., Rink, K., & Dietrich, P. (2015). Sustainable intensive thermal use of the shallow subsurface—a critical view on the status quo. *Groundwater*, *53*(3), 356–361. Retrieved from `https://ngwa.booklibrary.wiley.com/doi/abs/10.1111/gwat.12206` doi: 10.1111/gwat.12206

Villasenor, E. B. (2019). *Conceptual and numerical modelling of mine water rebound in the team valley, gateshead* (Unpublished doctoral dissertation). Newcastle University.

Vilà, M., Fernández, M., & Jiménez-Munt, I. (2010). Radiogenic heat production variability of some common lithological groups and its significance to lithospheric thermal modeling. *Tectonophysics*, *490*(3), 152–164. Retrieved from `https://www.sciencedirect.com/science/article/pii/S0040195110002064` doi: 10.1016/j.tecto.2010.05.003

Vincent, C., Rowley, W., & Monaghan, A. (2010). Thermal and burial history modelling in the midlothian-leven syncline in the midland valley of scotland using BasinMod and HotPot. *Scottish Journal of Geology*, *46*(2), 125–142. Retrieved from `http://sjg.lyellcollection.org/lookup/doi/10.1144/0036-9276/01-376` doi: 10.1144/0036-9276/01-376

Vélez Márquez, M. I., Blessent, D., Córdoba, S., López-Sánchez, J., Raymond, J., & Parra-Palacio, E. (2018). Geothermal potential assessment of the nevado del ruiz volcano based on rock thermal conductivity measurements and numerical modeling of heat transfer. *Journal of South American Earth Sciences*, *81*, 153–164. Retrieved from `https://linkinghub.elsevier.com/retrieve/pii/S0895981117301785` doi: 10.1016/j.jsames.2017.11.011

Walch, A., Mohajeri, N., Gudmundsson, A., & Scartezzini, J.-L. (2021). Quantifying the technical geothermal potential from shallow borehole heat exchangers at regional scale. *Renewable Energy*, *165*, 369–380. Retrieved from `https://www.sciencedirect.com/science/article/pii/S0960148120317602` doi: 10.1016/j.renene.2020.11.019

Wang, H., Qi, C., Du, H., & Gu, J. (2009). Thermal performance of borehole heat exchanger under groundwater flow: A case study from baoding. *Energy and Buildings*, *41*(12), 1368–1373. Retrieved from `https://www.sciencedirect.com/science/article/pii/S0378778809001820` doi: 10.1016/j.enbuild.2009.08.001

Wang, H., Qi, C., Du, H., & Gu, J. (2010). Improved method and case study of thermal response test for borehole heat exchangers of ground source heat pump system. *Renewable Energy*, *35*(3), 727–733. Retrieved from `https://www.sciencedirect.com/science/article/pii/S0960148109003516` doi: 10.1016/j.renene.2009.08.013

Wang, H., Yang, B., Xie, J., & Qi, C. (2013). Thermal performance of borehole heat exchangers in different aquifers: a case study from shouguang. *International Journal of Low-Carbon Technologies*, *8*(4), 253–259. Retrieved from `https://academic.oup.com/ijlct/article-lookup/doi/10.1093/ijlct/cts043` doi: 10.1093/ijlct/cts043

Wang, L., Cardenas, M. B., Wang, T., Zhou, J.-Q., Zheng, L., Chen, Y.-F., & Chen, X. (2022). The effect of permeability on Darcy-to-Forchheimer flow transition. *Journal of Hydrology*, *610*, 127836. Retrieved from `https://www.sciencedirect.com/science/article/pii/S0022169422004115` doi: 10.1016/j.jhydrol.2022.127836

Wang, X., Wang, Y., Wang, Z., Liu, Y., Zhu, Y., & Chen, H. (2018). Simulation-based analysis of a ground source heat pump system using super-long flexible heat pipes coupled borehole heat exchanger during heating season. *Energy Conversion and Management*, *164*, 132–143. doi: 10.1016/j.enconman.2018.03.001

Waples, W. a. (2004). A review and evaluation of specific heat capacities of rocks, minerals, and subsurface fluids. part 1: Minerals and nonporous rocks. *Natural Resources Research, Vol*, *13*(2), 97–122.

Wardell, K., & Wood, J. (1966). *Ground instability problems arising from the presence of old, shallow mine workings.* Midland Soil Mechanics and Foundation Engineering Society.

Watanabe, N., Zehner, B., Wang, W., Mcdermott, C. I., Taniguchi, T., & Kolditz, O. (2011). Numerical analysis and visualization of uncertainty effects in thermo-hydro-mechanical coupled processes in a hot-dry-rock geothermal reservoir. *Proceedings of ModelCARE 2009, Wuhan, China, September 2009*.

Watson, S., Westaway, R., & Burnside, N. (2020). Revaluating Glasgow's heat flow dataset to account for corrections for palaeoclimate: a case study of the Maryhill borehole. In *Proceedings World Geothermal Congress 2020, Reykjavik, Iceland.*

Watson, S. M., & Westaway, R. (2020). Borehole temperature log from the Glasgow Geothermal Energy Research Field Site: a record of past changes to ground surface temperature caused by urban development. *Scottish Journal of Geology*. Retrieved from `http://sjg.lyellcollection.org/lookup/doi/10.1144/sjg2019-033` doi: 10.1144/sjg2019-033

Watson, S. M., Westaway, R., & Burnside, N. M. (2019). Digging deeper: The influence of historical mining on Glasgow's subsurface thermal state to inform geothermal research. *Scottish Journal of Geology*, *55*(2), 107–123. Retrieved from `http://sjg.lyellcollection.org/lookup/doi/10.1144/sjg2019-012` doi: 10.1144/sjg2019-012

Watzlaf, G., & Ackman, T. (2006). Underground mine water for heating and cooling using geothermal heat pump systems. *Mine Water and the Environment*, *25*(1), 1–14. Retrieved from `https://doi.org/10.1007/s10230-006-0103-9` doi: 10.1007/s10230-006-0103-9

Westaway, R., & Younger, P. L. (2013). Accounting for palaeoclimate and topography: A rigorous approach to correction of the british geothermal dataset. *Geothermics*, *48*, 31–51. Retrieved from `https://linkinghub.elsevier.com/retrieve/pii/S0375650513000266` doi: 10.1016/j.geothermics.2013.03.009

Westaway, R., & Younger, P. L. (2016). Unravelling the relative contributions of climate change and ground disturbance to subsurface temperature perturbations: Case studies from tyneside, UK. *Geothermics*, *64*, 490–515. Retrieved from `https://linkinghub.elsevier.com/retrieve/pii/S0375650516300657` doi: 10.1016/j.geothermics.2016.06.009

Wheildon, J. (1981). *Investigation of the S.W. England thermal anomaly zone*. Commission of the European Communities. Directorate-General Information Market and Innovation. (Open Library ID: OL14934046M)

Wheildon, J., King, G., Crook, C., & Thomas-Betts, A. (1984). *The Eastern Highlands granites: heat flow, heat production and model studies. book in series: Investigation of the geothermal potential of the UK*. British Geological Survey.

Wheildon, J., & Rollin, K. (1986). *Heat flow in Geothermal Energy: the potential in the United Kingdom* [Report]. British Geological Survey.

Whitlock, C., Browne, D., & Chandler, W. (2000). NASA surface meteorology and solar energy data set for renewable energy industry use. In *Rise & Shine 2000, 26th Annual Conference of the Solar Energy Society of Canada Inc. and Solar Nova Scotia, 21 – 24 October 2000.*

Whittles, D. N., Lowndes, I. S., Kingman, S. W., Yates, C., & Jobling, S. (2006). Influence of geotechnical factors on gas flow experienced in a UK longwall coal mine panel. *International Journal of Rock Mechanics and Mining Sciences*, *43*(3), 369–387. Retrieved 2023-08-29, from `https://www.sciencedirect.com/science/article/pii/S1365160905001139` doi: 10.1016/j.ijrmms.2005.07.006

Whitworth, K. (2012). *Overview of mine water in the UK coalfields advice on mine water recovery and mine gas* (Report Control for the Coal Authority No. A031899-2). WYG Engineering.

Whitworth, K. R. (2002). The monitoring and modelling of mine water recovery in UK coalfields. In P. L. Younger & N. S. Robins (Eds.), *Mine Water Hydrogeology and Geochemistry* (Vol. 198, p. 0). Geological Society of London. Retrieved from `https://doi.org/10.1144/GSL.SP.2002.198.01.04` doi: 10.1144/GSL.SP.2002.198.01.04

Wieber, G., Stemke, M., Wonik, T., Enzmann, F., & Kersten, M. (2019). Stratification Dynamics and Geothermal Potential of a Deep Shaft in the Flooded Wolf Mine, Siegerland, Germany. *Mine Water and the Environment*, *38*. doi: 10.1007/s10230-019-00602-8

Witherspoon, P. (2000). Investigations at berkeley on fracture flow in rocks: From the parallel plate model to chaotic systems. *Geophysical Monograph Series*, *122*, 1–58. (ISBN: 9781118669662) doi: 10.1029/GM122p0001

Wolkersdorfer, C. (2008). *Water management at abandoned flooded underground mines.* Retrieved from `http://www.springer.com/dal/home/geosciences/hydrogeology?SGWID=1-40515-22-173789307-0`

Wood, B. D., He, X., & Apte, S. V. (2020). Modeling turbulent flows in porous media. *Annual Review of Fluid Mechanics*, *52*(1), 171-203. doi: 10.1146/annurev-fluid-010719-060317

WYG. (2006). *Interpretation report on the fluid conductivity/ temperature logging and discrete water sampling of the east of wear shafts.* [East of Wear Reports D900705]. White Young Green.

WYG. (2006). *Report on the options for control of mine water in the east of wear area.* White Young Green.

Yang, W., Kong, L., & Chen, Y. (2015). Numerical evaluation on the effects of soil freezing on underground temperature variations of soil around ground heat exchangers. *Applied Thermal Engineering*, *75*, 259–269. Retrieved from `https://www.sciencedirect.com/science/article/pii/S1359431114008217` doi: 10.1016/j.applthermaleng.2014.09.049

Younger, P. (2001). Mine water pollution in scotland: nature, extent and preventative strategies. *Science of The Total Environment*, *265*, 309–326.

Younger, P., & Adams, R. (1999). *Predicting mine water rebound.* doi: 10.13140/2.1.4805.5681

Younger, P., & Robins, N. (2002). Challenges in the characterization and prediction of the hydrogeology and geochemistry of mined ground. *Geological Society, London, Special Publications*, *198*(1), 1-16. Retrieved from `https://sp.lyellcollection.org/content/198/1/1` doi: 10.1144/GSL.SP.2002.198.01.01

Younger, P. L. (2016). A simple, low-cost approach to predicting the hydrogeological consequences of coalfield closure as a basis for best practice in long-term management. *International Journal of Coal Geology*, *164*, 25–34. Retrieved from `http://linkinghub.elsevier.com/retrieve/pii/S0166516216302701` doi: 10.1016/j.coal.2016.06.002

Younger, P. L., Banwart, S. A., & Hedin, R. S. (2002). *Mine Water: Hydrology, Pollution, Remediation*. Springer Netherlands.

Zanchini, E., Lazzari, S., & Priarone, A. (2012). Long-term performance of large borehole heat exchanger fields with unbalanced seasonal loads and groundwater flow. *Energy*, *38*(1), 66–77. Retrieved from `https://www.sciencedirect.com/science/article/pii/S0360544211008644` doi: 10.1016/j.energy.2011.12.038

Zhai, X. Q., Cheng, X. W., & Wang, R. Z. (2017). Heating and cooling performance of a minitype ground source heat pump system. *Applied Thermal Engineering*, *111*, 1366–1370. Retrieved from `https://www.sciencedirect.com/science/article/pii/S1359431116304227` doi: 10.1016/j.applthermaleng.2016.03.117

Zhang, C., Tu, S., Zhang, L., Bai, Q., Yuan, Y., & Wang, F. (2016). A methodology for determining the evolution law of gob permeability and its distributions in longwall coal mines. *Journal of Geophysics and Engineering*, *13*(2), 181–193. Retrieved from `https://academic.oup.com/jge/article/13/2/181-193/5113409` doi: 10.1088/1742-2132/13/2/181

Zhu, K., Bayer, P., Grathwohl, P., & Blum, P. (2015). Groundwater temperature evolution in the subsurface urban heat island of cologne, germany. *Hydrological Processes*, *29*(6), 965–978. Retrieved from `https://booklibrary.wiley.com/doi/abs/10.1002/hyp.10209` doi: 10.1002/hyp.10209

Zhu, W., Chen, L., Zhou, Z., Shen, B., & Xu, Y. (2019). Failure propagation of pillars and roof in a room and pillar mine induced by longwall mining in the lower seam. *Rock Mechanics and Rock Engineering*, *52*, 1193–1209.